



Proceedings of the 2020 session of the
13th *fib* International PhD Symposium in Civil Engineering

held in Paris, France
August 26-28, 2020.

Edited by: Fabrice Gatuingt & Jean-Michel Torrenti

© Fédération Internationale du Béton – International Federation for Structural Concrete

Every effort has been made to ensure that all published information has been reviewed by suitably qualified professionals and that all information submitted is original, has not been published previously and is not being considered for publication elsewhere. Further, the *fib* has made every effort to ensure that any and all permissions to quote from other sources has been obtained. The editor and the publisher are not responsible for the statements or opinions expressed in this publication.

fib Books of Abstracts are not able to, nor intended to, supplant individual training, responsibility or judgement of the user, or the supplier, of the information presented. Although the Scientific Committee did its best to ensure that all the information presented in this publication is accurate, no liability or responsibility of any kind, including liability for negligence, is accepted in this respect by the organization, its members, employees or agents.

All rights reserved. No part of this publication may be reproduced, modified, translated, stored in a retrieval system or transmitted in any form or by any means – electronically, mechanically, through photocopying, recording or otherwise – without prior written permission from the *fib*.

This publication is available on Internet under the following Creative Commons license
Some rights reserved



Published: <http://creativecommons.org/licenses/by-nc-nd/4.0/>

ISSN : 2617-4820

ISBN : 978-2-940643-06-6

Printed in Switzerland.

Photo of the first page:

Viaduct of the new coastal road in Reunion Island (France) courtesy of the Vinci Company

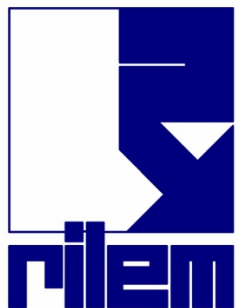
Symposium Sponsors



École Française du béton
<https://www.efbeton.com>



Association Universitaire de Génie
Civil
<https://augc.asso.fr>



International Union of
Laboratories and Experts in
Construction Materials, Systems
and Structures
<https://www.rilem.net>



Master Builders Solutions
<https://www.master-builders-solutions.com>

***fib* President's message**

Dear PhD candidates,

The *fib* is very happy about the 13th *fib* International PhD-Symposium In Civil Engineering and very pleased with the organization of Chairman Jean-Michel Torrenti and his colleagues.

The PhD Symposia are very pleasant events, with clever young researchers meeting socially and sharing experiences. Unfortunately, it is not possible to meet in person this year.

The PhD Symposia were initiated in 1996 by *fib* Honorary President György Balázs, who saw the value of such events.

Now it is your turn to benefit from presenting your own work and enjoy the work of others. You can take the opportunity to perfect your presentation technique but remember that no one knows your material better than yourself. And it is difficult to present complicated topics you know so well to others, who are experts but not in your field. Communication will be important in your whole career.

Best of luck, and make sure to seize this opportunity.

Tor Ole Olsen

President of the International Federation for Structural Concrete (*fib*)

Preface

A long-standing tradition of the *fib*, the PhD Symposia started in 1996. They were established by Prof. Balázs in Budapest to support young researchers and practitioners. Since then, the *fib* National Groups have already organised twelve symposia. The PhD symposia have become highly-recognised events, boasting the participation of international experts attending the symposia as PhD students' supervisors or keynote speakers. A two-year interval between each symposium allows for a thorough preparation of the event and for a sufficient amount of new information. The spirit of these symposia is to allow for a relaxed and friendly atmosphere, which befits the young generation.

The 13th *fib* Symposium was to be held in Paris, following the previous symposium in Prague in 2018. But 2020 was a very special year, and we have to deal with a world pandemic. Due to this unfortunate event, we decided to split the symposium into two parts. In 2020 (26 to 28 August), we have an online symposium dedicated to the students that are defending their PhD this year. In 2021 (21 to 23 July), we hope we will be able to organise a more traditional PhD symposium in Paris with the students that will finish their PhD later. The online symposium will be a new experience, and we will learn from its organisation for future *fib* events.

Two organisations are involved in the preparation of these events: The University Gustave Eiffel and the École normale supérieure Paris-Saclay, with the support of the French association of civil engineering (AFGC - representing the national *fib* group) and the University - Association of Civil Engineering (AUGC) and, of course, of the *fib*.

After a classic review process, the 40 selected papers for 2020 are divided into four themes for the oral presentations with two parallel sessions over three days. Thirty minutes are allowed for each presentation in order to have the opportunity for a long discussion, which is a part of the spirit of these PhD symposia. The best papers will be rewarded by our sponsors (BASF-Masterbuilders and EFB-école française du béton) and by the *fib*. It is a great pleasure for us to express our gratitude to all the sponsors who contributed to the organisation of the symposium.

For 2020, a keynote enriches the program. Bernard Mathieu (<https://www.hop3.eu/experts/bernard-mathieu>) will present his views about the existential challenge of concrete in a carbon-neutral economy. This topic is very important, especially for young researchers, who will certainly be involved in this challenge.

The social programme usually is very important in the PhD symposium for networking between young participants. It is not possible this year, and we will do our best for the second part of the symposium in 2021

Finally, let us wish to all participants – especially PhD students – an interesting event. We hope that this Symposium will help them to progress in scientific work and perhaps also in the *fib* activities.

Jean Michel Torrenti, University Gustave Eiffel & Fabrice Gatuingt, École normale supérieure Paris-Saclay.

Scientific committee

Sofiane Amziane - Chair

Maria Aiello, Karim Aït-Mokhtar, Pedro de Oliveira Almeida, György Balázs, José Bastien, Beatrice Belletti, Konrad Bergmeister, Hans-Dieter Beushausen, Francesco Biasioli, Stéphanie Bonnet, Mikael Braestrup, Abraham Corriols, Edoardo Cosenza, Manfred Curbach, Radim Čajka, Avraham Dancygier, Frank Dehn, Wit Derkowski, Vyacheslav Falikman, Michael Fardis, David Fernández-Ordóñez, Stephen Foster, Hans-Rudolf Ganz, Fabrice Gatuingt, Elhem Ghorbel, Petr Hájek, Steinar Helland, Nico Herrmann, Sung Gul Hong, Dick Hordijk, Gintaris Kaklauskas, Milan Kalný, Akio Kasuga, Alena Kohoutková, Lidia La Mendola, Ahmed Loukili, Xilin Lu, Koichi Maekawa, Yann Malecot, Riadh Al-Mahaidi, Giuseppe Mancini, Antonio Marí, Alberto Meda, Aurelio Muttoni, Harald Müller, Takafumi Noguchi, Albert Noumowe, Tor Ole Olsen, Alessandro Palermo, Peter Paulík, Marisa Pecce, Hugo Corres Peiretti, Carlo Pellegrino, Arnaud Perrot, Giovanni Plizzari, Marco di Prisco, Radomír Pukl, Sébastien Remond, Paolo Riva, Anna Saetta, Koji Sakai, Marco Savoia, Johan Silfwerbrand, Alfred Strauss, Fernando Stucchi, Luc Taerwe, Jean-Michel Torrenti, François Toutlemonde, Lucie Vandewalle, Jan Vitek, Sherif Yehia, Yamei Zhang, Bin Zhao

Organizing committee

Jean Michel Torrenti – Chair

Fabrice Gatuingt
Farid Benboudjema
Jean Luc Clément
Olivier Plé
Jean-Philippe Sellin

Table of contents

Disclaimer	I
Sponsors	II
fib President message	II
Preface	IV
Scientific committee	V
Organizing committee	VI
Innovation in materials and structures	1
Application of bonding concrete to reinforcement using adhesives in steel-concrete composite structures, Horb Oleksandr [et al.]	2
Development of new-generation, biodegradable board thermal insulation, Csanády Dániel [et al.]	10
Drying shrinkage and mechanical properties of concrete based on Corbicula shells, from river sediments, as coarse aggregates, Beddaa Hamza [et al.]	18
Effects of using polypropylene and steel fibres on Ultra High Performance Concrete subjected to elevated temperatures, Seyam Ahmed [et al.]	25

Experimental and numerical investigation of bond behaviour of synthetic macro-fibre in concrete, Garnevičius Mantas [et al.]	33
Experimental investigation of reinforcement strategies for concrete extrusion 3D printed beams, Gebhard Lukas [et al.]	40
Influence of constant hygric stress on the load-bearing behaviour of high-performance solid absorber made of high-strength fibre concrete, Kiesche Martin [et al.]	48
Influence of matrix properties and embedded length on the pull-out behaviour of yarns in cement/calcareous filler matrices, Slama Anne-Claire [et al.]	55
Influence of the sizes and the loading platform form on the strength of concrete elements at local compression, Kuznietsova Iryna [et al.]	63
Load-deformation behaviour of concrete tension ties with weft-knitted textile reinforcement, Lee Minu [et al.]	70
Mechanical and mineralogical characteristics of mortars with crushed and river sand, Elat Emmanuel [et al.]	78
Numerical study on the micro-mechanical behaviour of artificial granular materials, Benmebarek Mohamed Amine [et al.]	86
Residual stiffness analysis of flexural concrete elements with composite reinforcement systems, Sultani Haji Akbar [et al.]	94
Sealing of service penetrations in timber buildings with the method wood in wood, Scherer Thomas [et al.]	102
The Applicability of Superabsorbent Polymer as a Protective Carrier in the Bio-based Self-healing Concrete, Schreiberova Hana [et al.]	110
Wood Ashes from Electrostatic Filter as a Replacement for the Fly Ashes in Concrete, Lazik Piotr-Robert [et al.]	118

Structural analysis and design **125**

Advanced analysis on the behavior of a structure in reinforced concret frames with the height regime P + 8E - Comparative study between the variant of monolithic and prefabricated structures -, Hausi Sorin Bogdan [et al.]	126
Bond behavior between high-strength concrete and steel reinforcement under high cycle fatigue push-in loading, Spartali Homam [et al.]	134

Characterization of the anisotropic tensile response of UHPFRC, Valente Rui [et al.]	142
Dimensioning Approach of Partially Prestressed Concrete Beams: Optimization of Simply Supported Beams, Nadim Abdel Nour	149
Effects of unidirectional tensile stresses on punching shear of RC slabs, Fernandez Pablo [et al.]	157
Experimental Study on Flexural Behavior of Concrete Girders Prestressed with Stainless Steel Strands, Al-Kaimakchi Anwer [et al.]	165
Experimental and numerical studies of nodes of light steel-reinforced concrete structures, Hasenko Anton [et al.]	173
General method of structural analysis of reinforced concrete columns under axial load an biaxial bending, Barylyak Bogdan [et al.]	179
Impact of Modulus of Elasticity on Deflections of Concrete Structures, Vasatko Radek	187
Masonry strengthening under the combined action of vertical and horizontal forces, Usenko Dmytro [et al.]	193
Model uncertainty quantification for column removal scenario calculations using the energy-based method, Ding Luchuan [et al.]	200
Numerical Plastic Analysis of Non-Prismatic Reinforced Concrete Beams Strengthened by Carbon Fiber Reinforced Polymers, Ibrahim Sarah Khaleel [et al.]	208
Punching shear at edge flat slab-column connections, Abu-Salma Deema [et al.]	216
Simplification of the procedure for determining the fire resistance of heat insulating brickwork, Kruse Heiner [et al.]	224
The change of stress-strain state in biaxial bended reinforced concrete -section beams depending on the load, Prykhodko Yuliia [et al.]	230
Durability and life assessment	237
Accelerated carbonation of recycled concrete aggregates, Sereng Marie [et al.]	238
Experimental study of the concrete creep potential that is already damaged by Alkali Aggregates Reactions (AAR) in a new finite elements approach, Lacombe Clement [et al.]	246

Fracture mechanics parameters in assessment of high strength concrete's frost degradation, Borowska Sylwia [et al.]	254
Leaching of concrete : a comparison of performance indicators, Gauthier - Pouyane Aliénor [et al.]	263
Numerical Modelling for Reactive Transport due to the Water-dependent Activities within Building Materials, Xiong Qingxiang [et al.]	271
Numerical investigations on the influence of concrete cover on bond behavior of reinforcement in concrete after fire, Das Arunita [et al.]	279
Monitoring and structural assessment	287
A new assessment methodology for fair-faced concrete surfaces based on digital image processing, Ajtayné Károlyfi Kitti [et al.]	288
Carbon-fibred mortar: Effect of sand content and grain size distribution on electrical properties, Allam Hamza [et al.]	296
Transmission length test for prestressing cable after loss of mechanical anchorage, Walczak Rafał	304
Validation of a numerical model for singly reinforced corroded concrete beams, Nasser Hussein [et al.]	312
Author Index	320
Previous fib International PhD Symposia	323

Innovation in materials and structures

Application of bonding concrete to reinforcement using adhesives in steel concrete composite structure

Oleksandr Horb, Yurii Davydenko, Oleksandr Shkurupii, Pavlo Mytrofanov

*Name of Institute,
National University «Yuri Kondratyuk Poltava Polytechnic»,
Pershotravnevyj Ave. 24, Poltava (36011), Ukraine*

Abstract

The article contains information about the application in building practice of the method of bonding liquid concrete mixture to the external and internal reinforcement in the form of profiled and sheet steel to ensure the joint work of steel and concrete in the bearing structures. An algorithm for the investigated structures calculations taking into account the physical and mechanical adhesive joint properties was considered. The results of the experiments are compared with the theoretical calculations. The possibility of applying the proposed ensuring the joint steel and concrete work method in the manufacture of real building structures bearing elements was proved.

1 Problem statement

Among the latest achievements in the field of construction the leading place is occupied by development of progressive constructive elements based on the rational combination of steel and concrete in complex structures. All research aimed at reducing material costs, reducing the complexity of basic technological processes and the total cost of the final product.

To a large extent, the tasks can be solved by the wider use of steel-concrete composite structures (SCCS), in which steel reinforcement in the form of sheets, profiled flooring, rolling elements, rectangular or cylindrical closed profiles and conventional rods works more efficiently with the concrete component due to their intended use in relevant areas.

However, developers of composite structures face the problem of ensuring the joint work of concrete and steel. In such cases, traditional anchors are often used, which are too expensive and time consuming. Acrylic adhesives are increasingly being used in construction to solve this problem. The connection of ready-made concrete blocks to each other and metal plates to concrete elements was investigated by means of joining acrylic glues of different compositions. But still not enough research structures in which freshly laid concrete mix is glued to steel elements.

Today, among SCCS, one of the most researched and most common are compressed reinforced concrete elements reinforced with steel sheets, I-beams with side cavities filled with concrete and reinforced concrete slabs on profiled flooring. In these structures the problem of joint work of steel and concrete is relevant, because the cost of complex anchors (including the cost of material and installation) can reach 20% of the total cost.

Thus, the study of strength, deformability and load-bearing capacity of reinforced concrete elements while ensuring the joint work of their components with acrylic glue, developing methods for their calculation is the actual problem.

2 Analysis of recent research and publications

Modern scientific trends demonstrate the increasing interest of researchers in the use of polymer multicomponent materials in construction. In Ukraine, the main centers of such research are the leading universities of Kharkov, Kyiv and Poltava. They proved that it is optimal to use multicomponent acrylic glue to ensure the joint work of concrete and steel in load-bearing elements [1]–[4]. It is simple and reliable to manufacture, has high durability, low viscosity, which does not depend on ambient temperature, and fits well. Compared to this glue, even modern anchors are much more expensive and material-intensive, and their installation is more time consuming and requires the use of special equipment. Based on the experience of previous foreign scientists research [5]–[10], it was decided in traditional steel-concrete structures for the connection of steel and concrete used instead of the usual anchoring of joints based on acrylic adhesives.

To determine the strength and deformation of multilayer elements, the theory of composite rods was adapted, which allows to take into account the physical and mechanical characteristics of the glue. The obtained calculation algorithms showed good agreement with experimental data and suitability for introduction into engineering practice

3 Formulation of the article goals

The purpose of writing this article is to analyze and publish the results of experimental and theoretical researches of steel-reinforced concrete elements made by the method of gluing liquid concrete mixture to a fixed steel formwork.

4 The main material

Given the research objectives for obtain experimental results that will make it possible to draw conclusions about the work features of SCCS using glue connection authors have designed two groups of experimental samples (Fig. 1). The most effective composition of the adhesive (AST-T acrylic plastic) was used for construction works with the ratio of components – 1:1:2, where 1 – polymer (powdered component – methyl ester of methacrylic acid), 1 – hardener (liquid component – suspension polymer based on methyl acrylate), 2 – filler (quartz sand with a grain size of 0.315 mm).

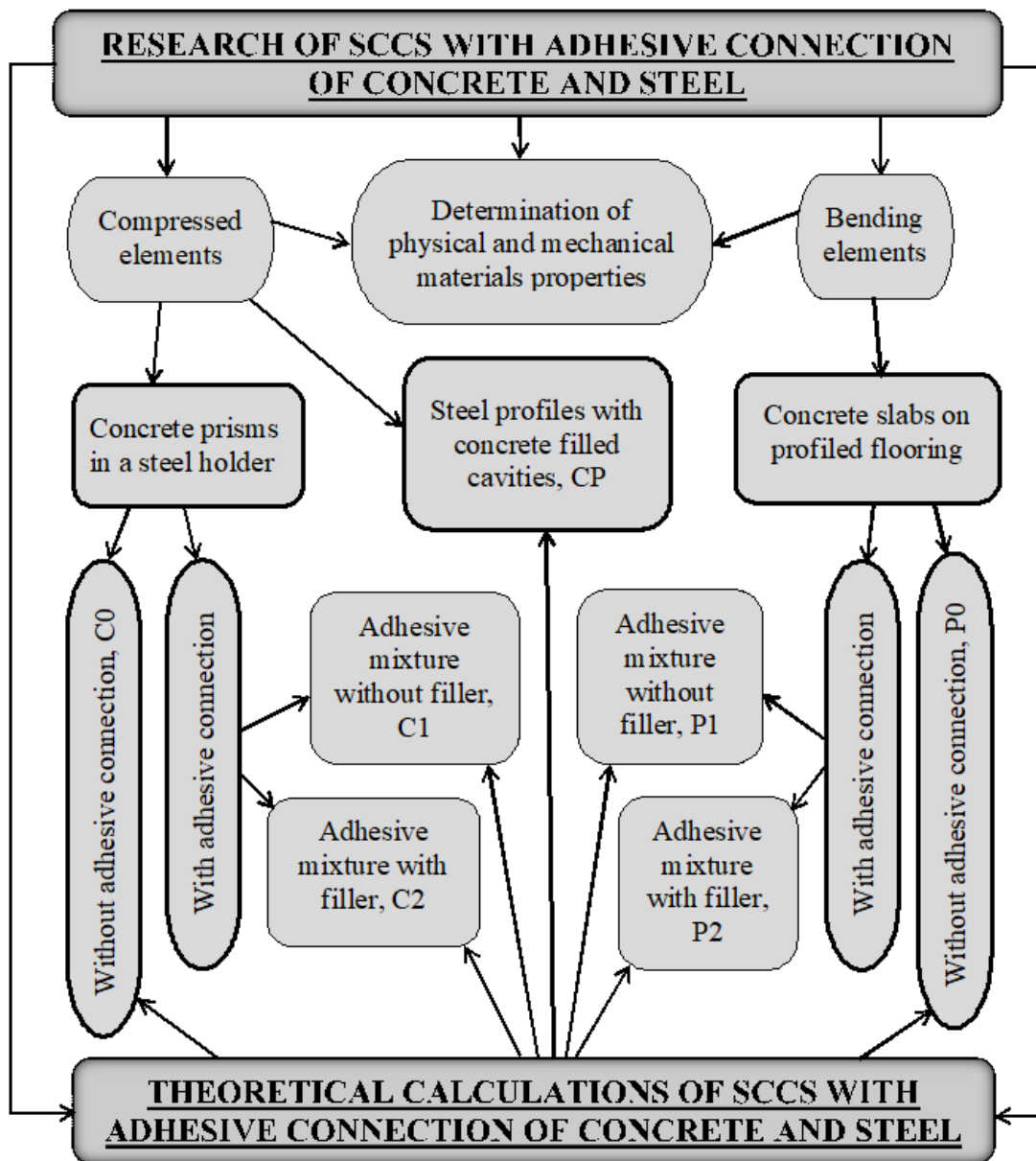


Fig. 1 Experimental studies scheme of structures with concrete and steel adhesive joints.

Samples of compressed elements – steel-reinforced concrete racks of I-beam cross-section with concrete-filled cavities and concrete prisms 630 mm high are framed by steel plates on four sides along the perimeter. The racks are formed by welding I-beam №16 with a length of 1.92 m with end steel plates measuring 160×82×4 mm (Fig. 2, a). In sample CP before concreting the surface of the metal part in contact with the concrete is lubricated with acrylic glue in compliance with the appropriate technology. The second type of samples is formed by welding two vertical formwork sheets measuring 630×150×4 mm and two horizontal formwork sheets measuring 150×150×12 mm (Fig. 2, b). The formed form is filled with concrete in horizontal position. The samples differ from each other by the presence of an adhesive connection, i.e. samples C0 do not have an adhesive connection, and in samples C2, C3 this connection is present (Table 1).

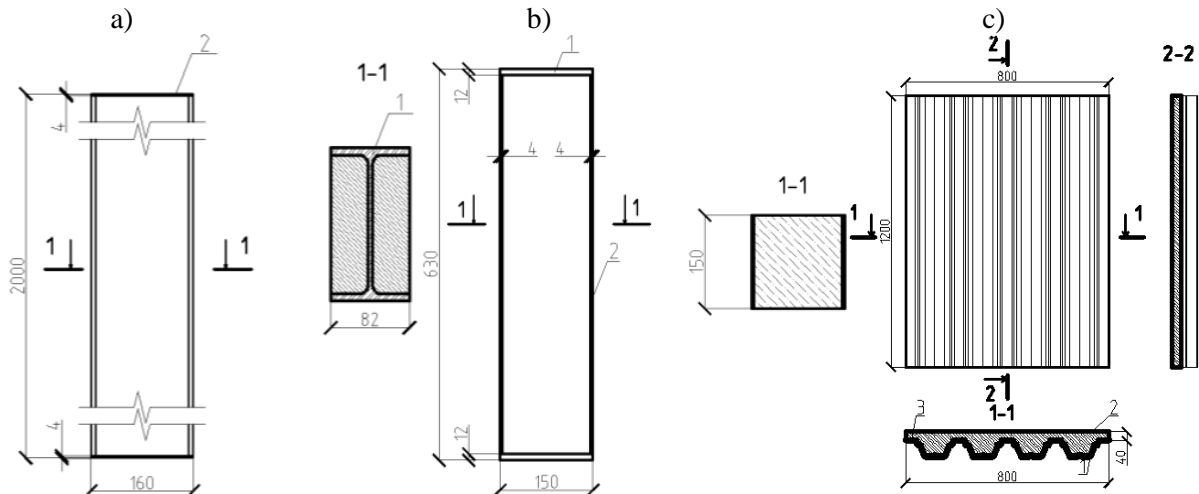


Fig. 2 Design of samples a): 1 – I-beam №16, 2 – end plates; b): 1 – end plates, 2 – external sheet reinforcement; c): 1 – profiled flooring H75-750-0.8, 2 – monolithic concrete slab, 3 – adhesive joint.

Designed prototypes of monolithic slabs on the profiled flooring are rectangular in plan 800×1200 mm, which are formed by the bearing profiled flooring H75-750-0.8 with a zinc coating with a thickness of 275 g/m², on top of which is arranged a monolithic concrete slab with a thickness of 40 mm with filling corrugations (Fig. 2, c). In two samples of the P2 series, before concreting, the surface of the metal part in contact with the concrete is lubricated with acrylic glue.

Table 1 Characteristics of experimental samples.

Number	Test method	Series of samples	Graphic model	Dimensions l×w×h, mm	Presence of adhesive connection
1	compression	CP		160×82×2000	+(with filler)
2		C0		150×150×630	-
3		C1			+(without filler)
4		C2			+(with filler)
5	bend	P0		1200×800×115	-
6		P1			+(without filler)
7		P2			+(with filler)

The experimental research program includes the study of changes in the stress-strain state of the test specimens under the action of longitudinal force (CP, C0, C1, C2) (Fig. 3, left) and bending moment (P0, P1, P2) (Fig. 3, right, Fig. 4).



Fig. 3 Samples in preparation for testing.

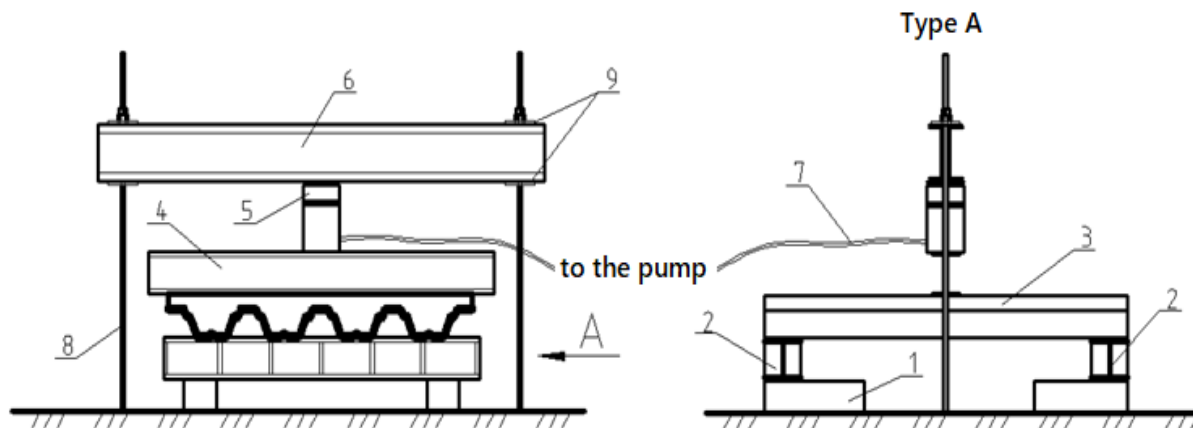


Fig. 4 Installation scheme for plates testing: 1 – stand, 2 – support, 3 – plate, 4 – distributing traverse, 5 – jack, 6 – limiting traverse, 7 – oil pipeline, 8 – bars, 9 – nuts.

The bearing capacity of compressed elements depends on the stability of the steel part, both general and local. That is, the destruction of the I-beam occurred due to the loss of overall stability along the sinusoid (446 kN). The effectiveness of the adhesive joint is evidenced by the fact that the concrete, even after the load-bearing capacity has been exhausted, does not chip off even in places of maximum deformation.

As a result of tests it was determined that the bearing capacity of test samples C0, C1, C2 (Fig. 5, left) depends on the strength of the steel frame and concrete prism connection, which in turn depends on the presence and type of adhesive mixture used for connection steel and concrete. Thus, the lowest bearing capacity among the prisms was the sample C0, in which the contact of steel and concrete was provided only due to the adhesive properties of the concrete mixture, namely 290 kN. Samples using an adhesive joint between concrete and steel showed significantly better results, exceeding the previous value by 1.76 and 2.28 times (C1 – 510 kN, C2 – 661 kN).

Speaking about the bearing capacity of the plates, it should be noted that the use of the adhesive mixture with the filler allowed to increase the bearing capacity of the sample P0 in comparison with P1 and P2 by 2.1 and 3.7 times, respectively (Fig. 5, right).

During the testing of the slabs it was found that the predominant steel part deformations over the concrete block deformations indicate the primacy of the stretched part destruction. This was expressed in the sheet separation from the concrete with the subsequent local stability loss of the vertical ribs, which led to bending of the sheet at the maximum internal forces site and instantaneous cracking of the slab in the same section.

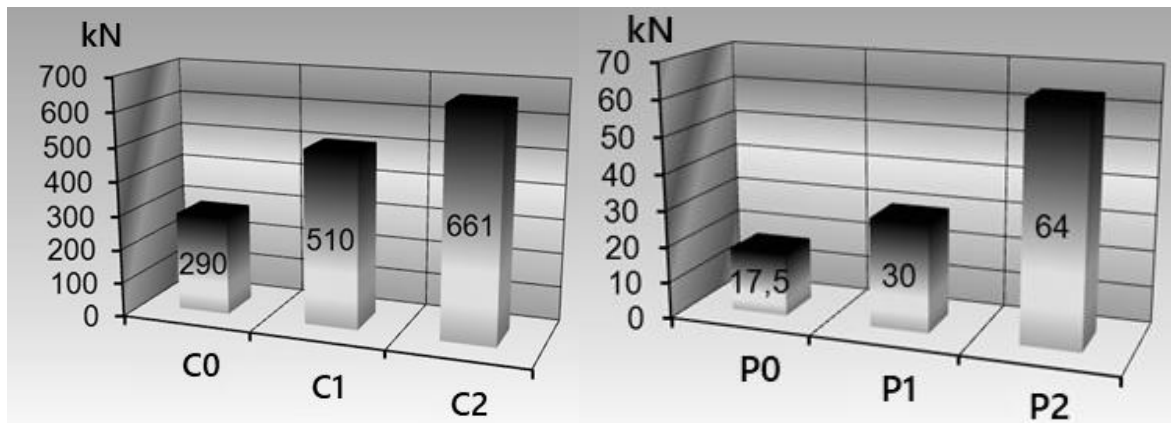


Fig. 5 Bearing capacity of samples.

During the research, strain gauges were used to measure the relative deformations, which were glued in the places where the greatest stresses were expected to appear (Fig. 6). After processing the measurement results, dependence graphs of the relative deformations on the load within the materials elastic stage were obtained (Fig. 7).

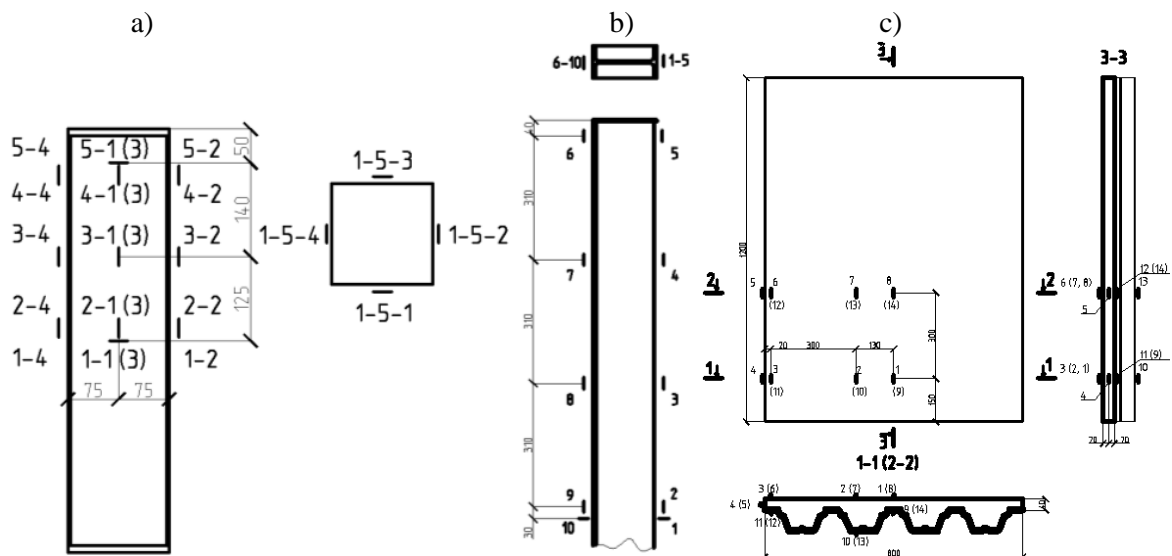


Fig. 6 layout of strain gauges: a) short racks, b) I-beam columns c) monolithic slabs on the profiled flooring.

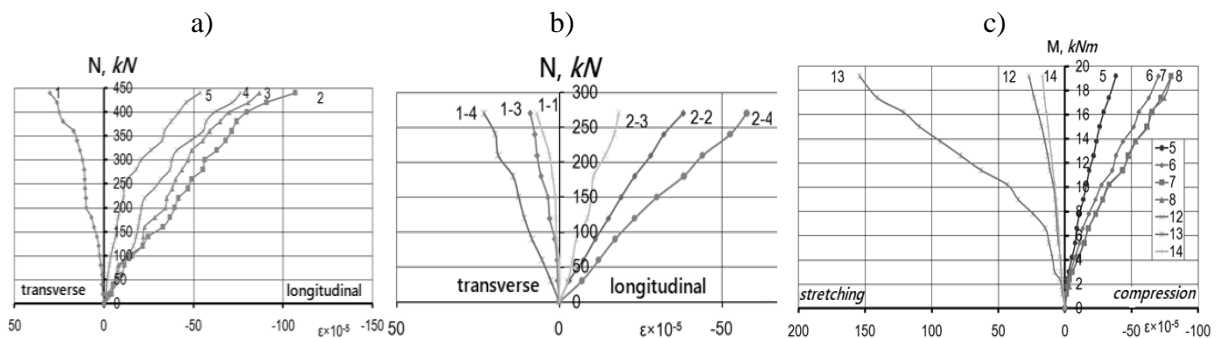


Fig. 7 Dependence of relative deformations on load: a) short racks, b) I-beam columns c) monolithic slabs on the profiled flooring.

The destruction of slab samples occurred due to the separation of corrugated board from the concrete block (Fig. 8, right). This process began with the extreme faces, where the complex stress-strain state of structures caused by the mutual influence of the components on each other was less pronounced. Next, samples P1 and P2 had a gradual separation of the steel sheet with visual fixation of the loss of

local stability of the ribs in the middle of the span, as evidenced by a significant increase in deflections with low bearing capacity (Fig. 8, left).

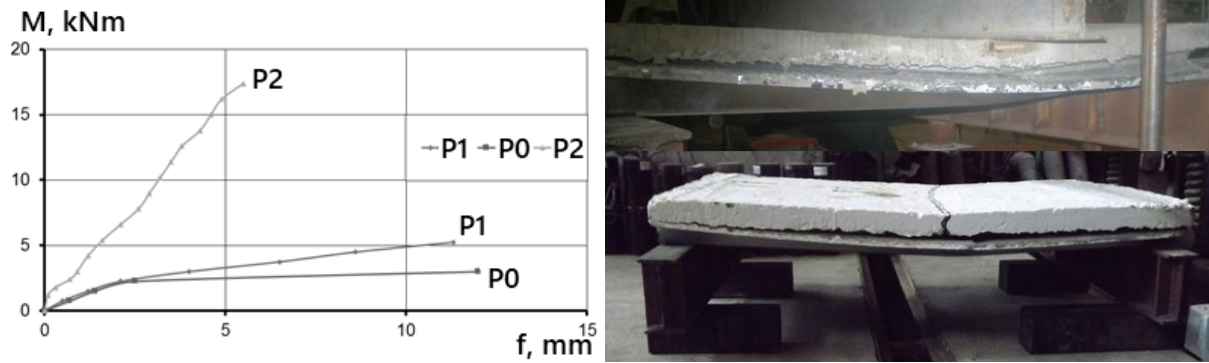


Fig. 8 Dependence of deflections on the load and the appearance of samples after failure.

Table 2 Algorithm for determining the reduced to a rectangular cross section samples bearing capacity according to the theory of composite rods, where b – sample width, f_{cd} , f_y – strength of materials, M – moment from external load, v – the distance between the steel and concrete rods centers of gravity, h_0 – working height of section.

Number	Determined value	Formulas
1	compressed and stretched zones bearing capacity checking	$M \leq M_c = b \cdot x \cdot f_{cd} \cdot z_c$; $M \leq M_s = A_s \cdot f_y \cdot z_c$
2	inner pair of forces arm	$z_c = h_0 - 0,4 \cdot x$
3	height of the compressed zone	$x = \frac{(N^0 - T)}{b \cdot f_{cd}}$
4	axial force in rods	$N^0 = \frac{M^0}{v}$
5	total moment	$M^0 = V_0 \cdot \xi_c^2 \cdot b \cdot h_0 \cdot f_{ctk} + A_s \cdot R_s \cdot v + T \cdot v$;
6	shear force	$T \cong \frac{0,8M}{h_0}$
7	reinforcement area	$A_s = \frac{2M^0 - Th_0}{f_y h_0}$

The optimal method for determining the bearing capacity of steel-reinforced concrete structural elements under the action of bending moments is the calculation according to the theory of composite rods (Table 2). Composite rod – is a non-monolithic rod, the cross section of which consists of several separate parts that are not tightly enough connected to each other, which makes it necessary to take into account the pliability of the connections. Among the SCCS, the most typical examples of composite rods are elements with external rigid reinforcement (beams and racks framed with steel sheets, slabs on profiled flooring, etc.) and reinforced concrete I-beams with side cavities filled with concrete. The cross section of the samples was reduced to a rectangular shape with one horizontal adhesive seam (Fig. 9) to simplify the calculation algorithm.

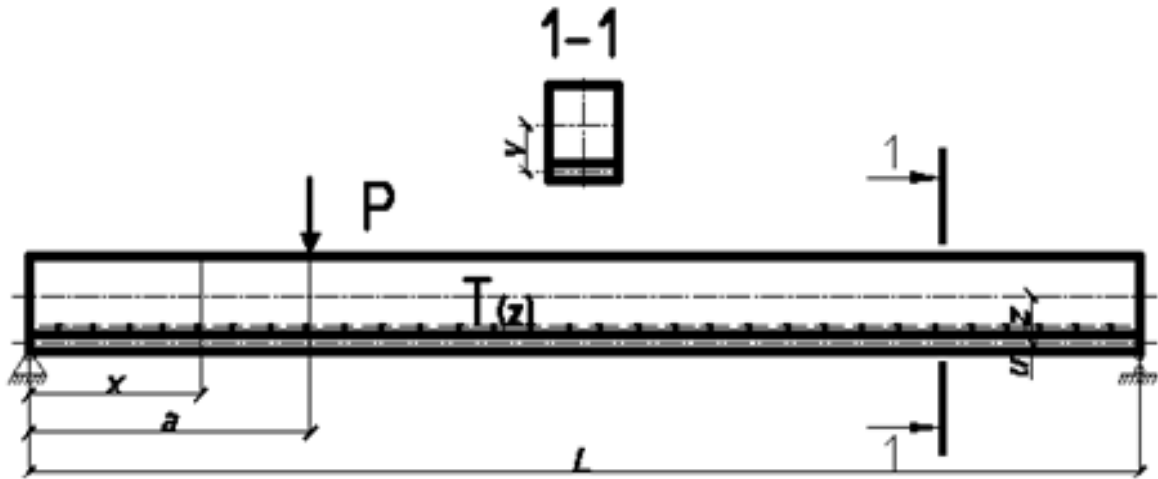


Fig. 9 Estimated model of bending element (T – shear force along the contact boundary between the rods).

Traditional methods for determining the bearing capacity of normal sections under central compression do not have significant differences with the theory of composite rods, and when eccentricities appear, the calculation is carried out by analogy with bending elements.

The highest accuracy in the calculations of the plates was achieved using the method taking into account the adhesive joint material properties according to the theory of composite rods and the discrepancy did not exceed 4% (Table 3). This was achieved in the case of the adhesive mixture with a filler use, which made it possible to work the components of the cross section together until complete destruction. In slab elements without adhesive joints and with adhesive joints without filler, the steel and concrete parts lost their bond in the early stages of loading, which led to a significant reduction in bearing capacity due to their separate operation.

The inability to take into account the effect of the type of adhesive joint on the final bearing capacity in the approximate methods gives an inaccurate result. Acceptable calculation results of the I-beam column by both methods are explained by the creation of concrete volume-stress state, which eliminates the significant influence of the adhesive on the bearing capacity.

Table 3 Comparison of the experimental and theoretical research results.

Series of samples	Bearing capacity, kNm			Divergence, %	
	Experiment values	Theoretical values		Two-layer	Three-layer
		Two-layer	Three-layer		
P0	5.25	18.15	-	-	-
P1	9		11.45	-	+27.2
P2	19.2		19.87	-5.5	+3.5
C0	290	638	-	-	-
C1	510		502	+20.1	-1.6
C2	661		667	-3.6	+0.9
CP	446		470	461	+5.1

5 Conclusion

At all stages of loading in structures with glue connection of steel and concrete with the help of acrylic glue with filler, their compatible work is ensured. Detachment and loss of local stability steel elements was observed only at the moment of destruction. These circumstances suggest that these structures are reliable in work and operation, and the proposed method application of ensuring the steel and concrete

joint work by gluing – an effective and promising type of connection of components of load-bearing structures in various fields of construction. All samples were tested for static short-term loads, and therefore there is a need for further studies of the proposed adhesive joints for long-term and dynamic loads. It is very important to further study the fire resistance of the proposed structures, especially their external steel reinforcement. Also today the behavior of the adhesive joint under the action of extreme temperatures is insufficiently studied

References

- [1] Zolotov, S., Firsov, P., & Muhamad, H. (2020). Evaluation of Stress-Deformed Condition Level of Glued Materials for the Without Anchor Steel-Concrete Joint. In *Lecture Notes in Civil Engineering* (Vol. 47, pp. 95–102). Springer. https://doi.org/10.1007/978-3-030-27011-7_12.
- [2] Zolotov, S., Pustovoitova, O., Firsov, P., Kais, H., & Kamchatna, S. (2019). Stress-strained state of steel-adhesive bonding on the acrylic adhesives. In *IOP Conference Series: Materials Science and Engineering* (Vol. 708). Institute of Physics Publishing. <https://doi.org/10.1088/1757-899X/708/1/012117>.
- [3] Davydenko, Y., Horb, O., & Avramenko, Y. (2018). Adhesive-bonded joint influence on deflection of composite steel and concrete beams with strengthening by external steel reinforcement. *International Journal of Engineering and Technology (UAE)*, 7(3), 349–353. <https://doi.org/10.14419/ijet.v7i3.2.14551>.
- [4] Shkurupiy, A. A., Mytrofanov, P. B., Davydenko, Y. O., & Horb, A. G. (2019). Statistical characteristics of strength distribution of normal sections of bended reinforced concrete elements and their analysis. In *IOP Conference Series: Materials Science and Engineering* (Vol. 708). Institute of Physics Publishing. <https://doi.org/10.1088/1757-899X/708/1/012072>.
- [5] Brede, Markus. (2018). *Fracture Mechanics of Adhesive Joints*. https://doi.org/10.1002/9783527803743.ch1_04.
- [6] Mora, Veronica & Mieloszyk, Magdalena & Ostachowicz, Wieslaw. (2018). Model of moisture absorption by adhesive joint. *Mechanical Systems and Signal Processing*. 99. <https://doi.org/10.1016/j.ymsp.2017.06.042>.
- [7] Quiertant, M. & Benzarti, K. & Schneider, Julien & Landrin, F. & Landrin, M. & Boinski, F. (2017). Effects of Ageing on the Bond Properties of Carbon Fiber Reinforced Polymer/Concrete Adhesive Joints: Investigation Using a Modified Double Shear Test. *Journal of Testing and Evaluation*. 45. <https://doi.org/10.1520/JTE20160587>.
- [8] Yang, Jincheng & Haghani, Reza & Al-Emrani, Mohammad. (2019). Innovative prestressing method for externally bonded CFRP laminates without mechanical anchorage. *Engineering Structures*. 197. <https://doi.org/10.1016/j.engstruct.2019.109416>.
- [9] Jeevi, G. & Nayak, Sanjay & Kader, M. (2019). Review on adhesive joints and their application in hybrid composite structures. *Journal of Adhesion Science and Technology*. 33. 1-24. <https://doi.org/10.1080/01694243.2018.1543528>.
- [10] Gift, Mohan & Jaganathan, Selvakumar & Alexis, S. John. (2016). Analysis of crack propagation in an adhesive joint. *International Journal of Chemical Sciences*. 14. 485-496.

Development of new-generation, eco-friendly thermal insulation board

Dániel Csanády, Olivér Fenyvesi

*Department of Construction Materials and Technologies
Budapest University of Technology and Economics,
Műegyetem rkp., Budapest (1111), Hungary*

Abstract

Nowadays the environmentally friendly thermal insulations become more popular, but most of them have poor insulation performance. The commonly used artificial materials have better performance than natural materials, but they have a higher price and a bigger environmental footprint. This research aims to develop a natural, eco-friendly straw-based insulation board. At the first phase of the research, the most favourable conditions of natural straw were searched. It was investigated that what kind of modifications can reduce the thermal conductivity of the natural fibres and which type of binder could ensure the fire resistance. After all manufacturing processes, the material has to remain still environmentally friendly. Results of two types of investigated bonded and non-bonded straw showed obviously, which is the most optimal density (in compacted condition) for the insulation boards. Due to our results, the macro- and microstructural modifications could reduce the thermal conductivity by 8% and 11% respectively. The treatment and the special binder provide the fire resistance for almost 30 minutes, while the insulation remains eco-friendly.

1 Introduction

Sustainability is essential properties of all building materials. Thus, it is important to monitor the quality of the built-in materials [1]. Nowadays the refurbishment of a building includes the thermal insulations, and new structure can build only with applying thermal insulating materials. Standards regulate the thermal transmittance, so this also affects the thickness of insulation.

There are some natural or reused material based thermal insulations in the low-density range which have satisfactory performance[2], but these are not applicable for facades which have specific requirements. The available environmentally conscious insulation materials which are suitable on facades still have poor performance, so large thickness is needed to use to satisfy the regulations [3]. The consequence of this situation is a high amount of built-in material, which means unnecessary use of energy and resources. But the thermal insulation of the building with any type of material is effective itself if only the operating energy demand is considered. In most cases, the applied insulation materials are mineral wools and polymer foams [4]. These materials need a considerable amount of embedded energy during manufacture [5] [6]. The melting of the mineral wools base material requires very high temperature, and its binder is also a synthetic polymer resin[7]. The base material of insulating foams is fossil petroleum. Both of these types of material generate waste in the future which needs to be deposited or need to find efficient recycling technology (current technologies are not efficient enough) [8]. Some type of reuse of grinded foams need a cement-based binder, so these have also high embedded energy [9].

The fire resistance of commonly used polymer foams (mainly polystyrene) is inferior, and they generate toxic gases during a fire [10]. Mineral wools are classified as A1 fire reaction category by the standards (MSZ EN 13501-5-2006), but the resin of the fibres also can generate toxic gases.[10]. Most of the natural fibre-based insulation contain polymer resins or contain toxic flame retardants [11]. Because of these reasons, such a fire-resistant environmentally friendly insulation is needed, which has competitive performance and price and also a minimal environmental footprint. Because straw can be found in almost every country and it has a very suitable structure for application as insulation, it was chosen as a base material. Besides these, the developed material can be used in many ways. For example, nowadays, thermal insulation filled masonry blocks appears in more and more manufacturers in Europe. This is well illustrated by the growing research number dealing with these materials using different artificial and natural-based thermal insulation materials to fill the

masonry blocks [12] [13]. The straw insulation is used in this type of bricks. Besides, it reduces the environmental footprint of the product.

2 Methodology/research program

2.1 Objective

The development of new material is usually a complicated task, but in the case of using natural raw material, it becomes more complicated. The material has to provide at least the same insulation performance as commonly used insulations, and it has to satisfy many criteria while it stays still environmentally friendly. The other obstacle is that the applied stem (fibre) is not artificial, where almost every property is well controlled during production. Every straw stems have specific natural material properties (macro and microstructure). With the modification of initial material structure in macro and micro levels, the suitable material properties can be reached. The applied binder is also a new material because there was not any kind of binder in that which can be used economically and it is acceptable in case of building material, that satisfies all of the criteria of eco-friendliness. With thermal insulation, more than two tons of eq. CO₂ can be saved in each year/family house. But with the newly developed straw insulation material, it can be saved more. Because it has deficient production energy demand, the stems absorb CO₂ during their growth and the binder also can absorb CO₂. So it generates less CO₂ emission than conventional thermal insulations.

The research was separated into four main parts: 1, Behaviour of stems without binder; 2, Behaviour of stems with a binder; 3, Properties of individual stems; 4, Binder composition. These parts contain several subsections. The supreme objectives were as follows: Biodegradability, fire-resistance, optimized thermal conductivity, good moisture permeability, low carbon emission during the manufacturing process and proper sound absorption. Most of the objectives have been reached already. The laboratory prototypes are satisfied with most of the criteria (Fig. 1).



Fig. 1 Laboratory prototypes of the straw insulation

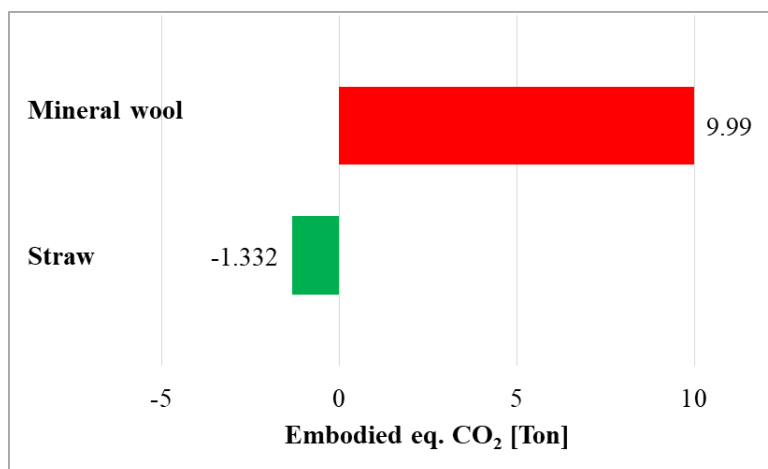


Fig. 2 Embodied eq. CO₂ in the facade thermal insulation of the same 200 m² family house

2.2 Materials

The investigated straw types were barley (type1) and a wheat (type2) straw. Type1 was compacted to a big bale, so most of the stems were injured, but it also contained intact stems. Type2 was made directly for us in loose bales, so most of the stems were intact. These materials were investigated in absolute raw condition and with modified structure too. Besides this, stems were examined in bonded and non-bonded conditions. The bonded specimens were different in phase 1 and phase 2 of the research. In phase 1, non-treated fibres were used with natural fibre length distribution, and a simple inorganic binder was used. In phase 2, treated fibres were used with defined fibre length, and a modified inorganic binder was used.

2.3 Measurements

2.3.1 Thermal conductivity

Every thermal conductivity measurements are done based on the guarded hot plate method. The measure conditions are regulated by MSZ EN 12667:2001 [14] and MSZ EN 1946-2:1999 [15]. All of the presented thermal conductivity results were measured at 10 °C mean temperature and based on a minimum of three individual test results. In the case of all presented experiments, all properties and conditions were constant. The investigated straw types were a barley (type1) and a wheat (type2) straw.

The first step was searching the optimal density, which results in the minimum thermal conductivity. It was also done in case of the bonded and non-bonded condition. In those cases, 150*150*50 mm (length, width, height respectively) specimens with ESP frame were used. These specimens were dry state during measurements and made according to the description of phase 1. The binder-fibre mass ratio was constant during these measurements.

In the next phase of research, the material properties of individual fibres were optimized. That stem length was searched, which gives the minimum thermal conductivity value. In another series of experiments (but parallel with the latter) the modification of microstructure (by different treatments) and its effect on thermal conductivity were also investigated. The treatment methods used different liquids, but the same stem-mass ratio. The length of the treatment time and the temperature was also the same. The pile of stems were filled to a thin-walled paper box which did not affect the results. The dimensions of the box were the following: 20 mm heights 300 mm width and length (paper type: 120 g/m²) (Fig. 3). In the investigation of the stem length effect, only the lambda value was measured. In the case of fibre treatments, the mass loss was measured, and the cross-section of treated stems was also investigated by SEM (Fig. 4).

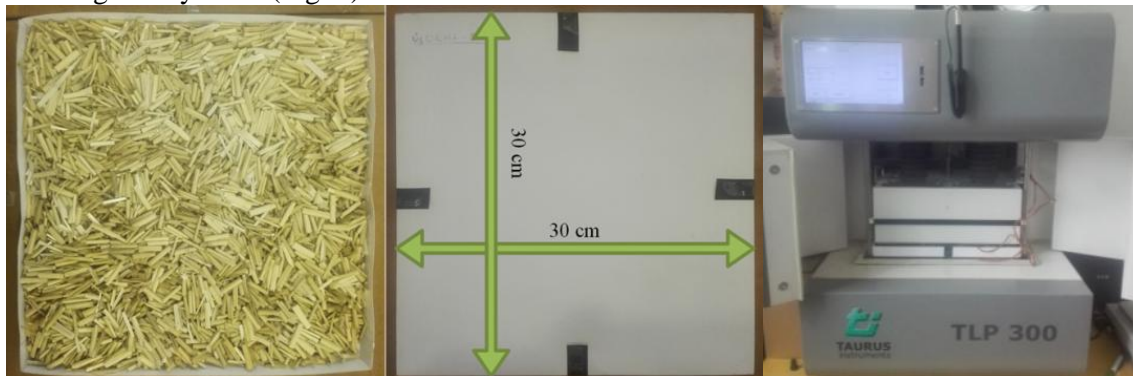


Fig. 3 The measuring box filled with unit length fibres, (left) opened condition, (middle) closed condition, (right) specimen in the measuring equipment

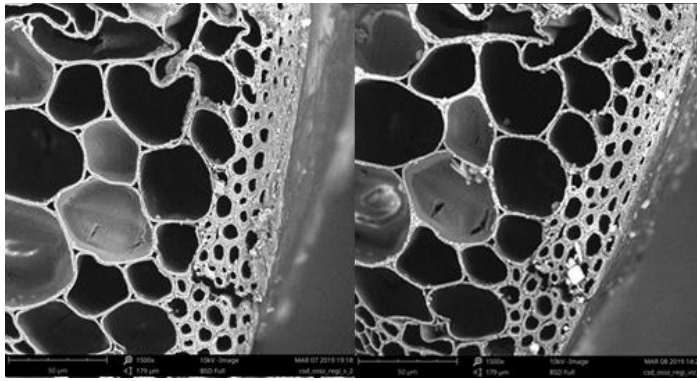


Fig. 4 The scanning electron microscope record from the cross-section (left) before and (right) after treatment

2.3.2 Binder

In the present phase of research, the binder is a modified inorganic liquid, and the previous modifications are also used, in the new generation of specimens (phase 2 specimens). The binder has lots of functions in the final insulation board. It gives mechanical strength, protects the fibres against fire, water, insects, so it improves durability. Besides, it can ensure all of these functions must be environmentally friendly too. All of these functions of the binder was tested, but in this article, only some of them are published.

2.3.3 Fire resistance

The binder is one of the essential components of the fire resistance because it forms a protective layer for the organic fibres against inflammation (worthily of note materials categorized by "reaction to fire" by standards, structures have "fire resistance", but this word is easier to handle and understandable). The treatments of stems affect the fire resistance in a positive direction. The fire resistance tests was a unique measurement method using a gas lamp, a thermocouple, and associated digital thermometer was applied (Fig.5). Thermocouples were fixed to the centreline of the protected side of the specimen (sensor 1: against a gas burner flame, sensor 2: 4 cm laterally away from sensor 1). For each test, the specific performance of the gas lamp was the same, and the distance between the surface of the specimen and the front of the gas lamp tube was constant (50 mm). The maximum temperature of the gas flame was between 920-1100 °C. The test ends when the measured temperature reaches 200 °C, because at this temperature materials may melt, self-ignite. After the fire load, the tested specimen has to be cut in half, and the shape of the burned surface in the loaded cross-section examined. The maximum temperature of the flame was between 920-1100 °C. The measured temperature values were shown as a function of time. The insulating and integrity performance of the tested material ("I" and "E") was also investigated. So how long the straw insulation can withstand the generated heat or the flames and prevent it from breaching the other elements of the building. Our insulation was compared to mineral wool with the same density, which is known as fire-resistant thermal insulation. The sensor positions were absolutely the same as it is mentioned in 2.3.3.



Fig. 5 Components of the experimental set-up used for measure fire resistance (left): 1.: gas lamp, 2.: digital thermometer, 3.: thermocouples, 4.: thermocouples fixing plate, 5.: specimen fixing stand, 6.: straw specimen. The specimen during the test (right)

3 Laboratory test results

The relation between thermal conductivity and density is clear from all types of measurements results. The results of non-bonded specimens give the minimum point of the thermal conductivity at the same density. The curve of bonded specimens has two local minimum (which are almost the equal value) one of them also belongs to that density like in case of bonded ones. From the diagram, it is clear that the binder increases the thermal conductivity (Fig. 6).

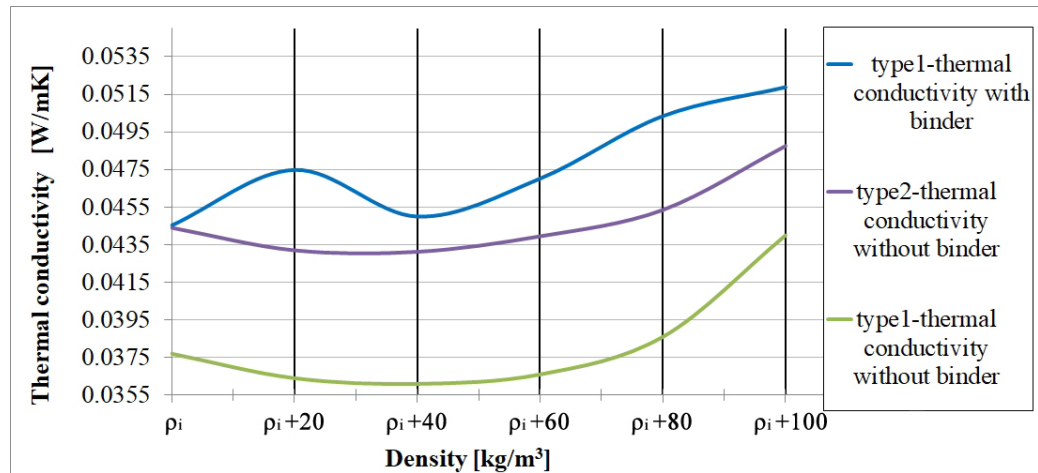


Fig. 6 Relationship between density and thermal conductivity

From the results, it is visible that stem length had a measurable effect on thermal conductivity (Fig. 7). The resulted curve has an interesting shape, in the investigated region, it consists of two curves with two local minimums.

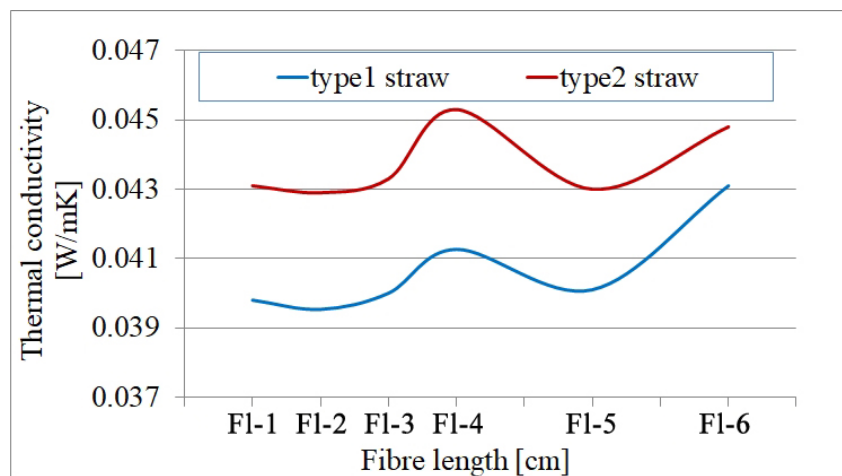


Fig. 7 Relationship between fibre length and thermal conductivity (F1-Fibre length)

The measurements of the treated stem thermal conductivity gave very instructive results. There are such fibre treatment methods which can reduce the thermal conductivity by 15 % (Fig. 8). Besides this, some of the treatment methods did not affect or increase the thermal conductivity.

The phase 2 specimens contain the new binder and all of natural stem structure modification. In general, these specimens have 17% lower thermal conductivity than phase 1 samples (Fig. 8).

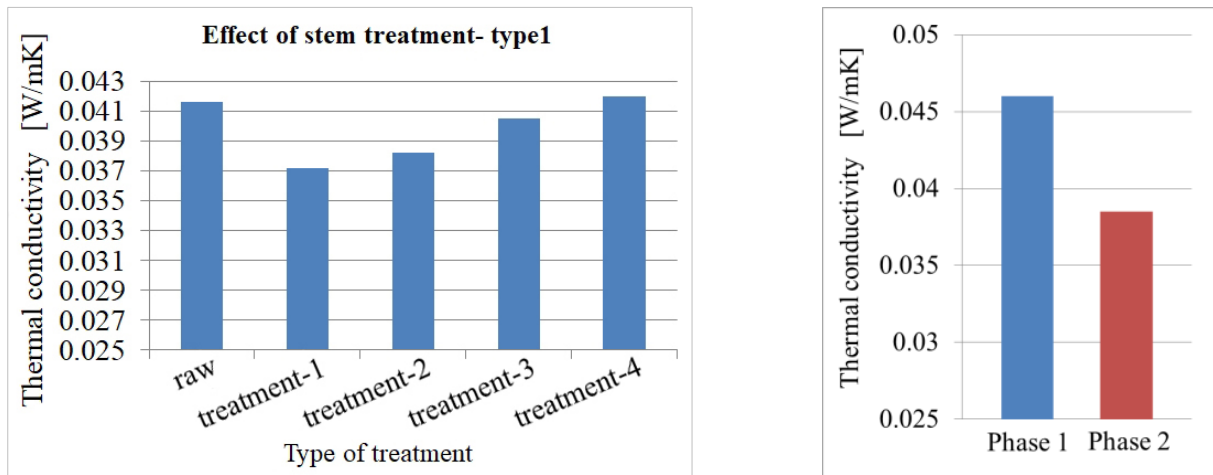


Fig. 8 Effect of treatments on thermal conductivity (left). Mean thermal conductivity of bonded specimens from research phase one and two (right)

Fire resistance test of 5 cm thick straw insulation shows that the protected side of the insulation needed 25 minutes to reach 200 °C while the loading flame temperature was between 900-1100 °C. The lateral sensor showed only a delay for 16 minutes long, after that the heating rate become dramatically slower than the opposite sensor's heating rate. The time-temperature curves of straw insulation consist of more accelerating and decelerating period. One of the most crucial observation is that all of the investigated specimens showed self-extinguishing behaviour. There was no fire spread only the carbonization was spread on the surface and cross-section of the specimen. The mineral wool specimens needed 18 minutes to reach 200 °C at the protected side (the diagram shows the mean of three specimens), so the straw specimens can inhibit the heat spread favourable, in case of high temperatures (Fig. 9). In the following tests should be examined how long time is needed for the straw insulation to burn through. For comparative the protected side of mineral wool temperature after fire load with the same length has to be measured.

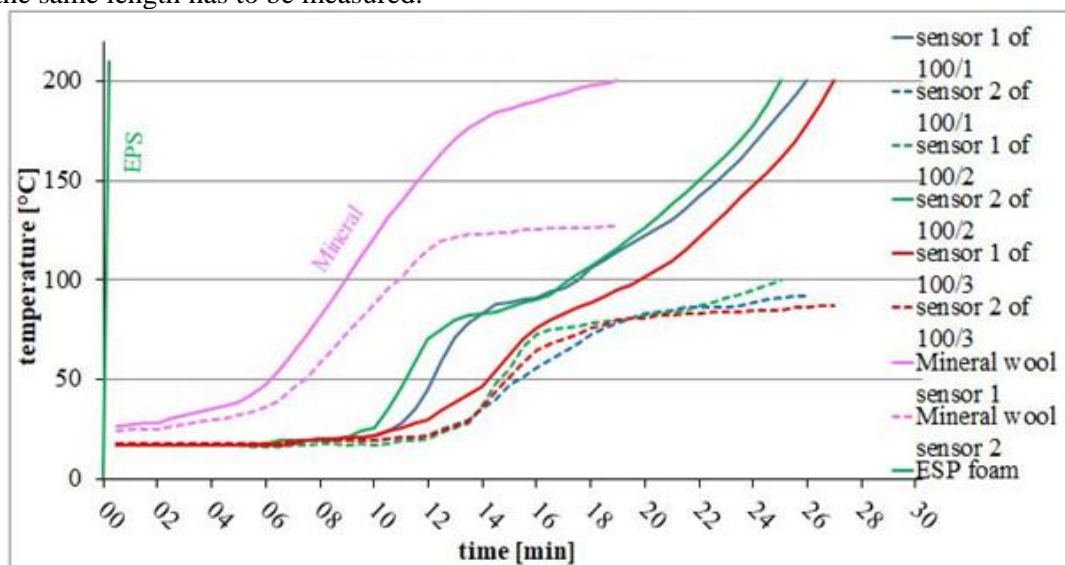


Fig. 9 Time-temperature curves of fire resistance tests

4 Conclusions

- The laboratory test results of different straws give the same curve characteristic when the thermal conductivity is shown in function of density, but their absolute value shifts on the ordinate. Because the porosity and stem wall thickness is different for each variety, and it has a strong influence on thermal conductivity. But the other properties in specimens are mostly the same.

- The applied binder increases the thermal conductivity of raw straw because it is a more dense medium which is more favourable for heat transfer, and the binder changes the contacts between fibres better.
- The thermal conductivity of straw with natural length can reduce either by 8 %. The thermal conductivity changes while stem length changes are changing. It is because of several parameters change inside the stem multitude while only the stem length is changing. For instance, this change results in a different number of the contact point between stems, and it affects the maximum length the heat can carry within one stem. Besides these things, it affects the gaps among stems which affects to the convection and radiation. All of these changes result in a different heat transfer process.
- Treatment can change the thermal conductivity of fibres either by 11 %. These results were following microscopic observations because the porosity of straw was inversely proportional to thermal conductivity.
- The time-temperature curves of straw insulation consist of more accelerating and decelerating section. This is because the generated char protected the intact parts while the huge ventilation did not take it from the loaded section. And this phenomenon was repeated while the specimen reached 200 °C. While the char protects the underlying material, the possible humidity can evaporate only more slowly. This phenomenon makes the curve's slope smaller. When all of the humidity leaves the next layer of the underlying material, the temperature will increase.
- The thermal properties of natural straw can be significantly changed by the application of macro- and microstructure modification, and these modifications are also effective if the stems are bonded to form a composite.

Based on the test results, the material can be used as a facade thermal insulation board, and its properties can be further improved by further development. In the future should be investigated the bonding of plaster in case of cyclic vapour loading and have to be measured the force required to break the fixing dowel.

References

- [1] Nagy B., Simon T. K., Nemes R., 2020, "Effect of built-in mineral wool insulations durability on its thermal and mechanical performance," *J. Therm. Anal. Calorim.*, 139:169–181
- [2] Dieckmann E., Onsiog R., Nagy B., Sheldrick L., Cheeseman C., 2020, "Valorization of Waste Feathers in the Production of New Thermal Insulation Materials," *Waste and Biomass Valorization*, pp. 1–13
- [1] Asdrubali F., D'Alessandro F., Schiavoni S., 2015 "A review of unconventional sustainable building insulation materials," *Sustain. Mater. Technol.*, 4:1-17
- [2] Sarwar D., Hosseinian-Far A., Yozsefi Y, 2019, "Greening the green: an investigation of circular economy in the improvement of building thermal insulation," Paper presented at University of Northampton's Annual Research Conference proceedings Northampton, June 20-21
- [3] Qi G., Shan F., Zhang Q., 2013 "Research and development of mineral wool production with high temperature industrial residual materials," *Materials Science Forum*, 743-744:301-305
- [4] Dissanayake D. M. K. W., Jayasinghe C., Jayasinghe M. T. R., 2017, "A comparative embodied energy analysis of a house with recycled expanded polystyrene (EPS) based foam concrete wall panels," *Energy Build.*, 135:85–94
- [5] Kowatsch S., 2010, "Mineral wool insulation binders", *Phenolic Resins: A Century of Progress*, Berlin: Springer, 209-242

- [6] Väntsi O., Kärki T., 2014, “Mineral wool waste in Europe: A review of mineral wool waste quantity, quality, and current recycling methods,” *Journal of Material Cycles and Waste Management*, vol., 16:62–72
- [7] Gadea J., Rodríguez A., Campos P. L., Garabito J., Calderón V., 2010, “Lightweight mortar made with recycled polyurethane foam,” *Cem. Concr. Compos.*, 32:672-677
- [8] Stec A. A., Hull T. R., 2011, “Assessment of the fire toxicity of building insulation materials,” *Energy Build.*, 43:498–506
- [9] Petter Jelle B., 2016, “Nano-based thermal insulation for energy-efficient buildings,” *Start-Up Creation: The Smart Eco-Efficient Built Environment*, Woodhead Publishing, 129–181.
- [12] Nagy B., 2019, “Designing insulation filled masonry blocks against hygrothermal deterioration,” *Eng. Fail. Anal.*, 103:144–157
- [13] Nagy B., Stocker G., 2019, “Numerical analysis of thermal and moisture bridges in insulation filled masonry walls and corner joints,” *Period. Polytech. Civ. Eng.*, vol. 63,:446–455
- [14] MSZ EN 12667:2001, “Thermal performance of building materials and products. Determination of thermal resistance by means of guarded hot plate and heat flow meter methods. Products of high and medium thermal resistance,” Budapest, 2001.
- [15] MSZ EN 1946-2:1999, “MSZ EN1946-3:1999 Thermal performance of building products and components- Specific criteria for the assessment of laboratories measuring heat transfer properties - Part 3 : Measurements by heat flow meter method,” Budapest, 1999.

Drying shrinkage and mechanical properties of concrete based on *Corbicula* shells, from river sediments, as coarse aggregates

Hamza Beddaa^{1, 2, 3}, Amor Ben Fraj¹, Francis Lavergne¹, and Jean Michel Torrenti³

¹*Cerema, Project-team DIMA, 120 rue de Paris, BP 216 Sourdun, 77487 Provins Cedex, France*

²*Clamens, Rue des Carrières Z.I. SUD, 77270 Villeparisis, France*

³*Gustave Eiffel University, IFSTTAR, 14 Boulevard Newton, Champs-sur-Marne F-77455, France*

Abstract

Dredged river sediments are considered as a promising alternative for aggregates. In the Paris region, these sediments contain a significant content of *Corbicula* shells. This paper seeks to investigate drying shrinkage and mechanical properties of concrete containing *Corbicula* shells, as coarse aggregates (0%, 2.5%, 5%, 7.5%, 10% and 20% by volume). The obtained experimental results show that the *Corbicula* shells can be used as coarse aggregates without substantially affecting the physical properties and the drying shrinkage of concrete. However, a quasi-linear decrease in the compressive strength with increasing the shell's content is observed (a decrease of 5%, at 28 days, for a replacement of 5% by volume). Young's modulus shows also the same trend as compressive strength.

1 Introduction

The sand fraction of dredged river sediments can advantageously be a substitute to conventional aggregates for concrete, as its soluble organic content is likely limited and its fine part is discarded, and may not significantly affect the hydration, the setting time and the evolution of the compressive strength [1], [2]. Nevertheless, this new resource may include a significant weight fraction of centimetric dry shells, either unimpaired or crushed. While the lightest of these shells can be removed by blowing, some of the heaviest shells can hardly be separated from the sandy river sediment. It is known that shells affect the compressive strength of concrete and the amount of shells in concrete aggregates is limited to 10% weight according to European Standards EN12620 [3].

While the decrease of mechanical performance induced by shells is often measured and reported, hints about its physical origin are scarce and valuable. Both the compressive strength [4]–[9] and the Young modulus [6], [10] are reported to decrease as significant weight fractions (> 10 wt.% substitution of fine or coarse aggregates) of shells are incorporated. Drying shrinkage strains also increase [5], [10]. This increase in shrinkage is related to the large difference between the properties of shells and substituted aggregates. On the one hand, shells are flat stiff inclusions, which might lead to higher stress concentrations in the cement paste in the vicinity of the shell. On the other hand, the surface of the shell may not bound to the cement paste [5], [6], or the shell itself is pictured as soft [10]. Scanning Electron microscopy unveils little cracks and higher porosity in the Interfacial Transition Zone near the outer layer of the shell (periostracum) and cavities near its inner layer (nacre) [6]. The lack of adhesiveness has also been attributed to the organic content of the shell itself, especially the chitin from the inner nacre layer [7]. In addition, the absorption of shell is higher than that of the conventional aggregates and it may affect the workability of the fresh concrete [4], [5], [7], [8]. The flakiness of the crushed shells or the non-convexity of unimpaired shell particles may also increase the water demand [6], alter the rheology of the concrete, the efficiency of vibrations, thus increasing the amount of entrapped air and reducing both density and mechanical performances. Finally, incorporating significant weight fraction of shells (> 10wt. %) may affect the durability of the material as its porosity and chloride diffusion coefficient are increased [11].

The shell species present in the dredged sediments of the Ile-de-France region are *Corbicula*, *Dreissena* and *Viviparus* [12]–[14]. While the latter two are light and can be easily removed by blowing, *Corbicula* is dense and its separation from sediment sand is difficult to achieve by a practical procedure.

This paper, therefore, seeks to investigate the effect of a progressive substitution of conventional coarse aggregates by Corbicula shells (Fig. 1) on the total shrinkage and the mechanical properties of concrete.



Fig. 1 Corbicula shells

2 Materials and methods

2.1 Materials

The cement used for this study is Portland cement type CEM I 52.5 from Calcia plant. Alluvial sand and coarse aggregates (0/4 mm and 4/20 mm respectively) from the Ormes Quarries are used (their properties are listed in Table 1). The shells used in this experimental campaign as a substitute for coarse aggregates (CA) are Corbicula shells (CS), obtained (by sorting) from the river sediments of the Ile-de-France region. In fact, the corbicula shellsea are invasive in all the main French basins. The physical properties of aggregates and shells are represented in Table 1: the density and water absorption are measured in accordance with European Standard EN1097-6 [15], while flakiness index is measured according to the European Standard EN933-3 [16].

Table 1 Properties of aggregates and corbicula shells.

Sample	Sand	Coarse aggregates (CA)	Corbicula shells (CS)
Water absorption (%)	4.70	2.32	4.50
Density	2.41	2.53	2.24
Flakiness index (%)	-	31	100

2.2 Concretes formulation

The study is conducted on six different mixtures of concrete. The only change from one concrete to another is the volume substitution rate of CA by CS, which takes the values of 0, 2.5, 5, 7.5, 10 and 20%. The required concrete is C30/37 class with a good workability (16-21 cm). The water/cement ratio is set to 0.55 for all formulas. Table 2 lists the quantities of various ingredients composing 1 m³ for different concretes. The total water is calculated by considering the water absorption coefficient of aggregates and shells in order to avoid any modification of the workability or hydration process.

2.3 Methods

2.3.1 Workability

Slump is measured using the Abrams cone for all mixes in accordance with European Standard EN12350-2 [17].

2.3.2 Physical properties

The density and porosity accessible to water are measured by the volumetric method on 11 cm × 5 cm cylindrical specimens according to the French Standard NF P18-459 [18] with some modifications; the sample has been saturated for 72 hours instead of 44 hours and the considered drying temperature is

80°C instead of 105°C in order to avoid the shells damage. The test is carried out on three samples for each substitution rate and the average is reported in Table 3.

2.3.3 Mechanical properties

The compressive strength is measured in accordance with European Standards EN 12390-3 [19], on cylindrical specimens 11 cm × 22 cm. The elastic modulus was measured on the same specimens using LVDT sensors. The samples are demolded 24 hours after being cast, stored in water, and then loaded at the age of 28 or 90 days. For different mixtures, the tests are performed on three samples loaded at the same age.

2.3.4 Shrinkage

The total shrinkage test is carried out on 7 × 7 × 28 cm³ prismatic specimens. Measurements began immediately after demoulding and continued for up to 90 days. Throughout this test period, the specimens are kept in a storage room set at 20 °C and 50 % humidity. The reported shrinkage is averaged from three measurements recorded on three different samples.

Table 2 Quantities of ingredients per m³ of concrete.

Ingredients	% Substitution rate (by volume)					
	0	2.5	5	7.5	10	20
Cement (kg)	335	335	335	335	335	335
Sand (0/4 mm) (kg)	881.10	881.10	881.10	881.10	881.10	881.10
Coarse aggregates (4/20 mm) (kg)	814.40	794.04	773.68	753.32	732.96	651.52
Corbicula shells (4/20 mm) (kg)	0	18.02	36.03	54.05	72.07	144.13
Efficient water (kg)	184.25	184.25	184.25	184.25	184.25	184.25
Total water (kg)	244.29	244.63	244.97	245.31	245.64	247.00
W/C ratio	0.55	0.55	0.55	0.55	0.55	0.55

3 Results and discussions

3.1 Slump

Table 3 shows that the slump of concretes based on CS (CCS_x where x is substitution rate) is similar to that of control concrete (CCS₀). The non-change of the slump value can be attributed to the higher unit weight of CS as that of conventional CA and taking into account the absorbed water of the different ingredients. These results show that the increase in the flakiness index and the surface area of the overall aggregates, due to a substitution of up to 20% by volume, has no effect on slump. Thus, the main factor impacting slump is the density of the incorporated shells.

Table 3 Physical properties of concrete based on CS.

Properties	Concrete name					
	CCS0	CCS2.5	CCS5	CCS7.5	CCS10	CCS20
Slump (cm)	21	20	21	21	20	20
Saturated concrete density (± 0.01)	2.28	2.29	2.29	2.29	2.29	2.29
Porosity at 90 days (%) (± 1)	18,3	18,6	19,0	18,7	18,9	18,6

3.2 Physical properties

The density and porosity values of concretes incorporating shells are similar to those of control concrete (Table 3). This can be attributed to the high density and low absorption coefficient of CS. In addition, the incorporation of shells instead of aggregates that are also flattened does not significantly affect the granular disposition of the concrete. Indeed, the curved shape of the shell particles may increase the water demand, the amount of trapped air and the porosity of the surrounding mortar, but the thickness of this affected mortar is very thin (< 0.1 mm) [6], it is therefore difficult to note its effect on the overall concrete density or porosity.

3.3 Compressive strength and elastic modulus

Fig 2 (left) shows the compressive strength values of all studied concretes at 28 and 90 days. From the obtained results, the compressive strength decreases as the percentage of CS in the mixture increases. This decrease is quasi-linear, for instance the substitutions of 5%, 10% and 20% decrease the compressive strength, at 90 days, by 2.2 MPa, 4.9 MPa and 10.4 MPa respectively.

This effect of shell on the compressive strength is attributed, by several studies [6], [8], to the fragility of shell compared to conventional aggregates and the increase of the total porosity due to shells form which disturb the granular packing. Since the shells used for this study are hard and the porosity of the concrete remains unchanged with incorporating shells, the possible explanation for this decrease seems to be the weak bond shell-mortar. Indeed, from Fig 3 the difference in adhesion with the mortar between CA and CS could be noted. The ITZ of the shell shows an absolute lack of adhesion (a detachment) especially for the outer face. The flattened shape of the shells acts as a barrier to bleeding water, besides their curved shape promotes the trapping of water and air bubbles, resulting in high porosity at the inner face (Fig 3). The ITZ of the gravel is also imperfect, but has only very small gaps and less porosity compared to shells (Fig 3). In addition, the high flakiness index of shell increases the surface area of the ITZ and the effect becomes more pronounced. It should also note that the ITZ size is so tiny to increase the total porosity of the concrete, however it is capable of significantly affecting its mechanical properties [20]-[22].

The elastic modulus results of the studied concrete follow the same trend of the compressive strength (Fig. 2 (right)). The decrease in the elastic modulus may also be attributed to the poor mechanical properties of shells-mortar ITZ [21], [22].

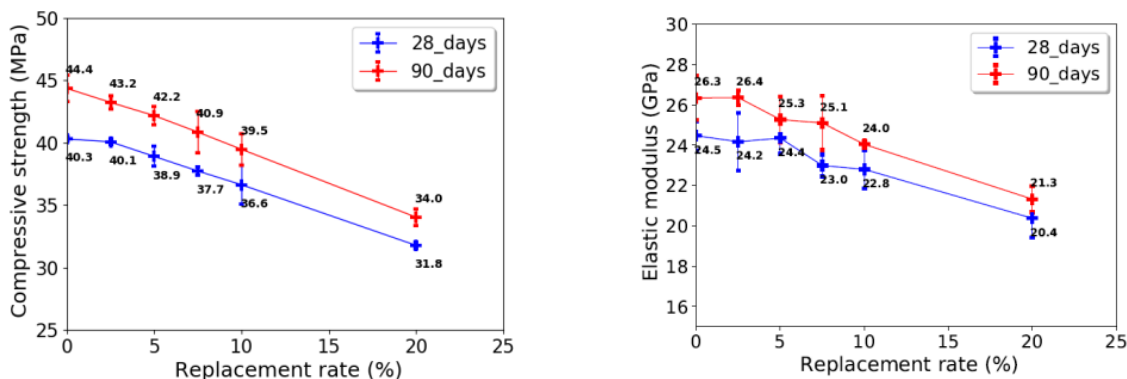


Fig. 2 Compressive strength at 28 and 90 days of different shells-based concretes (left). Elastic modulus at 28 and 90 days of different shells-based concretes (right).

3.4 Shrinkage

To assess the total shrinkage behaviour of concrete incorporating shells, Corbicula type, as coarse aggregates, a series of tests are carried out for 3 months and the results are reported in Fig 4 (left). The results show that replacing up to 20% by volume of CA by CS did not affect the concrete shrinkage. The weight loss over 3 months has been also measured in $7 \times 7 \times 28$ cm³ samples (Fig 4 (right)). The results are in accordance with those of shrinkage: the use of CS as CA does not affect the concrete weight loss. This finding supports that reported in [6]. The low absorption coefficient of CS, the substitution by volume and using the same W/C ratio result in the same cement paste volume fraction and properties. Thus, the same variation in volume of the different concretes, which is mainly related to that of the cement paste, must be obtained. According to Fujiwara [24], some aggregates may possibly

shrink and therefore the shrinkage of the concrete depends on the mechanical properties of the aggregates, in particular their elastic stiffness. The similar behaviour of concretes incorporating CS and control concrete, with respect to shrinkage, suggests that the mechanical properties of CS and conventional coarse aggregates are also comparable.

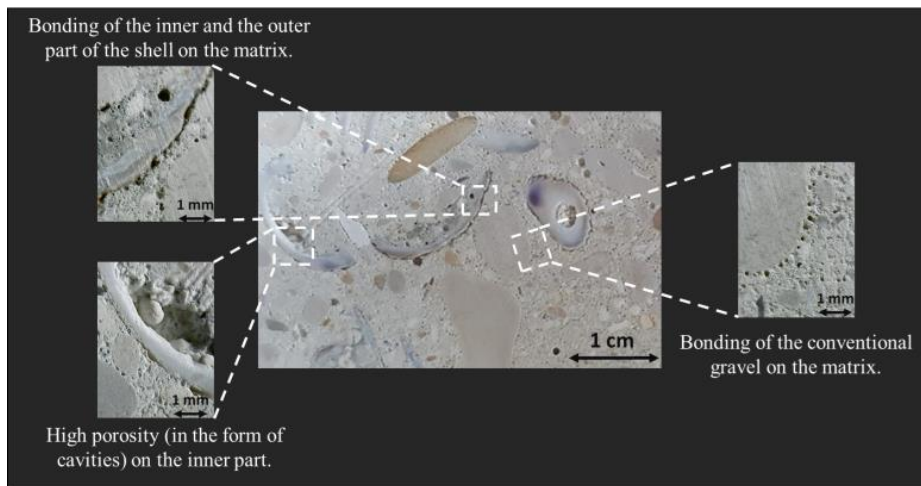


Fig. 3 Observation of aggregate-mortar bonds.

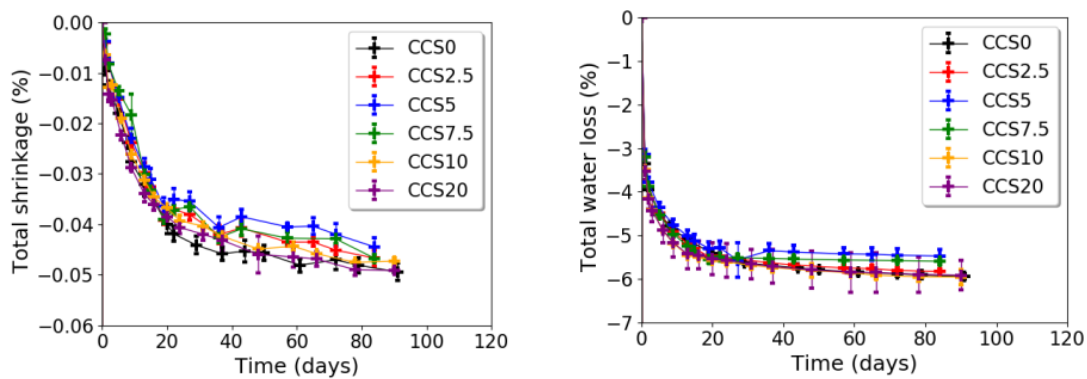


Fig. 4 Total shrinkage (left). Water loss (right).

4 Conclusion

This paper has sought to evaluate the effect of the presence of Corbicula shells in concrete, as ubiquitous shells in the Ile-de-France deposit. These shells are used as a substitute for coarse aggregates with volume rates of 2.5, 5, 7.5, 10 and 20%. Experimental tests performed on Corbicula shell-based concretes show that there is no effect on the physical properties of fresh or hardened concrete, such as slump, density and porosity. The poor quality of the shell-mortar interfacial transition zone (ITZ), seems to be the main factor causing the decrease in compressive strength and the elastic modulus (as the shells used are not soft). The curved shape of the shells promotes water trapping, which increases the porosity of the internal interfacial of the shell and decreases the mechanical properties of the concrete. Regarding to the total shrinkage of the concrete, it is similar for all formulas. This proves that the used shells have comparable mechanical properties to those of conventional coarse aggregates.

Acknowledgements

The authors hereby gratefully acknowledge the financial support received from all SEDIFLUV project partners, the Paris Region, France's Navigable Waterways Authority (VNF/DTBS), and the Clamens and Cerema organizations.

References

- [1] Beddaa, Hamza and Ben Fraj, Amor and Lavergne, Francis and Torrenti, Jean Michel. 2019. Effect of potassium humate as humic substances from river sediments on the rheology, the

- hydration and the strength development of a cement paste. *Cement and Concrete Composites* 104:103400. doi: <https://doi.org/10.1016/j.cemconcomp.2019.103400>
- [2] Beddaa, Hamza and Ouazi, Ilyass and Ben Fraj, Amor and Lavergne, Francis and Torrenti, Jean Michel. 2020. Reuse potential of dredged river sediments in concrete: Effect of sediment variability. *Journal of Cleaner Production*.
- [3] EN12620. 2008. Aggregates for concrete.
- [4] Falade, Funso. 1995. An investigation of periwinkle shells as coarse aggregate in concrete. *Building and Environment* 30:573-577. Doi: [https://doi.org/10.1016/0360-1323\(94\)00057-Y](https://doi.org/10.1016/0360-1323(94)00057-Y)
- [5] Kuo, Wen-Ten and Wang, Her-Yung and Shu, Chun-Ya and Su, De-Sin. 2013. Engineering properties of controlled low- strength materials containing waste oyster shells. *Construction and Building Materials* 46:128-133. doi: <https://doi.org/10.1016/j.conbuildmat.2013.04.020> .
- [6] Martinez-Garcia, Carolina and Gonzalez-Fonteboa, Belén and Martinez-Abella, Fernando and Carro-Lopez, Diego. 2017. Performance of mussel shell as aggregate in plain concrete. *Construction and Building Materials* 139:570-583. doi: <https://doi.org/10.1016/j.conbuildmat.2016.09.091>
- [7] Chakravarthy, Nahushananda and Mutusva, Tatenda. 2015. Investigation of properties of concrete with seashells as a coarse aggregate replacement in concrete. *International Journal of Science and Technology* 1:285-295. URL <https://grdspublishing.org/index.php/matter/article/view/131>
- [8] Nguyen, Dang Hanh and Boutouil, Mohamed and Sebaibi, Nassim and Leleyter, Lydia and Baraud, Fabienne. 2013. Valorization of seashell by-products in pervious concrete pavers. *Construction and Building Materials* 49:151-160. doi: <https://doi.org/10.1016/j.conbuildmat.2013.08.017>.
- [9] Richardson, Alan Elliott and Fuller, Thomas. 2013. Sea shells used as partial aggregate replacement in concrete. *Structural Survey* 31:347-354. doi: <https://doi.org/10.1108/SS-12-2012-0041>.
- [10] Yang, Eun-Ik and Kim, Myung-Yu and Park, Hae-Geun and Yi, Seong-Tae. 2010. Effect of partial replacement of sand with dry oyster shell on the long-term performance of concrete. *Construction and Building Materials* 24: 758-765. doi: <https://doi.org/10.1016/j.conbuildmat.2009.10.032>
- [11] Cuadrado-Rica, Héctor and Sebaibi, Nassim and Boutouil, Mohamed and Boudart, Bertrand. 2016. Properties of ordinary concretes incorporating crushed queen scallop shells. *Materials and Structures* 49:1805-1816. doi: <https://doi.org/10.1617/s11527-015-0613-7>
- [12] Marescaux, Jonathan and Van Doninck, Karine. 2010. New records of Corbicula clams in French rivers. *Aquatic Invasions* 5: 35-39. Doi: <https://doi.org/10.3391/ai.2010.5.S1.009>
- [13] Bouquerel, Jonathan. 2008. Canals: privileged environments for invasive macroinvertebrates. Study of the Nord-Pas-de-Calais region. Study report. Agency of the Artois-Picardy Water and University of Science and Technology of Lille I, digital ecology and ecotoxicology laboratory, 81 pages. URL : [http://consultation.eau-artois-picardie.fr/OAI_Docs/ae-gis/2438/B_22072_\(2.08Mo\).pdf](http://consultation.eau-artois-picardie.fr/OAI_Docs/ae-gis/2438/B_22072_(2.08Mo).pdf)
- [14] Tachet, Henri and Richoux, Philippe and Bournaud, Miche and Usseglio-Polatera, Philippe. 2000. *Freshwater Invertebrates: systematics, biology, ecology*. 588 pages.
- [15] EN1097-6. 2014. Tests for mechanical and physical properties of aggregates - part 6 : determination of particle density and water absorption.
- [16] EN933-3, 2012. Tests for geometrical properties of aggregates - part 3 : determination of particle shape flakiness index.
- [17] EN12350-2, 2012. Testing fresh concrete - part 2 : slump test.
- [18] NF P 18-459. 2010. Concrete - Testing hardened concrete - Testing porosity and density.
- [19] EN12390-3. 2012. Testing hardened concrete - part 3 : compressive strength of test specimens.
- [20] Vargas, P and Restrepo-Baena, Oscar and Tobon, Jorge. 2017. Microstructural analysis of interfacial transition zone (ITZ) and its impact on the compressive strength of lightweight concretes. *Construction and Building Materials* 137:381-389. Doi: <https://doi.org/10.1016/j.conbuildmat.2017.01.101>
- [21] Abu Taqa, Ala G and Abu Al-Rub, Rashid K and Senouci, Ahmed and Al-Nuaimi, Nasser and Bani-Hani, Khaldoun A. 2015. The effect of interfacial transition zone properties on the elastic properties of cementitious nanocomposite materials. *Journal of Nanomaterials*. Doi: <https://doi.org/10.1155/2015/258384>

- [22] Lee, Kwangmyong and Park, Jang-ho. 2008. A numerical model for elastic modulus of concrete considering interfacial transition zone. *Cement and concrete Research* 3: 396-402. Doi : <https://doi.org/10.1016/j.cemconres.2007.09.019>
- [23] Fujiwara, Tadashi. 2008. Effect of aggregates on drying shrinkage of concrete. *Journal of Advanced Concrete Technology* 6: 31-44. doi: <https://doi.org/10.3151/jact.6.31>

Effects of using polypropylene and steel fibres on Ultra High Performance Concrete subjected to elevated temperatures

Ahmed Maher Seyam, Samir Shihada, Rita Nemes

*Department of Construction Materials and Technologies,
Budapest University of Technology and Economics,
Múgyetem rkp 3. Budapest H-1111, Hungary*

Abstract

This research aims to study the effect of using polypropylene and steel fibres, known as cocktail fibres, on fire resistance of Ultra High-Performance Concrete. Three different mixes are prepared to obtain the effect of high temperature for different durations on the strength properties. Samples were heated to 250 °C and 500 °C temperature, for durations 2.5 hours and 5 hours. Two types of tests were carried out for all specimens, i.e., compressive and flexural-tensile strength tests.

Results of the compressive strength tests showed that mixes containing 16% steel fibres and 0.75% polypropylenes fibres, all by mass, improved the fire resistance of the concrete mix by 50% and 150% when the samples were exposed to 250 °C and 500 °C for 2.5 hours respectively, compared with concrete mix without fibres. Moreover, residual compressive strength was improved by 77% and 153% when the samples were exposed to 250°C and 500 °C for 5 hours respectively.

Results of flexural tensile strength tests showed that mixes containing 16% steel fibres and 0.75% polypropylenes fibres, all by mass, improved the fire resistance of the concrete mix by 105% and 61% when the samples were exposed to 250 °C for 2.5 hours and 5 hours respectively, compared with concrete mix without fibres. Moreover, residual flexural tensile strength was improved by 58% at the ambient temperature when mixes containing 16% steel fibres and 0.75% polypropylenes fibre.

1 Introduction

Over the past decades, construction materials have been developed with aims to better performance and improving their properties. Therefore, concrete materials are developed to derive a higher strength and performance than the ordinary concrete, and now we have an ultra-high-performance concrete (UHPC). UHPC is a developed mix that has gained more interest in the concrete construction industry.

Different types of fibres are added to the concrete mixture to improve one or more of its properties. Improvements include reduction of plastic shrinkage, improving resistance to fire and abrasion, and decreasing permeability. Steel fibre reinforced concrete (SFRC) is probably the most investigated fibre reinforced concrete type. Using steel fibres in concrete improves the tensile strength as well as improves the fracture behaviour of concrete to be more ductile [1].

Fibres reinforced concrete with polypropylene (PP) have been widely used in recent years as well. Polypropylene fibres are relatively inexpensive, easy to split into finer sizes, durable in the environment of cement matrix and they did not rust. Based on recent studies, the relative compressive strengths of concretes containing polypropylene fibres were higher than those of concretes without polypropylene fibres. Moreover, PP fibres improves the ductility, reduce the water permeability and the plastic shrinkage [2].

Additionally, researchers have tried to combine steel fibre with other type of fibres to improve different properties of the concrete mixture including the resistance to elevated temperature. Pliya et al., [3] studied the contribution of cocktail of polypropylene and steel fibres in improving the behaviour of high strength concrete subjected to high temperature. Results showed the significant improvement of the residual mechanical properties of concretes containing the cocktail of fibres compared to concretes without fibres [3]. Sideris et al., [4] investigated the performance of thermally damaged fibre reinforced concretes, and they studied effects of adding steel fibres and polypropylene fibres separately and combined. Results concluded that adding steel fibres to the concrete mixes increased the residual strength when it is subjected to temperatures up to 300 °C, yet spalling is still occurred. Such an explosive behaviour was not observed when polypropylene fibres were added in the mixtures [4].

In this research, effects of using steel fibres and polypropylene fibres combined under elevated temperature were studied.

2 Constituent materials & experimental program

2.1. General overview

The laboratory investigation consists of tests for hardened concrete including compressive and flexural strengths tests. The influence of polypropylene fibres “PP” and steel fibres “SF” was studied in order to obtain the optimum percentage for the mix and to reduce the loss in compressive strength due to high temperature by preparing different mixes with different percentages of “PP” and “SF”.

2.2. Characterizations of constituent materials

Constituent materials used in this research included ordinary Portland cement, silica fume, quartz sand, steel fibres and polypropylene fibres. In addition, superplasticizer was used to ensure suitable workability. Proportions of these constituent materials have been chosen carefully in order to optimize the packing density of the mixture.

Cement paste is the binder, holds the aggregate (fine, micron fine) together and reacts with mineral materials in hardened mass. The property of produced mix depends on the quantities and the quality of its constituents. Because cement is the most active component and usually has the greatest unit cost, its selection and proper use is important in obtaining the most economically the balance of properties desired of mixture. The cement used throughout the experiments is ordinary Portland cement (CEM I 52.5 N).

Silica fume with a dry bulk density of 0.65 ± 0.1 kg is used complying with (ACI 548.6R-96) [5] specification. SF is a by-product resulting from the reduction of high-purity quartz with coal or coke and wood chips in an electric arc furnace during the production of silicon metal or ferrosilicon alloys. The silica fume was supplied by SIKA Company.

Aggregate is relatively inexpensive and strong making material for concrete. It is treated customarily as inert filler. The primary concerns of aggregate in mix design for Ultra High Performance Fibre Reinforced Concrete (UHPFRC) are grain size distribution, maximum size and strength. Providing that concrete is workable, the large particles of aggregate are undesirable for producing UHPFRC. The nominal size ranges from 0.15 to 0.6 mm for quartz sand (fine aggregate) which are locally available in Gaza Strip markets.

Polypropylene is a plastic polymer that has been further improved and is now used as short discontinuous fibrillated material for producing fibre reinforced concrete or as a continuous mat for production of thin sheet components. Furthermore, the application of these fibres in construction is increased largely because addition of fibres in concrete improves the tensile strength, flexural strength, toughness, impact strength and also failure mode of concrete. Length of PP fibres is 15 mm, and 0.90 g/cm^3 unit weight with a melting point of $175 \text{ }^\circ\text{C}$. Application of polypropylene fibres provides strength to the concrete while the matrix protects the fibres.

The steel fibres used in mixtures exhibit a high tensile strength and were selected to study the effect of using it in improving fire resistant for the ultra-high performance concrete. Straight stainless-steel fibres have aspect ratio $L/d \approx 65$, tensile strength $\approx 655 \text{ MPa}$, and density is 7.8 g/cm^3 .

The chemical admixture used is superplasticizer which is manufactured to conform to ASTM-C-494 specification types G and F. This plasticizing effect can be used to increase the workability of fresh concrete, extremely powerful water reduction, excellent followability, reduced placing and compacting efforts, reduce energy cost for steam cured precast elements, improve shrinkage and creep behaviour, reduces the rate of carbonation of the concrete and finally improves water impermeability. This type is known as "Sika ViscoCrete -10" [6].

In all trial mixtures, where the w/c was constant, i.e., 0.24. During mixing no segregation was observed and all mixtures were homogenous, and fibres were well distributed through every batch.

2.3. Preparation of UHPFRC

After selection of all needed constituent materials and amounts to be used (mix designs); all materials are weighed properly. Then, mixing with a power-driven tilting revolving drum mixer, started to ensure that all particles are surrounded with cement paste, silica fume and all other materials and fibres should be distributed homogeneously in the concrete mass.

All mixes and tests were conducted in Soil & Materials laboratory at the Islamic University of Gaza, Palestine.

Mixing procedure was carried out according following steps [7]:

1. Placing all dry materials (cement, silica fume, quartz sand, steel fibres and polypropylene fibres) in the mixer pan, and mixing for 2 minutes.
2. Adding 40 % of superplasticizer to the mixing water.
3. Adding water (with 40% of superplasticizer) to the dry materials, slowly for 2 minutes.
4. Waiting 1 minute then adding the remaining superplasticizer to the dry materials for 30 seconds.
5. Continuation of mixing to changes from a dry powder to a thick paste.
6. After final mixing, the mixer is stopped, turned up with its end right down, and the fresh homogeneous concrete is poured into a clean plastic pan.

The casting of all specimens used in this research was completed within 20 minutes after being mixed. All specimens were cast, cured and covered to prevent evaporation, curing duration was being 28 days.

3 Results and discussion

3.1 Introduction

Series of tests were carried out on the concrete specimens to study and evaluate the effects of polypropylene and steel fibres on improving fire resistance of ultra-high performance concrete. All mixtures were subjected to hardened concrete tests in order to be classified as UHPFRC. Some mixing ingredients were fixed and the others were variable. Table (1) summarizes the different mix proportions. The percentage of silica fume, quartz sand, superplasticizer and water was used was the same percentage obtained by (Madhoun A., 2013) [8]:

Table 1: Different mix proportions of UHPFRC by weight of cement

Mix No.	Cement	Silica Fume	Quartz Sand	Super-plasticizer	Steel Fibre	PP Fibre	Water
Mix-1	1.00	15 %	125%	3%	0 %	0%	24%
Mix-2	1.00	15 %	125%	3%	16%	0.75%	24%
Mix-3	1.00	15 %	125%	3%	16%	1.50%	24%

3.2 Hardened properties results

Laboratory tests were conducted to evaluate and study the hardened properties. Results are the density, compressive strength and tensile strength tests. For each concrete mixture, 6 samples were tested under the same condition, so the number given in the below table is average value, staticall methods and CoV was taken in consideration. Mean results for concrete mixtures at several ages are summarized in Table 2 and Figures 1 through 3. These results are the base line in comparing the strength reduction of the samples after being subjected to the heating tests.

Table 2: Compressive and tensile strengths for samples without heating

Mix No.	Density kg/m ³	Compressive strengths MPa			Flexural strengths at 28 days, MPa
		7 days	14 days	28 days	
Mix-1	2335	84.8	109.1	138.2	14.2
Mix-2	2372	113.4	154.6	176.9	22.5
Mix-3	2345	119.7	146.8	171.4	21.7

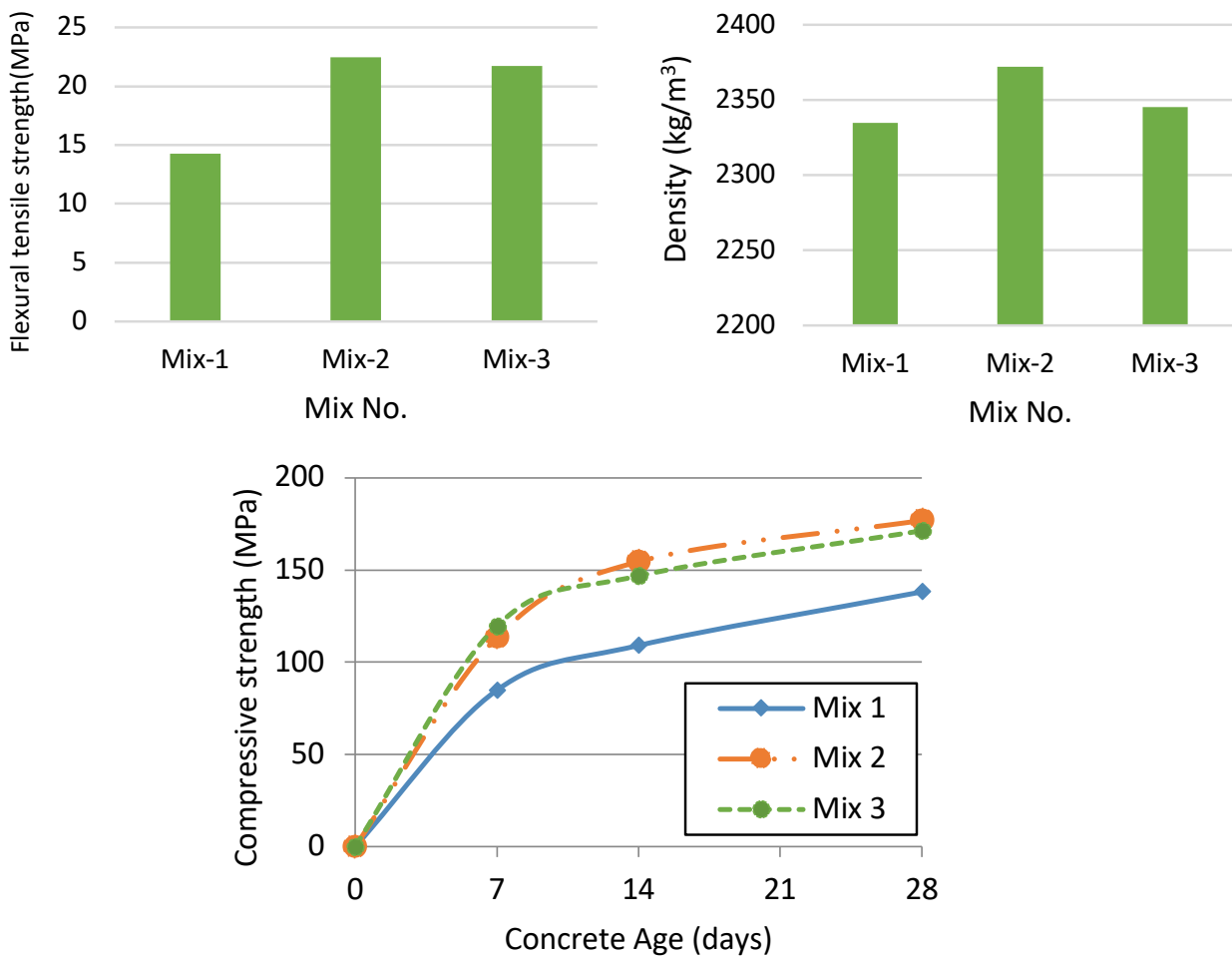


Figure 1: Mean compressive strengths vs. age for unheated samples

Results shown in Table 2 and Figure 1 demonstrate that it is possible to develop UHPC with different polypropylene and steel fibres amounts.

It can be observed that increasing the polypropylene content from 0% to 0.75% and increasing the steel fibres content from 0% to 16% effectively increases the compressive and the flexural tensile strength of concrete. But increasing the polypropylene content from 0.75% to 1.5% when 16% of steel fibres used decreases the compressive strength.

Figure 2: Mean flexural tensile strengths for unheated samples

Figure 3: Mean density for unheated samples

3.2.1 Compressive strength test results of heated samples

Results of the compressive strength tests are shown in Table 3, Figure 4 and Figure 5 for different percentages of polypropylene fibres (0%, 0.75% and 1.5%), different percentages of steel fibres (0% and 16%), different heating temperatures (room temperature, 250 °C and 500 °C) and heating durations (2.5 and 5 hours).

Table 3: Compressive strengths for heated samples

2.5-hour heating					
Mix No.	% of Polypropylene fibres	% of Steel fibres	Average compressive strength, MPa		
			Room temp.	250 °C	500 °C
Mix-1	0.00 %	0 %	138.2	113.3	40.0
Mix-2	0.75 %	16 %	176.9	170.2	102.6
Mix-3	1.50 %	16 %	171.4	166.9	84.0
5-hour heating					
Mix No.	% of Polypropylene fibres	% of Steel fibres	Average compressive strength, MPa		
			Room temp.	250 °C	500 °C
Mix-1	0.00 %	0 %	138.2	92.5	21.8
Mix-2	0.75 %	16 %	176.9	164.5	55.4
Mix-3	1.50 %	16 %	171.4	152.5	46.4

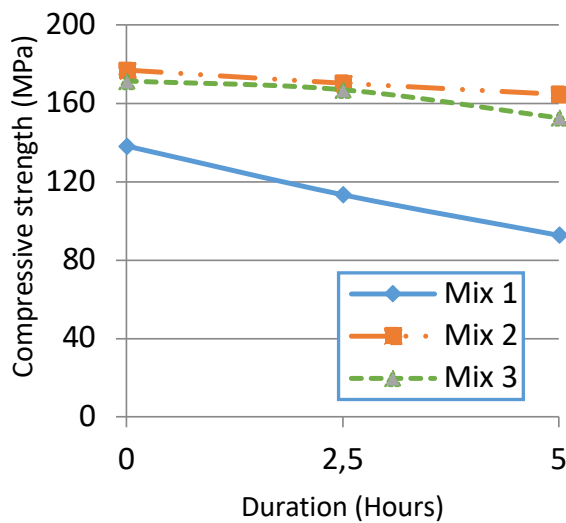


Figure 4: Compressive strength results for samples heated to 250 C°

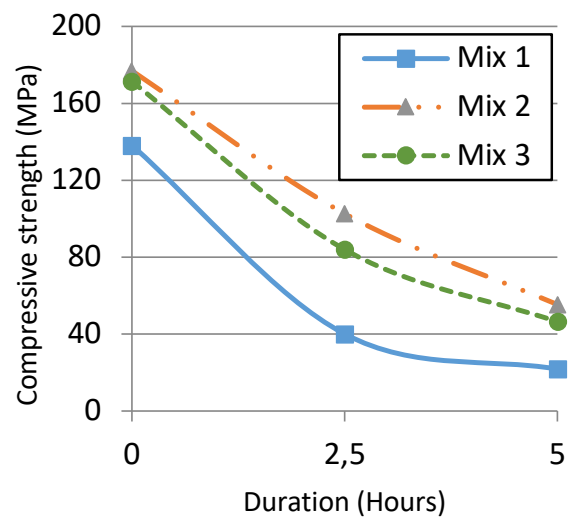


Figure 5: Compressive strength results for samples heated to 500 C°

Table 4: Percentages of reduction in compressive strength with difference % of PP and steel fibres, relative to the control specimens.

Heating to 250 °C					
Mix No.	% of Polypropylene fibres	% of Steel fibres	Percentage of reduction in compressive strength (%)		
			0 hours heating	2.5 hours heating	5 hours heating
Mix-1	0.00%	0 %	0	18	33
Mix-2	0.75%	16 %	0	4	7
Mix-3	1.50%	16 %	0	2	11
Heating to 500 °C					
Mix No.	% of Polypropylene fibres	% of Steel fibres	Percentage of reduction in compressive strength (%)		
			0 hours heating	2.5 hours heating	5 hours heating
Mix-1	0.00%	0 %	0	71	84
Mix-2	0.75%	16 %	0	42	69
Mix-3	1.50%	16 %	0	51	73

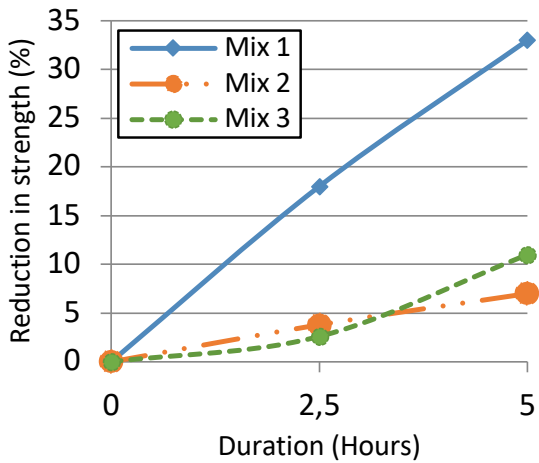


Figure 6: Reduction in compressive strength for samples heated to 250 °C

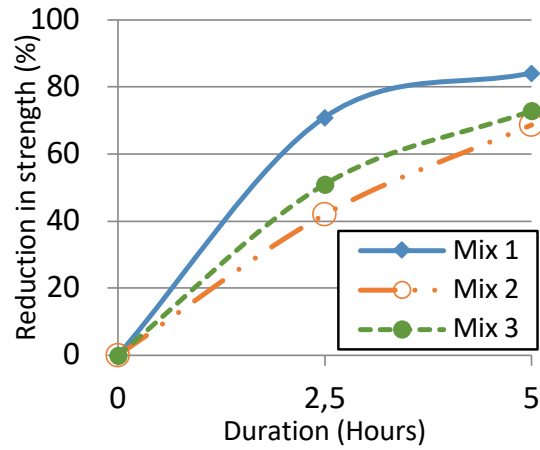


Figure 7: Reduction in compressive strength for samples heated to 500 °C

From Tables 2 through 4 and Figures 2 through 8, it is noticed that for samples without of polypropylene and steel fibres, the reductions in compressive strengths are larger than those with polypropylene. For example, the percentage of strength loss for samples with 0 % polypropylene and 0% steel fibres heated at 250 °C for 5 hours was 33%, and when heated at 500 °C for 5 hours was 84.2%. On the other hand, the loss for samples with 0.75% polypropylene and 16% steel fibres heated at 250 °C for 5 hours was 7% and when heated at 500 °C for 5 hours the loss was 68.7%.

From these results, it is concluded that the addition of polypropylene and steel fibres reduces the loss of concrete strength when it was heated to high temperature. The optimum percentage of polypropylene and steel fibres recommended to be used based on this investigation for improving the concrete resistance against fire is 0.75% and 16% by weight of the cement.

Additionally, it is noticed that polypropylene and steel fibres not only improve the concrete resistance for fire, but also improves its initial strength before heating, as shown in Table 2 and Figure 1. The compressive strength is increased by 28% when using 0.75% PP and 16% SF while increased by 24% when using 1.5% PP and 16% SF. Previous studies confirmed similar findings [9], [3].

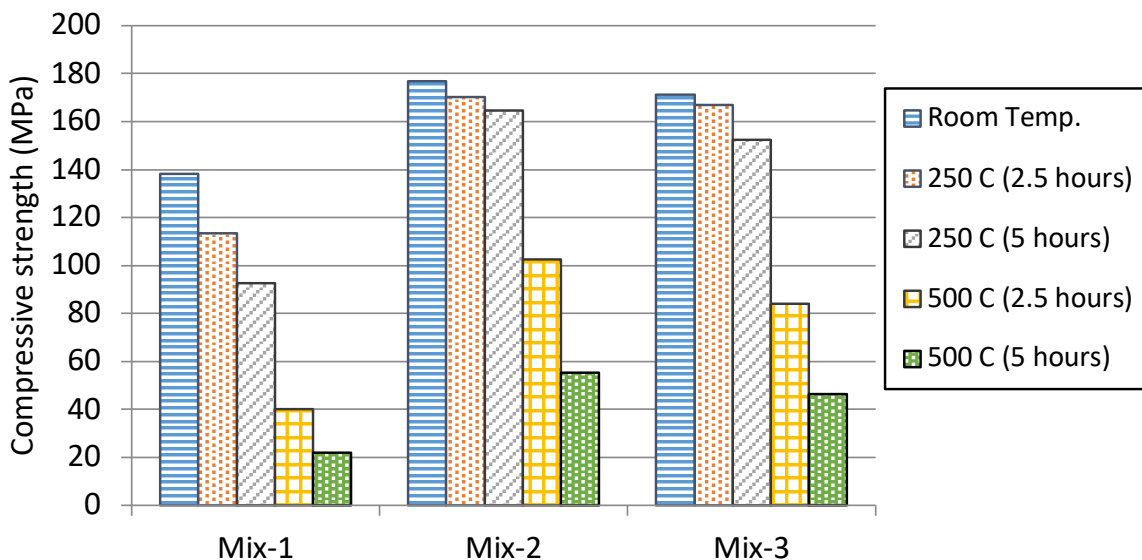


Figure 8: Compressive strength results for heated and unheated samples

3.2.2 Flexural tensile strengths test results after heating tests

Results of the flexural tensile strength tests are shown in Table 5 and Figures 9, for different percentages of polypropylene fibres (0%, 0.75% and 1.5%), different percentages of steel fibres (0% and 16%),

different heating temperatures (Room temperature and 250°C) and heating durations (0, 2.5 and 5 hours).

Table 5: Flexural tensile strength for heated samples

Heating to 250 °C					
Mix No.	% of Polypropylene fibres	% of Steel fibres	Average flexural tensile strength, MPa		
			0 hour	2.5 hours	5 hours
Mix-1	0 %	0 %	14.2	8.9	4.7
Mix-2	0.75 %	16 %	22.5	18.3	7.6
Mix-3	1.50 %	16 %	21.7	14.9	7.2

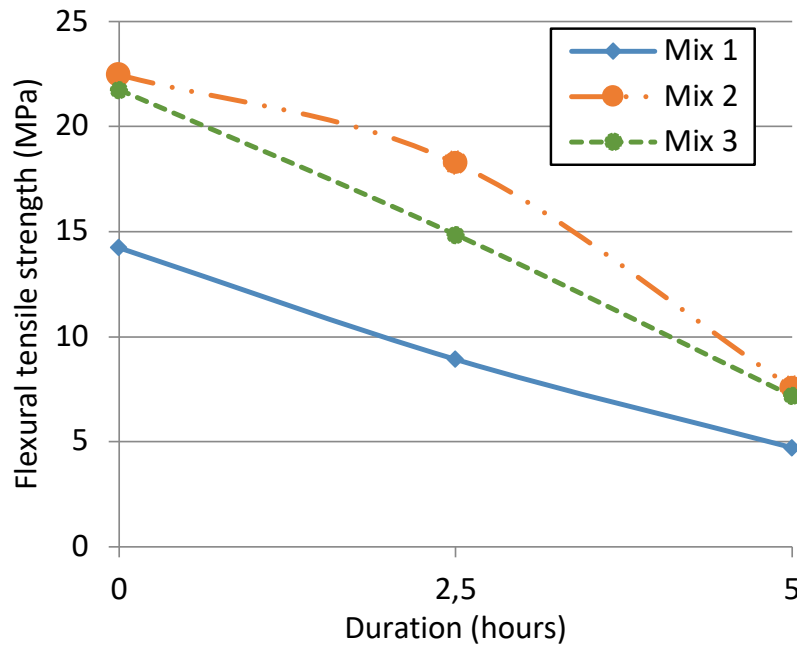


Figure 9: Flexural tensile strength results for samples heated to 250 °C

From Table 5 and Figure 9, it is noticed that for reference samples that does not include polypropylene and steel fibres, the reductions in flexural tensile strengths are larger than those with polypropylene and steel fibres. For example, the percentage of strength losses for samples with 0.0% PP and 0.0% steel fibres heated at 250 °C for 2.5 hours was 37.7 %, and when heated to 5 hours at the same temperature was 66.8%. On the other hand, the loss in tensile strength for samples with 0.75% PP & 16% steel fibres heated at 250 °C for 2.5 hours was 18.69% and when heated at 250 °C for 5 hours the loss was 66.2 %.

3.2.3 Effects of polypropylene and steel fibres on concrete density

Table 2 and Figure 3 summarize the effect of polypropylene and steel fibres on the concrete unit weight. The results show that the density of concrete decreases when increasing the polypropylene fibre percentage in mix, but it increases when the amount of steel fibres increases. Similar results were noticed by previous studies [10] and [7].

4 Conclusion

In this research, specimens of various concrete compositions were made and subjected to different heating periods. Three types of concrete mixtures were formulated without or with polypropylene and/or steel fibres. Concrete mass loss and residual mechanical properties were studied. The following conclusions can be drawn from the experimental results:

- The addition of 0.75 and 1.5% of polypropylene fibre with 16% of steel fibre to the concrete mix increased the compressive and the flexural tensile strength. The compressive strength

values for mix without fibres (Mix 1) were increased by about 28%, 24% when fibres were added as in (Mix 2) and (Mix 3) respectively.

- The residual compressive strength values of fibre reinforced concrete were higher than reference mixture. Comparing with concretes without fibres (Mix 1), reduction of relative residual strength was 33% when it was heated at 250 °C for 5 hours, and when heated at 500 °C for 5 hours, the strength loss was 84.2%. Therefore, adding polypropylene and steel fibres influencing significantly and reducing the strength loss, and the reduction of relative residual strength for (Mix 2) heated at 250 °C for 5 hours was 7% and when heated at 500 °C for 5 hours the loss was 68.7 %.
- Compared with concretes without fibres (Mix 1), it is noticed that the reductions in flexural tensile strengths are larger than those with polypropylene and steel fibres. The percentage of strength losses for (Mix 1) heated at 250 °C for 2.5 hours was 37.7 %, and when heated to 5 hours at the same temperature was 66.8%. On the other hand, the loss tensile strength for (Mix 2) heated at 250 °C for 2.5 hours was 18.69% and when heated at 250 °C for 5 hours the loss was 66.2 %.
- The flexural tensile strength for mix without fibres (Mix 1) was increased by 58% when 0.75% of polypropylene and 16% of steel fibres were used as in (Mix 2).
- By using steel fibres in the concrete mix, the flexural tensile strength values are highly improved to resist high temperatures for 5-hour heating. Optimum percentage of PP and steel fibres recommended to be used based on this investigation for improving the concrete resistance against fire is 0.75% and 16% by volume of the mix (Mix 2).

In short, adding optimum amount of polypropylene and steel fibres on Ultra High Performance Concrete (UHPC) improves the fire resistance properties, by decreasing the rate of compressive and flexural strength loss as well as increasing the time of exposure before occurrence of failure.

5 References

- [1] Bošnjak J., Sharma A. and Grauf. K. 2019. "Mechanical Properties of Concrete with Steel and Polypropylene Fibres at Elevated Temperatures." *Fibers* 2019, 7(2), 9.
- [2] Najimi M., Farahani F.M. and Pourkhorshidi A.R. 2009. " Effects of polypropylene fibers on physical and mechanical properties of concretes." Paper presented at Third International Conference on Concrete and Development, Tehran, Iran, April 27–29.
- [3] Pliya P., Beaucour, A.-L., & Noumowé, A. 2010. "Contribution of cocktail of polypropylene and steel fibres in improving the behaviour of high strength concrete subjected to high temperature." *Construction and Building Materials*, 1926-1934.
- [4] Sideris K., Manita, P., & Chaniotakis, E. 2008. "Performance of thermally damaged fibre reinforced concretes". *Construction and Building Materials*, pp. 1232–1239.
- [5] ACI 548.6R-96 (2003). "GUIDE FOR THE USE OF SILICA FUME IN CONCRETE" ACI MANUAL OF CONCRETE PRACTICE PART 2.
- [6] SIKA Limited. 2019. "SikaViscoCrete-10, product data sheet." Accessed December 19. <https://sikaconcrete.co.uk/wp-content/uploads/2017/06/Sika-ViscoCrete-10-GB-DOP.pdf>.
- [7] Arafa M., Shihada S. and Karmout M. 2010. "Mechanical Properties of Ultra High Performance Concrete Produced in Gaza Strip." *Asian Journal of Materials Science*, 2 (1). pp. 1-12.
- [8] Madhoun AbdUlla 2013. "Mechanical Properties of Ultra High Performance Fiber Reinforced Self Compacting Concrete (UHPFRSCC)." MSc Thesis, Islamic University of Gaza.
- [9] Tai Y. S., Pan H. H., Kung Y. N. 2011. "Mechanical properties of steel fiber reinforced reactive powder concrete following exposure to high temperature reaching 800 °C." *Nuclear Engineering and Design*, Volume 241, pp 2416–2424.
- [10] Shihada Samir. 2011. "Effect of Polypropylene Fibres on Concrete Fire Resistance." *Journal of Civil Engineering and Management*, 17(2), pp. 259–264.

A BOND MODEL OF SYNTHETIC MACRO-FIBRE IN CONCRETE

Mantas Garnevičius, Linas Plioplys, and Viktor Gribniak

Vilnius Gediminas Technical University,
Sauletekio av. 11, Vilnius LT-10223, Lithuania

Abstract

Bond behaviour of a synthetic macro-fibre in concrete is the object of this research. The bond strength and stiffness are the parameters characterising the bonding mechanism that determines the efficiency of the reinforcing material. However, there is no general methodology developed to evaluate these properties. There also exists neither a straightforward procedure to estimate the bond quality of a synthetic macro-fibre nor a reliable numerical model to mimic the bond behaviour of such fibres. In this work, the bond mechanisms of 40 mm long synthetic macro-fibres are investigated using pull-out tests: 32 concrete cubes were made for that purpose. Two types of synthetic macro-fibres available at the market are investigated. In each test sample, three fibres were placed perpendicular to the top surface and two sides; two bonding lengths (10 mm and 20 mm) were considered. A gripping system was developed to protect the fibres from local damage. The obtained load-displacement diagrams demonstrated that mechanical parameters of the bond (strength and deformation modulus) of the “top” fibres are almost 20% weaker than that of the fibres positioned to the side surfaces. Therefore, the results of the “top” fibres were excluded from further analysis. One fibre type was chosen for numerical modelling because of sufficient strength of the fibre material to activate the bond-slip mechanism. A physically non-linear finite element model of the pull-out sample was developed. A bond model was proposed to simulate deformation behaviour of the fibre with the different bonding length.

1 Introduction

The RILEM recommendations TC 162 TDF [1] considers fibre-reinforced concrete (FRC) as ordinary concrete with modified material properties. This approach is acceptable for design, but it does not allow to estimate the fibre interaction mechanisms or to define causes of alteration of mechanical properties of FRC. The absence of research methodology complicates the analysis of fibre efficiency. Variety of shapes, geometry and materials applied for the manufacturing of fibres complicates the issue. Recent publications [2] demonstrated that synthetic fibres could be efficiently used in combination with steel fibres. However, the bond-behaviour of polymeric fibres was not investigated appropriately. Fibre length, concrete strength, the fibre content in concrete, fibre surface shape, the density of the concrete, and maximal size of the aggregates influence the bond performance [3, 4]. It is difficult to determine which of these characteristics or them combination is optimal for providing the most effective bond properties. Thus, the interaction (bond) mechanism of synthetic macro-fibres and concrete is the object of this research. This mechanism is responsible for the residual strength of FRC – the essential property describing the efficiency of the structural application of the fibres. The bond strength and the corresponding deformation modulus define the interaction mechanism. However, there is no universal methodology for evaluating these parameters. The load-deformation diagram is the test outcome. In this study, a pull-out test of a single fibre is applied to investigate the mechanical performance of the bond. Two types of synthetic macro-fibres available at the market are investigated. This study aims to develop a numerical model enabling to predict deformation behaviour of synthetic macro-fibre pulled-out from the concrete.

2 Experimental program

Bond parameters of synthetic fibres and concrete are the research object. As shown in Figs. 1a and 1b, two fibre types (designated as to *Type A* and *Type B*) are considered. The fibres were pulled-out using 100 mm cubes. Eight cubes were produced for each fibre type and embedment length. In total, 32 cubes were prepared. Three fibres (one on the top and two on the opposite sides) were inserted in

each cube (Fig. 1c). To assure a correct position, the fibres were marked as shown in Figs. 1a and 1b. The “side” fibres were positioned and fixed using expanded polystyrene, while the “top” fibre in the specimen was placed manually. All specimens were made in one batch. Proportions of m^3 of concrete are following: 300 kg of cement CEM I 42.5 R, 165 l of water, 100 kg of limestone powder, 787 kg of 0/4 mm sand, and 988 kg of 4/16 mm crushed aggregates; 0.75% (by the cement weight) of the superplasticizer *Mapei Dynamon XTend*. Compressive strength of the 100 mm concrete cubes at 28 day and final 153 day was equal to 39.14 MPa and 46.16 MPa, respectively.

After the curing, the actual length of the unbonded part of a fibre was measured. A plastic sleeve was used for protecting the unbonded part as shown in Fig. 2; the fibre was fixed using steel clamps designed for preventing localization of stresses induced by the gripping system.

The tests were carried out using a 70 kN capacity electromechanical machine. The deformation-control path with the 0.8 mm/min velocity was applied. The load was fixed using a load-cell with 2 kN capacity. As can be observed in Fig. 2, linear variable differential transformers (LVDT) were used for monitoring vertical displacements of the grips. Additional LVDT was used for monitoring vertical displacements of the cube. All devices (LVDT and the load-cell) were connected to personal computer through signal processing equipment ALMEMO 2890-9. The readings were taken every second.

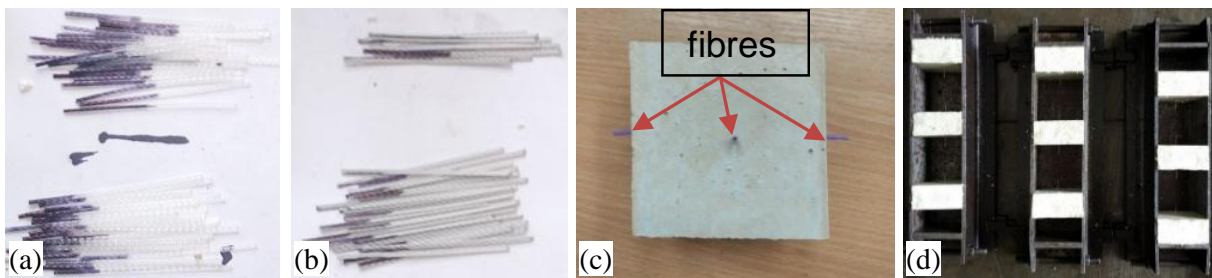


Fig. 1 Fibres highlighting the embedment length and test specimens: fibre Type A (a); fibre Type B (b); a typical cube with embedded fibres (c); forms for production of the specimens (d).

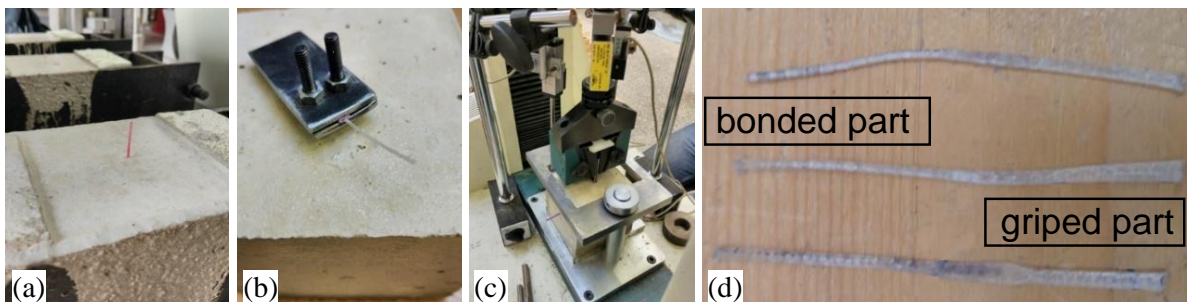


Fig. 2 Pull-out test: fibre protected with a plastic sleeve (a); steel clamps (b); testing machine (c); tested fibre samples (d).

3 Results and discussion

Figure 2d shows characteristic examples of the fibres pulled out the concrete specimens. Three failure types were identified: (I) extrusion (pull-out) of fibre from the concrete (nominal outcome); (II) failure of a fibre (uneven result); (III) damage before the test (uneven result). The latter outcome was mainly related with insufficient bond-strength of the “top” fibres. In all cases, bond characteristics of the fibres installed to the top surface of cubes were noticeably worse than the corresponding properties of the fibres positioned at the side surfaces. The further analysis, therefore, is based only on the test outcomes of the “side” fibres.

Figure 3 shows the load-displacement diagrams of the alternative fibres. A noticeable scatter is characteristic of these diagrams. Variations of the embedment length could be identified as a cause of the scatter though the bond defects could be also mentioned in this regard. A low flexural stiffness of synthetic fibres (concerning steel as the reference) could be mentioned as a cause of the latter defects. Analysis of the diagrams presented in Fig. 3 proves substantial differences in tensile resistance of the considered fibres. The increase of the length l_e (from 1 cm to 2 cm) has also different effect on the bond behaviour of the alternative fibres.

Table 1 summarizes the test results. It specifies the maximum reaction P_{max} and the corresponding displacement u_P ; the total deformation energy δ (evaluated as area beneath the load-displacement curve) and the corresponding displacement u_δ . **Table 1** includes only results of the fibres properly placed in the concrete, i.e. normal to the concrete surface, with minimal discrepancies of the length l_e from the target value, and without evident bond defects. Analysis of the results reveals that the loading capacity (the displacement energy δ) of the *Type A* fibre is almost twice of the *Type B* fibre. The average energy δ released for the length $l_e = 1$ cm is equal to 1077.4 Nmm and 559.2 Nmm; of the length $l_e = 2$ cm, it is equal to 2672.0 Nmm and 1469.7 Nmm, respectively. A similar tendency is characteristic for the ultimate load P_{max} . The test outcomes should be considered in the context of the structural behaviour when the number of the fibres crossing a crack could represent the fibre efficiency. In this context, a 100 g of product approximately contains 6,900 of the *Type B* fibres and only 3,840 of the *Type A* fibres. However, the beneficial mechanical properties of the latter fibre identified in this study might be important for resisting more intensive tensile stresses than the *Type B* counterpart resists. It should be the topic for further research.

Table 1 Summary of the pull-out tests results.

Notation*	P_{max} , N	u_P , mm	δ , Nmm	u_δ , mm
A1.1-1	176	4.90	938.3	10
A1.1-2	198	4.86	1039.5	10
A1.3-1	198	4.48	1175.3	10
A1.3-2	224	4.76	330.8	5.55
A1.4-1	213	5.02	1153.8	10
A1.4-2	190	2.61	1080.2	10
A2.1-1	197	5.79	656.6	7.21
A2.3-1	229	6.56	2651.2	20
A2.4-1	210	7.87	2440.2	20
A2.5-1	240	5.88	886.2	6.30
A2.5-2	220	6.78	2663.5	20
A2.6-1	234	5.90	2933.1	20
A2.6-2	238	8.62	903.6	8.64

Notation*	P_{max} , N	u_P , mm	δ , Nmm	u_δ , mm
B1.3-1	139	3.85	782.1	10
B1.3-2	86	2.46	409.1	10
B1.4-1	109	5.45	578.8	10
B1.4-2	98	3.03	535.3	10
B1.5-1	120	3.91	652.9	10
B1.5-2	71	3.17	644.7	10
B1.6-1	91	4.90	455.6	10
B1.6-2	84	3.69	415.0	10
B2.1-1	119	4.01	372.8	5.25
B2.1-2	141	4.74	267.3	4.95
B2.2-1	152	3.30	965.7	20
B2.2-2	150	3.43	1439.8	20
B2.3-1	178	4.43	2003.6	20

*Notations: the letter designates the fibre type; the first number indicates the embedment length (in cm); the remaining two numbers describe the cube number and the fibre number.

4 Numerical modelling

This section describes the development of a numerical model suitable to predict the deformation response of a synthetic macro-fibre. A commercial finite element (FE) software ATENA [5] is used for this purpose. The load-deformation diagrams shown in Figs. 3a and 3b are modelling objects. The continuous pulling-out behaviour of the *Type A* fibres (i.e. the breakage of fibres was not a characteristic output of the test) substantiates the choice of the modelling object.

Three stages of the deformation behaviour shown in Fig. 3 can be identified following the classification proposed in the referred work [6]:

- Complete bonding – the adhesive contact ensure a perfect connection between the fibre surface and surrounding concrete.
- Bonding failure starts when the pull-out force exceeds the adhesive shear resistance.
- Fibre slip induced by the loss of the adhesive contact; the fibre sliding induces friction forces opposite to the pulling direction.

A strong chemical bond between the concrete and the fibre is formed during the concrete hardening process. It alters the mechanical properties of the concrete around the fibre. This narrow area is called the “transition zone”. The reference [7] limits the area of this zone to about 0.005 mm. This area is too small compared to the fibre diameter. That complicates the development of a detailed model of this zone. Thus, a simplified bond model describes the above process under the assumption of identical parameters of the concrete (independently on that it belongs to the transition zone or not). However, there is no unified methodology to determine the parameters of the bond model [8]. This study employs a trial-and-error approach to model bond behaviour. The model parameters were tailored to represent the test result of the embedment length of 1 cm (Fig. 3a) adequately; the experimen-

tal outcomes of specimens having the 2 cm embedment length (Fig. 3b) were used to verify the developed model. Due to the weakness of the bond, the results of “top” fibres were not used for the analysis.

The 3D NON-LINEAR CEMENTITIOUS 2 USER material model was assumed for the concrete. It is based on the concept of smeared cracks and damage [9]. The fibre was modelled as a perfectly elastic material with a 3.35 GPa elastic modulus and a 0.1 Poisson ratio. These values were taken from the mill-certificate provided by the producer. The above parameters were preserved constant during the adjusting procedure of the model.

The problem is solved in 3D space using the isoparametric tetrahedral elements with four nodes. The element has 12 degrees of freedom and one integration point. The fibre geometry was approximated simplifying the development of the FE model. A rectangular shape replaced the round cross-section of the fibre. The producer specified the 0.9 mm equivalent diameter of the fibre (Fig. 1a). The simplified geometry was calculated to represent the area and perimeter of the fibre identical to the original ones. The 0.25×2.58 mm cross-section was obtained. The 100 mm cube represented the concrete part of the specimen. The 10 mm and 150 mm global size of finite elements with 100 times refinement at the contact interface satisfying the mesh comparability condition were assumed for the fibre and concrete part, respectively. The resultant number of FE was approximately equal to 4000. Figure 4 shows the FE models of different embedment lengths.

The prescribed deformations were applied to the free end of the fibre in a step-wise manner. The 0.25 mm loading step was chosen. Thus, the simulations of 1 cm and 2 cm embedment lengths included 50 and 100 loading steps, correspondingly. The movements of the bottom surface of the specimen (Fig. 4) were fixed in all directions. The solution procedure of the deformation problem employed the Newton-Raphson iteration procedure assuming 40 iterations at each loading step.

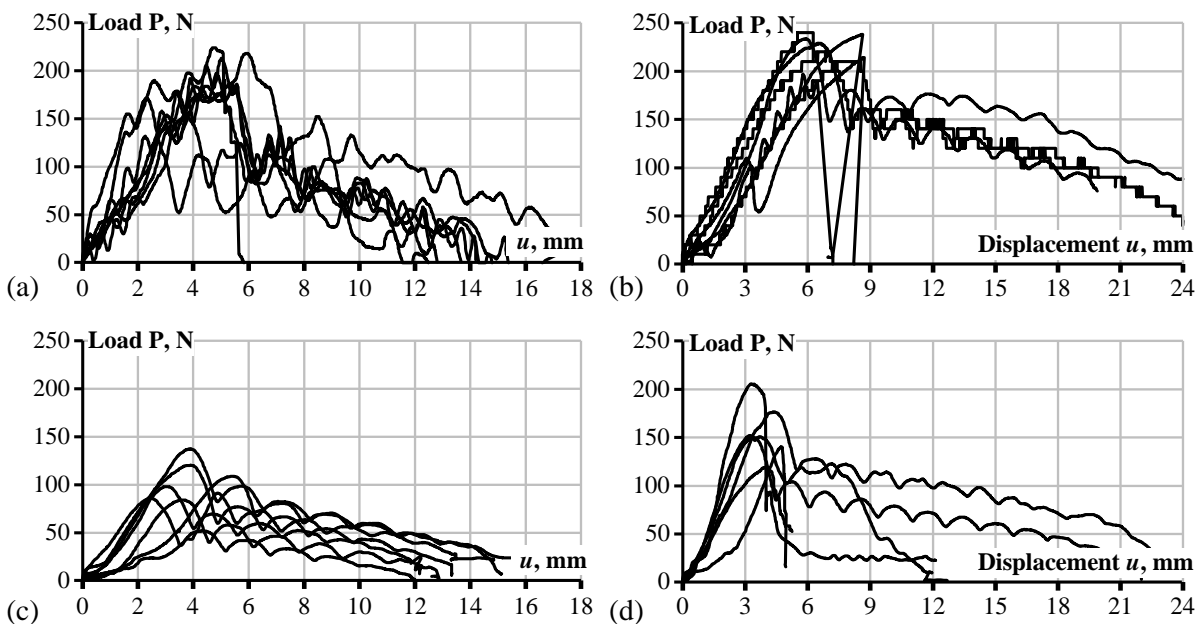


Fig. 3 Load-displacement diagrams of the pull-out tests: (a) and (b) *Type A* fibres with embedment length $l_e = 1$ cm and 2 cm; (c) and (d) *Type B* fibres with $l_e = 1$ cm and 2 cm, respectively.

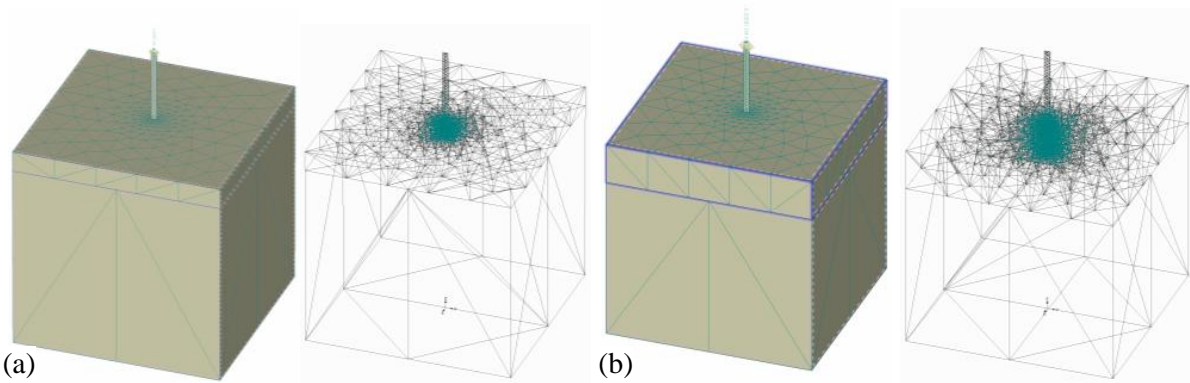


Fig. 4 FE models of different bonding size: (a) 1 cm and (b) 2 cm embedment length.

In ATENA, the term “bond model” is associated with interface behaviour of embedded reinforcing bars represented by 1D finite elements [5]. In this study, the contact between concrete and fibre was modelled by the interface element based on the Coulomb’s friction theory

$$\tau \leq C + \varphi \sigma, \quad (1)$$

where τ is the shear stress limit, C is the cohesion stress (slip threshold), φ is the friction coefficient, σ is the normal compression stress (negative). The parameters K_{nn} and K_{tt} define the interface stiffness in normal and tangential directions in the contact phase. In case of tension, the stress value is limited by the interface tensile strength f_{ib} . The interface contact is lost after exceeding the strength limit. The option “moving interface” was used to simulate the large interface displacements.

The above parameters were tailored to represent adequately the load-deformation diagrams shown in Fig. 3a. Figure 5a shows several initial solutions. The simulations were carried out until the prediction error does not exceed 15%. Figure 5b demonstrates the results. Table 2 lists the accepted parameters of the interface model. The diagrams of the specimens having 2 cm embedment length of the fibres (Fig. 3b) were used to verify the adequacy of the identified parameters of the interface model (Table 2). Figure 6 compares the simulation results of the test specimens with 1 cm and 2 cm bonding lengths.

Table 2 Parameters of the concrete and bond models.

Concrete model		Interface model	
Elastic modulus E_c	33.8 [GPa]	Normal stiffness K_{nn}	1500 [GN/m ³]
Poisson ratio ν	0.2	Tangential stiffness K_{tt}	1500 [GN/m ³]
Compressive strength f_c	33.3 [MPa]	Tensile strength f_{ib}	15.0 [MPa]
Tensile strength f_t	2.77 [MPa]	Cohesion threshold C	7.0 [MPa]
Fracture energy G_f	6.92 [kJ/m]	Friction coefficient	0.20 [-]

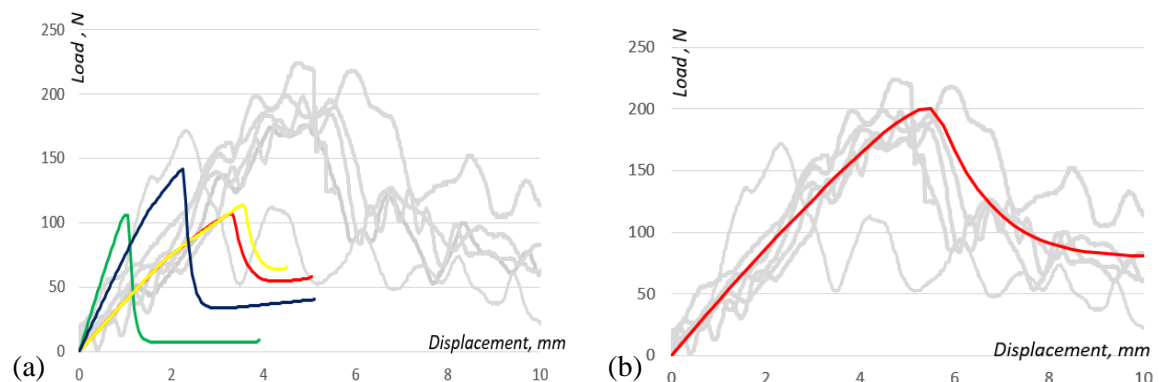


Fig. 5 Load-displacement simulation results of the 1 cm bonding length: (a) initial simulations; (b) the resultant predictions using the model parameters described in Table 2.

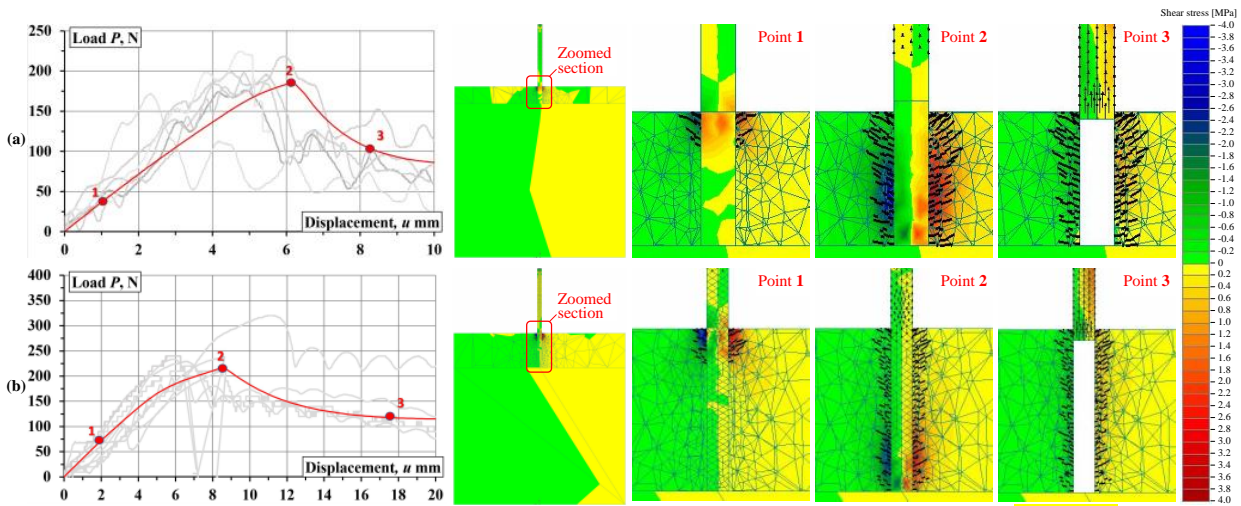


Fig.6 Simulation results (shear stresses) of different bonding lengths using the interface parameters described in Table 2: (a) 1 cm length; (b) 2 cm length.

The load-displacement diagrams presented in Fig. 6 demonstrate adequate prediction results of both bonding lengths. The predicted distributions of the shear stresses correspond to the loading points indicated at the load-displacement diagrams. The areas below the displacement diagrams (the deformation energy) obtained experimentally and simulated numerically were calculated to estimate the prediction adequacy. The experimental and simulated deformation energies of the 1 cm bonding length were correspondingly equal to 1077.4 Nmm and 1118.3 Nmm. That corresponds to the 4% approximation error. The corresponding results of the 2 cm bonded fibre were approximated as 2672.0 Nmm and 2746.3 Nmm that determines the 3% error of the displacement prediction. That well agrees to the 1 cm fibre simulation outcome.

5 Conclusion remarks

Two types of fibres (designated as to *Type A* and *Type B*) available at the market were tested. Two embedment lengths l_e (1 cm and 2 cm) were considered. Eight cube specimens for each fibre length and type were produced. Three fibres were inserted in each cube sample. Load-displacement diagrams were the test outcome. Analysis of the test results reveals that the loading capacity (the displacement energy δ) of the *Type A* fibre is almost twice of the *Type B* fibre. The average energy δ released for the length $l_e = 1$ cm is equal to 1077.4 Nmm and 559.2 Nmm; of the length $l_e = 2$ cm, it is equal to 2672.0 Nmm and 1469.7 Nmm, respectively. Thus, the *Type A* fibre was chosen for the numerical simulation.

A commercial software ATENA was used to simulate the bond behaviour. The trial-and-error technique was used to set parameters of the bond model of the 1 cm embedment length. The 2 cm embedded fibres were used to verify the model. The identified interface contact model was found suitable to represent the deformation behaviour of synthetic macro-fibres. The prediction errors corresponding to the 1 cm and 2 cm simulation results do not exceed 4%.

References

- [1] Vandewalle, L. 2000. "RILEM TC 162 TDF: Test and design methods for steel fibre reinforced concrete." *Materials and Structures* 33:3-5.
- [2] Sivakumar, A., Manu Santhanam. 2007. "A quantitative study on the plastic shrinkage cracking in high strength hybrid fibre reinforced concrete." *Cement & Concrete Composites* 29:575-81.
- [3] Babafemi, Adewumi J., William P. Boshoff. 2017. "Pull-out response of macro synthetic fibre from concrete matrix: Effect of loading rate and embedment length." *Construction and Building Materials* 135:590-99.
- [4] Alberti, M.G., Enfeaque, A., Gálvez, J.C., Ferreras, A. 2016. "Pull-out behaviour and interface critical parameters of polyolefin fibres embedded in mortar and self-compacting concrete matrixes." *Construction and Building Materials* 112:607-22.

-
- [5] Červenka, Vladimír, Libor Jendele, Jan Červenka. 2018. *ATENA Program Documentation, Part 1, Theory*. Prague.
- [6] Breitenbücher R., Meschke G., Song F., Zhan Y. 2014. “Experimental, analytical and numerical analysis of the pullout behaviour of steel fibres considering different fibre types, inclinations and concrete strengths.” *Structural Concrete* 15:126-35.
- [7] Bentur A., Diamond S., Mindess S. 1985. “The microstructure of the steel fibre-cement interface.” *ASCE Journal of Materials Science* 20:3610-20.
- [8] Wang Y., Li V. C, Backer S. 1988. “Modelling of fibre pull-out from a cement matrix.” *International Journal of Cement Composites and Lightweight Concrete* 10:143-49.
- [9] Gribniak V., Cervenka V., Kaklauskas G. 2013. “Deflection prediction of reinforced concrete beams by design codes and computer simulation.” *Engineering Structures* 56:2175–86.
- [10] Gribniak, V.; Jakubovskis R., Rimkus A., Ng P.-L., Hui D. 2018. “Experimental and numerical analysis of strain gradient in tensile concrete prisms reinforced with multiple bars.” *Construction and Building Materials*, 187: 572–583.

Experimental investigation of reinforcement strategies for concrete extrusion 3D printed beams

Lukas Gebhard^{1,*}, Jaime Mata-Falcón¹, Ana Anton², Benjamin Dillenburger² and Walter Kaufmann¹

¹ Institute of Structural Engineering, Department of Civil, Environmental and Geomatic Engineering, ETH Zurich, Switzerland

² Digital Building Technologies, Department of Architecture, ETH Zurich, Switzerland

* Corresponding author

gebhard@ibk.baug.ethz.ch

Abstract

This study investigates the structural behaviour of different reinforcement concepts for extrusion-based 3D concrete printed beams. As longitudinal reinforcement, unbonded post-tensioning and passive bonded reinforcement are explored. As shear reinforcement, fibres and cables placed between the layers of concrete are analysed. The results of four-point bending tests show that unbonded reinforcement leads to highly brittle failure without a proper activation of the shear reinforcement. The beams with conventional bonded reinforcement behave monolithically, with little influence of the concrete layering. Cables, as well as fibres, increase the shear resistance significantly. While cables have higher efficiency, fibres lead to finer and more closely spaced cracks.

1 Introduction

New digital fabrication with concrete (DFC) technologies open up many new possibilities for the construction industry [1]. Among these technologies, Concrete Extrusion 3D Printing (CE3DP) is the most known process, where a robotic system can add concrete in successive layers to reconstruct a digital object. Due to extensive research efforts in this field, technological and material challenges have been overcome to a large extent. However, there is still a lack of consistent reinforcement strategies, which are essential for this technology to have a relevant impact on the construction market. These reinforcement strategies should result in a ductile behaviour of the structural elements, to allow for a plasticity-based design philosophy similar to the actual design of conventionally built structures. This study investigates two reinforcement approaches for the longitudinal reinforcement and two shear reinforcement strategies for 3D printed beams. The experimental campaign consists of four-point bending tests of the beams, which are tracked by digital image correlation (DIC).

2 Reinforcement strategies

Currently, there is a vast interest in the development of reinforcement strategies for DFC. The current state of the art is summarised in [2]. One of the main challenges of these reinforcement strategies is to provide a ductile structural system without, at the same time, hindering the potentials of digital fabrication. Therefore, the authors developed a novel reinforcement strategy where fibres are placed between layers of concrete in an aligned and controlled manner [3, 4] (Fig. 1). Since previous work showed that this reinforcement approach is not suitable as the main reinforcement, this reinforcement strategy is used to provide shear reinforcement. For comparison, steel cables are used as shear reinforcement, which is derived from previous work [5, 6]. For the longitudinal reinforcement, this study investigates the use of post-tensioning or conventional reinforcement, similar as in previous studies [7]. The objective of the combined reinforcement approach consists in activating the cables, as well as the fibres, as shear reinforcement, providing a post-cracking shear resistance once diagonal cracks develop, while the main tensile loads are carried by the longitudinal reinforcement.

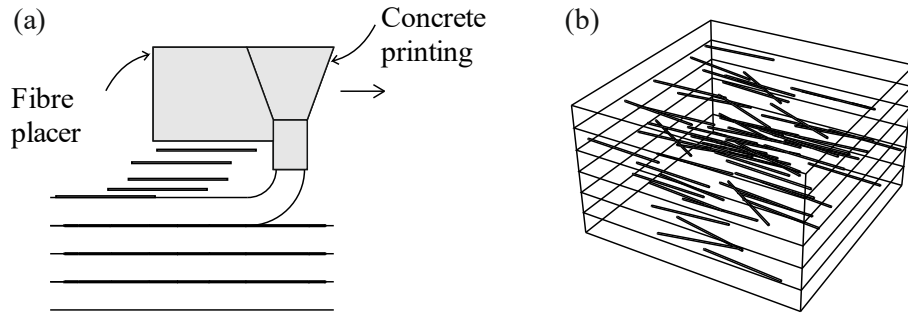


Fig. 1: Schematic sketch of the reinforcement concept for interlayer fibre reinforcement: (a) concrete layers printed by a nozzle with the continuous placement of fibres; (b) resultant layered concrete with aligned fibres in-between the layers [3].

3 Experimental campaign

3.1 Specimens and materials

Two series of beams with different longitudinal reinforcement were produced for this study (see the overview of samples in Table 1). The first series used unbonded post-tensioning (Series 01), and the second series used conventional bond reinforcement (Series 02). Series 01 only used fibres as shear reinforcement, while Series 02 explored fibres and cables as shear reinforcement. A reference beam without shear reinforcement was printed simultaneously to each beam with shear reinforcement. In total, Series 01 consisted of four beams (two with fibre reinforcement and two without) and Series 02 of five beams (one with cable reinforcement, two with fibre reinforcement and two with no shear reinforcement). The geometry of the samples is shown in Fig. 4. The beams from Series 01 had a nominal height (H) of 300 mm, a width (W) of 150 mm and a total length (L) of 1500 mm. The dimensions of Series 02 were slightly larger: H : 320 mm, W : 200 mm and L : 1720 mm. Due to the particularities of CE3DP, the actual printed width (WW , provided in Table 1) differed from the nominal values specified in Fig. 4.

The concrete used in this project was a fine-grained concrete with a maximum aggregate size of 2 mm. The average compressive strength for Series 01, measured at the same age of the tests, was 71.5 MPa (tested on eight cylinders 150x300 mm), and the tensile strength was 2.4 MPa (tested via

Table 1: Overview of samples: Average web width (WW), average prestressing stresses ($\sigma_{c,p}$), shear reinforcement type (SR), nominal shear reinforcement ratio (ρ_{SR}) and age at testing (Age).

Beam Nr.	Series	Codification	Printing session	Glued	WW [mm]	$\sigma_{c,p}$ [MPa]	SR	ρ_{SR} [vol%]	Age [d]
111	01	B-111-NR	11	Yes	45	-9	-	-	28
112	01	B-112-F03	11	Yes	45	-9	Fibres	0.3	31
121	01	B-121-NR	12	Yes	50	-7.5	-	-	29
122	01	B-122-F03	12	Yes	50	-7.5	Fibres	0.3	29
211	02	B-211-NR	21	No	62	-	-	-	28
212	02	B-212-C01	21	No	61	-	Cables	0.1	28
221	02	B-221-NR	22	No	57	-	-	-	28
222	02	B-222-F03	22	No	58	-	Fibres	0.3	28
231	02	B-231-F06	23	Yes	63	-	Fibres	0.6	50

double punch tests on four cylinders 150x150 mm). The same tests were used to assess the compressive strength of Series 02, with 67.5 MPa compressive strength (tested on six cylinders) and 2.3 MPa tensile strength (tested on six cylinders). All tested samples were made from the extruded accelerated concrete. The longitudinal reinforcement for Series 01 consisted of two high strength threaded rods with a diameter of 24 mm (M24 10.9). For Series 02, the conventional passive reinforcement were two B500B steel bars with a diameter of 26 mm and threads at both ends (i.e. bartec technology [8]) to enable anchorage. The cable reinforcement was a high strength steel cable composed of 19 wires, type 1x19 [9], with a nominal cable diameter of 1 mm and an average tensile failure load of 1.3 kN (measured on ten samples). The used fibres for both series are end hooked steel fibres of the type Dramix 3D 65/35 [10].

3.2 Production of the beams

3.2.1 Concrete extrusion 3D printing

The beams were produced by a set-on-demand [11] CE3DP system in the Robotic Fabrication Laboratory of ETH Zürich (Fig. 2.a). The system used two main components: Portland Cement based mortar (PC) and Calcium Aluminate Cement paste accelerator (CAC), which were actively intermixed inside the custom extruder-tool [12]. After extrusion, concrete starts hardening, thus enabling a vertical building rate of up to 3 meters per hour. Two progressive cavity pumps delivered PC and CAC into the extruder-tool, which was mounted on the 6th axis of the robotic manipulator (Fig. 2.b). The entire kinematic system consisted of an ABB 4600 robotic manipulator mounted on a 3-axis Güdel Gantry. Both pumps were manually supplied with materials and digitally controlled through the robotic interface. Motion commands were loaded as procedures into the robotic controller and executed in manual mode to allow human presence in the immediate proximity of the robot.

The beams were always printed vertically in pairs: one containing shear reinforcement and a reference one without reinforcement (Fig. 3.d). The nominal geometry of the beam was sliced with horizontal planes spaced at the layer-height (5 mm). The print path was designed to fabricate the shear reinforced beam and the reference one in a single printing session (i.e. four beam parts for Series 01 which were afterwards glued together into two beams and two full beams for Series 02). The transition from one beam to the next was made in one of the top corners of each section. The print path for Series 02 is shown in Fig. 3.d. The concrete filament width was controlled with the speed of the robot (e.g. for Series 02 a 25 mm layer-width was printed at a speed of 160 mm/s). The cross-section of Series 01 was produced with a single print path, while two adjoining print paths produced the cross-section of Series 02. The technology allows producing hollow sections, which in this study were used for inserting longitudinal reinforcement or left hollow.

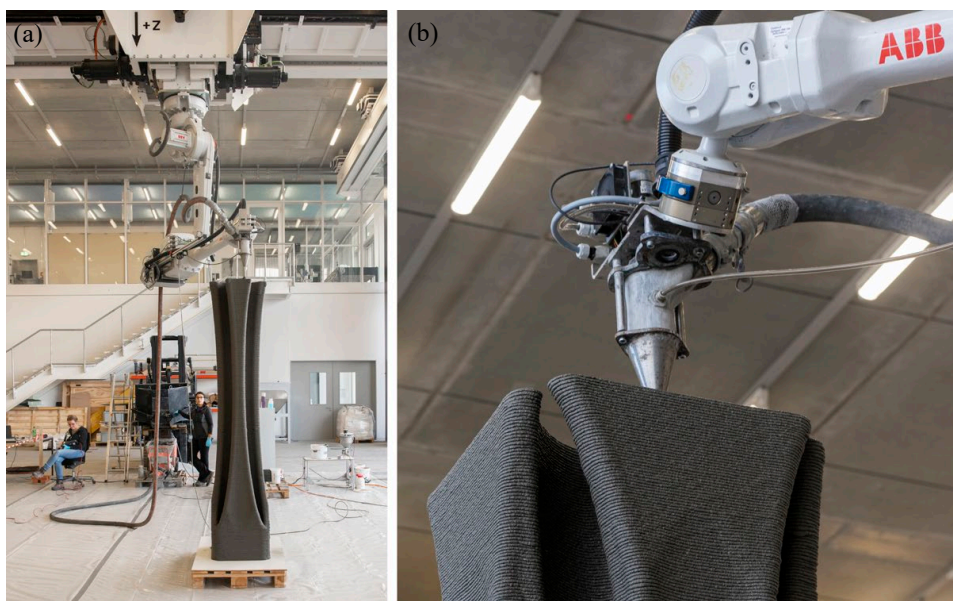


Fig. 2: CE3DP system developed at ETH Zurich, used to fabricate the beams: (a) kinematic system and progressive cavity pumps; (b) extruder tool [Photos by Axel Crettenand].

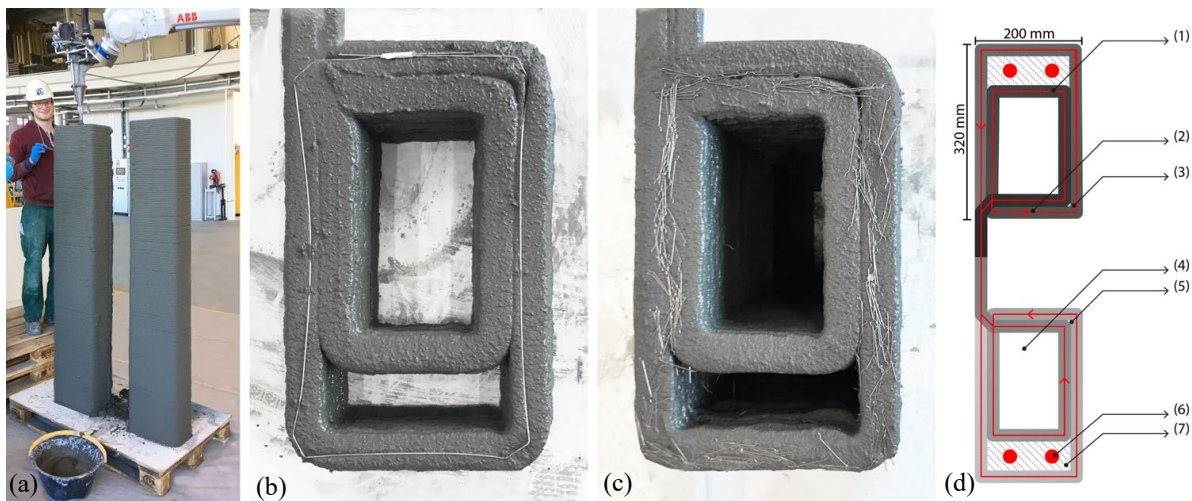


Fig. 3: Production of beams, Series 02: (a) Vertical printing of two beams; (b) cross-section with cable reinforcement; (c) cross-section with fibre reinforcement; (d) print path ((1) filament width 25 mm with gradient colour indicating the material deposition sequence, (2) direction of the print path, (3) beam without shear reinforcement, (4) hollow core of the beam, (5) shear-reinforced beam, (6) post-installed reinforcement, (7) cast concrete).

3.2.2 Placing of shear reinforcement

The two types of shear reinforcement (i.e. cables and fibres) were placed manually in-between the layers of concrete during printing for every second layer. The cables were pre-bent to fit the printing path and had an overlap in the upper flange of the beam of about 10 cm (Fig. 3.b). The total fibre content was determined with respect to the nominal concrete volume of each beam and afterwards subdivided for each interlayer. Due to the variations in the print path width, the final volume fractions deviated from the nominal ones (see Table 1). The fibres were first detached from each other by washing, then weighed to the correct amount, then placed on foils on top of magnetic strips and laid onto the concrete layer. After placing, first, the magnetic strip and afterwards, the foil was removed, leaving only the fibres in an aligned manner on top of the concrete (Fig. 3.c). For Series 01, fibres were only placed in the webs of the beams, whereas for Series 02, fibres and cables were placed all around the cross-section.

3.2.3 Preparation for testing

After hardening, the beam ends were cut to obtain flat surfaces for glueing and for placing the reinforcement anchor plates. For Series 01 two identical pieces were glued together with epoxy to reach the final length. The specimens of Series 02 were printed as one beam, except for Beam 231 which was also glued, assembling one piece without fibres and one with fibres. The side without fibres was externally shear reinforced to provoke failure in the fibre reinforced part. Since the printed surface presented some irregularities, local mortar beds were applied in the load induction and support areas in all cases. Next, the longitudinal reinforcement was placed in the void of the cross-section. As anchorage, a steel plate was used on both ends of the beams. For Series 02, to ensure bond between the reinforcement bars and the surrounding concrete, the void was grouted afterwards with the same concrete mixture used for printing, however, without the use of the accelerator. Series 01 used two prestressing bars for the post-tensioning. Each bar was composed of two rods connected by means of a mechanical anchor at midspan. For Beams 111 and 112, the prestressing force was applied to have a constant compression of 9 MPa across the entire cross-section. For beams 121 and 122, the prestressing was adjusted to a compressive stress of 12 MPa at the bottom and 3 MPa on top. Prestressing forces were controlled by load-cells (see Section 3.3). Before testing, a thin layer of gypsum was applied on one side of the 3D printed concrete to obtain a smooth surface for the application of a speckle pattern for the DIC measurement.

3.3 Test setup and protocol

After preparation, the beams were placed in a loading frame. The loading configuration is shown in Fig. 4. The load was applied by means of a manual hydraulic pump. Series 01 was instrumented with

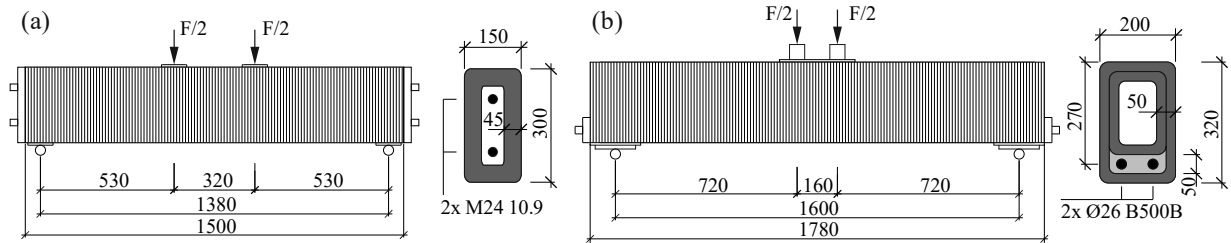


Fig. 4: Test setup and geometry of the specimens (dimensions in mm; cross-sections scaled by a factor of 1.5 compared to the test setup): (a) Series 01; (b) Series 02.

one load cell on each post-tensioning bar and one on each loading cylinder. For Series 02 the load was measured for the single loading cylinder and one of the supports. For both series, the entire surface was tracked with digital image correlation [13–15]. This allows tracking the entire displacement field including the beam's deflections at midspan, which are reported in the following. It is assumed that the thin gypsum layer follows the deformations of the concrete surface it was applied to. The crack pattern was computed from the DIC information by using the Automated Crack Detection and Measurement procedure [16].

4 Results

4.1 Series 01: unbonded post-tensioning reinforcement

Fig. 5 summarises the load-deformation curves for Series 01. Generally, all beams behaved similarly. In the first phase, all beams remained uncracked. After crack formation, the stiffness decreased, and the force could be further increased until the ultimate load was reached. The beam set of Beam 121 and 122 reached a higher ultimate load compared to the other set. This increase might have been due to the preferable initial prestressing state with -12 MPa at the bottom and -3 MPa on top and the larger web thickness. Beam 111 reached the lowest ultimate load and deformation. Both beams with fibre reinforcement showed mainly bending cracks, while the unreinforced beams also displayed significant cracking in the longitudinal direction. For Beam 111, this was likely due to large out of plane deformations. For Beam 121 these longitudinal cracks formed in the area of connection between the two prestressing rods, which might have introduced some lateral pressure into the web. No initiation of shear cracks could be observed in any of the tests. However, all beams experienced longitudinal cracks inside the upper flange (only visible from the top), indicating the necessity of also reinforcing the flanges. For both beam sets, the beam with fibre reinforcement reached a higher ultimate load than the reference specimens without shear reinforcement. All specimens failed in a brittle manner. However, while the beams without shear reinforcement failed in a highly explosive manner, the beams with fibres in the webs failed locally in the compression zone keeping the overall structure intact.

The lack of shear failures and shear cracks for specimens with unbonded longitudinal reinforcement was already reported by Leonhardt and Walther in 1962 [17]. In that study, it was stated that no shear failures could be reached without bond in the longitudinal reinforcement since the load was carried by strut-and-tie action. In this way, high forces can be resisted if the tensile force in the reinforcement can be properly anchored. However, for non-symmetrical loading, this system is problematic and could lead to sudden catastrophic failure, since no ductility can be provided. The influence of having bonded longitudinal reinforcement is assessed in a second test series, whose results are presented in the following.

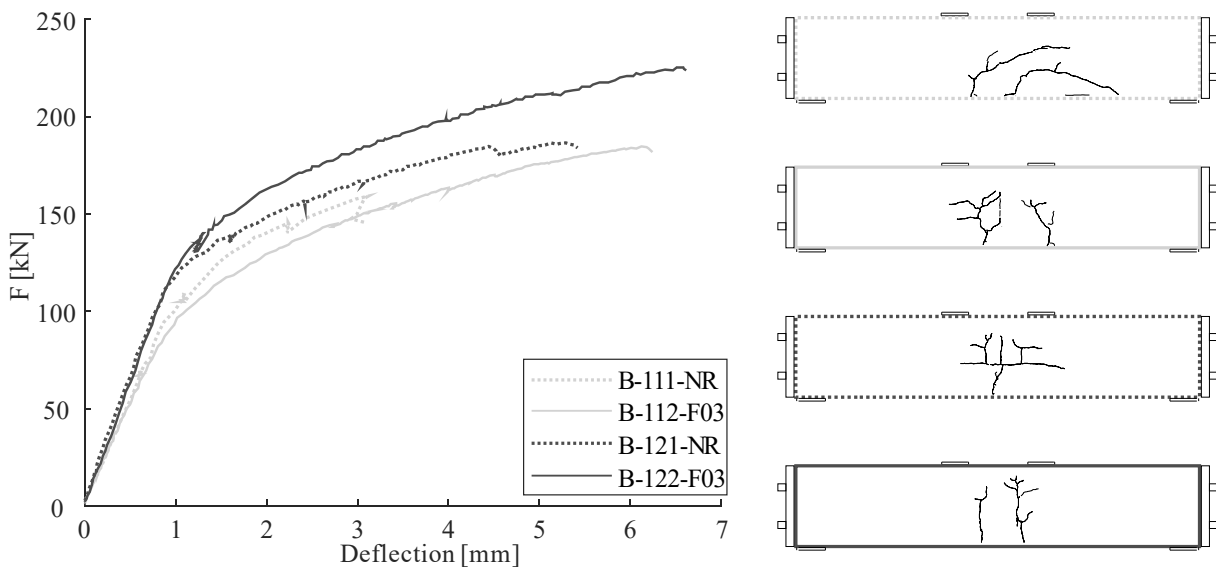


Fig. 5: Load deformation curves and crack patterns right before failure for Series 01.

4.2 Series 02: bonded passive reinforcement

Fig. 6 shows the load-deformation curves and the crack patterns for Series 02. For all beams, shear cracks were observed, and the failure was due to shear (diagonal tension). The two unreinforced beams (dotted lines) showed the lowest ultimate load. In both beams, shear cracks initiated at around 100 kN. While Beam 221 failed upon the formation of shear cracks, in Beam 211 the load could further be increased. This increase was likely due to interlock of the shear crack and the wider web thickness. In both cases, sudden load drops occurred after the first shear cracks formed, and the final failure was highly brittle.

The cable reinforced beam (Beam 212) formed the first shear cracks at a similar load as its reference beam without shear reinforcement, but the load could afterwards be increased to close to 300 kN. At the ultimate load, almost all cables over the length of the dominant shear crack ruptured simultaneously, leading to brittle failure. The rupture of the cables indicates that bond was sufficient to anchor the cables. The beam with 0.3% of fibres (Beam 222) could not reach the same ultimate load as Beam 212, even though the mechanical reinforcement content of the two beams was designed to be similar. After the formation of the first shear cracks, the aligned fibres were able to bridge the crack until they were pulled out at a maximum load of about 220 kN. For Beam 231 the fibre content was doubled. Consequently, the ultimate load could be significantly increased. However, the increase in ultimate load was not proportional to the increase in fibre content. This might have been due to the higher amount of fibres in the same layer resulting in a lower bond or to the presence of additional resistance mechanisms different than the fibre contribution. In both beams with fibre reinforcement, the fibres started to pull out, and at a certain point, the process became unstable, resulting in brittle failure.

As seen in the crack patterns, all specimens developed shear cracks. However, for the beams with fibre reinforcement, the crack spacing was smaller than for the cable reinforced beam. This could be beneficial for applications in which the service limit state is decisive. If the load-bearing capacity is decisive, the cables have higher efficiency, given that they are continuous and can be fully anchored. Contrary to previous work on metal cables as reinforcement, no issues with cable slipping were encountered in the present study [5].

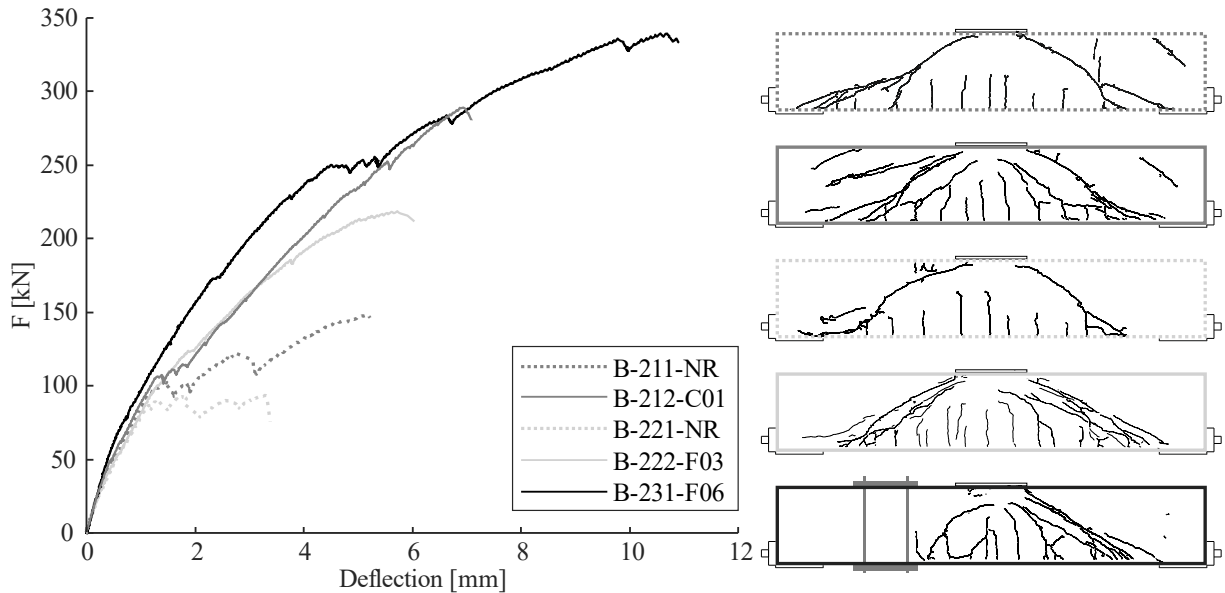


Fig. 6: Load deformation curves and crack patterns right before failure for Series 02.

5 Conclusions

This study presented two different reinforcement strategies for longitudinal reinforcement and two approaches to include shear reinforcement between the layers of printed concrete. The use of prestressing bars without bond as the main reinforcement led, for the studied load configuration, to high ultimate loads. However, since there was no bond between the reinforcement and the concrete, no shear cracks could be initiated, all the deformation was localised in a few bending cracks, and the failure was brittle. In some digitally fabricated structures, this approach is already used, since it allows installing the reinforcement after concrete production and, after prestressing, keeping the concrete in a state of pure compression. When using this reinforcing strategy, the concrete around the post-tensioning bars should be reinforced to avoid a catastrophic collapse in case the concrete is damaged.

In the case of conventional bonded reinforcement as longitudinal reinforcement, the structure behaved monolithically with the reinforcement. This allowed the formation of multiple bending cracks, with smaller crack openings and the formation of shear cracks, which can activate the shear reinforcement if present. This results in a more predictable system with smaller crack openings. However, the use of conventional reinforcement does hinder the geometric freedom of digital fabrication. A higher degree of geometric flexibility might be achieved when using flexible post-tensioning cables, which can be injected afterwards, as explored in this study. Whenever non-straight post-tensioning is used, the resulting deviation forces – which are beneficial for the global load-bearing behaviour if an appropriate tendon layout is chosen, but cause local tensile (splitting) forces – need to be accounted for, which would also require transversal reinforcement. For both longitudinal reinforcement strategies, the layering of the concrete seemed to have no impact on the overall structural behaviour.

Cables, as well as fibres, can be used as interlayer shear reinforcement for layered digital fabrication processes. The results showed that, in both cases, the shear resistance could be increased significantly compared to the samples with no shear reinforcement. While cables showed a higher efficiency, fibres resulted in closer and thinner cracks. The bond in the interlayer is crucial when inserting reinforcement in the interlayers. For cables, this means that the cables should be fully anchored. This can be achieved by changing the direction of the cable or by providing adequate anchorage length. For cables, this bonding issue can be seen as a global issue, while for fibres, it is more of a local problem.

Both shear reinforcements were placed manually during the production of the samples. While the automation of cable placement also for large scale application has already been addressed [18], the automation of the fibre placement still remains a considerable challenge.

Furthermore, it needs to be mentioned that all beams of this study did fail in a brittle manner and did not achieve a sufficiently ductile behaviour in order to conduct a design according to the theory of plasticity. Ensuring ductile failure mechanism in digitally fabricated reinforced concrete structures requires future research efforts.

Acknowledgements

The authors gratefully acknowledge the students Jonathan Ensslin, Moritz Studer, Jean-Luc Imhof and Vanessa Studer for their valuable support during the production, preparation and testing of beams. The authors would also like to express their gratitude to the technical teams of the ‘Structures Lab’, the ‘Robotic Fabrication Lab’ and the ‘Concrete Lab’ at ETH Zurich and also to the Swiss National Science Foundation, which partially funded this work within the National Centre for Competence in Research in Digital Fabrication (project number 51NF40-141853).

References

- [1] Wangler, T., Roussel, N., Bos, F.P., Salet, T.A.M., et al., Digital Concrete: A Review. *Cem. Concr. Res.* 2019, *123*, 105780.
- [2] Asprone, D., Menna, C., Bos, F.P., Salet, T.A.M., et al., Rethinking reinforcement for digital fabrication with concrete. *Cem. Concr. Res.* 2018, *112*, 111–121.
- [3] Gebhard, L., Mata-Falcón, J., Markić, T., Kaufmann, W., Aligned interlayer fibre reinforcement for digital fabrication with concrete, in: *RILEM-Fib X International Symposium on Fibre Reinforced Concrete, BEFIB2020 (Accepted)*, Valencia 2020.
- [4] Gebhard, L., Mata-Falcón, J., Anton, A., Burger, J., et al., Aligned interlayer fibre reinforcement and post-tensioning as a reinforcement strategy for digital fabrication, in: *Digital Concrete 2020 (Accepted)*, Springer International Publishing, Eindhoven 2020.
- [5] Bos, F.P., Ahmed, Z.Y., Jutinov, E.R., Salet, T.A., Experimental Exploration of Metal Cable as Reinforcement in 3D Printed Concrete. *Materials* 2017, *10*, 1314.
- [6] Salet, T.A., Bos, F.P., Wolfs, R.J., Ahmed, Z.Y., 3D concrete printing—a structural engineering perspective, in: *High Tech Concrete: Where Technology and Engineering Meet*, Springer Cham, 2018.
- [7] Bos, F., Wolfs, R., Ahmed, Z., Salet, T., Large Scale Testing of Digitally Fabricated Concrete (DFC) Elements, in: Wangler, T., Flatt, R.J. (Eds.), *First RILEM International Conference on Concrete and Digital Fabrication – Digital Concrete 2018*, Springer International Publishing, 2019, pp. 129–147.
- [8] Debrunner Acifer AG Bewehrungen, Bartec Schraubenverbindungen Dokumentaiton. 2018.
- [9] Jakob AG, Jakob Rope Systems Catalogue Hoisting Lifting C2. 2019.
- [10] Bekaert, Dramix® 3D technical documents. *Bekaert* n.d.
- [11] Gosselin, C., Duballet, R., Roux, Ph., Gaudillière, N., et al., Large-scale 3D printing of ultra-high performance concrete – a new processing route for architects and builders. *Mater. Des.* 2016, *100*, 102–109.
- [12] Anton, A., Bedarf, P., Yoo, A., Reiter, L., et al., Concrete Choreography : Prefabrication of 3D Printed Columns, in: Burry, J., Sabin, J., Sheil, B., Skavara, M. (Eds.), *Fabricate Making Resilient Architecture*, UCL Press, 2020.
- [13] Correlated Solutions, VIC 3D Software, Reference Manual v7. 2014.
- [14] Haefliger, S., Mata-Falcón, J., Kaufmann, W., Application of distributed optical measurements to structural concrete experiments, in: *SMAR 2017 Proceedings*, ETH Zurich, 2017, p. 159.
- [15] Mata-Falcón, J., Haefliger, S., Lee, M., Galkovski, T., et al., Combined application of distributed fibre optical and digital image correlation measurements to structural concrete experiments. *Eng. Struct. J.* 2020, *submitted for publication in 2020*.
- [16] Gehri, N., Mata-Falcón, J., Kaufmann, W., Automated Crack Detection and Measurement based on Digital Image Correlation. *Constr. Build. Mater.* 2020, *submitted for publication in 2020*.
- [17] Leonhardt, F., Walther, R., Schubversuche an einfeldrigen Stahlbetonbalken mit und ohne Schubbewehrung zur Ermittlung der Schubtragfähigkeit und der oberen Schubspannungsgrenze, Deutscher Ausschuss für Stahlbeton, Berlin 1962.
- [18] Salet, T.A.M., Ahmed, Z.Y., Bos, F.P., Laagland, H.L.M., Design of a 3D printed concrete bridge by testing. *Virtual Phys. Prototyp.* 2018, *13*, 222–236.

Influence of constant hygric stress on the load-bearing behaviour of high-performance solid absorber made of high-strength fibre concrete

Martin Kiesche M.Sc, Prof. Dr.-Ing. Matthias Pahn

*Department of Concrete Structure and Structural Design,
Technical University of Kaiserslautern,
Paul-Ehrlich-Straße, 67655 Kaiserslautern, Germany*

Abstract

Thermally activated concrete components, as large-area solid absorber, represent an efficient solution for the generation and supply of heat from renewable energies for buildings. The applications range from the temperature control of interiors, heat recovery via external concrete components to heat storage in the massive supporting structure. The heat-exchanging function in concrete curtain walls is made possible by a system of fluid-carrying pipe registers made of polyethylene (PE) and can provide a thermal output of 80 - 90 W/m² - with a considerable time delay due to the physical properties of the building. A thermally inert system is inefficient for heat generation from fluctuating regenerative energy sources. Disadvantageous for the thermal performance are the concrete cover of the pipe registers, the pipe register made of PE and the given pipe distance. The thermal output can be increased by up to 50 % if the concrete cover of the pipe registers is significantly reduced and the PE pipe register can be dispensed with. Large-area high-performance solid absorber as a filigree concrete curtain wall are thus considered to be a component that is strongly dissolved in its core and additionally subject to hygric stress. So far, no findings are available on this. Thus, the aim is to determine the influence on the load-bearing behaviour of high-performance solid absorber using fibre-reinforced high-performance concrete. To determine the residual stresses from continuous hygric stress, the penetration depth in fibre-reinforced high-performance concrete is determined by permeation. From internal swelling and surface drying, the concrete cross-section is under pressure in the core and under tension at the surface of the facade. The residual stress condition thus affects the bending load-bearing capacity of the high-performance solid absorber. To determine the influence on the load-bearing capacity, 4-point bending tests are carried out on plates.

1 Methodology

Up to now, thermally activated components have been manufactured as a massive concrete component with a fluid-carrying pipe register made of polyethylene (PE) and mainly used as thermal storage [1], [8], [9], [10] und [11]. Due to their thermal inertia, the massive concrete components are considered inefficient for heat generation from fluctuating regenerative energy sources. A filigree curtain wall made of high-performance concrete absorbs regenerative environmental heat via fluid-carrying cavity structures. The filigree design and the large proportion of cavity structures influence the load-bearing behaviour of the curtain wall panels. In addition, the direct contact with the fluid inside the cavity structure results in constant hygric stress, which causes compressive stresses in the cross-sectional core from water pressure and concrete swelling. For high-performance concretes, no knowledge is yet available on swelling strain. The additional stress from internal swelling of the high-performance concrete and surface shrinkage reduces the bending resistance of the component.

In this paper, the water penetration depth in high-strength concrete under pressure is determined in order to draw conclusions about the minimum concrete cover and the swelling area in high-strength concrete. From the swelling area the internal pressure and tensile stresses are calculated with the swelling strains and compared with the experimentally determined bending resistances. The bending resistances are determined in 4-bending tests.

2 Functionality

The high-performance solid absorber is mounted as a curtain wall on a substructure as a single-span beam (acc. Fig. 1 left). The curtain wall is full faced glued to the substructure. The adhesive has sufficient deformability, so that a statically determined position in x and y direction can be assumed. The curtain wall consists of a fibre-reinforced fine-grained concrete. The advantage of the concrete recipe (acc. Table 1) is its high-strength properties, the fine-pored structure and the low shrinkage deformation during setting. The fluid-carrying cavity structures have a diameter (d) of 10 mm and are arranged in the centre of gravity axis of the curtain wall (acc. Fig. 1 right).

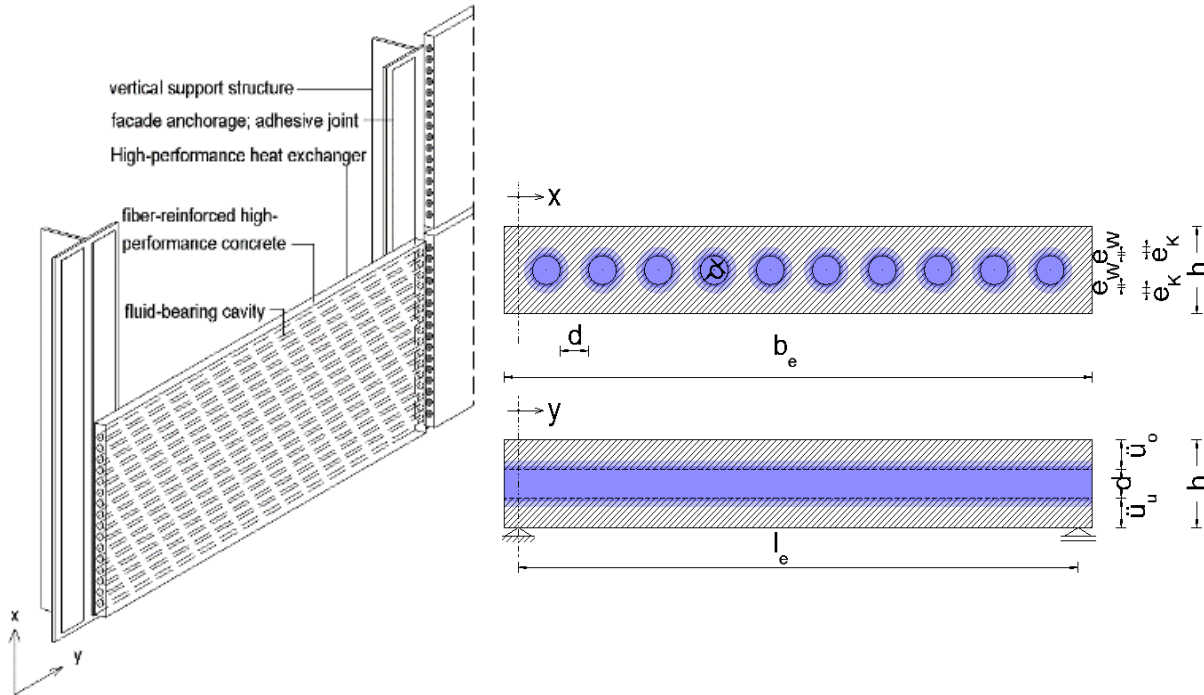


Fig. 1: Schematic view of the high-performance facade absorber (left); cross-section x and y water penetration area (right)

Table 1: Concrete mixture high performance concrete

High-strength fibre concrete	Vol [%]	Density [kg/m ³]	Mass [kg/m ³]
CEM I 42,5 R-HS/NA		3100	500
Metakaolin		500	27.5
Microsit H10		900	222
Quartz flour 1600		1200	167
Silica sand 0/2		1420	875
Basalt chippings 1/3		1650	413
Water		1000	170
Superplasticizer ACE 30		1060	32.5
Anti-crack glass fibres	0.02	2500	0.6
Glass short fibres 24mm	2.00	2500	50

3 Theory

3.1 Derivation of the swelling stresses

The concrete coverings at the top (c_o) and bottom (c_u) ensure the hygric, thermal and mechanical resistance of the curtain wall. The curtain wall is subject to the stresses of wind pressure and wind suction, water pressure and hygric deformations from concrete sources in the core. The hygric stresses create internal stresses in the curtain wall (acc. Fig. 2). Due to the statically determined support, the internal stresses do not lead to any external resulting internal forces. The concrete swelling causes an internal compressive stress ($\sigma_{E,Q}$) in the core of the cross-section, which is cancelled at the edge of the cross-section by an equivalent internal tensile stress ($\sigma_{E,T}$). The integral of the stresses over the section height must therefore be zero. The cross-section edge of the curtain wall is thus permanently under tension during operation.

The residual tensile stresses must be considered as permanent stress in the design. The load-bearing capacity check of the curtain wall is stress based, in the linear-elastic range on the basis of non-reinforced curtain walls [2]. The maximum bending stress of the curtain wall results, regardless of the cracking behaviour of the fibre concrete, when the initial crack is reached. Thus, the bending resistance of the curtain wall can be reduced by the amount of the tensile residual stresses.

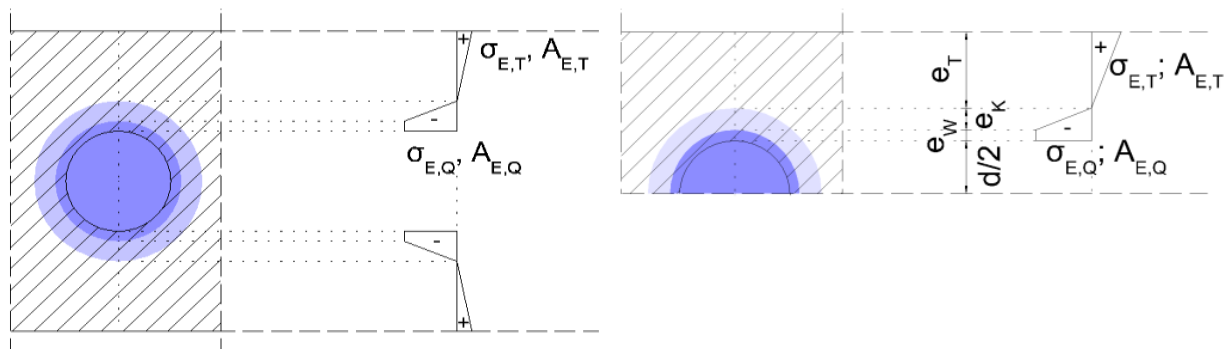


Fig. 2: Internal stress curve from concrete swelling

The inherent compressive stresses ($\sigma_{E,Q}$) result from Hooks' law from the product of the elastic modulus (E_{cm}) of the concrete and the swelling strain (ϵ_Q). Over the penetration depth by permeation (e_W) the internal compressive stress remains constant. The capillary area is connected to the pressurized water area with a capillary penetration depth (e_K). It can be assumed that the moisture content in the capillary area decreases linearly up to the maximum capillary penetration depth. Thus, the internal pressure stresses also decrease linearly up to the residual stress zero point. In order to avoid external internal forces, the area of the internal compressive stresses ($A_{E,Q}$) must be equal to the area of the internal tensile stresses ($A_{E,T}$). To calculate the internal tensile stresses at the cross-section edge, the elastic modulus and the swelling strains of the concrete and the water penetration depths from water pressure and capillary transport must be known. The modulus of elasticity of high-strength fibre-reinforced concrete can be determined using the tests according [3] under compressive loading. Grube [4] has investigated the swelling expansions of hardened cement paste. The swelling strains of a concrete component amount to approx. 20 % of the shrinkage strains. This is independent of the type and mass fraction of the cement in the concrete mix design. Thus, the swelling strains for the high-strength fibre concrete (acc. Table 1) can be calculated from the shrinkage strains. For the penetration depth due to permeation for high-strength fibre concrete, no information is available so far. The high packing density and the low water-cement ratio indicate a penetration depth of less than 25 mm. The penetration depth by permeation can be determined according to the tests of [5]. Due to the low total porosity and the changed pore size distribution in a high-strength fibre concrete, a low capillary water penetration can be assumed, which is to be equated with the water penetration by permeation.

4 Experimental investigations

4.1 Determination of material properties and penetration depth by permeation

4.1.1 Modulus of elasticity

Three cylindrical test specimens with a diameter of 80 mm and a height of 160 mm were produced to determine the modulus of elasticity under compressive stress. The lower and upper test stress was calculated on the basis of the compressive strength. The compressive strength was determined in a preliminary test on prisms of 40 x 40 mm. In three load cycles the strain was recorded with an extensometer. The modulus of elasticity results from the quotient of the difference in tension and the measured strain. The mean value from the partial results is used for further consideration (acc. Table 2).

Table 2: Modulus of elasticity of high strength fibre concrete

Test specimen	σ_u [N/mm ²]	σ_o [N/mm ²]	Elongation [‰]	E- Modulus [N/mm ²]
V1	3.30	23.00	0.448	43973.21
V2	3.20	23.00	0.456	43421.05
V3	3.10	23.00	0.446	44,618.83
		Average value:		<u>44,004.37</u>

4.1.2 Shrinkage deformations

Shrinkage tests are carried out on prism-shaped specimens in accordance with [6]. The shrinkage deformations are recorded in relation to a calibrated plastic zero specimen. The zero specimen provides a constant reference value over the measuring period and compensates for the differences in length of the test specimens caused by the manufacturing process. The shrinkage deformations are recorded at three prisms on pins embedded in the centre of the concrete (acc. Fig. 3 right). The shrinkage deformations over a concrete age of 28 days result in the mean shrinkage deformations (\bar{x}_{ε_s}) of 0.7267 mm/m (acc. Fig. 3 left). According to the investigations of [4], the average swelling of the high-strength fibre concrete amounts to 0.145 mm/m.

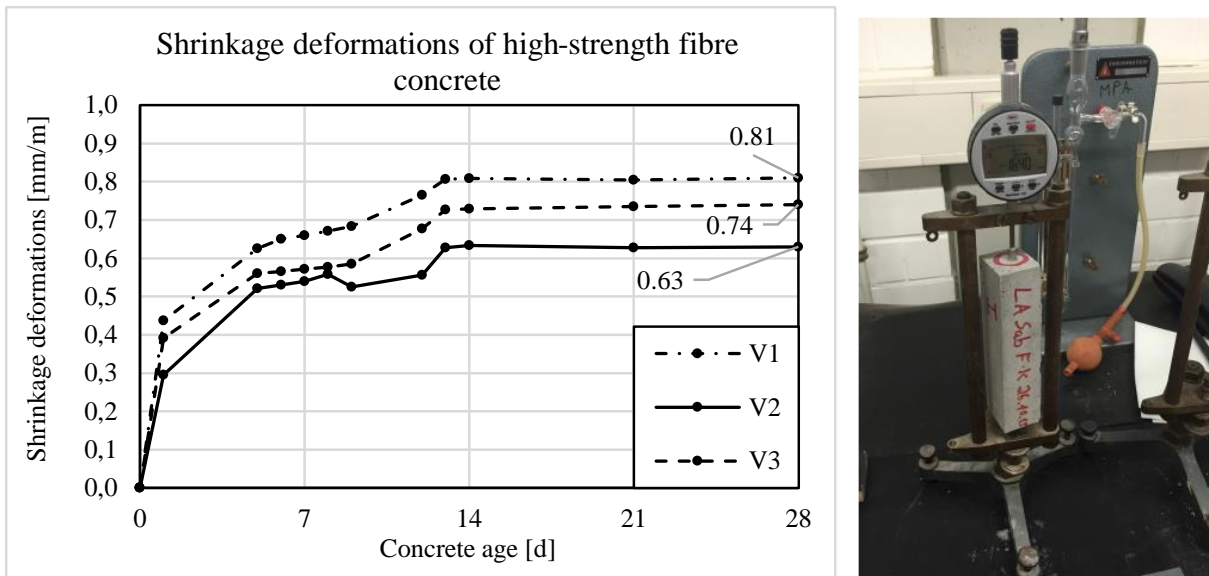


Fig. 3: Shrinkage deformations of high-strength fibre concrete (left); measuring device (right)

4.1.3 Water penetration depth by permeation

The test of water penetration depth by permeation was carried out according to the test standard [5] on three test specimens measuring 200 x 200 x 100 mm. The test surface of the test specimens was roughened by sandblasting after stripping the formwork. The test specimens were clamped in the test device to determine the penetration depth (acc. Fig. 4 left) over a concrete age of 28 days. A water pressure of (5 ± 0.5) bar was set on the test device and maintained for the test procedure of (72 ± 2) hours. After completion of the test procedure, test specimens were removed from the apparatus and immediately split into two halves. At the edge of the bridge, the maximum water penetration depth could be marked by permeation. The tests showed a maximum water penetration depth by permeation (e_W) of 2 mm into the high-strength fibre concrete (acc. Fig. 4 right).

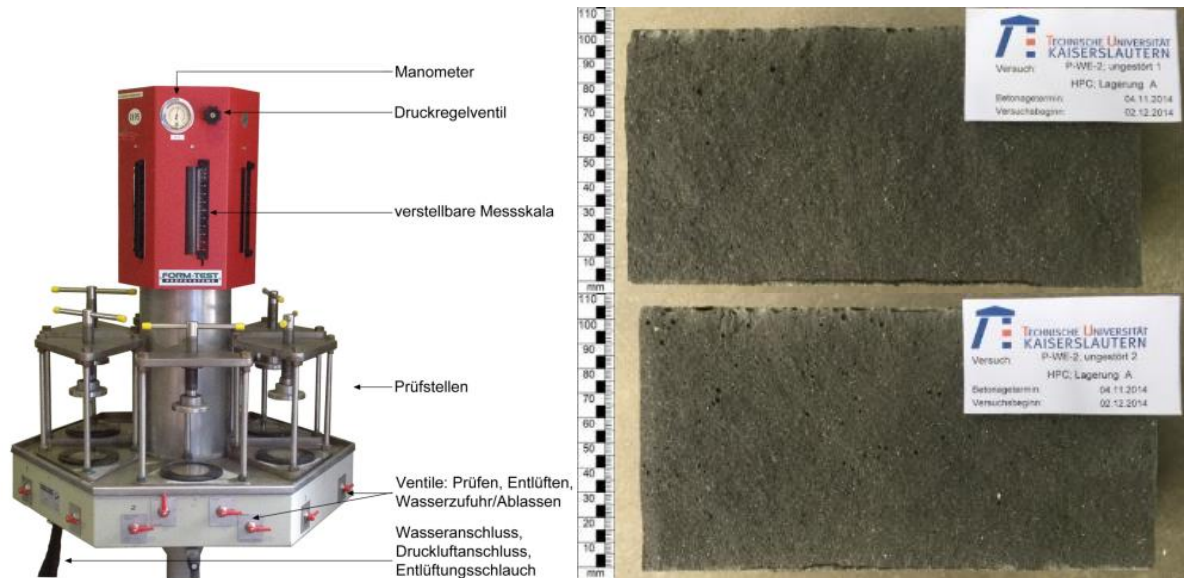


Fig. 4: Testing device for determining the water penetration depth by permeation (left), water penetration depth by permeation (right)

4.2 Investigation of the bending load capacity

To check the bending load-bearing capacity, plates with the dimensions of 700 x 150 x 30 mm were produced. Steel rods with a diameter of 8 mm and surrounding spiral tubes were used to create the cavities (acc. Fig. 5, left). After stripping the formwork, the steel bars and the spiral hoses could be pulled out of the panel (acc. Fig. 5, right).

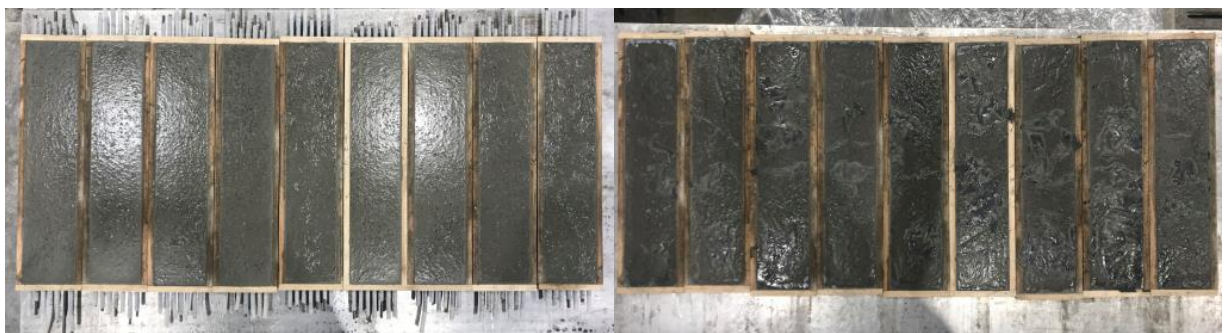


Fig. 5: Test specimen with cavity formwork (left), without cavity formwork (right)

The specimens were stored at $(20 \pm 2)^\circ\text{C}$ for 28 days. After storage, the cavities of three test specimens were filled with water (Wet) for 7 days. The voids of the reference test specimens (Dry) were not filled with water.

Fig. 6 on the right shows the test setup of the 4-point bending test. The force was absorbed under the middle piston via a 20 kN load cell. The displacement transducers on the front and rear side take up the deflection of the test specimen. The deflection was recorded in the centre of gravity of the test specimen. Fig. 6 left shows the average force-deflection behaviour of the dry and the wet test specimens. Both curves show a similar cracking behaviour. After the initial crack, the fibres in the test body absorb and maintain at this plateau until the fibres are completely pulled out. In the linear-elastic range, the curves differ in stiffness and maximum initial cracking force. The initial cracking force decreases by approx. 40 % due to the inherent tensile stresses at the edge of the cross-section caused by swelling of the test specimen interior.

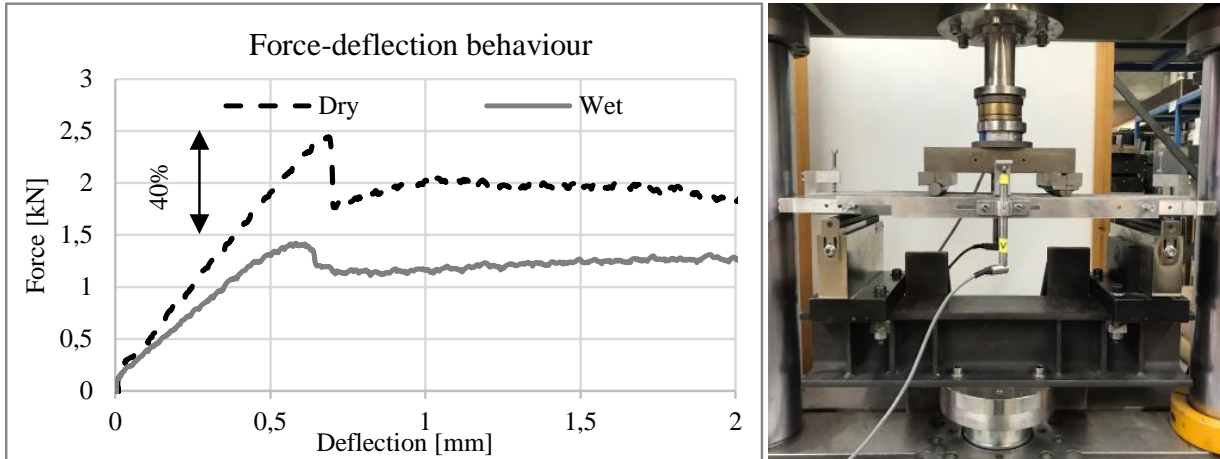


Fig. 6: Comparison of the bending load capacities (left), test setup (right)

5 Evaluation and Results

By determining the material parameters and the water penetration depth by permeation, the inherent tensile stress from the swelling of the cross-sectional core can be calculated with the theoretical considerations and compared with the difference between the initial cracking stresses of the reference test specimens and the wet test specimens.

The residual tensile stresses can be calculated using the following approach: The areas of the internal pressure and internal stress must equalize over the cross-section. It follows that the internal tensile stresses are directly dependent on the quotient of the area of the internal compressive stresses and the dry area of the concrete cover (c_o).

$$\sigma_{E,T} = \frac{A_{E,Q}}{e_T} \quad (1)$$

The area of the inherent compressive stresses can be calculated with the approach shown in Fig. 2 using the inherent compressive stresses from the swelling and the water penetration depths from permeation and capillary suction.

$$A_{E,Q} = e_W * \sigma_{E,Q} + e_K * \frac{\sigma_{E,Q}}{2} \quad (2)$$

$$\sigma_{E,Q} = E_{cm} * \varepsilon_Q \quad (3)$$

The swelling strains reach 20% of the mean shrinkage strains $\bar{x}\varepsilon_S$. With a concrete cover (c_o), a water penetration depth by permeation (e_W) of 2 mm and a water penetration depth by capillary suction (e_K) of 2 mm, inherent tensile stresses of 3.19 N/mm² occur at the cross-section edge. This corresponds to a difference in the bending tensile stresses of 35 %. The calculated difference corresponds approximately to the reduction of 40 % of the bending load capacity from the test results (acc. Fig. 6).

6 Conclusion and outlook

The difference between the calculation and the test results can be traced back to the assumptions made for the source expansions and the water penetration depth from capillary suction. With the calculation approach presented, it is possible to determine the influence of the residual stresses from the hygric stresses on the flexural strength of high-performance solid absorber. Nevertheless, the influence is slightly underestimated, which leads to the design being carried out on the uncertain side. The underestimation can be attributed to the unknown swelling strains and the capillary penetration depth.

The swelling strains and shrinkage strains are mainly controlled by the cement. The correlation of the strains does not depend on the type of cement and the mass fraction. Therefore, it can be assumed that the degree of swelling strains corresponds to the assumptions made and has rather a minor influence on the underestimation of the inherent tensile stresses. In the further course of the research work, the swelling strain of the high-strength concrete will be determined by means of sensor fibres.

A greater influence can be attributed to the water penetration depth from capillary suction. In high-strength concretes, hardly any capillary pores are to be expected due to the high packing density, which greatly reduces the water penetration depth. In the assumptions made, the water penetration (e_W) depth due to capillary suction (e_K) is underestimated, which also leads to an underestimation of the intrusion stresses ($\sigma_{E,T}$) at the edge of the cross-section.

In the further course of the research work, tests based on [7] are planned. In addition to determining the water penetration depth by capillary suction, the aim of the tests is to determine the drying range and draw conclusions about the minimum concrete cover to ensure the serviceability of high-performance solid absorber.

The residual stresses from concrete shrinkage were not considered in the presented model, since the measured shrinkage deformations were predominantly completed after 14 days and the test specimens were stored under identical climatic conditions up to a concrete age of 28 days.

References

- [1] Jastrow, R., Optimierung eines Wärmepumpen-Heizsystems mit Betonabsorbern. Messungen in der Solar-Thermie-Wohnanlage Oberhausen-Rheinhausen und mathematisches Modell, Düsseldorf: VDI Verlag, 1997.
- [2] M. Schultz-Cornelius, Konzept zur Bemessung von unbewehrten Fassadenplatten aus Ultrahochleistungsbeton in mehrschichtigen Stahlbetonwandtafeln, Kaiserslautern: Technische Universität Kaiserslautern, 2020.
- [3] Deutsches Institut für Normung, „Prüfung von Festbeton – Teil 13: Bestimmung des Elastizitätsmoduls unter Druckbelastung,“ Beuth Verlag, Berlin, 2019.
- [4] H. Grube, „Ursachen des Schwindens von Beton und Auswirkungen auf Betonbauteile,“ Bau + Technik, 1991.
- [5] Deutsches Institut für Normung, „Prüfung von Festbeton - Wassereindringtiefe unter Druck,“ Beuth Verlag, Berlin, 2019.
- [6] Deutsches Institut für Normung, „DIN EN 12617-4 Bestimmung des Schwindens und Quellens,“ Beuth Verlag, Berlin, 2002.
- [7] Beddoe, R.; Springenschmidt, R., „Feuchtetransport durch Bauteile aus Beton,“ *Beton- und Stahlbetonbau*, Bd. 94, Heft 4, pp. 158 - 166, 1999.
- [8] Pahn, M.; Bayer, D.; Krumke, S. O.; Caspari, C.; Gauer, T.; Schluppkotten, D. M. et al. (2019): Großdemonstrator - Multifunktionale Betonfertigteile für energetisch nutzbare Gebäudetragsstrukturen. Abschlussbericht. Abschlussbericht Forschungsinitiative Zukunft Bau. Stuttgart: Fraunhofer IRB Verlag (Forschungsinitiative Zukunft Bau, F 3135).
- [9] T. Gauer, M. Pahn, Multifunctional components for the active energetic use of the building envelope, in: 14th Conference on Advanced Building, pp. 715–725.
- [10] Pahn, M.; Caspari, C. (2018): Multifunctional precast elements. In: *BFT-International* 84 (2), S. 32–33.
- [11] Caspari, C.; Pahn, M. (2017): Multifunktionale Betonfertigteile – Großdemonstrator „Small-house IV“. In: O. Kornadt, S. Carrigan, S. Hoffmann, D. Lorenz, M. Pahn und Völker, C. & Vogel, A. (Hg.): Bauphysik in Forschung und Praxis. Bauphysikstage. Kaiserslautern. Universität: Eigenverlag der technischen Universität Kaiserslautern, S. 53–56.

Influence of matrix properties and embedded length on the pull-out behaviour of yarns in cement/calcareous filler matrices

A.C. Slama, J.L. Gallias, B. Fiorio

*L2MGC,
CY Cergy Paris Université,
5 Mail Gay-Lussac, 95000 Neuville-sur-Oise, France*

Abstract

The impregnation mechanism of multifilament yarns by a cementitious matrix, because of the heterogeneity of those materials, is more or less incomplete and random. Since this impregnation defines the mechanical properties of the composite, it must be evaluated and predictable. In this study, we focus on the influence of the matrix properties on the impregnation of the yarn and its link with the mechanical behaviour. By studying the link between the pull-out behaviour and the various matrix properties used to embed the yarn, it was found that it's the fluidity of the matrix that influences the impregnation, leading to a significant improvement of the maximum load for matrices with higher fluidity. The embedded length also has a role on the mechanical properties.

1 Introduction

Short monolithic fibres mixed in mortar are widely used nowadays [1] [2]. However, in textile cement matrix composites, a new technology is growing in the last few decades in research and industrial fields: TRC, textile reinforced concrete [3] [4]. They consist in textile structures made of continuous multifilament yarns (carbon [5], glass [6]...) that are embedded in fine grained and fluid cement matrices [7]. This type of reinforcements has many advantages compared to steel reinforcements (light, flexible, non-corrosive) but a main drawback that is slowing down its development: its impregnation mechanism is very specific and hard to visualize and model [8] [9] [10]. It leads to a difficult prediction of the mechanical properties of this type of composites [11] and so it is mainly used in prefabricated non-structural elements [12]. To generalize its use in other applications, it is necessary to understand its specificity and study the parameters influencing the bond between the multifilament yarn and the matrix. Several studies [13] [14] [15] concluded that the ductility of this type of composite is especially interesting because it leads to better behaviour of the composite, so the link between the matrix and the yarn shouldn't be too strong to keep this ductility. Moreover, this property can be used in masonry, to repair existing damaged structures or to create new one [16] [17]. In the light of those conclusions, our study focuses on the mechanical behaviour of yarn embedded in matrices with low mechanical resistance. To do so, various matrices composed of a mix of cement and calcareous filler presenting different rheological and mechanical properties were used to embed a glass multifilament yarn. The matrices were chosen in order to enable a slippage of the yarn and so a ductile behaviour. Pull-out tests were then performed, on samples with various embedded length of yarn, to evaluate the influence of this parameter on the mechanical behaviour.

2 Material and methods

2.1 Glass multifilament and matrices

The glass multifilament yarn used in this study is a direct roving from Owens Corning range Cem-1 5325. It has a linear weight of 2400 tex, approximately 1600 filaments and a weak sizing. This yarn is chosen because its linear weight is high, which leads to less damage during the manipulation. Furthermore, its weak sizing enables better penetration of the matrix in-between the filaments.

The matrices are inspired by the standard mortar formulation (1 part of cement, 3 parts of standard sand and 0.5 part of water), according to NF EN 196-1 standard. However, to obtain a wide

range of mechanical strength and fluidity, a part of the CEM I 52.5R cement is substituted in volume with calcareous filler and various water to binder ratios (W/B) are used. The workability is measured according to the norm NF P18-452 using a workability meter, the compressive strength according to the norm NF EN 196-1 on 4*4*16 prismatic specimens of mortar without yarn after 28 days of curing under water. Their composition and properties are summed up in Table 1.

Table 1 Matrices composition and properties

Matrix	Binder	W/B ratio (%)	Workability (s)	Compressive strength (MPa)
M50 50F	50% cement + 50% c. filler	50	3	27.0 ± 0.5
M50 70F	30% cement + 70% c. filler	50	4	9.3 ± 0.2
M47 70F	30% cement + 70% c. filler	47	6	10.5 ± 0.2
M45 70F	30% cement + 70% c. filler	45	8	12.7 ± 0.1

2.2 Sample manufacturing and pull-out test

The test samples are manufactured in a 4*4*16 steel mold and composed of a 10 cm free length, L_f ; of yarn and an embedded length, L_e , of yarn in the matrix along the principal axis of the prism. This embedded length is obtained by sawing the 4*4*16 samples, after 27 days of storage in water. Different embedded lengths were tested, varying from 1 to 8 cm. To investigate the mechanical bonding of a multifilament yarn in a mortar, pull-out tests have been performed on an Instron testing machine, at a low speed of 2mm/min. In order to enable the clippage of the end of the free length in the jaw of the testing machine and to prevent shearing of glass filaments, this extremity of the yarn was stuck between two epoxy plates of 2.5*5 cm. This manufacturing process and the pull-out test device are illustrated in Figure 1.

For each sample, the pull-out test is stopped when the displacement reaches the embedded length of the sample.

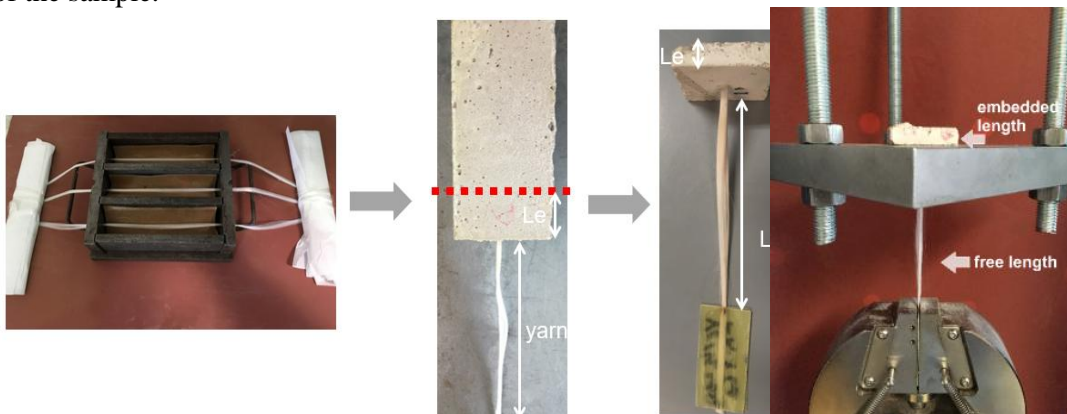


Figure 1 Sample manufacturing process (left) and device for the pull-out test (right)

2.3 Mechanical and physical parameters

After the pull-out test is stopped, the free length is composed of the epoxy plate at one side and the extracted length at the other. In the embedded length, some filaments that failed during the test and were not extracted of the mortar remain, and there is a void left by filaments extracted (visible by the hole left on the sawed surface of the sample, see Figure 2). The extracted mass M_{ext} of yarn for each sample is also measured by cutting the extracted length L_{ext} of yarn from the cement matrix after pull-out test and weighing it (see Figure 2).

On the load/displacement curves obtained from the pull-out test, two mechanical parameters are computed: the maximum load P_{max} and the residual load P_{res} (as shown in Figure 4).

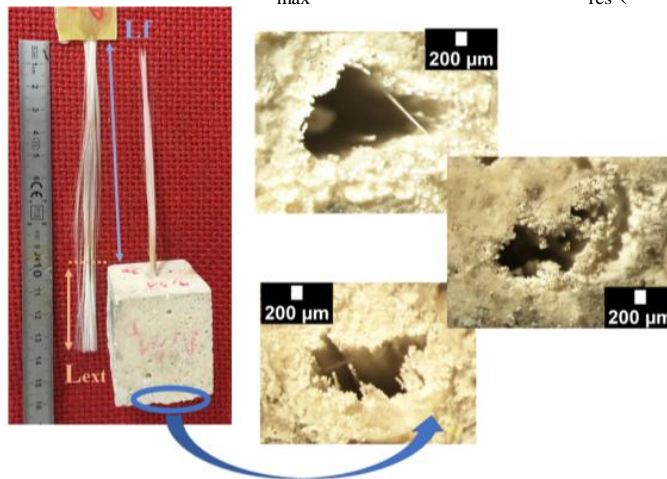


Figure 2 M_{ext} measurements and variety of voids left by extraction found for several samples

3 Results and discussion

3.1 Influence of the embedded length

To study the influence of the embedded length, several samples with the same matrix were sawed at different lengths. The chosen matrix is M50-00 70F. The different embedded lengths tested are 1 cm, 2 cm, 4 cm and 8 cm. Average values of P_{max} and P_{res} is computed for each considered embedded length. Those average values are shown in Figure 3. It is visible that the embedded length has a significant influence both on the P_{max} and P_{res} values. It is because, on a higher embedded length, the number of filaments/matrix bonds is higher, leading to a higher strength to break it and a higher friction value to extract the filaments on a higher length. However, this influence is not proportional to the embedded length. Indeed, for the P_{max} values for $Le=2cm$ and $Le=4cm$ samples, there is no significant difference. Moreover, between sample with $Le=1cm$ and $Le=8cm$, the P_{max} values are only multiplied by approximately 4 and not 8. It enables to conclude that the yarn is not sollicitated equally on its entire embedded length: the load transfer along this length is not efficient because of the incomplete impregnation of the yarn. Therefore, the area at the Le/Lf interface, where the load is applied, has a stronger influence on the maximum load obtained during the pull-out test. Other mechanism might also influence the pull-out maximum load, such as the behaviour and damaged of the free length of yarn, the impregnation of the yarn or the defect during manufacturing of the samples.

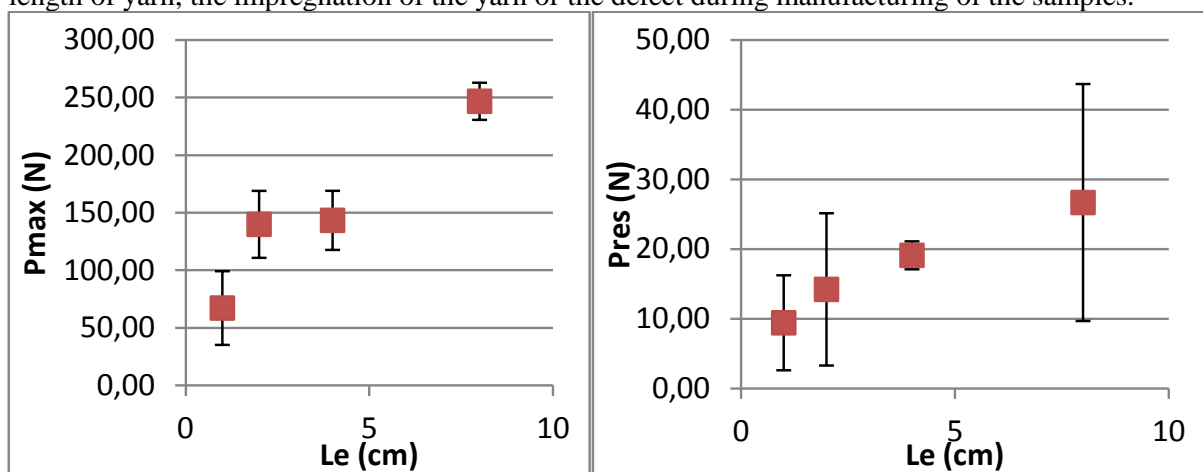


Figure 3 Average P_{max} (left) and P_{res} (right) values matrix M50-00 70F according to the embedded length, scatter based on standard error

3.2 Description of the global pull-out behaviour

Despite a high variability of the results, presented in Table 2, a global pull out mechanical behaviour can be described. First, an ascendant slope is encountered, which constituted the pre-peak phase. It corresponds to first the tensioning of the filaments and their alignment and then the beginning of the weakest filaments and filaments/matrix bonds failures. Then, P_{max} is reached and, after, successive debonding and/or breaking of the filaments leads to a soft descendant branch during the post-peak phase. When the displacement is high enough, the post-peak phase reaches an inflexion point, that characterises the residual load P_{res} . This point marks the beginning of the post-peak residual phase governed by filaments slippage along the embedded length. This last phase ends at a displacement equal to L_e . It is visible on the load/displacement curve in Figure 4.

Some samples also exhibit no filaments sliding and extraction, all the filaments fails during the pull-out test. The samples with this behaviour are in minority in the case of matrices with calcareous filler, and they are due to a high damage of the the free length of those samples, so they are excluded from this study.

During the test, it was observed that the sliding at the extremity of the embedded length begins approximately when the maximum load is reached, so the filaments sliding and extraction has an influence on the P_{max} and P_{res} values. However, when P_{max} and P_{res} are studied, they are not linked (except that they both depends of L_e). It is because P_{max} values seem to be more linked to filaments' own strength and failure and filaments/matrix bond's strength, whereas P_{res} values seems to be influenced by other mechanisms, such as matrix/filaments friction and the presence of small part of matrix that are detached and prevent the filament extraction, leading to a higher value of the residual phase.

Those hypotheses are confirmed by the study of the link between the mechanical parameters P_{max} and P_{res} and the extracted mass M_{ext} . A study for all the samples with matrix M50 70F is conducted. Because it was established that L_e has a significant influence on P_{max} and P_{res} values, the samples are distinguished according to their embedded length.

In Figure 5, it is visible that, if all the samples for each embedded are considered, there is a link between M_{ext}/L_e and P_{max} values. For samples with higher quantity of filaments extracted, the maximum load is superior, except for samples with $L_e=4$ cm. It indicates that the extracted filaments can be: filaments that were not impregnated by the matrix, and their participation in the load bearing is weak, but also filaments that were impregnated by the matrix, and since the matrix has a weak strength and the filament/matrix bond is weak, this bond is inferior to the filament strength and more filaments get detached from the matrix and are extracted. It is this phenomenon that leads to a higher maximum load value for a higher extracted mass of filaments.

Concerning the residual phase, this study is shown in Figure 6. It is visible that M_{ext}/L_e is also linked to P_{res} values. The P_{res} values are globally superior for superior M_{ext}/L_e , which indicates that more filaments extracted lead to more friction between the filaments and the matrix during extraction and explains those higher P_{res} values.

Table 2 Results of the pull-out tests

Matrix	L_e (cm)	Number of samples	Average P_{max} (N)	Average P_{res} (N)
M50 50F	2	3	121 ± 38	14 ± 3
M50 70F	1	6	67 ± 32	9 ± 7
	2	5	129 ± 26	10 ± 4
	4	4	143 ± 26	19 ± 2
	8	3	247 ± 16	27 ± 17
M47 70F	2	6	96 ± 35	11 ± 5
	4	4	147 ± 25	19 ± 1
M45 70F	4	6	139 ± 29	15 ± 4

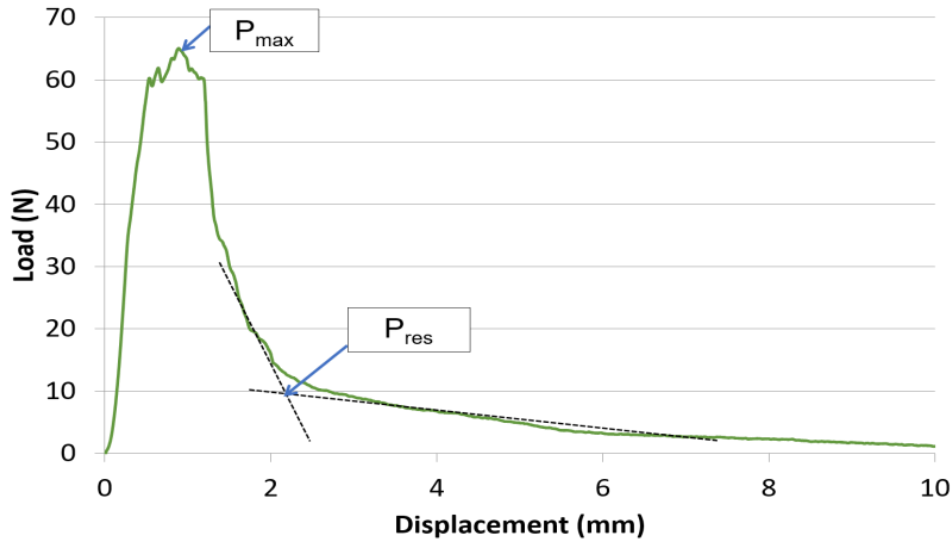


Figure 4 Example of a load/displacement curve from a pull-out test and mechanical parameters

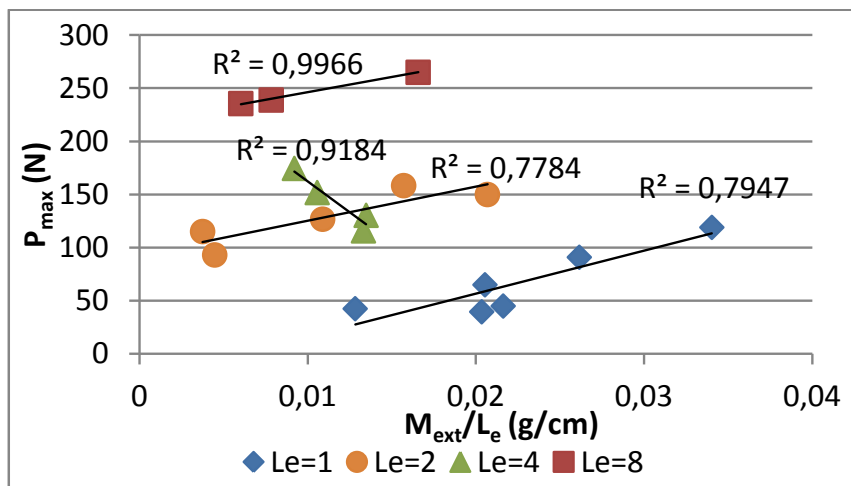


Figure 5 P_{max} according to M_{ext}/L_e for each sample of M50 70F matrix, different L_e

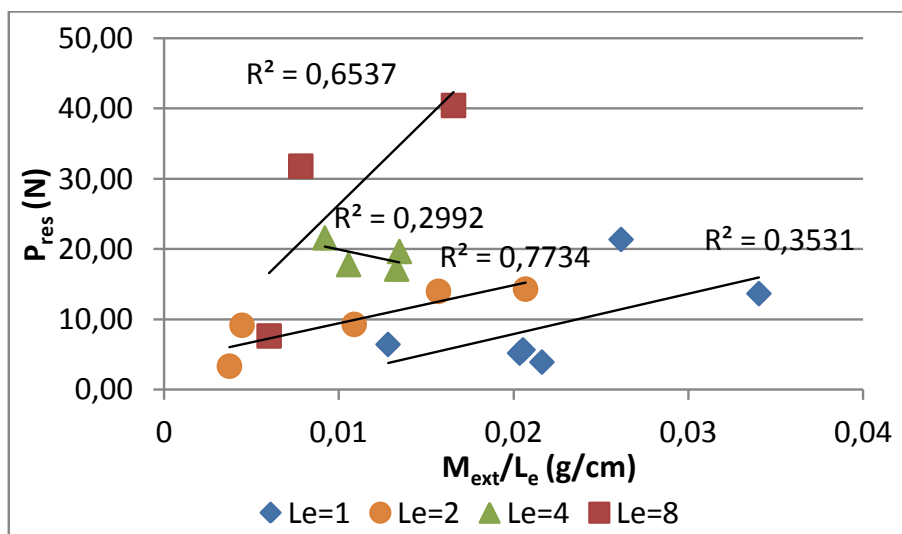


Figure 6 P_{res} according to M_{ext}/L_e for each sample of M50 70F matrix, different L_e

4 Influence of the matrix properties

To study the influence of the matrix properties on the pull-out mechanical results, it is necessary to divide the values of the mechanical parameters by the embedded for each sample, because it has been established that L_e has a significant influence on those values, even if they are not directly proportional to L_e . This division must be done to be able to compare all the samples.

4.1 Influence of the mechanical properties

To evaluate the influence of the mechanical properties of the matrix on the pull-out results, matrix with 50% of calcareous filler (compressive strength around 30 MPa) are compared to matrices with 70% of filler (compressive strength around 10 MPa). The results, presented in Table 2 and Figure 7, shows that the values of the mechanical parameters of the pull-out test are not influenced by the mechanical properties of the matrix for those matrices with calcareous filler and compressive strength inferior to 30 MPa. It means that the maximum load and the residual phase are not linked to the matrix density, so this density doesn't influence the failure or slippage mechanism of the filaments. The bond and the filaments strengths are the parameters influencing those phenomena.

However, M_{ext}/L_e is linked to the compressive strength of the matrix, a higher compressive strength leading to fewer M_{ext} as it can be seen in Figure 8. It can be explained by two factors: the matrix with lower compressive strength is detached easier and more particles of this matrix are extracted with the filaments, leading to higher M_{ext}/L_e values, or a matrix with higher density can block more the filaments extraction and it explains the lower M_{ext} values. However, this phenomenon seems to have no significant influence on the maximum load and residual phase, so it can be concluded that the filament extraction is not a direct influencing factor for those mechanical parameters.

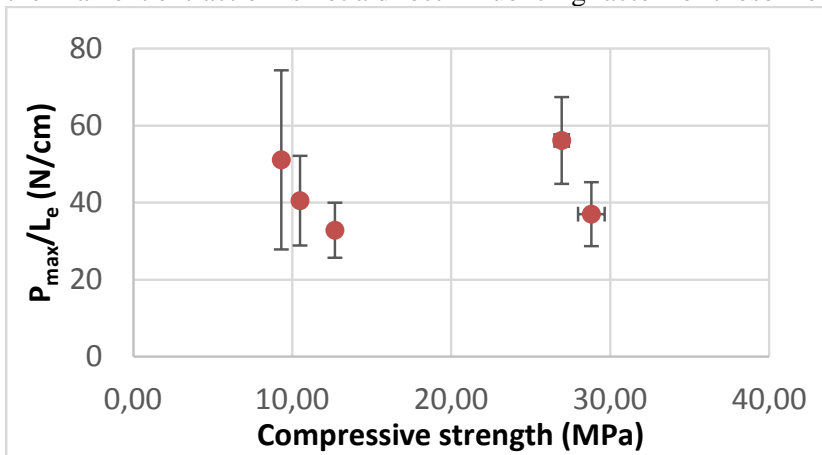


Figure 7 Average P_{max}/L_e values of pull-out samples according to the compressive strength of the matrix, scatter based on standard error

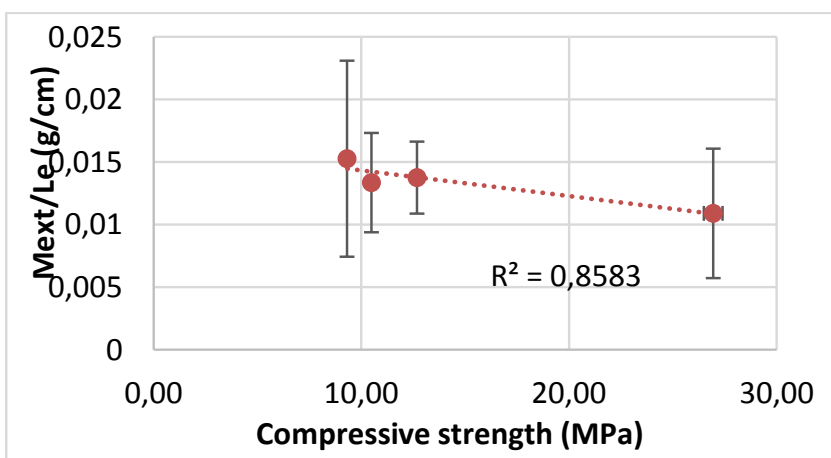


Figure 8 Average M_{ext}/L_e values of pull-out samples according to the compressive strength of the matrix, scatter based on standard error

4.2 Influence of the workability

According to several studies [18], increasing the workability of the matrix has a beneficial effect on the mechanical properties of the resulting composite. In fact, it was shown that the bond between the filaments of the multifilament yarn and the matrix is a crucial point for the mechanical properties of the composite [19] [20]. To increase this bond, specific mortars were manufactured, they are fine grained concrete with high fluidity thanks to high quantity of superplasticizer. The fluidity was also modified using fly ashes, which also enables to reduce the alkalinity of the mortar and avoid yarn chemical damages because of this alkalinity.

In the case of the present study, workability was varied by using different W/B ratios: W/B=0.50, W/B=0.47 and W/B=0.45. Thanks to this, the workability ranges from 3 sec to 10 sec approximately. As it has been shown in section 4.1, the mechanical properties of the matrices have no influence on the pull-out results, so all the matrix can be compared according to their workability, regardless of their different mechanical strengths.

It is visible in Figure 9 that a higher fluidity leads to higher average P_{\max}/L_e values for the considered matrices. It can be explained by the fact that, as it was concluded in the previous section with the study of the extracted mass of filaments, the P_{\max} values are mainly linked to the filaments/matrix debonding, and a higher fluidity leads to better impregnation, so a higher strength of the filaments/matrix bond (especially leading to more anchor points for each filament).

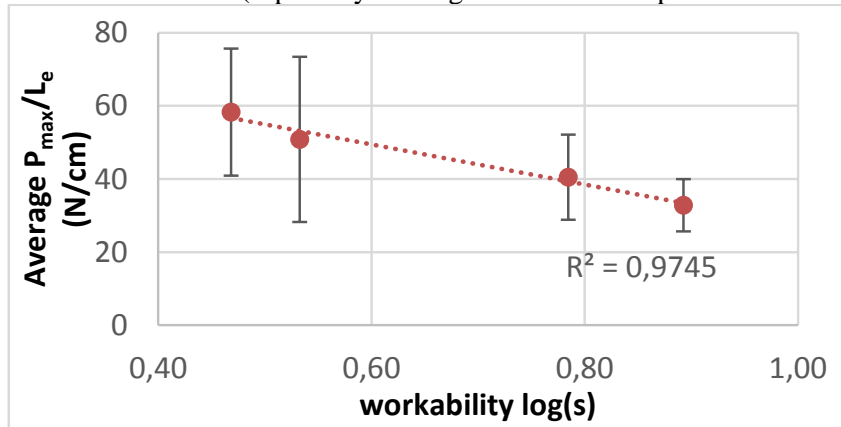


Figure 9 Average P_{\max}/L_e values of pull-out samples according to the workability of the matrix, scatter based on standard error

5 Conclusion

By studying the different mechanical parameters computed on the pull-out curve, and the quantity of filaments extracted during the pull-out test, it is possible to describe the pull-out behaviour of this composite and to understand the mechanism influencing each phase of it.

The pull-out behaviour can be divided in two phases: the first phase includes the pre-peak, peak and post-peak phase, and corresponds to the tensioning of the filaments, their elongation and their successive failure. It is linked to the filaments' organisation in the yarn, the filaments' own mechanical behaviour and the filaments/matrix bonds. This conclusion is reinforced by the fact that the maximum load at the peak is proportional to the extracted mass of filaments, which means that filaments debonding and failure are the main mechanism occurring during this phase. This phase is also linked to the rheological properties of the matrix, and a higher fluidity leads to a better yarn impregnation, so a higher filaments/matrix bonds strength, and a higher maximum load for the pull-out test.

The residual phase is governed by other mechanisms. L_{ext} is equal to L_e , even for the highest embedded lengths. It means that, for several filaments, debonding occurred all along the embedded length and the bond strength between those filaments and the matrix is inferior to the tensile strength of the filaments. However, since the maximum load is not linked to the residual load, computed at the beginning of the residual phase, it means that this debonding mechanism has no influence on the residual phase. The residual load values are mainly linked to the friction between the filaments and the matrix during the filaments' extraction.

For those matrices with cement and calcareous filler, the mechanical properties of the matrices don't have a significant influence on any of the phases of the curve. It is the rheological properties of

the matrix and the embedded length of the samples that are the key factors to explain the maximum load and residual load values for all the samples.

6 References

- [1] R. Figueiro, *Fibrous and Composite Materials for Civil Engineering Applications*, Elsevier, 2011.
- [2] P. Bartos, Review paper: Bond in fibre reinforced cements and concretes, *International Journal of Cement Composites and Lightweight Concrete*. 3 (1981) 159–177. [https://doi.org/10.1016/0262-5075\(81\)90049-X](https://doi.org/10.1016/0262-5075(81)90049-X).
- [3] A. Naaman, Textile Reinforced Cement Composites: Competitive Status and Research Directions, in: *International RILEM Conference on Material Science*, RILEM Publications SARL, 2010: pp. 3–22.
- [4] T. Triantafillou, *Textile Fibre Composites in Civil Engineering*, Woodhead Publishing, 2016.
- [5] A. Badanoiu, J. Holmgren, Cementitious composites reinforced with continuous carbon fibres for strengthening of concrete structures, *Cement and Concrete Composites*. 25 (2003) 387–394. [https://doi.org/10.1016/S0958-9465\(02\)00054-9](https://doi.org/10.1016/S0958-9465(02)00054-9).
- [6] V. Laws, A.A. Langley, J.M. West, The glass fibre/cement bond, *J Mater Sci*. 21 (1986) 289–296. <https://doi.org/10.1007/BF01144734>.
- [7] T. Brockmann, W. Brameshuber, *Mechanical and fracture mechanical properties of fine grained concrete for textile reinforced composites*, Mainz, 2006.
- [8] J. Hegger, N. Will, 8 - Textile-reinforced concrete: Design models, in: T. Triantafillou (Ed.), *Textile Fibre Composites in Civil Engineering*, Woodhead Publishing, 2016: pp. 189–207. <https://doi.org/10.1016/B978-1-78242-446-8.00009-4>.
- [9] B. Banholzer, T. Brockmann, W. Brameshuber, Material and bonding characteristics for dimensioning and modelling of textile reinforced concrete (TRC) elements, *Materials and Structures*. 39 (2006) 749–763. <https://doi.org/10.1617/s11527-006-9140-x>.
- [10] R. Chudoba, M. Konrad, M. Mombartz, M. Vorechovský, K. Meskouris, Multiscale modeling of textile reinforced concrete within a consistent modeling framework, in: Salzburg, Austria, 2005.
- [11] J. Hegger, N. Will, O. Bruckermann, S. Voss, Load-bearing behaviour and simulation of textile reinforced concrete, *Mater Struct*. 39 (2006) 765–776. <https://doi.org/10.1617/s11527-005-9039-y>.
- [12] C.G. Papanicolaou, 10 - Applications of textile-reinforced concrete in the precast industry, in: T. Triantafillou (Ed.), *Textile Fibre Composites in Civil Engineering*, Woodhead Publishing, 2016: pp. 227–244. <https://doi.org/10.1016/B978-1-78242-446-8.00011-2>.
- [13] M. Butler, V. Mechtcherine, S. Hempel, Experimental investigations on the durability of fibre–matrix interfaces in textile-reinforced concrete, *Cement and Concrete Composites*. 31 (2009) 221–231. <https://doi.org/10.1016/j.cemconcomp.2009.02.005>.
- [14] M. Butler, V. Mechtcherine, S. Hempel, Durability of textile reinforced concrete made with AR glass fibre: effect of the matrix composition, *Mater Struct*. 43 (2010) 1351–1368. <https://doi.org/10.1617/s11527-010-9586-8>.
- [15] Z. Cohen, A. Peled, Controlled telescopic reinforcement system of fabric–cement composites — Durability concerns, *Cement and Concrete Research*. 40 (2010) 1495–1506. <https://doi.org/10.1016/j.cemconres.2010.06.003>.
- [16] L.A.S. Kouris, T.C. Triantafillou, State-of-the-art on strengthening of masonry structures with textile reinforced mortar (TRM), *Construction and Building Materials*. 188 (2018) 1221–1233. <https://doi.org/10.1016/j.conbuildmat.2018.08.039>.
- [17] P.D. Askouni, C. (Corina) G. Papanicolaou, Textile Reinforced Mortar-to-masonry bond: Experimental investigation of bond-critical parameters, *Construction and Building Materials*. 207 (2019) 535–547. <https://doi.org/10.1016/j.conbuildmat.2019.02.102>.
- [18] A. Peled, B. Mobasher, Properties of Fabric–Cement Composites made by Pultrusion, *Materials and Structures*. 39 (2006) 787–797. <https://doi.org/10.1617/s11527-006-9171-3>.
- [19] B. Banholzer, *Bond Behaviour of a Multi-Filament Yarn Embedded in a Cementitious Matrix*, 2004.
- [20] A. Peled, E. Zaguri, G. Marom, Bonding characteristics of multifilament polymer yarns and cement matrices, *Composites Part A: Applied Science and Manufacturing*. 39 (2008) 930–939. <https://doi.org/10.1016/j.compositesa.2008.03.012>.

Influence of the sizes and the loading platform form on the strength of concrete elements at local compression

Iryna Kuznietsova, Oksana Dovzhenko, Volodymyr Pohribnyi, Iryna Usenko

*Educational-Scientific Institute of Architecture and Construction,
National University "Yuri Kondratyuk Poltava Polytechnic",
24, Pershotravnevyj Ave., Poltava 36011, Ukraine*

Abstract

To solve the strength problem of concrete and fiber concrete elements under central one-sided local compression, a variational method in the theory of ideal plasticity is used. The functionality of the virtual velocities method is investigated at steady state. As a plastic potential, the condition of concrete strength is used in the form of a paraboloid of rotation. A kinematic scheme was developed based on the generalization of the failure character. A pyramid with localization of plastic strain on the lateral faces is considered. The dependences are obtained of the failure resistance under triaxial state of stress on the ratio of the height and dimensions of the cross section of the element to the dimensions of the stamp through which the load is transmitted. Comparison of theoretical and experimental strength is made.

1 Introduction

The reliability of buildings and structures made of reinforced concrete depends to a large extent on the effectiveness of the structural decisions of the supporting sections and the joins of the elements of the bearing systems. In this case, consideration is given to ensuring their strength.

Concrete strength under local compression should be checked when transferring large concentrated loads from trusses, arches and beams of buildings and structures to massive concrete supports, walls or columns, in areas of concrete crimping with prestressed reinforcement with anchors at the ends, in places of columns support of tall buildings on slab or column foundations, in joints of precast columns under centering gaskets and supporting of heavy technological equipment to the foundations, when arranging the power floor, takeoff and landing runways at airfields, at the supporting of the mounting racks in the mines and mine working and in a number of other cases. Therefore, the rules for the design of concrete and reinforced concrete structures provide a chapter on their calculation for the effect of local load. The purpose of this calculation is to enable the designer to objectively assess the degree of reliability of the load-bearing structure, to reduce the material intensity of the reinforced concrete structure, and even, with appropriate justification, to refuse local indirect reinforcement. Taking into account the great variety of operation cases of elements under the action of local load, which exists in practice, the specificity of the stress-strain state of the zone of their failure should be taken into account when calculating the strength [1], [2].

One of the ways to increase the strength of the supporting sections of structures is to increase the resistance characteristics of concrete, in particular by adding fibers. Basalt fiber is one of the strongest mineral fibers. It has a number of significant advantages, namely high mechanical properties at a fairly low cost. Its use allows increasing the strength of concrete and reducing the weight of structures. Basalt fibers provide concrete with three-dimensional strength, are resistant to physical damage during mixing, are non-corrosive, which is characteristic of steel fiber, easily distributed over the volume of the element, do not form clots unlike polypropylene. According to the materials of experimental studies, the optimal size of basalt fiber has been established [3].

Numerous experimental-theoretical studies [4]–[12] of concrete elements under the local loading contribute to a deeper study of the problem. It should be noted that the empirical approach to the calculation of strength is the most common, in which particular attention is paid to determining the "calculated" area of the element [4]–[8]. However, there is an understanding of the need to take into account the influence of the element height [7], [8], the location of the load [5], the type of concrete [6], [9] and other factors of influence [10]. When applying empirical dependencies, there is a complexity of taking into account multifactorial influences and there is some ambiguity in the estimation

the pyramid by the height of the element leads to the crushing of concrete with a slight drop in the load on the downward branch of deformation.

Thus, almost simultaneously, three forms of concrete destruction are realized: shear, tear and crushing.

Normal σ_n and tangent τ_n stresses are applied on the lateral surfaces of the pyramid. The relationship between them is determined by the condition of the concrete strength at the triaxial state of stress [20], geometrically represented in the coordinates of the principal stresses by the paraboloid of rotation and is written in the form:

$$|\tau_n| = \sqrt{m(\sigma_n + m/4 + n^2/(12m))} \quad (1)$$

where $m = f_{c,prizm} - f_{ct}$, $n = f_{c,prizm} + f_{ct}$, here $f_{c,prizm}$ and f_{ct} – prism compressive strength and axial tensile strength of concrete.

In the region of cleavage stress equal to the concrete resistance of the axial tension.

At the entire failure surface of the element a limit state in the area of compression and tension reaches simultaneously. The functionality of virtual velocities principle [21] is investigated at steady state, which is equivalent to solving the boundary problem, discontinuous solutions are used. However, on the shear surface, plastic strains are localized [22] and there are velocity jumps in both the tangential and the normal direction, which is caused by the dilatation of the concrete in the failure stage. Velocity jumps in the compressed zone are generally expressed through the parameters that depend on the velocity direction of rigid units separated by shear surface and the values of the angles of the failure surface inclination.

The condition of concrete strength in the area of non-uniform compression is considered as a condition of plasticity. In this case, the plasticity surface is placed in the middle of the strength surface and lags behind it by a value that reaches zero. As a result of intense directional strain, movement over the paraboloid surface occurs without disturbing the strength condition, which is accompanied by a change in the stress state of the element. That is, there is no quantitative difference between the strength and plasticity equations, which allows the use of a mathematical apparatus of the plasticity theory under a given relationship between stresses in the condition of concrete strength.

For this problem, the unknown and varying parameters are the ratio of velocity components in the horizontal V_2 and vertical V_1 directions and the inclination angle γ of the failure surface along the long side of the stamp to the vertical.

The relation between the angle γ and the angle of the pyramid faces along the short side γ_1 is established by the equation $\tan \gamma_1 / \tan \gamma = b_{loc} / l_{loc}$.

The dependency for determining the value of failure resistance under local compression is written as:

$$f_{c,loc} = \frac{m}{2 \tan \gamma} \left[B^2 k + \frac{(1 + k \tan \gamma)^2}{4(k - \tan \gamma)} + \frac{1 + k^2 (1 + k_1^2 \tan^2 \gamma)}{4k_1^2 \tan \gamma} + f_{ct} \frac{k}{k_1} (4\alpha_1 \alpha_2 \tan \gamma - k_1) \right] \quad (2)$$

where $B^2 = [1 + \chi / (1 - \chi)^2] / 3$, $\chi = f_{ct} / f_{c,prizm}$, $k = V_1 / V_2$, $k_1 = b_{loc} / l_{loc}$, $\alpha_1 = b / l_{loc}$, $\alpha_2 = h / l_{loc}$.

When a square stamp is used, formula (2) takes the form:

$$f_{c,loc} = \frac{m}{2 \tan \gamma} \left[B^2 k + \frac{(1 + k \tan \gamma)^2}{4(k - \tan \gamma)} + \frac{1 + k^2 (1 + \tan^2 \gamma)}{4 \tan \gamma} + f_{ct} k (4\alpha_1 \alpha_2 \tan \gamma - 1) \right] \quad (3)$$

The value of the failure load corresponds to the minimum power of plastic strain in the compressed zone.

The results of the solution of the strength problem by the variational method in the plasticity theory indicate the influence of the ratio of the element height to the size of the loading platform, as well as the ratio of the cross-sectional area of the sample and the loading area, on the concrete strength under local compression.

The values of the relative failure resistance under the action of one-sided local compression $f_{cd,loc}/f_{cd}$ taking into account the influence of the ratio of the geometric parameters of the element and the sizes of the stamp b/l_{loc} and h/l_{loc} (Fig. 1) and the strength characteristics of concrete and fiber concrete on compression are given in the table 1.

Table 1 The value of the relative resistance of the concrete failure under local compression $f_{cd,loc}/f_{cd}$ at different ratios of thickness and height of the element to the width of the stamp b/l_{loc} and h/l_{loc} .

b/l_{loc}	h/l_{loc}	Concrete class				
		C16/20	C25/30	C32/40	C40/50	C50/60
for square stamp						
3	3	3.55	3.46	3.38	3.35	3.34
	4	3.97	3.88	3.75	3.7	3.69
	5	4.36	4.22	4.09	4.03	4.02
	6	4.72	4.56	4.41	4.34	4.33
	7	5.07	4.93	4.72	4.64	4.63
	8	5.41	5.21	5.02	4.93	4.92
for rectangular stamp $b_{loc}/l_{loc}=2$						
3	3	2.33	2.28	2.25	2.23	2.22
	4	2.55	2.49	2.44	2.42	2.41
	5	2.76	2.68	2.62	2.60	2.59
	6	2.96	2.87	2.80	2.77	2.75
	7	3.15	3.04	2.97	2.94	2.92
	8	3.33	3.22	3.13	3.09	3.07
for square stamp						
3	5	4.36	4.22	4.09	4.03	4.02
4		4.96	4.77	4.62	4.54	4.53
5		5.52	5.31	5.12	5.02	5.01
6		6.05	5.81	5.59	5.49	5.47
7		6.55	6.28	6.04	5.92	5.90
8		7.04	6.74	6.47	6.34	6.32
for rectangular stamp $b_{loc}/l_{loc}=2$						
3	5	2.76	2.68	2.62	2.60	2.59
4		3.09	2.99	2.91	2.88	2.86
5		3.39	3.27	3.18	3.15	3.13
6		3.69	3.55	3.44	3.40	3.38
7		3.97	3.82	3.69	3.64	3.61
8		4.23	4.06	3.92	3.87	3.84

By implementing the kinematic scheme of failure shown in Fig. 1 under local compression the tensile strength f_{ctd} also affects on the strength of the elements, in addition to the concrete resistance to compression f_{cd} . The placement of basalt fibers in concrete leads to a significant increase in the value of f_{ctd}/f_{cd} and an increase in the relative resistance to destruction of $f_{cd,loc}/f_{cd}$. Thus, when f_{ctd}/f_{cd} is increased 1.5 times $f_{cd,loc}/f_{cd}$ increases by 20% for square stamp and by 15% for rectangular stamp with $b_{loc}/l_{loc}=2$ for the ratio of thickness and height of the element to the width of the stamp $b/l_{loc}=3$ and $h/l_{loc}=5$.

3 Comparison of theoretical and experimental strength

Comparison data of theoretical and experimental strength are given in table 2.

Table 2 Comparison of experimental and theoretical strength of concrete specimens under local compression.

Authors	b/l_{loc}	h/l_{loc}	f_c [MPa]	f_{ct} [MPa]	$f_{c,loc}^{test}/f_c$	$f_{c,loc}^{calc}/f_c$	$f_{c,loc}^{calc}/f_{c,loc}^{test}$		
Ince R. and Arici E. [4]	2.5	2.5	9.63	1.23	4.72	3.61	0.76		
					3.45	3.61	1.05		
					2.90	3.61	1.24		
			24.02	2.27	4.23	3.32	0.78		
					3.64	3.32	0.91		
					2.70	3.32	1.23		
			24.05	2.27	24.05	2.27	5.41	3.32	0.61
							3.99	3.32	0.83
							3.25	3.32	1.02
	27.42	2.48	3.57	3.29	0.92				
	48.00	3.60	48.00	3.60	4.39	3.14	0.72		
					3.46	3.14	0.91		
					2.45	3.14	1.28		
	4	4	23.60	2.24	7.66	4.90	0.64		
					6.36	4.90	0.77		
4.83					4.90	1.01			
Au T. and Baird D. L. [7]	2	1	31.03	2.69	2.06	2.46	1.19		
	2	2	31.03	2.69	2.07	2.85	1.38		
	2.45	1.22	31.03	2.69	2.77	2.66	0.96		
Gladyshev B. M. [23]	2.5	2.5	12.30	1.45	2.88	3.53	1.22		
	3	3	19.62	1.55	3.06	3.60	1.18		
	4	4	10.08	1.00	4.96	4.99	1.01		
			15.50	1.60	4.85	5.07	1.05		
			24.21	1.21	3.47	3.85	1.11		
Piradov A. B. [24]	5	5	19.62	1.55	5.28	5.62	1.06		
	6	6	24.21	1.21	5.34	5.48	1.03		
	6.67	6.67	3.87	0.40	8.99	8.73	0.97		
			10.08	1.00	8.60	8.55	0.99		
			10.62	1.00	8.05	8.32	1.03		
			15.12	1.50	8.05	8.55	1.06		
			29.88	1.70	6.75	6.47	0.96		
Mitrofanov V. P., Dovzhenko O.O. [25]	3	3	29.80	2.38	2.70	3.62	1.34		
	4	4			4.11	4.58	1.11		

The proposed kinematic scheme (Fig. 1) is compared with the pattern of specimens failure [4], [7], [23]–[26]. Analysis of the failure character indicates that the violation of the element integrity begins with the movement of the stamp vertically downwards, with further splitting and exit of the tear-off pad on the side surfaces of the element in the middle of their part. With square and rectangular stamps and non-uniform load transfer, stress concentration occurs near the corners of the stamps. Then the change of the direction of the splitting plane is possible to the corners of the element, which is not observed when using a round stamp (Fig. 2).

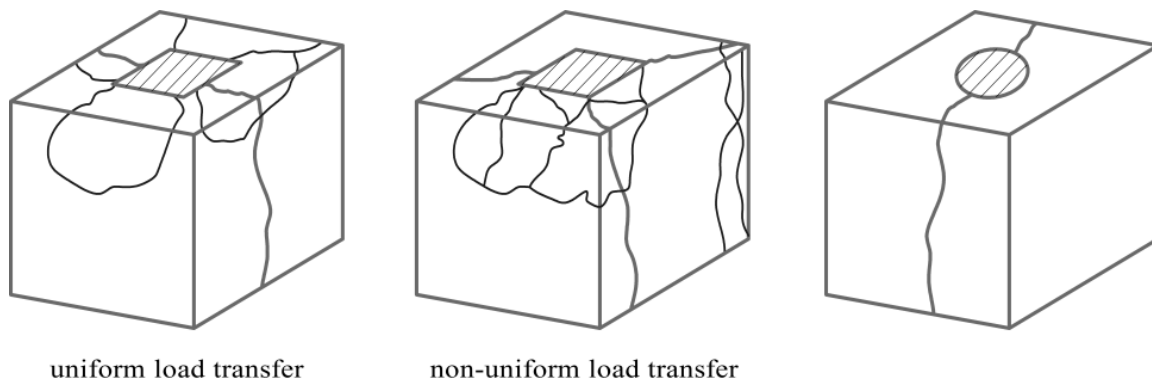


Fig. 2 Generalized failure character of concrete specimens under one-sided local compression with a square stamp (left) and round stamp (right).

4 Conclusions

To calculate the strength of concrete elements under local compression, the theory of concrete plasticity is promising. The application of the variational method and the principle of virtual velocities are suggested. According to research, strength, in addition to the ratio of the load area and the cross-sectional area, is influenced by the ratio of the height of the element to the width of the stamp and both characteristics of the concrete strength. Resistance to destruction of $f_{cd,loc}$ reaches the maximum value at a square stamp. The proposed kinematic failure scheme has found experimental confirmation. In the case of the pyramid formation under the loading platform and its displacement into the body of the element its splitting occurs with the output of the separation plane on the side faces. Simultaneously shear and detachable forms of failure are realized. The placement of basalt fibers increases the value of $f_{cd,loc}$, increases the value of the ratio f_{cd}/f_c and increases the plastic properties of concrete.

Acknowledgements

The authors thank the leadership of the National University “Yuri Konratyuk Poltava Polytechnic” and the head of the department of reinforced concrete and masonry structures and strength of materials for creating favorable conditions for the preparation of the article.

References

- [1] Yahya, N. A., Dhanasekar, M., Zain, M., Oh, C. L. and Lee, S. W. 2018. “Bearing Strength of Concrete for Difference Heights of Concrete Blocks.” *Published under licence by IOP Publishing Ltd IOP Conference Series: Materials Science and Engineering* 431 072011, 07 September 2018 – 15 November, 2018. doi:10.1088/1757-899X/431/7/072011.
- [2] Cao, Z., Yin, X., Cai, J. 2015. “Compression Bearing Capacity Analysis of Concrete in Edge and Corner under Prestressed Constraint.” *Proceedings of 5th International Conference on Civil Engineering and Transportation (ICCET 2015)*, Guangzhou, China, November 28-29: 571–575.
- [3] Perfylov, V.A. 2015. *Melkozernystye fibrobetony*. Volgograd: VolgGASU. (In Russian).
- [4] Ince, R. and Arici, E. 2004. “Size Effect in Bearing Strength of Concrete Cubes.” *Construction and Building Materials* 18:603–09. Accessed 17 June 2004. doi:10.12989/sem.2005.19.5.567.
- [5] Venckevicius, V. 2005. “About the Calculation of Concrete Elements Subjected to Local Compression.” *Journal of Civil Engineering and Management* 11 (3):243–48. Accessed September 2005. doi:10.3846/13923730.2005.9636355.

- [6] Rak, N.A. 2017. "Metodyka Rascheta Soprotyvleniya Stalefybrobetonnykh Elementov Mestnomu Szhatyiu." *Vestnyk Polotskoho Hosudarstvennogo Unyversyteta. Stroytelstvo. Prykladnye Nauky. Stroytelnye Konstruktsyy* 16:93–97. (In Russian).
- [7] Au, T. and Baird, D. L. 1960. "Bearing Capacity of Concrete Blocks." *Journal of the America Concrete Institute* 56:869–80.
- [8] Roberts-Wolimann, C. L., Banta, T., Bonetti, R. and Charney, F. 2006. "Bearing Strength of Light-Weight Concrete." *ACI Materials Journal* 103 (6):459–66.
- [9] Ravindrarajah, R. S. 1999. "Bearing Strength of Concrete Containing Polystyrene Aggregate." Paper presented at the Proc. the RILEM 8th Int Conf Durability of Building Materials and Components 8:505–14.
- [10] Breitenbücher, R., Meschke, G., Song, F., Hofmann, M., Zhan, Y. 2014. "Experimental and Numerical Study on the Load-Bearing Behavior of Steel Fiber Reinforced Concrete for Pre-cast Tunnel Lining Segments under Concentrated Loads." FRC 2014 Joint ACI-fib International Workshop Fibre Reinforced Concrete: from Design to Structural Applications: 417–29. July 2014.
- [11] Antakov, A.B. 1999. "Prochnost Elementov Yz Lehkykh Yacheystykh Betonov Pry Mestnom Deistvyy Nahruzky." Dys. k.t.n., Kazanskaia Hosudarstvennaia Arkhytekturno-Stroytelnaia Akademyia. (In Russian).
- [12] Yahya, N. A. and Manicka, D. 2017. "Strategies for Mitigation of the Failure of Concrete Pedestals Supporting Bridge Girder Bearings." PhD Thesis. Queensland University of Technology.
- [13] Panovko, Ya. G. 1985. *Mekhanika Deformiruyemogo Tverdogo Tela. Sovremennyye kontseptsii, oshibki i paradoksy*. Moscow: Nauka. (In Russian).
- [14] Rabotnov, Yu. N. 1988. *Mekhanika Deformiruyemogo Tverdogo Tela*. Moscow: Nauka. (In Russian).
- [15] Nielsen, M.P. and Hoang, L.C. 2011. *Limit Analysis and Concrete Plasticity*. CRC Press, Taylor & Francis Group.
- [16] Dovzhenko, O., Pohribnyi, V., Pents, V., Mariukha, D. 2018. "Bearing Capacity Calculation of Reinforced Concrete Corbels under the Shear Action." *MATEC Web Conferences* 230. doi:10.1051/mateconf/201823002005.
- [17] Dovzhenko, O., Pohribnyi, V., Yurko, I. 2018. "Concrete and Reinforced Concrete Strength under Action of Shear, Crushing and Punching Shear." *IOP Conf. Series: Materials Science and Engineering* 463: 022026. doi:10.1088/1757-899X/463/2/022026.
- [18] Pohribnyi, V., Dovzhenko, O., Maliovana O. 2018. "The Ideal Plasticity Theory Usage Peculiarities to Concrete and Reinforced Concrete." *International Journal of Engineering & Technology* 7 (3.2):19–26. doi:10.14419/ijet.v7i3.2.14369.
- [19] Pavlikov, A., Harkava, O., Prykhodko, Yu. and Baryliak, B. 2019. "Highly Constructed Pre-cast Flat Slab Frame Structural System of Buildings and Research of Its Slabs." Proceedings of the International fib Symposium on Conceptual Design of Structures, Madrid, September 26–28.
- [20] Geniyev, G. A., Kissyuk, V. N., Tyupin, G. A. 1974. *Teoriya Plastichnosti Betona i Zhelezobetona*. Moscow: Strojizdat. (In Russian).
- [21] Kolmogorov, V.L. 1986. *Mekhanika Obrabotki Metallov Davleniyem*. Moscow: Metallurhyia. (In Russian).
- [22] Dovzhenko, O., Pohribnyi, V., Karabash, L. 2018. "Experimental Study on the Multikeyed Joints of Concrete and Reinforced Concrete Elements." *International Journal of Engineering & Technology* 7 (3.2):354–59. doi:10.14419/ijet.v7i3.2.14552.
- [23] Gladyshev, B.M. 1987. *Mekhanicheskoe Vzaimodejstvie Elementov Struktury i Prochnost Betona*. Kharkov: Vishha shkola. (In Russian).
- [24] Piradov, A.B. 1973. *Konstruktivnye Svoystva Legkogo Betona i Zhelezobetona*. Moscow: Strojizdat. (In Russian).
- [25] Pohribnyi, V., Dovzhenko, O., Kuznietsova, I., Usenko, D. 2018. "The Improved Technique for Calculating the Concrete Elements Strength under Local Compression." *MATEC Web Conferences* 230. doi:10.1051/mateconf/201823002025.
- [26] Bonetti, R. 2005. "Ultimate Strength of the Local Zone in Load Transfer Tests.": MSc Thesis Virginia Polytechnic Institute and State University, Blacksburg.

Load-Deformation Behaviour of Concrete Tension Ties with Weft-Knitted Textile Reinforcement

Minu Lee, Jaime Mata-Falcón and Walter Kaufmann

*Institute of Structural Engineering (IBK),
Swiss Federal Institute of Technology Zurich (ETHZ),
Stefano-Franscini-Platz 5, 8093 Zurich, Switzerland*

Abstract

The use of non-corrosive high-strength fibrous materials as textile reinforcement allows the construction of more slender elements when compared to members with conventional steel reinforcing bars. This paper explores the load-deformation behaviour of weft-knitted textile reinforcement embedded in a fine grain concrete. In this experimental study, flat concrete specimens with a thickness of 12-16 mm are loaded in uniaxial tension. The study focuses on the comparison of various knitting patterns, materials and geometric features in the knitted textile. Results show that the post-cracking behaviour can be improved for certain configurations in terms of ultimate strength and deformation capacity. The failure mode is governed by the material of the fibres and their coating.

1 Introduction

Textile reinforcement is made from high-strength continuous fibres, which exist in a wide variety from synthetic polymers such as aramid or carbon fibres to inorganic materials such as glass fibre [1], that form rovings, i.e., bundles of thicker strands. Usually, these rovings are coated or fully impregnated with a resin (e.g. epoxy) to improve their resistance against abrasion and the inter-fibre friction, thereby enhancing the stress transfer and distribution within the strand of multiple filaments and hence, increasing the roving's strength [2]. The majority of existing literature covers flat sheets from orthogonally woven grids of straight rovings (e.g. [3], [4]), but little attention has been given to weft-knitted textiles, which have a great advantage in their geometric definition: They allow for complex shapes without the need of stitching multiple patches together [5]. CNC knitting machines allow to locally vary the length and width of the textile by adding or omitting loops and to include spatial features such as channels or ribs [6]. The KnitCrete technology developed at ETH Zürich [7] uses a weft-knitted textile as stay-in-place formwork. The textile is tensioned in a scaffolding frame and it is initially coated with a thin layer of fast-setting cement paste. After hardening, this first layer serves as a stable and stiff formwork for the subsequent application of concrete. The technology was successfully applied in the construction of the KnitCandela pavilion, which was collaboratively realised by Block Research Group (ETHZ) and Zaha Hadid Architects in Mexico City [8]. However, the approach did not explicitly address the integration of reinforcement within the fabrication procedure. Possibilities arising from knitting are summarised in [6]. A potential solution is the activation of the weft-knitted textile as reinforcement – rather than just as lost formwork – by utilising high-strength fibrous materials. Special care needs to be given to the interface between coated textile and the concrete to ensure proper stress transfer. This paper presents an experimental study consisting of uniaxial tension tests on flat concrete sheets with one centred layer of coated textile reinforcement (Fig. 1). The investigations focus on various knitting patterns, types of fibres and coating as well as spatial features within the textiles to enhance the bond between reinforcement and concrete.

2 Experimental campaign

This section summarises the materials, the preparation of the specimens and the test setup including the test protocol and measurement devices.

2.1 Materials, specimens and production

Fibres made of three different materials were used for the textile reinforcement: aramid (AR), carbon fibre (CF) and E-glass (GF), which all have a high tensile strength and adequate to high elasticity modulus, but are sensitive to lateral loading. The notional material properties are shown in Table 1.

Table 1 Properties of textile rovings.

Material	$f_{t,u}$	E_t	ρ_t
	[MPa]	[GPa]	[g/cm ³]
Aramid	3'000	100	1.44
Carbon fibre	4'300	240	1.76
Glass fibre	2'700	73	2.55

Two different types of coating were examined: a highly fluid cement paste consisting of a blended ordinary Portland cement, a polycarboxylate ether based superplasticiser and stabilising nanoparticles [7] (mix design courtesy of Chair of Physical Chemistry of Building Materials at ETH Zürich), and furthermore, a low-viscous two-component epoxy suitable for hand lamination of textile fibres.

The coated textiles were embedded in a fine grain concrete with a maximum aggregate size of $D_{max} = 2$ mm and a w/c -ratio of 0.4, which was mixed in the laboratory (Fig. 1c). The flexural tensile strength was obtained from small prisms (40 mm×40 mm×160 mm) according to EN 196-1 [9]. The material tests for the different batches were conducted at 8 and 13 days after casting, without a significant difference. The uniaxial tensile strength was calculated using Eq. (1) taken from fib Model Code [10]. Considering the depth of the prism $h_b = 40$ mm, the mean flexural tensile strength of 9.5 MPa results in a uniaxial tensile strength of 4.2 MPa.

$$f_{cm} = \alpha_{fl} \cdot f_{cm,fl} \quad \text{where} \quad \alpha_{fl} = \frac{0.06 \cdot h_b^{0.7}}{1 + 0.06 \cdot h_b^{0.7}} \quad (1)$$

A total of 28 specimens – with dimensions of 200 mm width, 800 mm height and thicknesses between 12 and 16 mm – were manufactured and tested to failure. The textile reinforcement was produced in a CNC knitting machine (Steiger Libra 3.130) and then tensioned in a wooden frame by hand (Fig. 1a). The pre-stress mostly serves to reduce deflections during application of the coating and has no significant relevance for the mechanical behaviour since the forces are very low when compared to the tensile strength of the yarn. The fabrics were coated and left for 3 days to harden in a climate chamber at 20°C and 90% relative humidity in case of cement paste (Fig. 1b) and one day at room temperature in case of epoxy. The coated textile was cut according to the specimen size, embedded onto a first layer of concrete with a thickness of 5 mm, and finally sealed with another top layer of 5 mm concrete cover (Fig. 1c). The concrete was vibrated on a shaking table during the placing of the reinforcement to minimise air voids. The specimens were put in the climate chamber to harden for at least 8 days.

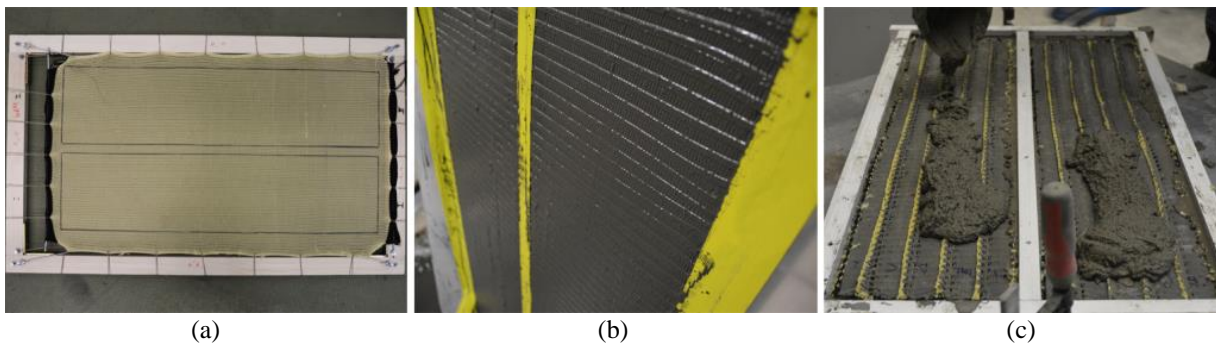


Fig. 1 Production of specimens: (a) tensioning and (b) cement paste coating of textile; (c) casting of concrete.

A double bed knitting machine allows for an almost infinite range of possibilities [5] depending on the sequence of activated needles which form the loop in the textile. Fig. 2 shows an overview of different typical knitting patterns and their schematic formation in the double needle bed. The first two patterns in Fig. 2a and Fig. 2b show a single layer fabric that alternates between the needle beds. The interlocked textile in Fig. 2c is a double-layer textile that is formed by mirroring the activated needles with every new row. Those knitting patterns could only be made from aramid with relatively thin yarns (160 tex; 1 tex corresponds to 1 g per meter of yarn) since the knitting needles cannot grab thicker yarns, and carbon or glass fibre yarns do not allow for such small bending radii and would break during fabrication.

In the following, those textiles will be referred to as ‘directly knitted reinforcement’. Furthermore, the knitting machine allows for the integration of straight rovings (called inlays) within the knitted textile (white yarns in Fig. 2d), which enables the use of thicker yarns and more brittle materials. In this case, the base knitted textile was made from a non-structural acrylic yarns as it served only as a holder for the straight high-strength rovings.

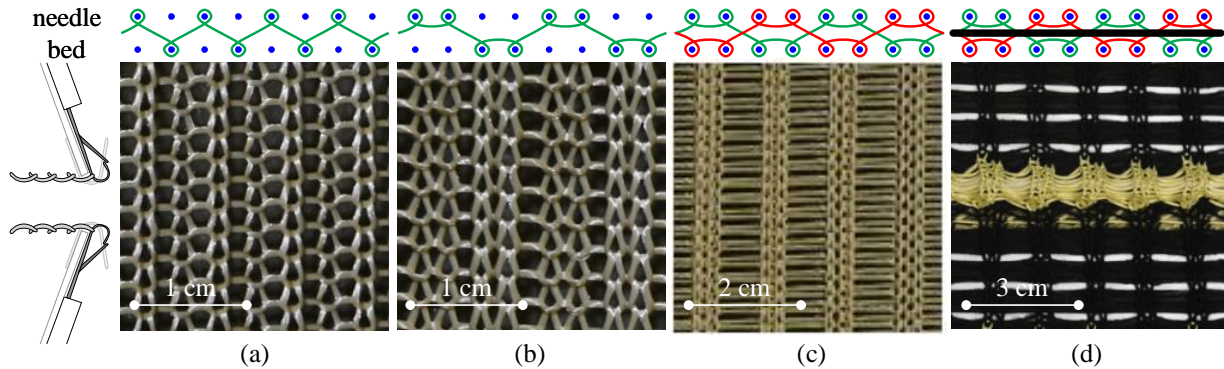


Fig. 2 Knitting patterns: single-layers (a) 1-1 and (b) 2-2; double-layer (c) interlock; (d) interlock with inlays and ribbed texture.

Table 2 Configurations, dimensions and reinforcement content of tested tension ties.

Pattern	Direction	Texture	Fibres & fineness	Coating	#	b	t	A_c	A_t	
						[mm]	[mm]	[mm ²]	[mm ²]	
1-1	Warp	Flat	Aramid 160 tex	Cement paste	1	200.7	11.8	2368	12.2	
					2	200.0	13.0	2600	11.8	
	Weft				1	200.0	12.2	2440	8.2	
					2	200.8	13.3	2671	7.9	
2-2	Warp	Flat	Aramid 160 tex	Cement paste	1	200.3	12.1	2424	14.4	
					2	200.7	12.2	2449	13.3	
	Weft				1	200.3	11.7	2344	8.6	
					2	200.3	11.6	2323	8.7	
Inter	Warp	Flat	Aramid 160 tex	Cement paste	1	201.0	15.0	3015	16.0	
					2	200.3	14.3	2864	15.1	
	Weft				1	201.0	14.0	2814	19.1	
					2	200.7	13.9	2790	18.9	
	Warp	Ribs	Aramid 160 tex	Cement paste	1	200.3	17.3	3465	16.0	
					2	200.7	15.7	3151	16.0	
Weft	1				201.0	15.8	3176	13.3		
	2				201.2	14.2	2857	13.3		
Inlay	Weft	Ribs	Aramid 800 tex	Cement paste	1	200.7	13.4	2689	15.6	
					2	200.8	12.6	2530	15.6	
					Epoxy	1	199.8	13.8	2757	15.6
				2		200.0	15.0	3000	15.6	
				Carbon fibre 800 tex		Cement paste	1	200.2	13.7	2743
					2		201.0	13.9	2794	12.7
			Epoxy		1		199.8	14.6	2917	12.7
					2	200.0	14.4	2880	12.7	
					Glass fibre 2400 tex	Cement paste	1	200.5	13.8	2767
			2				201.6	14.1	2843	16.9
			Epoxy	1			200.7	14.7	2950	16.9
				2		200.3	13.5	2704	16.9	

The coated textile forms a flat surface that might act as a cold joint over its whole area. Therefore, ribs – that are formed by folding and closing the textile as shown in Fig. 2d – were introduced in some configurations as spatial features to enhance bond conditions between the textile reinforcement and the concrete. A thin aramid yarn with a fineness of 160 tex was used for the ribs. Cement paste coating was applied in all specimens with the thinner aramid yarns whereas for the specimens with inlays, both cement paste and epoxy coating were examined. The directly knitted textile reinforcement was tested in parallel and orthogonally to the knitting direction (called weft and warp) whereas the textiles with inlays were only loaded in weft direction (although it is technically possible to include inlays in warp direction, the structural outcome is the same since both orthogonal directions in woven textiles are independent of each other). The configurations of all specimens (with a repetition of 2), their dimensions and their reinforcement contents are summarised in Table 2.

2.2 Test setup and protocol

The test setup is based on the recommendation of RILEM TC 232-TDT [11]. The specimens were clamped with stiffened plates over a length of 150 mm with a layer of neoprene with a thickness of 2 mm in between, resulting in a free length of 500 mm (Fig. 3). The plates were connected to the testing machine via threaded rods with spherical bearings on either side to create hinged-hinged boundary conditions, which minimises eccentricities in the load introduction. The specimens were loaded in displacement control. The speed was adjusted during the test according to the following scheme:

- Pre-cracking 0.15 mm/min
- During crack formation 0.5 mm/min
- After full crack formation 1.0 mm/min

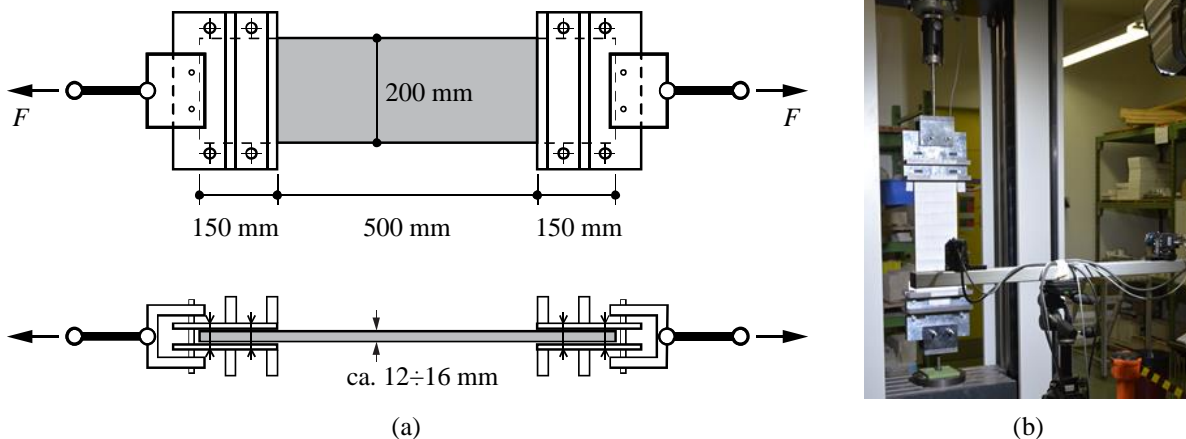


Fig. 3 Test setup (based on the recommendation of RILEM TC 232-TDT): (a) Schematic illustration and dimensions; (b) installed specimen and setup for DIC measurement.

A three dimensional digital image correlation measurement system was used to assess the actual deformations of the specimens and to further investigate the crack kinematics. Therefore, a speckle pattern was applied on one side of the specimen. VIC-3D software by Correlated Solutions was used for the correlation of the results. Small plates with a printed speckle pattern were attached directly onto the specimen in the clamped area to mitigate the effect of slip and deformation of the neoprene in the measurement of the overall elongation.

3 Results and discussion

Basic results of the experimental campaign are presented in the following. Fig. 4 shows the stresses in the textile reinforcement against the mean strains of all specimens where the reinforcement consists of the directly knitted yarn, whereas Fig. 5 summarises all specimens with straight inlays. The nominal textile stresses (σ_t) were calculated by dividing the force from the load cell by the textile cross section. The mean strains (ϵ_{tm}) were obtained from the total elongation divided by the free length of 500 mm.

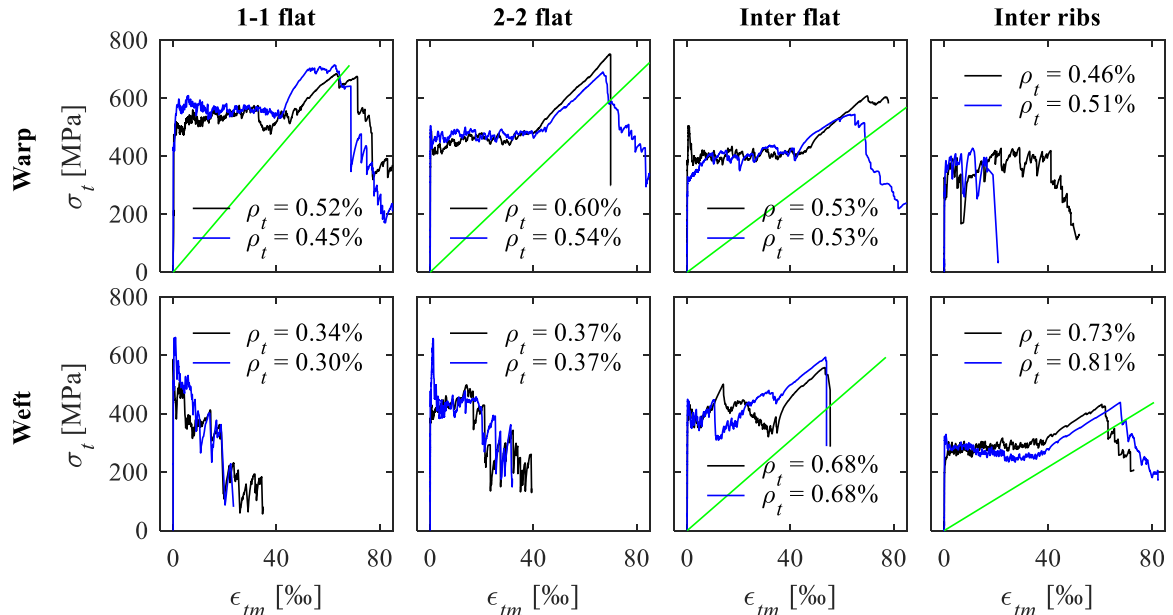


Fig. 4 Textile stress-mean strain-relationship of specimens with directly knitted reinforcement.

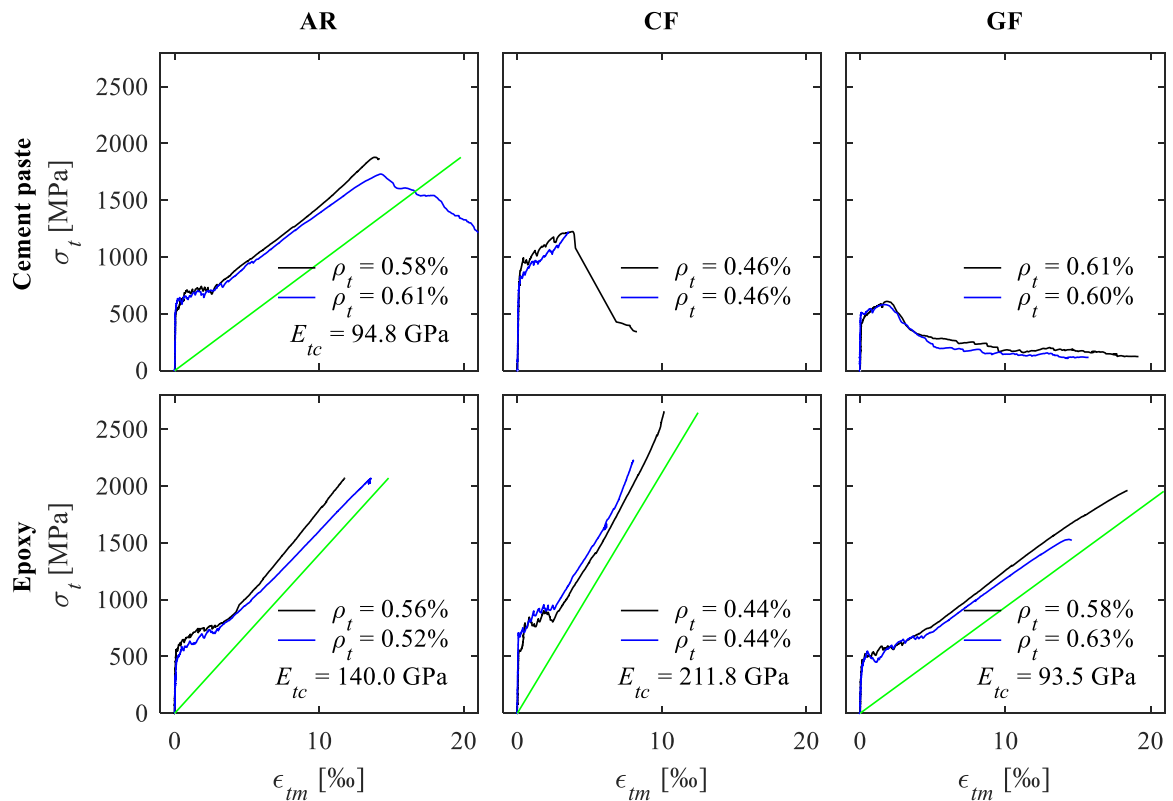


Fig. 5 Textile stress-mean strain-relationship of specimens with straight inlay reinforcement.

3.1 General load-deformation behaviour in pre- and post-cracking phase

Two different types of post-cracking behaviour were observed. Most specimens displayed stable multiple cracking and strain hardening once all cracks are formed. The crack spacing was between 10 mm and 20 mm (determined from visual inspection). However, in some specimens with directly knitted reinforcement (such as the flat interlock pattern and interlock with ribs, both loaded in weft direction), the load decreased right after initial crack formation. This phenomenon has already been observed in strain hardening cementitious composites and potential causes were addressed by Yu et al. [12]. In the present tests, eccentricities caused in the manufacturing of the specimens and in the preparation of the test setup may cause rotations and thus, bending out-of-plane.

In most cases, the failure mode was brittle with a sudden steep drop of textile stresses after reaching the peak load. A progressive failure followed once the tensile strength had been reached in one fibre since the material exhibits no ductility and thus, the stresses cannot be redistributed within the reinforcement. However, in deformation controlled tests, the subsequent failure of individual yarns can cause a softening behaviour, which was mostly observed in the directly knitted reinforcement since the yarn rupture caused a local opening of the interlocked loops (as shown in Fig. 6a), but the remaining textile is able to carry some residual stresses. Spalling of the concrete occurred with increasing deformation in the post-peak phase since the textile-concrete interface started to debond and the lateral contraction of the textile initiated buckling of the cover at the edges of the flat tension tie. The integration of ribs in the knitted fabric creates a mechanical connection between the textile and the cover concrete, which hindered spalling.

Some specimens did not display stable cracking and failed directly or shortly after the initial crack had formed. They normally exhibited a softening behaviour, which in case of the straight inlays, seemed to be caused by a pull-out of the fibres rather than progressive failure of the yarns as explained above. From visual inspection, it appears that only the outer fibres of the rovings were ruptured and the inner core was pulled out (Fig. 6b). This failure mode has also been observed in commercially available woven textile reinforcement [4] and is caused by insufficient internal friction of the filaments within the roving.

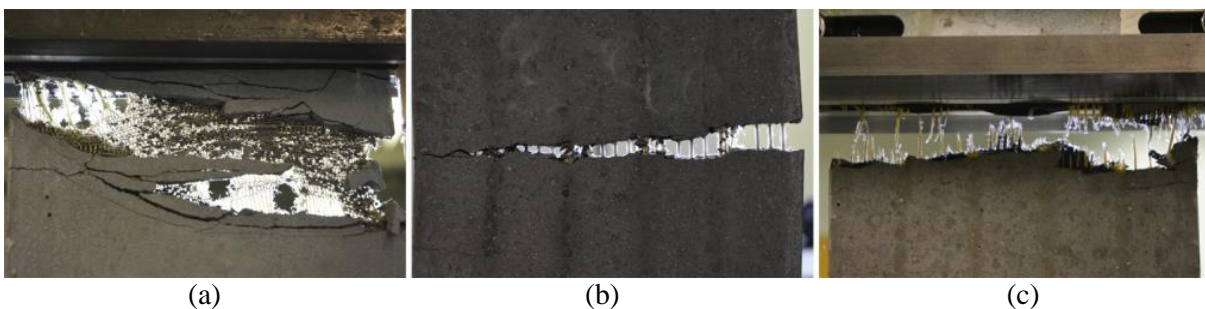


Fig. 6 Failure modes: (a) Subsequent failure of interlocked loops and spalling of cover concrete; (b) rupture of outer fibres and pull-out of inner core; (c) full rupture of fibres.

3.2 Strength and utilisation

The utilisation is defined as the maximum nominal tensile stress in the textile divided by the notional tensile strength adopted from the material documentation. The directly knitted textiles displayed low degrees of utilisation. The single-layer knitting patterns (1-1 and 2-2) showed utilisation ratios of around 24% whereas the interlocked double-layer textiles only reached utilisation between 14% and 17%. Therefore, specimens with low reinforcement content already failed upon cracking. The interlocked loops within the knitted textiles leads to small bending radii (with 180°-bends) and to concentrated introduction of lateral forces at the bends of the yarn, which explains the observed significant reduction in strength. The interlocked double-layer knitting pattern exhibits a much denser structure and the integration of ribs creates additional weakening impairing the utilisation.

The specimens with straight inlays performed much better (utilisation between 50% and 70%) since the rovings are only loaded in their axial direction. The contribution of the aramid fibres in the ribs was neglected in the determination of the utilisation since they exhibit much lower stiffness than the straight rovings and, therefore, do not get significantly activated. Eventually, the nominal textile stresses do not reach the full notional tensile strength due to several reasons: (i) Stresses spread across the cross section of a roving via internal friction between individual filaments, which depends on the type of coating and the depth of penetration into the roving [4]. The core fibres might not be loaded yet while the outer fibres of the roving already reach the tensile strength. (ii) Eccentricities in the specimen and in the test setup may cause a deviation of the roving at the crack edges and, therefore, damage the yarn and introduce highly concentrated lateral forces on the reinforcement [3]. (iii) The brittle nature of the fibre material prevents a redistribution of stresses after the first fibre breaks, which makes it more prone to premature failure due to local material deficiencies. A suitable coating or impregnation of the yarns can reduce or even mitigate those effects, whereas in the comparison of cement paste and epoxy, the latter had a more beneficial influence. The specimens with carbon and glass fibre inlays coated with cement paste failed shortly after initial cracking. These fibres are more sensitive to lateral loading than aramid

and can be easily broken even by hand when sharply folded. However, their epoxy-coated counterparts showed much higher failure loads with clean rupture of all rovings (Fig. 6c). From visual inspection of the broken yarns, it seems that the epoxy penetrated better into the yarn due to its lower viscosity and smaller particles while the cement paste only covered a lesser depth but most of the core remained loose.

3.3 Stiffness of reinforcement and tension stiffening in the composite behaviour

The slopes of the load-deformation-curves in the hardening phase represent the stiffnesses of the textile reinforcement (E_{tc}), which were determined from linear regression and the mean of the two specimens per configuration (see green lines in Fig. 4 and Fig. 5). The directly knitted textile reinforcement displayed a much lower stiffness when compared to the notional material stiffness since most of the deformation is due to stretching (with concomitant lateral contraction) of the textile fabric as a whole rather than actual deformation of individual yarns. The interlocked double-layer knitting pattern exhibited a more flexible behaviour than the single layer fabrics (1-1 and 2-2) and the integration of ribs decreased stiffness even more.

The specimens with straight inlays showed much higher stiffness and the behaviour was dependent on the fibre material and the coating type. The aramid yarns with cement paste coating displayed a much lower stiffness when compared to the specimens with epoxy coating, which even exceeded the notional material stiffness from the material documentation (Table 1). The coated textile reinforcement acts as a composite (textile-coating) within a composite (reinforcement-concrete). Therefore, more investigations and separated tests on the rovings with and without coatings are currently carried out to assess the contribution of different components in the double-composite behaviour. The specimens with glass fibre rovings exhibited the same phenomenon whereas the carbon fibre inlays displayed a lower stiffness compared to the notional material stiffness.

In all specimens with a hardening phase, there was a distinct effect of tension stiffening. The interaction between reinforcement and concrete leads to a stress transfer between the two components and a shift of the load-deformation curve (Fig. 7). The Tension Chord Model [13], well established in conventionally reinforced concrete – assuming a constant bond shear stress as long as the reinforcement is elastic – can be adjusted to account for the different type of reinforcement and used for the assessment of the bond stresses following Eq. (2). The mean crack spacings in Eq. (2), and the crack widths used for validation, can be obtained by automated crack detection and measurement (ACDM) [14] using digital image correlation (DIC). These evaluations are currently in progress.

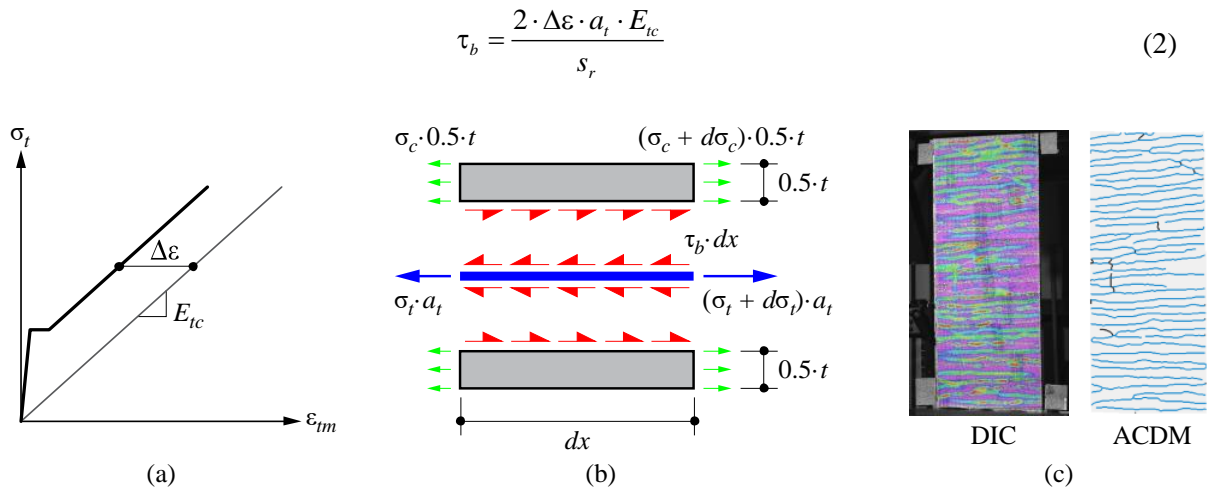


Fig. 7 Adapted tension chord model: (a) tension stiffening in stress-strain-relationship; (b) equilibrium of tensile and bond stresses; (c) crack detection using DIC and ACDM.

4 Conclusions

Results show that (i) in knitted textiles with high-strength fibrous materials, the ultimate strength of the rovings is significantly reduced due to the interlocked structure of the yarns and their vulnerability to lateral loading; (ii) the inclusion of straight rovings as inlays within the base fabric increases the utilisation of the fibres to an adequate level; (iii) glass and carbon fibres are considerably more brittle than

aramid and therefore, triggered by the concentrated deviation forces at the crack edges, fail shortly after crack formation when coated with cement paste; and (iv) the efficiency and stiffness can be highly improved by impregnating the fibres with epoxy instead. Regarding the behaviour of the textile-coating composite within the reinforcement-concrete composite, further research is required.

The load-deformation behaviour of the tension ties can be modelled using the tension chord model, which requires only few parameters and allows for the back-calculation of the bond stresses. This information can be used for the prediction of elements under different loading conditions such as bending or shear. A firm mechanical basis is needed to develop a consistent design model considering safety concepts for brittle materials and code compliance.

Acknowledgements

The authors gratefully acknowledge Dr. Mariana Popescu from Block Research Group (ETHZ) and Dr. Lex Reiter from the Chair of Physical Chemistry of Building Materials (ETHZ) for their technical and practical expertise as well as the students Seraina Buholzer and Salome Geiser for their valuable support during preparation and testing of the specimens shown in this paper. This research is supported by the National Centre for Competence in Research in Digital Fabrication, funded by the Swiss National Science Foundation (project number 51NF40-141853).

References

- [1] A. Peled, B. Mobasher, and A. Bentur, *Textile reinforced concrete*. Boca Raton, FL: CRC Press, Taylor & Francis Group, 2017.
- [2] T. Quadflieg, S. Leimbrink, T. Gries, and O. Stolyarov, ‘Effect of coating type on the mechanical performance of warp-knitted fabrics and cement-based composites’, *J. Compos. Mater.*, vol. 52, no. 19, pp. 2563–2576, Aug. 2018, doi: 10.1177/0021998317750003.
- [3] J. Hegger, M. Horstmann, S. Voss, and N. Will, ‘Textilbewehrter Beton: Tragverhalten, Bemessung und Anwendung’, *Beton- Stahlbetonbau*, vol. 102, no. 6, pp. 362–370, Jun. 2007, doi: 10.1002/best.200700552.
- [4] M. Fernández Ruiz and A. Muttoni, ‘Building in a lighter and more sustainable manner: textile reinforced concrete for thin structural elements’, cemsuisse, Schlussreport 201407, Dec. 2017.
- [5] M. Popescu, M. Rippmann, T. Van Mele, and P. Block, ‘Complex concrete casting: knitting stay-in-place formwork’, in *Proceedings of the IASS 2016 Tokyo Symposium: Spatial Structures in the 21st Century*, Tokyo, Japan, 2016, p. 1278.
- [6] M. Lee, J. Mata-Falcón, M. Popescu, P. Block, and W. Kaufmann, ‘Potential approaches for reinforcing complex concrete structures with integrated flexible formwork’, in *Proceedings for Digital Concrete 2020*, Eindhoven, Netherlands, Jul. 2020, vol. accepted for publication.
- [7] M. Popescu, L. Reiter, A. Liew, T. Van Mele, R. J. Flatt, and P. Block, ‘Building in Concrete with an Ultra-lightweight Knitted Stay-in-place Formwork: Prototype of a Concrete Shell Bridge’, *Structures*, vol. 14, pp. 322–332, Jun. 2018, doi: 10.1016/j.istruc.2018.03.001.
- [8] M. Popescu *et al.*, ‘Structural design, digital fabrication and construction of the cable-net and knitted formwork of the KnitCandela concrete shell’, *Structures*, p. S2352012420300655, Mar. 2020, doi: 10.1016/j.istruc.2020.02.013.
- [9] ‘DIN EN 196-1:2016-11, Prüfverfahren für Zement_ - Teil_1: Bestimmung der Festigkeit; Deutsche Fassung EN_196-1:2016’, Beuth Verlag GmbH. doi: 10.31030/2482416.
- [10] International Federation for Structural Concrete, *fib model code for concrete structures 2010*. Berlin: Ernst & Sohn, 2013.
- [11] RILEM Technical Committee 232-TDT (Wolfgang Brameshuber), ‘Recommendation of RILEM TC 232-TDT: test methods and design of textile reinforced concrete’, *Mater. Struct.*, vol. 49, no. 12, pp. 4923–4927, Dec. 2016, doi: 10.1617/s11527-016-0839-z.
- [12] J. Yu, C. K. Leung, and V. C. Li, ‘Why nominal cracking strength can be lower for later cracks in strain-hardening cementitious composites with multiple cracking?’, in *Proceedings of the 10th International Conference on Fracture Mechanics of Concrete and Concrete Structures*, Jun. 2019, doi: 10.21012/FC10.234225.
- [13] P. Marti, M. Alvarez, W. Kaufmann, and V. Sigrist, ‘Tension chord model for structural concrete’, *Struct. Eng. Int.*, vol. 8, no. 4, pp. 287–298, 1998.
- [14] N. Gehri, J. Mata-Falcón, and W. Kaufmann, ‘Automated Crack Detection and Measurement based on Digital Image Correlation’, *Constr. Build. Mater.*, vol. submitted for publication, 2020.

Mechanical and mineralogical characteristics of mortars with crushed and river sand

Emmanuel Elat^{1,2,*}, Alexandre Pierre¹, Prosper Pliya¹, Myriam Duc³, Michel Mbessa², Albert Noumowé¹

¹Laboratory of Mechanics and Materials of Civil Engineering (L2MGC), CY Cergy Paris University, 5 Mail Gay-Lussac-Neuville sur Oise, F-95031 Cergy-Pontoise Cedex, France,

²Laboratory of Mechanics, Materials, Structures and Production, (LMMPS), National Advanced School of Engineering, University of Yaounde I: P.O Box 8390 Yaounde-Cameroon,

³University Gustave Eiffel, Laboratory Soils, Rocks and Geotechnical Structures, 14-20 boulevard Newton - Champs-sur-Marne, 77447 Marne-la-Vallée cedex 2, France

Abstract

The aim of this study is to characterize the mixtures of crushed sand and river sand for an optimal use in the formulation of mortars and concretes. Physical, chemical and mineralogical characterization of aggregates was done, followed by the formulation of mortars by substituting 100%, 50% and 0% of river sand by crushed sand. The compressive strength and the water porosity were measured on mortar specimens, completed by a microstructural characterization using XRD, DTG, and SEM examinations. The results showed that ettringite, CSH and portlandite contents are similar in tested mortar while a slight difference of carbonation appeared with a lower carbonation in crushed sand. Besides, 100% river sand mortar was highly porous, with low compressive strength at 28 days, compared to crushed sand mortars containing more fines, less porous and with better compressive strength.

Key words: crushed sand, alluvial sand, mortar, compressive strength, mineralogical characteristics

1 Introduction

River sand is a material widely used in the construction of civil engineering infrastructures. However, its extraction became expensive and limited because of environmental protection. In addition, some regions in the world are located far from rivers, which reinforces the search of sand from various origins. The use of crushed sand from quarries in the production of cementitious materials is an alternative to reduce the overexploitation or to replace the river sand [1]. However, the use of crushed sand may have consequences on the mechanical behaviour and the durability of concretes [2]. Indeed, these sands present various characteristics compared to alluvial sands containing usually finer sized particles and with an adequate morphology to reduce the concrete porosity. These properties ensure granular continuity between cement and gravel for better cohesion of concrete [3].

In Cameroon, the exploitation of aggregate in quarries increased considerably in recent years, with the production of crushed sands. These sands are used in the manufacture of mortars and concretes, while the scientific recommendations on their use remained scarce. It explains the renewed interest in the influence of crushed sand on mortar properties.

Among literature, Menadi et al.[4] studied the strength and durability of concrete incorporating crushed limestone sand. The authors proved that up to 15% of fine content in crushed sand could be used without harmful effect on concrete strength. Cabreræ and al. [5] revealed also a correlation between the void content in mortar and the volume of paste required to start flowing such material.

Furthermore, the mineralogical source of crushed sands influence the concrete behaviour (with the same w/c ratio) as shown by Al-Ameeri [6] on three sands. The crushed sand from granite produced the best properties in term of compressive strength and workability. This behaviour has been attributed to the particular morphology of granite sand particles. Indeed, the texture and shape of the crushed sand particles have a great influence on the combination of cement paste and aggregates. The study concluded that crushed sand is a practical solution to limit the river sand exploitation, as long as the mechanical behaviour and the durability of concretes are not negatively impacted [7].

Based on such ideas, the aim of this study is to estimate the potential of crushed sands to replace alluvial sands, and to highlight the potential problem caused by this replacement for the purpose of better valorization. The study is carried out on three crushing sands and CEM II cement from Yaoundé (Cameroon). Physical, chemical and mineralogical characterization was carried out on sands while mechanical and microstructural tests were carried out on mortars. This work is part of the development of the use of crushing sands in the construction sector.

2 Materials and methods

2.1 Materials

2.1.1 Cement paste

The cement used in this study was a Portland cement NC CEM II of class 42.5 R with a fineness between 3900-4000 cm²/g, and a density of 3.14 g/m³. The cement came from the “Dangote company” located at Yaoundé (Cameroon). The chemical composition of cement determined by X-ray fluorescence (XRF) and its mineralogical composition are presented in Table 1 and Table 2, respectively. The water/cement (w/c) ratio was kept constant at 0.6 for all mortar’s mixtures.

Table 1 : Chemical composition of the cement. LOI: loss on ignition at 1000 T°C

Elt	SiO ₂	Al ₂ O ₃	Fe ₂ O ₃	MnO	MgO	CaO	Na ₂ O	K ₂ O	TiO ₂	P ₂ O ₅	LOI
(%)	25.99	7.23	6.35	0.13	2.56	48.91	1.02	0.91	0.97	0.26	2.67

Table 2 : Mineralogical composition of cement (composition given by the supplier).

Constituents	C ₃ S	C ₂ S	C ₃ A	C ₄ AF
Proportions (%)	50-65	15-20	≤ 7	≤ 5

2.1.2 Sands

Crushed sands whose characteristics are given in Table 3 and Table 4 came from three quarry aggregate mining sites in Yaoundé (Cameroon). The quarry operated by Arab Contractor, Gracam and Razel produced sands noted SA, SG and SR, respectively. The river sand came from the Sanaga River (running from north to south Cameroon) and it was noted SS. Petrographic analysis from thin slices of rock samples from the three quarries showed that rocks are all gneiss, with different textures and mineralogies. The fine fraction in sand, shown in Table 3, varies from 1.4% (SS) to 8.3% (SG). The fineness modulus remained quite similar for all sands (around 2,6). The sand equivalent (SE) test gives a SE percentage between 82.5 and 95.5%, reflecting the great cleanliness of sands, but with the risk of causing a defect in the plasticity of the concrete. [8].

Table 3. Fineness modulus and sand equivalent for tested crushed sands

Sand	Fines content (< 80 µm: %)	Fineness modulus	Sand equivalent (%)
SA	6.3	2.4	87.3
SG	8.3	2.7	89.9
SR	7.6	2.6	82.5
SS	1.4	2.6	95.9

Table 4. Chemical composition of crushed sand (%) from XRF (NF P 18-598). LOI: loss on ignition.

Sand	SiO ₂	Al ₂ O ₃	Fe ₂ O ₃	MnO	MgO	CaO	Na ₂ O	K ₂ O	TiO ₂	P ₂ O ₅	LOI
SA	65.50	15.69	7.76	0.16	2.74	1.37	1.76	2.68	0.95	0.14	0.57
SG	62.55	16.61	8.81	0.19	3.18	1.68	1.84	2.68	1.00	0.17	0.41
SR	67.53	13.73	7.66	0.14	2.43	2.22	1.82	2.13	1.03	0.19	0.48
SS	90.16	3.96	1.54	0.03	0.08	0.23	0.43	2.01	0.23	--	0.79

The chemical composition of sands determined by X-ray fluorescence (XRF) in Table 4 showed similar compositions for all crushed sands. Sands are mainly siliceous with aluminum and iron. The proportions of aluminum and iron ($\text{Fe}_2\text{O}_3 + \text{Al}_2\text{O}_3$) are 23.45%, 25.42%, 21.39%, for SA, SG, SR, respectively, while this proportion reached only 5.5% for the river sand SS. The percentages of alkali equivalents ($\% \text{Na}_2\text{O} + 0.658\% \text{K}_2\text{O}$) are 3.84%, 3.89%, 3.33% and 2.29% for SA, SG, SR and SS, respectively. The crushed sands had a calcium content (CaO) around 7 times higher than river sand.

Figure 1 shows the diffractograms of crushed sands SA, SG, SR and river sand SS. The quantitative analysis of XRD patterns with TOPAS software (Rietveld method) showed that the river sand is essentially composed by quartz SiO_2 (85.6%), biotite $\text{K}(\text{MgFe})_3(\text{OH})_2(\text{Si}_3\text{AlO}_{10})$ (0.05%) and feldspars such as microcline $\text{K}(\text{AlSi}_3)\text{O}_8$ (10.6%) and albite $\text{Na}(\text{Si}_3\text{Al})\text{O}_8$ (3.6%). The degree of crystallinity is about 87%. Similar crystalline phases were observed in crushed sands but they differ from river sand by the presence of a few additional phases. The average degree of crystallinity of the 3 crushed sands is around 96%. The main phases are quartz (57.2%), biotite (0.1%), mica (Annite) $\text{Si}_3\text{AlO}_{10}(\text{OH})_2\text{Al}_2\text{K}$ (4.1%), Andesine $(\text{Ca},\text{Na})(\text{Al},\text{Si})_4\text{O}_8$ (4%), Almandine $\text{Al}_2\text{Fe}_3(\text{SiO}_4)_3$ (15.1%) and feldspars such as microcline (9.5%) and albite (9.7%). Such mineralogy is in accordance to the geological origin of sands (Gneiss). However the identification of traces of dolomite $\text{CaMg}(\text{CO}_3)_2$ (0.25%) is not in accordance with the geological identification of the rock.

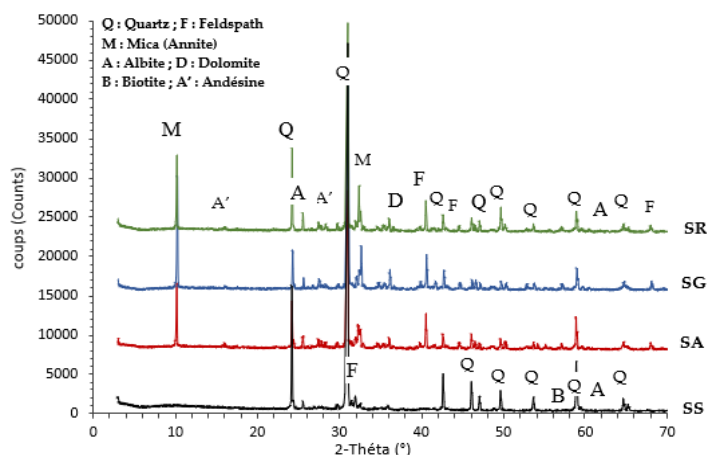


Fig. 1. XRD patterns of crushed sands SA, SG, SR and the river sand SS

2.2 Experimental program

2.2.1 Mixing procedure of mortars

The mixing procedure in this work is the Equivalent Concrete Mortar (ECM) method. Its principle is based on the existence of a simple correlation between the concrete rheological properties and the one of the mortar it contains [9]. It consists in replacing the granular skeleton with sand by keeping the same volume of cementitious paste and the same cement amount. We focused on the mixtures corresponding to mortars with 100%, 50% and 0% of SS and SR sands. The corresponding mortars are rated MSR100 (M: mortar, S: Sanaga sand, R: Razel sand, 100% Razel sand), MSR-50 (M: mortar, S: Sanaga sand, R: Razel sand, 50% Razel sand) and MSR-0 (M: mortar, S: Sanaga sand, R: Razel sand, 0% Razel sand), respectively. The w/c ratio 0.6 was similar for all the concretes while the CEM II/ B-P 42.5R cement content was fixed at 350kg/m^3 . The compositions of mortars are given in Table 5.

Table 5. Compositions of manufactured mortars (for 1 m^3)

Component (kg/m^3)	MSR0	MSR50	MSR100
Crushed sand	0	918	1900
River sand	1771	918	0
Cement	350	350	350
Water	206	206	206

Using such formulation, prismatic specimens of mortar 40 x 40 x 160 mm have been made according to the EN 196-1 standard and tested after water immersion curing for 28 days. Results are the average of three tested specimens.

2.2.2 Testing methods

The compressive and bending strengths of mortars specimens were measured with a loading rate of 1.0 kN/s according to the NF P 18-406 standard. The water porosity test was carried out according to NF P 18-459 standard. The specimen was dried at 105°C at the end of the water porosity test and not initially as recommended in the standardized method. It allowed to lower the microstructural damage induced by high temperature.

The measurement of endogenous shrinkage was carried out on mortar samples according to the conditions described in standard NF P 18-427 and under climatic conditions at $T=20\pm 2^\circ\text{C}$ and $50\pm 5\%\text{RH}$.

X-ray diffraction (XRD) analyses were applied on sands and mortars ground to pass through a 80 μm sieve. Analyses were performed using a Bruker AXS D8 Advance diffractometer, in theta-theta geometry, equipped with a cobalt source ($\lambda = 1.79 \text{ \AA}$), without monochromator and a lynx Eye fast detector. Identification was done with EVA software coupled with ICDD Pdf2 mineralogical data base. The quantitative analyses were done with TOPAS software (Rietveld Analysis).

A thermal analyzer NETZSCH STA 409 E was used to collect the thermogravimetric curve (TG) and the derived thermogravimetric curve (DTA). Analyses allowed to evaluate the portlandite $\text{Ca}(\text{OH})_2$, ettringite, C-S-H and calcium carbonate (CaCO_3) content in MSR0 and MSR100 mortars. The powder sample was heated from 20 to 1100 °C with a 10 °C/min heating rate under nitrogen to avoid carbonation during analysis.

The microstructure of mortars (after resin inclusion and polishing) was evaluated by Scanning Electron Microscope (SEM) using back scattered electrons mode. A chemical cartography was collected on polished surface by Energy Dispersive Spectroscopy (coupled with SEM). The morphology and the adhesion at paste/sand interface in mortars were evaluated [10].

3 Results and discussion

3.1 X-ray diffraction (XRD) on mortars

The XRD patterns of SR sand and mix-sand mortars MSR100 and MSR50 are presented on Fig. 2 while XRD patterns of SS sand and mix-sand mortars MSR0 and MSR50 are presented on Fig. 3.

The analysis shows that after cement addition, a few changes occurred on XRD patterns. Changes of peaks height may be due to a variation of the phase quantities (because of sands mixture, cement dilution or phase dissolution in alkaline medium) as well as a variation of particle aggregation. Indeed, the preferential orientation of phases during the filling of the XRD sample holder used is decreased in presence of cement paste. The preferential orientation mainly affects the sheet-formed phases becoming parallel to the plan of sample compaction in XRD sample holder. In presence of cement which allows the sheet dispersion and then their immobilization after hardening, the preferential orientation decreased inducing for example a decrease of annite peak at $d = 10.09 \text{ \AA}$ while its quantity may remain constant.

A small peak associated with portlandite ($d=4.92 \text{ \AA}$) was observed as expected in the presence of Portland cement and the detection of crystalline or amorphous hydrates C-S-H remained difficult as shown by the zoomed view on Fig. 5 (a, b). Zoom represents the specific 2theta range for main XRD peaks of cementitious hydrates and calcite/dolomite. In the case of SR sand, the trace of calcite ($d = 3.00/2.99 \text{ \AA}$) seemed to come from the sand itself (but its presence is not in accordance to the geology). Carbonation of the cement during curing occurred slightly with the development of a second peak associated to a new calcite form ($d = 3.04 \text{ \AA}$), also present on SS river sand mortar. The formation of calcite comes from the carbonation of Portlandite $\text{Ca}(\text{OH})_2$. Such phase is soluble in pore water and releases Ca^{2+} and OH^- ions. In the presence of CO_2 from the air, calcite may precipitate in such conditions. Calcite can also be obtained from the carbonation of cementitious hydrates that remain usually under amorphous state in a hardened cementitious paste. The change in the degree of crystallinity from TOPAS analysis also cannot help to detect an increase of amorphous product.

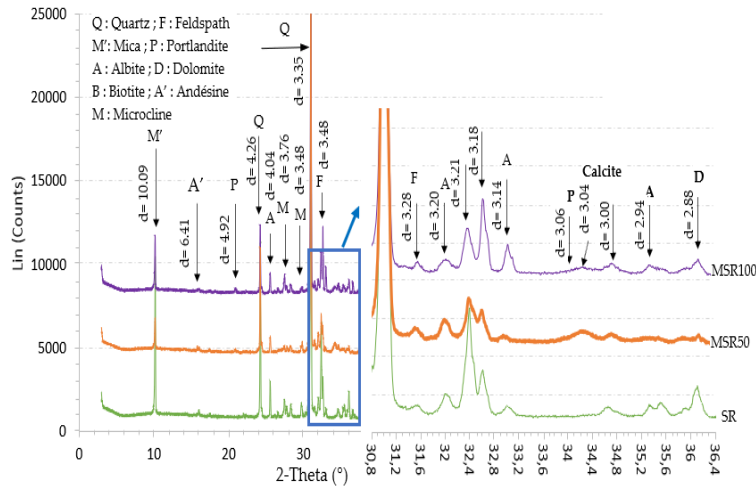


Fig. 2. XRD patterns of SR sand and mix-sand mortars MSR100 and MSR50

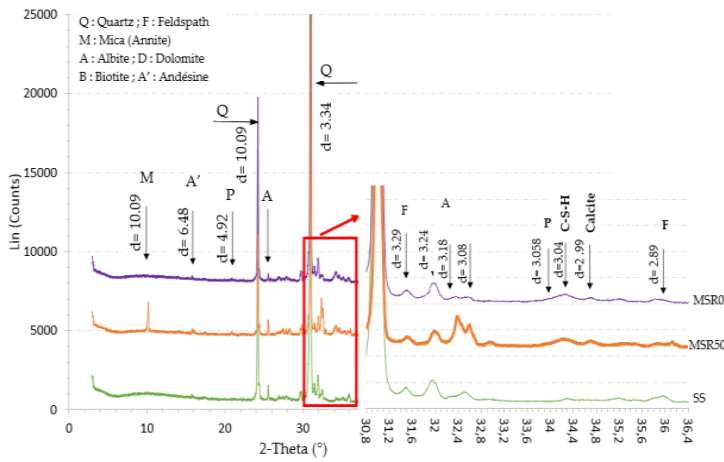


Fig. 3. XRD patterns of SS sand and mix-sand mortars MSR0 and MSR50

3.2 Water porosity

The water porosity values of mortars and the measuring system are presented in Fig. 4.

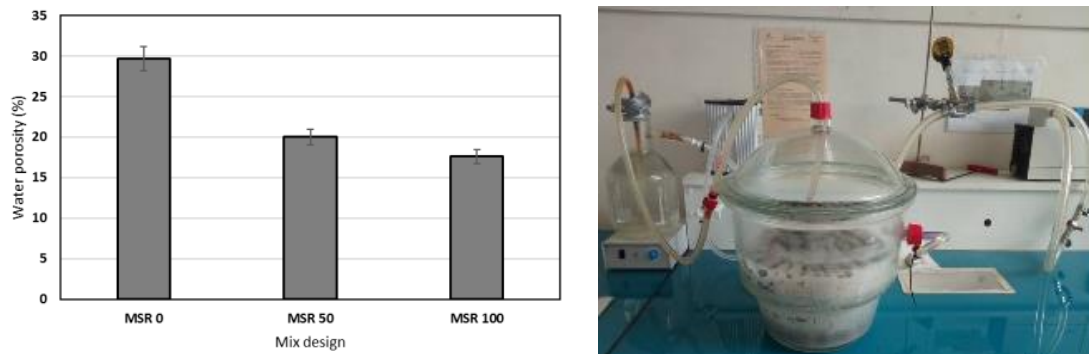


Fig. 4. a) The water porosity of different mortars, b) Sample saturation between measurement

The river sand mortar MSR0 showed a high porosity value ($P = 29.7\%$) compared to the crushed sand mortar MSR100 ($P = 18\%$). This difference was attributed to the low fine particle content in river sand ($< 80\mu\text{m} = 1.4\%$ against 6,5-8,5%). The mortar MSR50 manufactured with 50% of crushed sands presented an average porosity of 20% in Fig. 2. So, the presence of crushed sand in mortar decreased the water porosity, which is correlated to the improvement of compressive strength. On the other hand, the various formulations were made on the assumption of an identical w/c ratio, allowing a higher quantity of river sand and thus favouring a more interconnected porous structure.

3.3 Compressive strength and drying shrinkage

Figure 5 presents the compressive and bending strengths of mortars after 28 days curing in water.

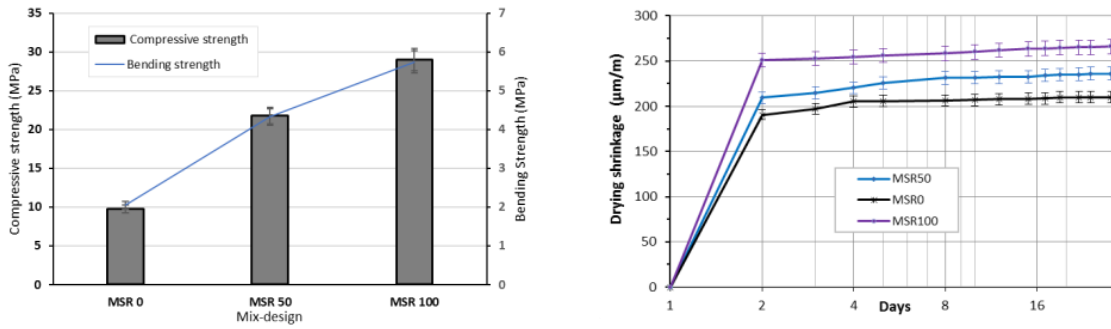


Fig. 5. Compressive strength and bending strength (a), drying shrinkage (b) measured on mortars

The results show that mortar containing only river sand has a very low compressive strength ($R_c = 9.5 \pm 0.4$ MPa) compared to crushed sand mortars ($R_c = 20$ -30 MPa). This situation can be explained by the low content of fine particles in the river sand ($< 80 \mu\text{m} = 1.4\%$) compared to the crushed sands ($< 80 \mu\text{m} = 7.6\%$). Indeed, a high fine content is necessary for cohesion at the interface between the cement matrix and sand as well as for a low porosity. This average difference was about 7 MPa between 100% crushed sand mortars and 50/50 mixed sands mortars. The average compressive strength value was around 22 MPa for MSR50.

The shrinkage curves for all mortars show a small variation of the shrinkage after the second day of drying (same speed). It reflects the creation of voids within the matrix induced by the consumption of pore water, which induces a capillary depression within the system and thus a so-called self-dehydration deformation [11]. However, the MSR100 mortar has a greater shrinkage speed than the MSR0. The shrinkage is moderate for the MSR50 mortar.

3.4 Thermogravimetric analysis

The Fig. 6 (a, b) shows the TG curves and the differential thermal analysis (DTA) for the mortars MSR0 and MSR100 after 92 days curing in water.

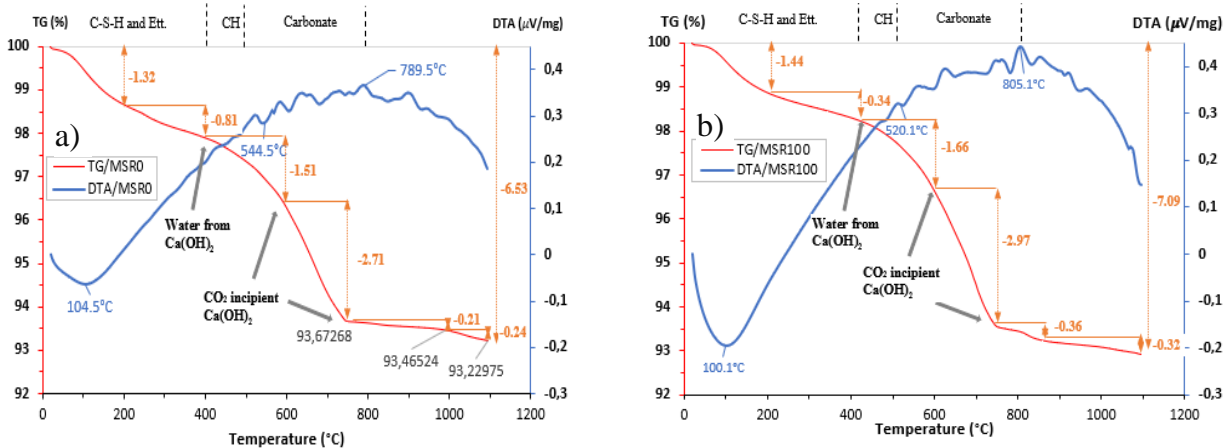


Fig.6. TG curves on MSR0 mortar (a) and MSR100 mortar (b).

The mass loss associated to each inflection points can be used to determine portlandite, C-S-H and calcite contents. For all analyses, the first mass loss between 20 and 400°C resulted mainly from the loss of free water and the dehydration of C-S-H and ettringite. The second mass loss around 460°C came from the decomposition of portlandite (CH). The third inflection point occurring between 600 and 800°C the consequence of the decarbonation of calcium carbonate (CaCO_3) produced by carbonation and other carbonated compounds [12]. The analysis shows that total mass losses or loss on ignition of MSR0 (LOI = 6.53%) and MSR100 (LOI = 7.09%) were similar. However, the mass losses at particular temperature appeared slightly different. The mass loss between 20 and 400°C

(dehydration of ettringite and CSH), between 410 and 480 °C (dehydration of CH) and between 580 and 750 °C (decarbonation) represented 1.32% and 0.81%, 2.71% (Fig.6a) for MSR0 mortar and 1.44%, 0.34%, 2.97% (Fig.6b) for MSR100 mortar. The carbonation of river sand mortar is slightly higher than the one occurring in crushed sand mortar. It could be link to the higher porosity of the river sand mortar. The other phases (CSH, ettringite or portlandite) seemed to be similar whatever the nature of the sand and no negative effect seemed to appear.

3.5 Energy dispersive spectroscopic (EDX) analysis

The Fig.7 shows the EDX chemical mapping of silicon (Si) and calcium (Ca) on MSR0, MSR50 and MSR100 mortars after their inclusion into resin and polishing.

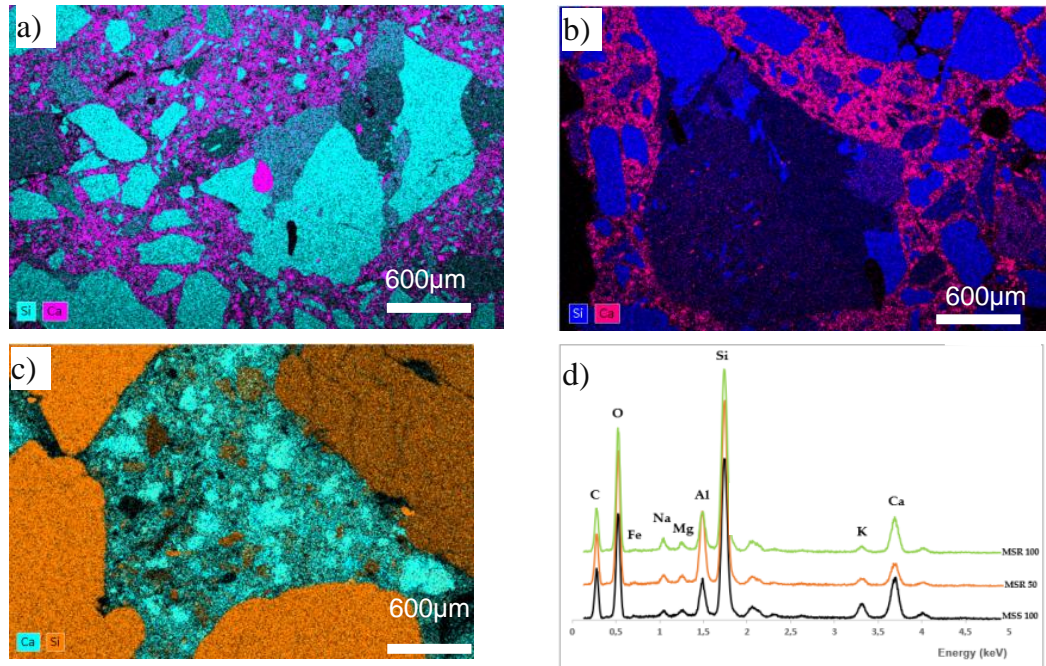


Fig.7. Silicon (Si) and calcium (Ca) mapping on mortar pastes (a) MSR100 (Si: blue, Ca: pink), (b) MSR50 (Si: blue, Ca: pink), (c) MSR0 (Ca: blue, Si: orange), (d) EDX spectra on concretes.

The 100% river sand mortar (Fig. 7c) showed silica aggregates (in orange) with irregular shapes, rounded angle and sizes ranging from 20 μm to several hundred micrometers, unlike 100% crushed sand mortars (Fig. 7 a). Crushed sand presented some angular particles (consequence of the crushing). The cement paste rich in calcium appeared in pink on Fig. 7a and b and in blue on Fig.7d and it filled the spaces between aggregates. The paste incorporated fine particles contained in crushed sands while the paste in 100% sand river mortar appeared more porous with non-homogeneous blue colour (the porosity appeared in black or dark blue in cement paste). In comparison, the cementitious matrix of the mixed sand mortars (Fig. 7 b) seemed more homogeneous with a better granular dispersion.

4 Conclusions

This study focused on the characterization of crushed sand and river sand as well as on their mixture in mortars. As a conclusion, the three tested crushed sands from Cameroon had a high proportion of fine particles (%), while the tested river sand presented a low fine content (%), which contributes to explain the difference of behaviour in mortars. Furthermore, thermogravimetric analysis (TG) revealed that the introduction of crushed sand didn't impact strongly the cementitious phases development. Ettringite, CSH or portlandite content from thermal analysis are similar in tested mortar while a slight difference of carbonation appeared with a lower carbonation in crushed sand that presented the lower water porosity (lower accessibility of CO_2 gas to the paste). Results are confirmed by XRD measurements showing the appearance of a small peak of calcite in mortar as well as portlandite.

The high fine content of the crushed sand does not have a negative influence on the compressive and bending strength of the mortars. MSR100 mortar has a high mechanical compressive strength compared to MSR0, moderate shrinkage is observed for the MSR50 mortar. Concerning the mortars

manufactured with sands mixtures, the compressive strength of hardened mortar is directly linked to the porosity. As expected, the compressive strength values of MSR50 mortars higher than 20 MPa proved that the mixture of river and crushed sands allowed the manufacture of mortars with satisfactory properties.

Results confirmed the ability to mix crushed sand with alluvial sand in the formulation of mortars, while increasing the mechanical strength and decreasing the water porosity. Now, this work has to be completed by durability test, especially the analysis of alkali-reaction.

Acknowledgements

This research work is part of a co-tutorship agreement between the CY Cergy Paris University (France) and the University of Yaoundé I (Cameroon). The authors gratefully acknowledge the financial support provided mainly by Campus France.

References

- [1] M. L. K. Khouadjia, B. Mezghiche, et M. Drissi, « Experimental evaluation of workability and compressive strength of concrete with several local sand and mineral additions », *Construction and Building Materials*, vol. 98, p. 194-203, nov. 2015, doi: 10.1016/j.conbuildmat.2015.08.081.
- [2] L. Zeghichi, Z. Benghazi, et L. Baali, « The Effect of the Kind of Sands and Additions on the Mechanical Behaviour of S.C.C », *Physics Procedia*, vol. 55, p. 485-492, janv. 2014, doi: 10.1016/j.phpro.2014.07.070.
- [3] J. Dang et J. Zhao, « Influence of waste clay bricks as fine aggregate on the mechanical and microstructural properties of concrete », *Construction and Building Materials*, vol. 228, p. 116757, déc. 2019, doi: 10.1016/j.conbuildmat.2019.116757.
- [4] B. Menadi, S. Kenai, J. Khatib, et A. Aït-Mokhtar, « Strength and durability of concrete incorporating crushed limestone sand », *Construction and Building Materials*, vol. 23, n° 2, p. 625-633, févr. 2009, doi: 10.1016/j.conbuildmat.2008.02.005.
- [5] O. A. Cabrera, L. P. Traversa, et N. F. Ortega, « Fluidez de morteros cementíceos con arenas machacadas », *Mater. construcc.*, vol. 60, n° 300, p. 115-130, déc. 2010, doi: 10.3989/mc.2010.50909.
- [6] A. Al-Ameeri, « using different types of fine aggregate to produce high strength concrete », *International Journal of Arts & Sciences; Cumberland Vol. 5, N° 7, (2012): 187-196*
- [7] B. Benabed, E.-H. Kadri, L. Azzouz, et S. Kenai, « Properties of self-compacting mortar made with various types of sand », *Cement and Concrete Composites*, vol. 34, n° 10, p. 1167-1173, nov. 2012, doi: 10.1016/j.cemconcomp.2012.07.007.
- [8] « Sand Equivalent », *Pavement Interactive*. <https://pavementinteractive.org/reference-desk/testing/aggregate-tests/sand-equivalent/> (consulté le avr. 04, 2020).
- [9] S. Yang et H. Lee, « Mechanical properties of recycled aggregate concrete proportioned with modified equivalent mortar volume method for paving applications », *Construction and Building Materials*, vol. 136, p. 9-17, avr. 2017, doi: 10.1016/j.conbuildmat.2017.01.029.
- [10] K. L. Scrivener, « Backscattered electron imaging of cementitious microstructures: understanding and quantification », *Cement and Concrete Composites*, vol. 26, n° 8, p. 935-945, nov. 2004, doi: 10.1016/j.cemconcomp.2004.02.029.
- [11] M. Bouasker, « Étude numérique et expérimentale du retrait endogène au très jeune âge des pâtes de ciment avec et sans inclusions », thesis, Nantes, 2007.
- [12] G. Villain, M. Thiery, et G. Platret, « Measurement methods of carbonation profiles in concrete: Thermogravimetry, chemical analysis and gammadensimetry », *Cement and Concrete Research*, vol. 37, n° 8, p. 1182-1192, août 2007, doi: 10.1016/j.cemconres.2007.04.015.

Numerical study on the micro-mechanical behaviour of artificial granular materials

M. Amine Benmebarek*, Majid Movahedi Rad

*Department of Structural and Geotechnical Engineering,
Faculty of Architecture, Civil Engineering and Transport Sciences,
University of Győr, Egyetem tér 1, Győr 9026, Hungary.*

Abstract

Numerical models for the simulation of the micro-mechanical behaviour of granular assemblies have a wide range of applications, for instance in material science, process engineering, environmental engineering, railway engineering and geotechnical engineering (in this study we examined one macro-grain but what important is behaviour of granular assemblies). In this examination, experimental tests and numerical computations using the discrete element method (DEM) are carried out to evaluate the micro-mechanical behaviour of the granular materials. For this purpose, artificial materials are taken into consideration for experimental Brazilian laboratory tests, and then according to the experimental results the DEM model is calibrated. Artificial crushable materials are produced by mixing cement and silt according to their mass ratio, in which cement can provide bonding and silt is the main filling material. In the DEM model, a 3D crushable granular material ‘macro-grain’ is built up from a large number of micro-grains which are associated according to crushable parallel bond properties. The behaviour of the single crushable grains and the fragmentation patterns under different contact configuration and load position are studied. The DEM simulation results show that the contact configuration type and load position affect the fragmentation patterns and loading capacity.

1 Introduction

The strength and breakage mechanisms of grains is a problem that has a great importance mostly in civil engineering and in the mineral industry. The breakage of individual grains and the resulting rearrangement of the solid particles are the primary mechanisms controlling the constitutive behavior of crushable granular materials subjected to high compressive stresses [1]-[4].

These complex microscale processes play a critical role in the performance and serviceability of several engineering applications, including embankments [5], rockfill dams [6] and railway tracks and geotechnical engineering [7].

The crushing of the grains leads to a modification of the grain size distribution, the shape of the grains, the ratios of critical strengths and the limit void ratios [8], [9].

Prior experimental observations uncovered that macro-grain crushing of a grain assembly under compression is affected by several factors, including, local micro-structure defects, particle size and shape, boundary conditions and coordination number [10]-[15].

During the loading processes, the particles of the granular assembly materials could slide, rotate, and crush or separate. The strength and the crushability of a granular assembly depend on the coordination number and location of the contact points. A high coordination number is known by its effect of increasing particle strength and of preventing crushing. Wang and Arson [16] have clarified this mechanism by the redistribution of the compressive forces concentrated at the contact points of the particles in a distributed pressure close to the hydrostatic pressure conditions.

Trial investigations of such factors of impact in laboratory experiments are difficult, expensive, time-consuming and usually constrained to macroscopic considerations [17]. Further, systematic experimental investigation of grain crushing for natural materials is often difficult due to the relatively high stress required to crush the grains and the variability and heterogeneity of natural deposits, which makes it difficult to obtain repeatable results [18].

In comparison to experimental investigations, numerical modeling offers the opportunity to see dynamic processes and spatial coordinates in given time. Important process parameters, such as the spatial redistribution of the compressive forces, the shear/tension failure modes, the distribution of micro-cracks can be examined. Detailed micro- and macro-scale informations can likewise be recorded.

In this context, according to McDowell [19], the discrete element method (DEM) has been one of the most widely recognized numerical approaches to model particle fracture in granular materials in that it provides a virtual laboratory to simulate mechanical tests without the size limitations encountered in the laboratory.

Furthermore, to obtain similar testing results, artificial materials are taken into consideration for experimental Brazilian laboratory tests then according to the experimental results the DEM model, carried out using the Itasca Particle Flow Code (PFC 3D), is calibrated. The behaviour of the single crushable grains and the fracture/crack patterns of the grains under different contact configuration and load position is studied.

2 Experimental work

2.1 Description of the material

In this investigation, the experimental work was conducted on artificially crushable materials made by blending uniformly silt, cement and water according to their ratio of mass, in which the silt was the main matrix while the cement provides bonding between the silt particles. The cement utilized was 325R Portland and the silt with dark color was taken from Raab river near Gyor city area.

In the current work, the mass proportion of cement to silt is controlled by experimentation to guarantee that the crushable materials are sufficiently strong to investigate their crushing properties subject to quasi-static loading. The silt, cement and water ratio was determined to be 100: 40: 71.

A group of six cylindrical samples with a height of 60 mm and a diameter of 60 mm of crushable material was prepared in order to estimate the peak loading before cracking. The samples were produced by filling the mixture in hollow tubes with length and diameter of 60 mm. The phases in the process for preparing the crushable cylindrical particles are as follow:

- Artificial material mixes were made in a container blender,
- based on their mass proportions, the cement and silt were first uniformly blended for around 1 min, and 50% of water was added, then the mixture was mixed for 1 min to allow absorption. The rest of water was added to this blend to form a uniform slurry by mixing for another 2-3 min,
- lubricating oil was then spread uniformly on the glass plate and put in hollow tubes to allow the remove of samples effectively after they were framed into cylindrical shapes,
- all samples were expelled from the molds after 24 h. After casting, samples were then cured at a temperature of 20 ± 3 C for 28 days.

2.2 Test procedure

In order to validate the DEM model, the Brazilian strength test was first performed to study the strength behavior of prepared samples of artificially crushable cylindrical materials. Displacement transducer were used for the measurement. The samples were loaded through plywood strips with a width of 1/6 of the sample diameter. The samples were compressed between two diametrically opposite loading strips as shown in Fig. 1.

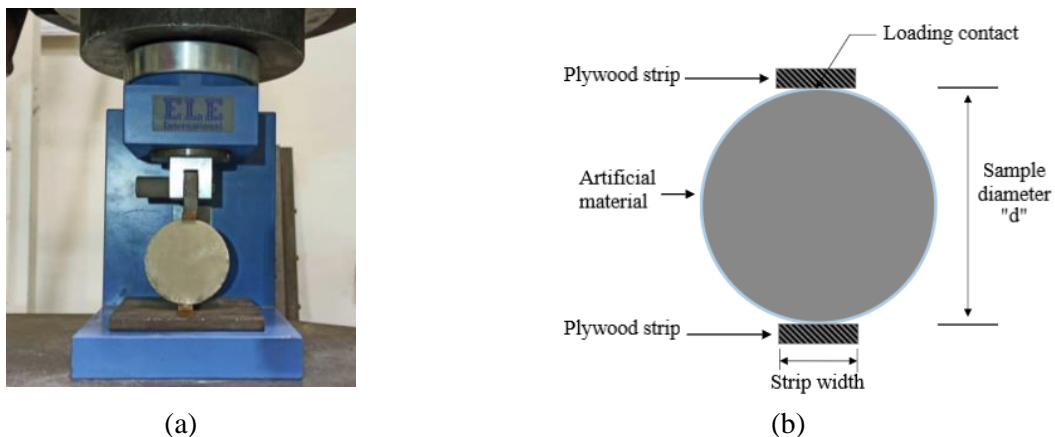


Fig. 1 (a) Setup of Brazilian test. (b) Sketch of the initial geometry of the sample in the splitting tensile test.

During the increase of the externally applied load frame with a constant loading velocity of $v=0.025$ mm/s, the reaction force was recorded as a function of displacement until the breakage of samples. Thus, the load-displacement data has been plotted for all of the samples.

2.3 Experimental results

In order to get an accurate result, the Brazilian laboratory test was repeated for the six samples. As the compressive force increases, the tensile crack propagates towards the loading point and the sample breaks into two main parts. It needed about 1-2 min from loading to failure of the artificial samples. In all tests a single crack was observed, accompanied sometimes by the formation of a thin wedge bellow the loading strips as shown in Fig. 2-(a).

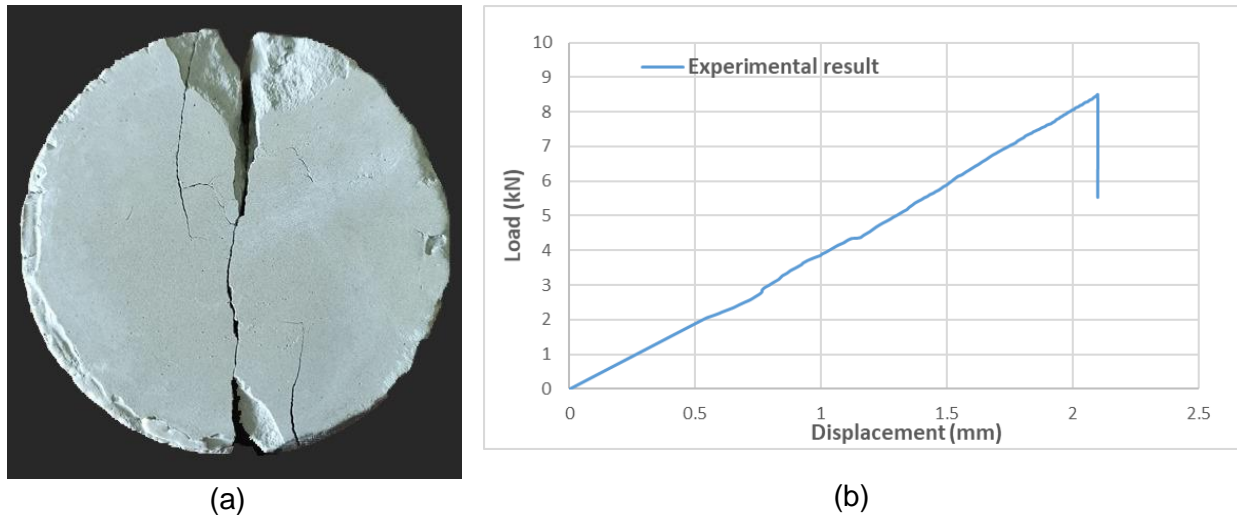


Fig. 2 (a) Typical failure observed for artificial cylinder samples subjected to Brazilian test. (b) Typical load-displacement diagram of artificial material in the Brazilian tests.

Similar load-displacement results were measured for all Brazilian laboratory tests. Fig. 2-(b) illustrates typical corrected load-displacement recorded for one of the samples. The correction includes the initial nonlinear displacement due to the loading contact defect and deformation of the plywood strip. A brittle failure was observed for all Brazilian tests. The applied force increases with the increase of the prescribed vertical displacement and it drops abruptly after the peak point. The average peak contact load 8.4 kN was reached at vertical diameter rapprochement of 2.2 mm

3 DEM model of crushable macro-grain

3.1 PFC3D model

All numerical simulations were carried out through the commercial PFC3D software [20]. PFC provides an embodiment of the Discrete-Element Method (DEM). In DEM, artificial crushable macro-grain breakage can be modelled using the cluster method with breakable agglomerates. Crushable macro-grains are represented by a cluster of smaller elements “balls” that are bonded together.

In the bonded balls implemented in PFC3D, the linear parallel bond consists of a linear model and a parallel bond interfaces. The linear model interface can carry only a non-tensional force and slipping in the shear (tangential) direction is governed by a Coulomb criterion. The parallel bond interface is also linear elastic and can carry both force and moment.

Balls can be bonded together to form clusters of different sizes and shapes. Interactions between bonded balls are governed simultaneously by three constitutive laws: a ball contact-stiffness model, a ball slip model and a bond model. Relative motion at the contact, occurring after the parallel bond has been created, causes a force and moment to develop within the bond material. This force and moment

act on the two contacting pieces and can be related to maximum normal and shear stresses acting within the bond material at the bond periphery. The cluster breaks when stresses in the bonds exceed the corresponding bond strengths. Parallel bonds mimic the role of a sticky grain cementing agent that can transmit forces and moments applied between the bounded particles.

Once the tensile strength or shear strength of a bond is achieved during loading, bonds break and neighboring pieces are free to behave as if they are in an unbonded state. For instance, frictional slip may occur locally, simulating the initiation and propagation of fractures. The main components of these two interfaces are listed in table 1.

3.2 Model calibration

We calibrate the bond parameters of the DEM cylindrical macro-grain model to better matching force–displacement curves obtained with our experiments during Brazilian crushing tests performed on cemented silt. With the purpose of reproducing the conditions of the experiment, the diameter of the micro-grains was set to 0.15 m. The loading platens were modeled by plate rigid walls.

Within the loading phase, the bottom wall was fixed and the top wall was under a constant velocity $v=0.01\text{m/s}$, which was chosen pretty small to simulate quasi-static loading conditions.

During the entire simulation, we monitored the force-displacement contact, as well as the number of broken bonds. The calibrated parameters are shown in Table 1.

Point out that since the balls and bonds obey a linear elastic behavior before breakage, the load–displacement curve is linear before the first peak. After the first fragmentation, internal forces in the macro-grain are relaxed, which explain the sudden drop of the contact forces after the peak.

Typical simulation results of calibrated model are shown in Fig. 3, in which we can see that when the first peak force is reached, the macro-grain breaks into two main parts (Fig. 2-a), which is in accordance with experimental results (Fig. 2-b).

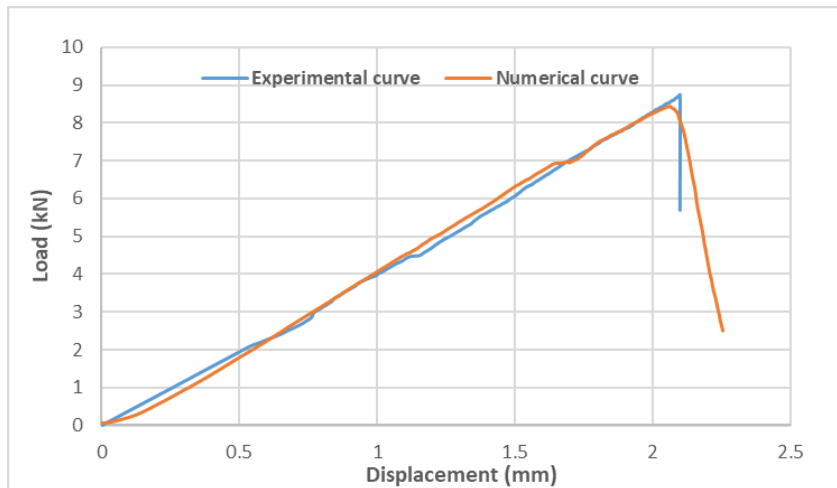


Fig. 3 Load-displacement diagram during the Brazilian test simulated by the DEM: calibration of DEM macro-grain model against experimental test results.

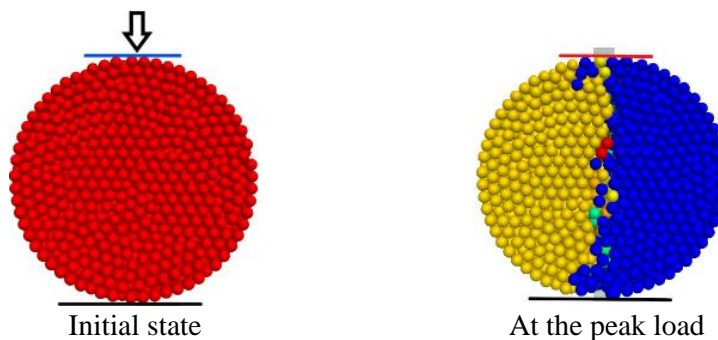


Fig. 4 Fracture patterns for calibrated model: before (left) and after the peak load

Table 1 Parameters used in the DEM simulation

Elementary particle size, D	mm	0.15
Installation gap, g_i	mm	0.002
Density	kg/m ³	2400
Young's modulus of the particle, E^*		GPa
Ratio of normal to shear stiffness of the particle, K_n/K_s		1
Particle friction coefficient, μ		0.5
Young's modulus of the parallel bond, \bar{E}	GPa	0.14
Ratio of normal to shear stiffness of the parallel bond, \bar{K}_n/\bar{K}_s		1
Tensile bond strength	MPa	1.3
Cohesion bond strength	MPa	7

4 Results of modeling contact effect

The bonds breakage in the crushable macro-grain is investigated for various coordination numbers and the corresponding location of the contact points. Two contact models were considered: grain-platens contact model and grain-cylinder walls contact model.

In case of grain-platens contact model (GPCM) the crushable macro-grain was loaded using rigid platens. For the grain cylinder walls contact model (GCCM), the crushable macro-grain was loaded using smaller diameter cylinder walls than our samples, which simulate the condition in a grain assembly more realistically. These two models are defined in more detail in the following.

4.1 Grain-platen walls contact model (GPCM)

In order to investigate the impact of location and number of rigid loading platens on the load-displacement behavior of the crushable cylindrical macro-grain, three other cases are considered in addition to the case 1 considered for the calibration of the model.

In case 2 four platens were in contact with the crushable cylindrical macro grain, the four equidistant platens perpendicular on the crushable macro grain were moved toward the center of the crushable macro-grain. In cases 3 and 4, three platens were in contact with the macro-grain in which the top platen was parallel to the horizontal axis and the other two plates were 45° from the horizontal axis. All platens were moved towards the center for the third case, while for the fourth case, only the top platen was moved towards the center and the two inclined platens were fixed.

4.1.1 Case GPCM-2

In the case GPCM-2, the four perpendicular platens were moving towards the center of the macro grain as shown in Fig. 5-(a). The fracture pattern shows when the peak is reached, the macro-grain breaks into four major pieces and a number of smaller fragments. The force-displacement contact diagram (Fig. 5-(c)) shows more complex post-peak behavior, and that is explained due to a several major failures in the macro-grain (Fig. 5-(b)). The highest load measured was 10.2kN which we can consider the main peak failure point with a displacement of 1.45 mm of the top wall. This displacement is half of total displacement of the top and bottom walls.

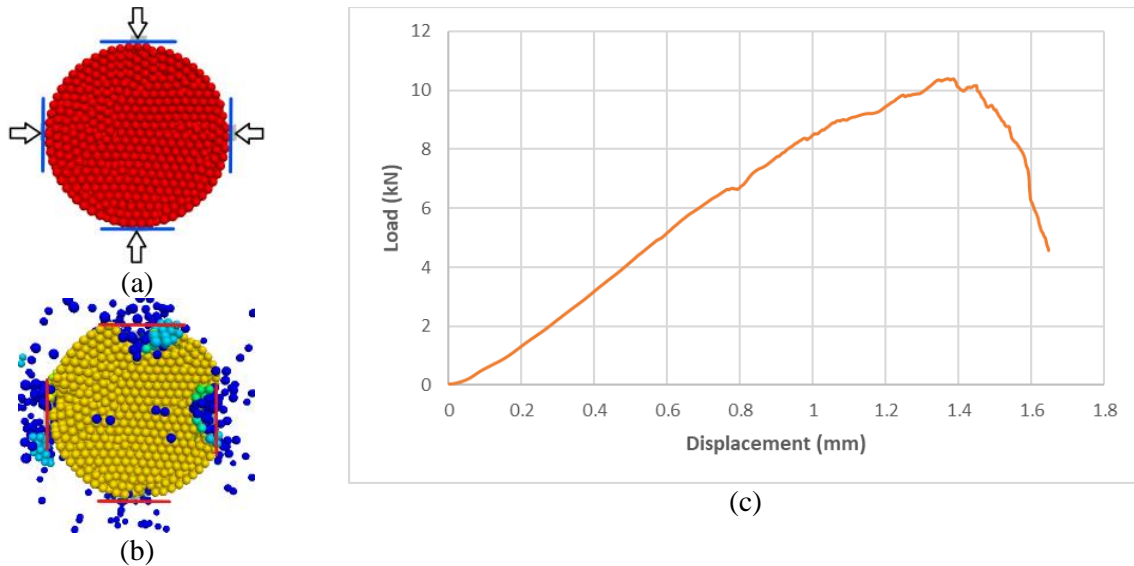


Fig. 5 Fracture patterns for case GPCM-2: (a) before and (b) after the peak load (c) force-displacement curve.

4.1.2 Case GPCM-3

In the case of top horizontal platen and two inclined platens all moving towards the center (Fig. 6-(a)), the fracture pattern shows that the macro-grain breaks into three parts (Fig. 6-(b)) limited by three major cracks perpendicular to each platen and intersect near the center of the macro-grain. The recording of loading-displacement (Fig. 6-(c)) indicates that the vertical contact load increases linearly and reaches a pre-peak of 9.5 kN at displacement of 1 mm, then continues to increase until a peak value of 11.4 kN with loading displacement of 1.27 mm (note that the displacement is smaller than the calibrated case because all the platens are moving while in first case it was only the top plate). The post-peak is marked by a drop of loading curve with some intermediate peaks.

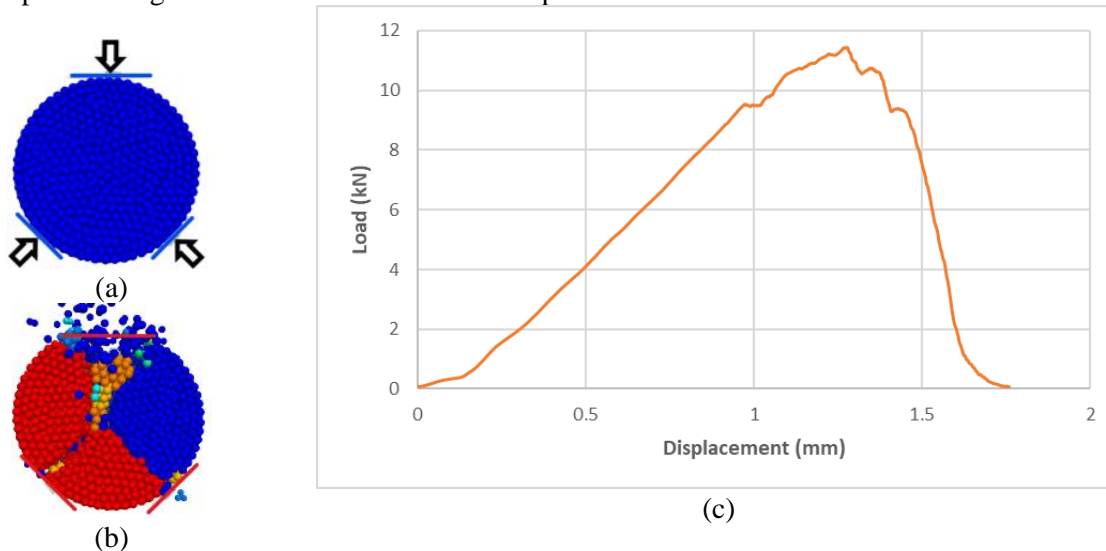


Fig. 6 Fracture patterns for case GPCM-3: (a) before and (b) after the peak load (c) force-displacement curve.

4.2 Grain-cylinder contact model (GCCM)

In order to examine the contact properties in a grain assembly near to reality, cylindrical rigid wall was set around the crushable macro-grain. The load was transmitted from the rigid cylindrical walls to the crushable macro-grain. Different boundary conditions were investigated like the previous grain-platen model as shown in Fig.8. The plot of the fracture pattern at the peak load of GCCM is similar to the cases of GPCM where both show cracks in the macro-grain and the breakage mechanism is nearly a sudden drop.

Essential results of peak loading with displacement of grain-cylinder model are summarized in Table 2. It should be pointed that the vertical displacement is corresponding only to the top cylindrical wall in case of GCCM-2 and GCCM-3. The loading capacity in these cases are smaller than the cases of grain platen model. It can be explained mainly by the reduction of contact surface linked to the curved surface in the cylindrical wall which has less contact between the crushable macro-grain and the cylindrical wall compared to platen wall.

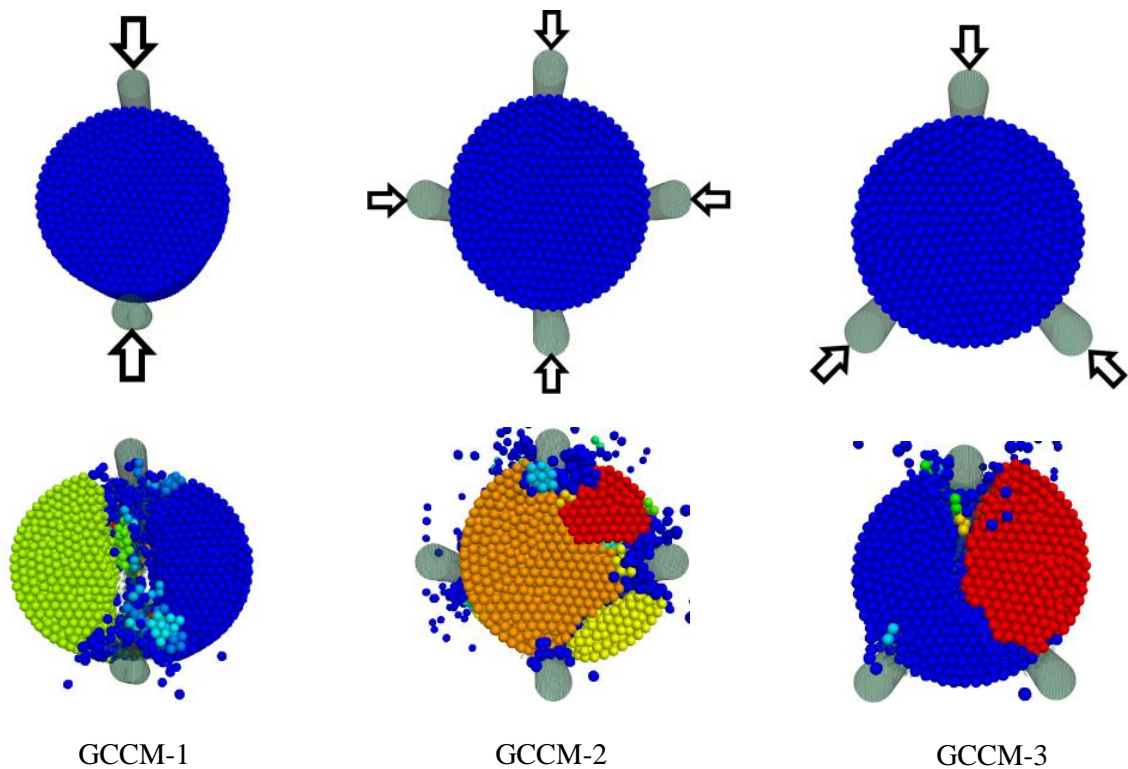


Fig. 7 Fracture patterns for cases GCCM: before and after the peak load.

Table 2 Simulation results for different contact models.

Contact	Peak load (kN)	Displacement at peak point (mm)	Number of fragments
GPCM-1	8.4	2.1	2
GPCM-2	10.2	1.45	1 major part with several minor parts
GPCM-3	11.4	1.27	3
GCCM-1	7.77	2.82	2
GCCM-2	8.33	1.46	3
GCCM-3	7.94	1.16	2

5 Conclusions

In order to examine the impact of different types of loading, different contact models, for example, grain platen wall and grain cylinder wall contacts, numerical investigation has been done using the DEM software PFC3D. First, the model parameters were calibrated to match well the results of the conducted Brazilian laboratory tests on an artificial material. Then the calibrated macro-grain model was used to simulate different number, location and shape of contact points. The results indicate that the boundary condition can have a huge effect on the peak loading and the fracture patterns. For the grain platen contact models, the peak loading of the crushable cylindrical macro-grain in the three platens loading case is greater than the four and two platens loading cases and this greater load may be

attributed to the macro grain breaks to three major fragments which implies more breakage inside the macro-grain in comparison to the other cases and that leads to a greater loading breakage. On the opposite side, in case of the grain cylinder wall contact model, the peak loading is lower than the case of grain walls. We found that smaller surface contact leads to a decrease in the loading capacity. In addition, the peak load increases with the increase of cylinder contact point number.

References

- [1] R. Alikarami, E. Andò, M. Gkiousas-Kapnisis, A. Torabi, and G. Viggiani. 2015. "Strain localisation and grain breakage in sand under shearing at high mean stress: Insights from in situ X-ray tomography." *Acta Geotech.* 10 (1): 15–30.
- [2] Y. D. Zhang, G. Buscarnera. 2017. "A rate-dependent breakage model based on the kinetics of crack growth at the grain scale." *Géotechnique* 67 (11): 953–967.
- [3] M. A. Chaudry, P. Wriggers. 2018. "On the computational aspects of comminution in discrete element method." *Comput. Part. Mech.* 5 (2): 175–189.
- [4] Y. D. Zhang, G. Buscarnera. 2018. "Breakage mechanics for granular materials in surface-reactive environments." *J. Mech. Phys. Solids* 112 (Mar): 89–108.
- [5] B. Kim, M. Prezzi, and R. Salgado. 2005. "Geotechnical properties of fly and bottom ash mixtures for use in highway embankments." *J. Geotech. Geoenviron. Eng.* 131 (7): 914–924.
- [6] E. Alonso, S. Olivella, and N. M. Pinyol. 2005. "A review of Beliche dam." *Géotechnique* 55 (4): 267–285.
- [7] B. Indraratna, Y. Sun, and S. Nimbalkar. 2016. "Laboratory Assessment of the role of particle size distribution on the deformation and degradation of ballast under cyclic loading." *J. Geotech. Geoenviron. Eng.* 142 (7)
- [8] L. Luzzani, M.R. Coop. 2002. "On the relationship between particle breakage and the critical state of sands" *Soils Found.*, 42 (2): 71-82
- [9] A. Sadrekarimi, S.M. Olson. 2011. "Yield strength ratios, critical strength ratios, and brittleness of sandy soils from laboratory tests Can". *Geotech. J.*, 48 (3): 493-510
- [10] Y. Salami, C. Dano, and P.-Y. Hicher, 2017. "An experimental study on the influence of the coordination number on grain crushing," *European Journal of Environmental and Civil Engineering.* 1–17
- [11] Y. D. Zhang, G. Buscarnera, and I. Einav. 2016. "Grain size dependence of yielding in granular soils interpreted using fracture mechanics, breakage mechanics and Weibull statistics." *Geotechnique* 66 (2):149–160.
- [12] M. Zhou, E. Song. 2016. "A random virtual crack DEM model for creep behavior of rockfill based on the subcritical crack propagation theory." *Acta Geotech.* 11 (4):827–847.
- [13] C. Sohn, Y. D. Zhang, M. Cil, and G. Buscarnera. 2017. "Experimental assessment of continuum breakage models accounting for mechanical interactions at particle contacts." *Granular Matter* 19 (4):67.
- [14] Ovalle, Carlos & Frossard, Etienne & Dano, Christophe & Hu, Wei & Maiolino, Siegfried & Hicher, Pierre-Yves. (2014). The effect of size on the strength of coarse rock aggregates and large rockfill samples through experimental data. *Acta Mech.* 225. 1-18.
- [15] Cavarretta, I and O'Sullivan, C (2012) The mechanics of rigid irregular particles subject to uniaxial compression *GEOTECHNIQUE*, 62 (8). pp.108.
- [16] P. Wang, C. Arson. 2016. "Discrete element modeling of shielding and size effects during single particle crushing." *Comput. Geotech.* 78: 227–236.
- [17] S. Xiao, M. T. Suleiman, and J. McCartney. 2014. "Shear Behavior of Silty Soil and Soil-Structure Interface under Temperature Effects". *Geo-Congress* 4105-4114.
- [18] C. Francesca, V. Giulia. 2011. "Experimental investigation of the evolution of grading of an artificial material with crushable grains under different loading conditions". *International Symposium on Deformation Characteristics of Geomaterials, IS-Seoul.* 957-964. 1~3, 2011.
- [19] G. R. McDowell, P. Yue and J.P.de Bono. 2015. "Micro mechanics of critical states for isotropically overconsolidated sand". *Powder Technology.* 283.
- [20] Itasca Consulting Group, Inc.PFC—Particle flow code, Manual. Minneapolis: Itasca.

Residual Stiffness Analysis of Flexural Concrete Elements with Composite Reinforcement Systems

Haji Akbar Sultani, Viktor Gribniak, Arvydas Rimkus, Aleksandr Sokolov

*Vilnius Gediminas Technical University,
Sauletekio av. 11, Vilnius LT-10223, Lithuania*

Lluís Torres

*University of Girona,
AMADE, Polytechnic School, University of Girona, Girona E-17003, Spain*

Abstract

Various materials and reinforcement technologies have been created, but this versatility causes a severe engineering problem – there is no versatile technique suitable for the development of efficient reinforcement system. In reinforced concrete systems, residual stiffness of the element can estimate the efficiency of the reinforcement. The stiffness is closely related to the structural integrity of cracked sections resisting the deformation increase of the member. This study introduces a simplified approach for the flexural stiffness analysis. It employs a new testing layout designed with the purpose to form multiple cracks in a small laboratory specimen. The proposed analytical model is based on the following assumptions: smeared crack concept; linear strain distribution within the section depth; elastic behaviour of reinforcement and compressive concrete; a rectangular distribution of stresses in the tensile concrete. The latter assumption enables obtaining a closed-form solution of the residual stiffness problem in terms of the equivalent tensile stresses in the concrete. The achieved solution requires neither iterative calculations nor a description of the loading history. The proposed methodology is also acceptable for estimating residual stiffness of elements with various combinations of reinforcement. The application of the proposed technique is illustrated experimentally. Several composite reinforcement schemes, including internal steel and glass fibre reinforced polymer (GFRP) bars, carbon fibre reinforced polymer (CFRP) sheets and near-surface mounted (NSM) strips in different combinations, are considered. The analysis of the test results reveals a substantiate efficiency of the external CFRP reinforcement systems concerning the internal reinforcement as the reference. The application of the CFRP sheets substantially increases the effectiveness of the tensile concrete. In essence, the decay of the equivalent stresses acting to the tensile concrete does not exceed 50% of the tensile strength of the concrete in the presence of the external reinforcement. However, the formation of a critical shear crack caused the failure of all specimens with composite reinforcement. That is a consequence of low resistance of the fibre reinforced polymer materials to a shear load.

1 Introduction

There is a general steady increase of application of innovative construction materials and concrete, as the case of using fibre reinforced polymers (FRP) as reinforcement. Various materials and reinforcement technologies have been developed. However, there is no uniform methodology to compare the mechanical characteristics of different reinforcing systems. Residual stiffness of the element can estimate the efficiency of reinforcement systems.

The purpose of this study is to offer a rational way of composing efficient composite reinforcement systems. Residual stiffness of flexural members is the focus of the research. It is closely related to the structural integrity of cracked sections of the concrete resisting the deformations of the element.

Tension-stiffening models can represent the stiffness in an averaged manner. Numerous studies investigated the tension-stiffening issue. However, only several works addressed flexural effects. Fundamental studies by Kaklauskas & Ghaboussi [1] and Torres et al. [2] could be mentioned in this context. Elaborate numerical procedures are an intrinsic attribute of the “exact” approaches [3]. Iterative nature of the algorithms often complicates applicability of the exact techniques: the calculation errors are accumulated following the load history [3]. The development of more reliable algorithms employed the reinforcement-related tension-stiffening concept was the consequence of the further improvements [4-6]. Such models, however, are not useful for the analysis of the elements reinforced with a combination of different types of internal bars, near-surface mounted strips and external sheets.

This study offers a new simplified approach for the flexural stiffness analysis introducing the equivalent stresses to measure the residual stiffness of the element. The proposed methodology is acceptable for estimating the residual stiffness of elements with different combinations of reinforcement. The developed analytical model requires neither iterative calculations nor a description of the loading history. The application of the proposed technique is illustrated experimentally representing a closed-form solution of the flexural stiffness problem in terms of the equivalent tensile stresses in the concrete.

2 Description of the beam specimens

The testing layout was designed with the purpose to form multiple cracks in a small laboratory specimen. That enables to reduce scatter of the result due to the crack formation peculiarities. The geometry of the beams was chosen using the iterative trial-and-error procedure. The satisfaction of the simplified modelling assumption (rectangular distribution of stresses in the tensile concrete) was used as the design criterion. In other words, the exact tension-stiffening diagram [3] had to have the shape as close as possible to rectangular.

Figure 1 shows the cross-sections of the specimens; Table 1 describes the parameters of the beams. In this table, h , b , and d are the height, width, and effective depth of the cross-section; A_r and E_r are the area and elasticity modulus of the reinforcement, respectively. The table also defines the compressive strength of the $\varnothing 150 \times 300$ mm concrete cylinder at 28 days ($f_{c,28}$) and at age (t) of testing (f_{cm}).

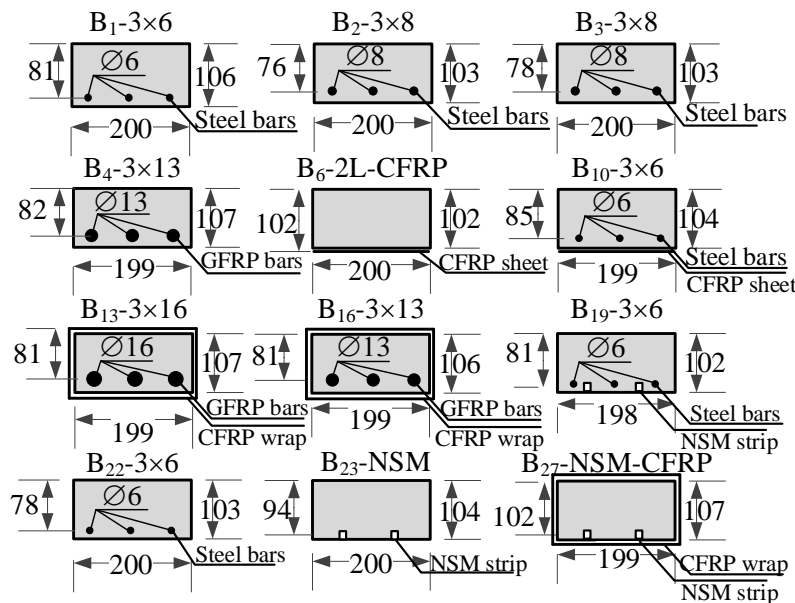


Fig. 1 Cross-sections of the beam specimens (dimensions are in mm).

Table 1 Main parameters of the beam specimens.

Specimen	h , mm	b , mm	d_1 , mm	d_2 , mm	A_{r1} , mm ²	A_{r2} , mm ²	E_{r1} , GPa	E_{r2} , GPa	$f_{c,28}$, MPa	t , days	f_{cm} , MPa	δ_1 , kPa	δ_2 , kPa
B ₁ -3×6	106	200	81	–	83.2	–	202.1	–	53.2	43	57.2	2.36	–
B ₂ -3×8	103	200	76	–	149.8	–	206.7	–	53.2	42	57.1	1.46	–
B ₃ -3×8	103	200	78	–	149.8	–	205.7	–	60.4	38	69.5	2.62	–
B ₄ -3×13-GFRP	107	199	82	–	380.1	–	46.0	–	55.9	39	68.6	2.67	3.32
B ₆ -2L-CFRP	102	199	–	103	–	23.2	–	230.0	61.8	48	69.7	4.82	7.45
B ₁₀ -3×6-2L-CFRP	104	199	79	105	83.2	23.2	202.1	230.0	58.3	49	61.9	3.52	4.64
B ₁₃ -3×16-GFRP (shear)	107	199	81	–	593.7	–	46.0	–	51.7	45	61.8	1.87	2.11
B ₁₆ -3×13-GFRP (shear)	106	199	80	–	380.1	–	46.0	–	60.4	46	69.5	2.52	3.23
B ₁₉ -3×6-NSM	102	198	78	92	83.2	28.0	202.1	170.0	63.1	57	70.3	2.31	–
B ₂₂ -3×6	103	200	78	–	89.2	–	202.1	–	58.3	57	61.9	2.33	–
B ₂₃ -NSM	104	200	94	–	28.0	–	170.0	–	61.0	62	68.1	2.95	4.05
B ₂₇ -NSM-CFRP (shear)	107	199	95	107	28.0	23.2	170.0	230.0	61.0	63	68.1	2.73	2.98

As it can be observed in Fig. 1, most of the tested specimens had a combined reinforcement. Therefore, Table 1 specifies two reinforcement types. Except for B₁₉-3×6-NSM, the subscript “1” of the parameters d , A_r , and E_r corresponds to the internal reinforcement (either bars or NSM strips), whereas the index “2” describes the external

sheets. Considering the specimen B_{19-3×6}-NSM, the subscripts “1” and “2” correspond to the internal bars and NSM strips, respectively. Physical parameters of the steel reinforcement were determined experimentally (through the tensile tests of three samples), whereas the values from the mill-certificates are provided for the non-metallic reinforcements.

The beams were cast using steel forms; they were unmoulded in 2-3 days after the casting. All specimens reinforced with internal bars were stored in water to reduce the shrinkage effect. The NSM system and CFRP sheets were attached to the dry specimens before the tests. The specimens were dried for approximately 24 hours before gluing the sheets.

3 Beam tests and discussion of the results

The 1000 mm long specimen is tested under a four-point-bending scheme with 600 mm pure bending zone and two 150 mm shear spans, a . That fits the Eurocode 2 [7] condition of elements not requiring design of shear reinforcement, i.e. $a \leq 2d$, where d is the effective depth of cross-section (Table 1).

The specimens were produced in several batches using the same concrete compositions. The composition of the concrete (for one cubic meter) is following: 356 kg of cement CEM I 42.5 R, 163 l of water, 177 kg of limestone powder, 890 kg of 0/4 mm sand, and 801 kg of 4/16 mm crushed aggregates; 1.97% (by the cement weight) of the superplasticiser *Mapei Dynamon XTend* and 3.5 kg of the admixture *SCP 1000 Optimizer*. The beams were reinforced with either 13 mm and 16 mm GFRP bars or 8 mm and 6 mm steel bars (Fig. 1). Several samples had NSM CFRP strips and external CFRP sheets attached to the tension surface of the specimen. The previous study [8] indicated the insufficient resistance of FRP composites to shear loads. In this study, three beams had CFRP wrapping in the shear zones to avoid premature failure of the specimens. These specimens are designated as “(shear)” in Table 1. Two CFRP loops (each of 100 mm width) were placed close to each other in the shear zone, as shown in Fig. 2b. The same unidirectional *MapeWrap C UNI-AX* CFRP sheets were used as external and shear reinforcement. The equivalent thickness of the dry material was 0.166 mm.

As shown in Fig. 2, the surface deformations were assessed using linear variable displacement transducers (LVDT) L_{10} - L_{15} attached in two continuous lines to the side surface of the specimen. The vertical displacements in pure bending zone were measured by nine LVDT (L_1 - L_9 , Fig. 2). The data logger ALMEMO 5690-2 collected the output results of all LVDT and the load cell. Figures 3 and 4 show the surface strains and vertical displacement assessment results.

Deformations and crack pattern of the opposite side surface of the specimens were fixed with the help of digital image correlation system (DIC). Two cameras IMAGER E-LITE 5M were used for this purpose. The cameras were placed on a tripod at the 3.0 m distance from the specimen. The gap between the cameras was equal to 0.4 m. The cameras, incorporating a charge-coupled device (CCD) detector, have a resolution of 2456×2085 pixel at the 12.2 fps rate. Such arrangement of the apparatuses enables a crosscheck of the test outcomes: the collected measurements enable to construct three each other independent moment-curvature diagrams, which can be used for the analysis.

Figure 5 demonstrates the evolution of the cracks identified by the DIC system highlighting the cracking sequence. The cracking patterns are related to certain bending moments indicated at the schemes. Figure 6 shows the final crack pattern of the beams.

The formation of a critical shear crack caused the failure of all specimens with composite reinforcement. That is a consequence of low resistance of the fibre reinforced polymer materials to a shear load. (The beam specimens had no shear reinforcement.) An increase in the area of FRP reinforcement has no significant effect on the shear resistance – the doubled number of CFRP sheets increase the load-bearing capacity only by 20%. The external wrapping acting in the shear zone (the specimens B₁₃, B₁₆, and B₂₇) also had no substantial effect on the shear resistance of the beam specimens. Although the load-bearing capacity of the strengthened specimens was increased by almost 30%, the formation of a critical shear crack caused the failure of the strengthened specimens. Another essential result was observed in the specimen B₁₉ reinforced with a combination of the 6 mm steel bars and NSM CFRP strips (Fig. 1). Notwithstanding the effect of the steel bars, the shear failure was the consequence of the bending test. That makes a requirement of the minimum shear resistance mandatory for the design of structural elements with composite reinforcement systems.

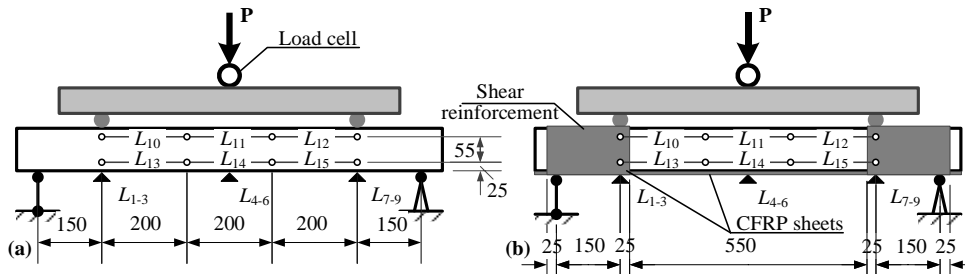


Fig. 2 Loading scheme of typical (a) and strengthened in shear (b) beams (dimensions are in mm).

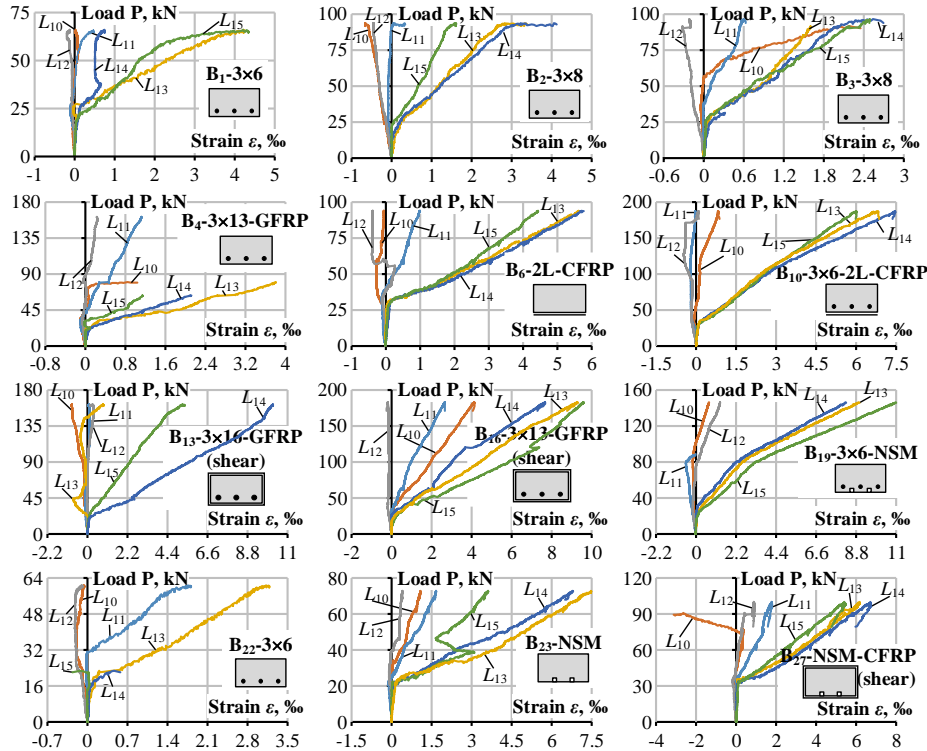


Fig. 3 Surface deformations of the beams.

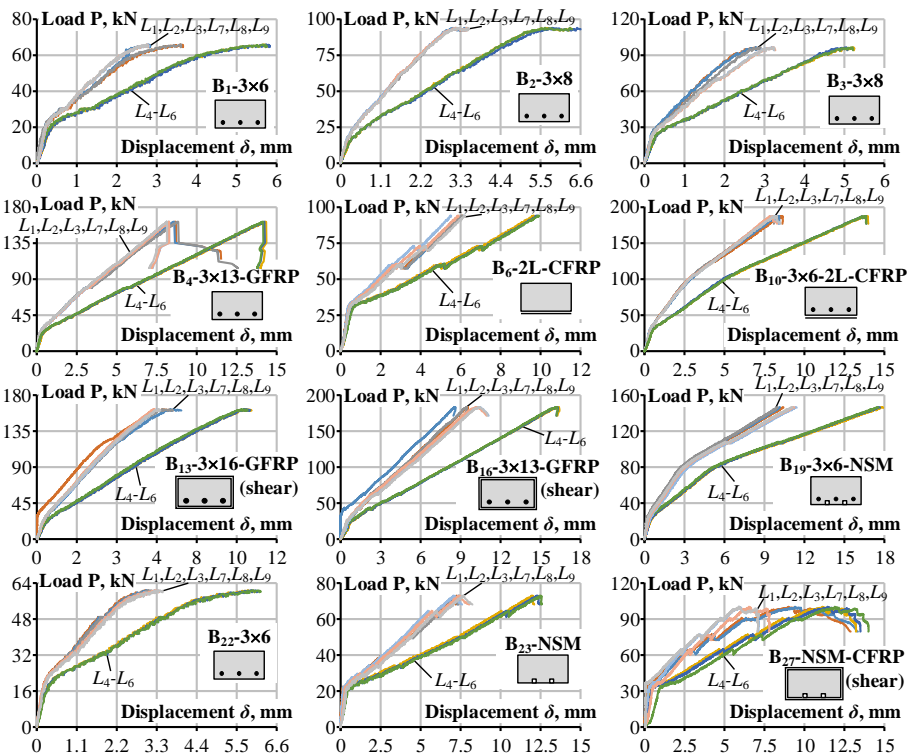


Fig. 4 Vertical displacements of the beams.

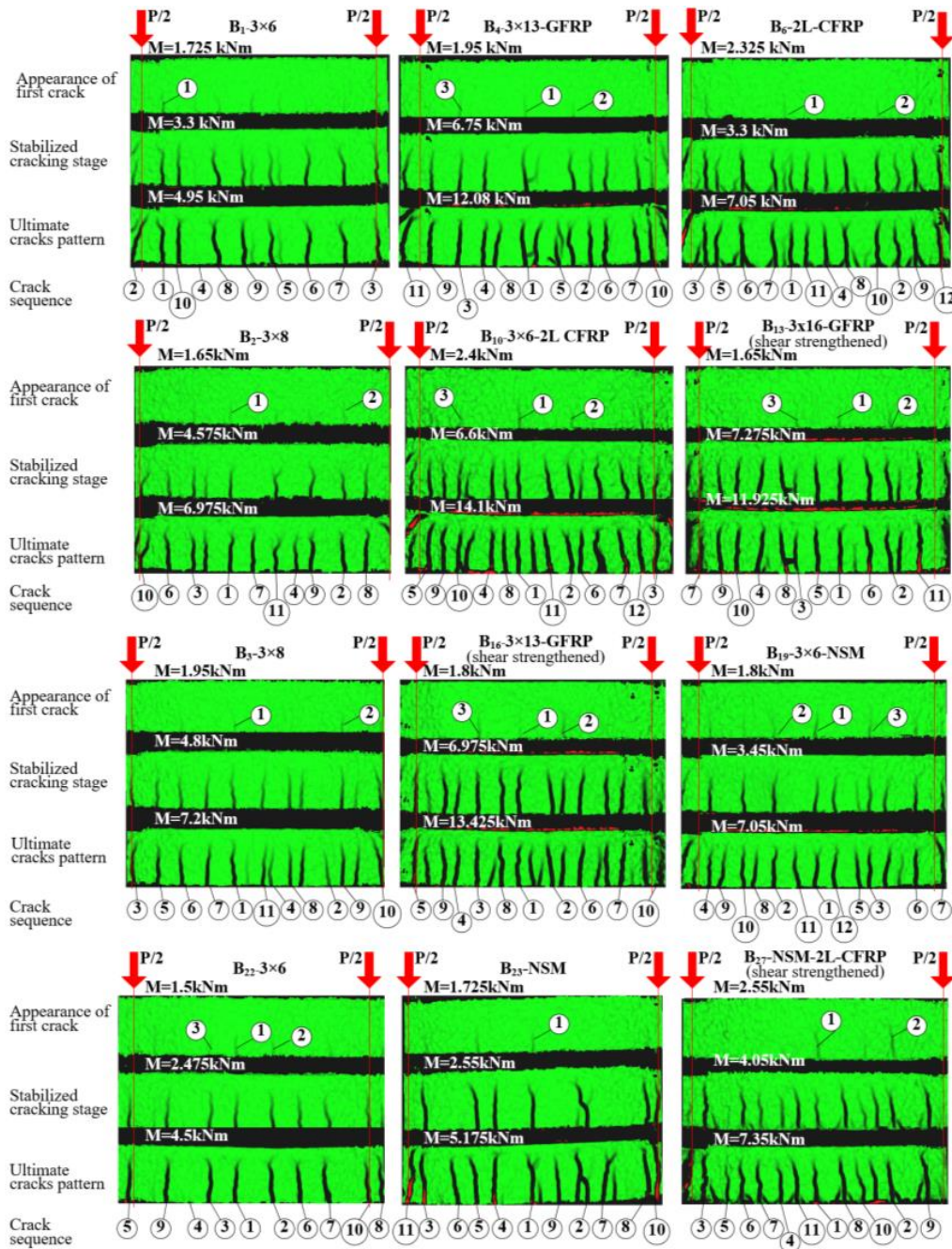


Fig. 5 Cracking schemes identified by the DIC system.

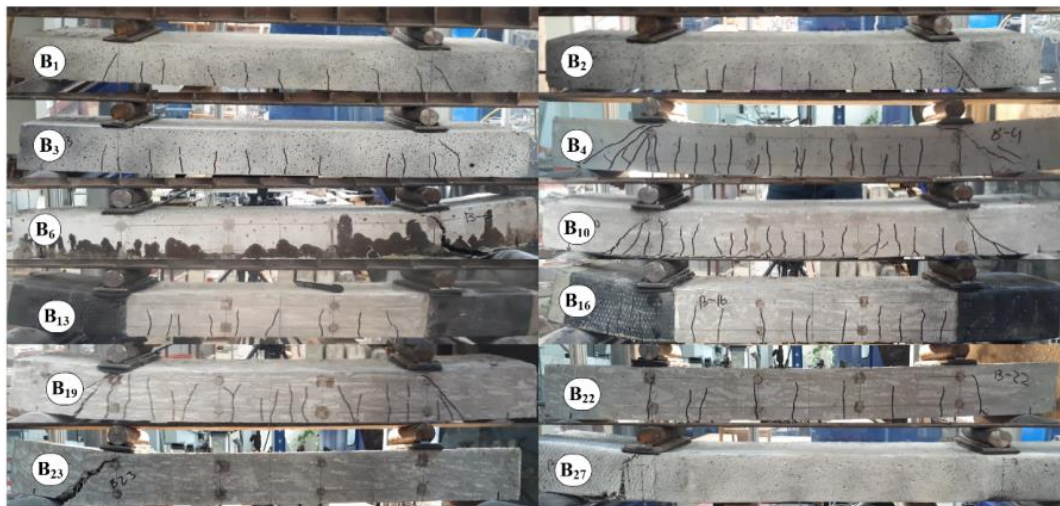


Fig. 6 Final crack pattern of the beams.

4 The residual stiffness analysis

The stiffness analysis is based on the moment-curvature response of the pure bending zone. The monitoring scheme (Fig. 2) enables the curvature estimation in different ways: from vertical displacements of LVDT L_1 - L_9 and from surface deformations identified using the LVDT L_{10} - L_{15} or DIC system. The averaged curvature can be obtained from the vertical displacement readings assuming a circular arc shape of the deflection curve along the pure bending zone [9] as follows

$$\kappa = \frac{2 \cdot \delta}{(l_b/2)^2 + \delta^2} = \frac{8 \cdot \delta}{l_b^2 + 4 \cdot \delta^2}, \quad \delta = \frac{\delta_4 + \delta_5 + \delta_6}{3} - \frac{\delta_1 + \delta_2 + \delta_3 + \delta_7 + \delta_8 + \delta_9}{6}, \quad (1)$$

where δ is the deflection over the pure bending zone; δ_i is the displacement obtained by LVDT L_i ($i = 1 \dots 9$, Fig. 2); l_b is the length of the bending zone (equal to 600 mm).

The surface strains were employed for the assessment of the curvature as follows

$$\kappa = \frac{(\varepsilon_{13} + \varepsilon_{14} + \varepsilon_{15}) - (\varepsilon_{10} + \varepsilon_{11} + \varepsilon_{12})}{3 \cdot h_\varepsilon}, \quad (2)$$

where ε_i is the strain estimated using the reading by the LVDT L_i ($i = 10 \dots 15$, Fig. 2); h_ε is the distance between the gauging lines (equal to 55 mm). A similar procedure was applied to estimate the curvature using the DIC system that is capable of determining relative displacements between any points recognised at the monitoring surface [10].

The analysis of the alternative curvature values enables of identifying the measurement errors. For instance, an illumination alteration or movement of the camera can corrupt the DIC results; the crack appearance at the LVDT support can distort the measurement results; a cyclic load can cause the erroneous outcomes of the LVDT devices. The presence of the overlapping measurements increases the reliability of the monitoring results that can be verified by comparing the alternative outcomes.

Figure 7a shows the moment-curvature diagrams constructed using the surface deformations captured by the DIC system. Figure 7b gives the corresponding equivalent stiffness values. The latter diagrams were derived using the proposed analytical model. That implies the following assumptions: smeared crack approach; linear strain distribution within the section depth; elastic behaviour of reinforcement and compressive concrete; rectangular distribution of stresses in the tensile concrete. The latter assumption enables an explicit solution of the residual stiffness problem expressed in terms of the equivalent stresses, σ_t^* , acting to the tensile concrete.

Figure 8 describes the assumed model that employs the transformed section method, combining different types of reinforcement (Fig. 8a) in one modified component (Fig 8b). The following equations determine the effective depth d_r , area A_r , and elasticity modulus E_r of the transformed reinforcement:

$$d_r = \frac{\sum_{i=1}^3 E_i A_i d_i}{\sum_{i=1}^3 E_i A_i}, \quad A_r = \frac{1}{E_r} \sum_{i=1}^3 E_i A_i, \quad E_r = E_1, \quad (3)$$

where E_i is the elasticity modulus of the i -th reinforcement component; Fig. 8a defines other notations.

The modelling is based on the equilibrium equations of internal forces and bending moments to the centroid of the equivalent tensile stress diagram (Fig. 8d):

$$\mathbf{F}_t^* + \mathbf{F}_r - \mathbf{F}_c = 0, \quad \mathbf{F}_r \left(d_r - \frac{h + y_c}{2} \right) + \mathbf{F}_c \left(\frac{h + y_c}{2} - \frac{y_c}{3} \right) - \mathbf{M}_{ext} = 0, \quad (4)$$

where \mathbf{F}_t^* is the *equivalent* resultant force of the tensile stresses in the concrete; \mathbf{F}_r and \mathbf{F}_c are the internal forces acting to the tensile reinforcement and the compressive concrete; y_c is the depth of the compressive zone. In the above equations, the internal forces can be expressed through the respective stresses:

$$\sigma_t^* (h - y_c) b + \sigma_r A_r - \sigma_c \frac{y_c b}{2} = 0, \quad \sigma_r A_r \left(d_r - \frac{h + y_c}{2} \right) + \sigma_c \frac{y_c b}{2} \left(\frac{3h + y_c}{6} \right) - \mathbf{M}_{ext} = 0. \quad (5)$$

For the given curvature, κ , the stresses in the tensile reinforcement and the most compressed concrete layer (Figs. 8c and 8d) can be expressed using the conditions of strain compatibility:

$$\sigma_r = \kappa (d_r - y_c) E_r, \quad \sigma_c = \kappa y_c E_c. \quad (6)$$

Taking into account expressions (6), equation (5) can be modified as

$$\kappa (d_r - y_c) E_r A_r \left(d_r - \frac{h + y_c}{2} \right) + \kappa y_c E_c \frac{y_c b}{2} \left(\frac{3h + y_c}{6} \right) - \mathbf{M}_{ext} = 0 \quad (7)$$

and expressed as a third order polynomial

$$C_3 y_c^3 + C_2 y_c^2 + C_1 y_c + C_0 = 0 \quad (8)$$

with coefficients

$$C_3 = \frac{\kappa E_c b}{12}, \quad C_2 = \frac{\kappa}{4}(2E_s A_s + E_c b h), \quad C_1 = \frac{\kappa E_s A_s}{4}(h - 3d), \quad (9)$$

$$C_0 = \frac{\kappa d^2 E_s A_s}{2} \left(2 - \frac{h}{d}\right) - \mathbf{M}_{ext}.$$

The polynomial (8) has three roots. From the condition $0 < y_c \leq h$, the position of the neutral axis is defined as $y_c = \frac{1}{3C_3} \left\{ 2\bar{C} \cos \left(\frac{1}{3} \cos^{-1} \left\{ -\frac{27C_3^2 C_0 - 9C_3 C_2 C_1 + 2C_2^3}{2\bar{C}^3} \right\} \right) - C_2 \right\}$, $\bar{C} = \sqrt{C_2^2 - 3C_3 C_1}$. (10)

The equivalent average stress in the tensile concrete is determined using equation (5); Fig. 8c defines the corresponding strain. The following formulas express those parameters:

$$\sigma_t^* = \kappa \frac{y_c^2 b E_c - 2(d - y_c) E_s A_s}{2(h - y_c) b}, \quad \varepsilon_t^* = \kappa \frac{h - y_c}{2}. \quad (11)$$

Figure 9 illustrates the residual stiffness tendencies observed in the specimens with composite reinforcement. The analysis of the residual stiffness (expressed in term of the equivalent stresses σ_t^*) reveals the substantial efficiency of the external CFRP reinforcement system concerning the internal reinforcing schemes as the reference. The area under the equivalent stress diagram can determine the deformation energy related to the relative contribution of the cracked concrete. Table 1 gives the energy values δ_1 and δ_2 corresponding to the deformation ε_t^* equal to 2‰ and 3‰. The maximal energy values are highlighted in the table. The efficiency decreases with increasing the reinforcement ratio. That is a well-known fact [1], but the effect of the external sheets should be the object of further research.

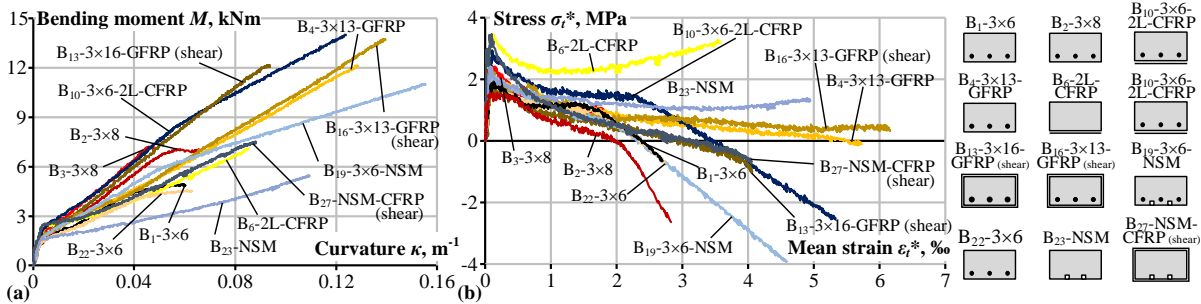


Fig. 7 The residual stiffness analysis: (a) moment-curvature diagrams of the beams; (b) the corresponding equivalent residual stresses in the tensile concrete σ_t^* , see equation (11).

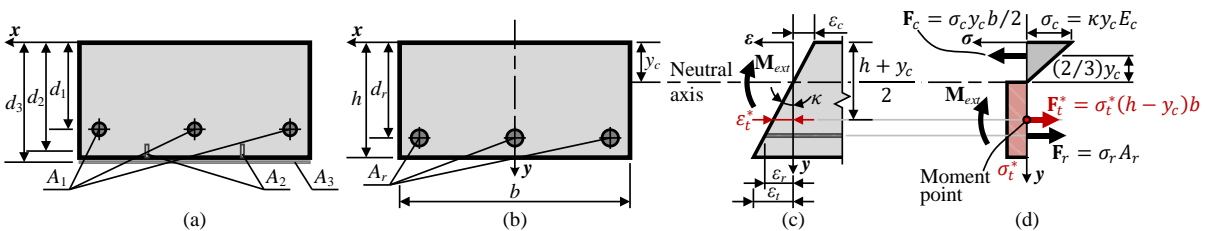


Fig. 8 Analytical model of the element subjected to bending moment \mathbf{M}_{ext} : (a) RC section; (b) transformed section; (c) strain profile; (d) stresses and internal forces acting to the section.

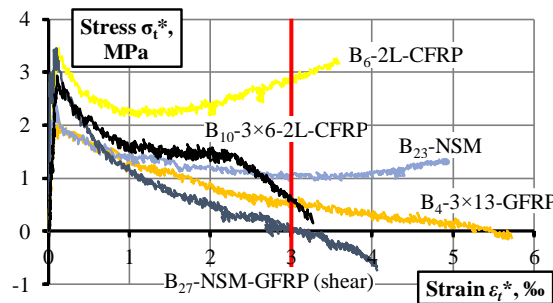


Fig. 9 Equivalent stress-strain diagrams of the selected specimens.

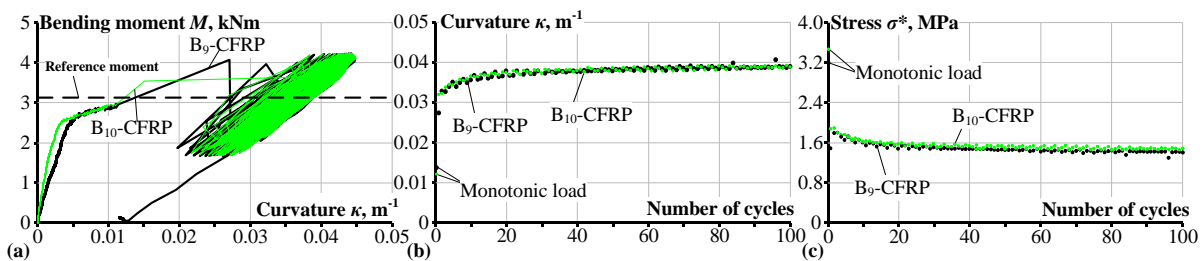


Fig. 10 Analysis of beam specimens subjected to cyclic load [8]: (a) moment-curvature diagram; (b) reference curvatures; (c) the resultant equivalent stresses σ_t^* .

The ability to analyse the residual stiffness of elements subjected to cyclic loading is an essential feature of the proposed analytical model. Figure 10a demonstrates the moment-curvature diagrams of the beam specimens subjected to cyclic load. The residual stiffness analysis is related to an arbitrarily set reference bending moment. The dashed line in Fig. 10a indicates the reference load. The curvature evolution is estimated by using one curvature value at each loading cycle that corresponds to the ascending of diagrams shown in Fig. 10a. Figure 10b reveals an increase in the curvature with load cycles. Figure 10c demonstrates the application results of the proposed analytical model clarifying the stiffness decay tendency.

5 Conclusions

- The proposed methodology is suitable for estimating residual stiffness of elements with various combinations of reinforcement: any kinds of internal bars, external sheets, and near-surface mounted strips can be used in different combinations.
- The external CFRP sheets demonstrated the most efficient deformation resistance among the considered reinforcement systems. This effect is to be the object of further research.

References

- [1] Kaklauskas, Gintaris, and Jamshid Ghaboussi. 2001. "Stress-Strain Relations for Cracked Tensile Concrete from RC Beam Tests." *ASCE Journal of Structural Engineering* 127(1):64–73.
- [2] Torres, Lluís, Francisco López-Almansa, and Luis Bozzo. 2004. "Tension-Stiffening Model for Cracked Flexural Concrete Members." *ASCE Journal of Structural Engineering* 130(8):1242–51.
- [3] Gribniak, Viktor, Gintaris Kaklauskas, Algirdas Juozapaitis, Romualdas Kliukas, and Adas Meskenas. 2017. "Efficient Technique for Constitutive Analysis of Reinforced Concrete Flexural Members." *Inverse Problems in Science and Engineering* 25(1):27–40.
- [4] Kaklauskas, Gintaris, Viktor Gribniak, Donatas Salys, Aleksandr Sokolov, and Adas Meskenas. 2011. "Tension-Stiffening Model Attributed to Tensile Reinforcement for Concrete Flexural Members." *Procedia Engineering* 14:1433–38.
- [5] Torres, Lluís, Cristina Barris, Gintaris Kaklauskas, and Viktor Gribniak. 2015. "Modelling of Tension-Stiffening in Bending RC Elements Based on Equivalent Stiffness of the Rebar." *Structural Engineering and Mechanics* 53(5):997–1016.
- [6] Kaklauskas, Gintaris, and Viktor Gribniak. 2016. "Hybrid Tension Stiffening Approach for Decoupling Shrinkage Effect in Cracked Reinforced Concrete Members." *ASCE Journal of Engineering Mechanics* 142(11), Paper ID-04016085: 1–11.
- [7] CEN (Comité Européen de Normalisation). 2004. *Eurocode 2: Design of Concrete Structures – Part 1: General Rules and Rules for Buildings, EN 1992-1-1:2004*. Brussels: CEN.
- [8] Gribniak, Viktor, Aleksandr Sokolov, Arvydas Rimkus, Haji A. Sultani, Murat C. Tuncay, and Lluís Torres. 2019. "A Novel Approach to Residual Stiffness of Flexural Concrete Elements with Composite Reinforcement." *Proc. of the IABSE Symposium – Towards a Resilient Built Environment Risk and Asset Management*, March 27-27, Guimarães, Portugal. Zurich: IABSE, 46–51.
- [9] Gribniak, Viktor, Gintaris Kaklauskas, Lluís Torres, Alfonsas Daniunas, Edgaras Timinskas, Eugenijus Gudonis. 2013. "Comparative Analysis of Deformations and Tension-Stiffening in Concrete Beams Reinforced with GFRP or Steel Bars and Fibers." *Composites Part B: Engineering* 50:158–70.
- [10] Rimkus, Arvydas, Askoldas Podviezko, Viktor Gribniak. 2015. "Processing Digital Images for Crack Localization in Reinforced Concrete Members." *Procedia Engineering* 122:239–43.

Sealing of service penetrations in timber buildings utilizing timber in timber installation

Thomas Scherer, Catherina Thiele, Dirk Lorenz

*Department of civil engineering,
TU Kaiserslautern,
Gottlieb-Daimler Str. 67, 67663 Kaiserslautern, Germany*

Abstract

An increasing number of taller buildings are constructed using wood as a material. Penetration seals become more relevant with increasing building height. In the completed research project ‘Leitungsdurchführungen im Holzbau’ (engl. ‘Pipe penetrations in timber construction’) full scale and small scale fire tests were conducted with the industry partner Hilti to examine penetrations and standard penetration sealing systems in combination with timber construction. Within further tests, penetrations of single conduits were examined. The test results show, that most of the tested typical penetration sealing systems can be used in timber construction as well. Selected single conduit penetrations in mass timber assemblies can be sealed without a classified sealing system.

1 Introduction

Timber construction has become increasingly important in Germany and many other countries in recent years, mainly due to ecological incentives. But timber construction also offers advantages from an economic point of view because of its high degree of prefabrication and short construction times. As a result of the afore mentioned points, larger and higher timber construction projects are increasingly planned and approved. The advantages of timber construction are partly limited. This is caused by constructional details for which no approved timber construction solutions have been found yet. Conduit penetrations are one of these details. In Germany, requirements for fire protection are regulated in the regional building regulations. Base for these is the model building code [1]. Further regulations are defined in technical building regulations. Regarding timber construction instructions are given in the model guideline for fire protective requirements on multi-storey timber buildings [2]. For the installation of conduits and the passing of wiring or piping through building’s components for sealing off areas the model conduit systems guideline [3] is relevant. Penetration seals are required in places where wiring / pipes are routed through walls with fire resistance requirements. Exceptions, called facilitations, are granted by the guideline for single cables, small cable bundles, and single pipes with specific dimensions. For timber constructions very few approved penetration sealing systems are available on the market. This is to be explained by the many different types of timber constructions. In order to be approved and thus tradeable the penetration sealing systems need to be tested in every timber construction they shall be approved for. The current solution for timber buildings in Germany is to use a component made of non-combustible building materials (e.g. concrete or mortar) at the point of cable bushing and to seal off the through penetrations in this component. This procedure requires an additional coordination effort, brings mineral building materials with moisture (liquid water), which can cause shrinkage and swelling, into the timber structure and represents an optical disturbance. The final aim is to provide a method which enables penetration sealing in timber buildings without the substitution of the buildings material in the penetration area and therefore facilitate building with wood. Further, the testing of each sealing system in each timber wall construction shall be avoided as testing is a major cost factor for producers. The completed research project ‘Pipe penetrations in timber construction’ [4] laid the foundation for an improved method of penetration sealing in timber components, called ‘timber-in-timber’. The first part of this article describes the results of this research project. Despite the timber in timber installation is only reasonable in Germany, the results of the tests of penetration seals in timber assemblies are relevant all over the world. The second part of the text (chapter 3) deals with further examinations regarding penetrations of single cables and pipes which were carried out by the authors. The tests have shown that selected penetrations of individual pipes and cables can be sealed off without a classified sealing system, if the facilitations of the conduit systems guideline, which currently may

not be used in timber construction, are observed. With this easier way of penetration sealing for single pipes and cables building costs can be decreased.

2 Reaserach project “Line penetrations in timber construction”

The aim of the research project was to determine the basic principles of penetration seals in timber construction and to provide companies and testing institutes with instructions on how to install and test penetration sealing systems in wood constructions. The overall result was the method ‘timer-in-timber’. Especially the weak points of the tested setups were evaluated in a first step to understand the critical areas. In the second step the basic idea of the project was to define a timber module, within which penetration seals can be installed and tested. The module can afterwards be inserted into various timber constructions (see Fig. 1 left). Using this approach, testing under constant conditions is possible and there is no need to substitute the wood at the point of penetrations. For penetration sealing systems the relevant performance criteria according to EN 1366-3 [5] in connection with EN 1363-1 [6] are integrity (E) and insulation (I) while the specimen is exposed to elevated temperatures according to the ISO heat curve (see Fig. 1 right) on one side. Regarding integrity, a defined cotton pad must not ignite, the physical penetration of emerging openings must not be impossible (see defined gap gauges in EN 1363), and there must not be any sustained flaming on the non exposed face. To fulfil the insulation criteria no measured temperature difference on the non exposed face shall exceed 180 K. Both performance criteria must be maintained during the whole test under elevated temperatures to achieve a corresponding classification.

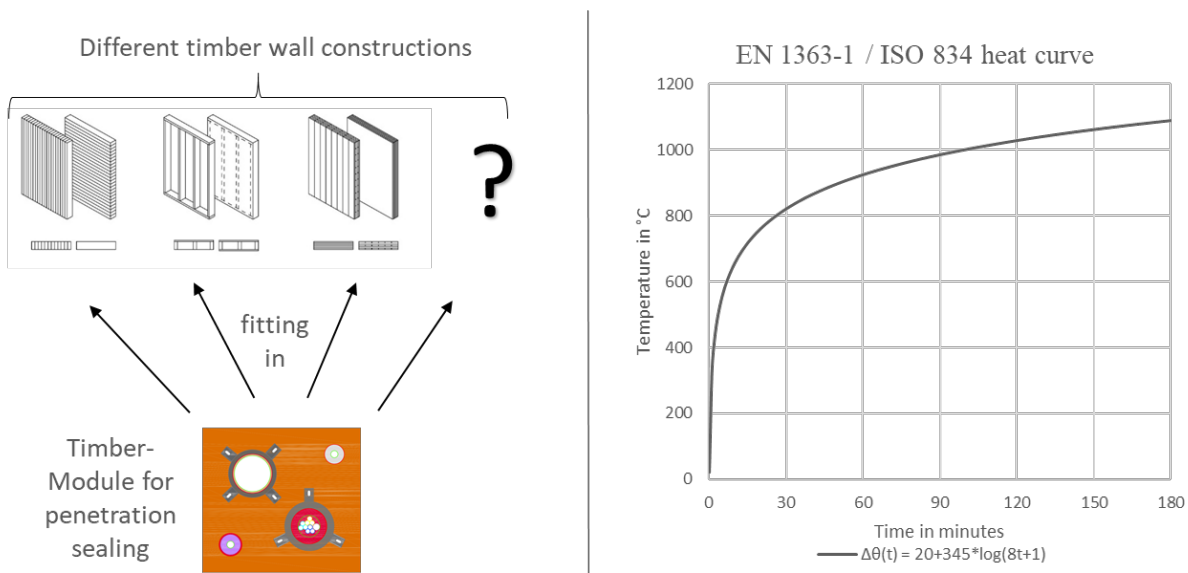


Fig. 1 Basic idea of the method 'timber-in-timber' (left), normative heat curve (right)

2.1 Fire tests

2.1.1 Small scale tests

First a suitable module needed to be found. The test duration was set to 120 min to enable the use of the modules in as many cases as possible. Basis for the dimensioning of the modules was the charring rate of wood according to [7]. Additionally, during longer tests more failure mechanisms can be examined. Two different possible structures were taken into account, a massive glued laminated timber (glulam) module and a layered module, consisting of oriented strand boards (OSB) and mineral wool (see Fig. 2). Both modules had dimensions of 440 mm * 440 mm. The glulam modules were 160 mm thick, the osb module had a total thickness of 132 mm. In both modules typical penetration sealing systems were installed and exposed to the heat source in accordance with EN 1366-3 [5]. ins

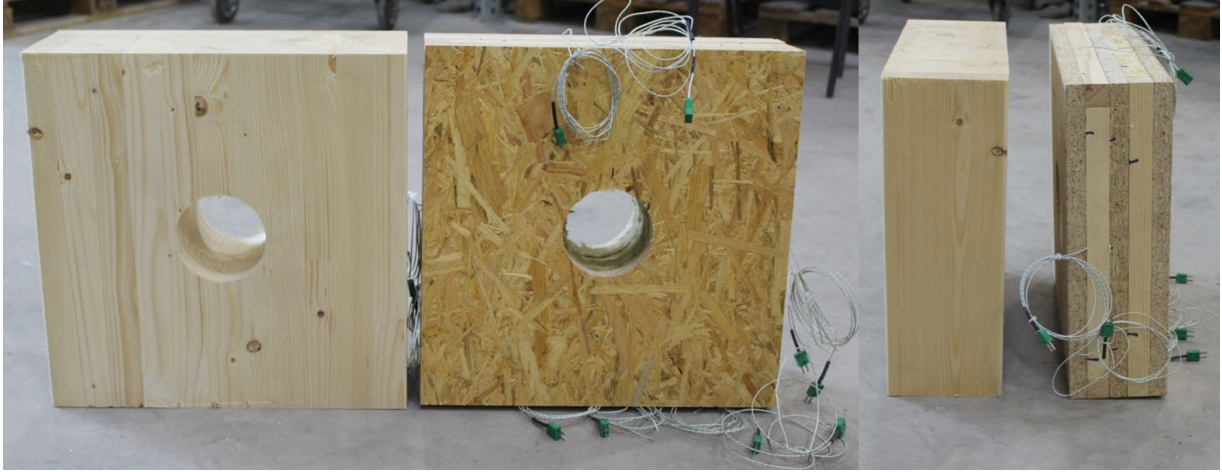


Fig. 2 Example: Front view and side view of glulam module (left) and OSB module (right)

Despite fulfilling the E and I criteria for about 60 minutes, the tests with coated mineral wool slabs did not provide good results. This can be explained by the loss of stability of the slab due to combustion of the reveal area, which leads to high temperatures on the non-exposed side and smoke leakage (see Fig. 3). To use coated mineral wool slabs safely in timber constructions the reveals should be lined according to [8] and [9] to generate comparable conditions to those in drywall or concrete constructions.



Fig. 3 Coated mineral wool slab with cables (service option “M” according to Annex A EN 1366-3) before the test and after 90 mins of exposure

All tests with other sealing systems, namely cable- and pipe collars, mineral wool linings, and bandages delivered satisfying results. Especially mineral wool linings for uninsulated copper pipes and bandages for insulated copper pipes would reach fire resistance classifications of over 90 minutes in combination with glulam modules (compare Fig. 4). As a result of the small scale tests, the glulam modules were chosen to be used for the examinations in full scale tests. Furthermore, the coated mineral wool slab was not longer examined and some small fixes were conducted regarding the installation of other penetration sealing systems.

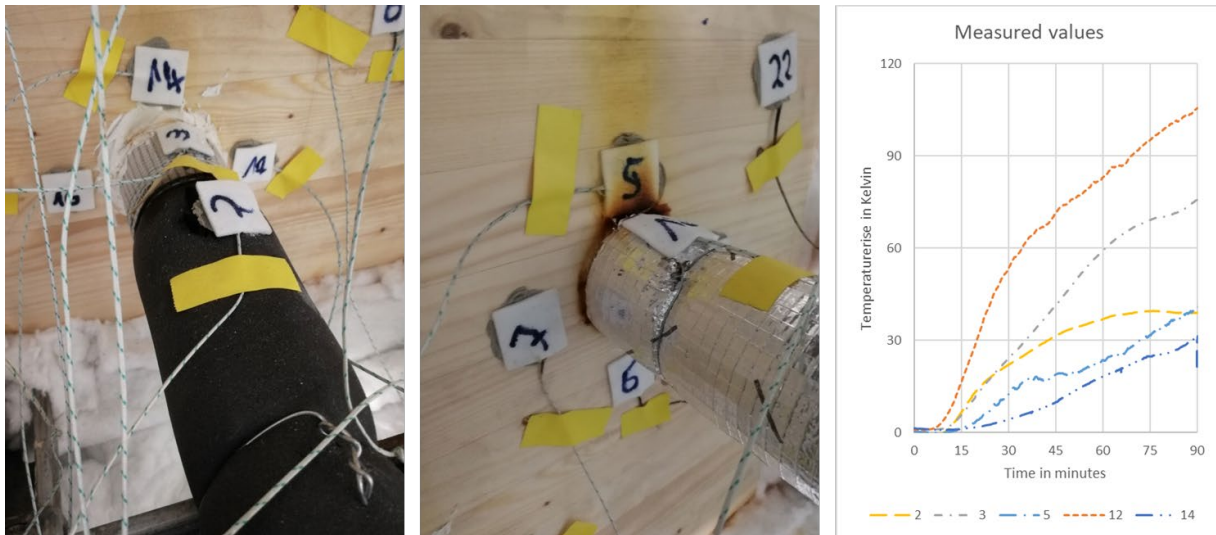


Fig. 4 Penetration seals for copper pipes (left bandage Hilti CFS-B [10] for combustible insulated copper pipe; middle Rockwool Conlit 150U [11] for uninsulated copper pipe) and measured values of a test (2: on the rubber insulation, 3: on the bandage, 5: on timber above insulation, 12: on insulation, 14: on timber above bandage)

2.1.2 Full scale tests

To confirm the applicability of the method, the modules were fitted into two different typical timber wall assemblies, a cross laminated timber (CLT) wall and a timber frame construction. The joint between the module and the wall construction is to be regarded as a critical detail. Due to the scope of the project and a lack of time the focus couldn't be laid on that joint. The joint was carried out safely by stuffing mineral wool and filling 50 mm of the joint from both sides with an intumescent caulk (Hilti – CFS-Fill / FS - ONE MAX). Eight modules were fitted into each wall construction, always two identical modules in each wall. Except of one module, the same modules as in the small scale tests were used. The module with the coated mineral wool slab was replaced by a mixed module with all other penetration sealing systems installed. The setup for the test in the CLT wall is shown in Fig. 5. In the second test the same modul arrangement was used. The wall construction is illustrated in Fig. 6. Both walls were exposed to heat according to EN 1366-3.

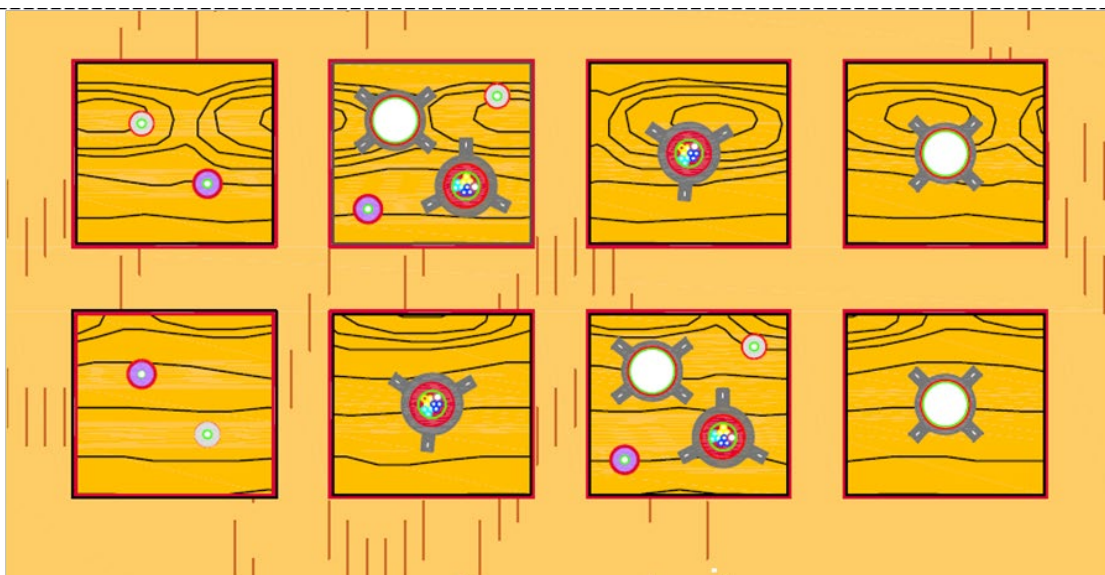


Fig. 5 Glulam modules with penetration sealing systems in a CLT wall (upper row: left: bandage and mineral wool; middle left: bandage, mineral wool, pipe collar, cable collar; middle right: cable collar; right: pipe collar)

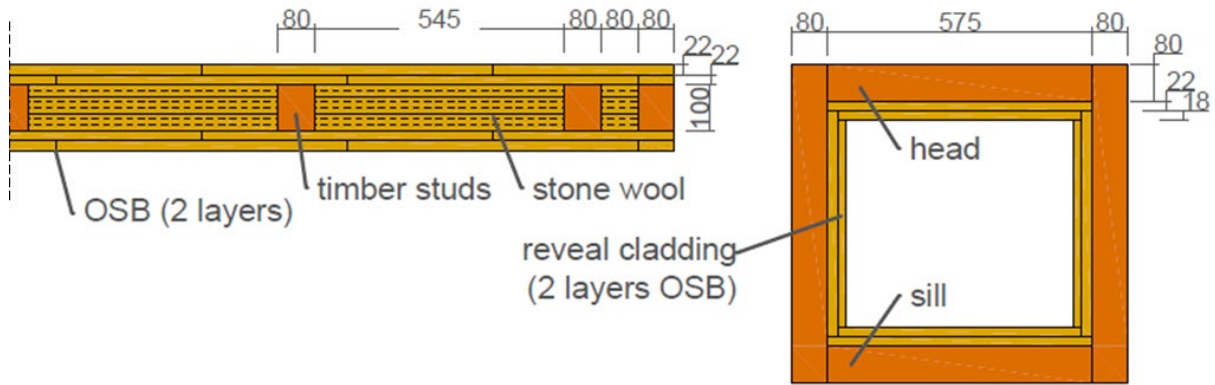


Fig. 6 Timber frame wall construction, left: section of the wall construction, right: opening design for module insertion

The test results [12], [13] show, that penetration sealing in timber modules is generally possible. It also confirmed that a closure of the linear joint with mineral wool and the caulk did provide a secure joint seal. During the first 90 minutes full scale test with the timber frame construction [12] fluctuations in the oven pressure, exceeding the standard pressure curve, occurred during the first half of the test. Thereby the physical impact on the sample was significantly higher. Nevertheless, all penetration sealing systems except the pipe collar could perform well. This is explainable by the negative impact of the pressure fluctuations during the crust formation. The second test confirmed the results of the first test. Only the two pipe collars in the right failed (compare Fig. 5). The upper one was ignited during extinguishing the initially ignited down one. Why the first collar failed can't be determined for certain. Most possibly the execution of the ring gap caused the failure. This detail was not carried out in accordance with the technical product documentation, but in an easier, less secure way. The ring gap was only filled 30 mm deep with firestop acrylic sealant [14], but no mineral wool stuffing was added. This detail was not regarded more precisely as it was not the aim of the project. Two of the four pipe collars and all other tested penetration seals maintained the performance criteria until the end of the test after 120 minutes. The results show, that these systems can be applied in timber constructions. Other penetration sealing systems base on the same operating principles. It is likely that their performance in timber modules is as good as that of the tested ones. In future, penetration sealing systems, which are intended to be used in timber buildings, could be tested in predefined timber modules. Due to the consistent testing conditions, extrapolation of results will be possible and the testing effort will be less. The timber modules can be installed at the penetration point in different timber assemblies. Different possibilities to carry out the gap between module and timber assemblies will be pointed out by the authors within upcoming projects. In addition, the industrie partner Hilti does now provide first tested solutions for selected wood constructions.

3 Single penetrations

In Germany the model conduit systems guideline [3] describes basically how penetrations need to be sealed. For selected single pipes and cables with relatively small diameters facilitations exist, which allow the sealing of penetrations without using a classified penetration sealing system in a defined setup. The facilitations differ between penetrations through walls with a classified fire resistance rating of 30 minutes and components classified for 90 minutes. This article regards only facilitations for walls with a rating of 30 minutes. According to [3] penetrations of single cables, small cable bundles (< 50 mm), and non-combustible pipes through non-combustible walls with a fire rating of 30 minutes can be sealed with non-combustible materials. If mineral fibers (with a melting point above 1000 °C) or an intumescent material are used, the size of the gap between the conduit and the surrounding component is limited to 50 mm. In small scale fire tests the applicability of this facilitation in timber construction was examined. The general test setup is shown in Fig. 7.

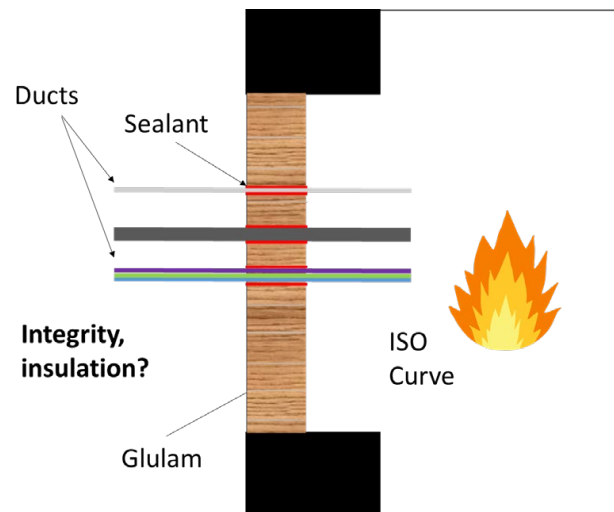


Fig. 7 General test setup for testing of single pipe and cable penetrations

As the material wood is combustible, a smaller ring gap was rated at a higher risk than the maximum allowed gap size of 50 mm. Copper pipes with diameters of 12 mm and 22 mm, a single cable (NYM-J 5x16), and a cable bundle (1 * (N)YM(ST) J_3x2,5/1,5; 2 * NYM-J 5x16) were installed in 60 mm glulam wall modules, each sealed with mineral fibres, intumescent material, firestop acrylic, and gypsum (see 8, middle). The ring gap sizes were between 5 mm and 15 mm for intumescent material and firestop acrylic and 10 to 20 mm for stonewool and gypsum. The conduits were arranged eccentrically in the borehole. The modules were exposed to fire according to Fig. 1 right for 30 minutes. Temperatures were measured on the unexposed side 25 mm above the conduits on the glulam (1) and on the conduits 25 mm away from the glulam surface (2) (see 8, left). On the Ø22 copper pipe (2) a rise of temperatures between 373 K and 406 K was measured after 30 minutes. On the timber surface (1) temperatures rose between 80 K and 107 K. Compared to that, the temperature rise on the Ø12 copper pipes was about 50 K less and the temperatures on the timber surface were about 25 K less. The sealing with stone wool lead to the highest temperatures on the copper pipe. This may be justified by the low thermal conductivity of stone wool. For the cable bundle measured temperatures were lower. The highest temperature rise on the bundle, nearly 200 K, occurred as well in connection with stone wool. The temperatures on the timber surface above the bundle can be compared with the temperatures over the Ø12 copper pipe. The sealing of single cables resulted in the lowest temperature rise of under 180 K on the cables and below 60 K on the timber surface. Averaged measured temperature rises for copper pipes, cables, and cable bundles, and the timber surfaces are shown in Fig. 9. During the tests no flames on the unexposed side occurred.

Only the results for the single cable and the bundles, which are not sealed with stone wool would meet the required temperature criteria for a classified penetration seal. The other penetrations with every kind of sealant result in high temperatures on the conduits on the unexposed side. As the temperatures on the conduits are significantly more influenced by the type of conduit and their own thermal properties and less by the type of sealant, it is not likely that the temperatures on the conduits would be significantly lower in combination with a concrete wall. Nevertheless, concrete is a better heat sink due to its higher thermal conductivity. Resulting temperature differences on pipes lead through wood should be compared to the temperature differences on pipes lead through concrete.

The temperatures on the timber component at the measure point are low enough to meet the temperature criteria of EN 1366-3. Still those temperatures need to be observed thoroughly as the surrounding material is combustible. According to [15] the ignition of wood is dependent on time and temperature. With rising temperature, wood ignites earlier. For an ignition within 30 minutes, the temperature has constantly to be about 180 °C. With an initial temperature of approximately 20 °C, the temperature on the timber surface at the measure point does not exceed 120 °C during the test. So at the measure point there is a low risk of ignition. The temperatures at the edge of the borehole may be significantly higher. Charring of the wood around the ring gap should be regarded as an important parameter and is an indicator for the temperature there.

During the tests no ignition on the unexposed surface occurred, despite charring of wood at the edge of the ring gap could be seen at some penetrations (see 8, right). The most charring occurred at

the penetrations which were sealed with intumescent material. By sealing with gypsum the durability of the sealment is to question as cracks can occur due to the different shrinkage and expansion behavior of timber and gypsum regarding different humidities. All requirements to meet the integrity criteria were fulfilled in the tests. Therefore, the risk of fire spread to the unexposed side in the tested assemblies is comparable to a corresponding penetration sealing in a non-combustible construction. The temperature differences on the conduits, especially on copper pipes, exceed the temperature limit for the insulation criteria. Hence, further insulation of the pipes after the penetration is recommended to prevent the ignition of nearby objects.



Fig. 8 Measure points (left), exemplary test assembly (middle), assembly after the test (right)

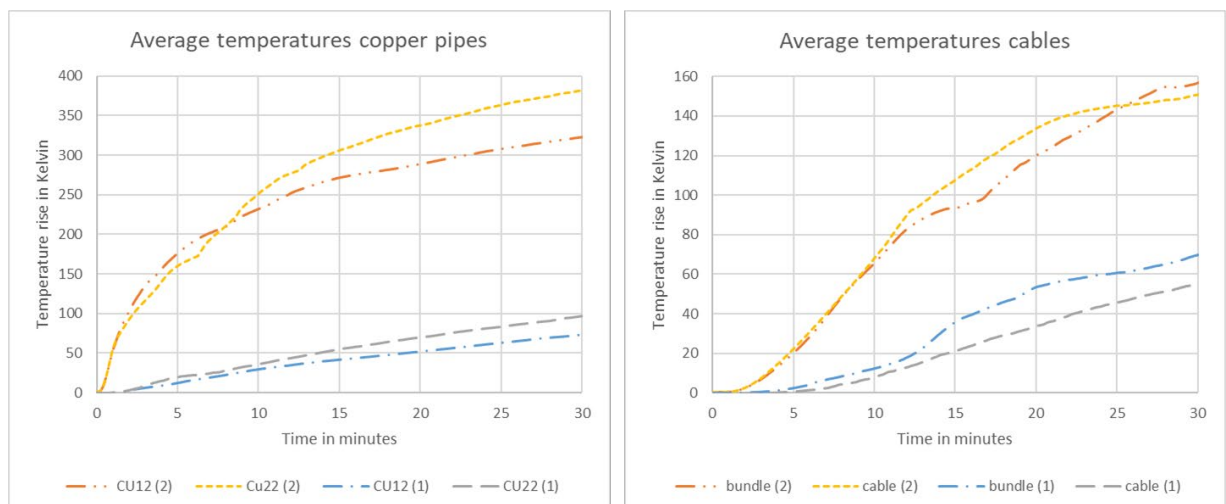


Fig. 9 Temperatures copper pipes (left), temperatures cables (right)

4 Conclusion

Due to ecological issues timber constructions move more into focus. Actually there is no modified solution to seal penetrations in timber buildings. The tested traditional penetration sealing systems can be used in timber assemblies with none or minor adjustments – when installed properly with respect to wood. Proper tested systems by various suppliers, e. g. [16] will provide good solutions in the near future. To avoid substitution of the timber construction in the penetration area, predefined timber modules should be used to install the penetration seals in. With constant testing conditions, experience will be made and fewer tests will be required.

In Germany selected single pipe or cable penetrations can be sealed without classified penetration sealing system according to the facilitations of the model conduit systems guideline. Some of this facilitations for 30 minutes fire resistance were tested in timber assemblies and can be used with a comparable risk of fire spread to non-combustible wall assemblies. As some pipes showed very high surface temperatures behind the penetration a further insulation of pipes, especially copper pipes is recommended.

References

- [1] Bauministerkonferenz. 2002. *Musterbauordnung (MBO)*. Last amended 22.02.2019.
- [2] Bauministerkonferenz. 2004. *Musterholzbaurichtlinie (M-HFH HolzR)*.
- [3] Bauministerkonferenz. 2016. *Muster-Richtlinie über brandschutztechnische Anforderungen an Leitungsanlagen - Muster-Leitungsanlagen-Richtlinie (MLAR)*.
- [4] Scherer, Thomas et al. 2019. *Leitungsdurchführungen im Holzbau: Abschlussbericht LeitHolz*. Stuttgart: Fraunhofer IRB Verlag.
- [5] European Committee for Standardization. 2009. *EN 1366-3 Fire resistance tests for service installations - Part 3: Penetration seals*.
- [6] European Committee for Standardization. 2012. *EN 1363-1 Fire resistance tests - Part 1: General requirements*.
- [7] European Committee for Standardization. 2010. *Eurocode 5 - Design of timber structures - Part 1-2: General - Structural fire design*.
- [8] Östman Birgit et al. 2010. *Fire safety in timber buildings*. Stockholm:SP.
- [9] Teibinger, Martin and Irmgard, Matzinger. 2013. *Brandabschottung im Holzbau – Planungsbroschüre*. Wien: Holzforschung Austria.
- [10] Hilti, „CFS-B Brandschutzbandage“. 2020. [Online]. Available: https://www.hilti.de/c/CLS_FIRESTOP_PROTECTION_7131/CLS_FIRESTOP_COL-LAR_WRAP_BANDAGE_7131/r4774?itemCode=429557. [Accessed February 2020].
- [11] Rockwool. „Conlit 150 U“. 2020. [Online]. Available: <https://www.rockwool.de/produkte/conlit-150-u/>. [Accessed February 2020].
- [12] Scherer, Thomas and Thiele, Catherina. 2019. „Versuchsbericht B1_Holzrahmenwand“. Kaiserslautern.
- [13] Scherer, Thomas and Thiele, Catherina. 2019. „Versuchsbericht B2_Brettsperrholzwand“. Kaiserslautern.
- [14] Hilti. „Hilti Firestop Acrylic Sealant CFS-S ACR“. 2020. [Online]. Available: https://www.hilti.de/c/CLS_FIRESTOP_PROTECTION_7131/CLS_FIRESTOP_SEAL-ANTS_SPRAYS_7131/r4883. [Accessed February 2020].
- [15] Metz, Ludwig. 1942. *Holzschutz gegen Feuer*. VDI. 1942. [Source was not available].
- [16] Hilti. 2019. „Brandschutzlösungen für den Holzbau“ [Online]. Available: <https://www.hilti.de/content/hilti/E3/DE/de/discover/magazine/directory/trends/firestop-wood.html>. [Accessed March 2020].

Applicability of Superabsorbent Polymer as a Protective Carrier in the Bio-based Self-healing Concrete

Hana Schreiberova, Josef Fladr, Karel Seps, Tomas Trtik, Zdenek Prosek, Alena Kohoutkova

*Faculty of Civil Engineering,
CTU in Prague,
Thakurova 7, 166 29 Prague 6, Czech Republic*

Abstract

Concrete with an enhanced self-healing ability caused by metabolic activity of certain bacteria has been widely studied in the recent decades. This paper deals with two of the major drawbacks which have been identified in the previous research – the inability of bacteria to survive the crystalline pressures in the hardening concrete and the need for a sufficient water supply for its metabolism. In order to solve these issues, in the current study, superabsorbent polymers (SAP) are applied to standard cement paste as a means of protection of the bacteria and also as a potential water reservoir. To prove the SAP applicability in the bio-based concrete, cement composite specimens with SAP, specimens with SAP and a biological self-healing agent and reference specimens were prepared. Subsequently, the sealing of artificially introduced cracks was recorded and the influence of the SAP addition on the materials self-healing ability was determined.

1 Introduction

Self-healing, in terms of autonomous detection and repair of defects, has attracted much attention in the field of concrete structures, especially due to the material's pronounced tendency to crack. The crack formation allows water and aggressive substances to enter the material, which results in further degradation and thus decrease in the structure durability.

Manual regular inspections and maintenance of concrete surfaces are highly laborious and economically demanding measures. Further, in many cases, due to the poor accessibility of certain structures, the manual approach can be complicated to nearly impossible. For these reasons, development of cementitious composite with a self-healing capacity to ensure prolonged durability is an economically important topic which is attracting widespread commercial interest.

Concrete with an enhanced self-healing ability based on metabolic activity of certain microorganisms has been widely studied in the recent decade. The self-healing, more specifically the autonomous crack-sealing, relies on the so-called biocalcification process – an ability of special types of microorganism (mostly bacteria) to produce calcium carbonate (CaCO_3) when supplied with appropriate nutritional compounds [1–5]. In the novelty material, bacteria in its resistant form of spores is incorporated directly into the concrete matrix during the mixing process. Further, standard concrete mix is enriched with the necessary nutrients – a source of calcium and some kind of a metabolic activator. Apart from this addition of the biological self-healing agent, the further processing of the mixture does not differ from the traditional procedures. The biocalcification process is triggered when a crack occurs, and water penetrates the material. The water presence together with the incorporated nutrients causes germination of the bacterial spores and subsequently the CaCO_3 precipitation.

Although numerous investigations reported a considerable self-healing potential of the bio-active cementitious composites [3,4,6–23], several obstacles remain not completely resolved. Principally, experiments showed that metabolic activity of the incorporated bacteria decreases significantly after approx. 7 days [3] from casting. This decrease may be a result of mechanical destruction of the bacteria by crystallization pressures in the aging concrete, thus it points out the importance of the bacteria protection [5,6,8,11,12,14]. Furthermore, especially in the case of horizontal structures, it might be problematic to ensure a sufficient water supply, which is crucial for the biocalcification process. Both of these drawbacks of the biological approach to self-healing concrete are being dealt with in this paper by application of superabsorbent polymers.

Superabsorbent polymer (SAP) is a designation for a polymer with an absorption capacity up to hundred times its own weight. In recent studies, SAP has been investigated as an addition into concrete which could positively influence autogenous shrinkage [24,25], frost resistance [26], waterproofing [27], and enhanced the materials natural self-healing ability [28,29]. Based on the promising results of the SAP addition, a combination of SAP and the bio-based self-healing concrete principles have been proposed and investigated in a few studies. Theoretically, the polymer could not only protect the bacteria from the harmful pressures in aging concrete, but also to provide the needed moisture thanks to its striking absorption abilities.

In the paper of Giriselvam et al. [30], concrete specimens containing unsporulated bacteria, nutrients and SAP in various concentrations were produced and investigated. In this study, the addition of SAP resulted in better healing of cracked specimens compared to the solely bacterial samples. However, the water uptake of the applied SAP was reported to be only 86 g/g SAP which is not in line with the expectations. For this reason, the results might not be generally applicable. Further, no SAP samples without bacteria were produced, thus the protective effect of the SAP is not clearly detectable.

In the study carried out by Kua et al. [31], SAP was primarily applied to further enhance the autogenous crack-sealing. The protection of bacteria was ensured in this experiment by their immobilization in biochar. In this paper, closure of cracks with width over 0.6 mm was reported in the case of combination of SAP, biochar-immobilized bacterial spores and polyvinyl alcohol fibres.

Although some research of the SAP application in the bio-based self-healing concrete has been done, more work is needed in order to determine all of the influencing factors, as the results may vary dramatically depending on the specific type of the applied materials. The current experiment presented in this paper deals with application of bacterial spores of *Bacillus pseudofirmus*, SAP and two nutritional compounds (calcium lactate and yeast extract). The self-healing potential is determined on several series of cement composite beams which were cracked by three-point bending test and further cured in water to trigger the healing.

2 Experimental investigations

2.1 Materials

In order to determine the applicability of SAP in the bio-based self-healing concrete, cement mortar containing ordinary Portland cement, distilled mixing water with/without bacterial spores, sand, SAP, and nutritional admixtures was prepared.

The biological healing agent, bacteria *Bacillus pseudofirmus* (LMG 17944), was selected based on the experiments described elsewhere [3,19,32,33]. The cultivation and sporulation processes were performed based on the supplier recommendation (Belgian Coordinated Collections of Microorganisms).

As a means of protection of the bacterial spores, commercially available SAP (cross-linked acrylamide/acrylic acid copolymer, potassium salt obtained from Evonik Industries) was applied. Our previous investigations of the material characteristics indicated that its absorption capacity at room temperature in distilled water reaches up to 245 g solution/g SAP; however, with an increasing ion presence the absorption lowers drastically. In a nutrient solution (60 g/l calcium lactate and 17 g/l yeast extract), the absorption was as low as 15 g solution/g SAP [34]. Thus, it can be expected that the liquid uptake in fresh cement paste with nutritional compounds will be significantly limited.

The nutritional compounds and their dosages necessary for the bacterial calcium carbonate precipitation were selected based on the previous studies presented elsewhere and own preliminary examinations [35]. Calcium lactate ($C_6H_{10}CaO_6 \cdot 5H_2O$, purity > 98%, obtained from Carl Roth GmbH + Co. KG, Germany) as the calcium source and yeast extract (obtained from Carl Roth GmbH + Co. KG, Germany) as the metabolic activator have been successfully applied in numerous studies [36] [7] [3] [12] and proved to be suitable for the biological healing agent.

2.2 Mix proportion design

In Table 1, design proportions of the prepared cement mortars can be seen. Four series were prepared in total. The CTRL mix served as the control, as it contained neither bacterial spores nor SAP. Mix containing directly added spores without SAP (BAC) provides an evaluation of the contribution of SAP on protection of the spores, thus on the crack filling. Further, by comparing the CTRL_SAP mix

(only SAP added) with control mix, the contribution of the polymer itself to the self-healing can be determined. Finally, the mix SAP_BAC was prepared in order to evaluate the self-healing potential of the SAP-bacteria combination.

The mass of binder and sand was fixed to 586 kg/m³ and 1759 kg/m³, respectively. In the case of mixes containing SAP (CTRL_SAP and SAP_BAC), additional mixing water was applied in order to make up for the liquid uptake by the polymer. The water to cement ratio (w/c) in these mixes was 0.6, whereas in the remaining series only 0.5. The amount of the extra mixing water (21 g water/g SAP) was applied based on our previous investigations dealing with the SAP–cement mortar workability [34]. Further, all of the mixes, including the control (CTRL), contained calcium lactate (3.0 wt. % of cement) and yeast extract (0.85 wt. % of cement).

The SAP was applied to the respected mixes in dry state in the dosage 0.5 % by weight of cement. This value was chosen based on our previous investigations which were focused on determining the SAP influence on the mechanical characteristics [34]. Bacterial spores were introduced into the bacterial mixes by their careful dispersal in the mixing water. The final concentration of the spores in the solution was 10⁶ CFU/ml.

Table 1. Mix composition of the investigated cement mortars with nutrient compounds.

Material		CTRL	BAC	CTRL_SAP	SAP_BAC
CEM I R 42.5	[kg/m ³]	586	586	586	586
Distilled water	[kg/m ³]	293	293	355	355
Sand (1-2 mm)	[kg/m ³]	440	440	440	440
Sand (0.1-1 mm)	[kg/m ³]	1319	1319	1319	1319
SAP	[wt.% of cement]	0	0	0.50	0.50
Calcium lactate	[wt.% of cement]	3.00	3.00	3.00	3.00
Yeast extract	[wt.% of cement]	0.85	0.85	0.85	0.85
<i>Bacillus pseudofirmus</i>	[CFU/ml]	-	1x10 ⁶	0	1x10 ⁶

2.3 Specimen preparation

The nutritional compounds and SAP, if applied, were added alongside with cement and premixed for 1 min in order to achieve distribution as uniform as possible. Mixing water with/without dispersed bacterial spores was added as prescribed by the standard.

Prior to casting, consistency of CTRL and CTRL_SAP was determined using a cement flow table test according to relevant standards in order to determine the impact of the SAP and extra mixing water addition on the paste workability.

All of the mixes were casted into 40x40x160 mm³ moulds. Additionally, steel fibres were placed approx. 10 mm below the mould edge (Fig. 1). This reinforcement should further facilitate the crack creation by a three-point bending in later ages. Without the steel reinforcement, the specimens could be easily fractured completely and split in half. The moulds with the embedded steel fibres were then left covered at room temperature and humidity. After demoulding, the specimens were cured at 25 °C and approx. 90% RH for 28 days.



Fig. 1 A mould for three 40x40x160 mm³ specimens – a demonstration of the steel fibres placement.

2.4 Crack introduction and healing

In order to determine the self-healing potential of the SAP-bacteria concrete, cracks were introduced by a three-point bending test after the end of the curing period in every specimen. The placement and widths of the cracks were carefully recorded by photographic imaging. Additionally, the areas around the formed cracks were scanned by optical scanning microscope in order to obtain high resolution images. After the investigation of the pre-healed state, the samples were subjected to the healing process.

Continuous full immersion in water was applied in the healing period. The cracked samples were placed into open plastic containers filled with standard tap water and left open at room temperature for 28 days. After the healing period, the samples were removed from the containers and the crack sealing was inspected and recorded by high resolution photographic imaging and scanning optical microscopy.

3 Results

3.1 Flowability of the fresh pastes

Cement flow table test indicated that the addition of 0.5% SAP to cement weight along with 20.1% of mixing water results (CTRL_SAP) in similarly flowable paste to control (CTRL). As seen in Fig. 2, the spread diameter of control series without SAP and additional mixing water reached 18.6 mm and, not too differently, the CTRL_SAP paste spread diameter was measured to be 18.2 mm.

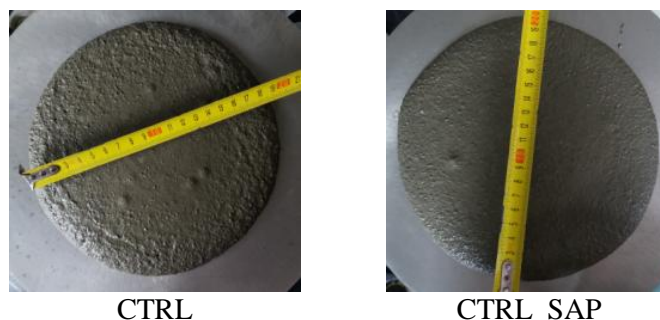


Fig. 2 Results of the cement table test performed on CTRL and CTRL_SAP series.

3.2 Healing efficiency

Self-healing efficiency, thus crack sealing, was in this paper evaluated by visual inspections through scanning optical microscopy and photographic imaging. The photographic images which compare the state before the 28-day long immersion in water and after the healing period can be seen in Fig. 3.

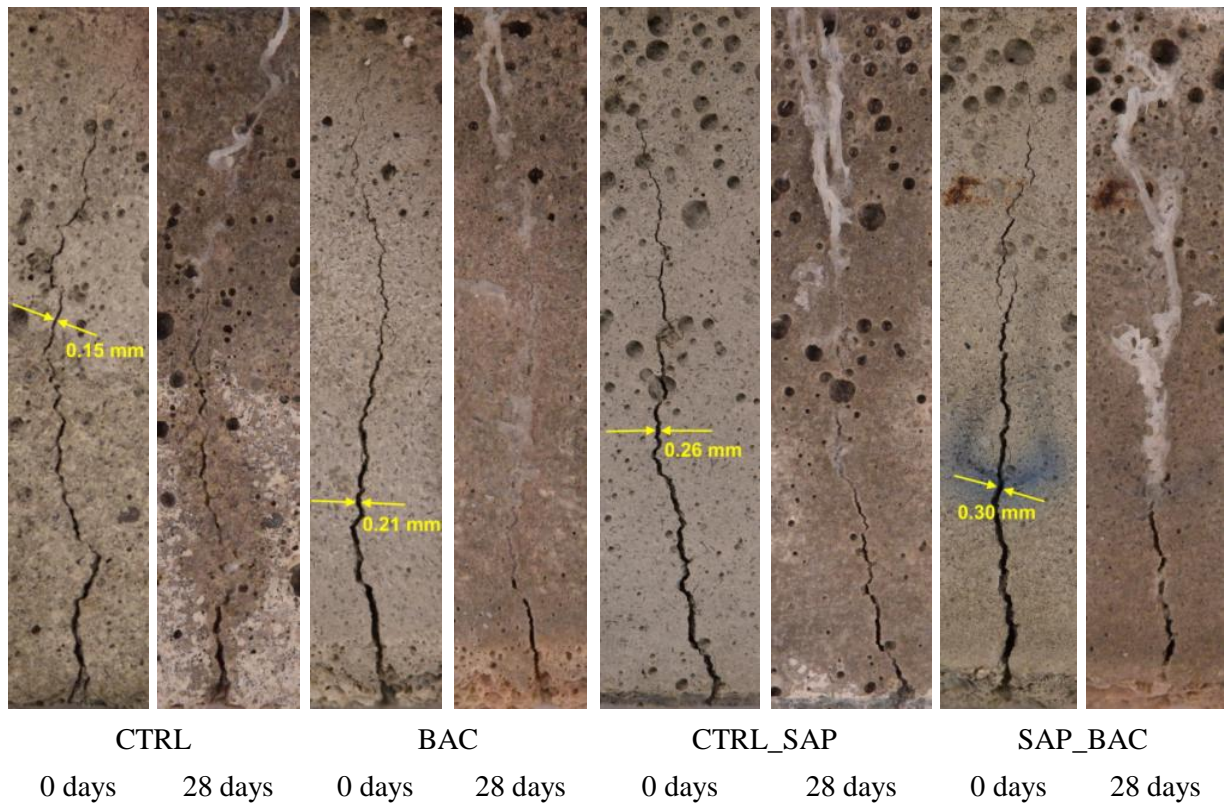


Fig. 3 Comparison of the cracked cementitious specimens before and after the healing process – the maximum initial width of the crack that was healed is marked.

It is evident from the results that certain crack-sealing has taken place in all of the investigated series. As it can be observed, newly formed white precipitates were detected in all of the samples. Following investigations revealed that maximum initial widths of the crack where the precipitates formed differed depending on the mix composition (Fig. 4). The samples were produced in duplicate, thus four different cracked surfaces were available for each mix composition. Based on the photographic imaging, the maximum initial width of the cracks that were healed were measured and their average value was determined for each mix.

In control samples (CTRL), the average maximum initial crack width was 0.18 mm. In the BAC samples where bacteria were incorporated, the width increased to 0.23 mm. In samples where only SAP was added, the average initial crack width reached 0.26 mm. Finally, in samples SAP_BAC containing both bacteria and SAP, the precipitates could be observed in crack with the average initial width up to 0.28 mm.

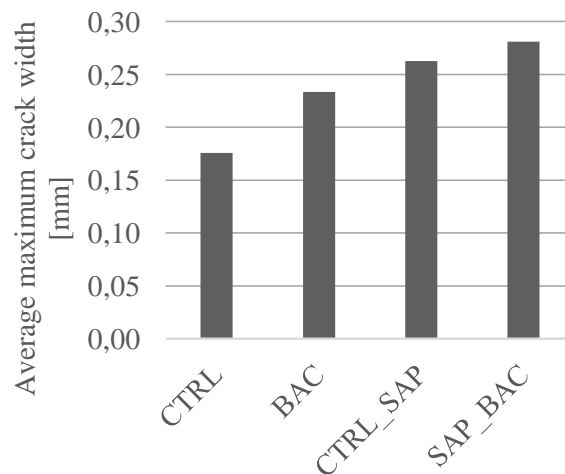


Fig. 4 Average maximum initial widths of healed crack.

The scanning microscopy enabled closer visual inspection of the crack sealing. In Fig. 5, a crack closed after the healing period can be seen. As visible from this example, the precipitates formed not only in the crack itself, but also in the area adjacent to it. The white depositions were primarily located in pores, although some of them remained empty.

The Fig. 5 captures crack in an SAP_BAC specimen, thus specimen containing bacteria and SAP. However, the microscopic investigation showed that the precipitates did not visually differ in the other series.

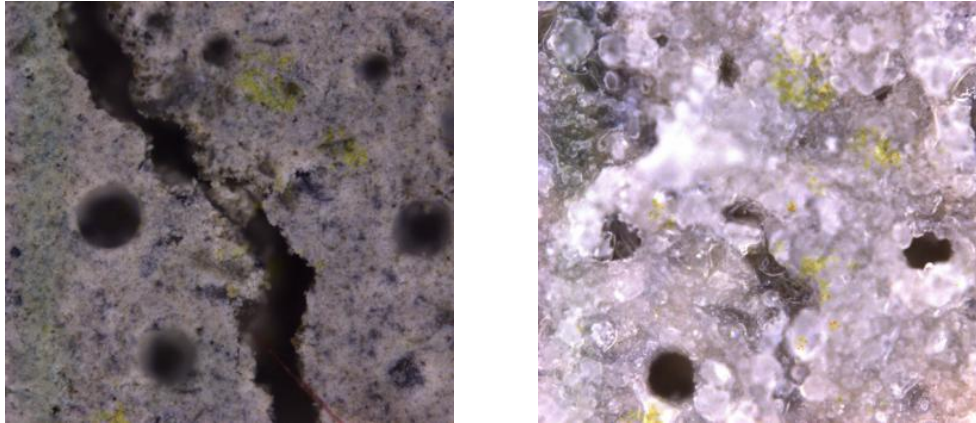


Fig. 5 A microscopic image of the crack before (left) and after the healing process (right) in a sample from the SAP_BAC series.

4 Discussion

In accordance with the assumptions, due to the autogenous self-healing capacity of cement composites, the crack closure was observed in all of the series including the control (CTRL). The positive impact of the SAP addition, especially in the case of crack widths below 0.5 mm, on the autogenous healing was reported elsewhere [31]. Comparable to these findings, in this paper, the maximum healed crack width of the CTRL_SAP series was 49.3% greater compared to the control series. However, it must be acknowledged that the extra mixing water added alongside with SAP in order to preserve the flowability may have improved the autogenous crack sealing itself.

The addition of the bacteria (BAC) increased the average healed crack width by 32.7% compared to the control. The highest value of the average maximum healed cracked after 28-day immersion in water could be observed in the samples containing both bacteria and SAP (SAP_BAC). The value was 59.84% higher compared to the control.

Although the results presented in this paper indicate positive impact of the SAP and bacteria addition on the cement composite self-healing ability, the maximum crack width healed in this experiment was only 0.32 mm. This value is not in line with earlier studies where cracks up to 0.70 mm wide were completely sealed [37]. It may be a result of an insufficient distribution of the healing agent (bacteria and nutritional compounds) in the mortar. Further, the SAP may successfully function as a moisture reservoir and increases the autogenous crack-sealing, but it may not provide enough protection of the bacteria spores against crystallization pressures. Thus, additional protection should be investigated in the future research.

5 Conclusions

In the current study, the combination of bacteria *Bacillus pseudofirmus*, nutritional compounds, and SAP was applied in cement composite in order to evaluate the biologically enhanced material's self-healing potential. The artificially cracked specimens were submitted to a 28-day long healing period and subsequently the crack closer was visually inspected. The following conclusions can be drawn based on the current experimental investigation:

- The SAP and extra mixing water addition increases the autogenous crack-sealing in cement composite.
- The bacterial self-healing agent (*Bacillus pseudofirmus*, calcium lactate, yeast extract) significantly improves the crack closure compared to plain cement composite samples.

- Protection of bacterial spores by SAP may not be sufficient and further additional methods of protection should be considered.

Acknowledgements

This paper was prepared thanks to the support of the science foundation of the Czech Republic (GACR), project "Self-healing of cementitious composites by bacteria-induced calcification" (no. 18-15697s) and project "Durability of concrete structure and assessment of its life cycle" (SGS19/149/OHK1/3T/11).

References

- [1] Henry Lutz Ehrlich, Dianne K. Newman AK. 2015. *Ehrlich's Geomicrobiology* CRC Press.
- [2] Castanier S, Le Metayer-Levrel G, Perthuisot J-P. 1999. "Ca-carbonates precipitation and limestone genesis — the microbiogeologist point of view" *Sediment Geol.* 126: 9–23.
- [3] Jonkers HM, Thijssen A, Muyzer G, Copuroglu O, Schlangen E. 2010. "Application of bacteria as self-healing agent for the development of sustainable concrete" *Ecol Eng.* 36(2): 230–5.
- [4] Al-Salloum Y, Hadi S, Abbas H, Almusallam T, Moslem MA. 2017. "Bio-induction and bioremediation of cementitious composites using microbial mineral precipitation – A review" *Constr Build Mater.* 154: 857–76.
- [5] Ersan YC, Boon N, De Belie N. 2018. "Granules with activated compact denitrifying core (ACDC) for self-healing concrete with corrosion protection functionality" Paper presented at the Conference: PRO 123: Final Conference of RILEM TC 253-MCI: Microorganisms-Cementitious Materials Interactions, Toulouse.
- [6] Tziviloglou E, Wiktor V, Jonkers HM, Schlangen E. 2016. "Bacteria-based self-healing concrete to increase liquid tightness of cracks" *Constr Build Mater.* 122:118–25.
- [7] Luo M, Qian C. 2016. "Influences of bacteria-based self-healing agents on cementitious materials hydration kinetics and compressive strength" *Constr Build Mater.* 121:659–63.
- [8] Chen H, Qian C, Huang H. 2016. "Self-healing cementitious materials based on bacteria and nutrients immobilized respectively" *Constr Build Mater.* 126:297–303.
- [9] Erşan YÇ, Gruyaert E, Louis G, Lors C, De Belie N, Boon N. 2015. "Self-protected nitrate reducing culture for intrinsic repair of concrete cracks" *Front Microbiol.* 6:1228.
- [10] Erşan YÇ, Belie N de, Boon N. 2015. "Microbially induced CaCO₃ precipitation through denitrification: An optimization study in minimal nutrient environment" *Biochem Eng J.* 101:108–18.
- [11] Wang JY, Snoeck D, Van Vlierberghe S, Verstraete W, De Belie N. 2014. "Application of hydrogel encapsulated carbonate precipitating bacteria for approaching a realistic self-healing in concrete" *Constr Build Mater.* 68:110–9.
- [12] Wang JY, Soens H, Verstraete W, De Belie N. 2011. "Self-healing concrete by use of microencapsulated bacterial spores" *Cem Concr Res.* 56:139–52.
- [13] Wiktor V, Jonkers HM. 2011. "Quantification of crack-healing in novel bacteria-based self-healing concrete" *Cem Concr Compos.* 33(7):763–70.
- [14] Wang JY, De Belie N, Verstraete W. 2012. "Diatomaceous earth as a protective vehicle for bacteria applied for self-healing concrete" *J Ind Microbiol Biotechnol.* 39(4):567–77.
- [15] Bang SS, Galinat JK, Ramakrishnan V. 2001. "Calcite precipitation induced by polyurethane-immobilized *Bacillus pasteurii*" *Enzyme Microb Technol.* 28(4–5) 404–9.
- [16] Wang J. 2018. "Screening of pH-responsive hydrogels for encapsulation of bacteria for concrete crack self-healing" Paper presented at the Conference: RILEM Technical Committee 253 Microorganisms-Cementitious Materials Interactions, Toulouse.
- [17] Alazhari M, Sharma T, Heath A, Cooper R, Paine K. 2018. "Application of expanded perlite encapsulated bacteria and growth media for self-healing concrete" *Constr Build Mater.* 160: 610–9.
- [18] Ersan Y. 2018. "Biotechnology offers more durable and sustainable cementitious composites" Paper presented at the Conference: RILEM Technical Committee 253 Microorganisms-Cementitious Materials Interactions, Toulouse.

- [19] Chiu CH, Chen CC, Ting WT. 2018. "Using lightweight aggregated as a carrier for bacterial spores in self-healing concrete" Paper presented at the Final Conference of RILEM TC 253-MCI. Toulouse.
- [20] Wang J, Mignon A, Trenson G, Van Vlierberghe S, Boon N, De Belie N. 2018. "Screening of pH-responsive Hydrogels for Encapsulation of Bacteria for Concrete Crack Self-sealing" Paper presented at the final conference of RILEM TC 253-MCI. Toulouse, 2018.
- [21] Ersan. 2016. "YC Microbial nitrate reduction induced autonomous self-healing in concrete" UGent.
- [22] Erşan YÇ, Verbruggen H, De Graeve I, Verstraete W, De Belie N, Boon N. 2016. "Nitrate reducing CaCO₃ precipitating bacteria survive in mortar and inhibit steel corrosion" *Cem Concr Res.* 83:19–30.
- [23] Erşan YÇ, Hernandez-Sanabria E, Boon N, de Belie N. 2001. "Enhanced crack closure performance of microbial mortar through nitrate reduction" *Cem Concr Compos.* 70:159–70.
- [24] Jensen OM, Hansen PF. 2001. "Water-entrained cement-based materials: I. Principles and theoretical background" *Cem Concr Res.* 31(4):647–54.
- [25] Jensen OM, Hansen PF. 2002. "Water-entrained cement-based materials: II. Experimental observations" *Cem Concr Res.* 32(6):973–8.
- [26] Reinhardt HW, Assmann A, Mönnig S. 2008. "Superabsorbent Polymers (SAPS) - An Admixture to Increase the Durability of Concrete" Paper presented at the 1st Int Conf Microstruct Relat Durab Cem Compos. Nanjing, China.
- [27] Mechtcherine V. 2016. "Use of superabsorbent polymers (SAP) as concrete additive" *RILEM Tech Lett.* (1):81–7.
- [28] Snoeck D, Van Vlierberghe S, Steuperaert S, Dubruel P, De Belie N. 2012. "Self-healing cementitious materials by the combination of microfibrils and superabsorbent polymers" *J Intell Mater Syst Struct.* 25(1):13–24.
- [29] Snoeck D. 2018. "Superabsorbent polymers to seal and heal cracks in cementitious materials" *RILEM Tech Lett.* 30:32–8.
- [30] Giriselvam MG, Poornima V, Venkatasubramani R, Sreevidya V. 2018. "Enhancement of crack healing efficiency and performance of SAP in biocrete" *IOP Conf Ser Mater Sci Eng.* 310(1).
- [31] Wei H, Gupta S, Aday AN, Srubar W. 2019. "Biochar-immobilized bacteria and superabsorbent polymers enable self-healing of fiber-reinforced concrete after multiple damage cycles" *Cem Concr Compos.* 100(February):35–52.
- [32] Jonkers H, Schlangen E. 2008. "Development of a bacteria-based self healing concrete" *Tailor Made Concr Struct.* (December):109–109.
- [33] Paine K, Sharma T, Alazhari M, Heath A, Cooper R. 2018. "Application and performance of bacteria-based self-healing concrete" Paper presented at the final conference of RILEM TC 253-MCI. Toulouse, 2018.
- [34] Schreiberová H, Fládr J, Trtík T, Chylík R, Bílý P. 2019. "An investigation of the compatibility of different approaches to self-healing concrete: The superabsorbent polymers and microbially induced calcite precipitation" IOP Conference Series: Materials Science and Engineering. Prague: IOP Publishing Ltd; 2019.
- [35] Schreiberová H, Bílý P, Fládr J, Šeps K, Chylík R, Trtík T. 2019. "Impact of the self-healing agent composition on material characteristics of bio-based self-healing concrete" *Case Stud Constr Mater.*
- [36] Chen C-C, Al. E. 2018. "Evaluation of effect of nutrients, calcium precursors, and bacteria on mechanical properties of mortar specimens" Paper presented at the final conference of RILEM TC 253-MCI. Toulouse, 2018.
- [37] Gupta S, Kua HW, Pang SD. 2018. "Healing cement mortar by immobilization of bacteria in biochar: An integrated approach of self-healing and carbon sequestration" *Cem Concr Compos.*
- [38]

Wood Ashes from Electrostatic Filter as a Replacement for the Fly Ashes in Concrete

M. Sc. Piotr-Robert Lazik, Prof. Dr.-Ing. Harald Garrecht

1. Introduction

The word "organic" currently has a good reputation worldwide. Everyone wants to eat organic products, have an organic lifestyle or use organic bags in the supermarket, all to protect nature and mother earth and to improve people's healthy lives. There are so many activists who fight every day to save the world. Some of those are more some less successful. They are looking for a solution that very often cannot be achieved for political or economic reasons.

And here we are, there is still a product that not many people pay attention to. A product that causes the greatest pollution in the world, more than car exhaust or volcanic eruption. It is cement and clearly, its manufacture. Cement is one of the most important binders, a key component of concrete in a world production of 4.1 billion tons. 2017 is the most widely used material overall. Have you ever considered what amount of CO₂ was emitted into the atmosphere by the production of 4.1 billion tons cement?

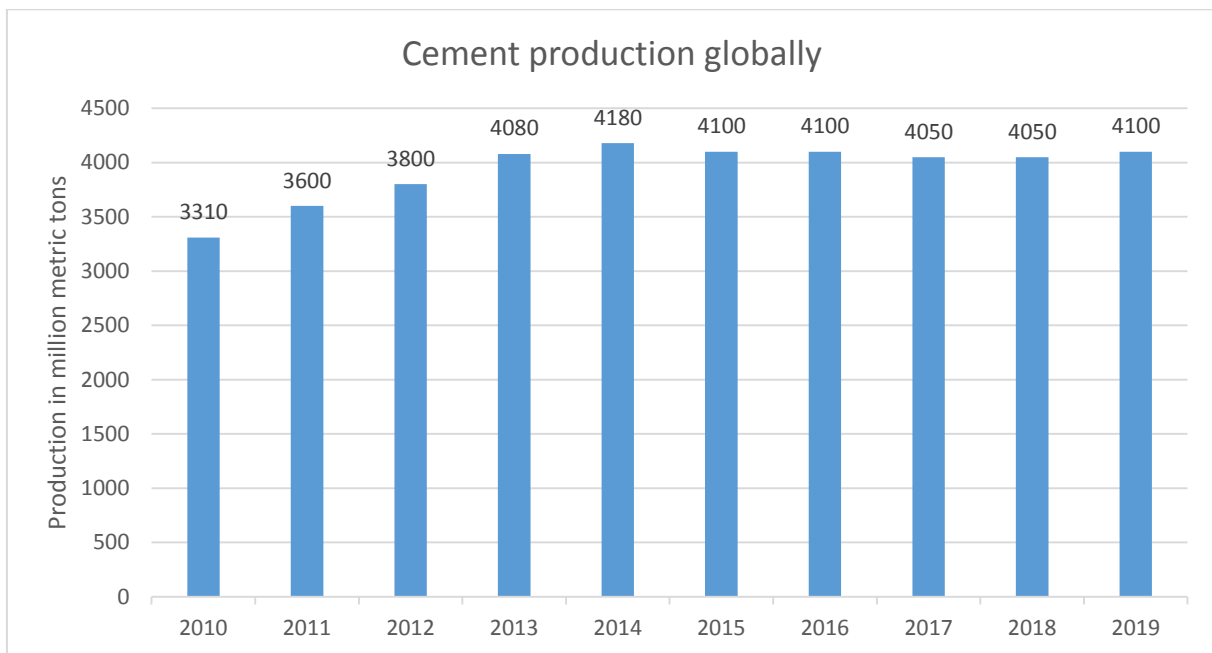


Fig. 1 Cement production globally from 2010 to 2019 worldwide. US Geological Survey.

First we have to answer a simple question. Can we forego cement in the concrete at all? Unfortunately not yet, cement is irreplaceable in concrete. Its properties give the concrete strength and are responsible for its durability. But that does not mean that the concrete could not be made more ecologically. In times where CO₂ reduction is the world most common effort, it is absolutely necessary to think products in the context to bioeconomy. Nothing is more bioeconomy than using available biological materials.

2. A way to organic concrete

Fly Ashes are considered to be one of the most important and popular component used in concrete. Their pozzolanic properties have a certain impact on the properties of fresh and hardened concrete, for example consistency and compressive strength. Unfortunately, in recent years in Germany as in Western Europe, we have had a huge shortage of this material. The reason for this phenomenon is the decreasing number of coal power plants in which Fly Ashes are a by-product. The use of by-products in concrete has not only strength aspects but also ecological ones. During the production of cement, a huge amount of CO₂ is produced. Using fly ashes as a substitute component and by-product in itself, we reduce the need for cement can be reduced, less cement means less CO₂ in the atmosphere. The most important property of fly ashes is that they can be used as a main component with virtually any type of cement and used almost in all types of concrete: normal concrete, lightweight concretes and ultra high performance concrete [1].

The standard DIN EN 450-1 defines fly ashes as a fine-grained dust consisting of spherical and glassy particles, which is produced by the use of finely ground coal. The pozzolanic properties of the fly ashes are mainly due to SiO₂ and Al₂O₃. The amount of reactive SiO₂ is at least 25 wt.%. According to DIN EN 197-1, lime-rich fly ash with a reactive CaO > 10 wt.% can be used as the main constituent for the production of fly ash cements CEM II/A-W or CEM II/B-W.

The application of fly ashes in Germany began in the 1960s with the constant increase in production. In the 90's fly ashes were already almost 100% used in the building industry, 75% of which is used in various types of concrete. It took scientists more than 10 years to see the visible success of fly ashes today. The delay was caused by the lack of approval of fly ashes to be used in concrete [1].

The coal is transported to the power plant by various means, depending on accessibility by truck, rail or ship. There it is added directly to the coal bunkers. The coal is then ground to a fine grain size in the coal mills. The grain fineness is adjusted, which is present at the 80 wt.% < 90 μm. The pulverized coal is further transported to the combustion chamber, where the organic components are burnt (Fig. 2). The fly ash is then obtained by electrostatic separation in multi-stage electrostatic precipitators. The combustion temperatures of hard coal are between 800°C and 1700°C depending on the type of furnace [2].

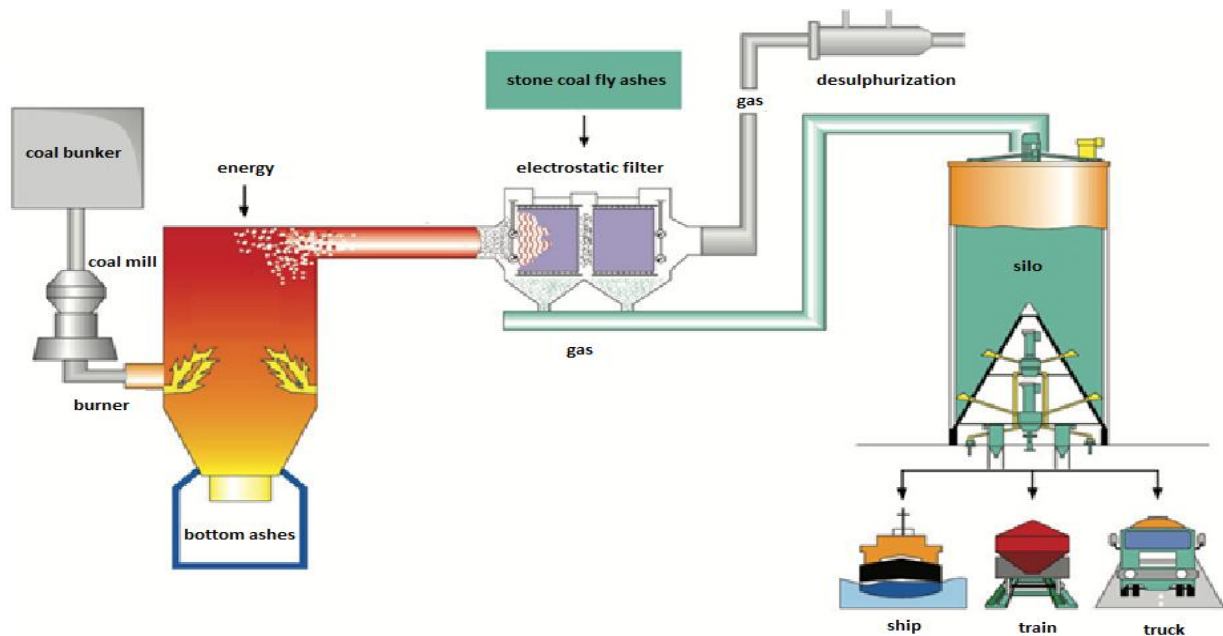


Fig. 2 Production process in the power plant [3]

- **Wood ashes from electrostatic filter and cyclone filter as a replacement for the fly ashes in concrete**

The delivered wood chips are first collected in a fuel store. The combustion chamber consists of three systems: grate, combustion chamber and afterburner. The furnace grate is located in the central point of combustion. Different types of construction are burned in the furnace. Thermo-chemical processes take place in the combustion chamber. Then they pass through the first filter stage, which is a cyclone separator, where most of the inorganic components are separated thanks to the air flow. In the meantime, another filter stage can follow in the form of an electrostatic precipitator, as in the case of fly ashes [4].

Table 1 Characteristics of wood ashes from cyclone and electrostatic filter [4]

Characteristic	Cyclone Ashes	Electrostatic Ashes
production	cyclone separator	electrostatic filter
particle size	2-160 µm	< 10 µm
mean particle size (kg/m ³)	2400 - 2700	2300 - 2600
density	0,3 - 0,5	0,15 - 1,12
pH	10 - 13	10 – 13

Due to the shift to regenerative energy (e.g. wood energy) several hundred tons of wood ashes from electric and cyclone filter are produced in Germany and the every year, in the UK even more. The wood from which the wood ashes arise are usually garden wastes, shrubs on the roadsides and tons waste from sawmills. In contrast to the bottom ash filter ashes cannot be used for nutrient recycling in agriculture and forestry but is mostly deposited. Only few research is done to find their usage in construction, to put it in another way - in concrete. The construction sector is so huge that there can certainly be found a place for them instead of storing them up. In order for this to happen, it is necessary to undertake appropriate tests. Without proper investigation, an acceptance to be used in construction is unlikely to be permitted.

Chemical composition of fly and wood ashes

In the first place, it is necessary to closely study the chemical structure of the wood ashes, and try to find similarities with fly ashes. Nowadays we know exactly how fly ashes behave. There are many chemical and physical methods with which to test the components of wood ashes, for example ICP method (Inductively Coupled Plasma). The content of heavy metals and other elements, which can cause problems in the binding of concrete must be eliminated. Only in this way their impact on the strength and durability of various types of concrete will be improved.

The chemical composition is characterized by three main components - SiO₂ (silicic acid), Al₂O₃ (alumina) and Fe₂O₃ (iron oxides). Most fly ashes from lignite-fired power plants are low in sulphate and rich in silicon. The table shows the composition of silicon-rich fly ash and Portland cement from 1997-2004.

Table 2 Chemical components of fly ashes and Portland cement. [5], [6]

Component [wt.%]	silicon-rich fly ash ¹⁾	Portland cement ²⁾
SiO ₂	36...59	19...23
Al ₂ O ₃	20...35	3...6
Fe ₂ O ₃	3...19	0,2...7
CaO	1...12	61...67
MgO	0,7...4,8	0,6...4
K ₂ O	0,5...6	0,4...1,5
Na ₂ O	0,1...3,5	0,06...0,4
SO ₃	0,1...2	2...4
TiO ₂	0,5...1,8	0,11...0,3

1) Values from monitoring of silicon-rich fly ash from 1997 to 2004, Testing according to DIN EN 450-1 [5]

2) Average range limits of Portland cement of strength class 42.5, containing loss on ignition [6]

In order to determine the components of wood ashes and to compare them with fly ashes, four different types of wood ashes from electrostatic precipitators and cyclone filters were investigated. The results were recorded in the Table 3

Table 3 Chemical components of wood ashes and selected fly ash [own research results].

Components [wt.%]	Wood Ashes				Fly Ashes
	1 ¹⁾	2 ²⁾	3 ³⁾	4 ⁴⁾	
SiO ₂	1,1	11,2	5,5	52,7	57,4
Al ₂ O ₃	0,2	2,4	0,7	7,9	19,0
Fe ₂ O ₃	0,1	1,8	0,5	3,3	13,1
CaO	3,8	31,1	37,9	17,3	3,5
MgO	1,5	4,3	4,8	2,4	1,4
K ₂ O	41,2	16,4	13,8	5,2	2,0
Na ₂ O	0,4	0,9	0,2	0,9	0,8
SO ₃	16,4	17,7	4,9	2,4	0,9
TiO ₂	< 0,1	0,2	< 0,1	0,6	0,9

1. electrofilter ashes (tree species Beech)
2. mixed electrofilter ashes - different tree species
3. cyclone ashes (tree species Beech)
4. cyclone ashes different tree species

As mentioned earlier, the first three components listed in the table above are responsible for the pozzolanic properties. As can be seen from the table, for the first three grades, the amount of reactive SiO₂ is less than 25 wt.% (according to standard EN 450-1 should be at least 25 wt.%). If one wants to compare the values with the requirements of standard EN 450-1 with fly ashes, the sum of the three components SiO₂, Al₂O₃ and Fe₂O₃ must be at least 70 wt.-%. In this case, the values are significantly lower. The values of reactive calcium oxide CaO should not exceed 10 wt.-%. The criterion was only met in electrofilter ashes Nr. 1. In accordance with DIN EN 197-1, wood ash with CaO > 10 wt.% can be used as the main constituent for the fly ash cements CEM II/A-W or CEM II/B-W.

However, to confirm the evidence, the strength tests (compressive strength) on normal concrete (2300 kg/m^3) with the water-cement value 0.4 were carried out and showed that despite much lower values of SiO_2 , Al_2O_3 and Fe_2O_3 , the wood ashes have reached almost the same strengths as the fly ashes. This leads to an important result, that the wood ashes must not be compared literally with the fly ashes standard EN 450-1.

A reference concrete with a water-cement value of 0.4 was produced, consisting only of cement CEM I 42, 5 N, aggregate and water. Afterwards the cement quantity was replaced by 25 wt.% each with fly and wood ashes from electrostatic precipitators (No. 1 and 2 in Table 3). The compressive strength was verified in accordance with the DIN EN 206-1/DIN 1045-2 standard on test specimens aged 28 days.

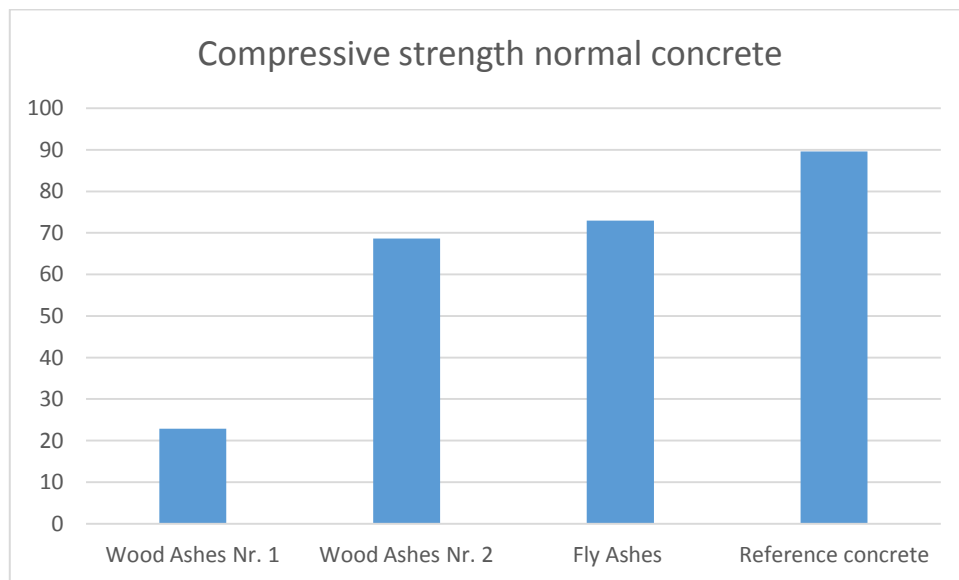


Fig. 3 Composition of compressive strength on concrete with wood and fly ashes [own research results].

The heavy metals in concrete can have unexpected consequences. German Institute for Structural Engineering has prescribed the limit values for fly ashes on heavy metals. The limits must meet the requirements of the Principles for the Assessment of the Effects of Construction Products on Soil and Groundwater in the currently valid version with regard to environmental compatibility. [7]

Table 4 Permissible heavy metal content on volatility of Construction Products on Soil and Groundwater ashes according to German Institute for Structural Engineering [7]

Element [mg/kg TS]		Limit values [mg/kg TS]	Analysis procedure
	Symbol		
Cadmium	Cd	10	DIN EN ISO 5961, DIN EN ISO 11885
Copper	Cu	600	DIN 38406-7, DIN EN ISO 11885
Nickel	Ni	600	DIN 38406-11, DIN EN SO 11885
Mercury	Hg	10	DIN EN 1483
Zinc	Zn	1500	DIN 38406-8, DIN EN ISO 11885

Table 5 Heavy metal content in investigated wood and fly ashes. [own research results].

Element [mg/kg TS]		Wood Ashes				Fly Ashes
	Symbol	1	2	3	4	
Antimony	Sb	<1	52	< 1	6,0	3,0
Arsenic	As	3,0	149	3,7	14,7	31,3
Cadmium	Cd	16,0	36,2	16,7	4,7	1,2
Copper	Cu	298,0	321,0	160,0	172,0	35,0
Molybdenum	Mo	< 2,0	34,0	8,0	6,0	36,0
Nickel	Ni	47,0	34,0	67,0	35,0	43,0
Mercury	Hg	< 0,07	0,43	< 0,07	< 0,07	0,10
Selenium	Se	< 1,0	9,0	< 1,0	1,0	14,0
Thallium	Tl	< 0,2	6,9	0,8	< 0,2	1,6
Zinc	Zn	1840	8970	666,0	722,0	118,0

A detailed analysis was carried out for fly ashes and the same for all wood ashes types as in table 3. The results are listed in Table 5. There are currently no requirements for heavy metals in wood ashes in concrete, so they will be compared to fly ashes.

As can be seen from the analysis, the amounts of zinc and copper in wood ashes differ significantly from the values for fly ashes. In the next investigations will be the influence of heavy metals on the concrete properties of hardened concrete determined. Since the pH-value of the concrete must remain alkaline to ensure corrosion protection of the steel, a few mixtures were made for each type of wood ashes and the pH-values of the fresh and hardened concrete were investigated. In both fresh and hardened concrete, all the values showed alkaline environment. The result is clear, the wood ashes despite increased amounts of heavy metals does not lower the pH of the concrete.



Fig. 3 Determination of the pH value on hardened concrete with the wood ashes No. 2, Table 5. Phenolphthalein as Indicator [own research results].

3. Economic aspects and goals

Survey was carried out with many construction companies and this confirmed that companies have a great interest in this material. A positive signal comes from the industry. First investigations and results which have been done, showed, that there is a huge potential in the wood ashes from electric and cyclone filter. But there's still so much to do. The replacement of at least 20 % of the amount of cement in every cubic meter of concrete with other components like wood ashes and at the same time maintain the strength of the concrete, will be an enormous successes worldwide. The cement plants can't be closed, they can only produce less cement and therefore the CO₂ emission is possible to decrease. This is the most simple, feasible and rational solution.

4 References

- [1] Lutze, vom Berg, Handbook fly ash in concrete: basics of production and use, 2009.
- [2] Cement paperback, HeidelbergCement, German Cement Industry 2017
- [3] Economic association mineral by-products e.V., "Economic association mineral by-products e.V.," September 2016. (online)
- [4] S. Achenbach, Aspects of high-quality cooperative disposal of wood ashes, 2019
- [5] R. Hüttl, "The mechanism of action of hard coal fly ash as a concrete additive," Technical University Berlin, Berlin, 2000.
- [6] J. Harder, „Trends in process filters in the cement industry,“ ZKG International, 2009
- [7] General building inspectorate approval, German Institute for Building Technology, 2015

Structural analysis and design

ADVANCED ANALYSIS OF THE BEHAVIOR OF A REINFORCED CONCRETE STRUCTURE WITH GF + 8F HEIGHT REGIME

-COMPARATIVE STUDY -

HAUȘI SORIN BOGDAN, ZAHARIA GELU MUGUREL, NECHITA OVIDIU PAUL

North Centre, Baia Mare

Technical University of Cluj Napoca

Street. Dr. Victor Babeș, Baia Mare 430083, Maramureș, Romania

Abstract

The purpose of this paper is to perform an advanced comparative analysis between a structure of reinforced concrete frames, a structure made of cast in site concrete, respectively in the version of precast concrete. Following the analysis, it is desired to observe the plasticization phenomenon of the frame node made in the two constructive variants, respectively, an analysis of the rigidities. The study of the node plasticization phenomenon, respectively the rigidity analysis, will be performed by a nonlinear analysis, by simulating the beam-column node with finite elements of "3d-solid" type with the help of a specialized finite element analysis computer software.

Key words: plastic articulation, mechanical beam-column joints, ductility, earthquake resistance, rigid knots, nonlinear numerical analysis.

1. Paper overview

For the case study, it is proposed to analyse a structure of reinforced concrete frames office building, with the ground floor plus 8 floors height regime. The proposed building has a regular shape in plan and elevation, with 3 span of 6 m transversely and 3 bspan of 6 m longitudinally. The total height of the structure is 36.80 m.

The construction is located in a seismic area, with the peak ground acceleration $p_{ga} = 0.25g$.

The structure analysis will be done for two variants of a technical solution, the first one being a structure of monolithic reinforced concrete frames, and the second one being a structure of prefabricated reinforced concrete frames. For the joints between the linear prefabricated elements as of beam-column type, column-column respectively, it is proposed a mechanical joints on site with high strength bolts, so as to finally obtain rigid nodes, equivalent in behavior with the concrete nodes of monolithic structures.

The modeling and nonlinear analysis of the frame node is performed using a specialized computer software. The final analysis model results from the use of 3D elements, defined as "Deformable" type elements and as "Solid" type elements in the case of concrete and metal plates, as "Wire" type elements in the case of reinforcement rods and stirrups respectively. For the correct application of the concentrated load, at the end of the beam section, the option "Rigid Body" was used to link the point of application of the force to the beam section and thus avoid the occurrence of stress concentrations and the premature failure of the beam. The applied force is of the "Concentrated force" type defined as "Amplitude".

The connection between the reinforcement bars and the concrete is made using the "Embedded region" option, the connection between the prefabricated elements and the embedded metal plates is made using the "Tie" option, a connection that does not allow relative slips and rotations between the connected surfaces. Between the beam and the prefabricated column, where we have only contact, the option "Surface-to-surface contact (Standard)" is used.

The reinforcement used for the models is B500C, and the concrete class C25/30. The reinforcement of the elements will be done according to the following details:

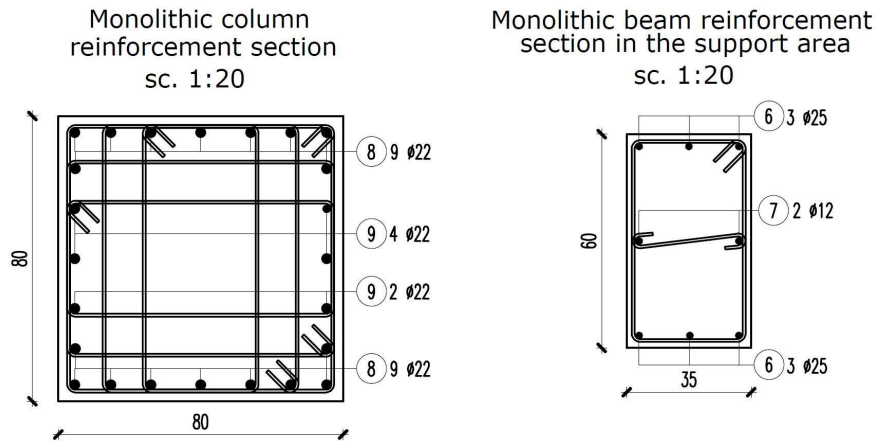


Figure: 1.a – Column and beam reinforcement section monolite variant

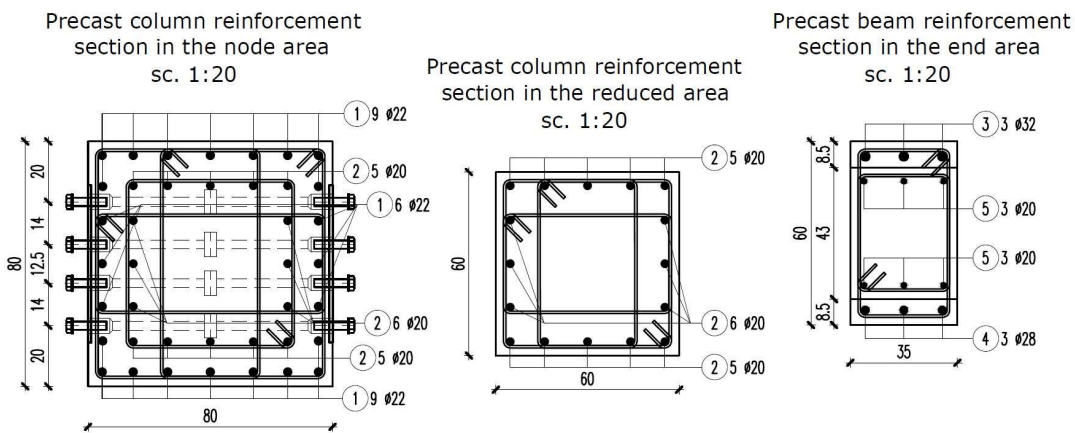


Figure: 1.b – Column and beam reinforcement section precast variant

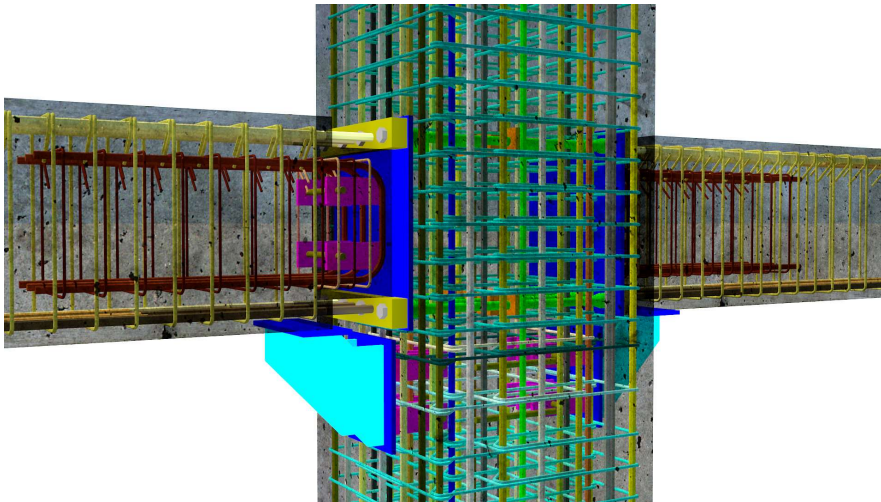


Figure: 1.c – 3D view of the reinforcement prefabricated node

The analysed frame nodes were considered as central nodes, located at the base of the structure at an elevation of + 4.50 m. The following pictures show schematically the analysed specimens, respectively the static scheme and the way in which the loads are applied.

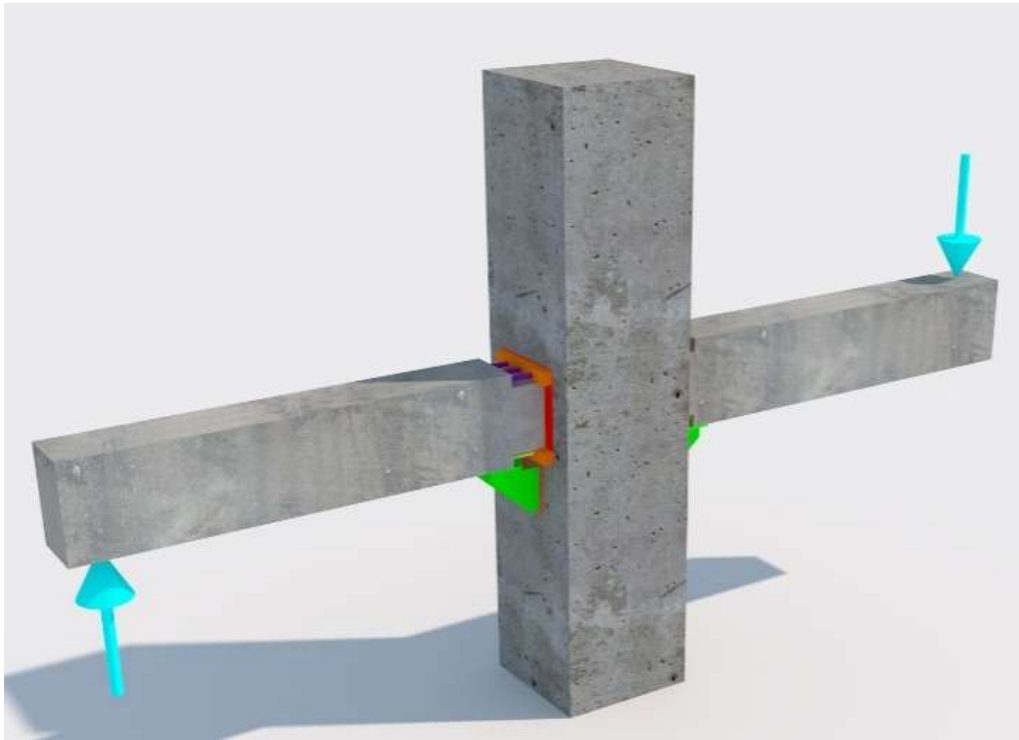


Figure: 1.d – 3D view of the proposed nodes for analysis



Figure: 1.e – 3D view of the proposed nodes for analysis

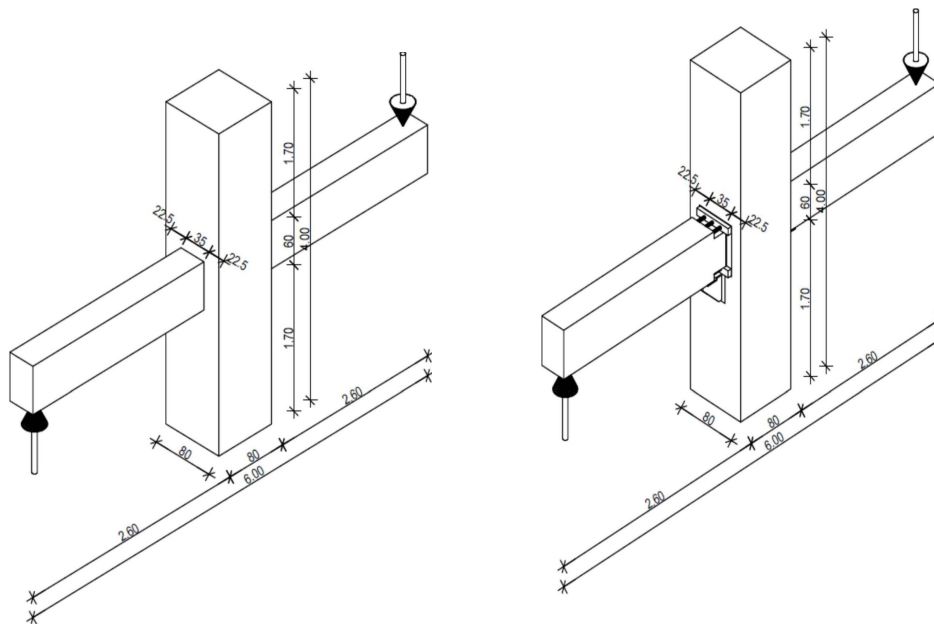


Figure: 2 – Technical details of the analysed specimens

According to the figures above, for the analysis of specimens, the static scheme is considered as follows: at the base of the column and at the top, the fixation is pinned type, meaning the translations are blocked and the rotations in the node plane are unblocked.

The application of the loads is done by forced movements at the top of the console, the loading regime is an alternating cyclic one. The application of the alternating loads will be done according to the graph below.

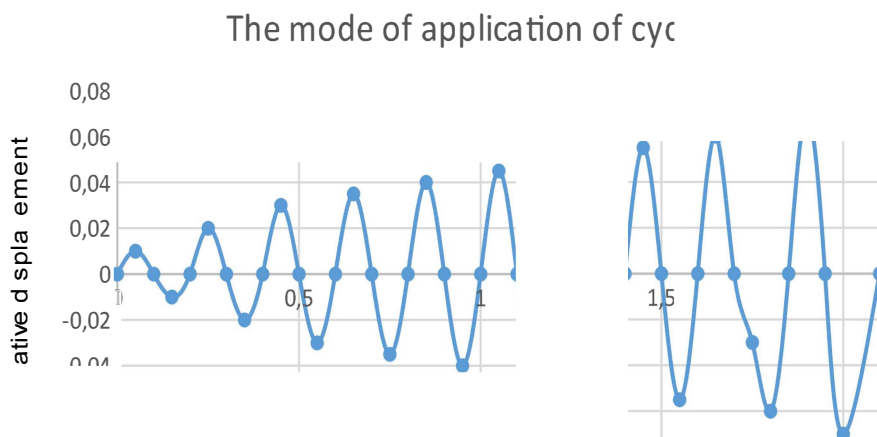


Figure 3: - The mode of application of the loads

The reason for modeling and analysing a monolithic node or a prefabricated node is to have a benchmark against which to make a comparison of the structural performance of the two systems, as a standard and for which there are specifications and clear calculation rules.

For the analysis of the nodes it is necessary to discretize the component elements into finite elements. On the mesh images of the elements it can be seen that near the contact area between the prefabricated beam and the prefabricated pillar, respectively for all the embedded metal elements, there is a dense network that has the role of making the correct connection between the different sections and materials that make up the calculation model. Due to the high level of complexity of the modelled assemblies, especially in the case of the prefabricated node, the mesh for the concrete elements is 50x50mm in size, to reduce the analysis time.

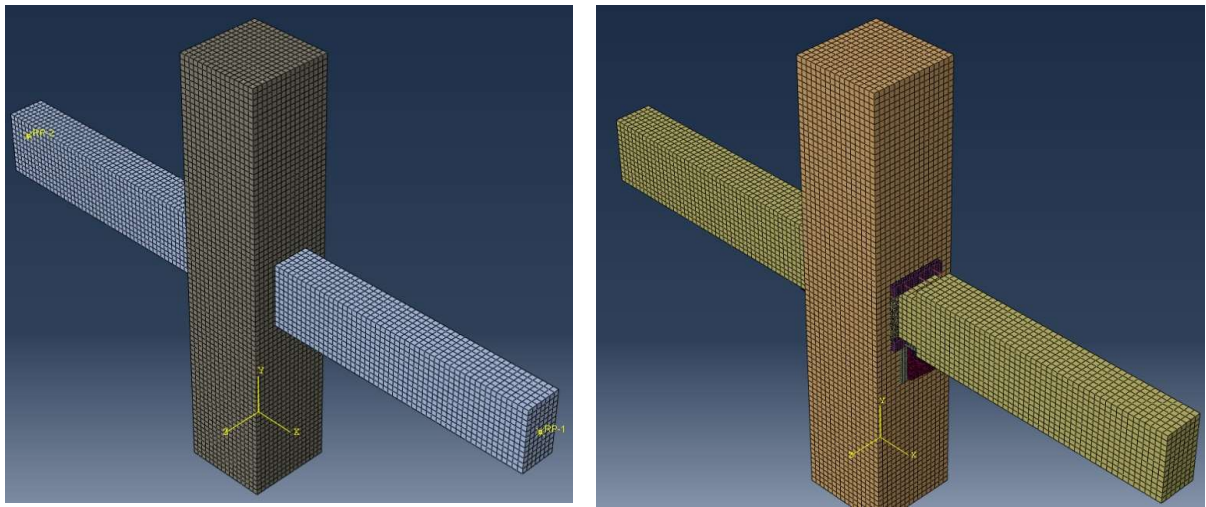


Figure: 4 - Spatial view of the frame nodes analysed with the corresponding mesh of each element

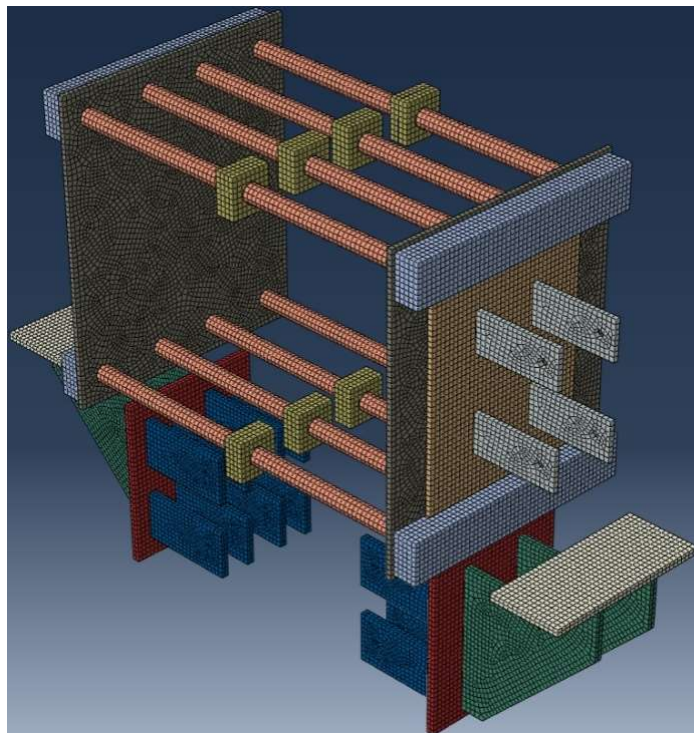


Figure: 5.b - Spatial view of the metal elements embedded with the mesh for each element

Below are some suggestive images in which the state of tensions can be seen, both for the concrete elements and for the metal parts embedded in the concrete or for the steel-concrete bars, as a result of the cyclic stresses to which the specimens are subjected.

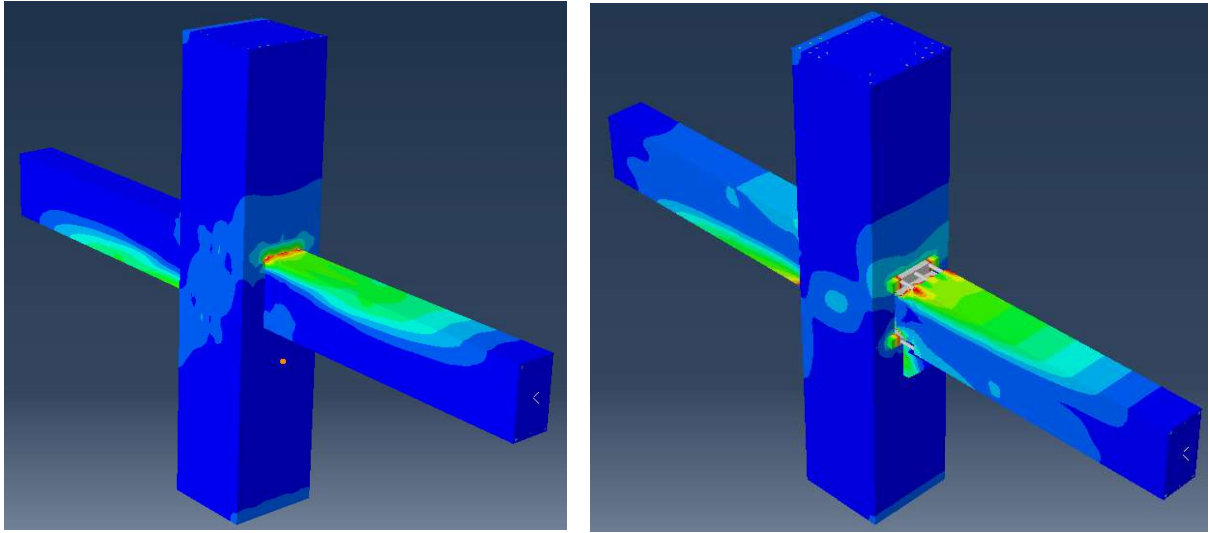


Figure: 6 - Spatial view with the state of tension after applying the stress

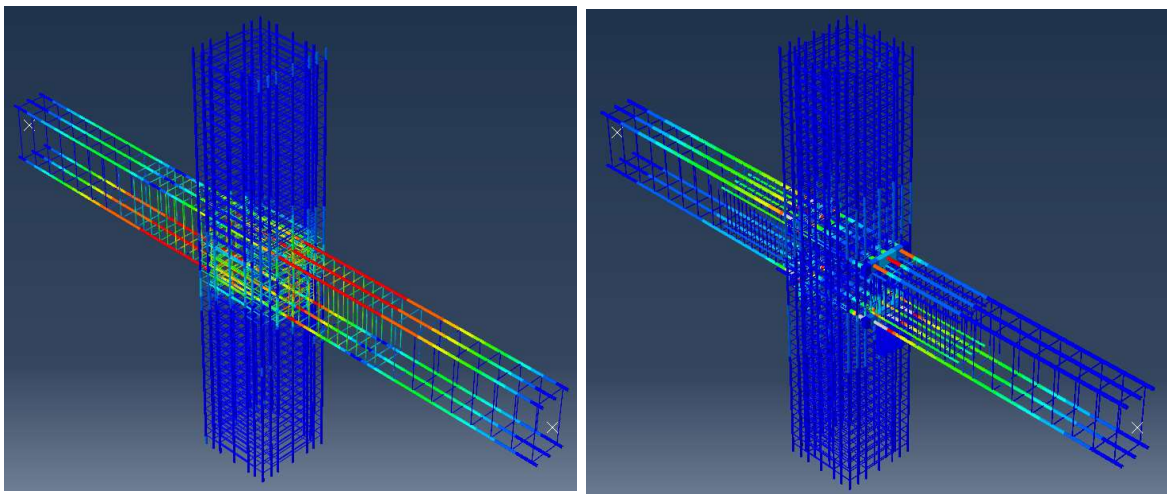


Figure: 7 - Spatial view with the state of tension in the reinforcement bars after applying the stress

The result obtained from the numerical analysis, for the precast model, regarding the absolute displacement at the top and the horizontal level force can be seen in the following graphs.

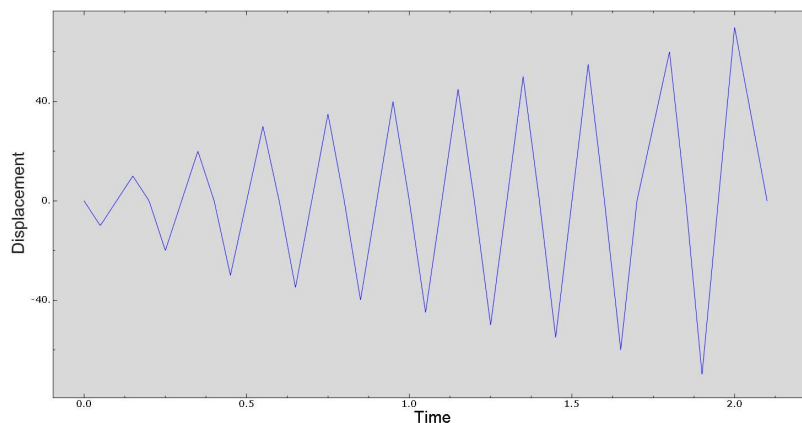


Figure: 8 – Absolute displacement variation

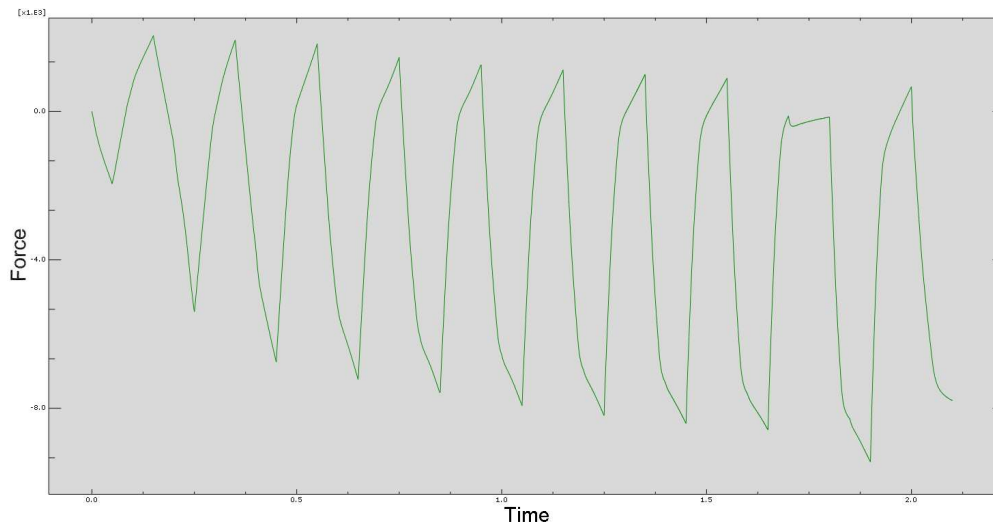


Figure: 9 – Horizontal level force variation

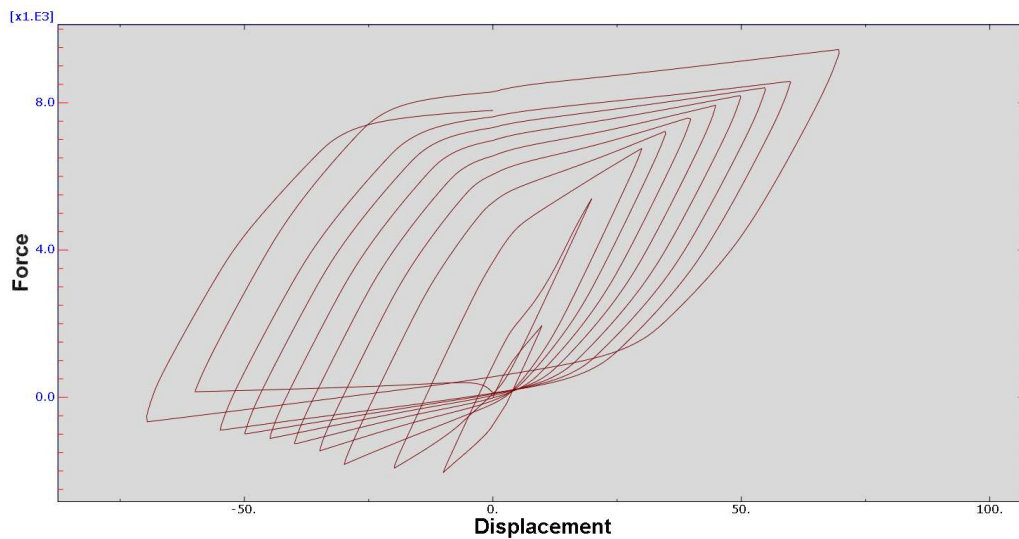


Figure: 10 – Displacement force curve for the column-beam node under cyclic loading

2. Conclusions

Following the numerical analysis, it can be seen that the models show quite accurately the behavior of the node subjected to a cyclic load and estimate correctly enough the limit load of the beam.

In the case of the prefabricated node, stress concentrations, in particular compression, are observed at the interface between the beam and the column or at the interface between the beam and that metal console. These concentrations are also the reason why it was proposed to place those metal consoles embedded on the end of the beam and at the front of the column on the contact area between the two elements.

The prefabricated node has a load-bearing capacity and a rotational capacity similar to that of the monolithic node, which is also the standard against which the comparison is made in terms of the behavior of the prefabricated node.

As can be seen from the analysis of the hysteresis curves, the cyclic response of the node is quite stable, which allows a large number of dissipative cycles before the loss of load-bearing capacity.

This article presents in particular the results obtained for the precast node, referring to the monolithic node. Following that in the future a comparison will be made between the results obtained for the precast node and the cast in site node. The analysis of the two constructive variants of structure in reinforced concrete frames is only at the beginning.

References

- [1] Panțel, Eugen, and Bia, Cornel., 2009. *Metoda elementelor finite pentru structuri de rezistență*. Cluj-Napoca: Editura Todesco.
- [2] Bia, Cornel, V., Ilie, and M.V., Soare., 1983. *Rezistența materialelor și teoria elasticității*, București: Editura Didactică și pedagogică.
- [3] Robert E. Englekirk, 2003. *Seismic design of reinforced and precast concrete buildings*.
- [4] Constantin C. Mihai, Vasile H. Hobjiță, Nicu S. Mihalache, 1996 *Noduri grindă-stîlp pentru structuri de beton armat*, Editura Tehnică București.
- [5] *fib Bulletin 78 (2016), Precast-concrete buildings în seismic areas. Fédération internationale du béton, Lausanne, Switzerland.*
- [6] SAFECAST (2012b), *Performance of innovative mechanical connections în precast building structures under seismic conditions, FP7 Project No. 218417*
- [7] SAFECAST (2012c), *Performance of innovative mechanical connections în precast building structures under seismic conditions, FP7 Project No. 218417, 2.4 Experimental behavior of new/improved connections.*
- [8] COD DE PROIECTARE SEISMICĂ – PARTEA I – PREVEDERI DE PROIECTARE PENTRU CLĂDIRI – INDICATIV P100-1/2013.

Bond behavior between high-strength concrete and steel reinforcement under high cycle fatigue push-in loading

Homam Spartali, Abedulgader Baktheer, Benjamin Camps, Josef Hegger, Rostislav Chudoba

*Institute of Structural Concrete,
RWTH Aachen University,
Mies-van-der-Rohe-Straße 1, 52074 Aachen, Germany*

Abstract

In the last decades, an increasing demand for renewable energy has been stimulating the development of more fatigue resistant wind turbines that can be exposed to millions of load cycles. Bond degradation caused by this high number of load cycles needs to be examined to guarantee the durability and safety of these structures. In this paper, experimental investigations of the bond behavior between high-strength concrete and steel reinforcement under monotonic and high-cycle fatigue loading are presented. In contrast to the pull-out test prevailing in literature, here a push-in compressive loading is applied. Therefore, a modified beam-end test specimen is used. Bond length, concrete strength as well as bar diameter are varied in the presented test program that consisted of 44 beam-end test specimens. The bond strength obtained from the push-in tests for bond length 2.5ds is comparable with the pull-out bond strength values. The results provide the basis for a detailed analysis of the effect of the splitting cracks on the growth of slip in the fatigue tests. Push-through and combined push-through \times splitting failure modes have been observed in the experimental program.

1 Introduction

The subject of bond fatigue in reinforced concrete structures has been attracting more attention in recent decades. This is because of the desire to utilize high-strength concrete in building resource-efficient, lightweight, high-strength and durable structures that are exposed to millions of load cycles such as wind turbines. At the same time, sufficiently sound description of the behavior of bond between high-strength concrete and steel reinforcement under fatigue loading is still missing in the literature.

One of the most prominent research efforts in this field is the test program carried out by [1]. A total number of 308 cylindrical pull-out specimens were tested with cyclic loading up to 1 million load cycles and with varied concrete strength up to cubic compression strength of 48 MPa. Other bond repeated loading tests were performed by [2], [3], [4]. Recent studies were performed also in [5], [6], [7]. Investigations focusing on the effect of the transverse tension on the bond behavior under cyclic loading have been reported by [8], [9].

All these studies used the normal-strength concrete matrix with compressive strength of up to 60 MPa. The behavior of bond between high-strength concrete and steel reinforcement under monotonic loading were studied experimentally by many authors e.g. [10], [11], [12], [13]. However, scarce research has been conducted for the case of cyclic loading. Moreover, to the knowledge of the authors no bond strength studies have been conducted elsewhere using a push-in test setup with high-cycle compressive loading. Therefore, it was necessary to characterize the bond between high-strength concrete and steel reinforcement under these loading and setup conditions.

2 Experimental program

2.1 Material properties

2.1.1 Concrete

Two different high-strength concrete classes were used in the tests. According to EuroCode 2 [14], these are the C80/95 and C100/115. However, in this paper they will be referred to as C80 and C120, respectively, depending on a convention among the partners of the collaborative research project

WinConFat focused on the fatigue behavior of wind turbine towers. The properties of the concrete mixtures for the two concrete types are summarized in Table 1. Batches with up to 9 beam-end specimens were casted at once to ensure similar concrete properties. In addition, material tests were performed with each batch to evaluate the development of the compressive strength and the Young's modulus along the period of experimenting. For that purpose, cylinders with a diameter of 150 mm and a height of 300 mm and cubes with an edge length of 150 mm were produced according to [15] and were stored in the laboratory with similar conditions to the beam-end specimens.

The average of the tested cylindrical compressive strength after 28 days was 84.2 MPa and 107 MPa for concrete C80 and C120, respectively. The average of Young's Modulus for concrete C80 was 37827.9 MPa and a value of 50033.6 MPa was obtained for concrete C120.

Table 1 Properties of the used concrete.

Concrete grade	Cement	W/C	Aggregate type	Maximum grain size
C80	CEM I 52,5 R	0,47	50% limestone, 50% quartz	16 mm
C120	CEM I 52,5 R	0,35	quartz	16 mm

2.1.2 Steel

Hot rolled highly ductile deformed bars of the class B500B [16] with yield strength $f_y = 500$ MPa and two different bar diameters of 16 mm and 25 mm were used. The steel bars are shown in Fig. 1.



Fig. 1 Steel bars used in the tests

2.2 Test set-up

The most common test setup for characterization of the bond behavior is the RILEM pull-out test [17]. In this test, a steel rebar is centrally positioned in a cubic concrete specimen and is exposed to the pull-out load. However, the results obtained from this test lead to overestimated bond strength because of the compressive stresses around the bond zone which originate from reaction forces on the supported surface of the cube. Moreover, the effect of splitting cracks along the bonded zone cannot be studied due to the inevitably large concrete cover. Another, more recent standardized test method for bond strength characterization is provided by the ASTM beam-end test [18]. The placement of supports and loading in this method corresponds better with the stress state in the tensile reinforcement of a RC beam and eliminates the undesired compressive stresses along the bond zone Fig.2.

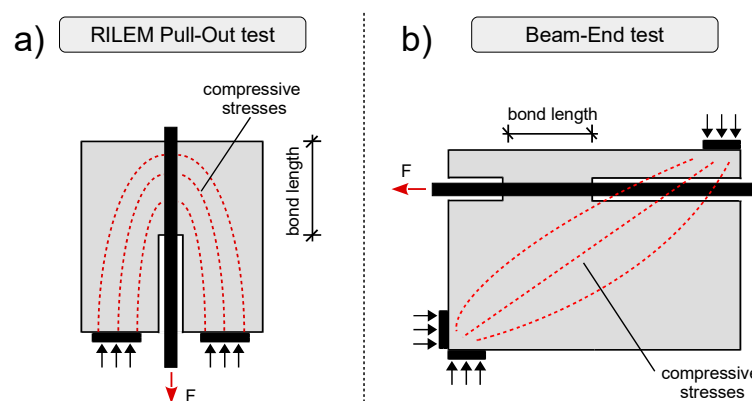


Fig. 2 Comparison of compressive stresses flow between beam-end test and RILEM test

It is to be mentioned that the bond behavior of rebars under compressive loading in RC elements accompanies an additional resistance mechanism stemming from the concrete cone breakout initiated at the tip of the rebar under compression. The full representation for this combined behaviour is not in the scope of the current test program which is primarily focused on bond behavior under the push-in condition.

For the reasons mentioned above, the beam-end test was chosen for the bond experiments presented here. However, multiple modifications have been conducted on the standard test specimen. First, the dimensions of the specimen were selected to be relative to bar diameter d_s ($L \times W \times H = 20 d_s \times 8 d_s \times 14 d_s$) according to [9] in order to have comparable specimens for the two different diameters Fig. 3 (a). Second, due to the push-in loading that should be applied, a wide recess was introduced to reduce the length of the bar in the loaded end zone, and hence to avoid buckling of the steel bar with. At the same time, the flow of compressive stresses was kept outside of the studied bond zone Fig. 2. Third, to have a realistic bond behavior similar to practical situations and to restrict splitting cracks, two stirrups were used along the bonded length for the tests with $2.5 d_s$ bond length and four were used for tests with bond length of $5 d_s$. Finally, three longitudinal bars were arranged on each side of the specimen to restrict the transversal cracks emerging due to the introduced recess Fig. 3 (b).

Two LVDTs (Linear variable differential transformers) were used to record the slip on the loaded and unloaded ends of the steel bar. In addition, one LVDT was mounted on the specimen surface over the bond zone to record the width of the longitudinal crack (splitting crack) along the bond and another one was mounted on the side of the specimen to record the width of the transversal crack Fig. 3 (b).

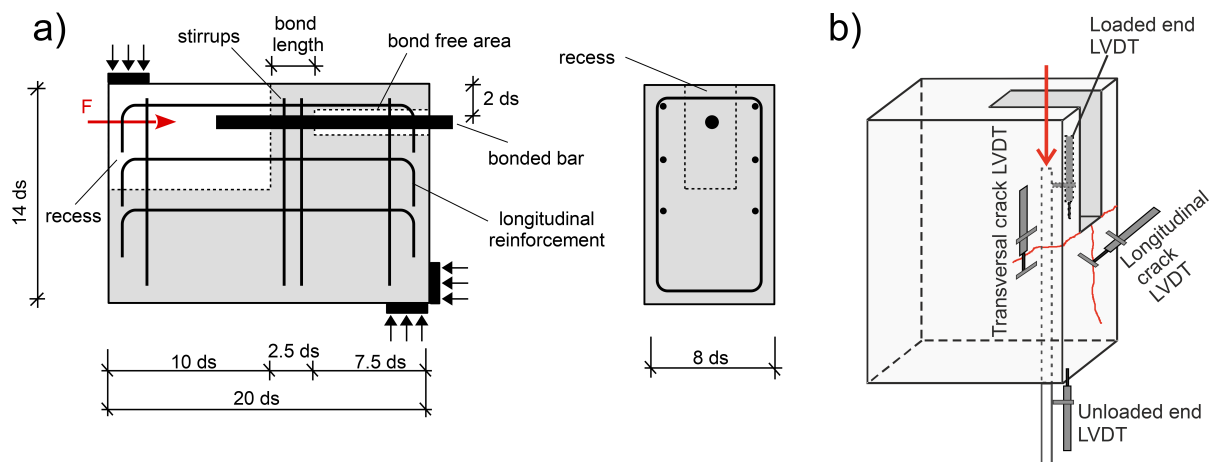


Fig. 3 a) Sketch of the modified beam-end specimen with the dimensions and reinforcement details; b) the setup of the 4 LVDTs with cracks positions

2.3 Loading scenarios

For the monotonic tests, a displacement-controlled loading with a rate of 1.0 mm/min was applied until reaching a predefined displacement at the unloaded end (8 to 12 mm). The value of the ultimate push-in load F_u obtained from the monotonic test was then used to define the limit values for the fatigue tests which were force-controlled. The cyclic tests were applied with a constant lower and upper load levels until fatigue failure. Loading frequency of 5 Hz or 10 Hz was used with upper load levels ranging between $S_{\max} = 0.7$ and $S_{\max} = 0.85$ and lower load levels between $S_{\min} = 0.2$ and $S_{\min} = 0.4$. If 10 million cycles were reached without having a fatigue failure, the specimen was loaded monotonically until failure.

3 Experimental results and discussion

3.1 Monotonic tests

In total, 29 monotonic tests were conducted in this test program. A summary of the results of these tests with statistical evaluation is presented in Table. 3. The observed failure mode for all monotonic tests can be classified as a push-through \times splitting failure mode.

The average of the ultimate push-in force for each set of tests is provided in addition to the respective bond strength supposing a constant stress distribution along the bond zone. The coefficient of variation (CoV) demonstrates the scattering of the ultimate force values. By comparing the CoV for C80 tests with a diameter of 16 mm and bond of 2.5 ds with the bond length 5 ds, it is to be noticed that the scatter of results is larger for shorter bond lengths from the same bar diameter. Also, the results of the C80 concrete show larger scatter in comparison with the values of the concrete C120.

The emergence of the splitting crack is vital for the interpretation of the failure process as it signifies the transition from a bond resistance mechanism controlled by the adhesion, mechanical friction and interlocking between steel ribs and concrete to a more complex tri-axial mechanism affected by the thickness of the concrete cover and the hoop stresses evolving around the bond zone. The force F_{crack} corresponding to the initialization of the splitting crack is provided in Table. 3 in addition to the ratio F_{crack}/F_u . The slip measured at the unloaded end when the ultimate force F_u is reached is also provided and denoted as $w(F_u)$.

Table 3 Results and statistical evaluation of the monotonic tests (LS1).

Tests	Concrete	ds [mm]	Lb	Num. tests	F_u [kN]	τ_u [MPa]	CoV [%]	F_{crack} [kN]	F_{crack}/F_u	$w(F_u)$ [mm]
T1 to T9	C80	16	2.5 ds	9	58.69	29.19	11.0	52.94	0.90	0.215
T10 to T15		16	5 ds	6	95.22	23.68	6.7	76.58	0.80	0.314
T16 to T19		25	2.5 ds	4	116.24	25.82	8.6	95.39	0.82	0.542
T28 to T33	C120	16	2.5 ds	6	72.30	35.96	5.2	67.18	0.93	0.202
T34 to T37		25	2.5 ds	4	167.58	34.14	7.2	158.95	0.95	0.157

The load-displacement curves measured at the loaded and unloaded ends are plotted in Figs. 4(a-c) for five different tests including all the investigated parameter combinations. The curves show a good match between the loaded and unloaded end response curves. Therefore, our assumption of a constant stress distribution in bond zone is valid and the measurements of the unloaded end will be adapted for all subsequent graphs in the paper. It is to be mentioned that despite the multiple precautions to avoid bar buckling in the force introduction zone, a small bending has occurred in some tests causing negative LVDT values at the pre-peak branch of the loaded end curves as shown in Fig. 4(a).

The push-in curves of the unloaded end for all monotonic tests are provided in Figs. 4(d-f). The development of the splitting cracks is illustrated in terms of slip versus crack width curves, plotted together with the corresponding push-in curves up to the slip level of 2 mm Figs. 4(g-i). These diagrams demonstrate the degradation of bond stiffness after the initiation of the splitting crack. This state is marked by an unfilled circle corresponding to the force F_{crack} . The force continues increasing with the reduced bond stiffness up to the ultimate value F_u , followed by the deterioration of the bond resistance with a rapid growth of the splitting crack opening until the termination of the experiment.

According to the FIB Model Code 2010[19], the bond strength of normal-strength concrete with pull-out failure can be calculated as a function of the concrete compressive strength as

$$\tau_u = 2.5 \cdot \sqrt{f_{cm, cyl}} \quad (1)$$

where $f_{cm, cyl}$ is the cylindrical compressive strength of concrete. Another, more complex expression for $\tau_{u, split}$ was also given in [19], which takes the confining conditions and the effect of concrete cover into account. For the case of high-strength concrete a formula was proposed in [20] as

$$\tau_u = 0.45 \cdot f_{cm, cyl} \quad (2)$$

In Fig. 5(a), each measured value of bond strength is plotted against the corresponding cylindrical concrete strength obtained from the accompanying material tests. For comparison, the graphs from

Model Code 2010 and [20] are also displayed. The results show that the formulas in the Model Code underestimate the bond strength values. For the constraining level and the configuration that we used in this test campaign, a ratio of 0.32 is obtained between the bond strength and the cylindrical concrete strength i.e. $\tau_u = 0.32 \cdot f_{cm, cyl}$. The bond strength values normalized w.r.t. the concrete strength are shown in Fig. 5(b). The effect of rebar diameter on the bond strength is represented in Fig. 5(c). The values suggest that larger bar diameters lead to smaller effective bond strengths.

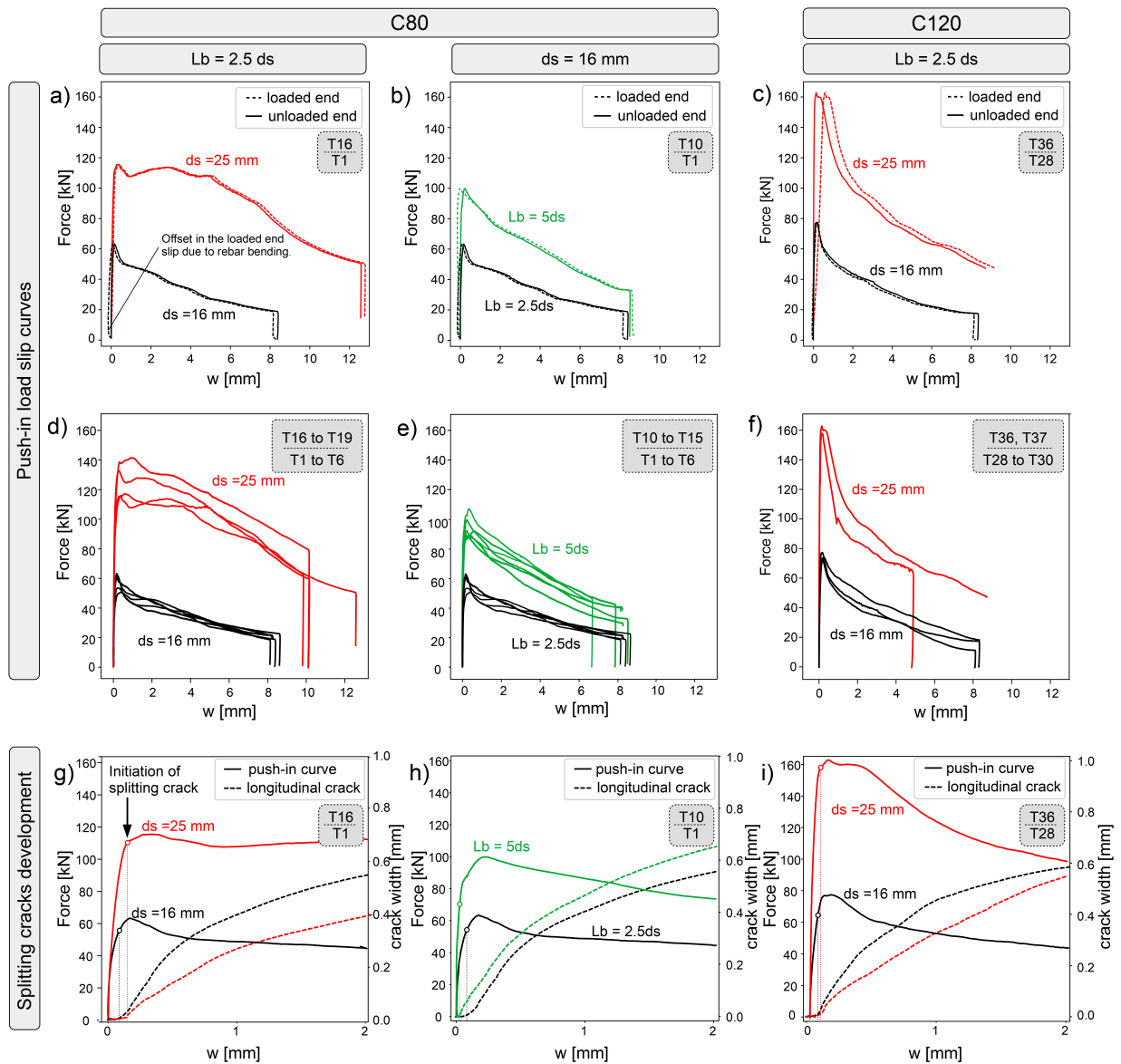


Fig. 4 Results of the monotonic tests; a-c) push-in curves for loaded and unloaded ends; d-f) push-in curves on the unloaded end for all monotonic tests; g-i) development of splitting cracks.

3.2 Fatigue tests

The total number of obtained cycles for each fatigue test is summarized in Table 3 together with the observed failure modes and upper and lower loading levels S_{max} and S_{min} . The tests T26 and T27 were terminated after achieving more than 10 million cycles without failure. In contrast to the push-through \times splitting failure mode, a pure push-through mode means that no splitting crack developed in the respective specimen. A pure splitting failure is not relevant here as this type of failure implies that no confining reinforcement were used. However, in our case two stirrups were used in the bond zone of every test to restrict the growth of the splitting cracks as mentioned earlier Fig. 3.

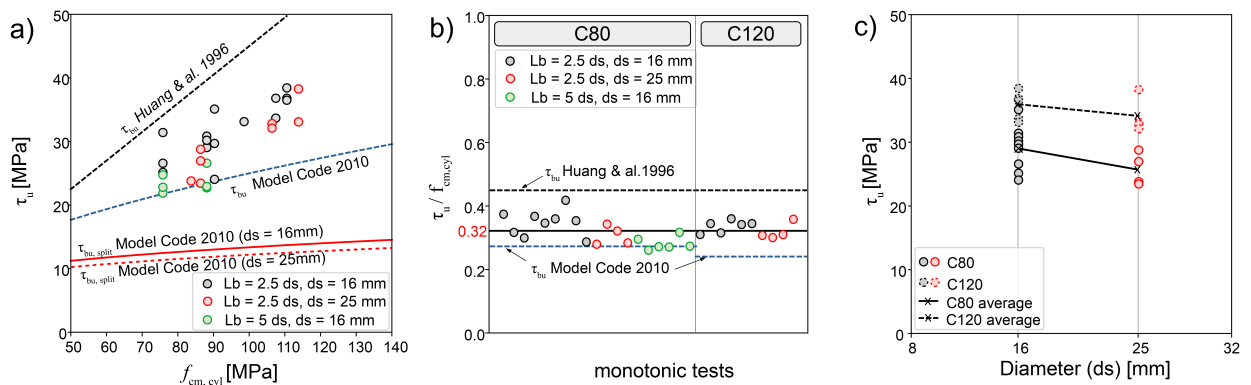


Fig. 5 Comparisons for bond strength values obtained in the monotonic tests; a) effect of the concrete grade on the bond strength; b) normalized bond strength with respect to the concrete compressive strength; c) effect of the rebar diameter on the bond strength

Table 3 Summary of the fatigue tests (Lb = 2.5 ds).

Tests	Concrete	ds [mm]	S_{max}	S_{min}	Cycles Number	Failure mode
T20 / T21	C80	16	0.8	0.4	20,388/8,345	push-through × splitting
T22 / T23		16	0.75	0.4	993 / 21,525	push-through × splitting
T24 / T25		16	0.7	0.4	7,254 / 23,033	push-through × splitting
T26 / T27		25	0.75	0.4	10,879,726* / 12,459,245*	no fatigue failure
T38/T39/T40	C120	16	0.75	0.2	1,185,480 / 235 / 3,147	push-through
T41/T42/T43		16	0.85	0.2	2,110 / 1,521,020 / 39,435	push-through × splitting
T44		16	0.85	0.2	245	push-through

The fatigue creep curves representing the growing push-in slip during the cyclic loading process for one test for each combination of varied parameters are illustrated in Figs. 6(a, b, d, e, g) with the corresponding splitting crack development. An accelerated slip growth is observed for cycles following the initialization of the splitting crack. The diagrams demonstrate that the higher the upper loading limit S_{max} , the earlier the splitting crack appears. Moreover, comparing the results of the concrete C120 and the concrete C80 one can conclude that the crack emerged much earlier in the C80 results for the same upper load levels. This explains the pure push-through failure of the C120 tests with an upper load limit $S_{max} = 0.75$ as in the case of Fig. 6(a) where no splitting crack has been detected.

Figs. 6(c, h) compare the fatigue lifetimes obtained from all cyclic tests with the Wöhler curves available in the literature. The scatter of the results is in the usual range observed in bond fatigue experiments. Taking into consideration the difference between our lower load level S_{min} and the lower load level of the presented Wöhler curves, these curves proposed in [1] show some overestimation of the fatigue lifetime for the tests of the concrete C80, and on the other hand, it relatively underestimates the lifetimes obtained from concrete C120.

4 Conclusions

The presented campaign of beam-end tests under push-in loading is a part of a larger campaign that includes C120, C80 and C40 concrete classes aimed at the characterization of the bond behavior between steel and concrete under high-cycle fatigue loading. Results for monotonic and fatigue tests conducted so far are introduced and discussed. As a result, following conclusions can be derived:

- The formulas for the calculation of bond strength suggested in the FIB Model Code 2010 underestimate the actual bond strength between high-strength concrete and the deformed steel rebars subjected to push-in loading. According to the configuration and confining

conditions used in this test campaign, the formula $\tau_u = 0.32 \cdot f_{cm, cyl}$ between bond strength and cylindrical concrete strength was obtained.

- The failure mode observed in the conducted beam-end tests was a combined push-through \times splitting failure in all monotonic tests and in most of the fatigue tests. However, some fatigue tests failed with a pure push-through failure without splitting cracks.
- Splitting cracks have a direct impact on the bond fatigue behavior and they accelerate the bond fatigue failure. This effect increases with the increase of the subcritical load level.

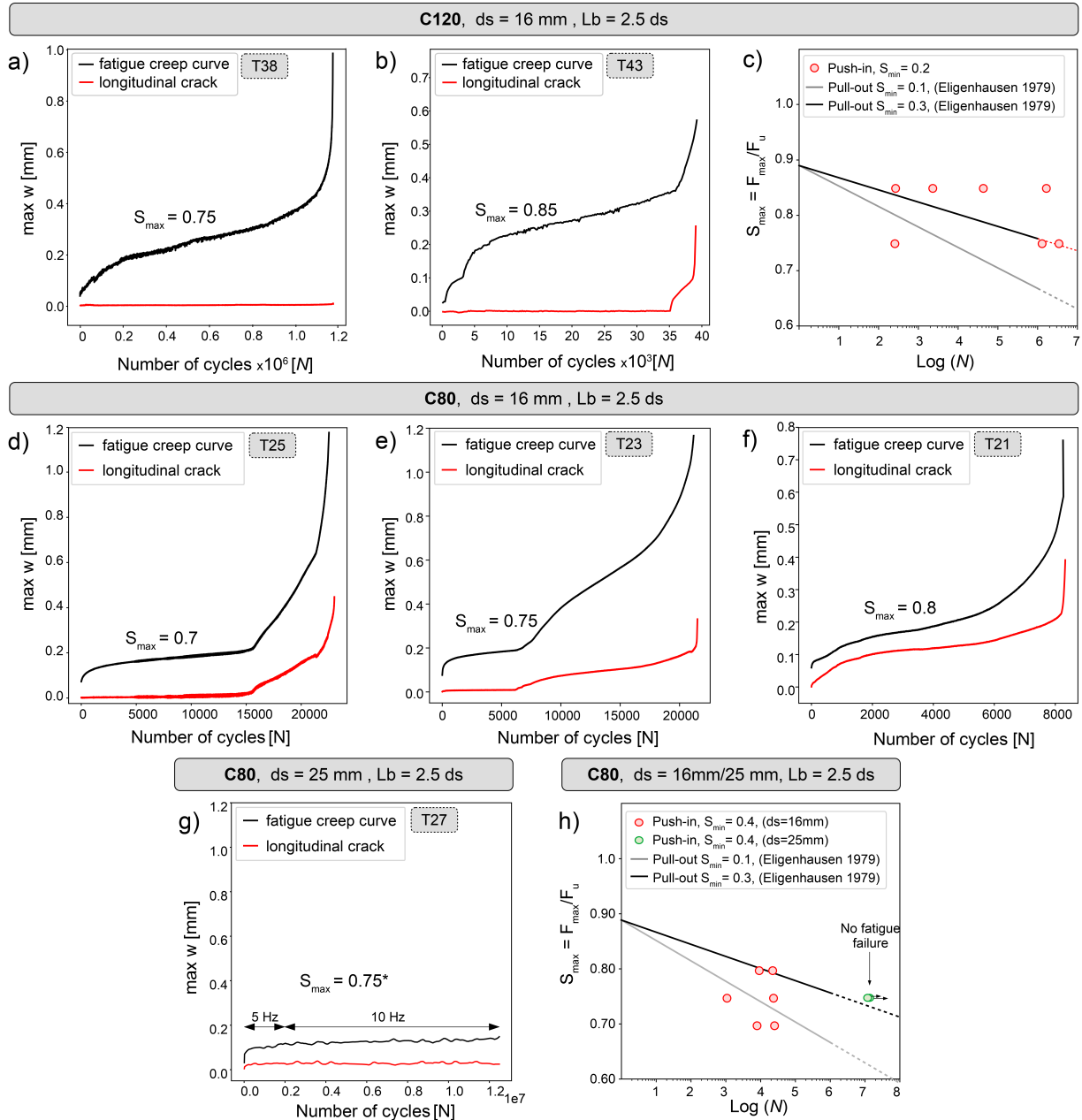


Fig. 6 Bond behavior under fatigue loading; a-b) fatigue creep curve with corresponding crack development c) comparison of the results for C120 with Wöhler curves; d-f) fatigue creep curves with corresponding crack opening evolutions g) fatigue creep curve with corresponding crack opening for C80 and diameter $d_s = 25 \text{ mm}$ with $S_{max} = 0.75$; h) comparison of C80 results with Wöhler curves

Acknowledgements

This research project is part of the collaborative research project WinConFat (0324016C2) funded by the Federal Ministry for Economic Affairs and Energy (BMWi). The authors acknowledge the support gratefully.

References

- [1] Rehm, G., Eligehausen, R. (1979). Bond of ribbed bars under high cycle repeated loads, *ACI Journal*, Vol. 76, No. 2, 297–309.
- [2] Gyorgy L. Balazs (1992). Fatigue of Bond, *ACI Materials Journal*, Vol. 88, No. 6, doi: 10.14359/1200.
- [3] Balázs, G., Koch, R. (1995). Bond characteristics under reversed cyclic loading, *Otto Graf Journal*, Vol. 6, No. 1, 47–62.
- [4] Balazs, G.L. (1998). Bond under repeated loading, *Special Publication*, Vol. 180, 125–144.
- [5] Lemcherreq, Y., Vogel, T. Experimental investigation of bond behaviour under repeated loading, In: *Proceedings of the 12th fib International PhD Symposium in Civil Engineering*, Fédération de l'Industrie du Béton (fib), 561–566.
- [6] Hu, X., Peng, G., Niu, D., Wang, J. (2019). Bond properties of deformed steel bars in concrete during construction under reversed cyclic loading, *Construction and Building Materials*, Vol. 223, 817–829.
- [7] Zhang, W., Zhang, Y., Li, H., Gu, X. (2020). Experimental Investigation of Fatigue Bond Behavior between Deformed Steel Bar and Concrete, *Cement and Concrete Composites*, 103515.
- [8] Lindorf, A., Lemnitzer, L., Curbach, M. (2009). Experimental investigations on bond behaviour of reinforced concrete under transverse tension and repeated loading, *Engineering Structures*, Vol. 31, No. 7, 1469–1476.
- [9] Lindorf, A., Curbach, M. (2011). Slip behaviour at cyclic pullout tests under transverse tension, *Construction and Building Materials*, Vol. 25, No. 8, 3617–3624.
- [10] Azizinamini, A., Stark, M., Roller, J.J., Ghosh, S.K. (1993). Bond performance of reinforcing bars embedded in high-strength concrete, *ACI Structural Journal*, Vol. 90, No. 5, 554–561.
- [11] Hegger, J., Kommer, B., Bulte, S., Sherif, A. (2005). Bond Anchorage Behavior of Pretensioned Tendons in High-Performance Concrete (HPC), *Special Publication*, Vol. 228, 495–512.
- [12] Wille, K., Naaman, A.E. (2012). Pullout Behavior of High-Strength Steel Fibers Embedded in Ultra-High-Performance Concrete, *ACI Materials Journal*, Vol. 109, No. 4.
- [13] Ganesan, N., Indira, P.V., Sabeena, M.V. (2014). Bond stress slip response of bars embedded in hybrid fibre reinforced high performance concrete, *Construction and Building Materials*, Vol. 50, 108–115.
- [14] Deutsches Institut für Normung e.V. (2010). Eurocode 2: Bemessung und Konstruktion von Stahlbeton- und Spannbetontragwerken – Teil 2: Betonbrücken – Bemessungs- und Konstruktionsregeln: Deutsche Fassung EN 1992-2:2005 + AC:2008, Beuth, Berlin, 91.010.30; 91.080.40; 93.040, DIN EN 1992-2:2010-12.
- [15] Deutsches Institut für Normung e.V. (2009). Prüfung von Festbeton - Herstellung und Lagerung von Probekörpern für Festigkeitsprüfungen: Deutsche Fassung EN 12390-2:2009, Beuth, Berlin, Vol. 91.100.30, DIN EN 12390-2:2009-08.
- [16] Deutsches Institut für Normung e.V. (2009). Betonstahl - Betonstabstahl, Beuth, Berlin, Vol. 77.140.15, DIN 488-2:2009-08.
- [17] RILEM, T.C. (1994). RC 6 Bond test for reinforcement steel. 2. Pull-out test, 1983, *RILEM recommendations for the testing and use of construction materials*, 218–220.
- [18] Standard ASTM (2010). Standard Test Method for Comparing Bond Strength of Steel Reinforcing Bars to Concrete Using Beam-End Specimens.
- [19] Fib model code for concrete structures 2010, Document Competence Center Siegmund Kästl eK, Germany, 2010. doi:10.1002/9783433604090.
- [20] Z. Huang, B. Engström, J. Magnusson, Experimental and analytical studies of the bond behaviour of deformed bars in high-strength concrete, in: 4th International Symposium on the Utilization of High Strength/High Performance Concrete, Vol. 3, 1996.

Characterization of the anisotropic tensile response of Ultra-High Performance Fibre Reinforced Cementitious Composites

Rui Valente, Aurélio Sine, Mário Pimentel and Sandra Nunes

CONSTRUCT-LABEST,
Faculty of Engineering of the University of Porto (FEUP),
R. Dr. Roberto Frias, 4200-465 Porto, Portugal

Abstract

The tensile behaviour of Ultra-High Performance Fibre Reinforced Cementitious Composites (UHP-FRC) is decisive in many structural applications. A non-destructive test method (NDT) based on the magnetic properties of the steel fibres is used to determine suitable fibre content and orientation parameters. These parameters are employed in a constitutive model providing the corresponding directional dependent tensile response, which varies throughout the structure. This information is then provided to the mechanical model of the beams used to simulate the four point bending tests (FPBT). The resulting numerical F - δ curves and crack patterns are confronted with those from experimental tests with a good match being generally attained.

1 Introduction

UHPFRC has higher compressive and tensile strengths than conventional concrete due to the more compact cementitious matrix and the presence of high-strength steel fibres. Moreover, UHPFRC has a distinct and complex tensile behaviour that is decisive in the overall structural performance. A suitable characterization of tensile behaviour leads to a better assessment of the structural performance, allowing the design of safer, sustainable and economical structures.

The linear dependency between the post-cracking tensile strength (f_{Um}) and fibre structure parameter (λ), given by Eq. (1), has been found in previous works [1].

$$\lambda = \alpha_0 \alpha_1 V_f \frac{l_f}{d_f} \quad (1)$$

This parameter, λ , reflects the influence of fibre orientation (α_0 is the fibre orientation factor), fibre efficiency (α_1 is the fibre efficiency factor), fibre content (V_f is the volumetric fibre fraction) and fibre shape (l_f and d_f are the fibre length and diameter, respectively).

More recently, studies have shown that not only f_{Um} , but also the strain at the onset of crack localization (ε_{Um}) and the limit of elasticity (f_{Ute}) depend on λ [2]. Those trends can be approximated by simplified functions, here called surrogate models, that are intended to be used for structural analysis [3].

The development of NDT based on the magnetic properties of steel fibres [4], [5] allows the estimation of fibre volume and orientation distribution required to find λ . This method is already being successfully used to study the effects of the uneven fibre distribution on the direct tensile response of the material [6]. In turn, λ determined from NDT can be used in combination with surrogate models to estimate the tensile constitutive laws. Structural analysis considering the variability of fibre volume and orientation is scarce and should be performed and validated through experimental tests.

Therefore, this work proposes the aforementioned procedures to perform structural analysis considering the anisotropic tensile behaviour of UHPFRC in order to predict the real structural response. As a result, the numerical calculation should be able to provide the structural strength and ductility for a given structural geometry and load pattern.

First, a brief insight on the tensile behavior is given which leads to the tensile constitutive laws used in the numerical analysis. Secondly, the experimental programme is described with emphasis on the NDT and the FPBT on thin plates. Then, the numerical model to simulate the FPBT is presented as well as the strategy to implement variable tensile constitutive laws throughout the plates. Finally, numerical and experimental results are presented, compared, and discussed.

2 Tensile behaviour and modelling

The limit of elasticity (f_{Ute}) is related with the onset of cracking and to a clear change in the linear shape of the stress-strain response. It usually corresponds to the matrix cracking strength but, under certain conditions, fibres can delay the propagation of microcracks resulting in the gradual loss of stiffness until the first significant bent on the tensile diagram, which defines the notional cracking strength of the composite. The f_{Utu} provided by steel fibres can be lower or higher than f_{Ute} . The first case leads to strain-softening response where fibres cannot resist the cracking load. Therefore, crack localization occurs when the first crack opens. The crack widens while the stress drops and fibres contribute to the fracture energy. When f_{Utu} is higher than the f_{Ute} , fibres can still transfer increasing tensile loads to the matrix. That leads to a series of closely spaced microcracks sequentially formed without significant stress variation. If crack localization occurs during the multicracking (or microcrack formation) stage, the material is said to be a low strain-hardening material. Otherwise, if it shows a stabilized cracking pattern while the tensile stress increases, it is said to be a large strain-hardening material.

The proposed constitutive laws (Fig. 1) are a simplified representation of the abovementioned tensile behaviours and are intended for nonlinear structural analysis using smeared crack models or continuum damage models. In the case of strain-hardening UHPFRC a bilinear stress-strain relation is adopted to describe the pre-peak behaviour. The four parameters defining this relation are the Young's Modulus (E_U), f_{Ute} , f_{Utu} , and ε_{Utu} . In the case of strain-softening UHPFRC, it is assumed a constant stress of f_{Utu} between ε_{Ute} and $\varepsilon_{deb} = w_{deb}/h_c$, where h_c is the crack bandwidth and w_{deb} is the crack opening marking onset of the pullout stage, according to model developed by Pfyf [7]. The same model was applied for the descending curve in both strain-softening and strain-hardening materials. The ultimate strain $\varepsilon_{Utu} = l_f/(2h_c)$ corresponds to an ultimate crack opening equal to half of the length of the longest fibre, l_f .

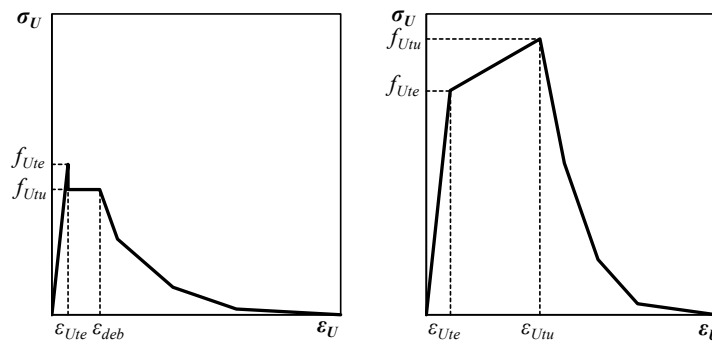


Fig. 1 General representation of material constitutive laws used for nonlinear numerical analysis: strain-softening behaviour (left); strain-hardening behaviour (right).

The tensile constitutive laws are defined through the parameters provided by the surrogate models proposed in [3] and depicted in the Fig. 2. These surrogate models allow taking into account the directionally dependent values of f_{Ute} , f_{Utu} and ε_{Utu} as a function of the directional variation of λ . Basically, the surrogate models are simple equations that reproduce the trends that are either observed experimentally through a series of uniaxial tensile tests for a wide range of λ values [8], or simulated resorting to detailed meso-mechanical models of the composite [2]. The parameters which define the surrogate models should be calibrated for a given matrix composition and geometry of the fibres.

The parameter λ_1 sets the onset of strain-hardening behaviour. For values of λ higher than λ_1 , the f_{Ute} was found to increase linearly with λ . The domain between λ_1 and λ_2 corresponds to the multicracking process translated by the fast change of ε_{Utu} for small changes of λ . The λ_0 is simply the average of λ_1 and λ_2 . The λ_2 sets the transition between the multicracking and crack saturation stage where the ε_{Utu} tends to stabilize in a constant value ε_{lim} . Up to λ_1 the stress marking the loss of linearity f_{Ute} is given by the matrix cracking strength f_{i0} . For higher values of λ , f_{Ute} varies linearly with the increase of λ . The relation of proportionality between f_{Utu} and λ is defined by the bond stress between the fibres and the matrix τ_f . The remaining model parameters, a and k , are adjusted to fit experimental observations.

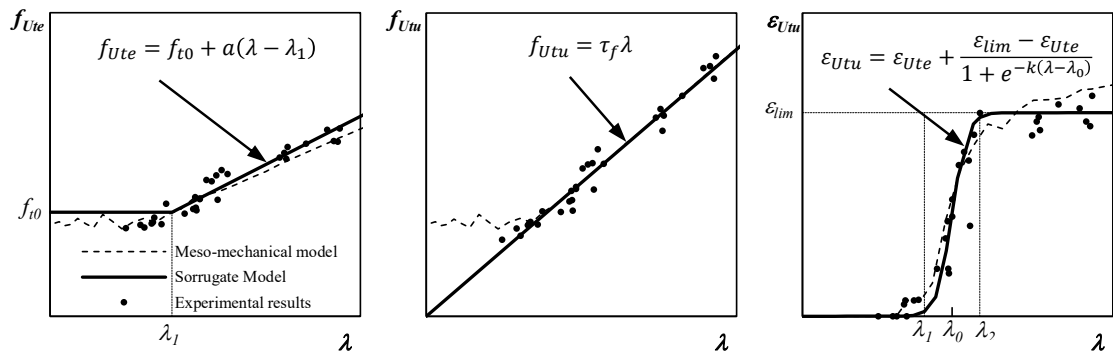


Fig. 2 Surrogate models for f_{Utu} (left), f_{Ute} (centre) and ε_{Utu} (right) as function of λ

In this case, the model parameters used in the experimental campaign are presented in the Table 1. The elasticity modulus of the composite is $E_U = 45\text{GPa}$.

Table 1 Surrogate model parameters

ε_{lim}	k	λ_1	λ_2	λ_0	τ_f	f_{i0}	a
0.47%	30	0.55	0.8	0.675	11MPa	6MPa	6.5MPa

3 Experimental Programme

3.1 Mixture Composition

The average particle size of the cement CEM I 42.5R is $14.6\mu\text{m}$. Limestone (LS) filler with $5.36\mu\text{m}$ and Silica Fume (SF) with particle size of 50 to 100 times smaller than cement particles are included. A super-plasticizer based on polycarboxylate ether is used to ensure the self-compacting properties. Steel fibres with different lengths, 9 and 12mm, were adopted. These are straight brass coated fibres with a diameter (d_f) of 0.175mm and a tensile strength of 2100MPa . The dosage of each constituent is indicated in the Table 2.

Table 2 Mixture Composition (kg/m^3)

Cement	SF	LS	Aggregate	Water	Plasticizer	Steel Fibres ($l_f=9\text{mm}$)	Steel Fibres ($l_f=12\text{mm}$)
794.90	79.49	311.43	940.99	153.76	22.20	117.75	117.75

3.2 Casting Method

The slab was casted from a constant pouring position as seen in the Fig. 3 (left). The vibrating table helped the flux of the fresh material. The tested plates were sawn from the thin slab according to the layout shown in the Fig. 3 (right). Due the viscosity of the fresh material the casting surface was rough, being difficult to ensure milimetric precision for the thickness of the plate.



Fig. 3 Casting of the thin slab (left) and the layout of the plates sawn (right)

3.3 Non Destructive Test

The surrogate models require the input of λ , which is defined in Eq. (1), so that constitutive law parameters can be obtained. The parameters related with fibres geometry, namely fibre length (l_f) and diameter (d_f), are constant and easy to characterize. Conversely, the orientation factor (α_0), efficiency factor (α_l), and fibre volumetric fraction (V_f) vary and are harder to determine. In the case of thin structural elements, both α_0 and V_f can be estimated using NDT, similar to what was done in [6].

The adopted NDT method is based on the measurement of the inductance of the magnetic circuit induced by U-shape ferrite inductor placed over the UHPFRC surface, as depicted in Fig. 4 (left). The inductance of the circuit can be correlated with magnetic permeability, μ_r , of the composite, as shown in [4]. Given that the steel fibres are the only ferromagnetic phase of the composite, it was also shown that the local V_f and α_0 can be obtained from any two orthogonal measurements of μ_r [5]. The equations adopted for obtaining V_f vary with the fibre geometry. The method provides information on the fibres located down to a depth of 40 to 50mm. Nevertheless, the structural element must be thin enough such that the variation of the fibre orientation in the thickness direction can be neglected throughout the structure. Therefore, the model might lose its validity for thicker plates.

The equation (2), suggested in [8], is used to obtain α_l directly from α_0 .

$$\alpha_l = 1.686 \cdot \sqrt{\alpha_0} - 0.406 \leq 1 \quad (2)$$

Considering the aforementioned, λ can be estimated in every intersection of the 50x50mm grid throughout the thin slab. Fig. 4 (centre) shows a coloured map representing the V_f distribution of the plate and the Fig. 4 (right) shows directions of preferential fibre orientation by means of ellipses whose geometry is based on the tensorial approximation of α_0 . On the one hand, three noncolinear inductance measurements in the same point are required to estimate a tensorial approximation of α_0 . On the other hand, two orthogonal inductance measurements are required to find V_f . For those reasons, three inductance measurements spaced out 45° were taken on every point of the 50x50mm grid.

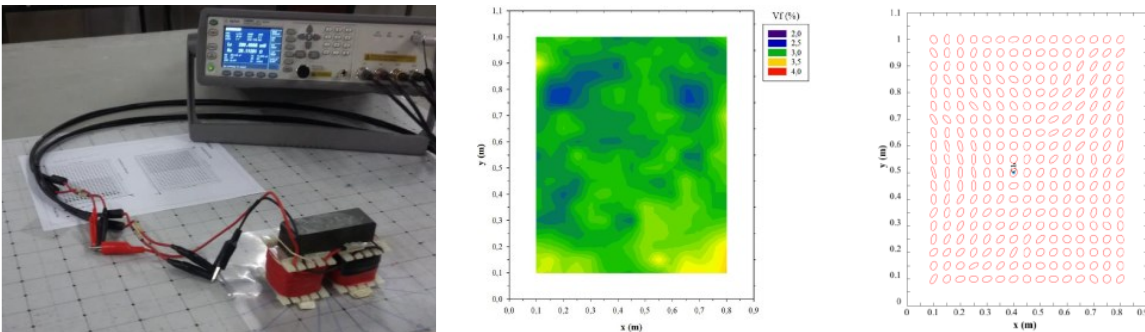


Fig. 4 LCR meter and magnetic probe (left); Colored map representing V_f (centre); Ellipse representation showing the maximum and minimum fibre orientation factors (right).

3.4 Four Point Bending Test

The Four Point Bending Test (FPBT) was carried out according to NF P 18-470 [9]. The loading and bearing systems have the necessary hinges so that the plate is in isostatic conditions in both longitudinal and transversal directions (Fig. 5). The mid span deflection (δ) is considered as being the average vertical displacement measured by the two linear variable differential transformers (LVDT) positioned at mid-span, one in each side of the plate. The LVDTs are vertically positioned at the geometric centre of the plate by means of stiff steel bars which are simply supported close to the supports and were the displacements are insignificant. The applied displacement rate was 0.25 mm/min.

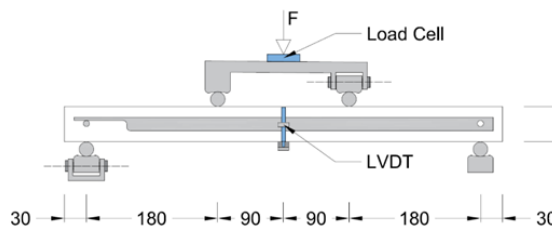


Fig. 5 Schematic representation of the Four Point Bending Test setup (mm)

A constant thickness (h) was admitted in the numerical analysis of each beam. However, due to the rough surface resulting from the casting procedure, the thickness of each beam was determined so that the elastic bending stiffness matches that from the experimental curve. In the Table 2, are presented both thickness (h) and width (b) of each plate.

Table 2 Thickness and width of the plates (mm)

Plate	1	2	3	4	5	6	7	8	9
h	30.1	30.8	31.6	32.3	32.3	34.6	31.8	33.8	33.7
b	95	98	94	97	100	93	97	98	97

4 Numerical simulations

The numerical analysis was carried out in the software *DIANA FEA 10.3* (Fig. 6). The finite element type chosen for the analysis were 1st order rectangular bricks. They comprise 8 nodes and a $2 \times 2 \times 2$ integration scheme. A total strain model with rotating cracks was adopted. The compression curve was simply modelled with linear elastic behavior because the compressed top layer of the plate does not reach the compression nonlinear stage during the analysis. The crack bandwidth (h_c) was defined according to the average distance between gaussian points in the longitudinal direction.

The constitutive laws depend on the values of λ which, in turn, varies over space and direction. Concerning the spatial variation, different blocks were created. The plan view of each block corresponds to the area of influence of each NDT measurement so that different constitutive laws could be assigned to them. Since the maximum tensile stresses occur in the longitudinal direction, transversal cracks are expected. For that reason, fibre structure parameters λ were estimated for the longitudinal direction of the plates which was then used to estimate the tensile constitutive laws. Moreover, the following properties were defined: $E_U = 45 \text{ GPa}$; $\nu = 0.2$, $\rho = 25 \text{ kN/m}^3$. Each block was discretised along their depth into 10 finite elements.

The external load was applied with distributed forces along the width of the specimen and, since it is a statically determinate system, the reaction forces were modelled the same way. Auxiliary supports were properly placed to provide stability to the analysis. The self-weight was included in the analysis despite its insignificant influence. The nonlinear analysis was performed with load control. The load increment started with 0.5kN and then it was automatically adjusted by the arch-length method (updated normal plane). The modified Newton-Raphson method with line search was used for the solution method. The convergence criterion was defined by a force norm lower than 1%. Moreover, a stop criterion was defined to interrupt the analysis when the peak load was achieved, since the post-peak is essentially influenced by the softening behavior of the composite, which is not the focus of this study.

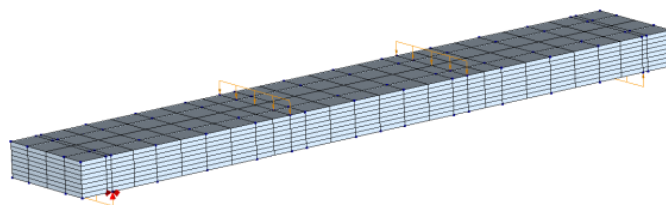


Fig. 6 Numerical model

5 Results and discussion

The numerical and experimental results are compared in terms of load-deflection curves ($F-\delta$) and the position of the crack localization, which governs the plate strength (Fig. 7). First, the plates go through an initial linear and elastic phase. The stiffness starts to decrease as the cracks start to arise in the bottom tensile surface of the plates. As the load increases, curvature grows and cracks propagate towards the top of the plate. Eventually, the bottom tensile layer gets into the tensile softening stage. However, flexural hardening behaviour is still possible, which allows increasing the load up to the bending strength of weakest cross-section.

A good match between experimental and numerical $F-\delta$ is achieved in the Plates 1, 3 and 9. The numerical model slightly overestimates the peak load of the Plates 2, 4, 5 and 6. The deflection at peak

load is also slightly overestimated in the models of the Plates 2, 5 and 6. The position of the critical crack is well predicted by the models of the Plates 1, 3 and 5.

Besides the simplifications inherent to surrogate models and interpretation of NDT results, there are other possible reasons that might be influencing the quality of the analysis. A constant thickness plate is being assumed but there is variability related to the rough surface, as previously mentioned. This variability might lead to the reduction of strength of locally thinner cross-sections. Consequently, the position of crack localization might be governed by the thickness variability instead of the post-cracking strength. Moreover, the flexural capacity of thinner cross-sections might dictate the peak load and that might justify the general overestimation of the peak load given by the numerical model, mainly in the cases of the Plates 7 and 8. In addition, the analysis is built upon the assumption that fibres are uniformly distributed along the depth of the plates, which does not occur in reality. Still, the significant variability of the structural response of the different beams sawn from the same plate could be reproduced with reasonable agreement.

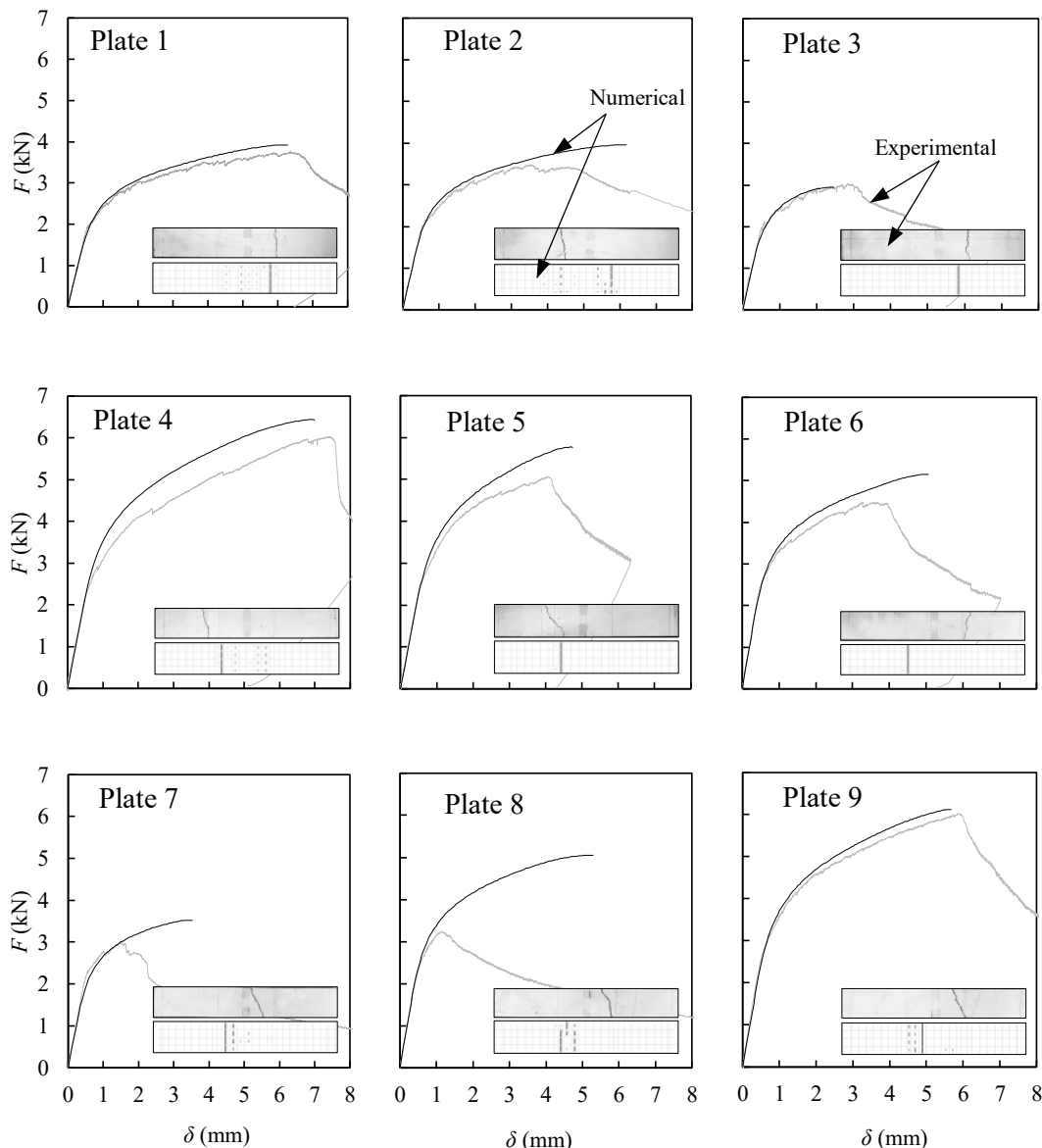


Fig. 7 Load-deflection and crack localization of both FPBT and respective numerical simulation.

6 Conclusions

A new method to perform structural analysis on UHPFRC structures is presented. The underlying tensile characterization process is based on the steel fibres orientation and content distribution, which can be estimated using NDT. The method is validated by means of experimental tests.

The proposed numerical method makes it possible to achieve similar trends in the structural response in terms of load-deflection, as those observed in the experimental tests of UHPFRC thin plates. The comparison between experimental and numerical results shows that the proposed method can be employed to perform improved assessments of post-cracking tensile behaviour provided by steel fibres on thin elements, without requiring destructive characterization tests.

In this work, a single λ or tensile constitutive law is assigned to each point of the plate because the principal tensile direction, which dictates the crack opening direction, is known beforehand and is parallel to the plate longitudinal axis. In cases of more complex geometries and load patterns, crack opening directions are not known beforehand and a more general description of the anisotropic tensile response is required. In the next stages of this research, the anisotropy is going to be characterized by the directional variation of λ and implemented in a constitutive model for nonlinear structural analysis.

Acknowledgements

This work was financially supported by: Base Funding - UIDB/04708/2020 and Programmatic Funding - UIDP/04708/2020 of the CONSTRUCT - Instituto de I&D em Estruturas e Construções - funded by national funds through the FCT/MCTES (PIDDAC); and by the project PTDC/ECI-EST/31777/2017 (UHPGRADE) funded by FEDER through COMPETE2020 - Programa Operacional Competitividade e Internacionalização (POCI) and by national funds (PIDDAC) through FCT/MCTES. Collaboration and materials supply by Concremat, Secil, Omya Comital, Sika, MC-Bauchemie and KrampeHarex is gratefully acknowledged.

The support by the Portuguese Foundation for Science and Technology (FCT) through the Ph.D. grant PD/BD/143147/2019 attributed to the first author and the support by the Fundação Calouste Gulbenkian through the PhD grant n°144945 attributed to the second author are also gratefully acknowledged.

References

- [1] Naaman, A.E.J.N.A.H.-p.c.m.s. and a.S.W.S. Publishing, *High performance fiber reinforced cement composites*. 2008: p. 91-153.
- [2] Abrishambaf, A., M. Pimentel, and S. Nunes, *A meso-mechanical model to simulate the tensile behaviour of ultra-high performance fibre-reinforced cementitious composites*. *Composite Structures*, 2019. **222**: p. 110911.
- [3] Pimentel, M., A. Abrishambaf, and S. Nunes, *Anisotropic tensile behaviour of UHPFRC: meso-scale model and experimental validation*, in *10th International Conference on Fracture Mechanics of Concrete and Concrete Structures*. 2019: Bayonne (France)
- [4] Nunes, S., M. Pimentel, and A. Carvalho, *Non-destructive assessment of fibre content and orientation in UHPFRC layers based on a magnetic method*. *Cement and Concrete Composites*, 2016. **72**: p. 66-79.
- [5] Nunes, S., et al., *Estimation of the tensile strength of UHPFRC layers based on non-destructive assessment of the fibre content and orientation*. *Cement and Concrete Composites*, 2017. **83**: p. 222-238.
- [6] Shen, X. and E. Brühwiler. *Characterization of tensile behavior in uhpfrc thin slab using ndt method and dic system*. in *Proceedings of the 2nd International Conference on UHPC Materials and Structures UHPC 2018-China*. 2018. RILEM Publications SARL.
- [7] Pfy, T., *Tragverhalten von stahlfaserbeton*. 2003, vdf Hochschulverlag AG.
- [8] Abrishambaf, A., M. Pimentel, and S. Nunes, *Influence of fibre orientation on the tensile behaviour of ultra-high performance fibre reinforced cementitious composites*. *Cement and Concrete Research*, 2017. **97**: p. 28-40.
- [9] AFNOR, *NF P18-470*, in *Concrete - Ultra-high performance fibre-reinforced concrete - Specifications, performance, production and conformity*. 2016, Association Française de Normalisation.

Dimensioning Approach of Partially Prestressed Concrete Beams: Optimization of T-shaped section with heels

Nadim Abdel Nour¹, Dominique Vié², Alaa Chateauneuf¹, Sofiane Amziane¹, Assad Kallassy³

¹ *University Clermont Auvergne, Institut Pascal, CNRS-UCA-SIGMA, BP 10448, F 63000 Clermont Ferrand, France*

² *Centre des Hautes Etudes de la Construction, 94110 Arcueil, France*

³ *Lebanese University, Faculty of Engineering II, Lebanon*

Abstract

The present article addresses the structural optimization of partially and fully prestressed concrete bridge girders. For this purpose, an optimization-oriented dimensioning approach for prestressed concrete is proposed in accordance with the Eurocode 2 provisions, it combines all service and ultimate limit states verifications simultaneously. An optimization procedure, based on Genetic Algorithms, is conducted on a T-shaped section with heels, with the total cost as the objective function. The design variables are the cross-sectional dimensions, the steel reinforcement and the quantity and configuration of prestressing tendons. Numerical examples are implemented to demonstrate the performance and effectiveness of this method.

KEY WORDS: Partial prestressing, Pivot rule, T-shaped heels, Structural optimization, Genetic Algorithms

1 Introduction

Prestressed concrete (PC) has been widely adopted in the design of bridge decks, allowing significant savings in material weight. An engineer's primary goal is to design an optimum structure that satisfies all performance requirements while minimizing the overall cost.

Many studies have proven the implementation of evolutionary algorithms into structural optimization, such as genetic algorithms, to be efficient for the resolution of non-linear complex problems. Marti [1] successfully applied the simulated annealing algorithm for the optimum design of PC precast bridges with double U-shaped cross sections. Aydin [2] minimized the cost of PC bridge I girders using a genetic algorithm and obtained a more economical solution than the real-life structure.

Given the complexity of the optimization problem involving several design variables and highly non-linear constraints, a suitable optimization-oriented approach for prestressed concrete design is not only effective but also indispensable to facilitate and simplify the optimization procedure, and the exploitation of results, as far as possible.

This paper deals with the structural optimization of partially and fully PC bridge T-shaped girder with heels, manipulating different span lengths. The design strategy developed for the design is outlined at first, and then the analysis is conducted as a single-objective optimization problem solved using genetic algorithms. Constraints to be satisfied include geometrical constraints and flexural verifications under service and ultimate limit states as per the Eurocode 2 provisions. The entire design and optimization procedure are coded on the computer program "scilab". Numerical examples are presented to demonstrate the efficiency of the developed approach and the results are analyzed.

2 Design strategy

The idea of full prestressing is to maintain the concrete in a compressed state at service loading; the principle of partial prestressing came later on, allowing the decompression of concrete and a certain amount of cracking in the service state. The design theory presented herein, the pivot rule method, is a new developed approach for dimensioning fully and partially pre-stressed concrete sections. It is inspired from common engineering practice seeking to optimize the design, and it can easily be implemented in optimization algorithms.

The main advantage of this method is the coherent combination of all limit states verifications in one formula including a common condition in the Eurocode provisions called “formwork condition”. This condition results from the upper and lower fiber stress constraints, based on which the minimum needed concrete section to meet the serviceability requirements is deduced. It is commonly called “condition de coffrage” in French, translated as a “formwork condition”.

The proposed method also introduces the prestressing force P as a probable value varying between two limits. The permissible domain of P is found based on a pivot rule, similar to the one used in reinforced concrete, demonstrating the benefit of partial prestressing.

2.1 Conventional design method

The former concrete prestressing French code BPEL prescribed direct limitations on tensile/compressive stresses in extreme fibers of the concrete section under all service limit states. These restrictions were replaced in Eurocode 2 (EC) by limitations on crack width and on stresses in concrete and in active/passive reinforcement depending on the service limit state (quasi-permanent, frequent or characteristic).

Today in common practice, engineers try to avoid the numerous Eurocode verifications by adopting supplementary limitations similar to those specified in BPEL.

Each service limit state is characterized by the following moments and stress limitations:

- M_{min} and M_{max} : minimum and maximum values of moment with ΔM being their difference
- and : concrete stresses on extreme concrete fibers
- and : stress limits at concrete top fiber under M_{min} and M_{max} respectively
- and : stress limits at concrete bottom fiber under M_{min} and M_{max} respectively

Stress limitations

Formwork condition

$$(1) \quad \text{---} \quad \text{---} \quad (2)$$

For each service limit state, two values of P ($P_{critical}$ and $P_{over-critical}$) are computed with their corresponding eccentricities, and the final prestressing force is the highest value.

2.2 New pivot rule method

This approach considers P to be an external force acting on the concrete section. The crack width limitation is replaced by a limitation on the stress in passive reinforcement by a correlation according to EC.

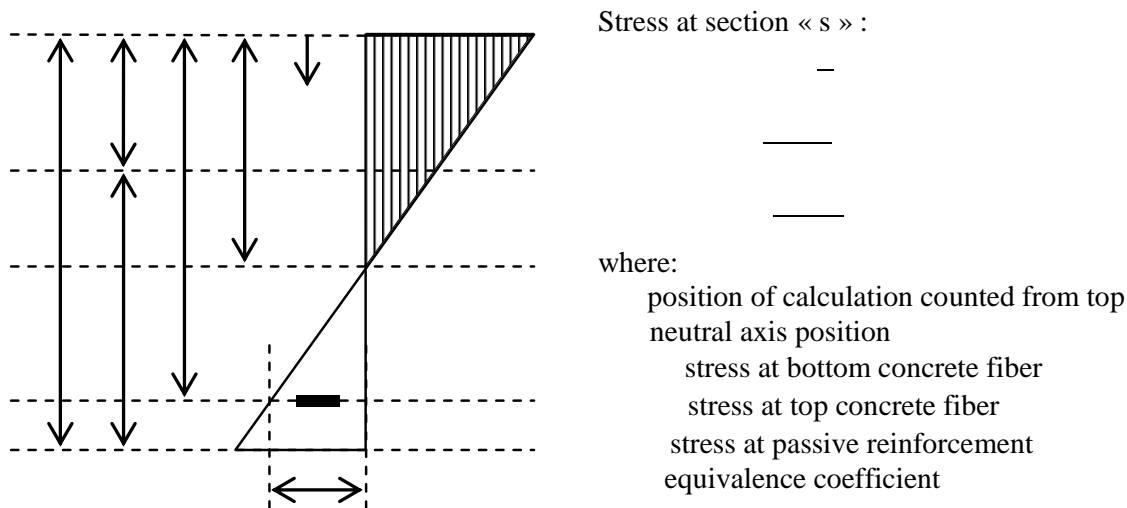


Fig. 1 Stress diagram along the height of the concrete section

In the case of a Tee section with heels where the width is considered to be linearly variable per segment, the mechanical properties can be obtained by successive integration based on the following equations, with area A_h , static moment $S_{h/x}$ and moment of inertia $I_{h/x}$:

$$(6)$$

The equilibrium equations of the bending moment and axial forces, expressed in terms of the mechanical properties of the section, result in the principle equation representing the basis of this approach.

$$(7)$$

The stress limitation is a rupture line represented in the plane (P, M^*) , prior to the calculation of the cable eccentricity e_o . The neutral axis position is calculated in terms of the prestressed force P by solving the following equation:

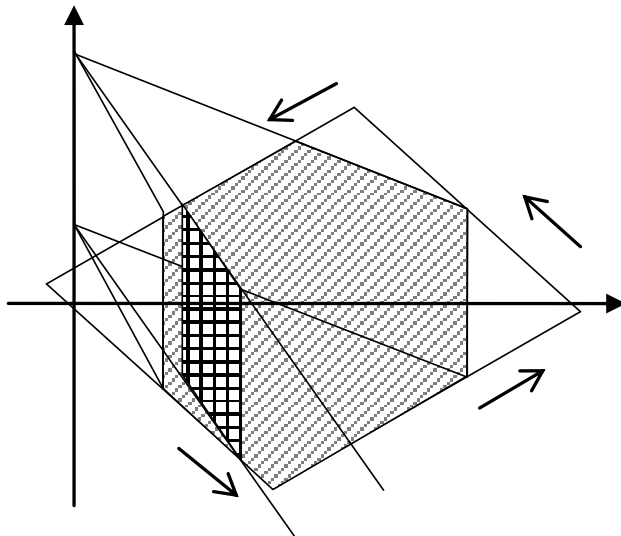
$$(8)$$

The idea is to find the value of the eccentricity e_o for which all service stress limitations are verified for all the applied external moments, taking into consideration the variation of the prestressing force. The actual applied state of stress is represented by a point in the plane (P, M^*) , and for the section to be verified, that point should be located inside the rupture line for all moment values between M_{min} and M_{max} and all force values between P_{min} and P_{max} .

2.3 Fully prestressed/uncracked section

When the section is fully compressed, the mechanical properties are computed in the range $[0, h]$. The position of the neutral axis is found by solving the equation $f(x) = 0$. The well-known stress equations at extreme concrete fibers for a fully prestressed section are then found.

The permissible domain is drawn by expressing the main stress limitations in the plane (P, M^*) . It is delimited by 4 lines parallel to each other two by two, forming a parallelogram.



Moving along the contour line of the permissible domain, at each of the lines (d1) to (d4), one stress limitation is reached. At the intersection of two lines, two stress limitations are reached simultaneously. No stress limitation is reached inside the domain.

The known values of P_{min} and P_{max} can be obtained graphically, and are multiplied by the coefficients α_{min} and α_{max} for each limit state.

Fig. 2 Permissible domain in full prestressing

At the top concrete fiber:
$$(9)$$

At the bottom concrete fiber:
$$(10)$$

For a fixed value of the eccentricity e_o , the total moment defined as M^* varies in terms of P :

$$(11)$$

The permissible range for the variation of the prestressed force P combining all service limit states:

2.4 Partially prestressed/cracked section

For an induced tensile stress less than the tensile stress limit, the full prestressing strategy applies. When this limit is exceeded, the section becomes cracked, the same expressions of the force P and the total moment M^* can be applied in terms of the neutral axis position.

Considering that the section is uncracked under M_{min} (pivots 1 and 3) and cracked under M_{max} , the same value of M_{min}^* is obtained, and M_{max}^* is computed on three different segments.

Pivot 2a = pivot 2, uncracked section — (13)

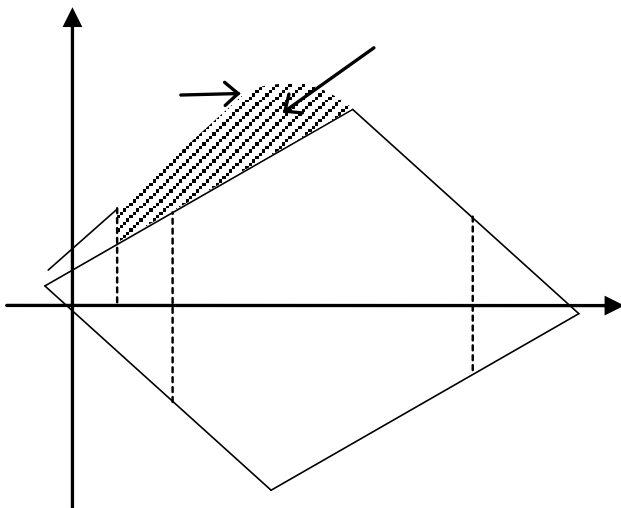
Pivot 2b, cracked section ————— (14)

Pivot 4b, cracked section — ————— (15)

For \dots , pivot 4b is reached; otherwise, pivot 2b is reached.

The same principle as followed in the full prestressing still applies for the computation of the forces $P_{critical}$, $P_{over-critical}$ and P_{max} . These values are obtained by resolving a polynomial equation obtained from equation (9) with the following general form:

(16)

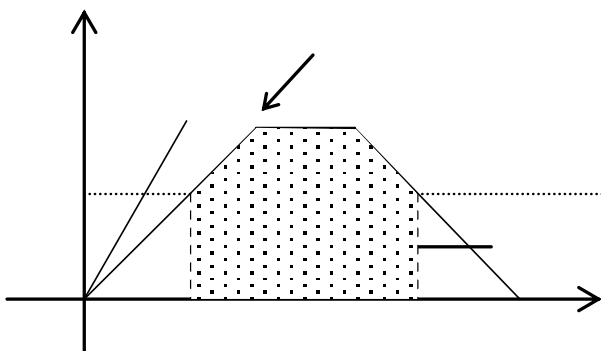


It can be clearly seen that the extended part of the permissible domain in partial prestressing consists of two curves representing the pivots 2b and 4b.

A significant gain in the value of M_{max}^* can be obtained in partial prestressing since the line (d4) representing pivot 4 is replaced by the curve 4b shifted further up.

Fig. 3 Extension of the permissible domain in partial prestressing

2.5 Formwork condition



It is worth mentioning that for sections presenting a value of $v/v' < 1$, a gain in the formwork conditions between full and partial prestressing can certainly be obtained.

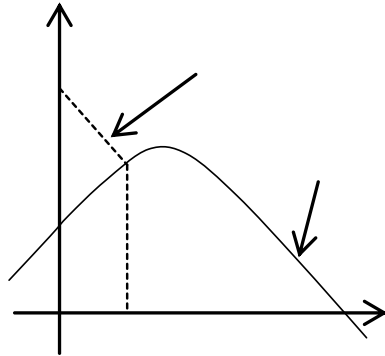
This condition is expressed independently from P and e_o .

Fig. 4 Formwork condition in full and partial prestressing

The formwork condition is evaluated, in full prestressing, based on the height of the parallelogram drawn in the plane ($\Delta M, P$). The height shall be sufficient to cover the variations of the exterior moments (M). The same principle applies to partial prestressing; with a gain in the maximum value of ΔM obtained based on the new equations of pivots 2b and 4b.

2.6 Ultimate bending verification

For a given steel reinforcement ratio, the exact force P_u needed corresponds to the value of P for which the interaction diagram intersects with the line . The section is verified if the obtained force P_u does not exceed the prestressing force P calculated in service limit state.



For the construction of the permissible domain (P, M), the values of the resultants P and M are calculated based. The section being divided in segments where the width is linearly variable, an integral I_i is introduced and computed for each segment.

Fig. 5 Interaction diagram in ultimate limit state verification

2.7 Shear verification in service limit state

The provisions of Annex QQ of EC [3] were applied for shear verification in the service limit state. At a distance “d” from the edge of the support, the following interaction equation needs to be verified:

$$\text{—————} \text{—————} \tag{17}$$

3 Optimization with a genetic algorithm

A genetic algorithm (GA) is an evolutionary optimization method inspired from Charles Darwin’s natural selection theory based on the concept of “survival of the fittest” [4].

3.1 Penalty function

Since GAs are mainly used for resolution of unconstrained optimization problem, a penalty function is used to account for violated constraints. It is the absolute sum of normalized violated constraints:

$$\tag{18}$$

Where n is the total number of constraints, and p_i is the violation factor of the i th constraint.

4 Optimum design of a prestressed concrete beam

The optimization problem is formulated as:

$$\begin{aligned} \text{Minimize } F &= \text{objective function} \\ \text{Subject to} &= \text{set of constraints} \\ &\text{design variables} \end{aligned}$$

4.1 Objective function

In this paper, the objective is to minimize the cost of the prestressed concrete beam calculated per linear meter. The penalized objective function is mathematically expressed as

$$\tag{19}$$

where C_c , C_s , C_p and C_f are the respective unit costs of concrete, steel reinforcement, prestressing steel and formwork. V_c , W_s , W_p and P_{er} are the concrete volume, the weight of steel reinforcement, the weight of prestressing steel and the perimeter of the section respectively.

4.2 Design variables

Table 1 Design variables

Variable	Description	Variable type
	height of the beam	continuous
	web width of the beam	continuous
	heel width of the beam	continuous
	heel height of the beam	continuous
	bottom sloped height	continuous
	number of steel reinforcement bars	discrete
	configuration of prestressing tendons	discrete

The heel of the section ensures the placement of the tendons with a minimum addition of concrete volume. For its dimensioning, a data table including all possible tendon configurations for 1 to 10 tendons is included in the program, see Figure 7.

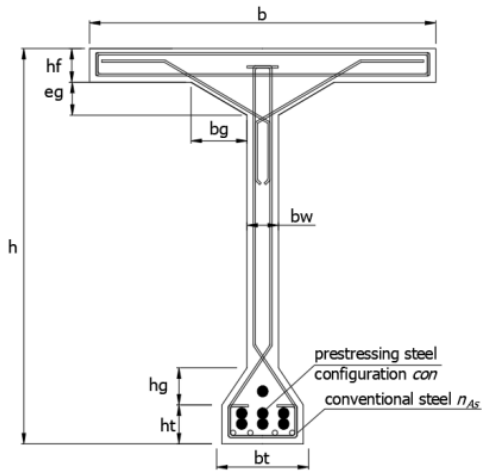


Fig. 6 Typical cross-section of the beam

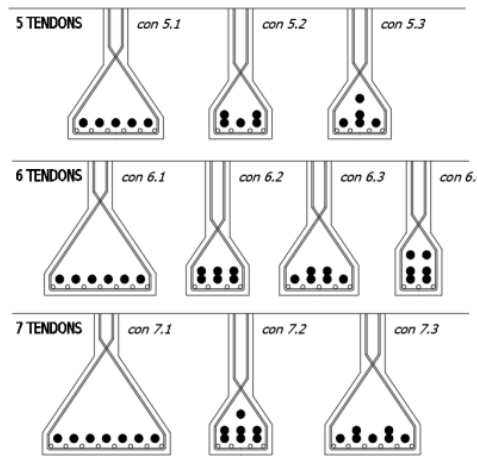


Fig. 7 Tendon configurations example

4.3 Constraints

Flexural constraints are defined as ratios between the applied solicitation (stress, shear, axial force) and the limit calculated as per the proposed approach.

Table 2 Constraints

Geometrical constraints	Depth of beam section	
	Width of web	
	Width of heel	
Flexural constraints	Minimum prestressing force	
	Maximum prestressing force	
	Formwork condition	
	Ultimate bending check	
	Shear verification	

5 Numerical example

The structural optimization procedure presented above was applied to a prestressed concrete 3-lane road bridge with a 10m-wide deck, composed of three T-shaped girders with heels. The study was computed on the edge beam, which carries the most severe loading, following a transverse distribution of the induced loads as per Courbon’s method.

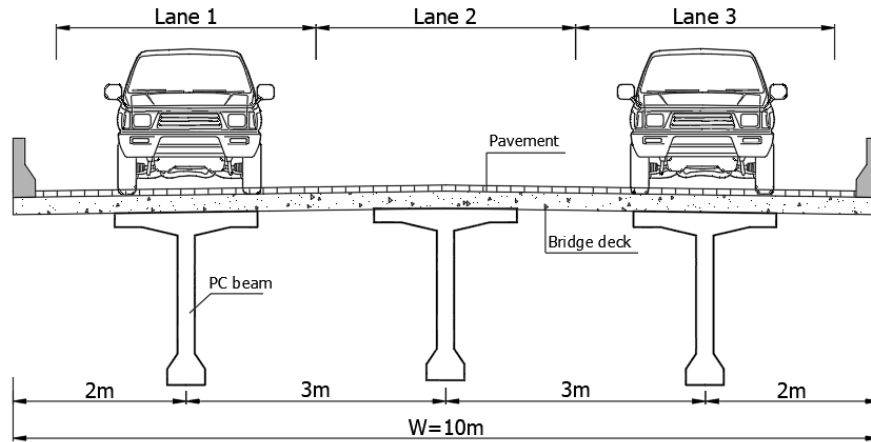


Fig. 8 Cross section of the studied bridge

Table 3 Analysis input parameters and assumptions

Geometric parameters	Loading assumptions
Beam top flange width	Traffic model LM1
Beam top flange thickness	Concrete unit weight
Top inclination width	Dead loads
Top inclination thickness	Distributed live load
Deck slab thickness	Truck loads
Material properties	Unit cost of materials
Compressive strength	Concrete volume cost
Tensile strength of passive reinforcement	Steel reinforcement cost
Tensile strength of prestressing steel	Prestressing steel cost
Tendon type	Formwork cost

5.1 Analysis and Results

- A significant decrease in the prestressing force and the number of cables is shown in partial prestressing. For a span of m , the prestressing force is reduced by \dots for a steel reinforcement ratio of 0. \dots when considering the section as partially prestressed, and the formwork ratio decreases by 30%.

Optimization assumptions	
Population size	100
Crossover rate	
Mutation rate	
Beam depth	
Web thickness	

	0.60%		0.80%	
	Full	Partial	Full	Partial
%Ast				
Prestressing				
P (MN)	14.95	10.92	15.10	9.04
Cables number	6	5	6	4
Area (m ²)	1.02	0.97	1.04	0.99

Table 4 Optimization results in full and partial prestressing

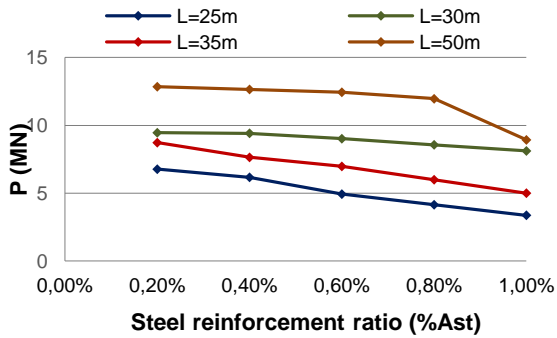


Fig. 9 Effect of steel reinforcement ratio %Ast on the prestressing force in partial prestressing

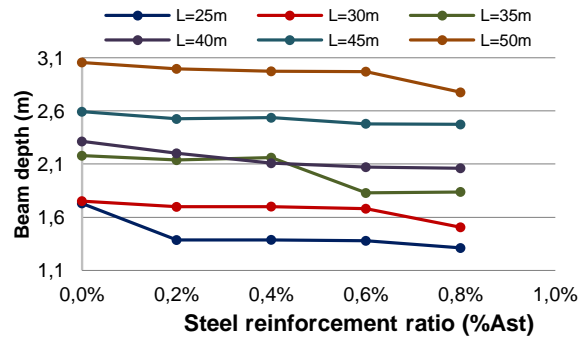


Fig. 10 Effect of steel reinforcement ratio %Ast on beam height in full prestressing

- Results of Figure 9 show that the decrease in the prestressing force reaches a reduction of 50% for an increase of the steel reinforcement ratio from 0.2% to 1.0%, for a span length of 25m.
- In fully prestressed sections, passive reinforcement is usually added for the ultimate verification. Figure 10 shows a gradual decrease in the optimal beam depth with the increase of the steel reinforcement ratio, accompanied by an increase in P due to a lower value of the cable eccentricity, since the cables are placed above the passive reinforcement.

6 Cost sensitivity analysis-Effectiveness of the proposed method

The proposed analytical method for prestressed concrete design is not directly related to the genetic algorithms but was developed in a way to facilitate the incorporation of any optimization calculations.

The effectiveness of the GA optimization method is clearly shown in the performed cost sensitivity analysis. The assigned unit costs of the concrete volume and the cables are modified and the obtained optimum solutions are analyzed. Resulting optimum solutions are shown in the below charts.

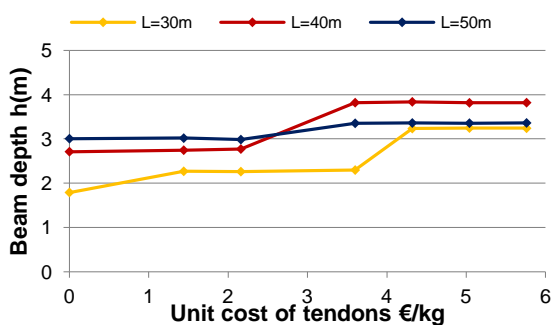


Fig. 11 Effect of the cables cost on the beam depth

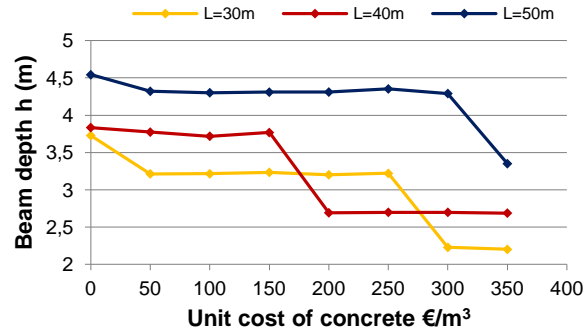


Fig. 12 Effect of the concrete cost on the beam depth

We can conclude that the optimum solution is directly affected by the unit costs. As opposed to conventional design methods, where the dimensions and reinforcement cannot be easily optimized, the formulated objective function can be easily modified based on the designer's objective (minimum cost, area, depth, ...), and the proposed GA optimization method will lead to a relatively rapid and accurate conversion towards the desired optimum solution.

7 References

- [1] J. Marti, F. Vidoza, V. Yepes and J. Alcalá. 2012. "Design of Prestressed Concrete Precast Road Bridges with Hybrid Simulated Annealing". *Engineering Structures* 48 (2013) 342–352.
- [2] Z. Aydn and Y. Ayvaz. 2009. "Optimum Topology and Shape Design of Prestressed Concrete Bridge Girders Using a Genetic Algorithm". *Struc Multidisc Optim*, no. 41, pp. 151-162
- [3] Eurocode 2, EN 1992-2:200, Annex QQ 5
- [4] J. Holland. 1992. *Adaptation in Natural and Artificial Systems*. MIT Press

Effects of unidirectional tensile stresses on punching shear strength of RC slabs

Pablo G. Fernández, Antonio Marí, Eva Oller, Magí Domingo

Civil and Environmental Engineering Department,
Universitat Politècnica de Catalunya,
31 Jordi Girona street, Barcelona (08034), Spain

Abstract

RC slabs can be subjected to transverse loads and in-plane tensile forces simultaneously, as it occurs in top slabs of continuous box girder bridges at intermediate supports, or in floor slabs supported on columns, due to skew in-plane compressions or imposed deformations as shrinkage. Tensile forces can reduce the punching capacity of the slabs, however, few studies have been carried out to quantify this effect. An experimental, numerical and theoretical investigation has been carried out, in which 5 1.65x1.65x0.12 m slabs have been tested under a point load and different degrees of unidirectional tensile force. Numerical predictions were made with FEA software ABAQUS and, from the theoretical point of view, the Compression Chord Capacity Model (CCCM) was extended to take into account the effect of in-plane tensile forces in the punching strength of the slabs. The experimental results showed that the ultimate punching load decreases linearly with the applied tensile force, and if that tensile force cracks the slabs, such reduction is higher. Results obtained with FEA and CCCM are in agreement with the observations made at the laboratory.

1 Introduction

The phenomenon of punching-shear has been extensively studied over the years, both theoretically and experimentally, but as far as the authors are aware, few studies have been carried out regarding punching-shear when there are tensile forces in the mid-plane of the slab [1]-[4]. Punching shear provisions included in the most frequently used design codes contemplate the effect of in-plane normal stresses in a different way. Model Code 2010 [5] formulation includes the load-rotation curves of the cross-section of the slabs, which are affected by in-plane normal stresses. ACI 318-14 [6] does not consider the effect of in-plane forces on the punching strength. However, ACI 349-06 [7] has a particular expression for the case of concrete slabs subjected to in-plane tensile stresses. Finally, EC-2 [8] includes the effect of axial stresses on punching shear by including the term $k_1 \cdot \sigma_{cp}$, but it does not differentiate between tension and compression, despite the response of concrete in one case or in the other is radically different.

RC slabs subjected to the simultaneous action of transverse concentrated loads and in-plane tensile forces can be found in continuous box girder bridges, at intermediate supports, where tensile stresses arise in top slab as result of hogging bending moments and may act together with a heavy vehicle load. Another common situation where this phenomenon takes place is on floor slabs supported on columns and subjected to a horizontal load, due to wind or earth pressure, on one of their sides. Skew compressions going from that side to the restraining columns of the opposite side may generate tensile stresses in the perpendicular direction, as can be seen in Fig. 1.

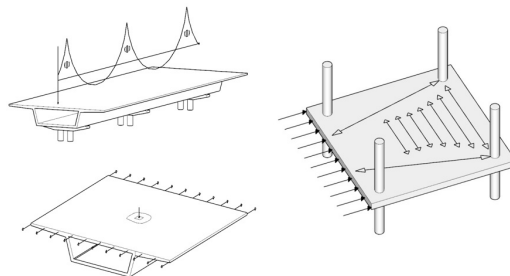


Fig. 1 Common situations where in-plane tensile stresses and a concentrate load may act together.

In this context, an experimental campaign has been carried out at the Laboratory of Technology of Structures and Materials of the Universitat Politècnica de Catalunya (UPC). The main objective of this program was to identify and quantify the effect of in plane tensile forces on the punching-shear strength of reinforced concrete slabs. On the other hand, it is intended to provide experimental results to contribute to extend the mechanically-based punching-shear resistance model “Compression Chord Capacity Model” (CCCM) [9], developed by some of the authors, to the case of in-plane tension.

From the 5 specimens tested, one was a control slab without in-plane forces (slab A0), whilst the other 4 slabs were subjected to different levels of tensile force. This article presents some results of the experimental campaign, such as load-displacement curves, crack patterns, and the decrement of the punching strength due to the tensile force applied. Experimental results have been compared with those obtained with the numerical simulations and the CCCM mechanical model.

2 Experimental campaign

2.1 Test specimens

A total of 5 slabs of 1650 x 1650 x 120 mm were cast at the laboratory. The dimensions of the slabs tested in the context of this experimental campaign are based on the punching-shear tests performed in [10]. The slabs were supported on 8 points placed at the vertices of a regular octagon, equidistant 765 mm from the point load’s vertical axis, applied on its center.

The specimens were subjected to tension in their plane, in only one direction, through 10 post-tensioning bars 25 mm in diameter and 600 mm in length, partially embedded in two opposite faces (5 bars on each side) (see Fig. 2). These bars were connected to the tensioning system to apply the tensile force to the slab. The value of the external tension applied during test is measured in relation to the tensile force producing the cracking of the slab’s cross section or $T_{cr} = A_c f_{ct}$, with A_c being the composite concrete and steel area of the cross section and f_{ct} the tensile concrete strength.

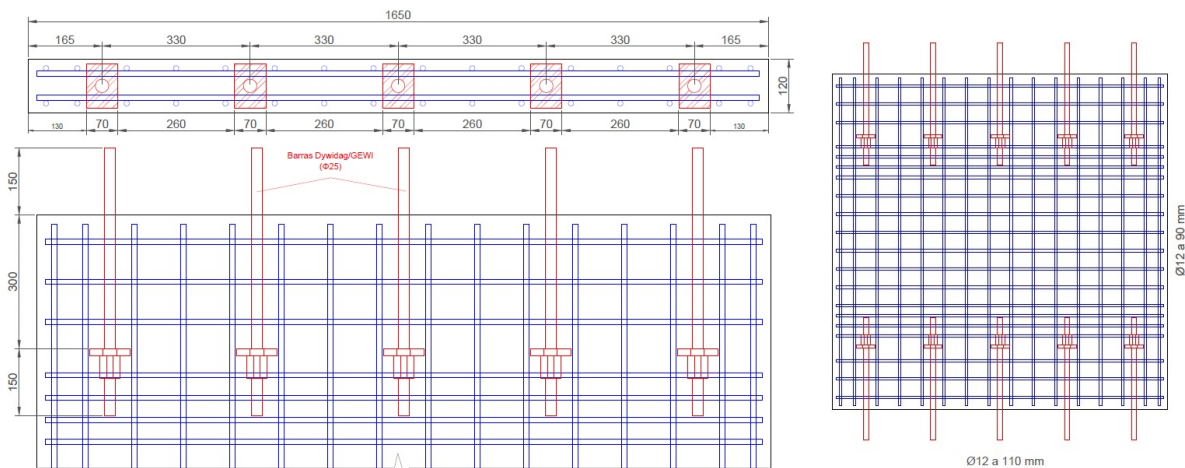


Fig. 2 Position of the post-tensioning bars inside the specimens.

The slabs were reinforced with two steel meshes arranged on the upper and lower faces. The tensile reinforcement ratio and effective depth of each slab are shown in Table 1. The punching load was transmitted to the slabs through a 145 x 145 x 30 mm steel plate located on its center. Due to the configuration of the experiment, all the slabs were tested face down with respect to their real position in a building, in which the reaction of the column goes upwards and the tensile reinforcement is arranged on the upper face.

Table 1 Reinforcement ratios and effective depths of the tension side reinforcement.

Parallel to tension			Perpendicular to tension		
Reinforcement area (mm ²)	Reinforcement ratio	Effective depth (mm)	Reinforcement area (mm ²)	Reinforcement ratio	Effective depth (mm)

1810	0.0108	99	1810	0.013	87
------	--------	----	------	-------	----

To characterize the materials before the control slab (A0) test, standard compression (UNE-EN 12390-3), splitting (UNE-EN 12390-6) and elastic modulus (UNE-EN 12390-13) tests were performed. The age of the concrete at that time was 160 days. The results of which are shown in Table 2.

Table 2 Mean values of material properties.

Concrete			Steel	
f_c (MPa)	f_{ct} (MPa)	E_c (GPa)	f_y (MPa)	E_s (GPa)
37.0	3.3	29	535	215

2.2 Test set up

Four of the five tested specimens were subjected to different levels of tension, whilst the control slab was tested un-tensioned. To apply the tensile force to the slabs, an auxiliary steel structure, whose plan dimensions were 2500 x 2840 mm was built. This structure consisted of a rectangular steel frame surrounding the slab (Fig. 3)

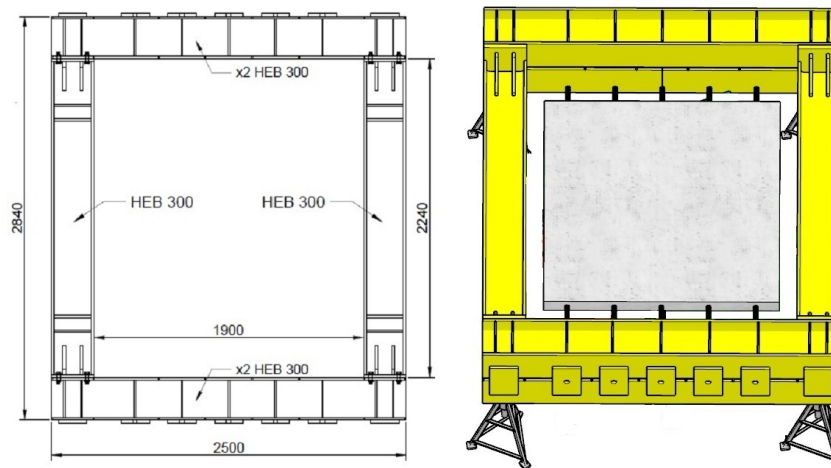


Fig. 3 Steel frame used to apply tensile force to the slabs

On one of the faces, a passive anchor for the tensioning bars was used, meanwhile bars were prestressed from the other end, with the help of hollow jacks connected to the protruding bars. The force applied to the slab was measured by a set of hollow load cells placed at both anchorages.

The steel structure was set at the appropriate height with the help of four height-adjustable supports designed for the experimental campaign and located under each of the four corners of the frame. For safety reasons, once the desired external force value was reached, the extension bars were anchored and the jacks were disconnected from them. The tensile force applied to the slabs in each test is presented in Table 3.

Table 3 Values of tensile forces applied on each test

Test #	T/T_{cr} at failure
1	0.00
2	0.44
3	0.69
4	1.02
5	1.26

To introduce the punching load, a hydraulic jack anchored in a loading frame, rigidly fixed to the floor slab, was used. Eight 120 x 120 mm load cells were placed at slab supports to measure the reactions, arranged in a circle centered with respect to the center of the loading frame. A piece of rubber was placed over each of the cells to allow free rotation in the supports. The 8 load cells were supported on 4 rigid easels arranged in such a way that the distance between the axis of two opposite supports was 1530 mm (Fig 4).

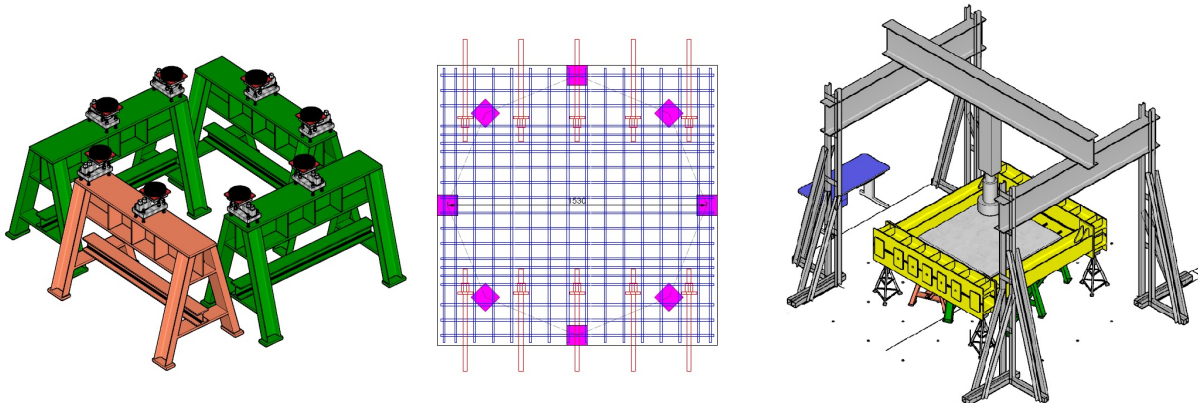


Fig. 4 Support schema of the slabs (left and center) and final positioning of all the elements under the loading frame (right)

3 Mechanical model. Extension of CCCM

3.1 Shear and punching models

The Compression Chord Capacity Model (CCCM) is a simplified shear strength mechanical model derived from a more general model called Multi-Action Shear Model (MASM), developed by A. Mari, et al. [11] and Cladera et al. [12]. It considers, as it is widely accepted, that the shear strength (V_{rd}) is the sum of: the shear resisted in the un-cracked compression head (V_c), the shear transferred across the web cracks (V_w), by aggregate interlock and residual stresses, the shear resisted by the longitudinal reinforcement, due to dowel action (V_{cl}), and the contribution of the transverse reinforcement (V_s), providing explicit expressions for each component. The CCCM model, groups the three first components into a single one, V_c , called concrete contribution.

Distributions of normal and shear stresses are assumed by combining beam and arch effects, so that the compression chord is subject to a biaxial stress state. It is considered that failure occurs when the principal stresses at one point of the compression head, at a critical section defined in [9], reach the Kupfer's biaxial failure envelope, in the compression-tension branch. To obtain the beam shear strength, equilibrium of forces and moments between the internal forces (V , M) and the stress resultants (Fig. 5) at the concrete chord (C , V_c), along the crack (V_w), at the stirrups (V_s) and at the longitudinal reinforcement (T , V_l) are taken in the portion indicated by Fig. 5. Then, relating forces with stresses and taking into account the failure criterion, the ultimate shear is obtained.

This model was extended to punching [9], considering the main differences between both phenomena, in order to incorporate them into the mechanical model. First, taking into account the shape of radial bending moment law $m_r(r)$, the position and inclination of the critical crack were formulated. Thus the position of the control perimeter was obtained. The second important effect incorporated was the multiaxial stress state in the slab compressed chord, due to tangential and vertical stresses in the vicinity of the column, enhancing the concrete capacity to resist shear stresses in the radial vertical plane. This phenomenon was incorporated in the model by modifying the compression-tension branch of Kupfer's biaxial failure envelope, using the confined concrete strength f_{cc} , from the EC-2 [8] formulation, instead of the unconfined strength f_c , so that a higher shear stress is needed to reach failure. Again, to obtain the punching strength of the slab, the equilibrium between internal forces and stress resultants is taken in a portion of the slab enclosed by the critical perimeter and the critical section (Fig. 6).

Solving the equilibrium equations, and assuming some simplifications explained in [9], the simplified expression for the punching strength (2) is derived, where ζ is the size effect given by Eq. (3) and x/d is the relative neutral axis depth obtained assuming cracked concrete, zero tensile stresses and linear stress distribution in the compression chord.

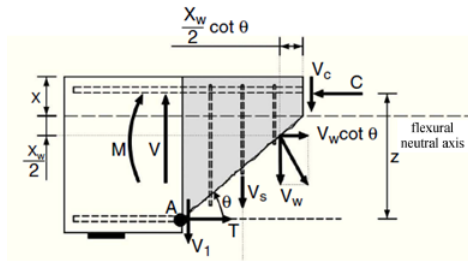


Fig. 5 Shear transfer mechanism and scheme of the equilibrium of the considered forces in the shear model.

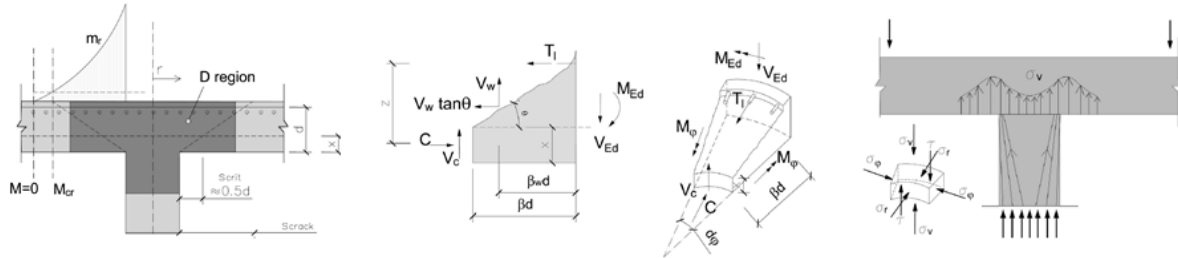


Fig. 6 Shear transfer mechanisms and scheme of the equilibrium of the considered forces in the punching model.

$$V_{rd,0} = 0.3 \cdot \zeta \left(1.125 \cdot \frac{x}{d} + 0.425 \right) f_{ck}^{2/3} \cdot u_{cri} \cdot d \quad (2)$$

$$\zeta = \frac{2 \left(\frac{d}{a} \right)^{0.2}}{\sqrt{1 + d/100}} \quad (3)$$

Due to the internal redundancy of the slabs, flexural reinforcement may yield before punching failure occurs, leading to a flexural-punching failure. First yielding will take place when the tangential moment reaches the lower yielding moment of the two orthogonal directions, since tangential moment per unit length is higher than the radial moment, and a redistribution of moments may take place from that point onwards. Anyhow, the punching strength can't be higher than the load that equals the radial moment to the yielding moment per unit length (V_Y) at the control perimeter.

$$m_r = \frac{V}{4\pi} \left[(1 + \nu) \ln \frac{r_0}{r_{cri}} \right] \approx \frac{V}{2\pi} = m_y = \rho f_y d^2 \left(1 - \frac{\rho f_y}{2f_c} \right) \quad (4)$$

$$V_{rd,0} \leq V_Y \approx 2\pi m_y \approx 2\pi f_y d^2 \left(1 - \frac{\rho f_y}{2f_c} \right) \quad (5)$$

In equation (4) it has been assumed, for the sake of simplicity, a mean value of $r_0/r_{cri} = 5$ and a Poisson's ratio for cracked concrete $\nu = 0.3$

3.2 Extension of CCCM-punching to in plane tensile forces

Since CCCM is a mechanical model, the effects of the tensile force were accounted for in two ways: by including it into the equilibrium equations, and using a previously derived reduction of the neutral axis depth due to the presence of that tensile force [13]. Then, a new simplified expression was derived (6). For the particular case of unidirectional tension, where half of the perimeter is subjected to tension and the other half remains un-tensioned, shear strength, is given by Eq. (7).

$$V_{rd,T} = \zeta \left[(1.125 - 0.85) \frac{x}{d} + 0.425 \right] f_{ck}^{2/3} \cdot u_{cri} \cdot d \quad (6)$$

$$V_{rd,total} = \frac{V_{rd,0}}{2} + \frac{V_{rd,T}}{2} = \left(V_{rd,0} - 0.425 \cdot \zeta \cdot \frac{T}{T_{cr}} \cdot \frac{x}{d} \right) f_{ck}^{2/3} \cdot u_{cri} \cdot d \quad (7)$$

Where T_{cr} is the force producing cracking in the RC slab due to pure tension. For values of $T > T_{cr}$, no contribution of the concrete to resist tension is considered, being resisted only by the reinforcement. For this cases, an effective tensile strength of steel $f_y^* = f_y - T/A_s$ is adopted, and used in Eq. (5). This reduction provokes that V_y , the punching strength associated to reinforcement yielding, becomes dominant, diminishing even more the strength and stiffness of the slab, as can be seen in section 5.

4 Numerical simulations

In addition to the experimental campaign, a numerical model was developed to contrast the obtained results at the laboratory and with the mechanical model CCCM. Simulations were carried out with Simulia Abaqus software, using the Abaqus/Explicit package [14].

4.1 Model generation

Taking account the existing double symmetry, both in geometry and loading, only a quarter of each slab was simulated, considering the corresponding boundary conditions in each symmetry plane. For concrete, cubic elements of 8 nodes (C3D8R) were used while for reinforcing bars, linear beam elements of 2 nodes (B31) were used [15]. The reinforcing bars were considered perfectly bonded to the concrete. The size chosen for the elements were 20 mm, so that 6 elements were arranged along the 120 mm of the slab's thickness. The slab supports were simulated by means of non-linear springs (SPRING A), with a very high stiffness in compression and practically zero stiffness in tension, thus allowing the partial lifting of the slabs. The introduction of the tensile force was simulated by applying the loads directly to the nodes located in the area of the anchor plates of the post-tensioning bars, whilst for the punching load, a displacement was imposed on the nodes located on the upper face of the slab, under the surface occupied by the load plate.

4.2 Materials

The Concrete Damaged Plasticity model [16] was chosen to simulate the behavior of concrete, which requires the definition of the uniaxial constitutive equations in compression and tension, in addition to the definition of a yielding surface. To define the yielding surface default values were used except for the dilation angle ($\psi = 37.5^\circ$) and $K = 0.8$. For compression, the Hognestad parabolic constitutive equation was selected, with a linear behavior up to 40% of f_c (σ_{c0}). For the tensile behavior the model proposed in section 5.1.8.2 of the Model Code 2010 [7] has been used. To define the elastic response, only the modulus of elasticity (E_c) and the Poisson ratio (ν) are needed. E_c was obtained in the corresponding characterization test (see Table 2), while for ν , as Abaqus/Explicit considers it a fixed value throughout the whole simulation process, including post-cracking regime, $\nu = 0$ was used [15].

5 Results

In this section, experimental, numerical and theoretical results are compared, focusing on the relative decrement of the punching strength to the tensile force applied. The numerical model was adjusted to fit the experimental results obtained in the control test. Once it was verified, simulations were performed for several values of T/T_{cr} , up to a maximum of $T/T_{cr} = 1.5$, in order to obtain a more complete behavior curve. Figure 6 shows the comparison between the load-deflection curves obtained experimentally and numerically for three of the test carried out at the laboratory. As can be seen, quite accurate results were obtained in terms of the ultimate load.

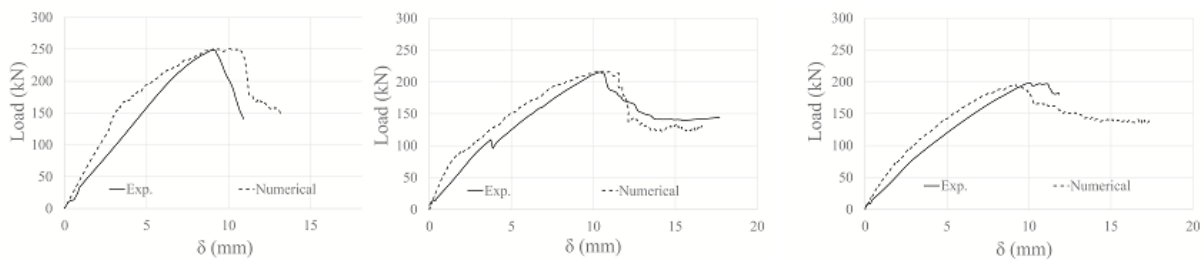


Fig. 6 Comparison between load-deflection curves obtained with the numerical model and experimentally for $T = 0$ (left), $T/T_{cr} = 0.69$ (center) and $T/T_{cr} = 1.02$ (right)

Figure 7 shows how the punching strength decreases as T/T_{cr} increases, and that this decrement is even bigger for values of $T/T_{cr} > 1$. A very good correlation between experimental, numerical and analytical models is observed as summarized in table 4.

Table 4 Relative decrement of the punching strength to the tensile force obtained with each method

Test #	T/T_{cr} at failure	$P_{u,0}/P_u$ (Experimental) ($P_{u,0}=249.1$ kN)	$P_{u,0}/P_u$ (CCCM) ($P_{u,0}=235.9$ kN)	$P_{u,0}/P_u$ (numerical) ($P_{u,0}=250.3$ kN)
1	0.00	1	1	1
2	0.44	0.91	0.92	0.93
3	0.69	0.86	0.87	0.88
4	1.02	0.79	0.81	0.81
5	1.26	0.72	0.72	0.73

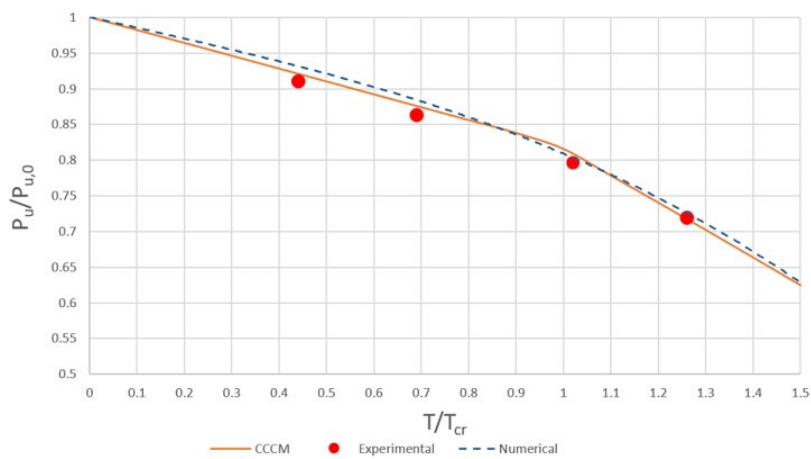


Fig. 7 Comparison of the relative decrement of the punching strength to the tensile force obtained numerically, theoretically and at the laboratory.

Finally, different crack patterns obtained numerically are shown in Fig. 8. As can be seen, the radial pattern obtained for $T = 0$ evolves into an orthogonal pattern for high values of T/T_{cr}

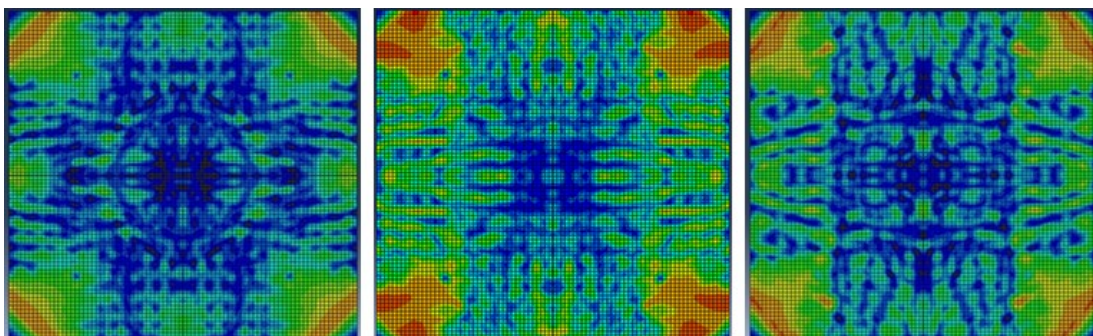


Fig. 8 Crack patterns (in blue) for $T = 0$ (left), $T/T_{cr} = 0.69$ (center) and $T/T_{cr} = 1.26$ (right). (Tensile force applied in horizontal direction in the pictures)

6 Conclusions

Based on the observations made during the experimental campaign and the results presented in this article, the following conclusions can be drawn:

- The decrease in the punching-shear strength can be well characterized by a bilinear function of the applied tensile force “ T ”. The first branch arrives up to a certain value “ T_{cr} ”, after which a higher reduction of the punching strength is observed.
- The maximum value of the reduction produced by the presence of a tensile force, for the tests carried out, was 28% with respect to the reference slab, for a load $T = 1.26 T_{cr}$. For the tensile value $T = T_{cr}$, the punching load reduction was approximately 20%
- Both the numerical model developed and the extended theoretical model CCCM have been able to accurately reproduce the results of an experimental campaign carried out by the authors. The experimentally observed behaviour has been captured both qualitatively and quantitatively, with an average error on the prediction of the ultimate load of 5%

Acknowledgements

This work has been carried out within the framework of research project BIA-2015-64672-C4-1-R, financed by the Ministry of Economy and Competitiveness (MINECO) of Spain. The authors want to deeply thank the personnel of the Structural Technology Laboratory of the Polytechnic University of Catalonia and Master student Laura Beltrán who collaborated in the execution of the tests.

References

- [1] Abrams, J.H. The Punching Shear Strength of Pre-cracked Reinforced Concrete in Biaxial Tension”, M.S. Thesis Cornell University, May 1979.
- [2] Jau, W.C, White R.N, Gergely P. Behavior of reinforced concrete slabs subjected to combined punching and biaxial tension. Report for U.S. Nuclear Regulatory Commission, 1982.
- [3] Regan, P.E. Punching shear in prestressed concrete slab bridges. Engineering Structures Research Group, Polytechnic of central London, 1983.
- [4] Bui T.T, Nana W.S.A, Abouri S, Liman A, Tedoldi B, Roure T. Influence of uniaxial tension and compression on shear strength of concrete slabs without shear reinforcement under concentrated loads. *Construction and Building Materials* 2017;147:86-101
- [5] Fédération international du Béton. Fib Model Code for Concrete Structures 2010 xol. 1. Lausanne: Ernst & Sohn; 2013
- [6] ACI 318-14. Building code requirements for structural concrete and commentary. American Concrete Institute, 2014.
- [7] ACI 349-06. Code Requirements for Nuclear Safety Concrete Structures. American Concrete Institute, 2007.
- [8] European Committee for Standardization. Eurocode 2: design of concrete structures: Part 1: general rules and rules for buildings. Brussels: European Committee for Standardization; 2002.
- [9] Mari A, Cladera A, Oller E, Bairán JM. A punching shear mechanical model for reinforced concrete flat slabs with and without shear reinforcement. *Eng. Struct.* 2018;166:413-26
- [10] Polak MA. SP-232: Punching shear in reinforced concrete slabs. Am Concrete Institute, Spec Publ, vol. 232; 2005. P.302. <http://dx.doi.org/10.14359/14960>.
- [11] Mari, A.; Bairán, J.; Cladera, A.; Oller, E.; Ribas, C. “Shear-flexural strength mechanical model for the design and assessment of RC beams”. *Struct. And Infr.* (2014) Eng. 11:1399–1419,
- [12] Cladera, A., Mari, A., Bairán, JM. Oller, E., Duarte, N. (2016) “The compression chord capacity model for the shear design and assessment of reinforced and prestressed concrete beams” *Structural Concrete (fib)*, Wiley, 18-2, pp1017-1032, ISSN 1464-4177
- [13] Fernández, P.G.; Mari, A.; Oller, E.; Domingo, M., Effects of tensile stresses on punching shear strength of RC slabs.(2019). 5th Int’l. Conf. Mech. Models Struct. Eng. CMMoST, Alicante, Spain
- [14] Abaqus Analysis user’s manual 6.14, Dassault Systems Simulia Corp., Providence, RI, USA; 2014
- [15] Genikomsou A, Polak MA. A Finite Element analysis of punching shear of concrete slabs using damaged plasticity model in ABAQUS. *Eng. Structures* 2015;98:38-48
- [16] Lubliner J, Oliver J, Oller S, Oñate E. A plastic-damage model for concrete. *Int J Solids Struct* 1988;25(3):299-326

Experimental Study on Flexural Behavior of Concrete Girders Prestressed with Stainless Steel Strands

Anwer Al-Kaimakchi, Michelle Rambo-Roddenberry

FAMU-FSU COLLEGE OF ENGINEERING,
FLORIDA STATE UNIVERSITY,
2525 POTTSDAMER STREET, TALLAHASSEE, FLORIDA 32310, USA

Abstract

Corrosion of reinforcement affects the design service life of concrete structures in harsh environments, and financial resources are needed to rehabilitate the structure. Corrosion-resistant reinforcement is proposed as an ideal option to tackle the corrosion issues in concrete structures in severe environments. Stainless steel alloys have a corrosion-resistant property and are viable for use as prestressing strands to replace carbon steel strands. Almost a decade ago, stainless steel material was used to form a seven-wire prestressing strand. The Duplex High Strength Stainless Steel (HSSS) Grade 2205 was found to be the ideal grade with the highest corrosion resistance and best mechanical behavior among other grades. The HSSS strands have lower mechanical characteristics compared to carbon steel strands. The HSSS strands used in this study had 1.9% ultimate strain and 256.65 ksi ultimate stress. The objective of this work was to study the flexural behavior of HSSS prestressed concrete girders. Four full-scale 42-ft-long AASHTO type II girders were cast, and a reinforced concrete deck was cast and made composite with the girders. The girders were designed using force equilibrium and the strain compatibility method. One of the girders had carbon steel strands and served as a control girder. The other three girders were prestressed with HSSS strands, two with the same initial prestressing force as the control girder and one with the same reinforcement ratio the control girder. All four girders were tested in flexure. The cracking and ultimate loads, ultimate deflection, and failure mode of HSSS prestressed concrete girders were compared to their carbon steel counterpart. Experimental results showed that the overall flexural behavior of the HSSS girders is different than those prestressed with carbon steel strands. When specimens had the same initial prestressing force, the ultimate capacity of the HSSS specimen was around 23.7% higher than that of the control specimen. Also, the ultimate capacity of the HSSS girder increased by 17.5% when the initial prestressing force increased by 18.2%. The failure mode was strand rupture in all three HSSS tested specimens; this is particularly important because it demonstrates the importance of the ultimate strand strain in design. The ultimate deflections of all HSSS girders were almost equal to the control girder even though they failed by rupturing of strands.

1 Introduction

Among the 616,096 bridges in the United States, 256,330 are reinforced concrete and 160,513 are prestressed concrete [1]. Non-prestressed and prestressed concrete bridges represent more than 67.5% of the current total number of bridges in the United States. Large number of those bridges are exposed to aggressive environments, which lead to deterioration. Corrosion of steel reinforcement is one of the most common types of deterioration and a major problem in concrete bridges. Therefore, concrete bridges exposed to harsh environments require regular inspection and maintenance. Utilizing corrosion-free and/or -resistant materials could be more economical in the long run. Stainless steel material has high corrosion-resistance and can be used in seven-wire prestressing strands. Corrosion-resistant strands offer longer service life to prestressed concrete bridges compared to those built with carbon steel strands.

The steel alloy is specified as stainless steel if all its raw materials comply with the specified range by ASTM A276 [2]. The main raw materials of stainless steel alloys include, but are not limited to, manganese, phosphorus, sulfur, silicon, chromium and nickel [2]. Many types of stainless steel alloys are available in the industry such as T316, XM29 and Duplex Grades 2101, 2304 and 2205. All these types can be used to form a seven-wire prestressing strand. Stainless steel strands are manufactured using the same technology as carbon steel strands. The only main difference between stainless and carbon steel strands is the chemical composition of the raw materials. The proportions of the raw

materials in the stainless steel alloys determine their mechanical characteristics and corrosion-resistance property. Previous works studying the material characteristics of multiple stainless steel strands concluded that duplex high-strength stainless steel (HSSS) strand Grade 2205 is the best option among other alloys [3-6]. HSSS strands have been successfully deployed in piles in multiple projects around the United States. Corrosion resistance of the stainless steel alloy can be enhanced by increasing the proportions of molybdenum and nickel [4]. However, those chemicals are expensive and therefore can significantly increase the cost of the prestressing strands.

In this study, three 42-ft long AASHTO type II stainless steel prestressed concrete girders were designed, fabricated and tested in flexure. The results were compared with a control girder, which was prestressed with carbon steel strands. The aim of this work was to study the flexural behavior of girders prestressed with stainless steel strands. The findings from this experimental work can be used in the development of future design specifications and guidelines.

2 Testing Program

2.1 Materials

The prestressing strands used in this study were duplex high-strength stainless steel (HSSS) Grade 2205 and carbon steel Grade 270. The size of both types was 0.6-in. diameter. Standard Specifications for Road and Bridge Construction issued by the Florida Department of Transportation (FDOT) specifies minimum mechanical properties for the HSSS strands [7]. The material characteristics of the HSSS strands, provided by manufacturer, are given in Table 1, and the stress-strain curve is shown in Fig. 1. The HSSS strands meet FDOT's minimum requirements as shown in Table 1. Currently, an ASTM standard is under development to specify minimum acceptable values of the mechanical characteristics of the stainless steel strands. The design guidelines of stainless steel prestressed concrete members shall be based on the minimum acceptable values specified by the ASTM. HSSS strands have different mechanical properties compared to carbon steel strands. HSSS strands have a rounded stress-strain curve once the elastic modulus is deviated and have no linear plateau before rupture. HSSS strands have low ductility, with only a 1.4% guaranteed ultimate strain. HSSS strands used in this study had 1.89% ultimate strain, which is 35% higher than the guaranteed ultimate strain and 54% of the minimum ultimate strain specified for carbon steel strands by ASTM A416 [8]. It should be noted that the material characteristics of the stainless steel strands varies as they depend on the composition of the raw materials. The raw materials might come from different sources and therefore the chemical composition cannot be guaranteed to be identical.

Table 1 Mechanical properties for 0.6-in. diameter HSSS strands

	Area	Breaking strength ksi	Ultimate stress ksi	Ultimate strain in./in.	Elastic modulus ksi
FDOT requirement	0.231	55.4	240	0.014	-
manufacturer	0.2328	59.75	256.65	0.0189	24300

Two types of shear reinforcement were used in this experimental program: glass fiber reinforced polymer (GFRP) and stainless steel rebars. GFRP and stainless steel rebars are viable stirrup options to make the entire prestressed member corrosion resistant. Two girders had GFRP rebars as transverse reinforcement while the other two had stainless steel rebars. The mechanical properties of the GFRP and stainless steel rebars are given in Table 2.

Two different concrete strengths were used for the girder and deck slab. A self-consolidating concrete was used for the girder with a specified concrete strength of 10 ksi, while the deck slab was cast with normal weight concrete with a specified concrete strength of 6.5 ksi.

2.2 Design and Fabrication

A design matrix showing the longitudinal prestressing and transverse reinforcement is given in Table 3. The girders were designed using force equilibrium and the strain compatibility method. Girder 1 is

the control girder, which had carbon steel strands as the main longitudinal prestressing and stainless steel rebars as transverse reinforcement. The eleven strands were pretensioned to 43.9 kips, which is equal to 75% of their ultimate strength. The prestressing ratio and total prestressing force were 0.647% and 482.9 kips, respectively, and the shear reinforcement ratio was 0.555%.

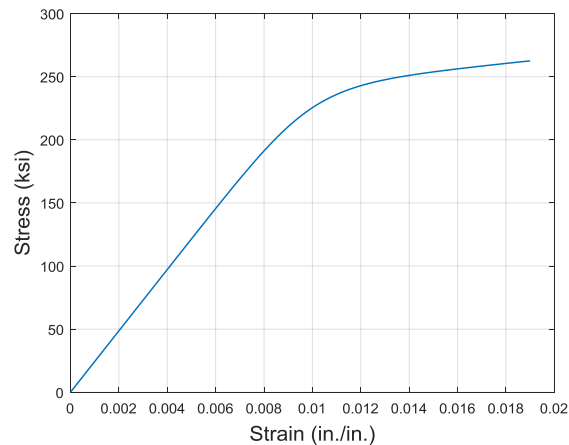


Fig. 1 Stress-strain curve for stainless steel strands

Table 2 Mechanical properties of stirrups

Type	Diameter in.	Area	Yield stress (0.2%) ksi	Ultimate stress ksi	Ultimate strain (in./in.)	Elastic modulus ksi
stainless steel	0.5	0.2	83.39	119.8	0.0265	29000
GFRP	0.526	0.217	-	131.4	0.0187	7042

Table 3 Design Matrix

		Transverse reinforcement	
		GFRP	Stainless steel
Longitudinal prestressing	11 carbon steel strands		Girder 1 (control)
	11 stainless steel strands	Girder 2	
	13 stainless steel strands	Girder 3	Girder 4

Girder 2 had eleven HSSS strands as longitudinal prestressing and GFRP rebars as transverse reinforcement. The objective of this design was to match the prestressing ratio with the control girder and compare their flexural behaviors. The eleven HSSS strands were pretensioned to 37.2 kips or 62.2% of their ultimate strength. The prestressing ratio and total prestressing force were 0.685% and 409.2 kips, respectively, and the GFRP shear reinforcement ratio was 0.603%.

Girders 3 and 4 had thirteen HSSS strands as longitudinal prestressing. The transverse reinforcement of Girder 3 was GFRP rebars, while Girder 4 had stainless steel rebars. The objective of the design was to match the total prestressing force with the control girder and compare their flexural behaviors. The HSSS strands were pretensioned to 37.2 kips, and to match the total prestressing force with the control girder, the total number of strands was increased to thirteen. The prestressing ratio

and total prestressing force were 0.810% and 483.6 kips, respectively. The GFRP and stainless steel shear reinforcement ratios for Girder 3 and Girder 4 were 0.603% and 0.555%, respectively.

The four 42-ft long AASHTO type II girders were constructed at Dura-Stress prestressing plant in Leesburg, Florida. All three HSSS girders were fabricated in one casting bed. Therefore, two strands had to be debonded for the whole length in Girder 2. The HSSS strands did not require any special equipment or procedures. Regular chucks were used to tension them. The girders were transported to the FDOT Structures Research Center in Tallahassee, Florida. At the FDOT lab, a deck slab was cast onto the girder and made it composite. The deck slab had a 10-in. thickness, including a 2-in. haunch, and 24 in. width. The interface shear reinforcement ratio was 0.278% for Girder 1 and 4 and 0.301% for girders 2 and 3. It should be noted that the concrete surface was smooth at the interface region between the deck slab and girder. All girders were designed to resist shear and fail in flexure. Shear reinforcement was designed based on the mechanical properties of carbon steel rebars. It was normal to use stainless steel rebars since their mechanical properties are higher than those of carbon steel rebars. The stainless steel shear reinforcement in Girder 1 was replaced on a one-to-one basis with GFRP rebars in Girder 2 and Girder 3.

2.3 Instrumentation and Testing

During the fabrication process, after tensioning strands and before casting concrete, two vibrating wire gages were installed in each specimen, at the bottom layer of the strands. Those vibrating wire gages were used to measure the prestress losses in the strands. The reference reading for each vibrating wire gage was taken after casting concrete and before releasing the strands. Thereafter, any reading compared to the reference reading can be used to determine the effective prestress in the strands at the time of that reading. For flexural testing, each specimen was instrumented with strain, deflection and strand slip gages. The strain gages were installed along the depth of the girder at three locations in the constant moment region. Multiple deflection gages were installed along the length of the girder, to measure the vertical displacement of the specimen during the test. The strand slip gages were installed on all bottom layer strands to monitor any slip in the strands during the flexural test. The load was applied by a hydraulic jack at a rate of 0.25 kip/sec. Two load cells, placed at the center of the load frame, were used to measure the applied load.

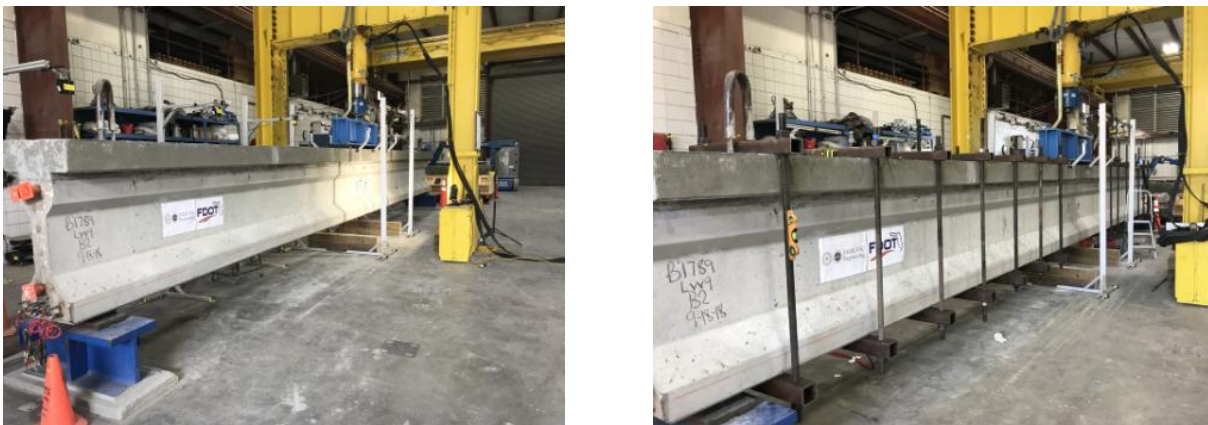


Fig. 2 Test setup for Girder 2; (left) before adding clamps and (right) after adding clamps.

All four girders were tested using a four-point loading scheme. The clear span was 40 ft with the point loads each spaced 3 ft from the midspan. The girder was placed on thick neoprene pads to create a simply-supported condition. Girder 2 was the first specimen to be tested among the four specimens (see Fig. (left)). Slightly after cracking load, a shear crack initiated at the end of the girder, and therefore it was decided to unload the specimen. One solution to prevent shear failure in a member is to externally reinforce it with steel rods [9]. In this work, it was decided to use external clamped steel rods (see Fig.2 (right)) to reinforce the section and prevent it from failing in shear. The steel rods were not attached to the steel frame and therefore did not influence the rotation of the specimen. Girder 2 was then loaded to failure. As mentioned before, the main objective of this experimental program was to study the flexural behavior of girders prestressed with stainless steel strands. For

consistency in the testing procedure, the other three specimens were also reinforced with the external threaded rods.

3 Results and Discussion

All four specimens were tested under static load up to failure except for Girder 1, which was unloaded before failure to save it for a future shear test. Experimental load-deflection curves for all tested girders are shown in Fig. 3. The load-deflection curve is divided into two regions, separated by initiation of the first flexural cracking. All specimens behaved linearly in the pre-cracking region. All HSSS girders exhibited similar post-cracking behavior up to failure, which was different than that for the control specimen. The mechanical characteristics of HSSS strands are different from those of carbon steel strands; therefore, it was expected that specimens prestressed with HSSS strands would behave differently after cracking load. Unlike carbon steel strands where they reach plateau after yielding, HSSS strands exhibit no discernible yield plateau. The capacity of all HSSS specimens increased up to failure, which reflects the stress-strain behavior of the HSSS strands.

GFRP rebars have lower elastic modulus and ultimate strain compared to carbon and/or stainless steel rebars. The stiffnesses of Girder 2 and Girder 3 were significantly reduced, and this was not taken into consideration during design. Because GFRP rebars are made from an anisotropic material, their longitudinal strength is much higher than their transverse strength. Therefore, interface shear failure was another issue in Girder 2 and Girder 3 because GFRP rebars do not provide high strength in the transverse direction and the interface region was smooth.

Table 4 shows the main test results captured during testing. Discussion and comparison of the experimental results are summarized below:

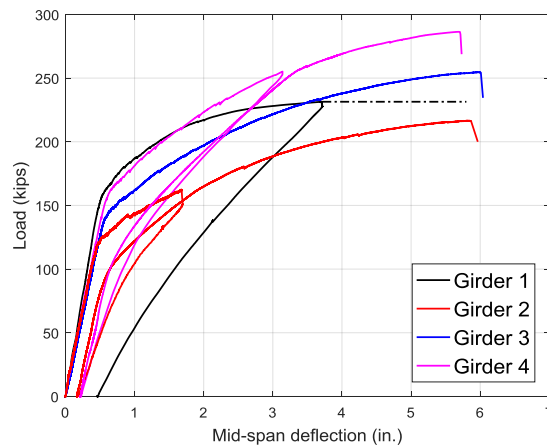


Fig. 3 Load-deflection curves for the tested girders

3.1 Girder 1 and Girder 4

Girder 1 and Girder 4 had a similar prestressing force but different prestressing type. Deflection increased linearly with applied load up to initiation of the first flexural crack. After cracking load, the behavior of Girder 4 was almost identical to Girder 1 up to a point where Girder 1 deflection increased more rapidly compared to Girder 4 (Fig. 3). Girder 1 was loaded until the load-deflection curve plateaued at 231.4 kips. The permanent deflection was 0.460 in. after unloading. Based on an analytical model, the calculated capacity and deflection for Girder 1 were 231.4 kips and 5.8 in., respectively. Girder 4 was loaded up to 90% of its calculated capacity and then unloaded. The permanent deflection was 0.216 in. after unloading. Then, it was loaded up to failure, to 286.3 kips. Even though Girder 4 failed by rupturing of all HSSS strands, it exhibited good deformability compared to Girder 1, and it also performed well in terms of capacity. The ultimate capacity of Girder 4 was approximately 23.7% higher than that of Girder 1.

Girder 1 and Girder 4 had approximately similar stiffnesses in the elastic region. The stiffness started to decrease in the plastic region, and the rate of decrease was higher in Girder 1 compared to Girder 4. This is attributed to the mechanical properties of the prestressing strands.

Table 4 Flexural test results

	Cracking load kips	Cracking deflection in.	Ultimate load kips	Ultimate deflection in.	Failure mode
Girder 1 (expected)	143.2	0.455	(231.4)	(5.800)	(Crushing of concrete)
Girder 2	115.6	0.445	216.7	5.835	Rupture of strands
Girder 3	132.6	0.530	254.7	5.969	Rupture of strands
Girder 4	143.6	0.535	286.3	5.693	Rupture of strands

3.2 Girder 3 and Girder 4

Girder 3 and Girder 4 had similar prestressing type and force but a different type of transverse reinforcement: GFRP for Girder 3 and stainless steel for Girder 4. The overall flexural behavior of Girder 3 was significantly reduced due to the use of GFRP stirrups. Deformation almost all comes from flexure. In structures design, we assume shear deformation are zero, unless it is a deep beam. The increase in deflection also be attributed to the low interface shear reinforcement and concrete surface condition at the interface region, which affected the composite interaction of the girder and deck slab. Even though Girder 3 and Girder 4 had the same prestressing type and force, the cracking and ultimate loads of Girder 3 were 7.7% and 11.0% lower than those of Girder 4, respectively. However, the cracking and ultimate deflections were almost equal for both girders. After flexural tests, Girder 3 and Girder 4 were visually inspected, and results showed that more cracks were originated throughout the length in Girder 3 than in Girder 4, as shown in Fig. 4. Increased cracks in Girder 3 attributed to the reduction in the member's stiffness due to the use of GFRP rebars.

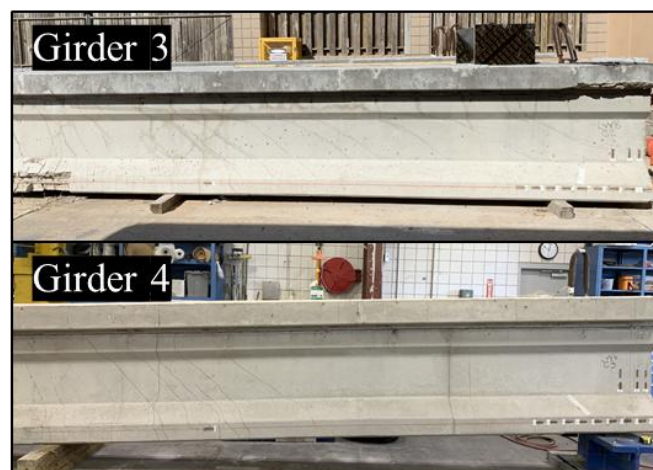


Fig. 4 Crack patterns at ultimate load for Girder 3 and Girder 4

3.3 Girder 2 and Girder 3

Girder 2 and Girder 3 had the same prestressing and transverse reinforcement type, but different prestressing force. Girder 3 had two additional prestressing strands, which increased the initial prestressing force by 18.2% compared to Girder 2. Although Girder 2 and Girder 3 failed approximately at the same deflection, an approximate increase of 17.5% in the ultimate capacity was achieved.

4 Failure modes

The failure mode depends on the type and ratio of prestressing. The HSSS strands used in this study had an ultimate strain of 1.89%, which is lower than the minimum specified ultimate strain for carbon steel strands. As designed, all specimens prestressed with HSSS strands failed by rupture of all strands. Fig. 5 shows Girder 4 at failure, where all HSSS strands in the bottom flange broke while the concrete at the top face was still intact. From Fig. 5, Girder 4 exhibited many flexural cracks before failure. Rupture of strands might be considered as brittle failure; however, all HSSS specimens failed at a large deflection, as shown in Fig. 3, with many flexural cracks in the mid-span. Therefore, regardless of failure mode, the stainless steel girders can achieve ultimate capacity and deflection as high as girders prestressed with carbon steel strands.



Fig. 5 Girder 4 at failure load (rupture of strands failure)

5 Design Guidelines

Current design guidelines developed for concrete members prestressed with carbon steel strands are based on decades of research and lessons learned from field applications. HSSS strands are relatively new to the construction industry, and limited research has been performed. A complete design guideline is still under development, and there might be still room for improving the mechanical characteristics of the HSSS strands. Three flexural design considerations are feasible when HSSS strands are used, and they are as follows:

1. Crushing of concrete failure where concrete top fiber strain reaches its ultimate value $\epsilon_{cu} = 0.003$, while the bottom layer of strands does not reach its ultimate strain $\epsilon_{pu} < 0.014$.
2. Balanced failure where the concrete top fiber strain and bottom layer of strands reach their ultimate values of $\epsilon_{cu} = 0.003$ and $\epsilon_{pu} = 0.014$, respectively. This design mode is theoretically possible to achieve but hard to achieve experimentally due to high uncertainty of many design parameters such as strength of concrete and effective prestressing force.
3. Rupture of strands failure where concrete top fiber strain does not reach its ultimate value, i.e., $\epsilon_{cu} < 0.003$, while the bottom layer of strands reaches ultimate strain, $\epsilon_{pu} = 0.014$, and ultimately rupture. All stainless steel specimens in this study were designed following this flexural design consideration.

6 Conclusion

Based on an experimental program including testing full scale 42-ft long AASHTO type II girders prestressed with HSSS or carbon steel strands and reinforced with GFRP or stainless steel rebars as shear reinforcement, the following conclusions can be drawn:

1. Flexural behavior of all specimens, whether prestressed with HSSS or carbon steel strands, was almost identical and linear up to the initiation of first cracking. HSSS girders exhibited different post-cracking behavior compared to that of the control girder. This is attributed to the differences in the mechanical properties between the two strands.

2. HSSS girder prestressed with the same initial prestressing force as the control girder had higher stiffness. The ultimate capacity of the HSSS girder was approximately 23.7% higher than that of the control girder.
3. The flexural behavior of all three HSSS girders were controlled by rupture of the HSSS strands. Even though all three HSSS girders failed by rupture of the strands, their ultimate deflections were almost equal to that of the control girder.
4. Direct replacement of the shear reinforcement from stainless steel rebars to GFRP rebars decreased the ultimate capacity of the member by 11%.
5. The ultimate capacity of the HSSS girder was increased by 17.5% when the initial prestressing force was increased by 18.2%.

7 Acknowledgement

The authors wish to express their gratitude and sincere appreciation to the Florida Department of Transportation for funding this study. Special thanks are extended to Sam Fallaha, Will Potter and Vickie Young for their continuous support and guidance. Also, we would like to thank Steve Eudy, Justin Robertson, Paul Tighe, Ben Allen, Miguel Ramirez and Michael Waters at the Florida Department of Transportation Structures Research Center for their assistance in testing specimens; the work was enjoyable and well executed because of their expertise and enthusiasm. The opinions, findings and conclusions expressed in this publication are those of the authors and not necessarily those of the Florida Department of Transportation or the U.S. Department of Transportation.

8 References

- [1] Federal Highway Administration. 2018. "National Bridge Inventory." February 1. <https://www.fhwa.dot.gov/bridge/nbi/ascii.cfm>
- [2] ASTM (American Society for Testing and Materials). 2017. "Standard Specification for Stainless Steel Bars and Shapes." ASTM A276. West Conshohocken, PA.
- [3] Moser, Robert D., Singh, Preet M., Kahn, Lawrence F., Kurtis, Kimberly E. 2012. "Chloride-Induced Corrosion Resistance of High-Strength Stainless Steels in Simulated Alkaline and Carbonated Concrete Pore Solutions." *Corrosion Science* 57:241-53.
- [4] Mullins, Gray, Sen, Rajan, Sagüés, Alberto. 2014. "Design and Construction of Precast Piles with Stainless Reinforcing Steel."
- [5] Schuetz, Daniel P. 2013. "Investigation of High Strength Stainless Steel Prestressing Strands." MSc. Georgia Institute of Technology.
- [6] Moser, Robert D., Kahn, Lawrence F., Singh, Preet M., Kurtis, Kimberly E. 2013. "Preliminary Studies of High-Strength Stainless Prestressing Steels." *ACI Special Publication* 291:1-10.
- [7] Florida Department of Transportation. 2020. "Standard Specifications for Road and Bridge Construction." February 1st. <https://www.fdot.gov/programmanagement/Implemented/SpecBooks/default.shtm>
- [8] ASTM (American Society for Testing and Materials). 2017. "Standard Specification for Steel Strand, Uncoated Seven-Wire for Prestressed Concrete." ASTM A416. West Conshohocken, PA.
- [9] Chehab, Alaa I., Eamon, Christopher D., Parra-Montesinos, Gustavo J., Dam, Thai X. 2018. "Shear Testing and Modeling of AASHTO Type II Prestressed Concrete Bridge Girders." *ACI Structural Journal* 115:801-11.

Experimental and numerical studies of nodes of light steel-reinforced concrete structures

Anton Hasenko, Oleksandr Semko, Oleksandr Drobotia, Vitalij Sirobaba

*Educational and Scientific Institute of Architecture and Construction,
National University "Yuri Kondratyuk Poltava Polytechnic",
Pershotravnevyj Ave. 24, Poltava (36011), Ukraine*

Abstract

The work of lightweight concrete in steel-concrete structures differs from heavyweight concrete. The article describes experimental and numerical studies of nodes of spatial steel-concrete composite columns from lightweight concrete in thin-walled shell. It was determined that a polystyrene concrete work in a closed steel shell increases the structures bearing capacity on average in 2 times. This spatial structure destruction occurs with clear signs of loss not local but general stability. This fact increases the spatial structure overall stability by more than 1.5 times.

1 Introduction

Born as a building structure about a century ago, steel-concrete structure has recently become more widely used in various fields of construction, proof of which is the development of relevant regulations [7]. This is a good combination of steel and concrete, through which compressed steel-concrete structures have a high strength, reliability, durability, meet the requirements of high manufacturability at relatively lower costs of materials [13]. These compressed elements are used as columns, individual compressed elements of farms or frames, road signs columns [11], etc.

A large number of steel-concrete structures studies are based on the combination of a steel shell more than 1 mm thick and heavy concrete with strength class above C8/10 [12]. Lightweight concrete in thin-walled shell structures have not been studied enough to date [15]. Under the thin-walled shell means a shell from light thin-walled steel profiles. Distinctive features of such profiles are significantly reduced metal consumption in comparison with traditional steel structures, rational constructive form of cross sections, use of high-strength steel with galvanized anti-corrosion coating. The work of lightweight concrete in steel-concrete structures differs from that heavyweight concrete [9].

In the course of parallel experimental study and finite elements' numerical simulation of light steel-concrete structures, it is possible to reveal their destruction nature or the stability's loss form [16]. Also it is possible to identify places of stresses concentration on their surface (the places of destruction) and to study in more detail the work of structure internal invisible parts [10].

2 Analysis of recent research and publications

The analysis of research of frames from easy thin-walled steel profiles nodes is reduced to consideration of the carried-out tests' of spatial structures results [8]. During the analysis of existing scientific publications, special attention was paid to the following questions:

- the choice of a rational type of nodes point fastening (it is necessary at the subsequent carrying out of finite-element modeling of node points work) [5];
- the main factors influencing the transition of the structure to the limit state (it is necessary at the further optimization of knots design) [4];
- features of structures from easy thin-walled steel profiles behavior under loading [14].

Fastening nodes (joints) should be divided into two groups: connections in structural nodes and connections along a wall or shelf to form a composite cross section. On the need for additional nodes installation along the length of the elements indicates a number of experiments. The number and type of these fasteners have a direct impact on the shape of the element stability loss. Fig. 1 shows three main known forms of elements from thin-walled steel profiles stability loss [6]. There are also transitional forms of stability loss. For example, the local shape can turn into cross-sectional distortion shape; cross-sectional distortion shape can turn into general shape (etc.). Forms of stability loss are dependent on each other, affect each other, and flow into each other [1].

Forms of elements from light thin-walled steel profiles stability loss

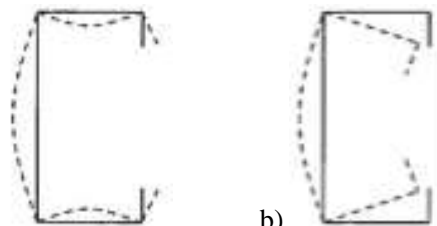
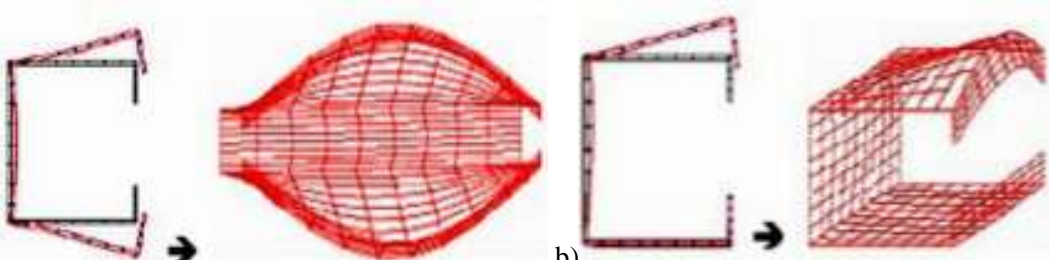
1	<p><u>Local form of stability loss</u> is a protrusion of the shelf, wall or bend from the axis alternately in one or other side of the element. In this case the angles between the shelf and the wall remain straight.</p> 
2	<p><u>Distortional form of stability loss</u> represents a stability loss with distortion of the cross section. For example, the side remains straight and the shelves protrude, causing the corners to change at their joints. Half-waves of stability loss along the length are distributed periodically, bending in one direction or another.</p> 
3	<p><u>General stability loss</u>, which is also characteristic of traditional profiles. It is determined first in the calculation, then check other forms of stability loss. Subspecies:</p> <p>3.1 <u>bending (Euler) form of stability loss</u>;</p> <p>3.2 <u>torsional shape of the loss of stability (twists the cross section, and the axes remain straight)</u>;</p> <p>3.3 <u>bending-torsional form of stability loss</u>.</p>

Fig. 1 Forms of elements from light thin-walled steel profiles stability loss.

Today, the results of numerical modeling of building structures using computer programs based on the finite element method are increasingly covered in the scientific literature. Computer simulation allows detailed research of rod elements in composite structures [2], as well as complete analysis of the three-axis stress-strain condition of structures [3].

When modeling elements from thin-walled profiles to simplify the model, the method of finite elements is usually modified (see fig. 2), which does not reduce the accuracy of the calculation results.

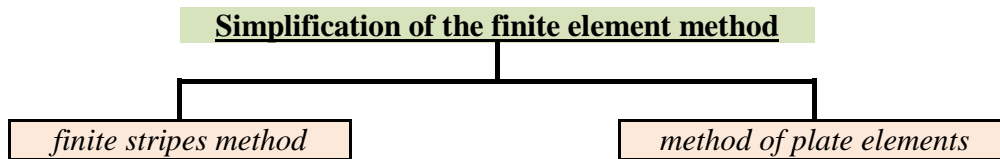


Fig. 2 Modification of the finite element method when calculating elements from thin-walled profiles.

Finite stripes method discretizes the cross section of the profile into longitudinal stripes, whereas along the length of the rod sampling is not provided. The method of finite strips is based on finding the critical loads for the three forms of loss of stability in the elastic stage (see fig. 1). This takes into account the interaction of the cross-sectional elements of the profile as a single rod.

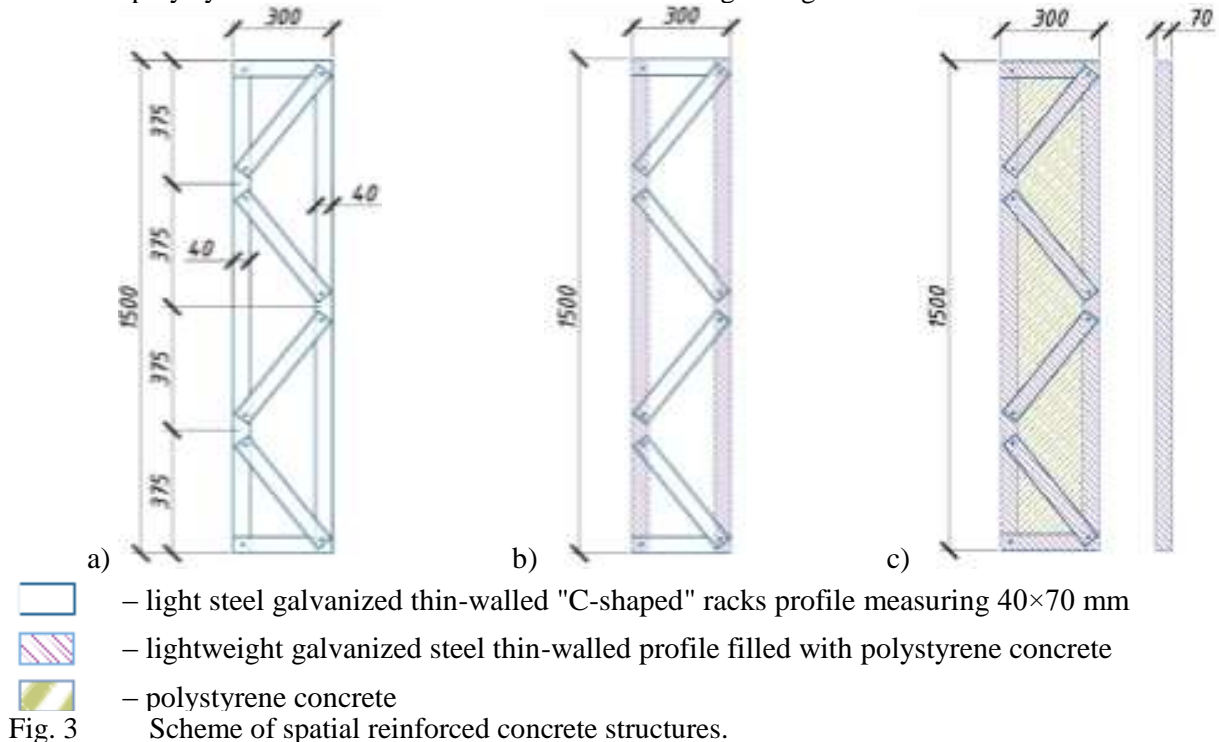
Method of lamellar elements replaces the section with a set of plates with different conditions of support along the contour. The influence of adjacent plates interaction (for example, between a wall and a shelf, a shelf and a bend) on the entire cross section stability loss is not always taken into account. In addition, if the profile cross section contains edge or intermediate elements of rigidity, the calculation is greatly complicated [17].

3 Formulating of the article's goals

The purpose of the work is to describe the experimental and numerical results of spatial steel-concrete composite columns nodes studies. The relevance of the topic is due to the efficiency of lightweight structures, the possibility of using this structures type both in new construction and in the existing steel structures strengthening.

4 The results of experimental and numerical studies of nodes of spatial steel-concrete composite columns

To evaluate the efficiency of concreting of spatial structure from light steel thin-walled structures with lightweight concrete with polystyrene filler, it was produced, experimentally studied and numerically simulated by finite element method the work of the three groups of samples. The test samples represented dimensional through columns with overall dimensions of 1500×300 mm, consisting of two "C-shaped" racks measuring 40×70 mm with a thickness of 0.42 mm and a system of brackets between them (see fig. 3). The elements of the spatial structure were connected to each other by exhaust rivets. The first group of samples was made without concrete (see fig. 3, a). In the second group only racks were concreted (see fig. 3, b). The third group was made with concreted racks and full filling of the space between the brackets with concrete (see fig. 3, c). Lightweight polystyrene concrete with a density of D750 was used for concreting spatial structures. Lightweight polystyrene aggregate with a diameter of 3-5 mm according to laboratory studies accounted for 60% of the total volume of polystyrene concrete [15]. Spatial columns were tested on the central compression (see fig. 4 and 5). Comparison of three types of columns assessed the effectiveness of the use of polystyrene concrete as a structural material for lightweight reinforced concrete structures.



The destruction of the first group of samples was the result of local sustainability profile racks shelves loss at the locations of the rivets and planes of the point load application and boundary conditions. The destruction of the second series of samples was the result of a total resistance loss of the concrete racks and the subsequent destruction of the mounting points of the brackets to the racks. The concreting of the spatial column was positively noted in the work of the structure. It should be noted that the brackets stability loss was observed after the cut of the rivets that attached these brackets to the racks. The deformations of the racks were made taking into account the overall stability of the element.

According to the results of experimental studies, it was determined that the work of polystyrene concrete in a closed steel shell space increases the bearing capacity of structures by 2 times. The nature of deformations of two-component reinforced concrete structures made from light steel thin-walled profiles and polystyrene concrete shows that the destruction occurs with clear signs of loss not

local but general stability. This fact increases the overall bearing capacity of the spatial structure by more than 1.5 times. The destruction of the nodes occurred as a result of the loss of local stability of the shelves of the compressed thin-walled profile of the brackets. In the case of stretched braces, the destruction of the node occurred as a result of cutting the rivets of the connection.

Numerical studies were performed using numerical simulation in the software package NASTRAN (NAsa STRuctural ANalysis) Femap 10.1.1 SC 32bit (training demo version SDRCFEMAP 8 / 1a S / N 000-00-00-DEMO-406F-00000000) finite elemental analysis. This program allows you to specify complete nonlinear diagrams of the materials used in the construction. Hexahedrons were used to model polystyrene concrete, and flat elements with a side size of 10 mm, which is 2.5% of the sample height, were used for the steel shell [16]. Photographs of the samples after experimental and numerical studies are shown in Figures 4 and 5.

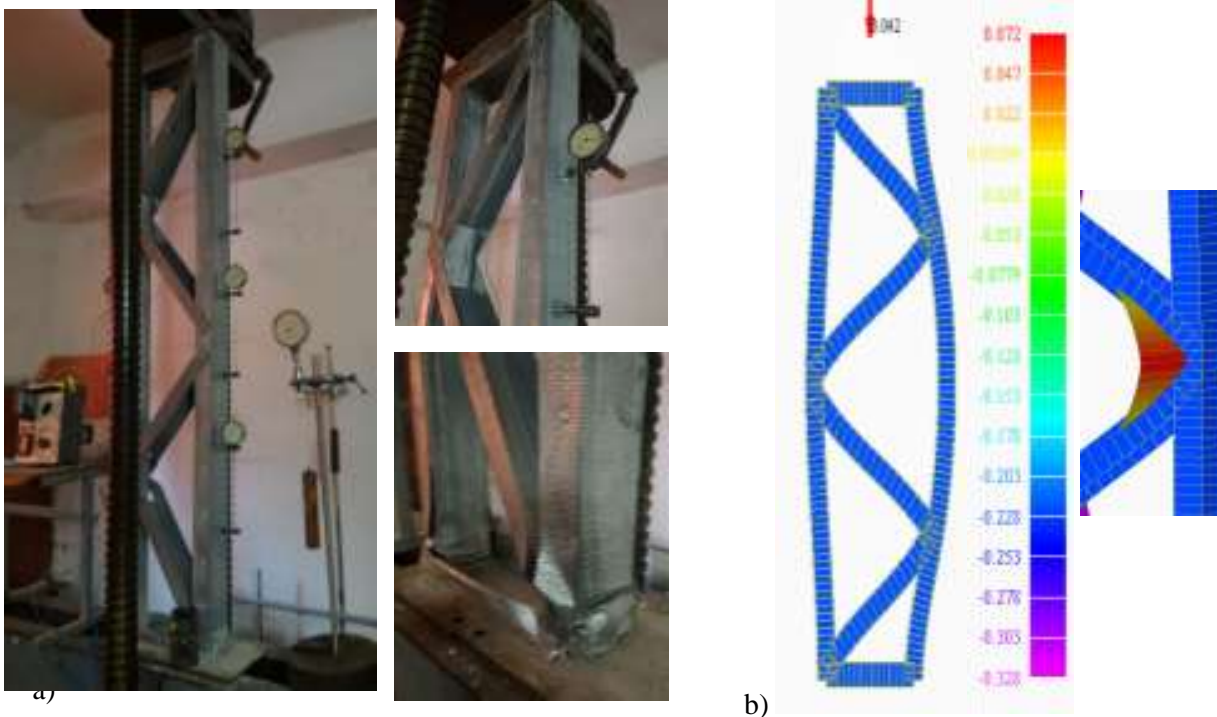


Fig. 4 Results of experimental (a) and numerical (b) studies of spatial columns made of light steel thin-walled profiles.

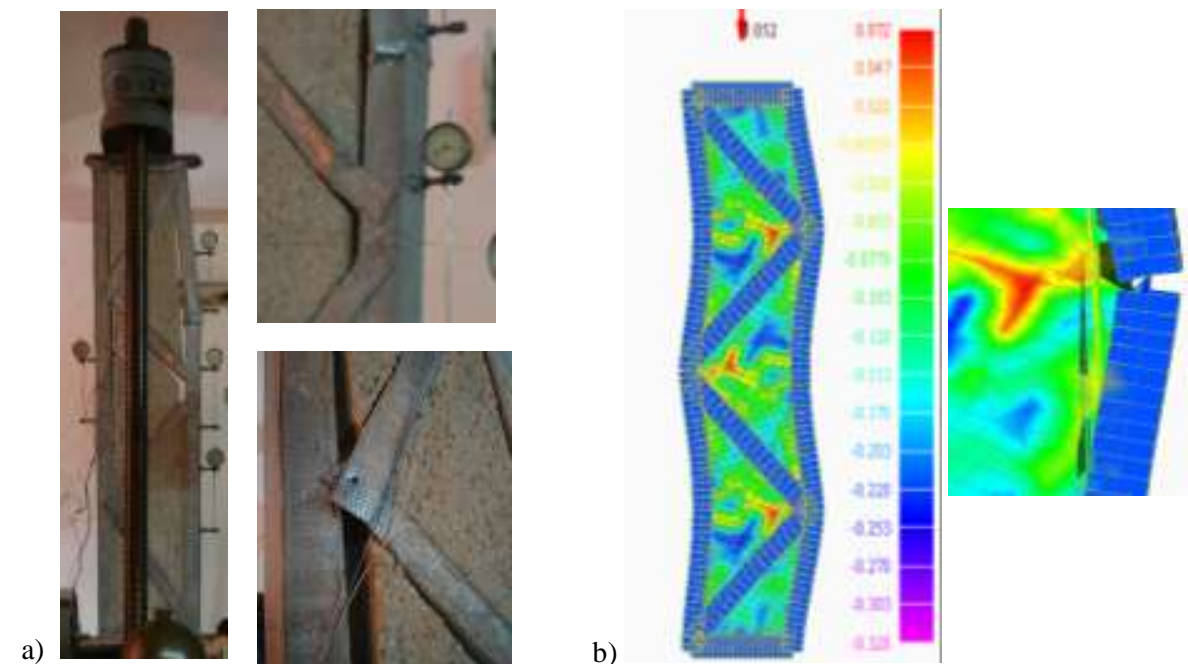


Fig. 5 The results of experimental (a) and numerical (b) studies of spatial lightweight steel-concrete columns.

In Figures 4, b) and 5, b) show the stress distribution in the nodes of spatial structures, which obtained as a result of numerical simulations. Analysis of the submitted stress distributions revealed the following. In the rod spatial structures, the weakest point is the nodal connection. In this case, the greatest stresses occur in the nodal zones of the braces. In the second case, when filling the interior of the structure with light concrete, the contact between the steel bars and the filling concrete is first broken. Then the fracture process repeats scenario of the first series of samples fracture.

5 General conclusions on the conducted studies and directions of further scientific researches

According to the results of experimental studies and numerical modeling of spatial steel-concrete structures of light thin-walled profiles filled with light polystyrene concrete, the loss of the total bearing capacity of the studied structures occurs primarily as a result of nodal joints destruction, which leads to a loss of local stability of the shelves in the elements. The failure of individual elements leads to a general stability loss of the entire spatial structure.

In order to increase the load-bearing capacity of the studied structures, it is proposed to perform a number of measures shown in Figure 6. These measures are related to the formation of the Pre-stresses in the elements of spatial structures. The purpose of *clamps installation along the length of the elements* is to provide joint work of a steel thin-walled cover and an internal core from polystyrene concrete. The step of installing such clamps (see fig. 7, a) is determined from the conditions of ensuring the local stability of shelves or walls of thin-walled profile. Pre-stresses by installing clamps along the length of the elements are provided by their tension (bolt or temperature). The purpose of *creation of the previous "negative" deflection before concreting* is the creation of pre-stresses in these elements (see fig. 7, b). Pre-stresses by creating a "negative" deflection are controlled by the magnitude of the pre-bending of the elements.

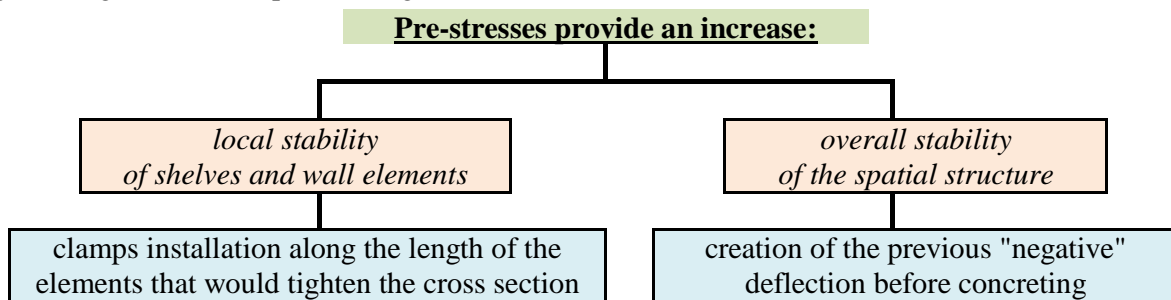


Fig. 6 Proposed measures to increase the load-bearing capacity of spatial reinforced concrete structures made of light thin-walled profiles filled with light polystyrene concrete.

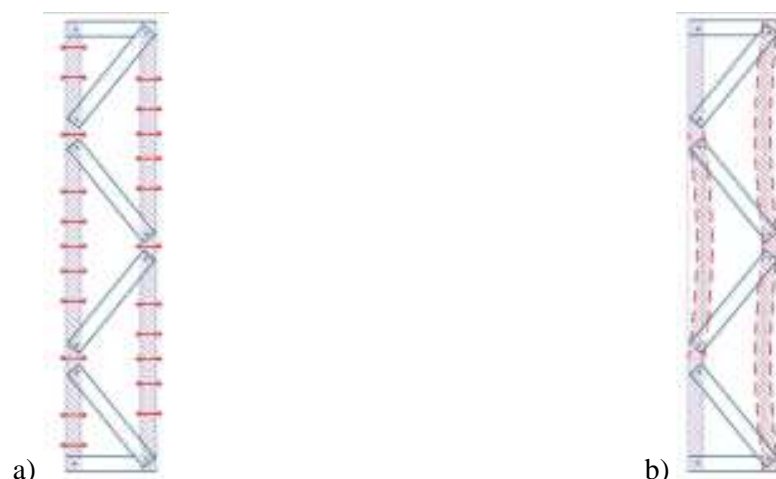


Fig. 7 Creation of previous stresses in the elements of the spatial steel-concrete structure: a) installation of clamps; b) creation before concreting of previous "negative" deflection.

Therefore, these measures will increase the stability of the elements. But to increase the overall load-bearing capacity of structures, it is also necessary to take measures to ensure the joint operation of steel rod elements and internal concreting.

References

- [1] Azizov T., Kochkarev D., Galinska T. 2020. “Reinforced concrete rod elements stiffness considering concrete nonlinear properties.” *Lecture Notes in Civil Engineering* 47: 1–6. https://doi.org/10.1007/978-3-030-27011-7_1
- [2] Beicha D., Kanit T., Brunet Y., Imad A., Moumen A. E., Khelfaoui Y. 2016. “Effective transverse elastic properties of unidirectional fiber reinforced composites.” *Mechanics of Materials* 102: 47–53.
- [3] Bishnu P.G., Daman K. P. 2016. “A new method of applying long-term multiaxial stresses in concrete specimens undergoing ASR, and their triaxial expansions.” *Materials and Structures* 49 (9): 3409–3508. doi: 10.1617/s11527-015-0734-z.
- [4] Cherednikov V., Voskobiinyk O., Cherednikova O. 2017. “Evaluation of the warping model for analysis of polystyrene concrete slabs with profiled steel sheeting.” *Periodica Polytechnica Civil Engineering* 61(3): 483–490.
- [5] Dmytrenko T., Semko O., Dmytrenko A., Derkach T., Voskobiinyk O. 2018. “Development and implementation of algorithms of building structure engineering calculations for shear fraction under pressing-through.” *MATEC Web of Conferences* 230. <https://doi.org/10.1051/mateconf/201823002004>
- [6] EN 1993-1-6: 2007. *Eurocode 3 Design of steel structures. Strength and Stability of Shell Structures*.
- [7] EN 1994-1-1. 2004. *Eurocode 4: Design of composite steel and concrete structures – Part 1.1: General rules and rules for buildings*.
- [8] Hasenko A.V., Pihul' O.V., Mahan I.V. 2010. “Modelyuvannya napruzhenno-deformovanoho stanu bezkapitel'nykh vuzliv monolitnoho zalizobetonnoho perekryttya iz stalebetonnomy kolonamy.” *Visnyk SNAU. Seriya : Budivnytstvo* 11 (14): 53–60.
- [9] Leshchenko M., Semko V. 2015. “Thermal characteristics of the external walling made of cold-formed steel studs and polystyrene concrete” *Inzhenerno-stroitel'nyy zhurnal* 8: 44–55. doi: 10.5862/MCE.60.6.
- [10] Liang K., Ruess M., Abdalla M. 2016. “An eigenanalysis-based bifurcation indicator proposed in the framework of a reduced-order modeling technique for non-linear structural analysis.” *International Journal of Non-Linear Mechanics* 81: 129–138. doi: 10.1016/j.ijnonlinmec.2016.01.013.
- [11] Lytvynenko T., Tkachenko I., Gasenko L. 2017. “Principles of the road beautification elements placing” *Periodica Polytechnica Transportation Engineering* 45(2): 94–100.
- [12] Mahas N.M. 2016. “Naskrizni zalizobetonni konstruktsiyi z zovnishnim lystovym armuvanniam.” *Stalezalizobeton. Continuance: zb. nauk. prats'. Pid red. Storozhenka L.I. Poltava, PoltNTU*: 245 – 261.
- [13] Pavlikov A.M., Mykytenko S.M., Hasenko A.V. 2018. “Effective structural system for the construction of affordable housing.” *International Journal of Engineering & Technology: Publisher of International Academic Journals: Science Publishing Corporation, RAK Free Trade Zone* 7, No 3.2: 291–298. doi: 10.14419/ijet.v7i3.2.14422.
- [14] Semko V.O., Hasenko A.V., Mahas N.M., Fenko O.G., Sirobaba V.O. 2019. “Stability of light steel thin-walled structures filled with lightweight concrete.” *IOP Conference Series: Materials Science and Engineering* 708(1). doi: 10.1088/1757-899X/708/1/012071.
- [15] Semko O.V., Hasenko A.V., Mahas N.M., Sirobaba V.O. 2018. “Bearing Capacity and Deformability of Three-Component Steel Reinforced Concrete Constructions Made of Lightweight Concrete.” *International Journal of Engineering & Technology: Publisher of International Academic Journals. Special Issue 8 – Science Publishing Corporation, RAK Free Trade Zone* Vol 7, No 4.8: 53–57. doi: 10.14419/ijet.v7i4.8.27213.
- [16] Semko O.V., Hasenko A.V., Sirobaba V.O. 2018 “Optymizatsiya rozmiriv ta typu skinchenykh elementiv pid chas modelyuvannya roboty nadlehkykh stalezalizobetonnykh konstruktsiyi.” Paper presented at the annual meeting for the conference: Stalezalizobetonni konstruktsiyi: doslidzhennya, proektuvannya, budivnytstvo, ekspluatatsiya, Poltava, PoltNTU, Vyp 13: 30–32.
- [17] Su Y.Y., Gao X.L. 2014 “Analytical model for adhesively bonded composite panel-flange joints based on the Timoshenko beam theory.” *Composite Structures* 107: 112–118.

General Method of Structural Analysis of Reinforced Concrete Columns under Axial Load and Biaxial Bending

Bohdan Baryliak, Andrii Pavlikov, Olha Harkava

*Educational-Scientific Institute of Architecture and Construction,
National University «Yuri Kondratyuk Poltava Polytechnic»,
Pershotravnevyj Ave. 24, Poltava, 36011, Ukraine*

Abstract

The paper proposes a generalized method for the strength analysis of biaxially bended reinforced concrete columns, developed on the basis of Eurocode 2 recommendations. The theorem on the location of external and internal forces in one plane, which forms an angle with the vertical axis of inertia of the section, is used. Analytical expressions were obtained to determine all parameters when calculating the strength of biaxially bended columns, namely: the angle of neutral axis inclination to the horizontal axis of inertia of the section, the neutral axis depth and the value of the destructive force at the given eccentricities of its application. The proposed generalized analysis method covers all possible positions of the neutral axis in a rectangular section of biaxially bended columns. The calculated dependencies can be used both in checking the bearing capacity of biaxially bended columns and in determining the required area of reinforcement, which confirms the generality of the adopted design model.

1 Introduction

As experience of building structures operation shows, columns of frames of industrial and civil buildings, engineering and special structures are subjected to biaxial bending. Most of the reinforced concrete members of structural systems of buildings, erected by atypical and individual projects, also operate in the conditions of biaxial bending. Additional factors that cause biaxial bending of reinforced concrete columns can be both technological and operational. Defects as well as damages of reinforced concrete structures that occur during operation are factors that cause complex deformation, such as biaxial bending. In addition to these factors, changes of the value and nature of the load application when strengthening building structures can also lead to biaxial bending effect. Because of these reasons, in the axially loaded members, as a rule, there is a displacement of the points of application of resultant forces in the compression and tensile zones of the section from the principal central axes of its inertia, i.e. the member undergoes biaxial bending [1].

Thus, in view of the above examples, it is safe to say that virtually all compressed structures undergo complex deformation. Nevertheless, at present the features of biaxial deformation of reinforced concrete are taken into account conditionally. In particular, the current norms [2] do not include recommendations for the strength analysis of reinforced concrete members for a significant number of cases of their operation in conditions of complex deformation. It is very often in strength analysis a complex stress-strain state is reduced to axial loading and bending moments about each of orthogonal principal axes of inertia separately. This approach naturally may lead to the distortion of the actual state of the structure and, as a consequence, the excessive consumption of materials or even to accidents. Designers are forced to resort to this simplification because the calculations of reinforced concrete structures for complex types of deformation are still quite difficult and are carried out with the use of time-consuming iterative methods. Particularly, the analysis is complicated also by the fact that even in a rectangular section of the column under biaxial bending, the compression concrete zone can take at least three geometric forms other than a rectangle.

2 Analysis of the latest sources of research and publications

The deformation model [3] and variational methods of deformable body mechanics are used [4], [5] to solve the problems of strength analysis of reinforced concrete members under complex stress-strain states. Methods for the strength analysis of reinforced concrete members undergoing biaxial bending have been developed by a large number of scientists. In particular, the problems of analysis biaxially

bended members are solved on the basis of a nonlinear deformation model [6], using two-linear stress-strain diagrams for concrete and reinforcement [1], or based on the concept of design strength of reinforced concrete [7]. The publication [8] notes the problem of estimating the technical condition of structures whose members have been damaged during operation, and because of this, they additionally undergo the phenomena of biaxial deformation. In the works [9] – [10], the problems of strength analysis of biaxially bended members are solved in the general form for cross sections of arbitrary configuration with and without openings, but this approach is difficult for practical implementation, and the proposed simplifications in the form of graphs and diagrams are very approximate. There is an objective need to develop a simplified technique for strength analysis of biaxially bended columns, which combines the required accuracy of calculations with the simplicity of their implementation.

3 Main material

As is well known, the compression concrete zone in a rectangular section of columns subjected to biaxial bending can take the form of a triangle, a trapezoid or a pentagon. Due to the different geometry, the design formulas are offered separately for each of the named forms of the compression concrete zone.

Initially, the problem of obtaining analytical formulas for determining all unknown parameters in the strength analysis of biaxially bended columns with a triangular compression concrete zone is being solved. Theoretical studies are based on the prerequisites for design according to the norms [2]. In this case, compression concrete is assumed a rectangular stress distribution according to [2, Fig. 3.5]. The relationship between stresses and strains in the reinforcement is described by a two-line diagram with a horizontal top branch without strain limit according to [2, Fig. 3.8].

To solve this problem, the design scheme for the cross-section of a reinforced concrete column is used (Fig. 1). The derivation of the design formulas is based on the general equations of equilibrium. Taking into account the accepted assumptions, the design equations of equilibrium in the plane of the coordinate axis Y perpendicular to the neutral axis are written:

$$\sum Z = 0: N_{Ed} + \sum_{i=1}^n N_{si} - N_c = 0; \quad (1)$$

$$\sum M_A = 0: N_c(y_{Ed} - y_{Nc}) + \sum_{i=1}^n N_{si}(y_{Ed} - y_{si}) = 0, \quad (2)$$

where N_{Ed} is the longitudinal force from the external load;

N_{si} is the resultant force in the i -th reinforcing bar;

n is the number of reinforcing bars in the section;

N_c is the resultant force in the compression concrete zone;

y_{Ed} is the coordinate of point of application of force N_{Ed} ;

y_{Nc} is the coordinate of the point of application of the N_c ;

y_{si} is the coordinate of the point of application of the N_{si} .

To simplify the equilibrium equations, the expressions for the resultant force N_c and the coordinate y_{Nc} of its application in the XOY coordinate plane are obtained in the following form:

$$N_c = \frac{\eta f_{cd} \lambda^2 X^2}{\sin 2\theta}, \quad (3)$$

$$y_{Nc} = \frac{X(3-2\lambda)}{3}, \quad (4)$$

where λ is the factor, defining the effective height of the compression zone, and η is the factor, defining the effective strength [2, 3.1.7(3)];

X is the neutral axis depth;

θ is the angle of inclination of the neutral axis to the horizontal axis of inertia of the section.

It is proposed to determine the resultant force N_{si} depending on the value of the stress σ_{si} corresponding to the strain ε_{si} in the design two-line diagram of the reinforcement stress-strain state, based on the expression:

$$N_{si} = \sigma_{si} A_{si}, \quad (5)$$

where A_{si} is the cross-sectional area of the i -th reinforcing bar.

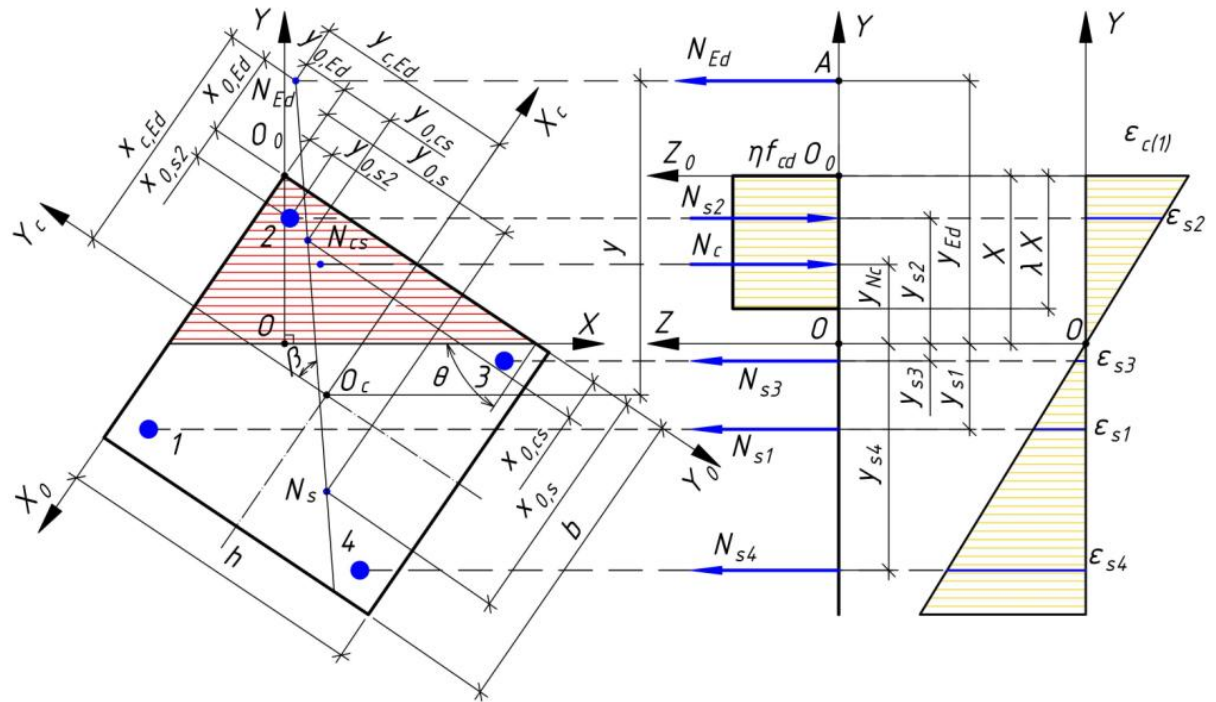


Fig. 1 Design scheme of the cross-section of the biaxially bended reinforced concrete column with a triangular form of the compression zone.

The value of the stress σ_{si} are determined by Hooke's law depending on the relative strain of the reinforcement

$$\sigma_{si} = E_s \varepsilon_{si}, \quad (6)$$

where ε_{si} is the strain in the reinforcement, which is determined using the hypothesis of plane cross-sections (Fig. 1):

$$\varepsilon_{si} = \frac{y_{si} \varepsilon_{c(1)}}{X}, \quad (7)$$

where $\varepsilon_{c(1)}$ is the relative strain of the concrete of the most compressed column rib (fiber strain of concrete).

The deformation criterion of strength is used to determine concrete compression extreme fiber strain $\varepsilon_{c(1)}$ at the moment of destruction. According to this criterion, the destruction of the reinforced concrete member occurs when strain in the concrete at the furthest from the neutral axis point reaches the ultimate value. Therefore, the strength of the biaxially bended reinforced concrete column is checked under the following condition of deformation of concrete:

$$\varepsilon_{c(1)} = \varepsilon_{cu3}, \quad (8)$$

where ε_{cu3} is the ultimate strain according to [4, Table 3.1].

The coordinates of the points of application of the N_{Ed} force and the N_{si} forces in the reinforcing bars in the rectangular section (Fig. 2) are determined as follows:

$$y_{Ed} = X + y - 0,5b \sin \theta - 0,5h \cos \theta, \quad (9)$$

$$y_{si} = X - x_{0,si} \sin \theta - y_{0,si} \cos \theta, \quad (10)$$

where $y = x_c \sin \theta + y_c \cos \theta$;

x_c, y_c are the coordinates of application the force N_{Ed} in coordinate system $X_c O_c Y_c$, which is placed in the geometric center of the section of the column, they are numerically equal to the eccentricities of the application of force N_{Ed} about the vertical and horizontal axes of inertia of the column cross section, respectively;

b is the cross-sectional breadth of the reinforced concrete column;

h is the height of the cross section of the reinforced concrete column;

$x_{0,si}, y_{0,si}$ are the coordinates of the position of the i -th reinforcing bar in the coordinate system $X_0 O_0 Y_0$.

Substituting dependencies (3) – (10) into equations (1) – (2), two equations are obtained with unknowns X , θ , N_{Ed} . In the general case of biaxial bending with axial force, the expression for determining the the neutral axis inclination angle for an elastic body is written as $\tan\theta = I_{Xc} / I_{Yc} \tan\beta$, in which I_{Xc} and I_{Yc} are the moments of inertia of the section about the axes X_c and Y_c , respectively. At the same time, experimental tests [3] have shown that for reinforced concrete members, which have elastic-plastic properties, such a condition is unacceptable. Therefore, for the analytical solution of the problem it is necessary to introduce an additional condition for determining the angle θ of the neutral axis inclination.

Using the theorem of the position of internal and external forces in one plane, two dependencies for the angle β of the inclination of the load plane to the vertical axis of inertia of the cross section in the coordinate system $X_0O_0Y_0$ can be written:

$$\operatorname{tg}\beta = \frac{x_{0,s} - x_{0,cs}}{y_{0,s} - y_{0,cs}}, \quad (11)$$

$$\operatorname{tg}\beta = \frac{x_{0,s} - x_{0,Ed}}{y_{0,s} - y_{0,Ed}}, \quad (12)$$

where $x_{0,Ed}$, $y_{0,Ed}$ are the coordinates of the application point of the force N_{Ed} in the coordinate system $X_0O_0Y_0$;

$x_{0,s}$, $y_{0,s}$ are the coordinates of the application point of the N_s force in the tensile reinforcing bars in the coordinate system $X_0O_0Y_0$, which are determined by the following formulas:

$$x_{0,s} = \frac{\sum_{i=1}^k \sigma_{si} A_{si} x_{0,si}}{\sum_{i=1}^k \sigma_{si} A_{si}}, \quad (13)$$

$$y_{0,s} = \frac{\sum_{i=1}^k \sigma_{si} A_{si} y_{0,si}}{\sum_{i=1}^k \sigma_{si} A_{si}}, \quad (14)$$

where σ_{si} is the stress in the i -th tensile reinforcing bar;

A_{si} is the cross-sectional area of the i -th tensile reinforcing bar;

$x_{0,si}$, $y_{0,si}$ are the coordinates of the position of the i -th tensile reinforcing bar in the coordinate system $X_0O_0Y_0$;

k is a number of tensile reinforcing bars;

$x_{0,cs}$, $y_{0,cs}$ are the coordinates of the application point of resultant force in the concrete of the triangular compression zone and in the compressed reinforcing bars in the coordinate system $X_0O_0Y_0$:

$$x_{0,cs} = \frac{N_c x_{0,c} + N_{sc} x_{0,sc}}{N_c + N_{sc}}, \quad (15)$$

$$y_{0,cs} = \frac{N_c y_{0,c} + N_{sc} y_{0,sc}}{N_c + N_{sc}}, \quad (16)$$

where N_c , N_{sc} are the resultant forces, respectively, in the compression concrete zone and in the compressed reinforcing bars;

$x_{0,c}$, $y_{0,c}$ are the coordinates of the application point of the force N_c of a triangular compression zone in the coordinate system $X_0O_0Y_0$ can be calculated by the following formulas:

$$x_{0,c} = \frac{\lambda X}{3 \sin \theta}, \quad (17)$$

$$y_{0,c} = \frac{\lambda X}{3 \cos \theta}, \quad (18)$$

$x_{0,sc}$, $y_{0,sc}$ are the coordinates of the point of application of the resultant in compressed reinforcing bars in the coordinate system $X_0O_0Y_0$, which can be determined by formulas (15) – (16), in which k is the number of compressed reinforcing bars.

Thus, by equating (11) and (12), it is obtained:

$$\frac{x_{0,s} - x_{0,Ed}}{y_{0,s} - y_{0,Ed}} = \frac{x_{0,s} - x_{0,cs}}{y_{0,s} - y_{0,cs}}. \quad (19)$$

Since the coordinates ($x_{0,c}$, $y_{0,c}$) of the point of application of the resultant N_c in the compression concrete zone depend on the angle θ according to (17) and (18), equality (19) taking into account (15) and (16) is inherently a dependence, which implicitly reflects the function $\theta = f(\beta)$. It allows

determining the angle θ of the inclination of the neutral axis in the section of the biaxially bended column.

The joint solution of equations (1) and (2), taking into account dependencies (8) and (19), makes it possible to calculate all unknown parameters of the stress-strain state of the biaxially bended reinforced concrete column at the moment of destruction for the case of a triangular compression zone that is, to solve the problem of strength analysis.

When changing the form of the compression concrete zone to a trapezoidal design scheme is converted to the form shown in Fig. 2.

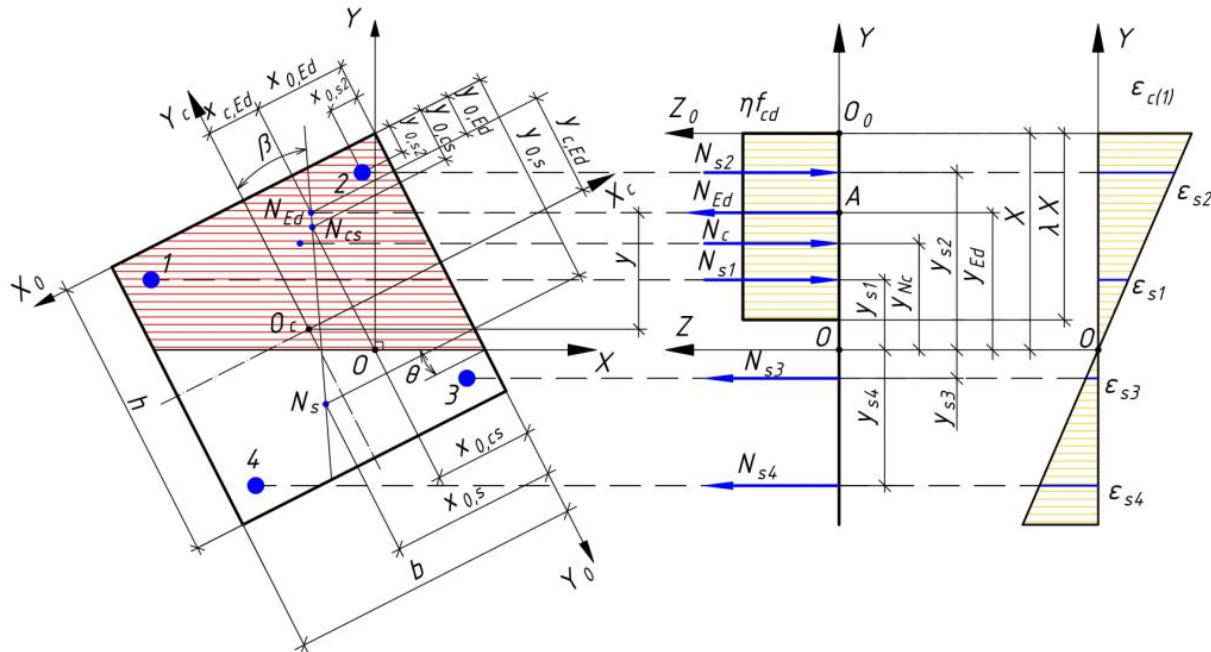


Fig. 2 Design scheme of the cross-section of the biaxially bended reinforced concrete column with a trapezoidal form of the compression zone.

The difference in the analysis from the triangular form of the compression concrete zone consists in using instead of (3) and (4) the following expressions for resultant N_c and y_{Nc} coordinate of its application in the XOY coordinate plane for the trapezoidal form of the compression concrete zone:

$$N_c = \frac{\eta f_{cd} b}{\cos \theta} \left(\lambda x - \frac{b \sin \theta}{2} \right), \quad (20)$$

$$y_{Nc} = \frac{3X^2 (2\lambda - \lambda^2) - b_{eff} \sin \theta (3X - b_{eff} \sin \theta)}{3(2\lambda X - b_{eff} \sin \theta)}. \quad (21)$$

The following formulas instead of (17) and (18) should be used to calculate the coordinates of the point of application of the resultant force in the trapezoidal compression concrete zone in the coordinate system $X_0O_0Y_0$:

$$x_{0,c} = \frac{b(3X\lambda - 2b \sin \theta)}{3(2X\lambda - b \sin \theta)}; \quad (22)$$

$$y_{0,c} = \frac{3X\lambda(X\lambda - b \sin \theta) + b^2 \sin^2 \theta}{3 \cos \theta (2X\lambda - b \sin \theta)}. \quad (23)$$

For the pentagonal form of the compression concrete zone (Fig. 3.) formulas (3) and (4) for resultant N_c and y_{Nc} coordinate of its application in the XOY coordinate plane take the following form:

$$N_c = \eta f_{cd} (A_{c1} + A_{c2} + A_{c3}), \quad (24)$$

$$y_{Nc} = \frac{A_{c1}y_1 + A_{c2}y_2 + A_{c3}y_3}{A_{c1} + A_{c2} + A_{c3}}, \quad (25)$$

where $A_{c1} = ha$; $A_{c2} = (b-a)c$; $A_{c3} = (b-a)c/2$; $a = (\lambda X - h \cos \theta) / \sin \theta$; $c = (\lambda X - b \sin \theta) / \cos \theta$;

$y_1 = \lambda X/2$; $y_2 = \lambda X - h \cos \theta/2$; $y_3 = X - (4\lambda X + h \cos \theta + b \sin \theta)/3$.

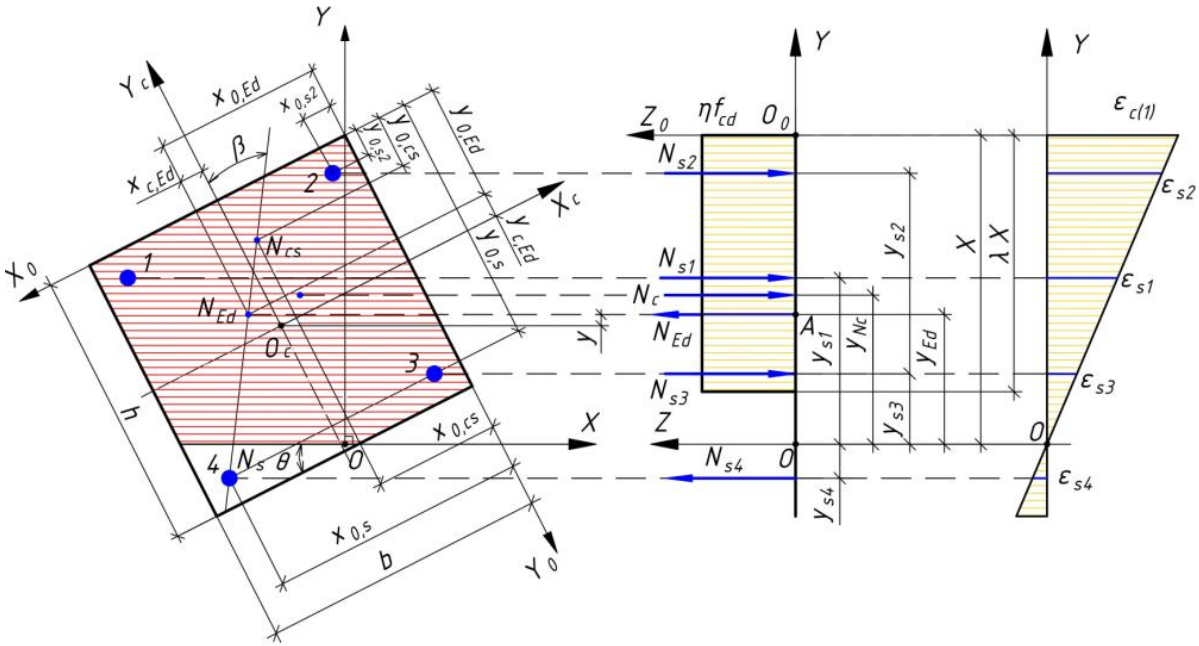


Fig. 3 Design scheme of the cross-section of the biaxially bended reinforced concrete column with a pentagonal form of the compression zone.

The coordinates of the point of application of the resultant force N_c in the pentagonal concrete compression zone in the coordinate system $X_0O_0Y_0$ can be calculated by the following formulas:

$$x_{0,c} = \frac{A_{c1}x_{0,1} + A_{c2}x_{0,2} + A_{c3}x_{0,3}}{A_{c1} + A_{c2} + A_{c3}}; \quad (26)$$

$$y_{0,c} = \frac{A_{c1}y_{0,1} + A_{c2}y_{0,2} + A_{c3}y_{0,3}}{A_{c1} + A_{c2} + A_{c3}}, \quad (27)$$

where $x_{0,1} = a/2$; $x_{0,2} = (b+a)/2$; $x_{0,3} = (b+2a)/3$; $y_{0,1} = h/2$; $y_{0,2} = c/2$; $y_{0,3} = (2c-h)/3$.

It is possible that all the reinforcing bars will be compressed in the pentagonal form of the compression concrete zone. In this case, the angle of inclination of the neutral axis should be determined from the conditions of coincidence of the points of application of the external force N_{Ed} and the resultant force N_{cs} in the compression zone.

Differentiation of cases of a neutral axis position and, accordingly, effective forms of a compression concrete zone, which are taken into account in its height λX , is carried out under such limit conditions:

$$\left. \begin{array}{l} \lambda X \leq b \sin \theta \\ \lambda X \leq h \cos \theta \end{array} \right\} \text{ – a triangular form;} \quad (28)$$

$$\left. \begin{array}{l} \lambda X > b \sin \theta \\ \lambda X \leq h \cos \theta \end{array} \right\} \text{ or } \left. \begin{array}{l} \lambda X \leq b \sin \theta \\ \lambda X > h \cos \theta \end{array} \right\} \text{ – a trapezoidal form;} \quad (29)$$

$$\left. \begin{array}{l} \lambda X > b \sin \theta \\ \lambda X > h \cos \theta \end{array} \right\} \text{ – a pentagonal form.} \quad (30)$$

The results of calculation values of the neutral axis inclination angle θ , the neutral axis depth X , and the strength N_{Em} (ultimate axial force at definite eccentricities about vertical and horizontal axes of inertia of the column section) of the columns by obtained formulas, are compared with experimental data for 25 column samples, which were taken from [3] (Table 1).

The test data for columns with rectangular section of dimensions of 250x350 mm (Fig. 4) are used for comparison. The columns were made of various types of concrete with a mean value of compressive strength $f_{cm} = 25$ MPa, the yield point of the longitudinal reinforcement was $\sigma_y = 420$ MPa.

The coordinates of application point of external load N_{Em} were changed depending on number J in a column code (Fig. 4) in such a way: $J = 1$ ($x_{0,Ed} = 125$ mm, $y_{0,Ed} = 0$ mm); $J = 2$ ($x_{0,Ed} = 62.5$ mm, $y_{0,Ed} = 0$ mm); $J = 3$ ($x_{0,Ed} = 0$ mm, $y_{0,Ed} = 0$ mm); $J = 4$ ($x_{0,Ed} = 0$ mm, $y_{0,Ed} = 62.5$ mm).

Table 1 Comparison of the results of theoretical strength calculations of biaxially bended reinforced concrete columns with experimental data [3].

Sample code	Neutral axis inclination angle θ°			Neutral axis depth X , mm			Destructive force N_{Em} , kN		
	Theor.	Exp.	$\frac{\text{Theor.}}{\text{Exp.}}$	Theor.	Exp.	$\frac{\text{Theor.}}{\text{Exp.}}$	Theor.	Exp.	$\frac{\text{Theor.}}{\text{Exp.}}$
K1-1.1	-20.0	-20.7	0.97	126	136	0.93	542	509	1.06
K1-1.2	33.8	35.6	0.95	212	237	0.89	429	486	0.88
K1-1.3	48.8	53.0	0.92	188	225	0.84	331	378	0.88
K1-2.1	-21.0	-20.2	1.04	94	103	0.91	543	580	0.94
K1-2.2	34.0	33.0	1.03	192	215	0.89	528	584	0.90
K1-2.3	49.2	54.2	0.91	188	209	0.90	370	415	0.89
K1-3.1	-23.0	-22.6	1.02	78	91	0.85	548	576	0.95
K1-3.2	34.0	32.9	1.03	192	210	0.92	528	589	0.90
K1-3.3	49.2	54.5	0.90	188	199	0.95	430	427	1.01
K2-1.1	-10.0	-11.7	0.85	68	77	0.88	369	400	0.92
K2-1.2	25.4	29.6	0.86	128	145	0.88	277	326	0.85
K2-1.3	38.5	50.0	0.77	139	127	1.10	125	137	0.91
K2-2.1	-10.8	-12.0	0.90	68	76	0.90	359	400	0.90
K2-2.2	25.7	30.6	0.84	129	145	0.89	325	345	0.94
K2-2.3	37.1	50.1	0.74	127	120	1.06	225	252	0.89
K2-3.1	-10.9	-10.9	1.00	66	72	0.92	369	396	0.93
K2-3.2	25.7	28.2	0.91	129	124	1.04	375	375	1.00
K2-3.3	37.1	50.6	0.73	127	120	1.06	236	260	0.91
K2-3.4	48.8	65.5	0.74	103	108	0.95	319	340	0.94
K4-1.1	-12.0	-12.1	0.99	96	121	0.79	477	515	0.93
K4-1.2	32.5	34.4	0.94	166	185	0.90	432	466	0.93
K4-1.3	45.4	53.4	0.85	167	162	1.03	311	350	0.89
K4-1.4	53.8	68.2	0.79	161	150	1.08	409	418	0.98
K4-3.1	-13.7	-16.0	0.86	85	96	0.89	513	600	0.86
K4-3.2	32.2	37.9	0.85	166	191	0.87	482	552	0.87
Expectation			0.8960			0.9329			0.9221
Arithmetical mean deviation			0.0774			0.0642			0.0368
Dispersion			0.0090			0.0066			0.0025
Root mean square deviation			0.0949			0.0812			0.0500
Variation coefficient			0.1059			0.0870			0.0542

The position of the neutral axis in the cross section of the experimental columns was determined using diagrams of strains of reinforcement and concrete, constructed according to the readings of strain gauges, which were glued on longitudinal reinforcing bars and on the concrete surface.

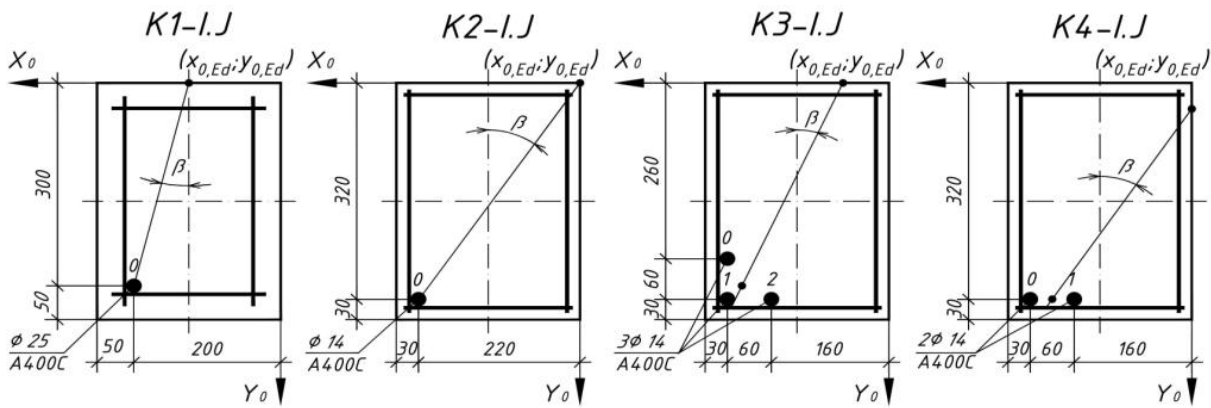


Fig. 4 Schemes of reinforcement and loading of samples of columns at biaxial bending.

4 Conclusions

The general method of structural analysis of reinforced concrete columns under axial load and biaxial bending is based on clear physical and geometric laws and does not contain simplifications that would significantly affect the result of the calculation. Analytical dependences for calculation of all parameters of the stress-strain state of biaxially bended columns at the moment of its destruction are received on the basis of the carried out theoretical researches. Dependences for any form of the compression concrete zone, which can be formed in rectangular section of a column, are deduced. The formed analytical apparatus is simple and can be implemented in any computer environment. The results of comparison of the calculations with experimental data indicate sufficient accuracy and feasibility of applying the developed method in practice.

References

- [1] Pavlikov A., Kosior-Kazberuk M., and Harkava O. 2018. "Experimental testing results of reinforced concrete beams under biaxial bending". *International Journal of Engineering & Technology* 7 (3.2): 299 – 305. Accessed February 20, 2020. doi: 10.14419/ijet.v7i3.2.14423.
- [2] EN 1992-1-1:2004. Eurocode 2: Design of Concrete Structures – Part 1-1: General rules and rules for buildings. fib Bulletin 34 (2006). Model code for service life design. Fédération Internationale du Béton (fib). Lausanne, Switzerland.
- [3] Pavlikov A. 2008. *Nelineina model napruzhenno-deformovanoho stanu kosozavantazhenykh zalizobetonnykh memberiv u zakrytychnii stadii: Monohrafiia*. Poltava: PolNTU.
- [4] Dovzhenko O., Pohribnyi V., and Yurko I. 2018. "Concrete and Reinforced Concrete Strength under Action of Shear, Crushing and Punching Shear." *IOP Conf. Series: Materials Science and Engineering* 463: 022026. Accessed February 20, 2020. doi:10.1088/1757-899X/463/2/022026.
- [5] Dovzhenko O., Pohribnyi V., Pents V., and Mariukha D. 2018. "Bearing Capacity Calculation of Reinforced Concrete Corbels under the Shear Action". *MATEC Web Conferences* 230: 02005. Accessed February 20, 2020. doi:10.1051/mateconf/201823002005.
- [6] Pavlikov A.M., Harkava O.V., Prykhodko Yu.O., and Baryliak B.A. 2018. "Experimental and Theoretical Testing Results of Reinforced Concrete Columns under Biaxial Bending". *International Journal of Engineering & Technology*, 7 (4.8): 145 – 151. doi:10.14419/ijet.v7i4.8.27230.
- [7] Pavlikov A., Kochkarov D., and Harkava O. 2019. "Calculation of reinforced concrete members strength by new concept". *Proceedings of the fib Symposium 2019: Concrete – Innovations in Materials, Design and Structures*: 820 – 827.
- [8] Orešković M., Klymenko Ie., Aniskin A., and Kozina G. 2018. "Analysis of Damaged Concrete Columns of Circular Cross-Section". *Technical gazette* 25, 2: 337-343. Accessed February 20, 2020. doi:10.17559/TV-20160621085905.
- [9] Bouzid T., and K. Demagh. 2011. "Practical method for analysis and design of slender reinforced concrete columns subjected to biaxial bending and axial loads". *Slovak journal of civil engineering*, 1: 24 – 32.
- [10] Chen S.F., Teng J.G., and Chan S.L. 2001. "Design of biaxially loaded short composite columns of arbitrary section". *Journal of Structural Engineering*, 127(6): 678 – 685.

Impact of Modulus of Elasticity on Deflection of Concrete Structures

Radek Vasatko, Jan L. Vitek

*Department of Concrete and Masonry Structures,
Czech Technical University in Prague,
Thakurova 7, Prague 160 00, Czech Republic*

Abstract

Deflection of reinforced concrete (not prestressed) structures is influenced by many parameters. Short term deflection is most affected by modulus of elasticity and by cracks in concrete. Long term deflection is in addition affected by shrinkage and creeping of concrete. At real structures we often encounter larger deflection than it is assumed in structural analysis. Sometimes this phenomenon tends to be explained by lower value of modulus of elasticity than that which is recommended in design standards. But usually the larger deflection is caused rather by too small thickness of the slab or small depth of the beam. The paper deals with behaviour of concrete slabs under bending moment load. It explains causes and their proportions of large deflections, especially long-term deflections.

1 Introduction

In assessment of concrete structures in serviceability limit states, linear distribution of strain and stress in the section is used, except areas in tension, where crack development is assumed. In calculation of deformations mostly the mean value of modulus of elasticity is used. The same value is also used in assessment in ultimate limit states because it is difficult to determine if its higher/lower value is favourable/unfavourable. In ultimate limit state the influence of the modulus of elasticity is negligible; the methods are mostly based on equilibrium. Following text deals with impact of modulus of elasticity on deflection of concrete structures.

2 Modulus of elasticity in static analysis

Modulus of elasticity is one of basic inputs in structure analysis. Most calculations are based on assumption that the structure behaviour is elastic. Under service conditions, stress in structures are small and behaviour of materials is linear. Therefore, the validity of Hook's law can be assumed.

$$\varepsilon_e = \frac{\sigma}{E} \quad (1)$$

where ε_e is elastic deformation, σ is stress and E is modulus of elasticity. So the modulus of elasticity is a basic parameter for calculation of deformation (deflection) of structures.

In structural analysis, modulus of elasticity is recommended in design codes. For example, in Eurocode 2 [1] the modulus of elasticity is defined just by its mean value. It is determined as value of secant modulus of elasticity at stress corresponding to 40% of mean value of concrete strength. This value is stated as approximate and it can be modified in dependence on the used aggregate. After this adjustment it is still approximate mean value of modulus of elasticity. Modulus of elasticity increases with concrete strength that increases with time. Based on agreement, in calculations values of modulus of elasticity and strength for age of 28 days are used if there is no need for more detailed analysis.

For determination of long-term behaviour of structure creep of concrete needs to be involved in the calculations. Mostly it is reflected by creep coefficient which denotes ratio between delayed deformation (creeping) and elastic deformation at constant stress. Therefore, also long-term deformation depends on modulus of elasticity.

$$\varepsilon(t, t_0) = \frac{\sigma}{E_c} [1 + \varphi(t, t_0)] \quad (2)$$

where E_c is tangent modulus of elasticity (assumed as $1.05 E_{cm}$), ϕ is creep coefficient, t_0 is age of concrete at the time when load is applied and t is age of concrete at time when we calculate deformation $\varepsilon(t, t_0)$.

3 Effect of modulus of elasticity on behaviour of concrete structures

Generally, structures are checked in two limit states: serviceability limit state and ultimate limit state. In serviceability limit state elastic behaviour of structures is assumed. It allows for using linear elastic calculations including the principle of superposition and the principle of proportionality. Development of cracks in the section leads to change of section stiffness that must be included to the calculation of deformations. On other hand the crack development has only small effect on internal forces since the redistribution of internal forces due to cracking is usually neglected.

In ultimate limit state non-linear behaviour of materials is assumed. In order to make the analysis easier it has been accepted to determine internal forces assuming linear behaviour (including principles of superposition and proportionality). But sections are assessed assuming non-linear behaviour of materials. Non-linear analyses of internal forces are carried out sporadically. Such calculations are very sophisticated and principles of superposition and proportionality cannot be applied.

3.1 Statically determinate structures

In statically determinate structures the internal forces are determined by static equilibrium equations. Internal forces are not dependent on properties of materials and structures. Therefore, internal forces are not dependent on modulus of elasticity. That's why modulus of elasticity has no effect on internal forces and also has no effect on dimensioning of structure elements. But in calculation of deformations, the modulus of elasticity plays a key role. Lower modulus of elasticity leads to higher deformations, rotations and deflections.

3.2 Statically indeterminate structures

In statically indeterminate structures the internal forces are determined by both, static equilibrium equations and compatibility of deformations – thus by modulus of elasticity. If the modulus of elasticity is the same in the whole structure (homogenous structure) it does not influence distribution of internal forces. But there are only few such structures. Mostly, the structures are not homogeneous and the value of modulus of elasticity influences both, internal forces and deformations.

3.3 Effect of modulus of elasticity on deflection of reinforced concrete structure

Deflections of concrete structures are influenced by many parameters. Short-term deflections are influenced especially by crack development and by modulus of elasticity. Above that, long-term deflections are influenced by creeping and also by shrinkage when the section is reinforced unsymmetrically.

At real structures (especially building structures) we often encounter larger deflection than it is assumed in structural analysis. Sometimes this phenomenon tends to be explained by lower value of modulus of elasticity than is stated in design standards. But usually the larger deflection is caused rather by small thickness of the section/slab. It leads to more significant crack development which causes increase of the deflection.

The following example shows impact of modulus of elasticity and impact of cracking of concrete on deflection of a reinforced concrete slab. To make the example transparent, the simply supported concrete slab has been considered. The thickness of the slab is 200 mm, the span is 4800 mm, and the concrete cover is 30 mm. The slab is reinforced by $\phi 16@150$ mm and is made from concrete of the strength class C30/37. The slenderness of the slab is approximately 29 and the reinforcement ratio is 0,83%. Creep coefficient is assumed by value 1.93 (for RH=70% and $t_0=28$ days).

This example is divided in two parts. In the first step, deterministic calculations were carried out. The short term and long-term deflections were calculated for both stages of sectional performance - cracked and uncracked, and for two values of modulus of elasticity. The first value of modulus of elasticity was taken from Eurocode 2 (32,8 GPa) and the second value is by 4 GPa lower (28,8 GPa). Results are shown in Table 1 and also at Fig. 1. In the analysis it was assumed the stiffness of section varies with length – sections near supports where the cracks don't develop are assumed with full stiffness whilst section in the middle of span are assumed with reduced stiffness.

Table 1 Overview of calculation results

	Short-term deflection [mm]		Long-term deflection [mm]	
	E = 32.8 GPa	E = 28.8 GPa	E = 32.8 GPa	E = 28.8 GPa
Cracked section	11.54	11.89	16.32	17.15
Uncracked section	3.01	3.41	8.18	9.13

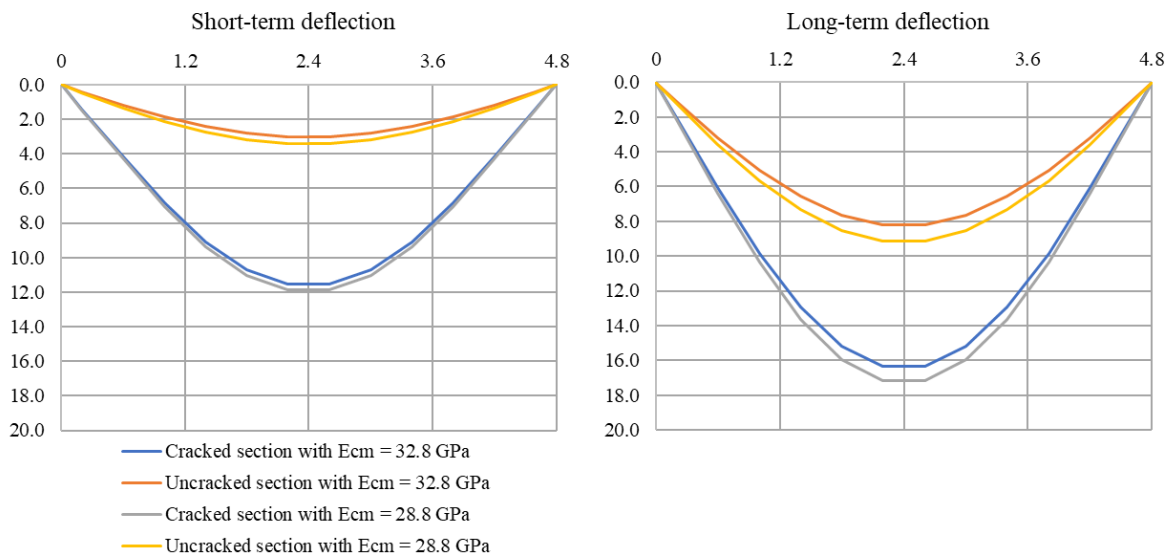


Fig. 1 Deterministic short-term and long-term deflection of the slab

From the performed calculations it was found out:

- As known, considering only elastic deflection is not correct. When including influence of crack development in this example, short-term deflection increases about 4 times, long-term deflection increases about 2 times.
- If the influence of crack development is considered then the modulus of elasticity has only very small influence on deflection (about 3% for short-term deflection, about 5% for long-term deflection).
- For determination of the deflection the influence of crack development is decisive. Influence of lower modulus of elasticity is significantly lower.

In the second step statistical analysis was carried out. The slab was divided into 6 elements in the longitudinal direction. In each element, the modulus of elasticity and the tensile strength of concrete were considered to be variable. The Latin Hypercube Sampling (LHS) method was used. Following three alternatives of analysis were carried out:

- Only the modulus of elasticity was variable (the tensile strength was constant).
- Only the tensile strength was variable (the modulus of elasticity was constant).
- Both, the modulus of elasticity and the tensile strength were variable.

The results of statistical calculations are summarised in Table 2. In the table, mean values and variation coefficients of short-term and long-term deflection are shown. There are also shown mean values and variation coefficients of inputs. The modulus of elasticity and its variation coefficient were taken from a set of about 70 measurements of modulus of elasticity (concrete class C30/37) carried out in different concrete plants in the Czech Republic [2]. Measurement results are shown in Fig. 2. Linear regression of E_{ci} is gained by least squares method. The tensile strength and its variation coefficient were taken from Eurocode 2 [1]. Assumed cumulative distribution functions of modulus of elasticity and of tensile strength of concrete are shown at Fig. 3.

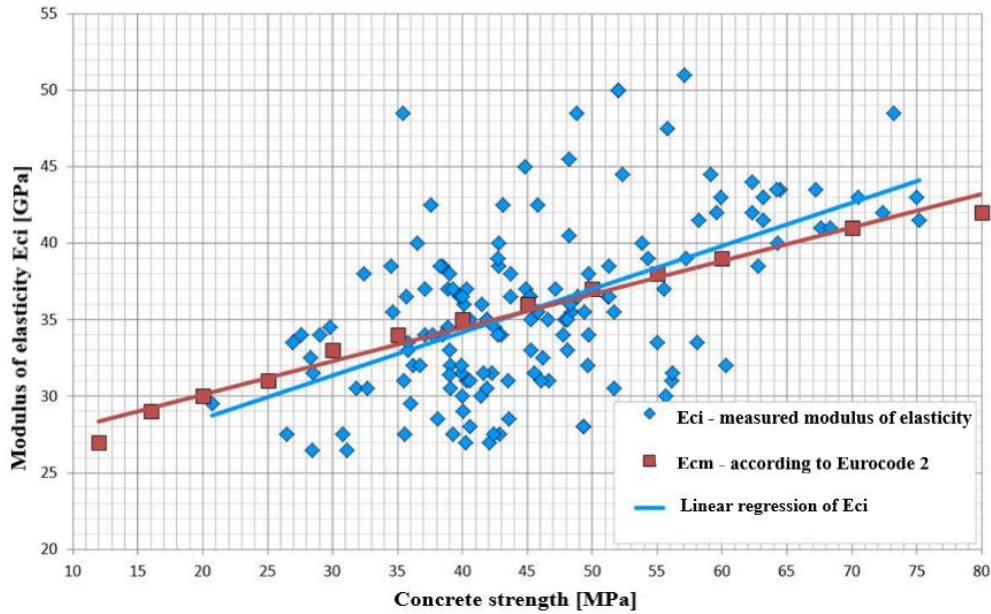


Fig. 2 Measured modulus of elasticity of real concrete, taken from [2]

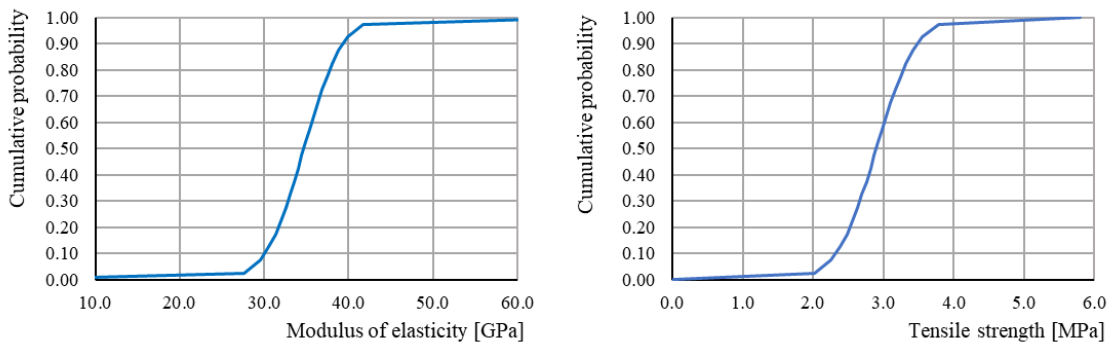


Fig. 3 Assumed cumulative distribution functions of the modulus of elasticity and of tensile strength of concrete used in calculations

Table 2 Short-term and long-term deflections [mm] and their variation coefficients [%] based on variable modulus of elasticity and tensile strength – cracked section

	Modulus of elasticity		Tensile strength		Short-term deflection		Long-term deflection	
	Mean value [GPa]	Variation c. [%]	Mean value [MPa]	Variation c. [%]	Mean value [mm]	Variation c. [%]	Mean value [mm]	Variation c. [%]
Variable modulus of elasticity	34.7	10.3	2.90	0.0	11.4	1.0	16.1	1.6
Variable tensile strength	34.7	0.0	2.90	15.5	11.2	4.5	15.8	3.1
Variable both, modulus and strength	34.7	10.3	2.90	15.5	11.2	4.2	15.9	2.7

As shown in the Table 2, the influence of the modulus of elasticity on slab deflection is small, similarly to the first part of this example. From the statistical analysis it was found out :

- Although the modulus of elasticity has a variation coefficient about 10.3%, the variation coefficient of a short-term deflection is 1.0%, and 1.6% for long-term deflection

- The influence of the variable tensile strength (crack development) is more significant, but the variability of deflection (both, short-term and long-term) is lower than variability of tensile strength. The variation coefficient of a short-term deflection is 4.5% and of a long-term deflection 3.1%, while the variation coefficient of a tensile strength is 15.5%.
- When considering a variable modulus of elasticity and a variable tensile strength, the influence of a variable modulus of elasticity is negligible, since the influence of a variable tensile strength is clearly dominant.
- Variation coefficient of long-term deflection is relatively small which doesn't match a reality. It is caused by assuming constant creep coefficient in the calculation. If the creep coefficient had been assumed as variable, the variability of long-term deflection would significantly increase. There was an aim to show primarily the influence of a modulus of elasticity and of a crack development, therefore the creep coefficient was assumed intently to be constant.

One more analysis was made to show the influence of a variable modulus of elasticity on deflection when the section is uncracked (maximum bending moment on the slab in lower than cracking moment). In this case only variability of modulus of elasticity was assumed. Results are shown in the Table 3. We can see A similar behaviour as in previous examples can be observed. The variation coefficient of deflections (short-term and long-term) is approximately 2.5 times lower than variation coefficient of modulus of elasticity (again a constant creep coefficient is assumed).

Table 3 Short-term and long-term deflections [mm] and their variation coefficients [%] based on variable modulus of elasticity – uncracked section

	Modulus of elasticity		Tensile strength		Short-term deflection		Long-term deflection	
	Mean value [GPa]	Variation c. [%]	Mean value [MPa]	Variation c. [%]	Mean value [mm]	Variation c. [%]	Mean value [mm]	Variation c. [%]
Variable modulus of elasticity	34.7	10.3	-	-	2.9	4.2	7.9	4.0

Results of the calculations are also shown at Fig. 3. The diagram shows a distribution of probability of short-term and long-term deflections involving the influence of distribution of probability of inputs – the modulus of elasticity and the tensile strength. From the figure, it is evident that deflection has lower variability than inputs.

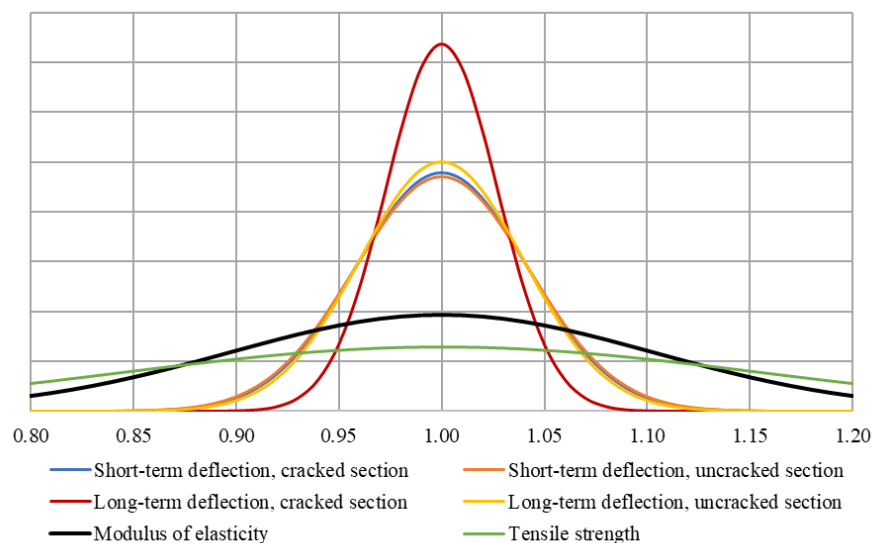


Fig. 4 Probability distribution of deflections in dependence on scatter of the modulus of elasticity and of the concrete tensile strength (creep coefficient is assumed to be constant)

4 Conclusion

A modulus of elasticity is a basic parameter for calculation of deflection of reinforced concrete structures. It has impact on determination and distribution of internal forces on statically indeterminate structures. Therefore, it is necessary to specify the modulus of elasticity in design codes. A modulus of elasticity has a large scatter which has a significant effect especially on deformations of structures with entire section in action (i.e. without cracks), for example prestressed structures. At reinforced concrete structures, the influence of crack development and the tensile strength variation prevails over the influence of a variability of the modulus of elasticity.

If a actual deflection of concrete structures is larger than that determined by the structural analysis, there is a high probability that the influence of cracking or creeping was not involved in the calculation correctly.

It should be noted that although results stated above are valid for a given slab, they illustrate the general behaviour and may be easily extrapolated for other reinforced concrete structures.

At prestressed concrete structures with uncracked sections, it is necessary to take the variability of the modulus of elasticity into account. The measured values (Fig. 2) illustrate a large statistical scatter of the modulus of elasticity.

Acknowledgements

The investigation is supported by the research project No. 16-04454S supported by the Grant Agency of the Czech Republic and by project No. TE01020168 supported by Technology agency of the Czech Republic. The support is gratefully acknowledged.

References

- [1] *Eurocode 2: Design of concrete structures – Part 1-1: General rules and rules for buildings. 2004+AI*, Ed. 2, 2011
- [2] Vítek, J. L., Kolísko, J., Coufal, R., Huňka, P., Števula, M.: *Modul pružnosti betonu, Technická pravidla (Modulus of elasticity of concrete – Technical rules) ČBS TP-05*, Prague, 2016 (in Czech)

Masonry strengthening under the combined action of vertical and horizontal forces

Dmytro Usenko, Oksana Dovzhenko, Volodymyr Pohribnyi, Oleksandr Zyma

*Educational–scientific institute of architecture and construction,
National University «Yuri Kondratyuk Poltava Polytechnic»,
Pershotravnevyj Ave. 24, Poltava (36011), Ukraine*

Abstract

The aim of the study, which is being carried out, is to improve the methodology for calculating the bearing capacity of stone structures under the combined action of horizontal and vertical loads. The use of the theory of plasticity and the principle of virtual speeds makes it possible to more accurately take into account the influence of determining factors on the masonry strength, to increase the reinforcement efficiency and the serviceability of stone buildings. The dependence of the strength of the masonry under crushing-splitting was established on the length of the lintel area of bearing on separation partitions and the effective level of compression of the masonry was determined. The values of the design resistance to crushing-splitting along the inclined section are given for various ratios of horizontal and vertical loads.

1 Introduction

Buildings with load-bearing brick walls are widely spread in civil engineering. They, as a rule, are under the combined action of vertical and horizontal loads. Among the latter, seismic impacts play the most significant role.

The territory of Ukraine is located in three seismically active zones, which include: the southern coast of Crimea, Transcarpathia (northeastern Carpathians) and the most powerful, one of the most seismically dangerous – the Romanian Vrancea zone. It is here that the power of earthquakes can reach maximum marks – 6–9 points.

The issue of determining the bearing capacity of reinforced concrete elements of frame structural systems in complex deformations was investigated in [1], [2]. During calculating the strength of masonry, there is ambiguity. An analysis of the effects of earthquakes made it possible to identify the main damage patterns of brick structures [3] depending on the direction of application and the ratio of the horizontal and vertical components of the load (Fig. 1 top): when the direction of the horizontal load is parallel to the longitudinal walls with a small value of the vertical load, inclined cracks in the separation partitions and in the areas under the slots, as well as horizontal cracks in the separation partitions at the top and bottom of the slots, are observed; at large vertical accelerations, there are inclined cracks in wide pylons with horizontal sections in the masonry between the slots and the failure of the lintels are observed; in the case of a load perpendicular to the longitudinal walls in the transverse walls with slight vertical accelerations in the presence of slots, inclined cracks form in the separation partitions and bands between the windows, as well as horizontal cracks in the separation partitions at the top and bottom of the slots – the damage is most developed on the lower floors.

So, one of the most vulnerable structures of brick buildings are the separation partitions.

2 Stages of deformation of brick walls and methods for their calculation

The separation partitions of the building during operation can be at different stages of deformation. In [3], three stages are distinguished (Fig. 1 bottom).

At the first stage of masonry deformation, when seismic forces are small, separation partitions work together with a window band over the entire contact area. The vertical load is transferred from the upper separation partition to the lower along the entire horizontal section.

Subsequently, in the tensile zones of the horizontal section of the separation partition at the levels of the upper and lower part of the slots adjacent to them, cracks form, the masonry monolithic is broken – this is the second stage of work. At this stage, the transmission of vertical and horizontal loads in the indicated sections is carried out only at a length of $a_c < 2a$ (where a is half the width of

the separation partition). With an alternating horizontal load due to the formation of cracks, adhesion in the masonry is broken along the entire contact above and below the separation partition.

The third stage is characterized by a reduction in the length of the compressed zone and the formation of a diagonal crack in the separation partitions.

The different deformation of separation partition on different floors of the building can be associated with a change in the value and ratio of vertical and horizontal loads, strength and stiffness of the separation partition (Fig. 1 top).

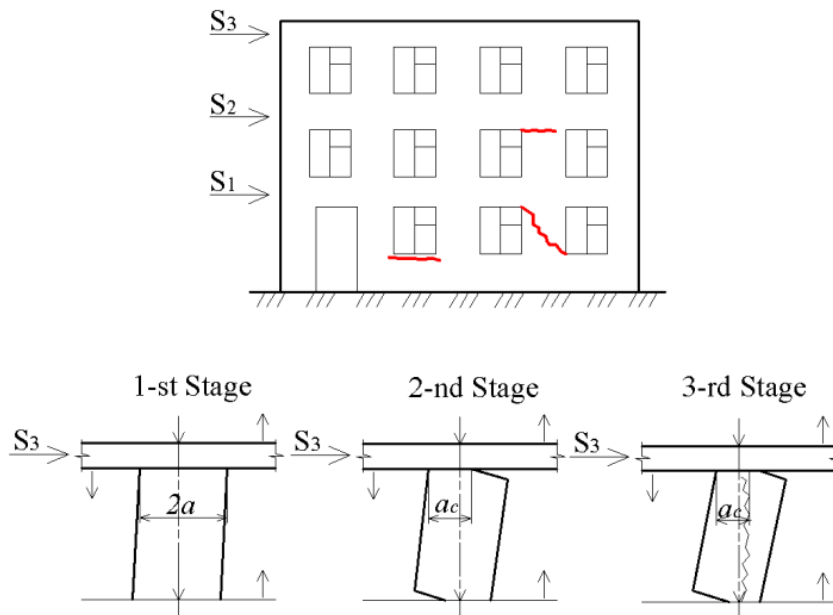


Fig. 1 Scheme of separation partitions damage under the combined action of vertical load and horizontal seismic load (top) and stages of deformation of the separation partitions (bottom).

According to [4], in the case of shear forces in the horizontal plane, the following types of failure are realized: shear (sliding), displacement with splitting, and bending. The shear occurs along the horizontal plane behind the seam (Fig. 2 left) or along a broken crack, which has horizontal and vertical sections (Fig. 2 right). Failure, which is accompanied by diagonal splitting (Fig. 3 left), occurs in the case of reduced brick strength. And also in walls, bending is observed, which is accompanied by the crushing of stones in the zone of compression or turning of the wall (Fig. 3 right). It is associated with subsidence of the walls, and not dominant for unreinforced masonry.

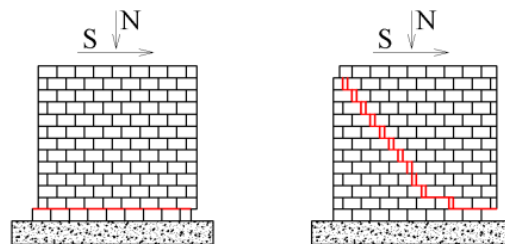


Fig. 2 The character of the brick walls failure under the action of vertical and horizontal loads: shear (sliding) along the horizontal line (left) and along the broken line (right).

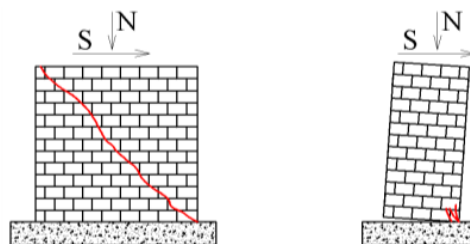


Fig. 3 The character of the brick walls failure under the action of vertical and horizontal loads: displacement with splitting (left); crushing by bending (right).

The most common monolithic masonry violation under the combined action of vertical and horizontal loads is failure along an inclined section.

Calculation of masonry walls that absorb vertical and horizontal loads, including wind and seismic loads, for shear, crushing, eccentric compression by bandaged and not bandaged section is carried out according to the formulas obtained on an empirical basis. They include a number of factors and components that decrease or increase the design resistance and differ in the standards of different countries [5], [6]. These dependencies do not allow to fully take into account the influence of determining factors.

As a theoretical base for calculating the strength of a wall under the combined action of vertical and horizontal base, the application of the theory of plasticity is promising.

3 Preconditions for the application of the theory of plasticity

For masonry at the stage of failure, the plasticity premise is applied and the model of a rigid plastic body is used [7].

Since stone structures work mainly on compression, the “pseudo-plastic” failure, which is accompanied by an increase in the volume (dilatancy) of the material, is of primary practical importance.

The kinematic failure mechanism, which is the basis of the calculation, considers the parts separated by the local area of plastic strain, which mutually move like hard disks due to its localization [8], [9]. Moreover, the development of plastic strain in the danger zone of the body until the ultimate load is reached occurs in a practically finite range of its value. A prerequisite for the implementation of the ultimate kinematic mechanism is the development of plastic strains in its most deformed and stressed area, which completely intersects the body and divides it into parts.

The development of kinematic mechanisms in pseudo-plastic bodies is associated with the formation of a layer of localization of irreversible strains, which can also be called the displacement surface. Its importance is that it serves as a justification for the use of velocity discontinuity surfaces, which make it relatively easy to obtain a solution to strength problems.

In the process of implementing the kinematic mechanism, external forces work on irreversible strains of a more compliant layer, while strains in more rigid elastic parts do not significantly affect the load resistance. The above creates the conditions for the use of a rigid-plastic body model. The sizes of the areas of inelastic strains are unknown in advance and are calculated from the ultimate load [10]–[12].

The plastic state is determined by the condition of plasticity as a relationship between the ultimate stresses that are achieved in the area of plastic strains. The strength condition is considered as a plastic potential.

A qualitative criterion for applying the theory of plasticity to stone structures is the possibility of at least a momentary existence of the plasticity condition over the entire area of the limit state of the masonry, the development of which is necessary for the transformation of the body into a kinematic mechanism. The rationale for the qualitative criterion for the possibility of applying the theory of plasticity to calculate the strength of reinforced concrete structures with externally brittle character of the failure is described in [10].

The relationship between strain rates and stresses is found from the associated law of yield:

$$\dot{\xi}_{ij} = \lambda \partial F / \partial \sigma_{ij} \quad (1)$$

where $\lambda = \dot{\xi}/m$, $\dot{\xi}$ is strain rate, $m = f_c - f_t$, here f_c and f_t are the resistances of the masonry to compression and tension.

The character of the stress-strain state of the reinforcement is taken depending on the state of the masonry that surrounds it. Reinforced stone structures and elements that have such a reinforcement intensity that the ultimate state of reinforcement is reached at the stage of masonry failure are considered. The power of plastic strain of reinforcement W_s reduced to a unit area S_f is found as a function of discontinuities (jumps) of the tangent and normal to failure surface for the velocity components.

4 Variational calculation method

When choosing as the basic for the calculation through the insufficient knowledge of the descending branch of the stress-strain relationship for masonry the theory of plasticity takes priority. Its use as a calculation apparatus allows us to consider elements in the failure stage, to use simplified physical and mechanical dependences with a section corresponding to the state of ideal plasticity. Moreover,

the required accuracy of the calculations is ensured by the use of kinematic schemes (failure mechanisms) of elements that are close to reality. The combination of simplicity and accuracy with the presence of the developed calculation apparatus makes the variational method in the theory of plasticity [13] attractive for use.

At the National University «Yuri Kondratyuk Poltava Polytechnic», a variational method in the theory of plasticity is developed to calculate the strength of masonry during crushing-splitting and shearing, which is based on the consideration of the failure stage and takes into account the complete set of influence factors [8], [14]. Diagonal failure can be considered as bilateral crushing-splitting (shear-cut-off) of masonry. In this case, the failure surface consists of two shear planes along the edges of the wedge, which is formed under the loading platform, and the failure splitting areas connecting the corners of the wedges. An important issue in the application of the technique is the designation of the dimensions of the loading platform, significantly affects the strength.

The masonry strength condition of Balandin - Geniev [15] is accepted as a plastic potential, which in tensor form has a simple expression:

$$F(\sigma_{ij}) = T^2 + m\sigma - T_{sh}^2 = 0 \quad (2)$$

where $T_{sh}^2 = f_{ct}^2/3$, T is the shear stress intensity, σ is the average stress. Under two dimensional stress state, condition (2) is geometrically an ellipse.

The functional of the method for a stone element in a two-dimensional stress state is:

$$J = \int_{S_i} m \left[2B \sqrt{1 + \frac{1}{4} \left(\frac{\Delta V_t}{\Delta V_n} \right)^2} - 1 \right] \Delta V_n ds - \int f_i^* V_i ds_f \quad (3)$$

where $B^2 = (1 + \chi/(1 - \chi)^2)/3$, $\chi = f_{xk1}/f_b$, f_i^* are the specified forces on parts S_f of the surface of the body; S_i – the surface of failure; ΔV_t , ΔV_n – discontinuities (jumps) of the tangent and normal to the S_i of the velocity components.

Problem-solving in discontinuous velocity functions is used.

5 Masonry reinforcement

For increasing the bearing capacity of brick walls, the most effective are measures to contain the transverse strains of the masonry. It is known that brick walls are reinforced with steel clips [16] and clips with composite materials [17], polystyrene concrete applications, shotcrete and concrete spray [18]–[21]. To ensure the joint work of the main structure and reinforcing elements using applications, depending on the required value of the increase in the bearing capacity, the use of concrete micro- or extended keys formed in pre-prepared horizontal toothings, as well as reinforcing anchor bars [22]. Modern technologies of the international concern “Sika” [23] allow us to create and apply new materials with enhanced mechanical properties, such as carbon fiber ribbons, as reinforcing elements.

During diagonal crushing-splitting, the strips are placed horizontally or in a direction perpendicular to the direction of crack development (Fig. 4).

During calculating, the reinforcing is considered as external reinforcement.

An additional term is introduced into the functional of the variational method, which takes into account the deformation capacity of carbon fiber at given speed.

The limit of failure resistance under the loading platform expressed through unknown parameters k and $\tan \gamma$ is calculated as:

$$\frac{f_{loc}}{m} = \frac{\left[2B \sqrt{(k - tg\gamma)^2 + 0.25(1 + ktg\gamma)^2} - (k - tg\gamma) \right]}{tg\gamma} + \frac{f_{xk2} k (\alpha tg\gamma - 1)}{mtg\gamma} + \frac{(2A_1 + A_2) \sigma_y k}{Bl_{loc} m} = 0 \quad (4)$$

here F_u is the resultant load; t is the thickness of the separation partition; l_{loc} is the width of the loading platform; $k = V_1/V_2$, here V_1 and V_2 are the speeds of rigid disks 1 and 2 in the kinematic scheme; γ is the angle of inclination of the failure surface in the compressed zone to the vertical; f_{xk2} is masonry resistance to the main tensile stress; $\alpha = 0.5l/l_{loc}$, l is the length of conditional inclined strip of the calculated inclined section of the separation partition; f_{yd} and A , respectively, is the design tensile strength and the total cross-sectional area of the reinforcement element.

The results of calculating the characteristic values of the relative strength of the separation partitions by the variational method in the theory of plasticity for different ratios of horizontal and vertical loads are given in Table 1.

Table 1 Relative failure resistance of masonry $\alpha_{loc}=f_{loc}/f_d$ for various compressive and tensile strengths during calculating the value of the vertical component of the ultimate force, which perceives the separation partition.

The masonry design resistance		h/l_{loc}	Relative compression stress σ/f_d	Raito S_{Ed}/N_{Ed}		
by compression f_d , MPa	by tensile f_{td} , MPa			0.2	0.6	1
1	0.16	4	0	1.39		0.98
			0.2	1.93		1.36
			0.4	2.33		1.65
			0.6	2.76		1.95
			0.7	2.98		2.11
		10	0	1.99		1.42
			0.2	3.06		2.16
			0.4	4.14		2.93
			0.6	5.21		3.68
			0.7	5.75		4.07
1.7	0.25	4	0	1.46		1.03
			0.2	1.89		1.34
			0.4	2.33		1.65
			0.6	2.76		1.95
			0.7	2.97		2.10
		10	0	1.94		1.37
			0.2	3.02		2.14
			0.4	4.10		2.90
			0.6	5.18		3.66
			0.7	5.73		4.05
2.2	0.3	4	0	1.45		1.03
			0.2	1.89		1.34
			0.4	2.32		1.64
			0.6	2.75		1.95
			0.7	2.97		2.10
		10	0	1.9		1.34
			0.2	2.98		2.11
			0.4	4.07		2.67
			0.6	5.15		3.64
			0.7	5.69		4.02

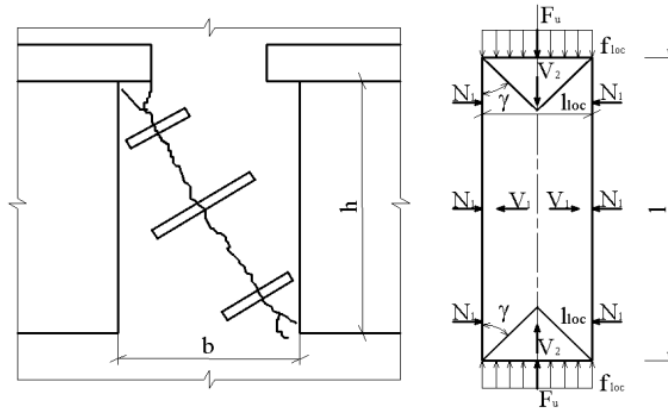


Fig. 4 The character of the failure with the arrangement of the reinforcing elements of the brick wall under diagonal crushing-splitting (left) and the kinematic scheme of failure (right).

To select the reinforcement and the value of the compression stresses $\sigma_c = \Sigma N_s / (th)$ where $N_s = f_{yd} A$, it is recommended to use formula (4) and the data from Table 1 subject to condition $\alpha_{loc} f_d t l_{loc} \geq N_{Ed}$.

The analysis of the character of the failure of the separation partitions, the kinematic scheme (Fig. 4) and the data in the Table 1 shows that: the maximum level of compressive stress of the masonry should not exceed $\sigma / f_d \leq 0.7$; to increase seismic resistance in order to include it into work of masonry sections under the slots, the angle of inclination of the diagonal of the separation partition to the vertical should not exceed the value of the direction angle of the resultant load; to reduce the influence of stress concentration and increase the strength of the compressed masonry directly under the lintel, the length of its area of bearing is recommended to increase compared to buildings operated in non-seismic regions.

6 Conclusions

The effectiveness of reinforcing stone structures is largely determined by the accuracy of the calculation. The use of the variational method in the theory of plasticity makes it possible to justifiably determine the value of compression stresses necessary to ensure the strength of the masonry under the combined action of horizontal and vertical loads and to designate the final gain solution.

The resistance of the masonry separation partition under crushing-splitting is affected by the level of compression stress and the length of the lintel area of bearing. The most effective masonry works with compression $\sigma = 0.7 f_d$. Increasing the width of the lintel area of bearing increases the bearing capacity of the separation partition. During the new designing, restoration and reconstruction of existing earthquake-resistant buildings with bearing stone walls, it is recommended to set the dimensions of the separation partition with the condition that the ratio of the width of the separation partition to its height doesn't exceed the value of the horizontal to vertical load ratio $b/h \geq S_{Ed} / N_{Ed}$.

Acknowledgements

Thanks to the teaching staff of the department of reinforced concrete and stone structures and the Educational-scientific institute of architecture and construction of the National University «Yuri Kondratyuk Poltava Polytechnic» for the support provided during the research.

References

- [1] Pavlikov, A., Harkava, O., Prykhodko, Yu. and Baryliak, B. 2019. "Highly Constructed Pre-cast Flat Slab Frame Structural System of Buildings and Research of Its Slabs." Proceedings of the International fib Symposium on Conceptual Design of Structures, Madrid, September 26–28.
- [2] Pavlikov, A., Kochkarov, D. and Harkava, O. 2019. "Calculation of Reinforced Concrete Members Strength by New Concept." Proceedings of the fib Symposium 2019 Concrete - Innovations in Materials, Design and Structures: held in Kraków, Poland, May 27–29.
- [3] Gasiev, G.A. 2015. "Seismosileniye Sten Kirpichnykh Zdaniy Vneshnim Armirovaniyem na Osnove Uglevoloknistoy Tkani." Phd diss., JSC "SIC CONSTRUCTION", Moscow. (In Russian).

- [4] Salmanpour, A. 2017. "Displacement Capacity of Structural Masonry." Phd diss., International Institute of Earthquake Engineering and Seismology, Iran.
- [5] Eurocode 6: Design of Masonry Structures - Part 1-1: General Rules for Reinforced and Unreinforced Masonry Structures. European Committee for Standardisation (CEN), Brussels, 2009.
- [6] Ledenov, V. 2015. *Prochnost i Treshchinostoykost Sten*. Tambov Publishing house FSBEI HPE "TSTU". (In Russian).
- [7] Dovzhenko, O., Pohribnyi, V. and Yurko, I. 2018. "Concrete and Reinforced Concrete Strength Under Action of Shear, Crushing and Punching Shear." *IOP Conf. Series: Materials Science and Engineering* 463: 022026. doi:10.1088/1757-899X/463/2/022026.
- [8] Pohribnyi, V., Dovzhenko, O. and Maliovana, O. 2018. "The Ideal Plasticity Theory Usage Peculiarities to Concrete and Reinforced Concrete." *International Journal of Engineering & Technology* 7 (3.2):19–26. doi:10.14419/ijet.v7i3.2.14369.
- [9] Dovzhenko, O., Pohribnyi, V. and Karabash, L. 2018. "Experimental Study on the Multikeyed Joints of Concrete and Reinforced Concrete Elements." *International Journal of Engineering & Technology* 7 (3.2): 354–59. doi:10.14419/ijet.v7i3.2.14552.
- [10] Mitrofanov, V., 2006. "Teoriya Ideal'noy Plastichnosti kak Elementarnaya Mekhanika Pseudoplasticheskogo Predel'nogo Sostoyaniya Betona: Osnovy, Ogranicheniya, Prakticheskiye Aspekty, Sovershenstvovaniye". *City utilities* 72:6–26. (In Russian).
- [11] Dovzhenko, O., Pohribnyi, V., Pents, V. and Mariukha, D. 2018. "Bearing Capacity Calculation of Reinforced Concrete Corbels Under the Shear Action." *MATEC Web Conferences* 230. doi:10.1051/mateconf/201823002005.
- [12] Dovzhenko, O., Pohribnyi, V., Klymenko, Ye., Oreškovič, M. and Maliovana, O. 2019. "Strength Calculation of Risers Near the Supports of Reinforced Concrete Three-Hinged Frames Based on the Concrete Plasticity Theory." *IOP Conference Series: Materials Science and Engineering* 708. doi:10.1088/1757-899X/708/1/012046.
- [13] Kolmogorov, V. 1986. *Mekhanika Obrabotki Metallov Davleniyem*. Moscow: Metallurhiya. (In Russian).
- [14] Pohribnyi, V., Dovzhenko, O., Kuznietsova, I. and Usenko, D. 2018. "The Improved Technique for Calculating the Concrete Elements Strength Under Local Compression." *MATEC Web Conferences* 230. doi:10.1051/mateconf/201823002025.
- [15] Geniyev, G., Kissyuk, V. and Tyupin, G. 1974. *Teoriya Plastichnosti Betona i Zhelezobetona*. Moscow: Strojizdat. (In Russian).
- [16] Rimshin, V., Aralov S. 2018. "K Voprosu Usileniya Kirpichnykh Sten Stal'nymi Oboymami i Kompozitsionnymi Materialami." *Promyshlennoye i Grazhdanskoye Stroitel'stvo* 12:38–41. (In Russian).
- [17] Myers, J. J. 2011. "Strengthening Unreinforced Masonry Structures Using Externally Bonded Fiber Reinforced Polymer Systems." An Overview of the American Concrete Institute 440.7r Design Approach 9th Australasian Masonry Conference Queenstown, New Zealand February 15–18.
- [18] Sardar, R., Ashraf, M. and Adil, M. 2015. "Shear Strength Evaluation of Strengthened Unreinforced Brick Masonry Walls by Using Shotcrete ARPN." *Journal of Science and Technology* 5:138–44.
- [19] Startsev, S., and Sundukova, A. 2014. "Usileniye Kirpichnoy Kladki Kompozitnymi Materialami i Vintovymi Sterzhnyami." *Stroitel'stvo Unikal'nykh Zdaniy i Sooruzheniy* 6(21):21–22 (In Russian).
- [20] Granovskiy, A., Dzhamyev B., Osipov P. and Simakov O. 2017. "Seysmostoykost' Kirpichnykh Sten Zdaniy, Usilennykh Kompozitnymi Materialami." *Promyshlennoye i Grazhdanskoye Stroitel'stvo* 4:44–49. (In Russian).
- [21] Kabantsev, O. and inclined Tonkikh, G. 2014. "Eksperimentalnoye Issledovaniye Seysmicheskoy Modernizatsii s Ispolzovaniyem Armirovannykh Voloknami Polimerov s Vneshney Svyazyu" *Bulletin of TGASU* 6: 58–69. (In Russian).
- [22] Tonkikh, G., Osipov, P., Temiraliuly, G. and Fedorov, S. 2017. "Eksperimentalnyye Issledovaniya Kamennoy Kladki, Usilennykh Kompozitnymi Materialami na Osnove Uglerodnogo Volokna." *Bulletin of TGASU* 6:98–111. (In Russian).
- [23] Sika Ukraine. 2020. "Sika Ukraine" Accessed April 1. <http://rus.sika.com/ru/group.html>.

Model Uncertainty Quantification for Column Removal Scenario Calculations Using the Energy-based Method

Luchuan DING, Wouter BOTTE, Ruben VAN COILE, Robby CASPEELE

*Department of Structural Engineering and Building Materials,
Ghent University,
Technologiepark Zwijnaarde 60, Ghent (9052), Belgium*

Abstract

Progressive collapse resistance of a building structure is often investigated by the notional removal of one or more vertical load bearing elements from the structural system. Usually, a nonlinear dynamic analysis is needed to perform such an analysis. To avoid the complex nonlinear dynamic analysis, the energy-based method (EBM) is a promising method to predict the maximum dynamic responses of a structural system, where the dynamic load-bearing capacity curve is derived from the static load-displacement curve based on the principle of energy conservation. In this contribution, the performance of the EBM is evaluated based on a validated finite element model of a tested RC slab. Subsequently, 60 samples are generated by using Latin Hypercube Sampling (LHS), taking into account probability distributions for the most important variables. Both static analyses and direct dynamic analyses are executed for every sample set. Based on the results of the stochastic analyses, the EBM is observed to perform well. Furthermore, in the analyzed case study, the model uncertainty of the ultimate load-bearing capacity obtained through the EBM compared to direct dynamic analysis is found to be represented well by a lognormal distribution with mean (i.e. bias) of 0.96 and a standard deviation of 0.13. Model uncertainties are also obtained in relation to ultimate displacements and displacements at different load levels.

1 Introduction

The Alternative Load Path (ALP) method is a widely used method for robustness assessments based on the notional member removal concept [1][2]. A sudden column removal scenario is usually used in the ALP method to check the capability of the structural system to develop alternative load paths to redistribute the unbalanced forces [3][4]. However, the analysis of such an event is complex since both nonlinear behaviors and dynamic effects are involved. Although a direct nonlinear dynamic analysis can provide an accurate result, it requires significant numerical expertise to perform the analysis and introduces high computational demands.

The energy-based method (EBM) is an alternative simplified approach for such kind of analysis, without the need to carry out any direct dynamic analyses. The EBM is based on the principle of conservation of energy, which makes it easy to understand and apply. This approach has been validated when applied to sudden column removal scenarios [5]-[8].

The EBM is based on several simplifications and, therefore, an approximate result is obtained which is a compromise between accuracy and complexity. Furthermore, several uncertainties exist within structural analysis which may have a significant influence on the overall behavior. Nevertheless, most of the existing studies neglect this [2][9][10] and therefore a probabilistic analysis might yield a more comprehensive evaluation of the performance of the EBM.

Consequently, this paper aims at evaluating the performance of the EBM. Firstly, the EBM is introduced in detail. Afterwards, a numerical model is built based on the experimental results of a RC slab to validate the EBM. Next, stochastic analyses are executed to evaluate the EBM in a probabilistic way and quantify the model uncertainty. Finally, concluding remarks are presented.

2 The energy-based method

Conservation of energy must be satisfied for a structural system undergoing deformations. Considering this, the energy-based method (EBM) can be easily described in physical terms [5][6]. Assuming a structural system subjected to a sudden column removal at a certain moment in time, the equilibrium for the gravity load and external loads will not be satisfied any more due to the unbalanced forces

originating from the column before the removal. Thus, the structure accelerates, deforming in order to accommodate the unbalanced loads. The released gravity potential energy during this moving process is transferred into strain energy and kinetic energy, increasing the velocity of the system until a maximum velocity is reached. Beyond this point, the upward forces resulting from the stress-strain state exceed the downward forces from the gravity loads and the external loads. The structure slows down again, while the additional absorbed strain energy leads to a reduction in the kinetic energy. Finally, the kinetic energy is reduced back to zero (i.e. the velocity is equal to zero). Neglecting the energy dissipated by other sources such as heat, the absorbed strain energy then equals the released potential energy and enables to quantify the maximum deflection.

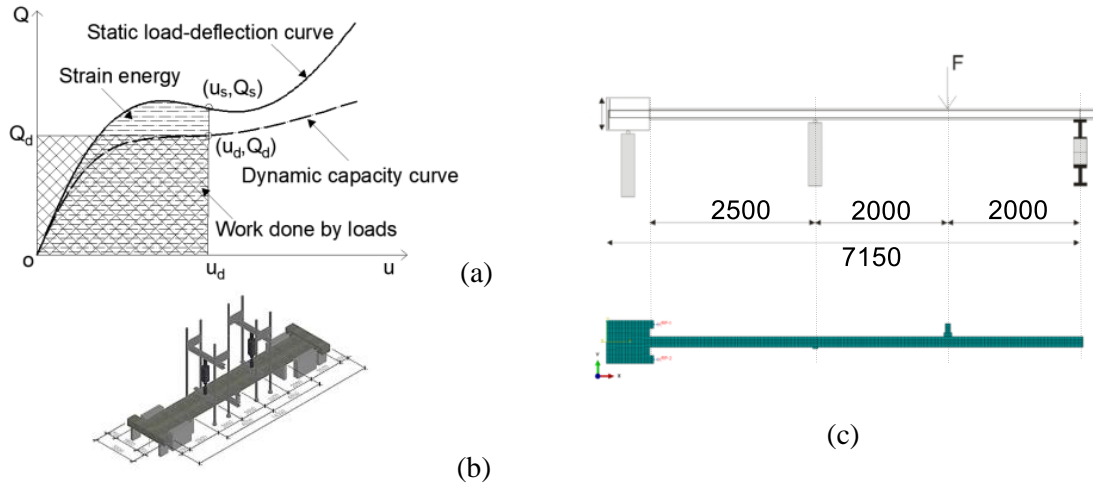


Fig. 1 Concept of the energy-based method (a) [6]; test set-up (b) [11]; detail of half of the test set-up and the corresponding FE model (c).

To apply the EBM, the strain energy is calculated first through a quasi-static nonlinear pushdown analysis. The strain energy is equal to the area under the static load-deflection curve (see Fig. 1 (a)). Considering that the released potential energy from the loads at the displacement u_d and the internal stored strain energy are equal at the same displacement level, i.e. the hatched rectangular area corresponding to (u_d, Q_d) equals the hatched area under the static load-deflection curve until (u_s, Q_s) , the dynamic load Q_d can be mathematically calculated by using (1),

$$Q_d(u_d) = \frac{1}{u_d} \int_0^{u_s} Q_s(u) du \quad (1)$$

where Q_d is the load in the dynamic load-deformation curve; Q_s is the load in the static load-deformation curve; u_d is the peak dynamic deflection; and u_s is the static deflection.

3 Validation of the energy-based method

3.1 Finite element model

An experiment on a real-scale one-way slab subjected to a removal of a support [11] is employed to develop a finite element model (FEM). The test set-up is illustrated in Fig 1 (b). The total length of the slab was 14.3m with two inner spans of 4m and two outer spans of 3.15m. The width of the specimen was 1.8m. Concrete of class C30/37 was used, while the flexural reinforcement consisted of 16 bars of type S500 with a nominal diameter of 10mm for both top and bottom reinforcements. The concrete cover was 20mm. Material properties of both the concrete and the steel are summarized in Table 1. In addition, only the inward movements were restrained by heavily reinforced edge beams at two ends of the slab since the experiment aimed at investigating tensile membrane action only. Additional details can be found in the related paper [11].

The FE software Abaqus is employed to perform the numerical analysis. Considering the symmetry of both geometry and loading, a 2D plane stress FEM of half of the slab is modelled. As cracks are expected to occur all over the slab, a dense mesh is applied, i.e. 8 elements through the slab depth, see Fig. 1 (c) and 2 (d). 4-node bilinear plane stress quadrilateral elements (CPS4R) are used to model the concrete. The parabolic stress-strain relationship is implemented for concrete in compression, while the

Hordijk tension softening model is used for concrete in tension, see Fig. 2 (a) and (b) [12]. The concrete damaged plasticity (CDP) model is used. For the reinforcement, 2-node linear truss elements (T2D2) are applied assuming perfect bond to the neighboring concrete elements. A multi-linear stress-strain relationship based on laboratory testing is employed for the reinforcement, i.e. the strain hardening of steel is considered as an elastic-plastic model which explicitly includes a sudden decrease in strength at rupture of the reinforcement bars to enable to model the observed failure phenomenon of the slab, see Fig. 2 (c). The parameters from Table 1 are used.

Table 1 Material properties for concrete and reinforcing steel [11].

Concrete		Steel			
f_c (MPa)	E_{ci} (GPa)	f_y (MPa)	f_t (MPa)	ϵ_u (%)	E_s (GPa)
36.2	31.97	555	605	8.31	207.9

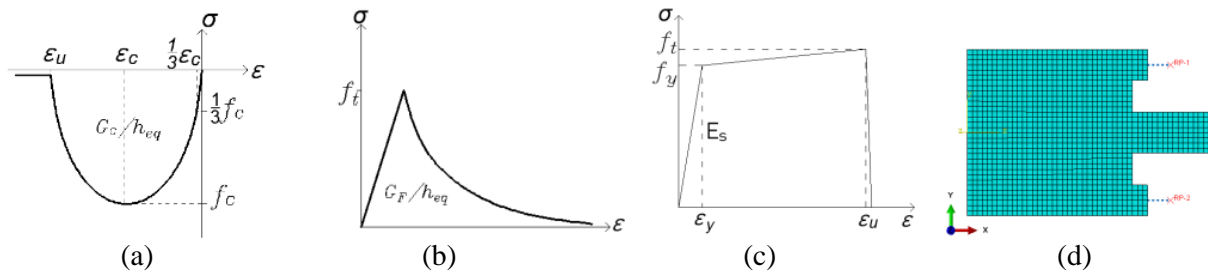


Fig. 2 Stress-strain relationships of concrete and reinforcement [12] and springs in the FEM: concrete in compression (a); concrete in tension (b); reinforcement (c); boundary condition (d).

Lateral displacements over the central support are prohibited considering the symmetry condition. As in the experimental test set-up, the outward movement of the edge beam is allowed. However, the inward movement is restrained through spring elements, see Fig. 2 (d). Two connector elements are employed to simulate springs, incorporating the relationship between the occurring horizontal force and the corresponding horizontal displacement. Based on the measured membrane force versus displacement measurements on the end blocks in the test setup, the spring stiffness is assigned as a constant value of 151.5kN/mm for each spring.

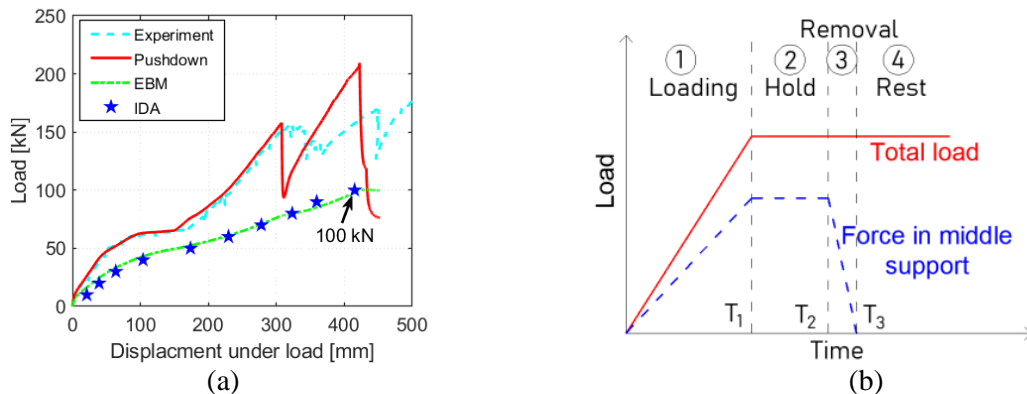


Fig. 3 Vertical load-deformation relationship (a); Loading scheme for the dynamic analyses (b).

To validate the FEM, the same loading scheme as the test is executed, which is divided into three loading phases. The self-weight and a service load of 60kN are initially applied, followed by the removal of the service load in phase 1. The central support is removed in phase 2, i.e. the two inner spans of 4m thus become one span of 8m. Eventually, a displacement controlled vertical load is imposed on the slab in phase 3 until the failure of the slab. Abaqus/Standard is employed to perform the static pushdown analysis. Geometrical nonlinearities are taken into account. The load-displacement curves obtained from both the experiment and the numerical pushdown analysis are presented in Fig. 3 (a), where good agreement between both is observed until the first load peak. Similar as observed in the experiment [11], the slab experiences an elastic stage, an elastic-plastic stage and a tensile membrane

action stage. Little difference is found between the values of the first load peaks, which are 158.1kN and 156.6kN, respectively. This first load peak corresponds to rupture of the reinforcement over the inner support. The subsequent structural response is highly complex which is reflected by the significant discrepancy between experiment and numerical analysis. In case structural failure is defined as first rupture of reinforcement, it can be concluded that the FEM has a good performance.

3.2 Comparing between the EBM and direct dynamic analyses

Based on the EBM and the results presented in 3.1, a dynamic load-bearing curve is calculated and presented in Fig. 3 (a). The ultimate dynamic load-bearing capacity is 100.4kN. The sudden decrease in strength occurring on the pushdown curve is not observed on the dynamic capacity curve since the latter is calculated from the former based on the energy balance. However, a slight softening stage on the dynamic capacity curve is observed between 80kN and 100kN.

As the dynamic capacity curve is directly derived from pushdown curve without performing any dynamic analyses, the effectiveness of the EBM can be validated by comparing the derived dynamic capacity curve with results of direct dynamic analyses. The incremental dynamic analysis (IDA) technique is employed here to execute the dynamic analyses on the same FEM, which performs a series of dynamic analyses from a lower load to a higher load until the collapse of the slab occurs. A loading scheme presented in Fig. 3 (b) is used. First, self-weight and vertical loads are applied in phase 1 from 0 to T_1 (1.5s). Secondly, the loads are kept the same from T_1 to T_2 (1.5s-2.0s). Thirdly, the support is removed in a time duration of 10^{-5} s from T_2 to T_3 . Thereafter, the structure keeps on oscillating with the other loads. Abaqus/Explicit is employed to execute the dynamic analyses.

The comparison of results of the incremental dynamic analyses (IDA) with that of the EBM is presented in Fig. 3 (a), in which every star represents a maximum displacement of the dynamic response under the corresponding vertical imposed load. The maximum dynamic load capacity is approximately 100kN, which agrees well with that of EBM, i.e. 100.4kN. For a higher imposed load, the structure fails in the dynamic analysis upon removal of the central support. The good agreement between EBM and IDA indicates that the EBM predicts the maximum dynamic response well. Influences of the strain rate effects and damping were investigated in another paper [7], which shows that strain rate effects are not significant and the influence of damping is limited. Therefore, these dynamic effects are not taken into account in this paper. Furthermore, it needs to be mentioned that the numerical results deviate from the observed experimental data after the first load peak was reached, but that this does not prevent to quantify the model uncertainty of the EBM compared to direct dynamic analyses as performed in the following. Nevertheless, this indicates the importance to quantify also a model uncertainty with respect to the prediction of the highly nonlinear post-peak behavior in case of large deformations and membrane actions, for which however at this stage only very limited data is available.

4 Uncertainty Quantification

4.1 Probabilistic models for the input variables

Based on previous investigations [2][10][13][14], eight parameters are selected as input random variables to quantify the uncertainty propagation when the EBM is used. These parameters are the material properties of concrete, the material properties of reinforcing steel, the cross-section of the reinforcement and the stiffness of the horizontal springs (see Fig. 2 (d)). The probabilistic models are presented in Table 2. The other input parameters are considered deterministic.

Table 2 Probabilistic models for the random variables.

Name	Unit	Distribution	Mean (μ)	COV
Density of concrete ρ_c	kg/m ³	N	2400	0.04
Concrete compressive strength f_c	MPa	LN	36.2	0.10
Reinforcement yield stress f_y	MPa	N	555	0.03
Reinforcement tensile strength f_t	MPa	LN	605	0.03
Reinforcement strain at maximum stress ε_{it}	%	LN	8.3	0.15
Young's modulus of reinforcement E_s	GPa	N	207.9	0.08

Cross-section of reinforcement A_s	mm^2	N	1256	0.02
Stiffness of horizontal spring k	kN/mm	LN	151.5	0.25

Latin Hypercube Sampling (LHS) is used in combination with the developed FEM to perform stochastic analyses, which allows to limit the number of calculations to an acceptable amount. As the standard LHS may bring undesired spurious correlation into the sample scheme, correlation Latin Hypercube Sampling (LHS) is used to avoid this unwanted effect [15]. Sixty Latin-Hypercube samples are generated based on the probabilistic models presented in Table 2. Eventually, each set of sampled realizations is used as an input for the FEM to determine the response predicted by the EBM and by IDA.

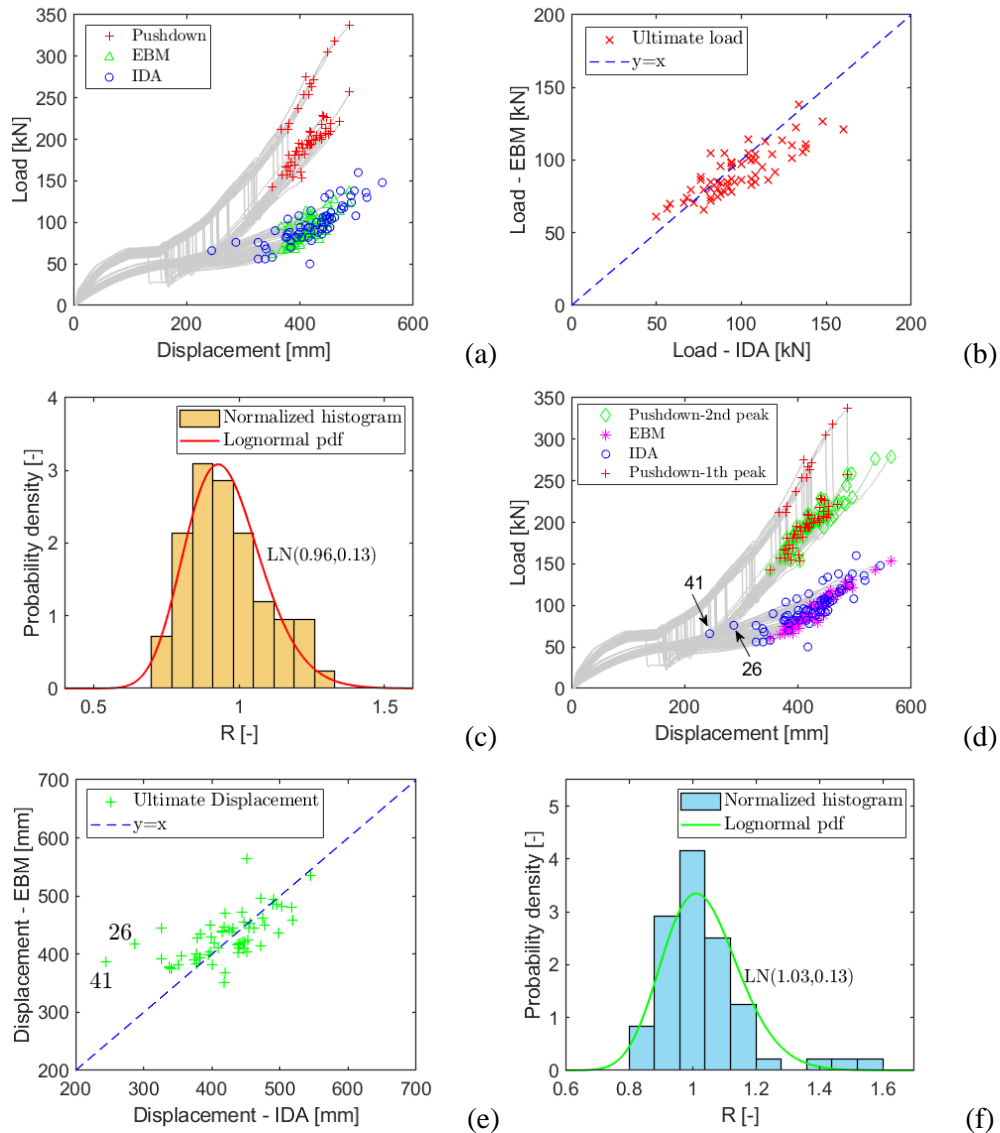


Fig. 4 Comparison for the ultimate capacities between EBM and IDA: load-displacement relationship (a); comparison of ultimate load-bearing capacity (b); histogram and PDF of the ratio (load) EBM/IDA (c); load-displacement relationship (d); comparison of displacement (e); histogram and PDF of the ratio (displacement) EBM/IDA (f).

4.2 Stochastic analyses

All LHS samples are evaluated considering both static pushdown analyses and direct dynamic analyses. For the latter, the IDA technique is employed for every slab realization. Firstly, a load interval of 10kN is employed from 40kN to 160kN, i.e. 13 dynamic simulations. To obtain a 2kN resolution for the maximum dynamic load, another 4 simulations are performed every 2kN in the interval between the last non-failed simulation and the first failed simulation. No smaller load interval is further considered as this requires much more calculations. Subsequently, the curves from the pushdown analyses are

converted into dynamic capacity curves (EBM) to be compared with the results of the direct dynamic analyses (IDA). The details are not presented here for every sample, however, in general, a good agreement is observed between the results of EBM and IDA.

The results of static pushdown analyses show an elastic stage, an elastic-plastic stage and a tensile membrane action stage for every realization. The dynamic capacity curves of EBM completely depend on the pushdown curves. Fig. 4 (a) present the comparisons between the EBM and IDA for ultimate load-bearing capacities. The ultimate static load-bearing capacities (pushdown) are also shown. Although differences can be observed for the corresponding displacements, the results of EBM are situated in the same load ranges as the results of IDA. Good agreement is found for the ultimate load-bearing capacities of the two cases, see Fig. 4 (b), where the ultimate load-bearing capacities of EBM against the ultimate capacities of IDA distribute along the diagonal line ($y=x$), i.e. the values are approximately equal to each other.

As the ultimate displacements may occur after the displacements corresponding to the ultimate load-bearing capacities in some pushdown curves, i.e. the second peak load is lower than the first peak load on the pushdown curves, see Fig. 4 (d), the dynamic capacities of EBM based on the pushdown curves will be larger in these cases. Therefore, a comparison of the corresponding ultimate displacements is also relevant. The dynamic capacities of EBM of the ultimate displacements are compared with the IDA. A good agreement is observed for the ultimate displacements of EBM against IDA as presented in Fig. 4 (e). However, two cases (26 and 41) significantly deviate.

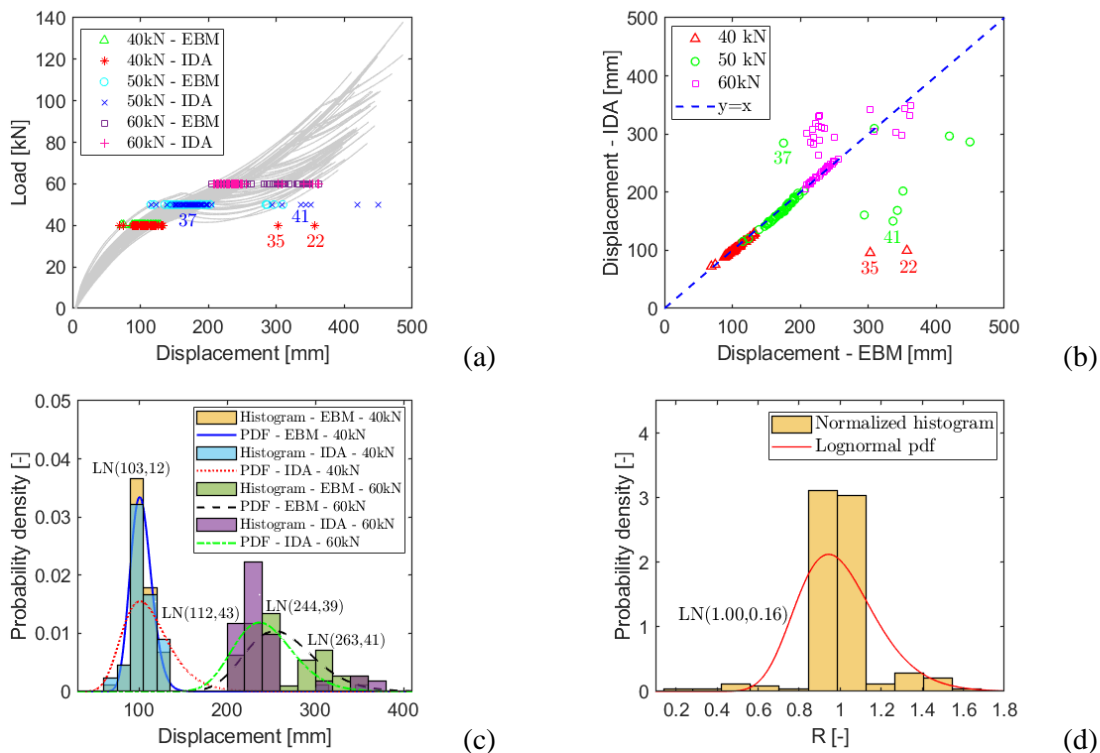


Fig. 5 Comparison of the displacements between EBM and IDA: load-displacement relationship (a); comparison of displacement (b); histograms and PDFs of the displacements (c); histogram and PDF of the ratio of the displacements corresponding to EBM/IDA (d).

The performance of the EBM for the ultimate capacities is observed to be well. The performance for other stages, i.e. the elastic-plastic stage and the tensile membrane action stage, is further assessed. As a load interval of 10kN is used in the IDA and the corresponding peak displacements are obtained, the displacements are used to compare with the EBM. Fig. 5 (a) shows the load-displacement relationships of dynamic cases under three load levels, i.e. 40kN, 50kN and 60kN, for both EBM and IDA. The displacements obtained through EBM against the displacements obtained through IDA are presented in Fig. 5 (b) for the three cases, respectively. The points distribute along the diagonal line, which indicates the displacements of EBM agree well with the displacements of IDA. However, considering a confidence level in three times of standard deviation, four cases could be considered as outliers, namely 22 and 35 in case of 40kN and 37 and 41 in case of 50kN, respectively. Further, it should be noted that only 56 samples remain available in case a load of 60kN is considered for the dynamic analysis, as the

ultimate dynamic load-bearing capacities of four cases, i.e. 22, 35, 48 and 54, are found to be smaller than 60kN. Histograms and probability density functions (PDFs) of displacements corresponding to a load of 40kN and 60kN for EBM and IDA are presented in Fig. 5 (c), respectively, where lognormal distributions are used to fit the PDFs. The PDFs for displacements are close to each other in case of 40kN, which indicates a good performance of the EBM. A larger variation is observed in case of 60kN, although the distribution for the EBM can be considered to be modeled still reasonably well. Therefore, comparing with the results of IDA, EBM can be considered overall to perform very well in both the elastic-plastic stage and in the tensile membrane action stage.

4.3 Uncertainty quantification

To evaluate the performance of EBM quantitatively, ratios of the displacements of the EBM to the direct dynamic analyses (IDA), see Fig. 4 (e) and 5(b), are calculated by using Eq. (2). Further, ratios of the ultimate load-bearing capacities, see Fig. 4 (b), are also calculated.

$$R = \frac{D_{EBM}}{D_{IDA}} \text{ or } \frac{P_{EBM}}{P_{IDA}} \quad (2)$$

where R is the ratio. D_{EBM} is the displacement for EBM; D_{IDA} is the peak displacements for IDA; P_{EBM} is the ultimate load-bearing capacity for EBM; P_{IDA} is the ultimate load-bearing capacity for IDA.

Histograms for the ratios of displacements are presented in Fig. 4 (f) and 5 (d). Fig. 4 (f) shows ratios of the ultimate displacements, where a lognormal distribution LN(1.03, 0.13) is used to fit the PDF. It should be noted that the two cases of significant deviation, i.e. 26 and 41, are taken into account. Fig. 5 (d) shows ratios of all the displacements under the three load levels, i.e. 40kN, 50kN, and 60kN, in which a lognormal distribution LN(1.00, 0.16) is found to represent the histogram. The four cases of large deviations are taken into account, i.e. 22 and 35 in case of 40kN, and 37 and 41 in case of 50kN, respectively. Fig. 4 (c) shows ratios of the ultimate load-bearing capacities, where a lognormal distribution LN(0.96, 0.13) is found to fit the histogram. The parameters of the model uncertainty distributions are summarized in Table 3. As the mean values are approximately equal to one, on average a good performance of the EBM is found by comparing with the IDA.

Table 3 Ratios of EBM/ IDA.

Case	R [-]	
	Mean (μ)	Standard deviation (σ)
Displacement - 40kN	0.96	0.13
Displacement - 50kN	0.94	0.15
Displacement - 60kN	1.08	0.16
Displacement - 40kN, 50kN and 60kN	1.00	0.16
Displacement - ultimate	1.03	0.13
Ultimate load-bearing capacity	0.96	0.13

5 Conclusions

The performance of the EBM is evaluated by comparing with the direct dynamic analyses. Considering a large scale test of an RC slab, a FEM is firstly validated. Next, stochastic analyses are executed considering eight stochastic input variables using Latin Hypercube sampling. The results of EBM are compared with the results of direct dynamic analyses to assess the performance of EBM in a probabilistic way.

Good performance is found for the FEM when compared with the experimental result. Furthermore, the EBM predicts the dynamic load-bearing curve well, as confirmed by dynamic load-bearing capacity evaluations.

Although there are some differences for several cases, good agreement can be found between EBM and direct dynamic analyses for the 60 realizations. On the basis of these simulations, probabilistic models have been proposed for the model uncertainty of EBM compared to direct dynamic analyses,

in particular in relation to the ultimate load-bearing capacity, the ultimate displacement and displacements at different load levels.

Acknowledgements

The authors would like to thank the China Scholarship Council for the financial support provided in relation to the PhD research of the first author.

References

- [1] Adam, J. M., Parisi, F., Sagaseta, J., and Lu, X. 2018. "Research and practice on progressive collapse and robustness of building structures in the 21st century." *Engineering Structures* 173:122-149.
- [2] Feng, D. C., Xie, S. C., Xu, J., and Qian, K. 2020. "Robustness quantification of reinforced concrete structures subjected to progressive collapse via the probability density evolution method." *Engineering Structures* 202:109877.
- [3] DoD 2009. "UFC 4-023-03: Unified facilities criteria - design of buildings to resist progressive collapse." Department of Defense, United States.
- [4] GSA 2013. "Alternate path analysis & design guidelines for progressive collapse resistance." General Services Administration, United States.
- [5] Izzuddin, B., Vlassis, A., Elghazouli, A., and Nethercot, D. 2008. "Progressive collapse of multi-storey buildings due to sudden column loss—Part I: Simplified assessment framework." *Engineering structures* 30(5):1308-1318.
- [6] Herraiz, B., Russell, J., and Vogel, T. 2015. "Energy-based method for sudden column failure scenarios: theoretical, numerical and experimental analysis." Proc. IABSE Symposium Report, International Association for Bridge and Structural Engineering, Helsinki, Finland, February 11-12.
- [7] Ding, L. C., Botte, W., Van Coile, R., and Caspeele, R. 2020. "Evaluation of the energy-based method for dynamic analysis under a sudden column removal scenario." Proc. The fib Symposium 2020: Concrete Structures for Resilient Society, Shanghai, China, November 22-24 (Accepted).
- [8] Yu, X. H., Qian, K., Lu, D. G., and Li, B. 2017. "Progressive collapse behavior of aging reinforced concrete structures considering corrosion effects." *Journal of Performance of Constructed Facilities* 31(4):04017009.
- [9] Ding, L. C., Botte, W., Van Coile, R., and Caspeele, R. 2018. "Robustness - evaluation of a stochastic dynamic system and the instant equivalent extreme - value event: The PDEM - based structural reliability evaluation of a dynamic system." *Beton - und Stahlbetonbau* 113:33-37.
- [10] Ding, L. C., Droogné, D., Botte, W., Van Coile, R., and Caspeele, R. 2019. "Structural Reliability Calculations Considering Concrete Tensile Membrane Action Using the Probability Density Evolution Method." Proc. 13th International Conference on applications of statistics and probability in civil engineering (ICASP13), Seoul, South Korea, May 26-30.
- [11] Gouverneur, D., Caspeele, R., and Taerwe, L. 2013. "Experimental investigation of the load-displacement behaviour under catenary action in a restrained reinforced concrete slab strip." *Engineering structures* 49:1007-1016.
- [12] Hendriks, M. A., de Boer, A., and Belletti, B. 2017. "Guidelines for nonlinear finite element analysis of concrete structures." Rijkswaterstaat Technisch Document (RTD), Rijkswaterstaat Centre for Infrastructure, 1016-1.
- [13] Botte, W. 2017, "Quantification of structural reliability and robustness of new and existing concrete structures considering membrane action." PhD diss., Ghent University.
- [14] Droogné, D., Botte, W., and Caspeele, R. 2018. "A multilevel calculation scheme for risk-based robustness quantification of reinforced concrete frames." *Engineering Structures* 160:56-70.
- [15] Olsson, A., Sandberg, G., and Dahlblom, O. 2003. "On Latin hypercube sampling for structural reliability analysis." *Structural safety* 25(1):47-68.

Numerical Plastic Analysis of Non-Prismatic Reinforced Concrete Beams Strengthened by Carbon Fiber Reinforced Polymers

Sarah Khaleel Ibrahim¹, Majid Movahedi Rad¹

¹Department of Structural and Geotechnical Engineering
Faculty of Architecture, Civil Engineering and Transport Sciences
Széchenyi István University
Egyetem tér 1, Győr 9026, Hungary

Abstract

The non-prismatic reinforced concrete (RC) beam considered a unique case in structural engineering as it has variable depth all over beam section and it doesn't have sufficient information in structural codes, this can put structural engineers in a challenge to predict how this beam will react under specific types of loads or with different geometrical variables and strengthening existence. In this research, concrete plastic damage constitutive model developed and used to explore the shear strength of non-prismatic RC beam structure. Furthermore, in order to improve the shear strength of existent RC beams, Carbon Fiber Reinforced Polymers (CFRP) strips are attached to the surface of the critical sections. For this aim, initially numerical model was calibrated according to the data obtained from laboratory tests then a series of numerical simulations with different variables are carried out to investigate the shear behavior and these variables were: haunch angle α value and CFRP strips existence (composite status). The numerical results show that changing beams geometry (haunch angle α value) can have an influence over shear strength, in addition, using CFRP strips has an obvious effect on the failure behavior of the non-prismatic RC beam structure. Finite element simulations are executed by using ABAQUS.

Keywords: concrete plastic damage, non-prismatic RC beam, CFRP, shear strength.

1 Introduction

Since the 1995 Hyogoken-Nanbu Earthquake, the use of horizontally haunched beams has been increasing to prevent brittle fractures of beam flanges in the beam-column connections of moment-resisting frames. The British and American codes do not contain any design equations considering haunched beams under shear and to replace this lack of information, many cases regarding this kind of beams were studied. El-Niema [1] proposed a formula which provides the ultimate shear force of reinforced-concrete non-prismatic beams exposed to shear in terms of concrete strength, dowel action, and stirrups contribution. The proposed formula is a modified using American Concrete Institute (ACI) code terms for shear design. Dado and Al-Sadder [2] studied the behavior of prismatic and non-prismatic cantilever beams under various types of loadings. Several numerical examples were studied considering prismatic and non-prismatic cantilever beams subjected to tip concentrated loadings, uniform and non-uniform distributed loads in horizontal and vertical directions. Archundia et al. [3] studied interpretations and final research results of testing ten simply-supported reinforced concrete beams (two prismatic and eight haunched) designed to fail in shear under cyclic loading. Five beams (four haunched and one prismatic) were tested with a shear reinforcement while the remaining five (one prismatic and four haunched) were tested without shear reinforcement. Ponnachan and Koshy [4] performed the analysis of reinforced concrete framed structures with haunched beams. This study emphasized the effects of different configurations of haunched beams on the seismic response of a structure and the main purpose was to carry out the nonlinear static analysis on RC building frames of ten storeys at seismic zones.

Therefore, and in order to study unique cases in the structural engineering that doesn't have sufficient information in structural codes, Finite element method based to analyse reinforced concrete structures has significantly developed. Models for material were applied for analysing the behavior of unconfined concrete, and the concrete damage plasticity (CDP) model was a possible constitutive model which was first established by Lubliner et al. in 1989 [5] and then it enhanced by Lee and Fenves in 1998 [6]. Because of the complexity of CDP theory, the procedure was simplified by Hafezolghorani et al. [7]. In their study they developed a simplified concrete damage plasticity (SCDP) model. The

SCDP model was then described in the forms of tables to simulate the behavior of unconfined concrete. Demin and Fukang [8] simplified several simple stress-strain relationships of the concrete material recommended in the related Codes, then the factors of the damage of the simplified plastic damage constitutive model were computed based on Sidiroff's energy equivalence principle. The calculation method of plastic damage parameters in ABAQUS program is further studied, and the modified constitutive model of concrete plastic damage is proposed and verified. Shen et al. [9] proposed a plasticity-based damage model for inelastic analysis of structural concrete. Drucker-Prager-type plasticity was adopted in the formulation of the constitutive equations. The aim of this investigation was to build a constitutive model that can simulate the history-dependent plastic damage behaviour of massive structural concrete under confinement.

Civil engineers have used Fiber Reinforced Polymer (FRP) materials to improve the performance of structural members under static and dynamic loading conditions. Because of the uncertainty in the behavior of such strengthened members, there are some design limitations. This reality is particularly important when considering the complexity of the nonlinear behavior of materials, the impact loading conditions and geometry of the members that have FRP systems. Roudsari et al. [10] developed a new model for analysing the structural members strengthened using FRP systems under impact loading conditions. In order to develop the proposed model, ABAQUS based finite element code was considered. Lee et al. [11] Analysed the performance of shear-deficient reinforced concrete beams strengthened using carbon fiber reinforced polymers (strips/sheets) through numerical simulations on four-point bending tests. The numerical simulations are executed using ABAQUS. Krour et al. [12] presented a new method for decreasing the internal stresses in a concrete beam strengthened with FRP plate by considering the effect of the fiber orientation in the FRP plate. Zhang et al. [13] presented numerical modelling of the structural behavior of CFRP (carbon fiber reinforced polymer) strengthened RC (reinforced concrete) beams under four-point bending. Simulation of debonding at the CFRP-concrete interface was focused, as it is the main failure mode of CFRP strengthened RC beams. Jahami et al. [14] examined the behavior of reinforced concrete beams strengthened by carbon fiber reinforced polymer (CFRP) under blast loading. Numerical analysis was then performed using ABAQUS software depending on the experimental data providing damage and deflection values. Mabrouk and Ramadan [15] presented a three-dimensional (3-D) finite element (FE) modelling of RC beams shear-strengthened with externally bonded CFRP sheets using ABAQUS software.

In this study, a constitutive model based on concrete plastic damage developed and used to investigate the shear strength of non-prismatic RC beam having different haunch angle α . Moreover, Carbon Fiber Reinforced Polymer (CFRP) strips were applied to the critical sections surface with different strips number to enhance the shear strength of RC beams. All these parameters were considered and their effects were studied.

2 Experimental program

In this research, the experimental results considered are presented by al-Attar et al. [16]. According to that experimental work, fourteen reinforced self-compacting concrete non-prismatic (haunched) beams with or without strengthening were established with overall length of 2000 mm, depth at supports (h_s) of 250 mm, width of 150 mm and different haunched angle (α) values that formed different mid-span depth (h_m), Fig. 1 shows beams geometry and loading and supporting conditions where All beams were tested under monotonic loading, up to failure, with two concentrated loads. Moreover, to obtain shear failure, beams have provided with steel reinforcement bars that have different diameters as demonstrated in Fig. 2.

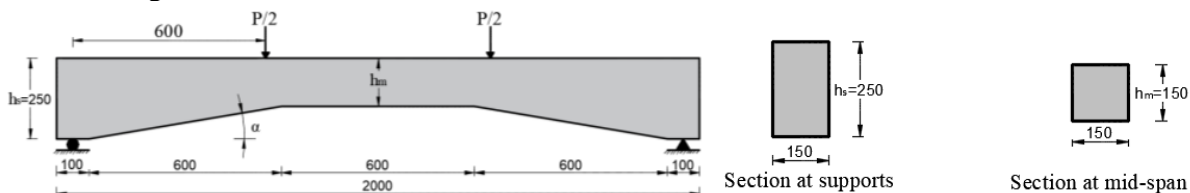


Fig.1 Beams geometry and loading condition.

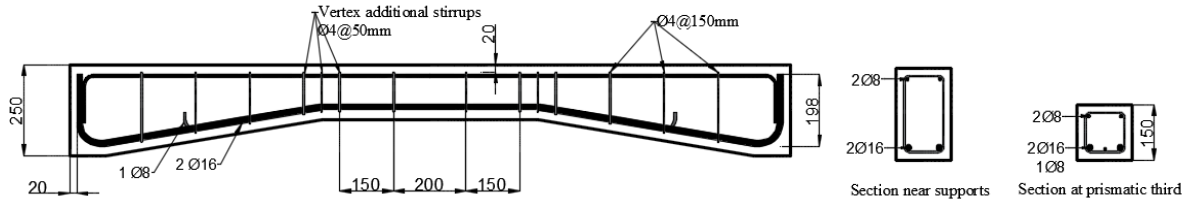


Fig. 2 Reinforcement details.

In this study, three cases with $\alpha=9^\circ$ and $h_s=150$ mm were chosen as a bench mark depending on the experimental specimens. The first beam (B1R) was without strengthening while the second and third (B1S2 and B1S3) was strengthened with 2 and 3 U-wrap CFRP sheets tilted by 45° as shown in Fig. 3. The experimental properties of materials are presented in Table 1.

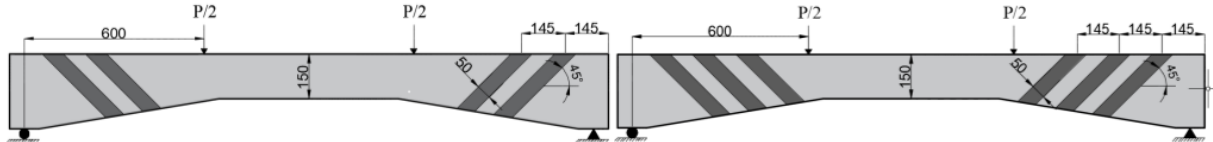


Fig. 3 CFRP distribution for beams: (left) B1S2 and (right) B1S3

Table 1 Materials properties

Material	Specifications	Yield strength (N/mm ²)	Compressive strength (N/mm ²)	Ultimate tensile strength (N/mm ²)	Flexural strength (N/mm ²)	Elastic modulus (N/mm ²)
Steel	$\phi = 16$ mm	490	-	558.58	-	210000
	$\phi = 8$ mm	556	-	632	-	210000
	$\phi = 4$ mm	548	-	629	-	210000
CFRP	T = 1 mm	-	-	4300	-	280000
Concrete	-	-	35	3.27	3.6	26420

3 Constitutive model of concrete

To study the performance of concrete in inelastic way, the isotropic damaged elasticity, the isotropic tensile and compressive plasticity are presented in the concrete damaged plasticity model. The overall strain value ε consisted of the elastic section ε^{el} and the plastic section ε^{pl} as clarified below:

$$\varepsilon = \varepsilon^{el} + \varepsilon^{pl} \quad (1)$$

$$\sigma = D^{el} : (\varepsilon - \varepsilon^{pl}) \quad (2)$$

$$\bar{\sigma} = D_0^{el} : (\varepsilon - \varepsilon^{pl}) \quad (3)$$

$$D^{el} = (1 - d)D_0^{el} \quad (4)$$

Equation (2) can be rewritten considering the nominal stress with the reduced elastic tensor showed in equation (4) giving the following equation:

$$\sigma = (1 - d)D_0^{el} : (\varepsilon - \varepsilon^{pl}) \quad (5)$$

The next stress–strain relationship formed the damage plasticity constitutive model:

$$\sigma = (1 - d) \cdot \bar{\sigma} \rightarrow \sigma = (1 - d_t)\bar{\sigma}_t + (1 - d_c)\bar{\sigma}_c \quad (6)$$

Where the scalar damage variables d_t and d_c are ranging from 0 (for undamaged case) to 1 (for fully damaged case). Basically, the damage model used for concrete took into account the failure process of tensile cracking and compressive crushing. The variables of the isotropic hardening are indicated by cracking strain $\varepsilon_t^{ck,h}$ and inelastic strain for compression $\varepsilon_c^{in,h}$, which consist of the plastic hardening strain $\varepsilon^{pl,h}$ plus the residual strain resulted by damages.

$$\varepsilon^{pl,h} = \begin{bmatrix} \varepsilon_t^{pl,h} \\ \varepsilon_c^{pl,h} \end{bmatrix}; \varepsilon^{pl} = h(\varepsilon^{pl,h}, \bar{\sigma}). \varepsilon^{\dot{pl}}, \dot{\varepsilon} = \varepsilon^{\dot{el}} + \varepsilon^{\dot{pl}} \quad (7)$$

The uniaxial tensile and compressive response of concrete is supposed to be influenced by plasticity damaging as shown in Fig. 4. The uniaxial tensile and compressive response of concrete according to the concrete damage plasticity model under compression and tension load are given by:

$$\sigma_t = (1 - d_t)E_0(\varepsilon_t - \varepsilon_t^{pl,h}) \quad (8)$$

$$\sigma_c = (1 - d_c)E_0(\varepsilon_c - \varepsilon_c^{pl,h}) \quad (9)$$

Hence, the effective uniaxial compressive and tensile stresses σ_t and σ_c are derived as following:

$$\bar{\sigma}_t = \frac{\sigma_t}{(1-d_t)} = E_0(\varepsilon_t - \varepsilon_t^{pl,h}) \quad (10)$$

$$\bar{\sigma}_c = \frac{\sigma_c}{(1-d_c)} = E_0(\varepsilon_c - \varepsilon_c^{pl,h}) \quad (11)$$

where tensile strain ε_t equals to $\varepsilon_t^{pl,h} + \varepsilon_t^{el}$, and compressive strain ε_c equals to $\varepsilon_c^{pl,h} + \varepsilon_c^{el}$.

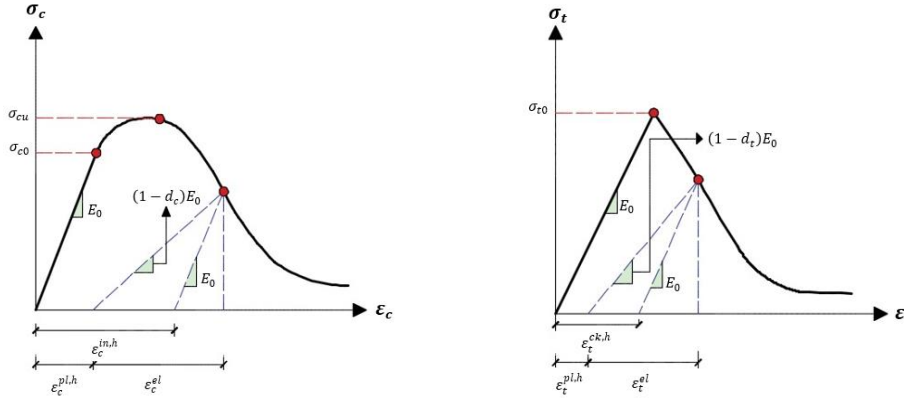


Fig. 4 Concrete response to uniaxial loading condition: (left) Compression, (right) Tension.

4 Materials and method (Finite element modeling)

Finite element failure analysing was carried out to model the nonlinear behaviour of the non-prismatic beams and damage plasticity model adopted in this study. The 8-node solid (C3D8) element was used in modelling of the concrete beam. The reinforcement bars were represented as beam elements where a 2-node linear beam in space (B31) element type was chosen. To simulate the bond between the longitudinal and the transverse reinforcements with concrete, embedded region was applied. Furthermore, the 4-node (doubly curved shell) element (S4) selected to stand for the CFRP. The bond between CFRP and concrete are considered as surface to surface contact, cohesive zone (glue), and the glue contact is defined by using friction coefficient equals to 0.1 which is available in ABAQUS manual [17]. Steel bearing plates (length = 150 mm, width=70 mm and thickness =30 mm) were installed points of loading to prevent local failure caused by crushing, and to model these plates, the (C3D8) 8-node solid element is used. The boundary conditions chosen to hold the beam were pin at the first support to produce rotation and roller set at the other support to produce rotation and horizontal movement. Also, in order to have the same experimental conditions, a vertical concentrated load was considered at each plate which placed at the top of the beam and this load was distributed by the coupling effect. Moreover, a fine mesh was applied to obtain results of sufficient accuracy where the total elements number of the beams was approximately equals to 9500 elements. Fig. 5 shows the numerical model while table 2 shows the numerical specimens' properties.

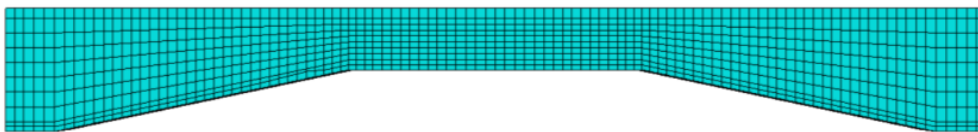


Fig. 5 The numerical model

Table 2 The numerical specimens' properties

Beam notation	α value (haunch angle)	CFRP strips no.
B1R	9 ⁰	-
B2R	11.7 ⁰	-
B3R	6.18 ⁰	-
B1S2	9 ⁰	2 U-wrap strip 45 ⁰
B1S3	9 ⁰	3 U-wrap strip 45 ⁰

5 RESULTS AND DISCUSSION

In this section, the numerical results of the models consisted of concrete, CFRP and steel is verified with experimental results. By comparing the numerical load carrying capacity with the experimental results it was realized that the ultimate loads and concrete crack patterns in these two cases are almost similar. Table 3 shows the numerical and experimental test results.

Table 3 The numerical and experimental test results

specimens	Experimental results		Numerical results	
	Δu (mm)	P_u (MPa)	Δu (mm)	P_u (MPa)
B1R	20	90	18.7293	86.27
B2R	-	-	20.824	53.812
B3R	-	-	19.74	123.53
B1S2	19.3	100	19.6	103.046
B1S3	19.6	110	23.422	110.62

The results of numerical analysis declare that the ultimate loads reached the maximum values for the specimens when 3 strips of CFRP are used. The deflection values were measured numerically at the middle of the beam specimen like the experimental test. The load-deflection relationship of all beams having different CFRP strips number in their experimental and numerical aspects are shown in Fig. 6 to 8.

On the other hand, Fig. 9 shows the effect of changing α value on the behaviour of non-prismatic beam and it can be noticed that increasing α value leads into less load capacity as the volume of concrete decreases causing earlier shear failure. In addition, as α value increase the deflection value increases too as slenderer beams act in more flexible manner causing more deflection values.

Moreover, it can be noted in Fig. 10 that all the models are almost acting in the same way at the beginning of the curves where the beams are still in the elastic stage. Gradually, at a higher loads the curves are starting to behave differently as the existence of CFRP strips affect on their behaviour and intend to lead into more brittle failure hence using CFRP strips causes less deflection values, however, their existence provided more strength for the beams. In Fig. 10 it is obvious that B1S2 model follows B1S3 until failure while the extra CFRP strips that B1S3 has pushes the curve into further strength to fail at 110.62 MPa. Also, that figure shows that the existence of the CFRP strips limits the stresses in the shear area and increases the cracks in the flexural area (mid-span of the beam). Also, according to the numerical results, the failure is considered a concrete sheatr failure which is the same failure type in the experimental cases.

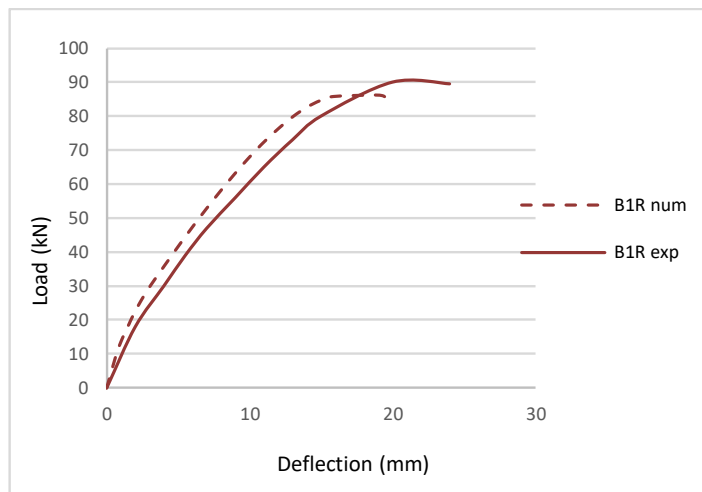


Fig. 6 B1R load-deflection relationship in numerical and experimental tests

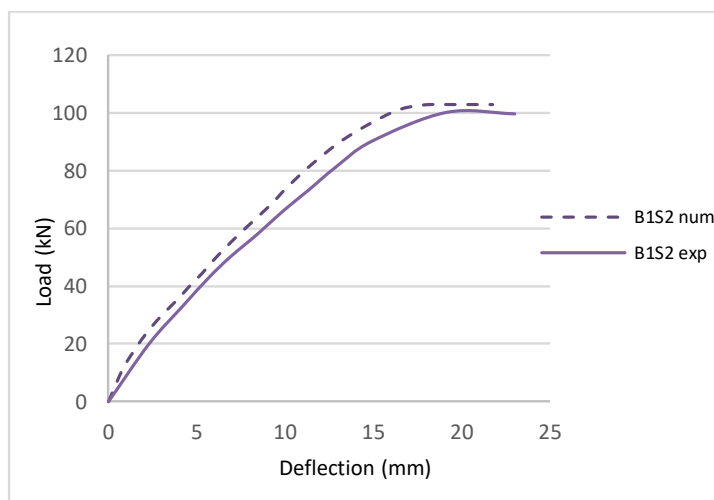


Fig. 7 B1S2 load-deflection relationship in numerical and experimental tests

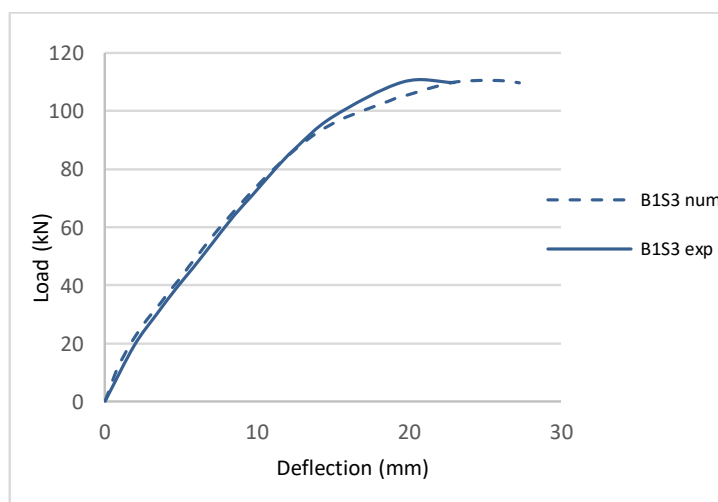


Fig. 8 B1S3 load-deflection relationship in numerical and experimental tests

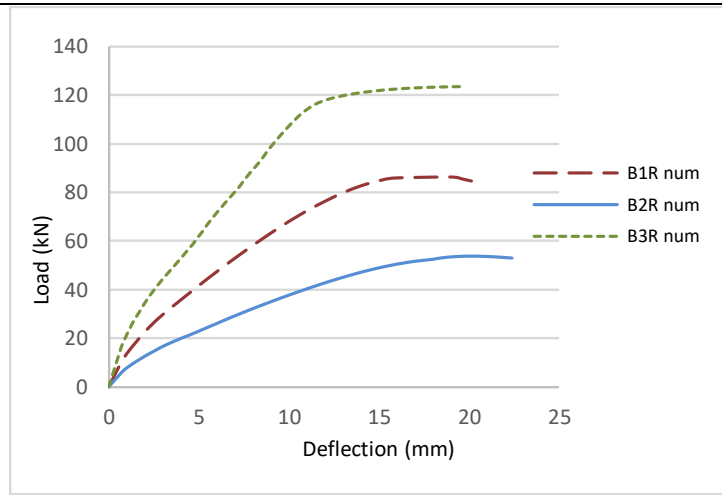


Fig. 9 The effect of α value on the non-prismatic beam behaviour

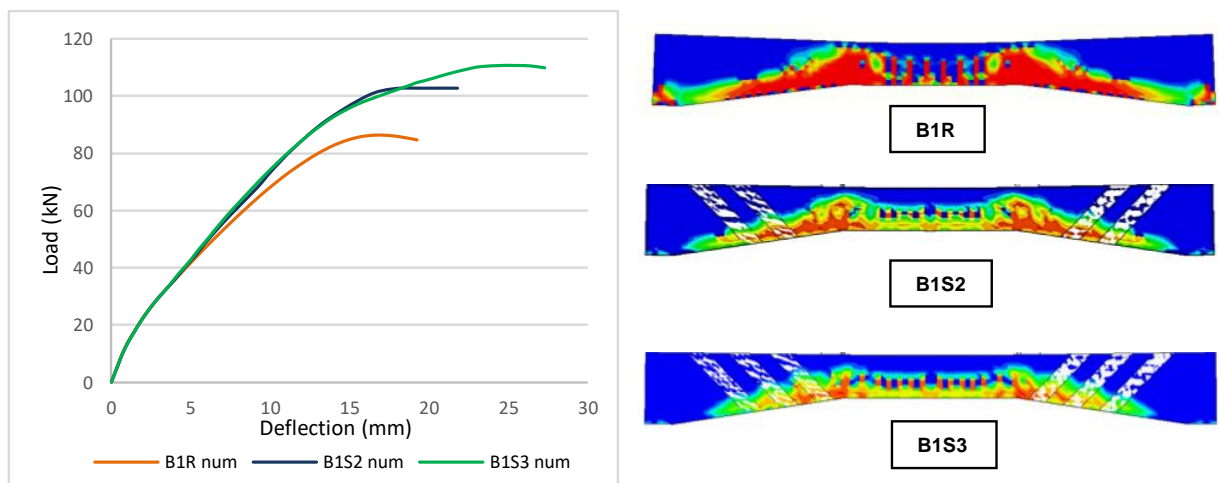


Fig. 10 The effect of CFRP existence on the beam behaviour numerically

6 CONCLUSIONS

From this study, these conclusions can be estimated:

1. Changing the α angle value had a significant effect on beam shear behavior and strength where increasing the angle value decreases the ultimate strength value as the concrete required to resist shear failure decreases and as a result beams fail in earlier loads, however, increasing α value provide more elastic behavior for non-prismatic beams as the section area decreases giving more deflection values.
2. On the other hand, according to the numerical results, the different number of CFRP strips holds an impact on the beam behavior. Comparing between numerical and experimental results it is noted that the existence of CFRP causes an increment in the ultimate load of the beams where it acts as extra support to resist the shear stress and confine the concrete section leading into more brittle and sudden failure.
3. The existence of CFRP affected clearly on the cracking pattern where it is obvious that while using CFRP strips the cracking in the mid-span of the beam increased in number and intensity and that consider a sign that most of the stresses has shifted far from shear area into flexural area. While the existence of the CFRP strips limits the stresses in the shear area.

REFERENCES

- [1] El-Niema, E.I., 1988. "Investigation of Concrete Haunched T-Beams under Shear." *Journal of Structural Engineering*, 114(4), pp.917-930.
- [2] Dado, M. and Al-Sadder, S., 2005. "A New Technique for Large Deflection Analysis of Non-Prismatic Cantilever Beams. " *Mechanics Research Communications*, 32(6), pp.692-703.
- [3] Archundia-Aranda, H.I., Tena-Colunga, A. and Grande-Vega, A., 2013. "Behavior of Reinforced Concrete Haunched Beams Subjected to Cyclic Shear Loading." *Engineering Structures*, 49, pp.27-42.
- [4] Ponnachan, J. and Koshy, V., 2018. "Study on Seismic Behavior of RC Structures with Different Parameters of Haunched Beam." *International Journal of Engineering Research & Technology (IJERT) ISSN: 2278-0181* pp.1-5.
- [5] Lubliner, J., Oliver, J., Oller, S. and Oñate, E., 1989. "A Plastic-Damage Model for Concrete." *International Journal of solids and structures*, 25(3).
- [6] Lee, J. and Fenves, G.L., 1998. "Plastic-Damage Model for Cyclic Loading of Concrete Structures." *Journal of engineering mechanics*, 124(8), pp.892-900.
- [7] Hafezolghorani, M., Hejazi, F., Vaghei, R., Jaafar, M.S.B. and Karimzade, K., 2017. "Simplified Damage Plasticity Model for Concrete. " *Structural Engineering International*, 27(1), pp.68-78.
- [8] Demin, W. and Fukang, H., 2017. "Investigation for Plastic Damage Constitutive Models of The Concrete Material. " *Procedia engineering*, 210, pp.71-78.
- [9] Shen, X., Yang, L. and Zhu, F., 2004. "A Plasticity-Based Damage Model for Concrete." *Advances in Structural Engineering*, 7(5), pp.461-467.
- [10] Roudsari, S., Hamoush, S., Soleimani, S., Abu-Lebdeh, T. and HaghghiFar, M., 2018. "Analytical Study of Reinforced Concrete Beams Strengthened by FRP Bars Subjected to Impact Loading Conditions. " *American Journal of Engineering and Applied Sciences*, arXiv preprint arXiv:1806.06929.
- [11] Lee, H.K., Ha, S.K. and Afzal, M., 2008. "Finite Element Analysis of Shear-Deficient RC Beams Strengthened with CFRP Strips/Sheets." *Structural Engineering and Mechanics*, 30(2), pp.247-261.
- [12] Krour, B., Bernard, F. and Tounsi, A., 2013. "Fibers orientation optimization for concrete beam strengthened with a CFRP bonded plate: A coupled analytical–numerical investigation." *Engineering structures*, 56, pp.218-227.
- [13] Zhang, D., Wang, Q. and Dong, J., 2016. "Simulation Study on CFRP Strengthened Reinforced Concrete Beam under Four-Point Bending." *Computers and Concrete*, 17(3), pp.407-421.
- [14] Jahami, A., Temsah, Y. and Khatib, J., 2019. "The Efficiency of Using CFRP as a Strengthening Technique for Reinforced Concrete Beams Subjected to Blast Loading." *International Journal of Advanced Structural Engineering*, 11(4), pp.411-420.
- [15] Mabrouk, A. and Ramadan, O., 2017. "Finite Element Modeling of RC Beams Shear-Strengthened with Side Bonded CFRP Sheets." Paper presented at the 6th Asia-Pacific Conference on FRP in Structures, Singapore, 19-21st July.
- [16] Al-Attar, T.S., Abdulqader, S.S. and Ibrahim, S.K., 2017. "Behavior of Tapered Self-Compacting Reinforced Concrete Beams Strengthened by CFRP." *Engineering and Technology Journal*, 35(3 Part (A) Engineering), pp.197-203.
- [17] Simulia, D.S., 2018. ABAQUS 2018 User's manual. Dassault Systems, analysis user's guide volume IV: Elements.

Punching Shear at Slab-Edge Column Connections

Deema Abu-Salma, Robert Vollum, Lorenzo Macorini

*Imperial College London,
South Kensington, London (SW7 2BU), United Kingdom*

Abstract

This paper is concerned with modelling punching shear failure at edge columns of flat slabs. Punching failure at edge columns is much less researched than at interior columns despite typical buildings having more edge than interior columns. The paper uses nonlinear finite element analysis (NLFEA) to study the influence of column aspect ratio and loading eccentricity on punching resistance at edge columns subject to inwards eccentricity. The analysis is carried out using 3D solid elements as well as a Joint Shell Punching Model (JSPM) in which nonlinear joint elements are combined with nonlinear shell elements. The JSPM uses joint elements incorporating the Critical Shear Crack Theory (CSCT) failure criterion to model punching failure. The joint elements are placed around the punching shear control perimeter which is located at $0.5d$ from the column face where d is the slab effective depth. The paper focusses on the analysis of punching shear at elongated columns orientated with the long side normal to the slab edge. This column arrangement is commonly used in residential buildings since it enables the column to be hidden within partition walls. Shear stress around the control perimeter is shown to concentrate towards the ends of elongated columns placed normal to the slab edge. Strength predictions obtained with the JSPM are shown to compare favourably with laboratory tests and numerical studies carried out with NLFEA with 3D solid elements.

1 Introduction

The paper focuses on the numerical modelling of punching resistance at edge columns which is best simulated using 3D solid elements since these capture the complex stress distribution around the column where punching failure occurs. Although capable of giving good predictions of punching resistance, nonlinear finite element analysis (NLFEA) using 3D solid elements is too computationally demanding for practical use. NLFEA using 2D shell elements is more computationally efficient but advanced procedures are required to model punching failure explicitly since conventional 2D shell elements do not capture through thickness shear failure. Two alternative approaches are adopted in the literature for overcoming this problem. In the first approach [1-2], a 3D state of stress and strain is modelled within each layer of the shell element. The out-of-plane normal strain is calculated from the assumption that the out-of-plane normal stress is negligible. In the second approach [3-6], 3-D connector elements are combined with nonlinear shell elements. This paper utilises the JSPM approach of Setiawan et al. [6] in which punching failure is modelled with joint elements positioned around a control perimeter located at $0.5d$ from the column face (where d is the slab effective depth). The joint elements are used to connect the nodes of the shell elements located to either side of the punching control perimeter. This paper extends the use of the JSPM to the modelling of punching failure at edge columns of flat slabs. Predictions of the JSPM are compared with the predictions of NLFEA with 3D solid elements as well as experimental test results.

2 Nonlinear Finite Element Analysis Using 3D Solid Elements

This paper calibrates the JSPM for punching at external columns using experimental data as well as the results of 3D NLFEA with solid elements. The 3D NLFEA with solid elements was carried out using ATENA [7]. Concrete was modelled using the fracture-plastic model Cementitious 2, which combines constitutive models for compression and tension. The hardening part of the compressive response is expressed in terms of strain while the softening part is expressed in terms of a limiting displacement w_d at which the compressive stress reduces to zero. This approach, which reduces mesh sensitivity, is equivalent to relating the softening response to the compressive fracture energy. Based on calibration studies, a fully rotating smeared crack approach was used with w_d equal to its default value of 0.5 mm. After concrete cracks, the compressive strength is reduced in the direction parallel to the cracks similarly to the Modified Compression Field Theory [8]. The compressive strength

reduction factor was limited to a minimum of 0.8. Based on a mesh sensitivity study, linear order hexahedra elements were adopted for meshing the column and slab. Linear order tetrahedra elements were used to mesh the loading plates. The slab was modelled with 10 elements through the slab thickness using a graded mesh similar to that adopted by Setiawan [9]. In this approach, a very fine mesh is used to mesh the slab within $2d$ of the column face. Reinforcement was modelled with a bilinear stress-strain relationship assuming perfect bond. Force-control and arc-length methods were used for loading the slabs. A convergence criterion of 0.01% was assigned for the energy error and 1% for the displacement, residual force and absolute residual force errors. According to previous studies by Setiawan [9], punching failure occurs when the radial compressive strains in the soffit of the slab located at $d/2$ away from the column face drop to zero (d is the slab average effective depth). This criterion is adopted in the calibration studies of this paper.

3 Nonlinear Finite Element Analysis Using 2D Shell Elements

The JSPM is implemented in the nonlinear finite element program ADAPTIC [10]. The slab is modelled using a layered-shell element based on the conventional Reissner-Mindlin hypothesis. In plane material nonlinearities are accounted for along with geometric nonlinearities [11]. Linear elements were used to model the columns, which were connected to the shell slab elements using rigid links. The material properties for concrete were as described previously in [6], [10-12]. Reinforcement was modelled with a bilinear stress-strain response and minimal strain hardening assuming perfect bond.

4 Validation of NLFEA with Experimental Test Results

The NLFEA modelling procedure adopted in ATENA was validated by modelling the four internal and six external slab-column connections listed in Table 1. All six of the external slab-column specimens were also modelled in ADAPTIC using nonlinear 2D shell elements without joint elements around the control perimeter. Slabs XXX and HXXX of El-Salakawy et al. [13] measured 1540 mm long by 1020 mm wide by 120 mm thick with an average effective depth of 88.75 mm. The slab was simply supported around one long and two short sides. A 250 mm square column was positioned midway along the free edge of the slab with its outside face flush with the slab edge. The column was loaded vertically and horizontally with a constant inwards eccentricity of 300 mm in slab XXX and 660 mm in slab HXXX. More details regarding the test setup can be found in [13]. The NLFEA model was evaluated by comparing both the failure load and the load-deflection response. Fig.1 (left) and Fig.1 (right) compare the measured load-deflection responses of slabs XXX and HXXX respectively with those obtained from ATENA and ADAPTIC. The load deflection responses obtained with ATENA were terminated at the failure load obtained using the strain-based failure criterion of Setiawan [9]. In the same figure, the load-deflection response obtained by Genikomsou and Polak [14] using ABAQUS is added for comparison. It is concluded that the deflections calculated with ATENA and ADAPTIC compare reasonably with those obtained by [14] as well as the experimentally observed deflection of XXX but not HXXX. ATENA also captures the measured failure loads reasonably well unlike the ADAPTIC analysis which only considers flexural failure.

5 NLFEA parametric study

Punching failure at elongated edge columns has hardly been studied despite the common occurrence of such columns in residential buildings. Finite element analysis (FEA) shows that shear stress in the slab concentrates at the inner end of the elongated column. The paper presents the results of a parametric study undertaken to study the influence of column aspect ratio and loading eccentricity on punching resistance at edge columns. The parametric study is based on slab L1 of Albuquerque et al. [15] (see Fig. 2) in which c_1 and c_2 refer to the longer and shorter sides of the column respectively. The column and slab edge were extended backwards from their position in L1 as shown in Fig. 2 to create specimens with column sizes of 1000 x 300 mm and 750 x 300 mm. These specimens are depicted L1c and L1b respectively. Eccentricities of 1000 and 1200 mm were investigated for connection L1c, while eccentricities of 500, 700 and 1200 mm were investigated for connection L1b. Two additional eccentricities of 500 and 700 mm were investigated for the 300 mm square column of L1 [15]. The largest eccentricities are proportionally at the upper end of those obtained from elastic FEA of a flat slab frame building with varying column sizes and spans. In practice, maximum eccentricities are likely to be less than considered in this study.

Table 1 Flat slab-column connections modelled with ATENA

Slab	Column size (mm x mm)	Column location	Loading type	V_{test}/V_{ATENA}	Source
PT22	260 x 260	Interior	Concentric	989/1012=0.98	[16]
PT31				1433/1489=0.96	
OC13	200 x 600	Interior	Concentric	568/573.5=0.99	[17]
LS06	300 x 300	Interior	Eccentric	582.3/501.3=1.16	[18]
XXX	250 x 250	Edge	Eccentric	125/117.9=1.06	[13]
HXXX				69/61=1.13	
L1	300 x 300	Edge	Eccentric	308/345=0.89	[15]
L2			Concentric	315/318.3=0.99	
L5			Eccentric	374/415=0.90	
L6			Eccentric	330/344=0.96	

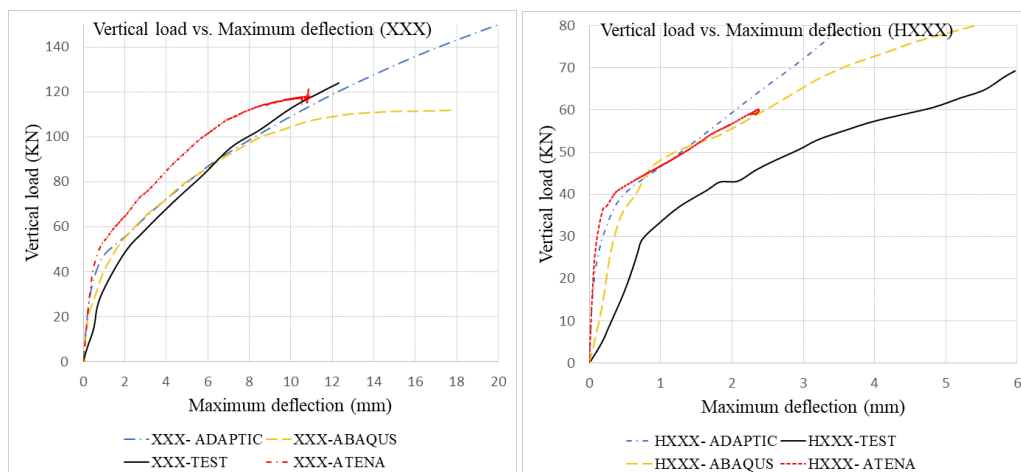


Fig. 1 Load-deflection response of slab XXX (left) and slab HXXX (right)

6 The Joint Shell Punching Model (JSPM)

The JSPM [6] was used to model all the slabs with edge columns modelled with ATENA using 3D solid elements. Nonlinear joint elements (jel3) were inserted between the nodes of the shell elements lying to either side of a square control perimeter positioned at $0.5d$ from the column face where d is the slab effective depth. These joints are depicted two-way since they are used to simulate punching failure. Weak jel3 elements with almost zero-resistance were positioned along parts of the control perimeter further than $1.5d$ from the column corners which are neglected in MC2010 [19] as indicated in Fig. 3. The dimensions c_1 and c_2 in Fig. 3 refer to the longer and shorter column sides respectively while d is the slab effective depth. The 6-degree of freedom jel3 element has 4 nodes of which nodes 1 and 2 form the joint and are initially coincident. Nodes 3 and 4 are used to define the x axis and the plane in which the y-axis is positioned respectively. In the JSPM, nodes 1 and 2 are positioned around the punching control perimeter, node 3 is positioned around the line of radial contraflexure where rotations are typically greatest and node 4 is placed on the column chord just above the slab centreline. The limiting joint shear resistance is calculated at each load step in terms of the relative slab-

column rotation which is given by the difference between the rotations at nodes 3 and 4. Initially k_{inc} behaves linearly with out-of-plane stiffness, depicted k_{inc} , calculated as follows:

$$(1)$$

in which E_c is the concrete elastic modulus, l_s is the joint spacing, ν is Poisson's ratio which is taken as 0.2 and k_{red} is an out of plane stiffness reduction factor that accounts for cracking.

The joint shear force is calculated in terms of the vertical joint separation until the joint fails in shear. Subsequently, the joint shear force is calculated in terms of its sector rotation using equation (2) of the CSCT. Each joint fails independently when its shear force reaches its resistance calculated in accordance with the critical shear crack theory (CSCT) of Muttoni [20], which relates shear resistance to relative slab-column rotation. The shear strength of each joint is calculated in terms of its sector rotation as follows:

$$(2)$$

where l_{si} is the spacing of joint i , f_c is the concrete cylinder strength, ψ_{si} is the relative slab-column sector rotation for joint i , which is continuously updated through the analysis, d is the average slab effective depth and d_g is the maximum aggregate size.

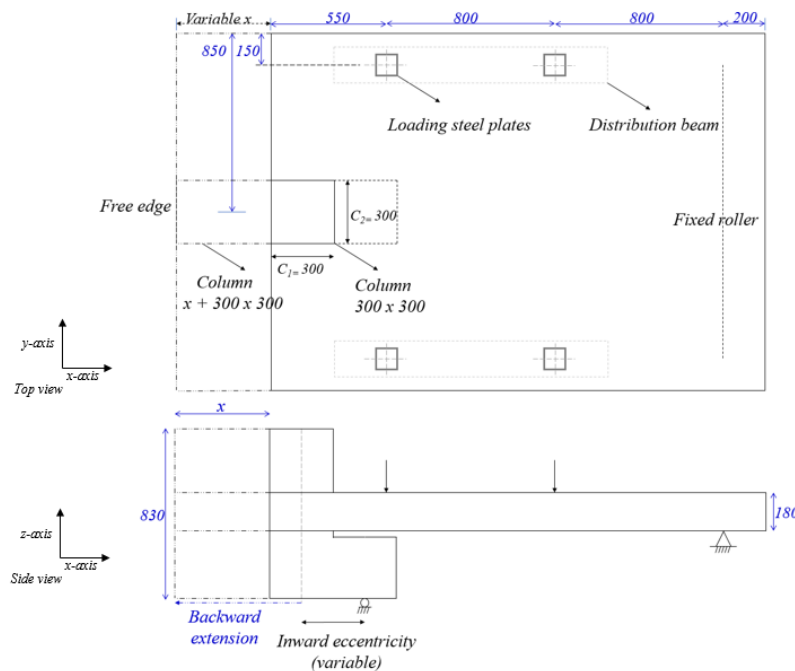


Fig. 2 Plan showing original and parametric test set-up regenerated from [15] (all dimensions in mm).

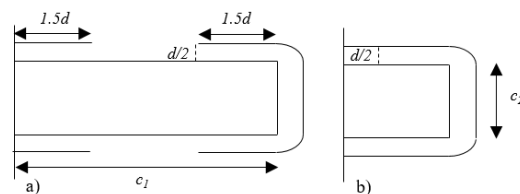


Fig. 3 Control perimeter by MC2010 [19] with a) $c_1 > 3d$ and $c_2 < 3d$ and c) c_1 and $c_2 < 3d$

6.1 Shear force distribution along the control perimeter

A parametric study was carried out to determine a suitable choice of k_{inc} for edge column connections. All slabs were analysed with $k_{inc} = 1e12$ N/mm (rigid). Additionally, k_{inc} was calculated with $k_{red} = 0.1, 0.5, 0.8$ and 1.0 for HXXX and XXX as well as $k_{red} = 0.1$ and 1.0 for L1, L2, L1b and L1c.

Without an additional failure criterion, global failure is triggered in the JSPM when all joints fail. In this case, the JSPM overestimates punching resistance since the extent of shear redistribution at punching failure is overestimated. The reason for this was investigated by plotting the shear force/length around the control perimeter at several load steps for each value of k_{inc} . The resulting shear force distributions were compared with shear force distributions obtained using ATENA at the same load steps. This is illustrated in Fig. 4 below which shows shear force distributions around the control perimeter of slab HXXX determined using the JSPM (with $k_{inc} = 1e12$ N/mm) and ATENA. Shear forces are shown for the JSPM at the failure loads obtained with ATENA (V_{ATENA}), experimentally ($1.15 V_{ATENA}$) as well as $1.22V_{ATENA}$. The shear force/length obtained with ATENA at V_{ATENA} is also shown for comparison. Fig. 4 shows that downward redistribution of joint shear forces occurred between V_{ATENA} and $1.22V_{ATENA}$. This arises because once a joint fails, it softens following the calculated CSCT resistance curve, which allows shear redistribution to the adjacent joints. Without intervention, the analysis continues until all joints fail which overestimates punching resistance. Consequently, an additional failure criterion is needed to adjust the JSPM predictions as found in [9] for eccentrically loaded internal slab column joints.

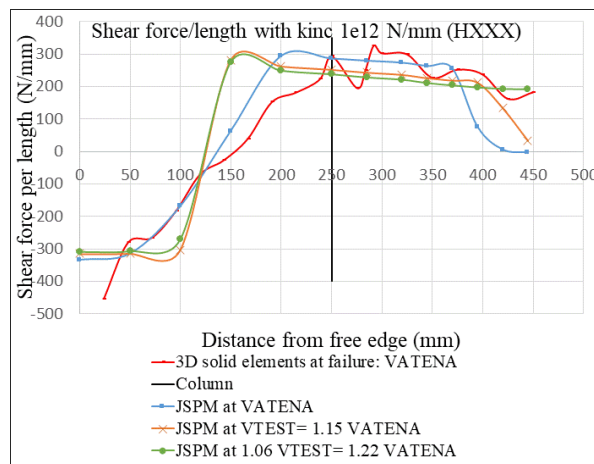


Fig. 4 Shear force/length distribution for specimen HXXX at different loads

Fig. 5 compares shear force per unit length distributions obtained with ATENA and the JSPM, with $k_{red} = 0.1$, for slab L1b with an eccentricity of 700 mm. The shear force/unit length is plotted around a rectangular perimeter at a distance of $d/2$ from the column face. Shear forces are shown in Fig. 5 (left) at loads of $0.47 P_{u, ATENA}$ and in Fig. 5 (right) at $P_{u, ATENA}$ as well as $0.93P_{u, ATENA}$. Fig. 5 (right) shows a shear reversal at the three joints next to the free edge at higher loads. The reason for this was investigated and found to be related to the proportion of unbalanced moment carried by eccentric shear, flexure and torsion. At $0.93P_{u, ATENA}$, eccentric shear and torsion carried 49.7% and 22% of the unbalanced moment respectively with the remainder carried by flexure. As the load increased to $P_{u, ATENA}$, the eccentric shear component of moment resistance reduced to 33.3% while the torsional component increased to 37.6% of the unbalanced moment. The JSPM shear force distribution at $P_{u, ATENA}$ is considered unrealistic.

7 Modified JSPM failure criterion

The failure load predicted by the JSPM depends on the joint at which global failure is assumed to be triggered as well as the adopted joint shear stiffness k_{inc} . Reducing k_{inc} flattens the shear force/length distribution, thereby, reducing the peak shear force and increasing the calculated punching resistance. Reducing k_{red} also reduces the proportion of unbalanced moment that is carried by eccentric shear. Fig. 6 below compares the experimental and predicted load-deflection responses of slabs XXX and HXXX of El-Salakaway et al. [13] with 250 mm square columns. The coefficient k_{inc} was assumed to be $1e12$ N/mm in the JSPM. Global punching failure of slabs with square columns (all with $c_1 < 3d$ where c_1 is defined in Fig. 3) was assumed to occur when the joint midway along c_1 failed. As shown in Fig. 6, this approach gives reasonable estimates of the experimentally observed failure load.

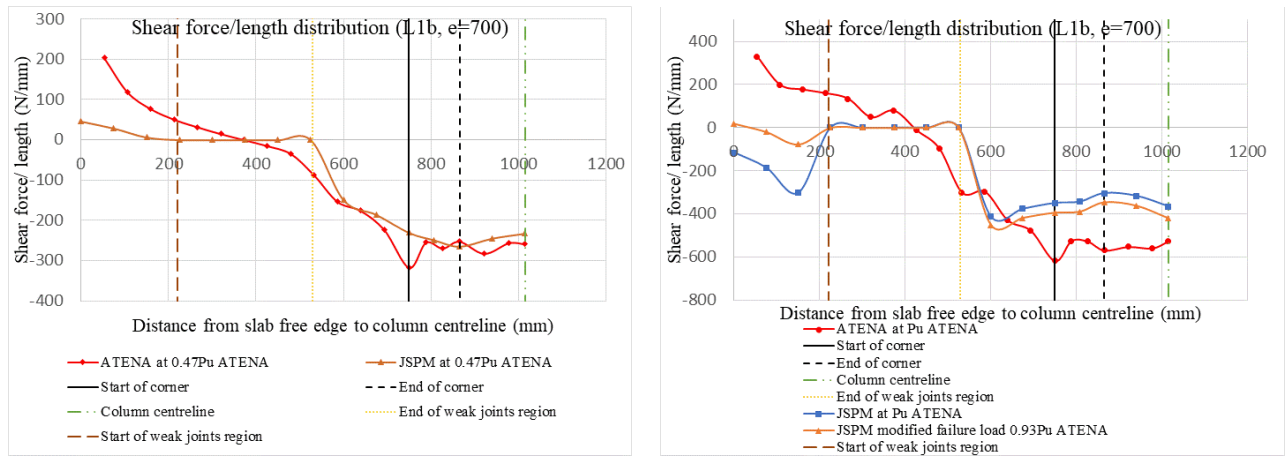


Fig. 5 Shear force/length distribution for specimen L1b ($e=700$ mm) before failure (left) and at failure (right)

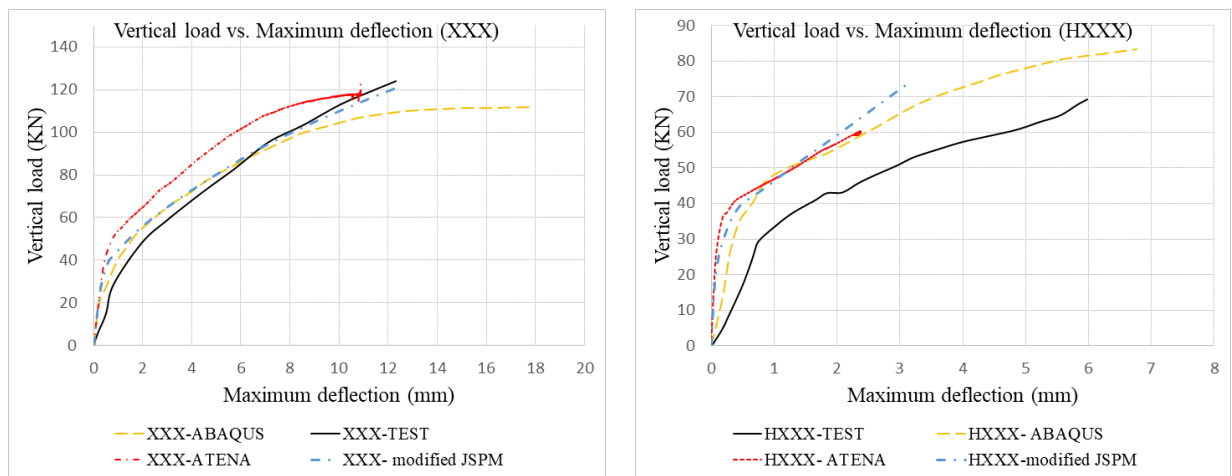


Fig. 6 Load-deflection response of slab XXX (left) and slab HXXX (right) with modified JSPM

In the absence of available experimental data, the JSPM predictions for elongated columns are compared with the ATENA predictions which are themselves subject to error. Punching failure was assumed to occur when the last two-way joint along side c_1 (see Fig. 3) at $1.5d$ from the inner column face failed. Dummy joints with minimal resistance were used along the central part of c_1 which is neglected in MC2010. Utilising this assumption, punching resistance at elongated edge columns tended to be underestimated if k_{inc} was taken as $1e12$. Improved estimates of punching resistance were obtained if k_{inc} was calculated with $k_{red} = 0.1$ as adopted by Setiawan et al. [6] for eccentrically loaded internal slab column connections. Predictions of the JSPM with $k_{red} = 0.1$ are illustrated in Fig. 7 for elongated columns. Fig. 7 (left) compares the load-rotation responses obtained with the JSPM and ATENA for slab L1b with an eccentricity of 700 mm. Also shown is the load-rotation response obtained with ADAPTIC omitting the joints of the JSPM. Similarly, Fig. 7 (right) shows the load-rotation behaviour of slab L1b with an eccentricity of 1200 mm. The modified JSPM predictions compare reasonably well with ATENA, while the shell model without joints is unable to predict the punching shear failure load. Table 2 summarises punching resistances obtained with ATENA and the JSPM with $k_{inc} = 1e12$ for square columns and k_{inc} calculated with $k_{red} = 0.1$ for elongated columns. In most cases, the JSPM predictions compare reasonably with the ATENA predictions.

8 Conclusion

This paper uses numerical analysis to investigate punching shear failure at edge columns of flat slabs. The effect of loading eccentricity and column size are investigated through the use of 3D solid elements, and the joint shell punching model (JSPM) of Setiawan et al. [6]. The effect of column elongation on punching resistance at edge columns is investigated seemingly for the first time. NLFEA is carried out with 3D solid elements using ATENA to investigate the influence of loading eccentricity

on punching resistance. Examination of the shear force/unit length around a rectangular control perimeter at 0.5d from the column face shows that shear redistribution occurs near failure with shear being redistributed from highly stressed to less stressed parts of the perimeter. The results of the NLFEA with ATENA are used to develop a provisional failure criterion for the JSPM at edge columns. Global punching failure is assumed to occur in the JSPM at initial failure of the two-way joint midway along the side c_1 (see Fig. 3). In the case of large columns with $c_1 > 3d$, global failure is assumed to occur when the joint along c_1 at 1.5d from the inner column face fails. Dummy joints with minimal resistance were positioned along segments of the control perimeter further than 1.5d from the column face which are neglected in MC2010. This approach limits shear distribution between the joints and prevents the JSPM from over predicting punching resistance. Further research is needed to generalise the applicability of the JSPM to other column sizes and eccentricities.

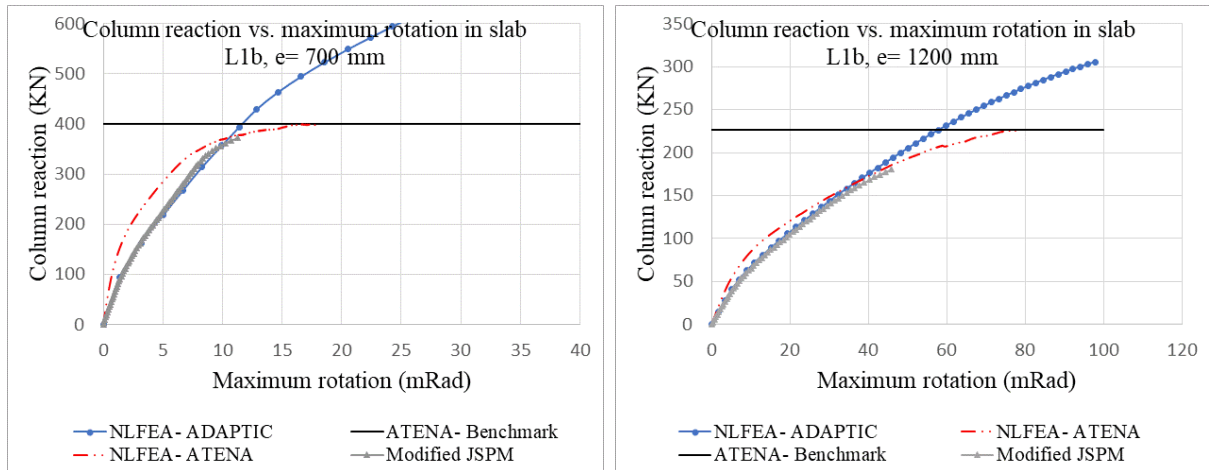


Fig. 7 Load-deflection response of slab L1b with eccentricity of 700 mm (left) and with eccentricity of 1200 mm (right) with modified JSPM predictions

Table 2 Modified JSPM load predictions

Slab	Column size (mm)	Eccentricity (mm)	V TEST (KN)	V ATENA (KN)	V JSPM modified (KN)	% Difference with TEST or ATENA
XXX	250 x 250	300	125	117.9	122	-2% (TEST)
HXXX	250 x 250	660	69	61	73	6% (TEST)
L2	300 x 300	0	315	318.3	373	18%
L1	300 x 300	300	308	345	380	23% (TEST)
L1	300 x 300	500	Not applicable	301	319	6%
		700		270	266	-1%
L1b	750 x 300	500	Not applicable	459	512	11%
		700		400	372	-7%
		1200		226	180	-20%
L1c	1000 x 300	1000	Not applicable	383	321	-16%
		1200		253	232	-8%

9 References

- [1] Polak, MA. 2005. "Shell finite element analysis of RC plates supported on columns for punching shear and flexure." *Engineering Computations* 22(4):409–28.
- [2] Hrynyk, TD., and Vecchio FJ. 2015. "Capturing out-of-plane shear failures in the analysis of reinforced concrete shells." *Journal of Structural Engineering* 141(12):04015058
- [3] Keyvani, L., Sasani, M., and Mirzaei, Y. 2014. "Compressive membrane action in progressive collapse resistance of RC flat plates." *Engineering Structures* 59:554–64.
- [4] Liu, J., Tian, Y., Orton, S.L., and Said AM. 2015. "Resistance of flat-plate buildings against progressive collapse." Part I: Modeling of slab-column connections *Journal of Structural Engineering*. 141(12).
- [5] Liu, J., Tian, Y., Orton, S.L., and Said, A.M. 2015. Resistance of flat-plate buildings against progressive collapse. Part II: system response. *Journal of Structural Engineering* 141(12).
- [6] Setiwana, A., Vollum, R.L., Macorini, L., and Izzuddin, B. 2019. "Efficient 3-D modelling of punching shear failure at slab-column connections by means of nonlinear joint elements." *Engineering Structures* 197.
- [7] Cervenka, V., Jendele, L., and Cervenka, J. 2018. *ATENA Program Documentation, Part 1, Theory*. Cervenka Consulting, Prague.
- [8] Vecchio, F.J., and Collins, M.P. 1986. "The modified compression-field theory for reinforced concrete elements subjected to shear." *ACI Structural Journal* 83(2):219–31.
- [9] Setiwan, A. 2019. "Efficient strategy for modelling punching failure of flat slabs." PhD diss., Imperial College London.
- [10] Izzuddin, B.A. 1991. "Nonlinear dynamic analysis of framed structures." PhD diss., Department of Civil Engineering, Imperial College, London.
- [11] Izzuddin, B.A., Tao, X.Y., and Elghazouli, A.Y. 2004. "Realistic modeling of composite and reinforced concrete floor slabs under extreme loading." Part I: analytical method. *Journal of Structural Engineering* 130(12):1972–84.
- [12] Elghazouli, A. Y., and Izzuddin, B. A. 2004. "Realistic modelling of composite and reinforced concrete floor slabs under extreme loading." Part II: Verification and application. *Journal of Structural Engineering* 130(12): 1985–1996.
- [13] El-Salakawy, E.F., Polak, M.A., and Soliman, M. H. 1998. "Slab-column edge connections subjected to high moments." *Canadian Journal of Civil Engineering* 25 (3): 526-538.
- [14] Genikomsou, A., and Polak, M. 2015. "Finite element analysis of punching shear of concrete slabs using damaged plasticity model in ABAQUS." *Engineering Structures* 98: 38-48.
- [15] Albuquerque, N. G. B., Melo, G. S. and Vollum, R. L. 2016. "Punching shear strength of flat slab-edge column connections with outward eccentricity of loading." *ACI Structural Journal* 113 (5): 1117-1129.
- [16] Sagaseta, J., Muttoni, A., Ruiz, M., and Tassinari, L. 2011. "Non-axis-symmetrical punching shear around internal columns of RC slabs without transverse reinforcement." *Magazine of Concrete Research* 63 (6), 441-457.
- [17] Teng, S., Gheong, H. K., Kuang, K. L., and Gneg, J. Z. 2004. "Punching shear strength of slabs with openings and supported on rectangular columns." *ACI Structural Journal* 101 (5): 678-687.
- [18] Ferreira, M. D. P. 2010. "Punção em lajes lisas de concreto armado com armaduras de cisalhamento e momentos desbalanceados." PhD diss., The University of Brasília.
- [19] fib (Fédération Internationale du Béton) 2013. "*fib Model Code for concrete structures 2010*." Fédération Internationale du Béton, Lausanne, Switzerland
- [20] Muttoni A. 2008. "Punching shear strength of reinforced concrete slabs without transverse reinforcement." *ACI Structural Journal* 105 (4): 440-450

Simplification of the procedure for determining the fire resistance of heat-insulating brick masonry

Heiner Kruse, Catherina Thiele, Christian Glock

Department of civil engineering,
TU Kaiserslautern,
Gottlieb-Daimler Str. 67, 67663 Kaiserslautern, Germany

Abstract

In terms of climate change, more heat-insulating brick masonry are continuously being used in construction of buildings. In practice, it takes a very long time for a newly developed brick to receive approval. Regarding the requirements of building physics, which also includes fire protection, a simplified investigation procedure should enable a quick classification of fire protection.

In order to achieve this goal, various test reports from fire tests with heat-insulating masonry are analysed and in a second step further fire tests are carried out in a targeted manner. Within the scope of the evaluation of the test reports, initial investigations have already shown that minimum fire resistance classes can be formed on the basis of the test reports, but that these classes must be viewed very conservatively and critically. At the end of the research project, economic minimum fire resistance classes for heat-insulating brick masonry should be excised, as they are currently available for standardised bricks in the national annex DIN EN 1996-1-2/NA:2013 [7].

1 Scientific, technical and economic importance

The demand for building materials with steadily increasing requirements for thermal protection, acoustic insulation and fire protection for masonry in residential construction has continuously grown. According to the housing market forecast 2030 published in May 2015 by the Federal Institute for Building, Urban and Regional Research (Bundesinstitut für Bau-, Stadt- und Raumforschung - BBSR), the number of households will increase by more than 500.000 in the period from 2015 to 2030 and will be approximately 1.3 % higher in 2030 than in 2015 [1].

According to the German Society for Masonry Construction (Deutsche Gesellschaft für Mauerwerksbau - DGfM), around 76% of all walls for the construction of new residential buildings were built of masonry in 2015 [2]. This market-leading use of masonry in residential construction will continue in the years after 2015, as shown in Figure 1.

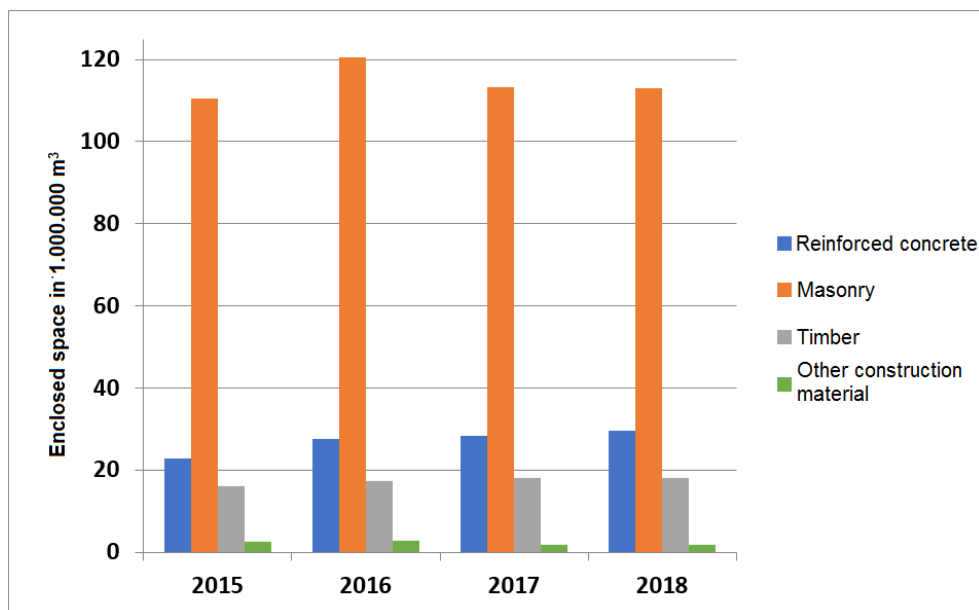


Fig. 1 Comparison of the building materials used in Germany for the construction of new apartments (enclosed space after building permits have been issued) [3].

A study carried out at the Technical University of Darmstadt, which considers the three sustainability dimensions of ecology, economy and socio-culture over the entire life cycle of residential construction, also presents the numerous sustainability-relevant advantages of masonry. Furthermore, a study by the working group for contemporary building e.V. (Arbeitsgemeinschaft für zeitgemäßes Bauen e.V. - ARGE//eV) showed the high economic efficiency of masonry in housing construction. According to this study, the average construction costs for masonry are 2 to 3.8 % lower than for concrete and 4.7 to 6 % lower than for timber construction. In addition, external walls made of masonry in apartment buildings are approximately 11 % less expensive compared to the use of reinforced concrete and have a cost advantage of approximately 15 % compared to timber constructions. The results clearly show that masonry is still the most economical construction method in terms of the necessary contribution to the creation of affordable and social housing [2].

If the masonry building materials from the statistics "Building and living - building permits for residential and non-residential buildings according to predominantly used building material" (Bauen und Wohnen - Baugenehmigungen von Wohn- und Nichtwohngebäuden nach überwiegend verwendetem Baustoff) in Figure 1 are considered separately, Figure 2 shows that the brick used in the construction of new apartments is the most frequently used representing building material for masonry [3].

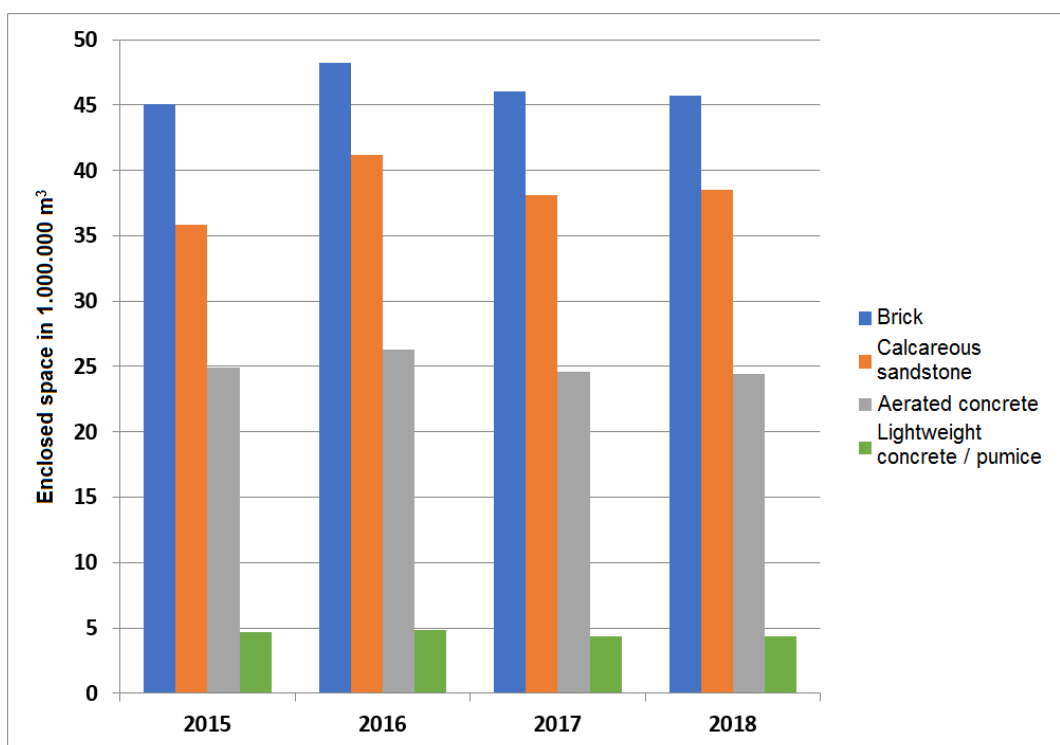


Fig. 2 Comparison of the masonry building materials used in Germany for the construction of new apartments (enclosed space after building permits have been issued) [3].

In line with the high demand for brick products for masonry construction described above, the brick and tile industry must react promptly with market-oriented products that meet the constantly increasing building physics requirements for thermal protection, acoustic insulation and fire protection. The innovative measures required for this include not only optimizations on the raw material side or during the burning process, but also targeted adjustments to the geometric hole pattern and web design as well as the use of fillers (lightweight materials) as highly insulating components. The improvement of only one physical property interacts in different ways with the other physical properties. For example, an improved thermal conductivity due to an increase in porosity caused by the raw material usually reduces the acoustic insulation or the permissible mechanical load-bearing capacity.

These requirements are set in the respective general building authority approvals or type approvals. For the declaration of the product and its possible applications, a proof of the physical building properties must be provided. This includes also a classification in fire resistance classes for fire protection. According to the current state of the art, these are large fire tests on storey-height walls for a product in

accordance with the European harmonised standards EN 1363-1:2012 [4], EN 1363-2:1999 [5] and EN 1365-1:2013 [6]. These tests are usually very expensive and time consuming. Due to economic efficiency, manufacturers of brick masonry are interested in the lowest possible number of fire tests. As a result, the optimum utilisation is not always achievable, either because of the desired fire resistance class, that has not been achieved or because of a too low classification, that limits the possible uses of an approved product in masonry construction. This inadequate classification is related to the test conditions, that require a fire test under continuous masonry loading. The height of the load is mainly calculated on the wall compressive strength, which is based on an f_k value, which is determined separately in the approval procedure.

The national annex DIN EN 1996-1-2/NA:2013 [7] contains a table of values for a classification of the fire resistance duration of masonry walls according to the current state of the art. By using these values, a quick classification of the fire resistance class can be made for different material properties in combination with different degrees of utilisation. However, the table of values for brick masonry given in the standard are only applicable when using normal masonry mortar and/or light masonry mortar. For heat insulating brick masonry, which is usually made with thin-bed mortar, there are no simplified table of values that would be necessary for a quick classification into fire resistance classes. In addition, the tables only apply to standard bricks and bricks with a gross density class ≥ 0.8 . Heat-insulating hollow bricks with large chambers and heat-insulating hollow bricks with small chambers, which predominantly have a gross density class < 0.8 , are as well excluded in the existing tables.

Furthermore, the approach of the research activity should define extended fields of application. Among other things, the subject of the investigations is aimed at acquiring knowledge that allows statements to be made on the extent to which the compressive strength of thermally insulating vertically perforated bricks correlates with different temperature stresses and which differences in the event of fire between thin-bed mortar and normal masonry mortar must be taken into account. For these investigations, different masonry bricks are to be assigned into groups regarding to their properties (total perforated cross section, web thickness, etc.) and analysed in tests with temperature and pressure loads.

By defining minimum fire resistance classes for different groups of heat-insulating brick masonry, a simple and quick classification of fire resistance shall be achieved in the future. The tests or calculated proofs of fire resistance required in the context of general building authority approval procedures could be omitted thereby.

2 Working hypothesis

The aim of this research project is, on the one hand, to define data on fire resistance or fire resistance class for heat-insulating brick masonry with different loads / degrees of utilisation under boundary conditions to be observed (brick dimensions, proportion of holes, etc.), on the basis of the results of the basic research and, on the other hand by evaluating existing fire tests and further experiments. Due to the elaboration of minimum fire resistance classes, these results form the basis for a new simplified assessment of fire resistance without or with reduced experimental effort. In order to determine the necessary minimum fire resistance classes, all relevant effects and material characteristics for the design must be determined and taken into account but also confirmed by experimental tests.

When defining extended areas of application, special attention should be paid to the possibility of specifying increased fire resistance durations for lower utilization factors or higher utilization factors for lower fire resistance durations. It should also be clarified whether the slenderness of masonry walls can be extrapolated, which would lead to a wider application area of the products. In addition to the determination of minimum fire resistance classes relevant to standards, the project will also investigate whether small-format fire tests could replace the time-consuming and costly large-scale fire tests with walls measuring 3 m x 3 m.

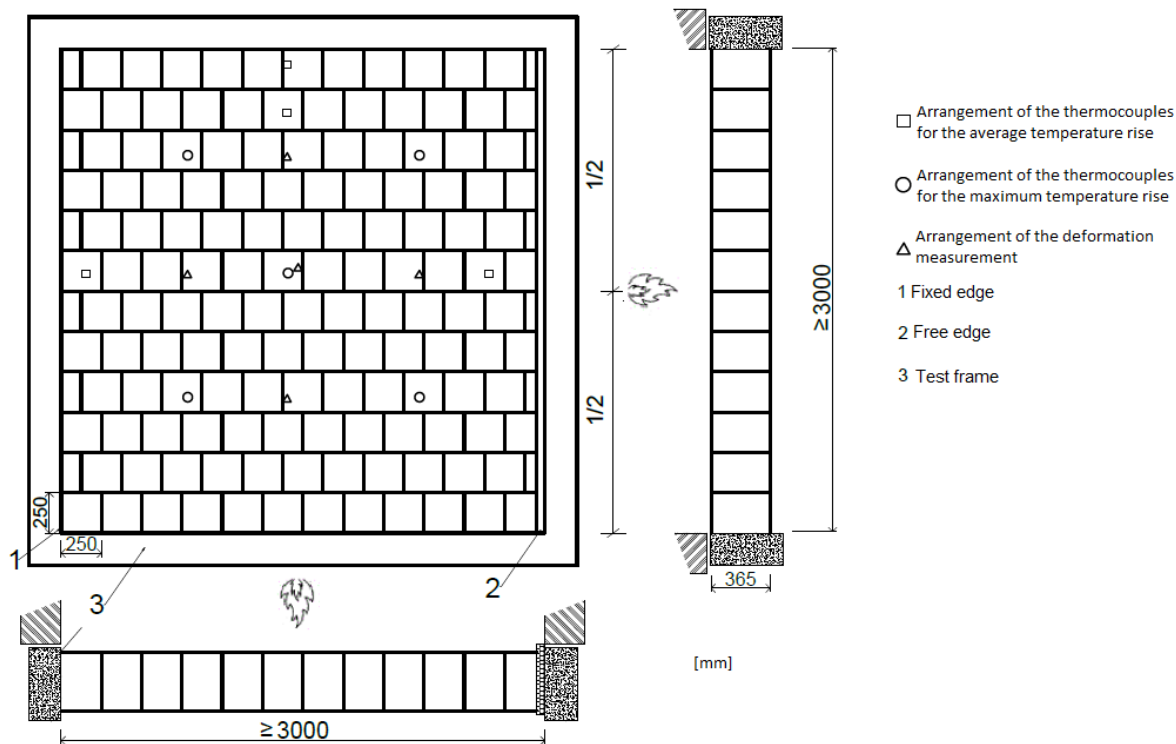


Fig. 3 An exemplary arrangement of thermocouples on the non-flamed side and arrangement of the deformation measurements for brick masonry walls according to EN 1364-1:2015 [8].

Small-format fire tests would be necessary if the defined minimum fire resistance classes are not sufficient for the manufacturer or if his product cannot be assigned to any group of bricks. The aim purpose is to show to what extent the small-scale tests can replace the large-scale fire tests with averaging costs of approximately 12.500 € per test and with a period of time from planning to evaluation of at least half a year. For this purpose, special attention is paid to the different types of failure of heat-insulating vertically perforated bricks in the event of fire. If comparable results can be achieved with smaller wall sections, a cost-effective and comparatively fast testing of masonry walls would be conceivable, which would also save valuable resources such as the basic materials for brick production as well as oil and gas used for firing the test furnaces.

3 Evaluation and first results

The research objectives are realised by means of fire tests and by evaluating information from previous fire tests on brick masonry walls. Based on an initial evaluation, it has already been shown that the characteristic features used in the approvals for classification into fire resistance classes have the greatest impact on the fire test results. However, the hole cross-section also shows a significant influence on the test duration. Referring to the test results, the first minimum fire resistance classes have already been formed. When the table 1 was created, the procedure was such that firstly rough relations between the tests were searched in the results. These were then further verified and the individual limit values were determined. The following table shows the results from all available test reports for load-bearing and space-enclosing walls.

Table 1 Classification in fire resistance classes depending on relevant parameters for load-bearing and room-enclosing walls (1-sided fire exposure).

Line	Thickness	Gross density class	Compressive strength class	α_{fi}	Fire resistance class according to [EN 13501-2] [9]
1	≥ 365	≥ 0.6	≥ 10	≤ 0.7	REI 60
2	≥ 365	≥ 0.6	≥ 4	≤ 0.6	REI 60
3	≥ 300	≥ 0.6	≥ 10	≤ 0.61	REI 90 / REI 60
4	≥ 300	≥ 0.6	≥ 4	≤ 0.6	REI 60
5	≥ 240	≥ 0.6	≥ 4	≤ 0.5	REI 90 / REI 60

However, the table above shows some contradictions for the fire resistance class. For example, according to lines 1 and 2 (thicknesses ≥ 365 mm), the maximum permissible resistance class is REI 60, but for thicknesses ≥ 300 mm, with certain requirements for gross density class, compressive strength and α_{fi} according to line 3, even REI 90. This can be explained by the fact that when drawing up minimum fire resistance classes for thicknesses ≥ 300 mm, only test results of walls with a thickness < 300 mm may be considered, since according to the regulations in EN 1365-1, section 13 [6] the test results may be transferred to walls with greater thicknesses. If there occurs no test with a failure (wall collapse) of less than 90 minutes in this amount of data, then for thicknesses ≥ 300 mm REI 90 is specified as the fire resistance class. If thicknesses of ≥ 365 mm are considered, it is possible that fire tests with a duration of less than 90 minutes may occur in this new data set. Therefore the classification for these thicknesses is REI 60.

The decrease in fire resistance duration with increasing thickness is not plausible and must be regarded critically, due to the still relatively limited data basis. Therefore, REI 90 should be changed to REI 60 in these cases. This is marked in orange in the table 1. Nevertheless, it should be noted that α_{fi} is more restricted at a thickness of ≥ 300 mm than at a thickness of ≥ 365 mm.

However, it is questionable whether a reduction of α_{fi} by 0.09 is sufficient to guarantee that every wall with the properties according to line 3 complies with REI 90. In order to confirm this, an evaluation of a larger amount of data by test results or further test reports would be necessary.

The requirement for line 5 must also be questioned, because especially for narrow masonry walls ≤ 240 mm only 11 evaluable test reports were available. In the most test reports, a thickness of 300 mm or 365 mm was tested.

According to line 2 and line 4 of table 1, all walls with these characteristics meet REI 60 and this statement may be secured regarding to the fact that in no test report in which walls have been tested, a failure has occurred before 60 minutes.

Further investigations carried out to date have shown that even the integrated insulation filling in a brick can cause spalling in the event of fire. This is due to thermal stresses, which are based on locally different thermal conductivities and the resulting temperature differences in the rows of holes in the bricks. Based on these findings, fire tests will be carried out with filled and unfilled vertically perforated insulating bricks. Further tests will also show the differences between different insulating materials.

4 Conclusion based on current knowledge

The establishment of minimum fire resistance classes based on test reports is possible in general, but these are very conservative, because a test result with a short test duration limits all other results to this duration. However, the determination of the limit values cannot be described in general terms when it is created. The problem in this case is that it is not possible to identify which test is decisive. If one test achieves a short test duration with relatively high utilisation and another test achieves a longer test duration with a lower utilisation, it cannot be determined which is the decisive case. It is possible that the second mentioned test with the utilization from the first test would achieve a shorter test duration than the first one.

The classification into individual brick groups sometimes leads to more economical fire resistance classes, but this also reduces the data basis. As part of the research project, planned fire tests should provide more detailed information on the described topic. The preliminary investigations are taken into

account, which have shown that in fire tests on heat-insulating brick masonry, a distinction must be made between filled and unfilled bricks. A distinction between large-chamber bricks and bricks with small holes should also provide more detailed information about different types of brick in the event of fire.

Further tests should also define an extended range of application of heat-insulating brick masonry and provide an answer to the question if large-scale fire tests in general could be replaced by smaller substitute tests in the future.

References

- [1] BBSR (Bundesinstitut für Bau-, Stadt- und Raumforschung). 2015. *Wohnungsmarktprognose 2030, Analysen KOMPAKT*. Bonn.
- [2] DGfM (Deutsche Gesellschaft für Mauerwerks- und Wohnungsbau e.V.). 2015. *Mehrgeschossbau: Massive Argumente pro Mauerwerk (Presseinformation)*. Berlin.
- [3] Statistisches Bundesamt (StBA). 2019. *Bauen und Wohnen: Baugenehmigungen von Wohn- und Nichtwohngebäuden nach überwiegend verwendetem Baustoff. Lange Reihen z. T. ab 1980*. Wiesbaden.
- [4] European Committee for Standardization. 2012. *EN 1363-1 Fire resistance tests - Part 1: General requirements*.
- [5] European Committee for Standardization. 1999. *EN 1363-2 Fire Resistance Tests - Part 2: Alternative and Additional Procedures*.
- [6] European Committee for Standardization. 2012. *EN 1365-1 Fire resistance tests for loadbearing elements - Part 1: Walls*.
- [7] Deutsches Institut für Normung e.V.. 2013. *DIN EN 1996-1-2/NA Nationaler Anhang Eurocode 6: Bemessung und Konstruktion von Mauerwerksbauteilen – Teil 1-2: Allgemeine Regeln – Tragwerksbemessung für den Brandfall*.
- [8] European Committee for Standardization. 2015. *EN 1364-1 Fire resistance tests for non-load-bearing elements - Part 1: Walls*.
- [9] European Committee for Standardization. 2016. *EN 13501-2 Fire classification of construction products and building elements - Part 2: Classification using data from fire resistance tests, excluding ventilation services*.

The change of stress-strain state in biaxial bended reinforced concrete T-section beams depending on the load

Yuliia Prykhodko, Andrii Pavlikov

*Department of Reinforced Concrete and Masonry Structures and Strength of Materials,
National University «Yuri Kondratyuk Poltava Polytechnic»
24, Pershotravnevyj Ave., Poltava 36011, Ukraine*

Abstract

The efficiency of the entire economic system in the country depends on one of its most important branch – building industry. For its rapid development, it is necessary not only to improve the quality indicators of materials, the technology of manufacturing and installation of buildings elements and structures, but also the design methods for structures under influence of complex deformation (compression, bending and torsion).

Reinforced concrete has become widespread used among building materials used for the constructing of load-bearing elements for industrial and civil buildings and engineering structures. The most cost-effective cross-sectional shape of reinforced concrete bending elements is T-shape. The difficulty of designing such elements is caused by the variety of the concrete compressed zone forms: triangular, trapezoidal, pentagonal, hexagonal. Therefore, in order to create a design method for biaxial bended reinforced concrete T-section beams, it is necessary to derive the analytic dependence of stress-strain state parameters for recognizing each group of forms using nonlinear deformation model. The obtained formulas will give an opportunity to accurately describe the stress-strain state in the normal section of the reinforced concrete T-section beam. The stresses and deformations will be represented depending on the following factors: the position of the neutral line, which is characterized by the angle θ of its inclination to the horizontal axis and the height X of the concrete compressed zone, as well as the value of the concrete relative strains level in the most compressed fiber η_m . As shown by the analysis, the values of these factors can generally vary within the following limits: $0 \leq \theta \leq 90^\circ$, $0 \leq X \leq h \cos\theta$, $0 \leq \eta_m \leq 2,7$, which can be used as boundary characteristics.

The given parameters values for the reinforced concrete beams stress-strain state under biaxial bending change depending on the load level. The process of obtaining a model of the stress-strain state of the biaxial bended reinforced concrete T-section beam since the beginning of the loading till the time of destruction was automated using the MS Excel and AutoCAD software.

1 Introduction

In today's world, the building industry is still considered to be one of the most important and influential in the world. It is connected with all economical and political spheres of social life. For the development of building industry it is necessary to constantly improve and automate methods of calculation of building structures [1 – 4]. In this case an important step is the use of stress-strain state modeling method in order to analyze the possibilities of the elements' work under compression, biaxial bending and torsion [5 – 6].

Particular attention is attracted by the necessity for process changing knowledge of the stress-strain state parameters in the normal section of the reinforced concrete T-section beams. Especially important is the knowledge about the compressed zone shapes, which are determined by the position of the neutral line in the cross section through the parameters: X – height of the concrete compressed zone, θ – angle of neutral line inclination and η_m – the value of the concrete relative strains level in the most compressed fiber. This paper identifies possible shapes of the compressed zone: rectangle, triangle, trapezoid, pentagon and hexagon [7 – 8]. For each form in the process of integration analytical dependences are obtained, by which it is possible to determine the coordinates of stress resultant application in such zones. For better visual perception, of stress-strain state models in the normal section of the reinforced concrete T-section beam were constructed.

2 Choice of coordinate system for theoretical studies

To create the stress-strain state model of the bended reinforced concrete T-section element, a nonlinear diagram of the stress-strain relationship for the compression concrete was used [9].

For the convenience of theoretical research of the stress-strain state, the stress distribution law in the coordinate system $X_0O_0Y_0$ depending on the coordinates x_0 and y_0 with $K = 2$ was used [3–4]. This made it possible to determine the stress value at any point of the reinforced concrete beam cross section. The stress distribution law in the compressed concrete zone of the normal cross-section has the form (Fig. 1 – 4):

$$\sigma_c(x_0; y_0) = f_{cd} \left[\frac{2\eta_m}{X} (X - x_0 \sin \theta - y_0 \cos \theta) - \frac{\eta_m^2}{X^2} (X - x_0 \sin \theta - y_0 \cos \theta)^2 \right]. \quad (1)$$

where f_{cd} – the calculated value of the concrete compressive strength; X – height of the concrete compressed zone; η_m – the value of the concrete relative compression strains level in the most compressed fiber; x_0 та y_0 – the coordinates of the point that is considered; θ – the angle of inclination of the neutral line to the horizontal axis.

3 The formulas of stress resultant in the concrete compressed zone N_c and its application coordinates $x_{0,Nc}$ and $y_{0,Nc}$ for different forms of compressed zone

3.1 Triangular shape (Fig. 1)

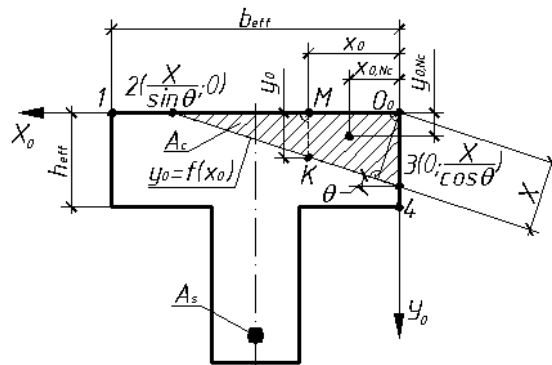


Fig. 1 Triangular shape of the reinforced concrete T-section element compressed zone

The stress resultant N_c in the compressed zone of concrete for this case:

$$N_c = \int_0^{\frac{X}{\sin \theta}} dx_0 \int_0^{\frac{X - x_0 \sin \theta}{\cos \theta}} \sigma(x_0; y_0) dy_0. \quad (2)$$

After integration we have that

$$N_c = \frac{f_{cd} X^2}{\sin 2\theta} \cdot \omega_1, \quad (3)$$

where ω_1 – the completeness coefficient of the stress distribution diagram in the compressed concrete zone of triangular shape under biaxial bending [table. 1].

Application coordinates of stress resultant N_c in the compressed concrete zone

$$x_{0,Nc} = \frac{S_{c,y0}}{N_c}, \quad (4)$$

$$y_{0,Nc} = \frac{S_{c,x0}}{N_c}. \quad (5)$$

In formulas (4) and (5):

$$S_{c,x0} = \frac{f_{cd} X^3}{\sin 2\theta \cos \theta} \cdot \varphi_{x1}, \quad (6)$$

$$S_{c,y0} = \frac{f_{cd} X^3}{\sin 2\theta \sin \theta} \cdot \varphi_{y1}, \quad (7)$$

where $\varphi_{x1}, \varphi_{y1}$ – the completeness coefficients of the stress distribution diagram in the compressed concrete zone of triangular shape under biaxial bending [table. 1].

3.2 Trapezoidal shapes (Fig. 2)

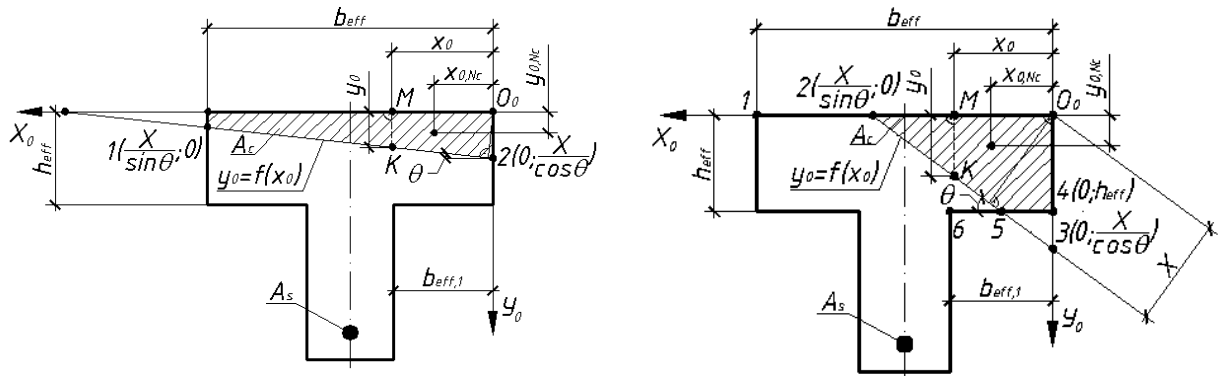


Fig. 2 Trapezoidal shapes of the reinforced concrete T-section element compressed zone: case 1 (left), case 2 (right)

The stress resultant N_c in the compressed zone of concrete for the first case (Fig. 2, left):

$$N_c = \int_0^{b_{eff}} dx_0 \int_0^{\frac{X-x_0 \sin \theta}{\cos \theta}} \sigma(x_0; y_0) dy_0 = \frac{f_{cd} X^2}{\sin 2\theta} \cdot \omega_2, \quad (8)$$

where ω_2 – the completeness coefficient of the stress distribution diagram in the compressed concrete zone of trapezoidal shape (case 1) under biaxial bending [table. 1]

The coordinates of stress resultant N_c are calculated by substituting into formulas (4) and (5):

$$S_{c,x0} = \frac{f_{cd} X^3}{\sin 2\theta \cos \theta} \cdot \varphi_{x2}, \quad (9)$$

$$S_{c,y0} = \frac{f_{cd} X^3}{\sin 2\theta \sin \theta} \cdot \varphi_{y2}, \quad (10)$$

where $\varphi_{x2}, \varphi_{y2}$ – the completeness coefficients of the stress distribution diagram in the compressed concrete zone of trapezoidal shape (case 1) under biaxial bending [table. 1].

The stress resultant N_c in the compressed zone of concrete for the second case (Fig. 2, right):

$$N_c = \int_0^{h_{eff}} dy_0 \int_0^{\frac{X-y_0 \cos \theta}{\sin \theta}} \sigma(x_0; y_0) dx_0 = \frac{f_{cd} X^2}{\sin 2\theta} \cdot \omega_3, \quad (11)$$

where ω_3 – the completeness coefficient of the stress distribution diagram in the compressed concrete zone of trapezoidal shape (case 2) under biaxial bending [Table. 1].

The coordinates of stress resultant N_c are calculated by substituting into formulas (4) and (5):

$$S_{c,x0} = \frac{f_{cd} X^3}{\sin 2\theta \cos \theta} \cdot \varphi_{x3}, \quad (12)$$

$$S_{c,y0} = \frac{f_{cd} X^3}{\sin 2\theta \sin \theta} \cdot \varphi_{y3}, \quad (13)$$

where $\varphi_{x3}, \varphi_{y3}$ – the completeness coefficients of the stress distribution diagram in the compressed concrete zone of trapezoidal shape (case 2) under biaxial bending [table. 1].

3.3 Pentagonal shapes (Fig. 3)

The stress resultant N_c in the compressed zone of concrete for the first case (Fig. 3, left):

$$N_c = \int_0^{b_{eff,1}} dx_0 \int_0^{h_{eff}} \sigma(x_0; y_0) dy_0 + \int_{b_{eff,1}}^X dx_0 \int_0^{\frac{X-x_0 \sin \theta}{\cos \theta}} \sigma(x_0; y_0) dy_0 = \frac{f_{cd} X^2}{\sin 2\theta} \cdot \omega_4, \quad (14)$$

where ω_4 – the completeness coefficient of the stress distribution diagram in the compressed concrete zone of pentagonal shape (case 1) under biaxial bending.

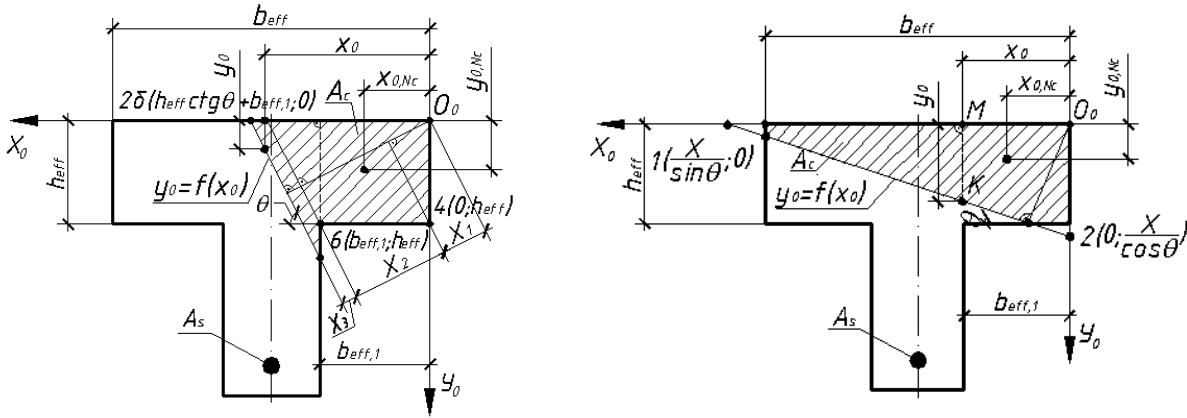


Fig. 3 Pentagonal shapes of the reinforced concrete T-section element compressed zone: case 1 (left), case 2 (right)

The coordinates of stress resultant N_c are calculated by substituting into formulas (4) and (5):

$$S_{c,x0} = \frac{f_{cd} X^3}{\sin 2\theta \cos \theta} \cdot \varphi_{x4}, \quad (15)$$

$$S_{c,y0} = \frac{f_{cd} X^3}{\sin 2\theta \sin \theta} \cdot \varphi_{y4}, \quad (16)$$

where $\varphi_{x4}, \varphi_{y4}$ – the completeness coefficients of the stress distribution diagram in the compressed concrete zone of pentagonal shape (case 1) under biaxial bending.

The stress resultant N_c in the compressed zone of concrete for the second case (Fig. 3, right):

$$N_c = \int_0^{\frac{X - h_{eff} \cos \theta}{\sin \theta}} dx_0 \int_0^{h_{eff}} \sigma(x_0; y_0) dy_0 + \int_{\frac{X - h_{eff} \cos \theta}{\sin \theta}}^{b_{eff}} dx_0 \int_0^{\frac{X - x_0 \sin \theta}{\cos \theta}} \sigma(x_0; y_0) dy_0 = \frac{f_{cd} X^2}{\sin 2\theta} \cdot \omega_5, \quad (17)$$

where ω_5 – the completeness coefficient of the stress distribution diagram in the compressed concrete zone of pentagonal shape (case 2) under biaxial bending.

The coordinates of stress resultant N_c are calculated by substituting into formulas (4) and (5):

$$S_{c,x0} = \frac{f_{cd} X^3}{\sin 2\theta \cos \theta} \cdot \varphi_{x5}, \quad (18)$$

$$S_{c,y0} = \frac{f_{cd} X^3}{\sin 2\theta \sin \theta} \cdot \varphi_{y5}, \quad (19)$$

where $\varphi_{x5}, \varphi_{y5}$ – the completeness coefficients of the stress distribution diagram in the compressed concrete zone of pentagonal shape (case 2) under biaxial bending.

3.4 Hexagonal shape (Fig. 4)

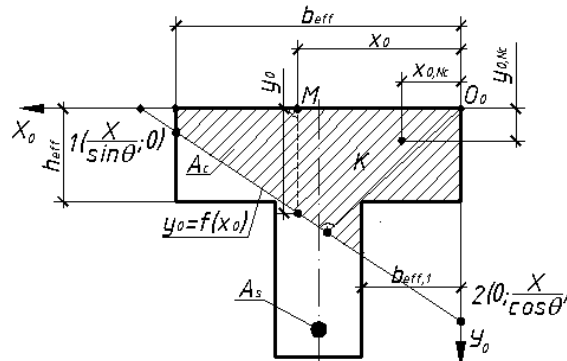


Fig. 4 Hexagonal shape of the reinforced concrete T-section element compressed zone

The stress resultant N_c in the compressed zone of concrete for hexagonal shape:

$$N_c = \int_0^{b_{eff,1}} dx_0 \int_0^{h_{eff}} \sigma(x_0; y_0) dy_0 + \int_{b_{eff,1}}^{b_{eff}} dx_0 \int_0^{\frac{X-x_0 \sin \theta}{\cos \theta}} \sigma(x_0; y_0) dy_0 = \frac{f_{cd} X^2}{\sin 2\theta} \cdot \omega_6, \quad (20)$$

where ω_6 – the completeness coefficient of the stress distribution diagram in the compressed concrete zone of hexagonal shape under biaxial bending.

The coordinates of stress resultant N_c are calculated by substituting into formulas (4) and (5):

$$S_{c,x0} = \frac{f_{cd} X^3}{\sin 2\theta \cos \theta} \cdot \varphi_{x6}, \quad (21)$$

$$S_{c,y0} = \frac{f_{cd} X^3}{\sin 2\theta \sin \theta} \cdot \varphi_{y6}, \quad (22)$$

where $\varphi_{x6}, \varphi_{y6}$ – the completeness coefficients of the stress distribution diagram in the compressed concrete zone of hexagonal shape under biaxial bending.

Table 1 shows the formulas for the triangular and trapezoidal forms of the compressed zone. Formulas for pentagonal and hexagonal forms are similarly derived.

Table 1 The completeness coefficients of the stress distribution diagram in the compressed concrete zone under biaxial bending

Geometric shape	Formulas for calculating the completeness coefficients of the stress distribution diagram
Triangle	$\omega_1 = \eta_m \cdot (4 - \eta_m) / 6;$ $\varphi_{x1} = \varphi_{y1} = \eta_m \cdot (5 - \eta_m) / 30$
Trapeze (case 1)	$\omega_2 = \eta_m \cdot [(4 - \eta_m) - 4 \cdot (1 - \gamma_1)^3 + \eta_m \cdot (1 - \gamma_1)^4] / 6;$ $\varphi_{y2} = \eta_m \cdot [(5 - \eta_m) - 20 \cdot (1 - \gamma_1)^3 + 5 \cdot (3 + \eta_m) \cdot (1 - \gamma_1)^4 - 4 \eta_m \cdot (1 - \gamma_1)^5] / 30;$ $\varphi_{x2} = \eta_m \cdot [(5 - \eta_m) - 5 \cdot (1 - \gamma_1)^4 + \eta_m \cdot (1 - \gamma_1)^5] / 30;$ $\gamma_1 = b_{eff} \cdot \sin \theta / X$
Trapeze (case 2)	$\omega_3 = \eta_m \cdot [(4 - \eta_m) - 4 \cdot (1 - \gamma_2)^3 + \eta_m \cdot (1 - \gamma_2)^4] / 6;$ $\varphi_{y3} = \eta_m \cdot [(5 - \eta_m) - 5 \cdot (1 - \gamma_2)^4 + \eta_m \cdot (1 - \gamma_2)^5] / 30;$ $\varphi_{x3} = \eta_m \cdot [(5 - \eta_m) - 20 \cdot (1 - \gamma_2)^3 + 5 \cdot (3 + \eta_m) \cdot (1 - \gamma_2)^4 - 4 \eta_m \cdot (1 - \gamma_2)^5] / 30;$ $\gamma_2 = h_{eff} \cdot \cos \theta / X$

4 Models of stress-strain state of the element in the compressed zone

Using the equilibrium equation of stresses in the normal section of biaxial bended reinforced concrete T-section beam with the use of MS Excel and AutoCAD software [10 – 11], models of stress-strain state at values $\eta_m=0,5$ in case of trapezoidal form of compressed concrete zone (Fig. 5) and $\eta_m=1,5$ in case of triangular form of compressed concrete zone (Fig. 6) are made.

Using the presented models (Figs. 5 – 6), analytical dependences were obtained to determine the basic parameters of the neutral line position in the cross section of the biaxial bended reinforced concrete T-section element.

As shown by theoretical research at low load levels, the stress distribution law has linear direction. With the increase of the load, the stress distribution diagram becomes warped, the height X of the concrete compressed zone and angle θ of neutral line inclination decrease.

In this paper, only two stress-strain state models of the biaxial bended reinforced concrete T-section beams under load change are presented. The algorithm for constructing models for other cases is similar. Consequently, it is possible to visualize the stress-strain state and to obtain the values of all its parameters, depending on the shape, which becomes compressed zone of concrete, at any load level.

5 Conclusions

Representing the process of the stress-strain state changing by modeling with the use of a non-linear diagram for the stress-strain relations description in concrete allows to determine with great accuracy all its parameters. The obtained formulas for their calculation allow to determine with sufficient accuracy the bearing capacity of biaxial bended reinforced concrete elements.

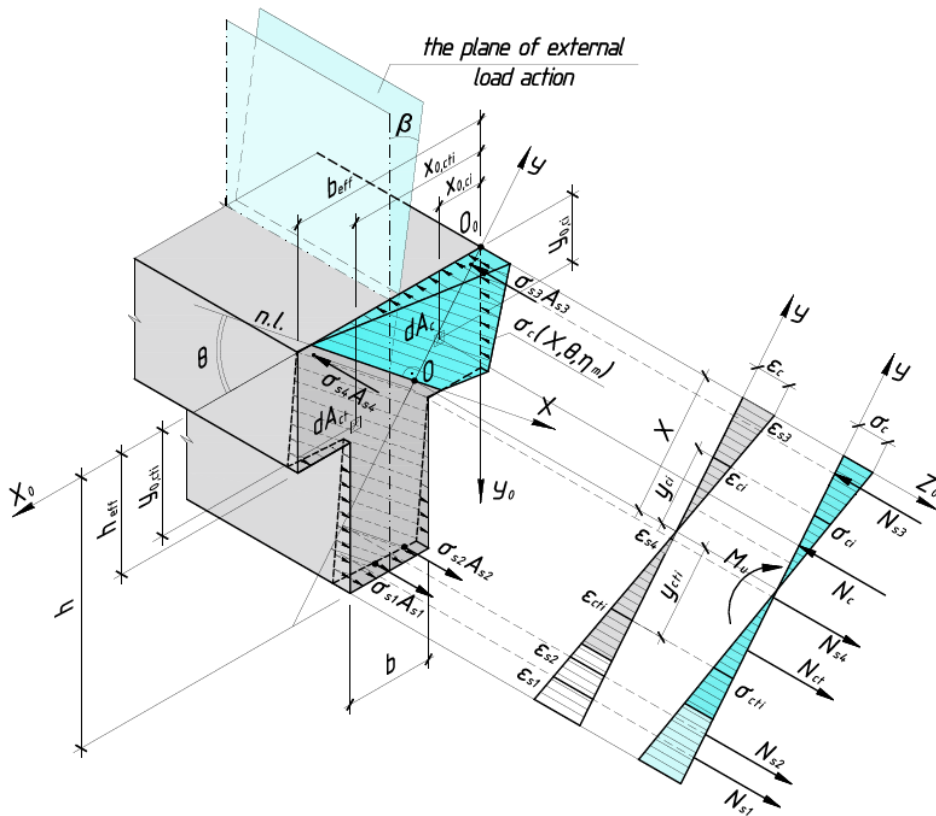


Fig. 5 The stress-strain state model in normal section of the biaxial bended reinforced concrete T-section crane beam in case of trapezoidal form of compressed concrete zone

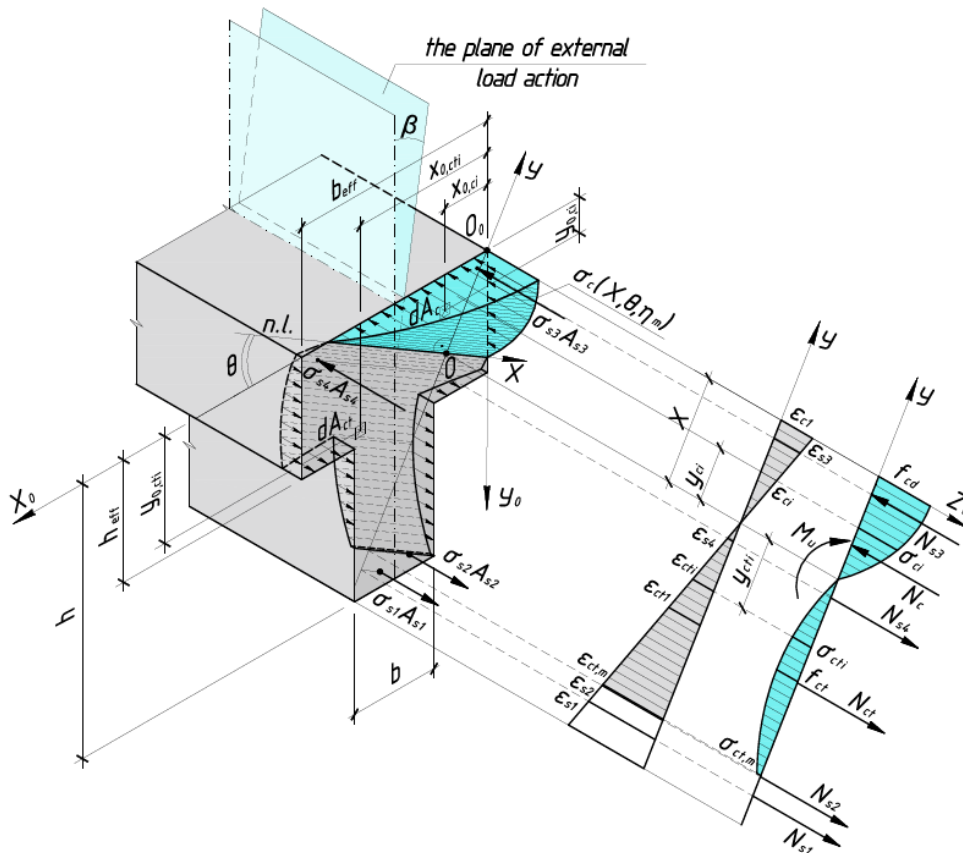


Fig. 6 The stress-strain state model in normal section of the biaxial bended reinforced concrete T-section crane beam in case of triangular form of compressed concrete zone

References

- [1] Pavlikov, A., Harkava, O., Prykhodko, Yu., and Baryliak, B. 2019. "Highly constructed precast flat slab frame structural system of buildings and research of its slabs." Proceedings of the International fib Symposium on Conceptual Design of Structures, Madrid, Spain, September 26–28.
- [2] Pavlikov, A., Harkava, O., Prykhodko, Yu., and Baryliak, B. 2018. "Experimental and Theoretical Testing Results of Reinforced Concrete Columns under Biaxial Bending." I International Scientific and Practical Conference "Technology, engineering and Science – 2018", London, Great Britain October 24 – 25.
- [3] Pavlikov, A., Kochkarev, D., and Harkava, O. 2019. "Calculation of reinforced concrete members strength by new concept." Proceedings of the fib Symposium 2019: Concrete – Innovations in Materials, Design and Structures, Kraków, Poland, May 27 – 29.
- [4] Pohribnyi, V., Dovzhenko, O., Kuznietsova, I., and Usenko, D. 2018. "The improved technique for calculating the concrete elements strength under local compression." *MATEC Web Conferences* 230, 02025
- [5] Pavlikov, Andriy. 2007. *Neliniina model napruzhenno-deformovanoho stanu v koso-zavantazhenykh zalizobetonnykh elementiv u zakrytychnii stadii*. Poltava: PNTU.
- [6] Pavlikov, Andriy. 2008. "Napruzhenno-deformovaniy stan navskisno zavantazhenih zalizobetonnih elementiv u zakritichnij stadiyi." PhD diss., Poltava National Technical Yuri Kondratuk University.
- [7] Kharchenko, Maryna. 2013. "Rozrakhunok mitsnosti kosozihnutykh zalizobetonnykh balok tavrovoho profilu z urakhuvanniam neliniinoho deformuvannia betonu ta armatury." PhD diss., Poltava National Technical Yuri Kondratuk University.
- [8] Babych, Ye. 2011. "Vyznachennia napruzhenno-deformovanoho stanu ta rozrakhunok zghynalnykh zalizobetonnykh elementiv tavrovoho pererizu." *Resursoekonomni materialy, konstruksii, budivli ta sporudy*.
- [9] EN 1992-1-1: Eurocode 2: Design of concrete structures – Part 1-1: General Rules and Rules for Buildings. European Committee for Standardisation (CEN), Brussels, 2004.
- [10] Billo, E. J. 2007. *Excel for Scientists and Engineers Numerical Methods*. John Wiley & Sons.
- [11] Katsikadelis, J. T. 2002. *Boundary elements: Theory and Applications*. Elsevier.

Durability and life assessment

Accelerated carbonation of recycled concrete aggregates

Marie SERENG, Assia DJERBI, Othman OMIKRINE METALSSI, Patrick DANGLA and Jean-Michel TORRENTI

MAST-FM2D, Univ Gustave Eiffel, IFSTTAR, F-77447 Marne-la-Vallée, France

Abstract

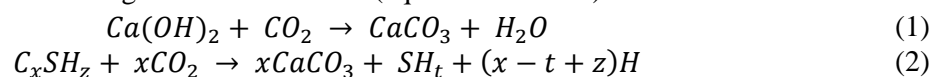
Accelerated carbonation is described as a treatment of recycled concrete aggregates (RCA) in order to uptake CO₂ and to improve their properties. To investigate the effectiveness of this treatment, some properties of RCA are studied: aggregates size, water content and CO₂ concentration. The main objectives are to obtain the maximum of CO₂ uptake on RCA with a simultaneous improvement of their properties, through the parametric study of carbonation parameters. The results show that a maximum of CO₂ uptake can be achieved for an optimum of water content, which depends on RCA properties. By their origin, RCA-CB 1-4 have the better CO₂ uptake of 49.9 g/kg. The increase of CO₂ concentration until 100% CO₂ can improve CO₂ uptake and fine RCA have a greater CO₂ uptake than coarse RCA (21.8 g/kg for RCA 1-4 mm with respect to 8.5 g/kg for RCA 12-20 mm). To finish, CO₂ uptake is demonstrated to have a significant effect on the decrease of water absorption coefficient, from 36 to 43%.

1 Introduction

The increase of construction waste has been growing in the last decades, due to the urban growth. It represents 224 thousand tons of waste generated in France in 2016 [1], up to 860 million tons for the whole European Union in 2015 [2]. Concrete waste are valued in recycled concrete aggregates (RCA). Recycling, allows to preserving natural resources and to promoting circular economy. The reduction of greenhouse gas as CO₂ is an important environmental concern, due to their effect on climate changes. The production of Portland cement emits CO₂ by decarbonation until 540 kg of CO₂ per ton of clinker and this production represents 5 to 7 % of global emissions worldwide [3]. Due to this fact, the national project FastCarb has the main objective to use carbonation reaction to improve CO₂ uptake in RCA. The aim is to optimize the maximal CO₂ quantity that can be stored in RCA in industrial conditions, to improve ecological impact of concrete. In the national project FastCarb, three industrial equipments are used to demonstrate the practical application and feasibility with a high volume of RCA. The first is a static process with the utilisation of a container (Clamens), the second equipment is rotating drum (Vicat) and the third is a fluidized-bed cooler (Lafarge).

RCA resulting from demolition concrete, by the original concrete and the crushing process, are composed with natural aggregates and attached mortar. The latest is responsible of lower RCA properties than natural aggregates, such as high porosity, high water absorption coefficient and low density [4]. These properties can affect fresh, hardened and durability properties of recycled aggregate concretes (RAC) [5]. The NF EN 206/CN French standard indicates the quantity of RCA that can be used to replace natural aggregates according to their exposure conditions [6]. Fine RCA (< 4 mm), due to their lower properties, inferior than coarse ones, are not incorporated in concretes. To improve RCA properties and to increase their substitution rate, treatments are required. Some mechanical, thermal and chemical methods have been demonstrated to be efficient to remove as much attached mortar as possible [7]. Treatments based on calcium carbonate biodeposition, PVA emulsions, pozzolan slurry, sodium silicate solution [5] and polymers treatment [8] can be used to directly strengthen attached mortar. These treatments have advantages and limits, especially on the aspects related to energy consumption, their duration and their cost [9].

Carbonation in brief is the reaction between cement hydrates (portlandite Ca(OH)₂ and calcium silicate hydrate C-S-H) and CO₂ dissolved in interstitial water, and leads to the formation of calcium carbonates CaCO₃, by the following chemical reactions (equations 1 and 2):



In nature, carbonation is qualified as natural carbonation, CO₂ concentration from the air is around 0.04% in volume and to carbonate structural concretes, several years are needed. The kinetics of the phenomenon depends on many factors such as the water content of concrete

As for natural carbonation, accelerated carbonation depends on several parameters, among which relative humidity, CO₂ concentration and concrete properties, for an effectiveness of the process [10]. Moreover, this reaction depends on the CO₂ solubility which is related to relative humidity (RH). In fact, at low RH, the dissolution of CO₂ is limited by the low amount of available water in pores, while CO₂ diffusion is slowed at high RH because of the high amount of water filling the pores. Furthermore, the diffusion is higher in a gas than in a liquid water. In the literature, the optimum of RH to obtain a maximum of carbonation is the 50-80% range [11], [12]. In a laboratory, CO₂ concentration can be increased up to 100%, to accelerate carbonation process. The French standard NF EN 12390-12 limits CO₂ concentration to 3% [15] because the aim of this norm is to reproduce natural carbonation with an acceleration of the process but without changing the phenomenology and the products nature. Different effects of CO₂ concentration are described on carbonation kinetics [11]. During carbonation at high CO₂ concentrations, Thiery describes a persistence of residual portlandite [14]. This phase is due to the occurrence of a layer of calcium carbonates which reduces the porosity of cementitious materials and therefore the accessibility to non-carbonated phases. The properties of cementitious materials can affect carbonation kinetics, especially porosity and the content of non-carbonated phases. Indeed, porosity of cementitious materials is related to the formulation and the water-to-binder ratio. High porosity or high water-to-binder ratio induces high penetration of CO₂ to reach non-carbonated available phases [11].

Carbonation has a negative effect on reinforced concretes, by the decrease of pH of 13 to 9 with the dissolution of CO₂ in water and the release of H⁺ ions. This decrease leads to a depassivation and corrosion of steel reinforcements, with the increase of carbonation depth.

On the other hand, carbonation is demonstrated as a potential technique to improve microstructure and mechanical properties of cement-based materials [15] and can be used as a treatment to improve RCA properties and to uptake CO₂, as a positive effect. RCA properties are improved by carbonation of recycled aggregates, as a decrease of porosity and water absorption, and the increase of density [16], [17]. The effectiveness of CO₂ storage by RCA depends on several factors: size of RCA, water content of RCA, CO₂ concentration [9]. The treatment by accelerated carbonation of RCA is imposed by their carbonation in a large curing chamber, as suggested by Zhan *et al.* [16]. In their study, RCA derived from laboratory preparations are kept in a full CO₂ atmosphere. They discussed the effect of size of RCA on carbonation percentage. They suggested that fine RCA (5-10 mm) can uptake 56% of CO₂, while coarse aggregates (14-20 mm) uptook 37% of CO₂. This conclusion is also confirmed by Fang *et al.*: for fine RCA (inferior to 2.4 mm), the uptake was around 55 g/kg of CO₂ [18]. Concerning water content of RCA, Zhan *et al.* demonstrated that 3.4% is an optimum of value to obtain the maximum of carbonation percentage [16]. Still in the literature, the increase of CO₂ concentration allows uptaking more CO₂. Liang *et al.* suggested that the maximum of CO₂ uptake of 12 g/kg is obtained for 45% of CO₂ concentration. Above this concentration, CO₂ uptake decreased due to the dense microstructure and the reduction of CO₂ diffusion [9].

Note that carbonation of recycled aggregates is not a problem for durability because the use of carbonated RCA is similar to the use of limestone aggregates. Nevertheless, in the FastCarb project concretes made with carbonated RCA will be tested to verify how the durability properties are affected by the accelerated carbonation.

This study shows the treatment of accelerated carbonation aggregates of two origins of RCA, RCA from demolition concretes and RCA from concretes derived from laboratory preparations, both having different properties. This article presents a new method of characterisation of CO₂ uptake, by taking into account the carbonation of portlandite. The process was carried out at two different CO₂ volume concentrations. At 100% CO₂, the objective is to determine the full potential of RCA to uptake CO₂. At 15% CO₂, the aim is to have the same concentration as the industrial concentration recovered in cement kilns, in order to transpose our application in industry. During the parametric study to determine the maximum of CO₂ uptake of RCA, the effect of water content was studied for all the aggregates, to obtain the optimum of water content, depending on their nature and their properties. The second purpose of this study is to conclude on the potentiel of carbonation to improve RCA properties, including water absorption coefficient (WAC).

2 Materials and experimental program

2.1 Materials

2.1.1 RCA from demolition concretes

The first types of RCA used for this study were RCA derived from demolition concretes, which are crushed on recycling plants. First RCA named RB are used in national project RecyBéton [19], [20]. Two sizes of RCA were studied, 1-4 mm and 10-20 mm. Their carbonation specifications are:

- RCA 1-4 mm (RB 1-4) are naturally carbonated, after a 6 years long storage,
- RCA 10-20 mm (RB 10-20) are already naturally carbonated at the surface,
- RB 10-20 have been crushed and sieve in RCA 1-4 mm (RB 1-4 C), to study the effect of natural carbonation on CO₂ uptake.

Second RCA were named CB, because coming from concrete beams that were crushed in a recycling plant (Clamens, Villeparisis – 77 (France)). They are two years old, thus were naturally less carbonated. Only the 1-4 mm fraction was studied (CB 1-4).

Properties of all the RCA are presented in Table 1. The evaluation of water absorption coefficient (WAC) is described in section 2.2.2. The portlandite contents of RCA are determined by thermogravimetric analysis (NETZCH STA 449 F5 Jupiter, temperature conditions: 0-1250°C (10°C/min)).

Table 1 Properties of RCA (derived from demolition concretes) studied

Properties	Dimension	RB 1-4	RB 10-20	RB 1-4 C	CB 1-4
WAC	%	4.2	5.1	5.4	6.8
Portlandite content	%	0	1 ± 0.06	0.5 ± 0.08	3.4 ± 0.3

2.1.2 RCA from concretes derived from laboratory preparations

Two RCA (Ordinary concrete (OC) and High performance concrete (HPC)) derived from laboratory concretes are used in this study. They were already studied in BHP2000 project [21]. The advantage to use these RCA types is that both their compositions and the cements CEMI 52.5 used for the manufacturing are known. Two sizes of RCA are used: 1-4 mm (OC 1-4 and HPC 1-4) and 12-20 mm (OC 12-20 and HPC 12-20). Concerning carbonation specifications, RCA are crushed in a laboratory environment and preserved of natural carbonation by storing them in a sealed bag. Table 2 presents WAC, portlandite contents and paste content SFSA (described by the soluble fraction by salicylic acid).

Table 2 Properties of RCA (derived from demolition concretes) studied

Properties	Dimension	OC 1-4	OC 12-20	HPC 1-4	HPC 12-20
WAC	%	4.8	4.1	4.2	3.6
Portlandite content	%	4 ± 0.2	2.9 ± 0.3	2.3 ± 0.2	2.1 ± 0.1
SFSA	%	45 ± 3.9	32 ± 5.4	35 ± 5.6	34 ± 1.2

2.2 Experimental program

2.2.1 Accelerated carbonation test of RCA

Water content is an intrinsic parameter of carbonation, as described in the introduction. In order to increase CO₂ diffusion in RCA, it is necessary to impose an optimum of water content, and this value depends on physico-chemical properties of RCA [9]. RCA carbonation test is carried out in a first part, by setting a water content on dry RCA at the initial state. Water content is imposed by the immersion of RCA during 24 hours and after by a controlled drying in order to obtain the desired water content.

In a second part, after setting a water content on RCA, samples were kept in a desiccator as a curing chamber and a concentration of CO₂ (15% or 100% of CO₂) is maintained during 24 hours, at atmospheric pressure (figure 1). Finally, at the end of accelerated carbonation test, RCA are dried at 80°C (until constant mass) to eliminate free water in RCA [22].

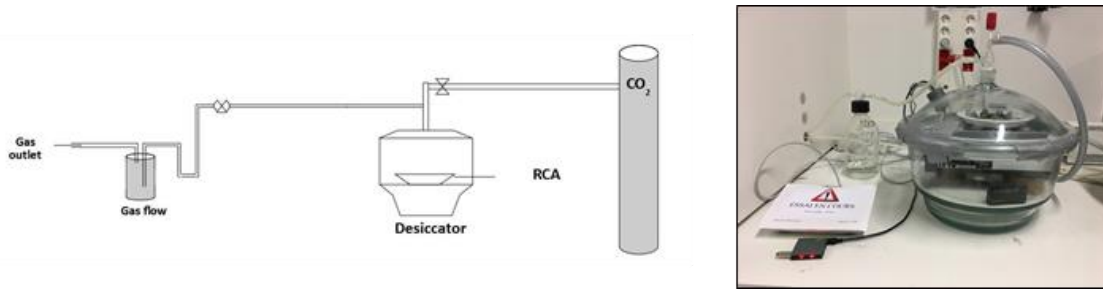


Fig. 1 Experimental setup of accelerated carbonation test of RCA

To determine CO₂ uptake (in g/kg), a mass monitoring is achieved to study the weight gain after accelerated carbonation test. It is determined by the ratio between the mass of dry RCA before carbonation $m_{ini\ dried}$, and the mass of dry RCA after carbonation $m_{final\ dried}$ (equation 3) [22]. At this ratio, a factor M_{gw} is added, M_{gw} being defined in equation 4. This factor is used to define water mass generated by carbonation of portlandite, which is considered in this study as the only hydrate which produces bound water by carbonation [23]. About C-S-H, Morandau *et al.* explains that their carbonation don't release water [23]. The amount of portlandite which can be carbonated is determined by TGA analysis and as indicated in equation 1, each mole of portlandite produces 1 mole of water (converted in mass to find M_{gw}).

$$CO_2\ uptake = \frac{(m_{final\ dried} - m_{ini\ dried}) + M_{gw}}{m_{ini\ dried}} \quad (3)$$

$$M_{gw} = m_{Ca(OH)_2-TGA} \times \frac{M_{H_2O}}{M_{Ca(OH)_2}} \quad (4)$$

$m_{Ca(OH)_2-TGA}$ is the mass loss due to the dihydroxylation of portlandite determined by TGA analysis, M_{H_2O} and $M_{Ca(OH)_2}$ respectively are molar mass of water and portlandite.

2.2.2 Determination of water absorption coefficient of RCA

Water absorption of RCA is measured by a simple test. Dry RCA are saturated under vacuum for 24 hours. After saturation, coarse RCA (10-20 mm) were dried with absorbent paper to determine saturated surface dry (SSD) state, which describes the state when RCA are dried at the surface, but saturated in volume by adsorbed water [24]. Then, they were dried at 80°C until constant mass. However, for fine RCA (1-4 mm), after saturation, their SSD state is determined by evaporimetric drying [25]. Then, RCA are also dried at 80°C. WAC (in percentage) is determined by difference between mass of RCA at SSD state (m_{SSD}) and mass of dry RCA (m_{dried}) as illustrated in equation 5:

$$WAC = \frac{m_{SSD} - m_{dried}}{m_{dried}} \times 100 \quad (5)$$

3 Parametric study of accelerated carbonation

3.1 Effect of RCA water content on CO₂ uptake

Figure 2 illustrates the effect of water content on CO₂ uptake. The curve trends are similar for both RCA. The highest CO₂ uptake has been reached for an optimum of water content comprised between 3.5 to 4% for RCA-OC 1-4 and HPC 1-4 (fig 2-B) and between 5.2 to 7.2% for RB 1-4, RB 1-4 C and CB 1-4 (fig 2-A). On both sides, minimum values of CO₂ uptake correspond to low or high water content, because of the effect of water content on carbonation. At high water content, CO₂ diffusion is slowed because of the quantity of water present in pores and at low water content is affecting the dissolution of CO₂ as previously explained.

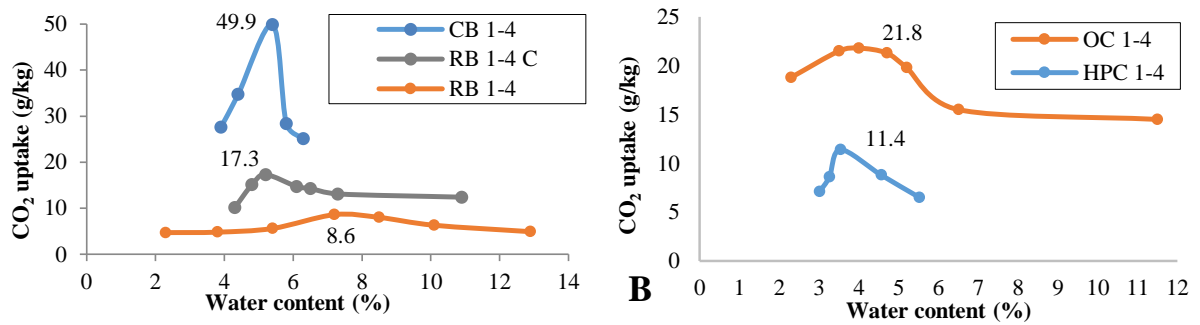


Fig. 2 Effect of RCA water content on CO₂ uptake (Fig. 2-A : accelerated carbonation test at 100% CO₂, Fig. 2-B : accelerated carbonation test at 15% CO₂)

Water contents values differ under RCA types, these values are in the average of WAC of RCA (tables 1 and 2) (it is not the case for RB 1-4, more investigations are needed). The trends of optimum of water content are also demonstrated by Zhan *et al.* [16], who obtained an optimum of water content of 3.4% for a maximum of CO₂ uptake of 1.7%, for RCA 10-14 mm derived from laboratory preparations. Pan *et al.* [26] suggested an optimum of 5% of water content for RCA derived from demolition concrete. The CO₂ uptake values are ranging between 8.6 g/kg and 49.9 g/kg. On Figure 2-A the difference on CO₂ uptake values is attributed to the effect of initial natural carbonation. Indeed, CB 1-4 have a low natural carbonation and have the maximum CO₂ uptake (49.9 g/kg). For RB 1-4 C, crushed from RB 10-20, they are naturally partially carbonated, their CO₂ uptake is of 17.3 g/kg. Finally, RB 1-4 which have a natural carbonation after a 2 year of storage, have the lowest CO₂ uptake of 8.6 g/kg. In the literature, Fang *et al.* [18] obtained a maximum of CO₂ uptake around 22 g/kg for RCA 5-10 mm derived from recycling plant, which consistent with our results. Xuan *et al.* [27] suggested a maximum of CO₂ uptake of 7.9 g/kg for RCA 5-20 mm, which have a low natural carbonation. The effect of natural carbonation is also reported in the literature by Xuan *et al.* [27], who explained that for a long storage of RCA, a partial natural carbonation can affect RCA. They suggest a maximum of 7.9 g/kg of CO₂ uptake for RCA 5-20 mm which are naturally carbonated. In Figure 2-B, the difference of CO₂ uptake between OC 1-4 and HPC 1-4, is related to the portlandite rate (table 2). OC 1-4 have more portlandite left which can be carbonated (4%) than HPC 1-4 (2.3%). Moreover, the water-to-cement ratios are different between the two RCA (0.49 for OC 1-4 and 0.32 for HPC 1-4). Thus HPC 1-4 have more non-hydrated phases than OC 1-4 and Liang *et al.* [9] described the effect of high compressive strength, like HPC 1-4 in our study, on the densification of cement paste, which reduces CO₂ diffusion.

3.2 Effect of the size of RCA on CO₂ uptake

Figure 3 illustrates the effect of the size of RCA on CO₂ uptake, for OC and HPC materials. The effect of water content is also demonstrated by the curve trends.

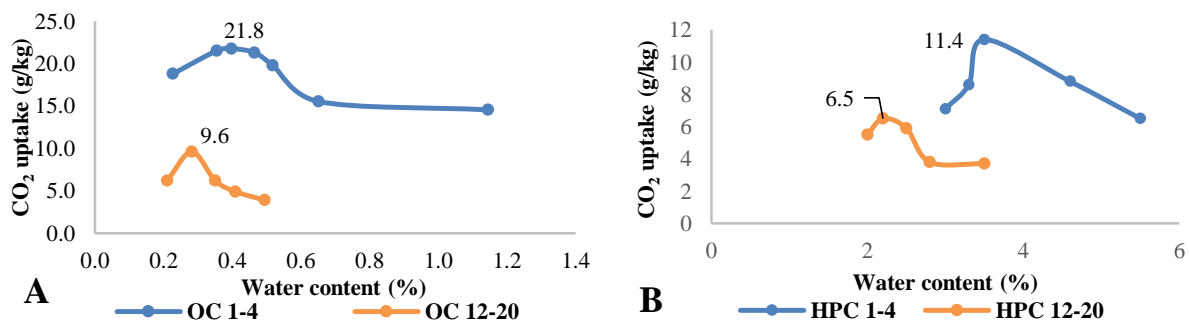


Fig. 3 Effect of the size of RCA on CO₂ uptake (Fig 3-A : OC, Fig 3-B : HPC)

On Figure 3-A, optimums of water contents are between 2.8% for OC 12-20 to 4% for OC 1-4. This optimum depends on RCA size, for fine RCA, the optimum of water content is higher than for coarse RCA and this is consistent with the effect of RCA size on water absorption coefficient. For HPC

in Figure 3-B, the same trend is observed, the optimum of water content for HPC 12-20 is 2.2%, while for HPC 1-4, the optimum is 3.5%. Maximum CO₂ uptakes were obtained for both RCA, for 1-4 mm fraction (21.8 g/kg for OC 1-4 and 11.4 g/kg for HPC 1-4) at 15% CO₂. This difference can be explained in a first part by a higher diffusivity of CO₂ in fine RCA than in coarse RCA, due to the RCA size. For coarse RCA, to increase the accessibility to CO₂, it will be necessary to increase the time of the experiment. These conclusions nevertheless need additional investigations. The second justification is the content on portlandite. Indeed, fine RCA contains a higher portlandite rate due to the content of cement paste (4% for OC 1-4 with respect to 2.9% for OC 12-20). This content affects CO₂ uptake. About HPC, the content of portlandite is relatively similar, but the content of cement paste (table 4) is different. It is possible to consider C-S-H carbonation, but this hypothesis needs more investigations. According to the literature, Fang *et al.* [18] explained that for RCA 1.18 mm, the maximum of CO₂ uptake is 54 g/kg with respect to 27 g/kg for RCA 15 mm, the difference being linked to RCA cement contents. This conclusion is consistent with our results. For RCA derived from laboratory preparations, Zhan *et al.* [16] suggested a maximum of carbonation percentage of 56% for RCA 5-10 mm, and of 37% for RCA 14-20 mm. Xuan *et al.* [17] reached the same conclusion with a percentage of carbonation of 2.2% for RCA lower than the 0.8% rate of 5 mm for RCA 5-10 mm.

3.3 Effect of CO₂ concentration on CO₂ uptake

Figure 4 illustrates the effect of CO₂ concentration on CO₂ uptake of RCA 10-20, which have a natural carbonation at the surface as a function of water content. The two tested CO₂ concentrations were of 15% and of 100%.

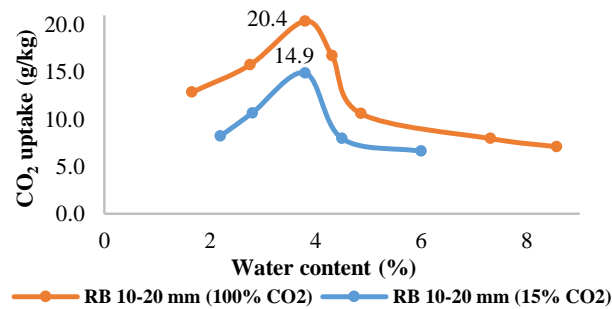


Fig. 4 Effect of CO₂ concentration on CO₂ uptake

As indicated in paragraphs 3.1 and 3.2, the curve trends demonstrate the effect of water content on CO₂ uptake, the maximum CO₂ uptakes of 20.4 g/kg and 14.9 g/kg being obtained for 3.8% of water content, respectively for RCA under 100% CO₂ and 15% CO₂.

The maximum of CO₂ uptake is obtained for carbonation under 100% CO₂ and the increase of CO₂ uptake between the two concentrations is around 37%. But the increase of CO₂ between 15% and 100% of CO₂ is not really significant. This is due to the dissolution rate of cement hydrates and calcium carbonates formed, as explain by Fang *et al.* [18]. The authors also that CO₂ concentration impacts CO₂ uptake, the higher the concentration, the greater its storage, but the increase beyond 15% is not significant on CO₂ uptake. They obtained a maximum of CO₂ uptake of 17 g/kg for 15% and 20 g/kg for 100% CO₂. Liang *et al.* [9] explained that after a maximum of CO₂ uptake of 12 g/kg obtained with 45% CO₂, CO₂ uptake decreased with the increase of CO₂ concentration, due to the layer of calcium carbonates formed by carbonation, and thus the difficulty of accessibility of phases which can be carbonated.

4 Effect of accelerated carbonation treatment on RCA properties

Figure 5 illustrates the effect of accelerated carbonation treatment and CO₂ concentrations on CO₂ uptake and on RCA properties, as water absorption coefficient. Tests are carried out on RCA-RB 1-4 C, at 15% and 100% CO₂ at the same optimum water content (5.2%).

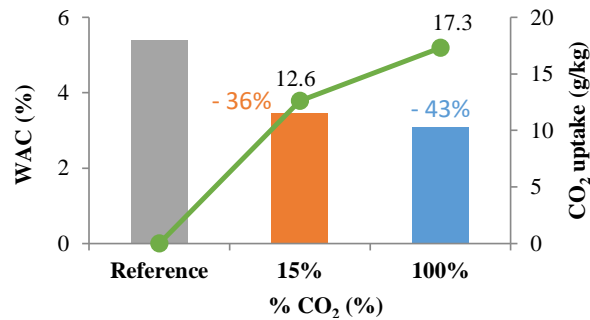


Fig 5 Effect of accelerated carbonation test and CO₂ concentration on CO₂ uptake and WAC

The maximum of CO₂ uptake of 12.6 g/kg was obtained for 15% CO₂ and the value of 17.3 g/kg was obtained for 100% CO₂. The increase of CO₂ uptake between the two concentrations was around 37%, this value is close to the increase of CO₂ uptake for RCA-RB 10-20. This trend on the effect of CO₂ concentration on CO₂ uptake has been observed by Fang *et al.* [18]. CO₂ uptake impacted water absorption coefficient. The increase of CO₂ concentration increased CO₂ uptake which reduced WAC of RCA. In fact, this decrease of WAC with 15% CO₂ is of nearly 36% and of 43% for 100% CO₂. These results are in agreement with the effect of CO₂ uptake, when CO₂ concentration is higher, CO₂ uptake increased and the formation of CaCO₃ during carbonation affected the porosity of RCA by clogging pores. The difference between WAC of RCA 1-4 C at 15 and 100% CO₂ is around 11%. Therefore, it seems that it is not necessary to use 100% CO₂ concentration to have a significant effect on the increase of CO₂ uptake and, after, on the decrease of WAC. In the literature, Pan *et al.* [26] suggested a decrease of WAC around 54% for RCA derived from concrete demolitions, under 20% CO₂, because of the effect of carbonation. Their results demonstrated that WAC decrease with the increase of CO₂ uptake and the minimum of WAC of 1.2% was obtained for 50% CO₂. Above this value of CO₂ concentration, WAC increased again. The value of WAC under 20% and 100% CO₂ were similar (2%), because the effect of the stabilization of carbonation.

5 Conclusions

From the results obtained in this study, it can be concluded that:

- Water content has a significant effect on CO₂ uptake. The optimum of water content depends on RCA properties, including water absorption. About CO₂ uptake, values are between 8.6 and 49.9 g/kg according to RCA types and natural carbonation impacts these values.
- There is an effect of size of RCA on CO₂ uptake by the content of portlandite which can be carbonated, but also by the effect of size for fine RCA, which impacts physical exchanges between gas and RCA, and increase CO₂ diffusion at the surface of RCA.
- The increase of CO₂ concentration leads to enhance the CO₂ uptake, but an increase of concentration above 15% is not significant.
- The improvement of RCA properties as the water absorption is demonstrated. Carbonation decreases WAC by pore-filling and formation of calcium carbonates.

6 Acknowledgements

The investigations and results reported herein are supported by the French Ministry for the Ecological and Inclusive Transition under the national project FastCarb.

References

- [1] Commissariat général au développement durable. 2019. « Bilan 2016 de la production de déchets en France ». Accessed March 2020. <https://www.statistiques.developpement-durable.gouv.fr/>
- [2] Yap, S.P., Goh, Y., Mo, K.H., Ibrahim, H.A. 2019. « Recycling of construction and demolition wastes into renewable construction materials » *Encycl. Renew. Sustain. Mater.* 2:520-526.
- [3] Zhang, D., Cai, X., Shao, Y. 2016. « Carbonation curing of precast fly ash concrete » *J. Mater. Civ. Eng.* 28-11:1-9., 2016.
- [4] De Juan, M.S., Gutiérrez, P.A. 2009. « Study on the influence of attached mortar content on the properties of recycled concrete aggregate » *Constr. Build. Mater.* 23-2:872-877.

- [5] Mefteh, H., Kebaili, O., Oucief, H., Berredjem, L., Arabi, N. 2013. « Influence of moisture conditioning of recycled aggregates on the properties of fresh and hardened concrete » *J. Clean. Prod.* 54:282-288.
- [6] Afnor. 2014. «NF EN 206/CN: Concrete - Specification, performance, production and conformity - National addition to the standard NF EN 206».
- [7] Mistri, A., Bhattacharyya, S.K., Dharmi, N., Mukherjee, A., Barai, S.V. 2020. « A review on different treatment methods for enhancing the properties of recycled aggregates for sustainable construction materials » *Constr. Build. Mater.* 233:1-12.
- [8] Spaeth, V., Djerbi Tegguer, A. 2013. « Improvement of recycled concrete aggregate properties by polymer treatments » *Int. J. Sustain. Built Environ.* 2-2:143-152.
- [9] Liang, C., Pan, B., Ma, Z., He, Z., Duan, Z. 2020. « Utilization of CO₂ curing to enhance the properties of recycled aggregate and prepared concrete : A review » *Cem. Concr. Compos.* 105:1-14.
- [10] Fernandez Bertos, M., Simons, S.J.R., Hills, C.D., Carey, P.J. 2004. « A review of accelerated carbonation technology in the treatment of cement-based materials and sequestration of CO₂ » *J. Hazard. Mater.* 112-3:193-205.
- [11] Drouet, E. 2010. « Impact de la température sur la carbonatation des matériaux cimentaires : prise en compte des transferts hydriques » PhD Diss., ENS Cachan.
- [12] Drouet, E., Poyet, S., Le Bescop, P., Torrenti, J.-M., Bourbon, X. 2019. « Carbonation of hardened cement pastes: Influence of temperature » *Cem. Concr. Res.* 115:445-459.
- [13] Afnor. 2020. « NF EN 12390-12: Testing hardened concrete - Part 12: Determination of the carbonation resistance of concrete - Accelerated carbonation method».
- [14] Thiery, M. 2005. « Modélisation de la carbonatation atmosphérique des matériaux cimentaires - Prise en compte des effets cinétiques et des modifications microstructurales et hydriques » PhD Diss., ENPC, LCPC.
- [15] Zhang, D., Ghoulah, Z., Shao, Y. 2017. « Review on carbonation curing of cement-based materials » *J. CO₂ Util.* 21:119-131.
- [16] Zhan, B., Poon, C.S., Liu, Q., Kou, S.C., Shi, C. 2014. « Experimental study on CO₂ curing for enhancement of recycled aggregate properties » *Constr. Build. Mater.* 67:3-7.
- [17] Xuan, D., Zhan, B., Poon, C.S. 2016. « Development of a new generation of eco-friendly concrete blocks by accelerated mineral carbonation » *J. Clean. Prod.* 133:1235-1241.
- [18] Fang, X., Xuan, D., Poon, C.S. 2017. « Empirical modelling of CO₂ uptake by recycled concrete aggregates under accelerated carbonation conditions » *Mater. Struct.* 50- 4:1-13.
- [19] Omary, S., Ghorbel, E., Wardah, G. 2016. « Relationships between recycled concrete aggregates characteristics and recycled aggregates concretes properties » *Constr. Build. Mater.* 108:163–174.
- [20] De Larrard, F. 2018. *Concrete Recycling : Research and Practice (Ouvrage de synthèse du PN RecyBéton)*. CRC Press.
- [21] Presses de l'école nationale des ponts et chaussées. 2005. *Synthèse des travaux du projet national BHP 2000 sur les bétons à hautes performances*.
- [22] Sereng, M., Djerbi, A., Omikrine Metalssi, O., Dangla, P., Torrenti, J.-M. 2018. « Effect of water contents of recycled concrete aggregates on carbonation kinetic » Paper presented at the 12th fib International PhD Symposium in Civil Engineering, Prague, Czech Republic, August 2018.
- [23] Morandau, A., Thiéry, M., Dangla, P. 2014. « Investigation of the carbonation mechanism of CH and C-S-H in terms of kinetics, microstructure changes and moisture properties » *Cem. Concr. Res.* 56: 153-170.
- [24] Afnor. 2014. « NF 1097-6: Tests for mechanical and physical properties of aggregates - Part 6: Determination of particle density and water absorption ».
- [25] Yacoub, A., Djerbi, A., Fen-Chong, T. 2018. « Water absorption in recycled sand: New experimental methods to estimate the water saturation degree and kinetic filling during mortar mixing » *Constr. Build. Mater.* 158:464-471.
- [26] Pan, G., Zhan, M., Fu, M., Wang, Y., Lu, X. 2017. « Effect of CO₂ curing on demolition recycled fine aggregates enhanced by calcium hydroxide pre-soaking » *Constr. Build. Mater.* 154:810–818.
- [27] Xuan, D., Zhan, B., Poon, C.S. 2016. « Assessment of mechanical properties of concrete incorporating carbonated recycled concrete aggregates » *Cem. Concr. Compos.* 65:67-74.

Creep potential of concrete damaged by Alkali Aggregate Reaction

Clément Lacombe, Alain Sellier, Thierry Vidal, Christine Noret*, Patrice Anthiniac*

*LMDC (Laboratoire Matériaux et Durabilité des Constructions),
Université Toulouse III Paul Sabatier,
135 Avenue de Rangueil, 31077 Toulouse Cedex 4, France*

** Tractebel ENGIE France
5 Rue du 19 Mars 1962, Gennevilliers, France*

Abstract

The durability of concrete structures, especially when concrete is affected by Alkali Aggregates Reaction (AAR), is a major concern. Indeed, the AAR swelling can induce changes in the stresses distribution within the structure which could affect its functionality. Previous studies have demonstrated the swelling mitigation in compressive stress directions, and the low effect of AAR on creep rate in this configuration. However, very few studies have investigated the creep behaviour of a concrete already damaged by AAR. Nevertheless, in real structures, compressive stresses may develop with AAR and become significant only after a certain level of swelling. That is the reason why it is necessary to characterize the creep rate of a concrete already damaged by AAR before loading.

The present study consists of an original experimental programme of creep tests carried out on concrete previously damaged by AAR in free swelling condition. Two concrete mixes were designed differing only by their aggregates. The first concrete incorporated reactive aggregates and the second non-reactive aggregates. Both mixes are similar regarding the proportions of cement, water, alkali content, sand and aggregates.

Under stress, a reduction of the swelling is observed which is the consequence of two phenomena. The first one is the effect of the AAR on the instantaneous elastic strain of the reactive concrete and the second one, is due by a higher creep rate of the affected concrete during the first 15 days after loading.

1 Introduction

Numerous studies have investigated the chemistry of the Alkali Aggregates Reaction (AAR) and its three main causes [1], namely alkali-sensitive aggregates, high relative humidity and alkali content in the cement. Other studies dealt with the structural effects of AAR, studying the mechanical properties and long-term strains of affected concretes.

The free swelling “S” curve induced by the reaction was proposed by Larive in 1997 [2], but these strains can be reduced or cancelled in the stress direction if the specimens are loaded before the reaction initiation [3]. In 1994, Charlwood had already observed these phenomena on real size structures and proposed an empirical law between the swelling rate and the compressive stress with an 8 MPa vanishing limit [4]. This first model and numerous others which followed were reviewed in 2017 [5].

In these models, AAR is modeled at different levels, from the smallest scale, i.e. the reaction products to the largest structure scale. One of these models considers swelling reduction directly using a rheological model coupled with a micro-mechanics cracking criterion that permits large structure analysis once incorporated into finite element softwares [6]. Others tried to explain these phenomena using numerical meso scale approaches with concrete matrix considered as a viscoelastic material that can absorb swelling. Depending on creep model used for the matrix, the creep velocity rate immediately around the aggregates could be able to absorb a part of the gel overpressure [7]. In order to take into consideration this phenomenon in future models, a first step consists of quantifying it experimentally.

In 2019, the time-dependent strains of concretes incorporating different types of reactive aggregates were quantified by Reinhardt et al [8]. In this study, the reaction was stopped when the samples were loaded. The experimental programme presented here is intended to clarify the interactions between creep behaviour and the ongoing AAR.

2 Experimental test programme

2.1 General

The investigation of two concretes, one reactive and the other not, is required to observe the effects of AAR on creep behaviour. Both concrete mixes were designed to reach similar mechanical strength and stiffness. In terms of storage and loading, the conditions were the same for both concretes. In parallel, the strains of free-swelling unloaded specimens were also recorded.

2.2 Choice of aggregates

The properties of both concrete mixes have to be similar before the development of the reaction. Consequently, the type of aggregates is important: for the non-reactive mix, crushed limestone aggregates were chosen. Crushed calcareous-siliceous aggregates (classified as potentially reactive according to the LCPC classification [9]) were used for the reactive ones. To justify this choice, the potentially reactive aggregates were characterized in accordance with standards and recommendations [10]– [11] and compared with the non-reactive crushed limestone in table 1.

Table 1 Mechanical properties of aggregates

Reactivity of the rock	Non-reactive [12]	Reactive
Uniaxial compressive strength	224 ± 25 MPa	178 ± 47 MPa
Young's modulus	80 ± 2 GPa	78.6 ± 0.2 GPa
Poisson's ratio	0.31 ± 0.01	0.31 ± 0.02

2.3 Concrete compositions

Both concrete compositions were designed with the same proportions of materials (presented in table 2). The grading curves were close with a maximum size of the largest grains of 12.5 mm.

The Na₂O equivalent content of both mixes was increased from 0.28% of cement content to 1.25% to ensure the AAR development.

Table 2 Concrete mixes

Components (for 1 m ³)	Non-reactive mix	Reactive mix
Non-reactive sand [0-2 mm]	680 kg/m ³	
Reactive sand [0-4mm]	/	672 kg/m ³
Non-reactive aggregates [4-12.5 mm]	1041 kg/m ³	/
Reactive aggregates [4-6 mm]	/	190 kg/m ³
Reactive aggregates [4-12.5 mm]	/	843 kg/m ³
Cement	410 kg/m ³	
Effective water/Cement ratio	0.46	

2.4 Exposure and loading conditions

The exposure conditions were the same for both concrete samples. These thermo-hydric conditions changed with time as follows: from the day after mixing, they were stored at 20°C in autogenous conditions for 28 days. After this curing, the specimens were immersed in a 1M hydroxide solution kept in barrels to avoid the leaching of alkalis. This was in accordance with previous experiments [13], and stored at 38°C to accelerate the reaction. Once a swelling of about 0.04% was reached for the reactive concrete mix, all the specimens were taken out of the solution and immediately sealed by aluminum foils to avoid desiccation and stored at 20°C. Once protected of desiccation, half of the samples remained free to swell while the others were uniaxially loaded at 30% of the lowest compressive strength of both mixes assessed after immersion.

2.5 Specimens and measurements

For each mix, strains were assessed on 3 unloaded specimens and on 2 loaded specimens. In parallel, 6 samples were used to characterize the mechanical properties. At each date of exposure condition change, the compressive strength and the Young's modulus were measured. All samples were cylinders with 113mm diameter and 220mm high. Longitudinal free strains of the unloaded specimens were measured using an indicator and plugs for the contact points (complied with the norm [14]) during the immersion time and after sealing. The creep tests samples were equipped with an inner LVDT sensor located in a niche centered in each specimen. This sensor allows to record the evolution of longitudinal strain during the curing period and under sustained loading.

3 Results and discussion

3.1 Designations and curve conventions

All the figures are presented with positive swelling strains while shrinkage and compressive creep strains are negative. NR is used for the non-reactive samples that are presented in blue, when R and the red curves are used for the reactive ones. The measurements system used is indicated with IS for the inner sensor and with P for the indicator and plugs system, and represented by continuous lines and dashed lines, respectively.

3.2 Autogenous shrinkage during curing

The strains due to autogenous shrinkage measured on two samples for each concrete using the inner sensors are presented in figure 1. After 28 days, a shrinkage strain of $178 \pm 3 \mu\text{m/m}$ was observed for the non-reactive concrete and $206 \pm 28 \mu\text{m/m}$ for the reactive one. This shrinkage measured at the end of the curing with the external sensor (corresponding to the mean value of three measurements) was $124 \pm 13 \mu\text{m/m}$ for the non-reactive concrete and $137 \pm 5 \mu\text{m/m}$ for the reactive one. The autogenous shrinkage is relatively high for both concretes and may be the consequence of the high alkali content [15].

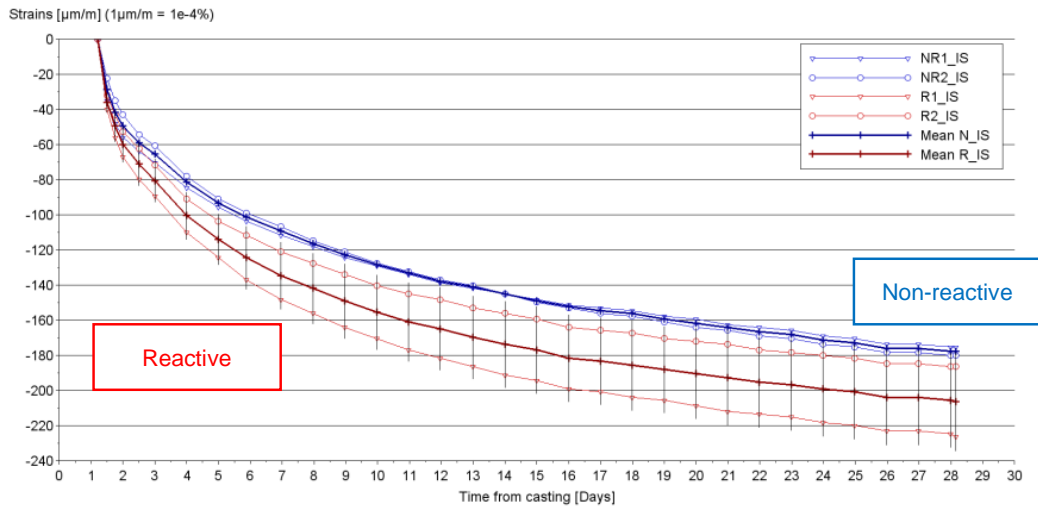


Fig 1 Autogenous shrinkage strains for reactive and non-reactive specimens during the 20°C autogenous curing (measurement by inner sensor)

3.3 Free strains and AAR expansions

The strains measured after the curing period are presented in figure 2, while figure 3 gives the strains evolution measured after samples sealing.

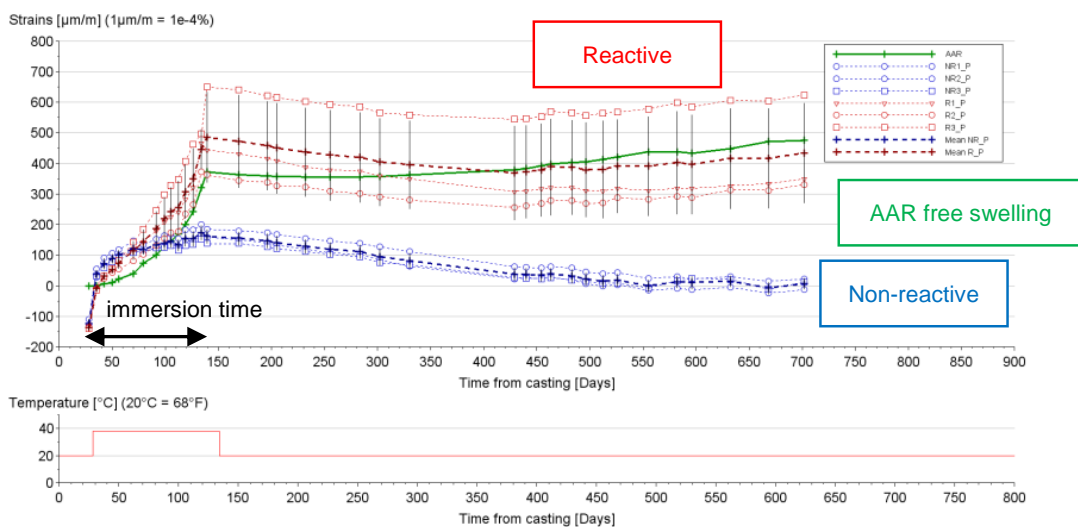


Fig 2 Evolution of the free strains of the reactive (red) and non-reactive (blue) specimens from 28 days to 700 days. (The AAR free swelling corresponding to the difference between the reactive and non-reactive concrete strain evolutions is represented by a green line)

3.3.1 Evolution in NaOH solution at 38°C

The AAR strain evolution (the green line in figure 2) corresponds to the difference between the strains of both types of concrete. This AAR strains curve begins one week after immersion to erase the strain due to the initial water absorption. At the end of the immersed period, the AAR swelling reaches a value of 0.032%. The strains directly measured on specimens were $446 \pm 64 \mu\text{m/m}$ and $173 \pm 24 \mu\text{m/m}$ for the reactive concrete and non-reactive one, respectively.

3.3.2 Free strains in autogenous conditions

At the beginning of the sealed condition period at 20°C, AAR is strongly slowed down and is maintained at a value of 0.038%. But after 420 days after casting, i.e. 300 days in autogenous condition, the kinetic increases again and reaches 0.048% at 700 days. Along with this slow AAR swelling rate, a shrinkage strain evolution was observed for both concrete types (figure 3).

The reduction in swelling rate can be attributed to the temperature decrease (from 38°C to 20°C) as previously observed in [2] - [16]. The change of moisture conditions also contributes to reduce the swelling rate. Nevertheless, the observed AAR swelling evolution with the increase of kinetic after 300 days in autogenous condition at 20°C confirms that this thermo-hydric condition is sufficient to allow the reaction development [17].

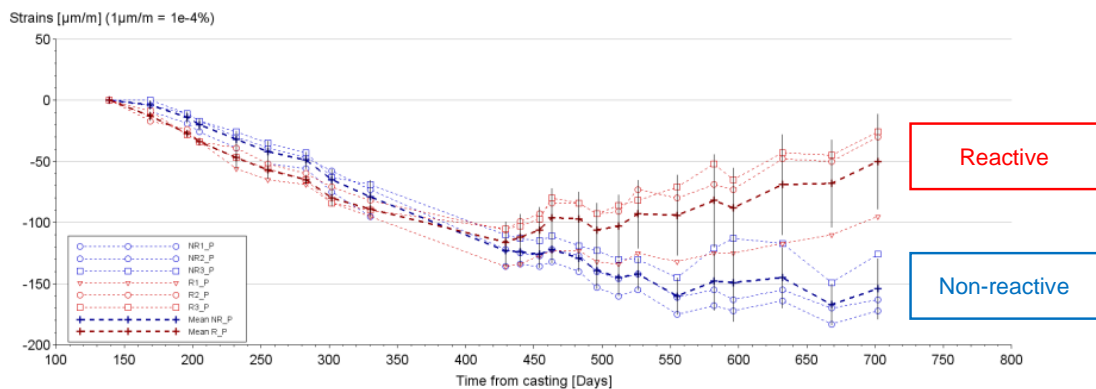


Fig 3 Evolution of free strains from the beginning of the autogenous stage

3.4 Evolution of mechanical properties

At each thermo-hydric condition change, the mechanical properties of both concretes were measured. The results before and after immersion at 35 days and 136 days, respectively, are presented in table 3.

Table 3 Mechanical properties before and after immersion time

Concrete Mix	Non-reactive	Reactive	Relative difference
Compressive Strength			
35 days	$45.3 \pm 1.2 \text{ MPa}$	$51.1 \pm 0.6 \text{ MPa}$	12.8 %
136 days	$56.2 \pm 1.0 \text{ MPa}$	$59.2 \pm 0.9 \text{ MPa}$	4.70 %
Evolution	+ 19.9 %	+13.7 %	/
Young's modulus			
35 days	$39.2 \pm 0.6 \text{ GPa}$	$37.3 \pm 0.4 \text{ GPa}$	4.79 %
136 days	$41.7 \pm 0.2 \text{ GPa}$	$36.1 \pm 0.4 \text{ GPa}$	13.4 %
Evolution	+ 6.01 %	- 3.36 %	/

The aim of the measurements at 35 days in autogenous condition at 20°C after casting was to compare the mechanical performance of both concretes before the beginning of the swelling. The compressive strength of the reactive concrete is slightly higher than the non-reactive one (difference of 12.8%), whereas it is the opposite for the Young's modulus results (difference of 4.79%).

At the end of the immersion period, i.e. 136 days, the AAR swelling reached 0.032%. The compressive strength of both concretes continues to grow but the increase is stronger for the non-reactive concrete (20% compared to 14% so a difference of 4.70%) showing that AAR certainly also affects this mechanical characteristic. The difference between the Young's modulus of both concretes reaches 13.4%. The Young's modulus of the non-reactive concrete increases due to cement hydration while the one of the concrete affected by AAR decreased by 3.36%. This reduction of mechanical properties during AAR agrees with previous observations [2]–[8] and is generally explained by micro-crackings in the cement paste and in the reactive aggregates.

3.5 Time-dependent strains under a uniaxial compressive load

The strains measured during the creep tests are presented in figure 6. These strains, assessed by inner sensors, are plotted with the free strains curves already analyzed in figure 4, and provide an overview of both tests conditions.

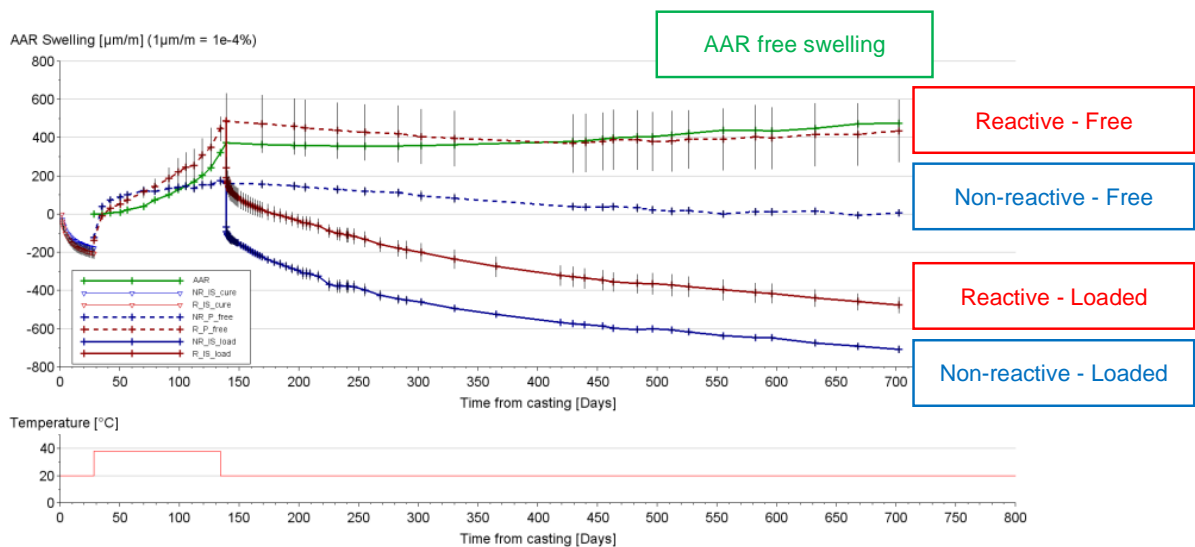


Fig 4 Total axial strains for both test conditions

3.5.1 Loading and elastic strains

A uniaxial compressive stress of 17 MPa was applied to all specimens. This value corresponds to 30% of the lowest compressive strength assessed the day of the loading (i.e. 56.2 MPa measured on the non-reactive concrete at 135 days (table 3)).

The elastic strains were 243 $\mu\text{m/m}$ and 228 $\mu\text{m/m}$ for the reactive and non-reactive concretes, respectively.

3.5.2 Strains under loading

As shown in figure 4, even after 570 days of creep, the total strain under loading of the reactive concrete, loaded after a free swelling period, was still 232 $\mu\text{m/m}$ higher than the non-reactive one. Before loading, this difference was equal to 320 $\mu\text{m/m}$. Thus, the compressive loading reduced the AAR free swelling by 25%.

This reduction is the consequence of two phenomena. Firstly, the instantaneous elastic strain of the reactive concrete is higher than the non-reactive one, due to the damage induced by the previous free swelling. Secondly, during the first 15 days after loading, the creep rate was superior in the reactive concrete.

Afterwards, both creep evolutions were quite similar, even when the AAR kinetic increased as observed on free strains samples, at the date corresponding to 300 days from loading.

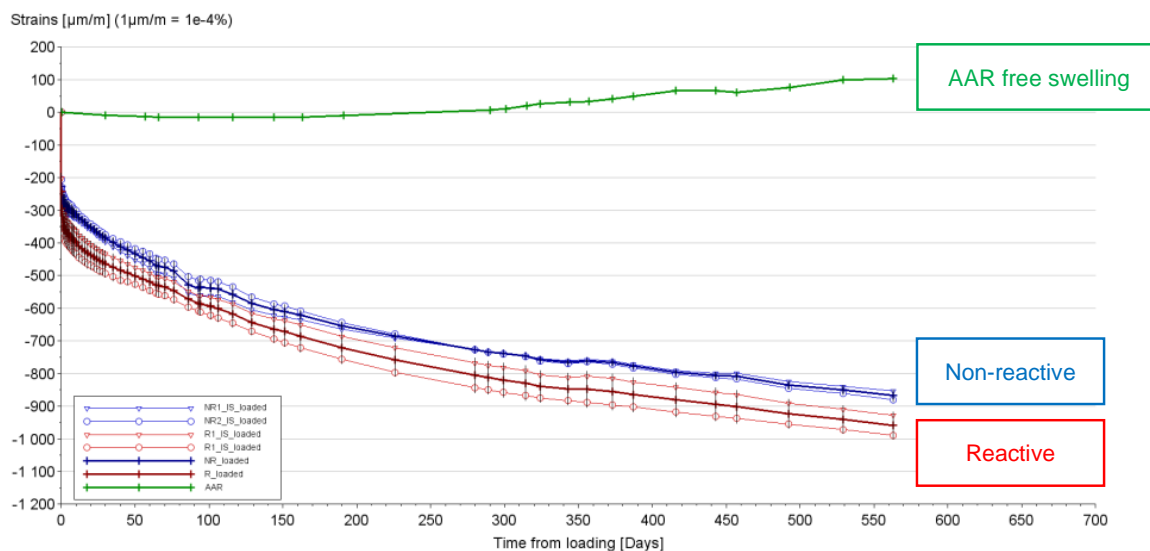


Fig 5 Strains under loading and AAR free swelling during the same period

The same observations were reported by Reinhardt et al [8] on concretes with different free swellings. After two weeks under stress and despite the reaction was already stopped in these tests, the creep velocities were similar whatever the AAR amplitude.

For the tests results detailed in the present paper, a compressive stress corresponding to 30% of the compressive strength provokes a swelling reduction of 25%. This reduction occurs during loading and in the first two weeks after loading. Beyond this period, the creep rate reaches a same level than for the non-reactive concrete, despite the AAR restarts.

4 Conclusions and modelling prospects

The quantification of the interactions between creep and AAR swelling has been done thanks to an experimental comparative study of a reactive concrete and a non-reactive one with similar initial mechanical performances.

This research work shows clearly that a compressive stress corresponding to 30% of the concrete compressive strength can reduce by 25% the free swelling occurred before the loading. A third of this absorption is the result of a high creep rate during the first two weeks of loading. The other part is due to the elastic behaviour of the damaged concrete. Even if the reaction continues, the creep rate remains the same for the concrete affected by AAR than for the non-reactive one.

These results will be considered to set up a structural model under development at LMDC Toulouse. The collaboration with Tractebel-Engie company aims to consider the local behaviour of cement paste around reactive aggregates in this model. This will be done via a micromechanics-based formulation that will consider cement paste creep and partial reclosing of AAR micro-cracks.

Acknowledgment

This work was carried out at LMDC Toulouse in collaboration with and with support from Tractebel-Engie company.

References

- [1] S. Diamond. 1975. "A review of alkali-silica reaction and expansion mechanisms." *Cement and Concrete Research* 5:329-346.
- [2] Larive C. 1997. "Apports combinés de l'expérimentation et de la modélisation à la compréhension de l'alcali-réaction et de ses effets mécaniques." PhD, Ecole Nationale des Ponts et Chaussées.
- [3] Multon S. 2003. "Evaluation expérimentale et théorique des effets mécaniques de l'alcali-réaction sur des structures modèles." PhD, Ecole Nationale des Ponts et Chaussées.
- [4] Charlwood R. G. 1994. "A review of alkali aggregate reaction in hydro plants and dams." *Hydropower and Dams* 1:73-80.
- [5] Esposito R. and Hendriks M. A. N. 2019. "Literature review of modelling approaches for ASR in concrete: a new perspective." *European Journal of Environmental and Civil Engineering* 23:1311-1331.
- [6] Grimal E., Sellier A., Le Pape Y. and Bourdarot E. 2008. "Creep, Shrinkage, and Anisotropic Damage in Alkali-Aggregate Reaction Swelling Mechanism—Part I: A Constitutive Model." *ACI Materials Journal* 105:227-235.
- [7] Dunant C. F. and Scrivener K. L. 2010. "Micro-mechanical modelling of alkali-silica-reaction-induced degradation using the AMIE framework." *Cement and Concrete Research* 517:525-40.
- [8] Reinhardt H. W., Özkan H. and Mielich O. 2019. "Creep of concrete as influenced by the rate of expansion due to alkali-silica reaction," *Structural Concrete* 20:1781-1791-.
- [9] LCPC. 1994. *Recommandations pour la prévention des désordres dus à l'alcali-réaction*.
- [10] NF P18-412. 1981. *Bétons - Caractéristiques particulières des machines hydrauliques pour essais de compression (presses pour matériaux durs)*. AFNOR.
- [11] RILEM. *Recommandations RILEM CPC8. Modulus of elasticity of concrete in compression, Materials and Structures*.
- [12] Makani A. 2011. "Influence de la nature minéralogique des granulats sur le comportement mécanique différé des bétons." PhD, INSA de Toulouse.
- [13] Rivard P., Bérubé M. A., Ollivier J. P. and Balliby G. 2007. "Decrease of pore solution alkalinity in concrete tested for alkali-silica reaction." *Materials and Structures* 40:909-921.
- [14] NF P18-594. 1978. *Granulats - Méthodes d'essai de réactivité aux alcalis*. AFNOR.
- [15] Jawed I. and Skalny J. 1978. "Effects of Alkalies on Hydration and Performance of Portland Cement." *Cement and Concrete Research* 37:52-8.
- [16] Diamond S., Barneyback Jr R. S., and Struble L. J. 1981. "On the physics and chemistry of alkali-silica reactions." Conference on Alkali-Aggregate Reactions in Concrete, Cape Town, South Africa.
- [17] Poyet S. 2003. "Etude de la dégradation des ouvrages en béton atteints par la réaction alcali-silice." PhD, Université de Marne-La-Vallée.

Fracture mechanics parameters in the assessment of frost resistance of high-strength concretes

Sylwia Anna Borowska, Marta Kosior - Kazberuk

Faculty of Construction and Environmental Sciences,
Bialystok University of Technology,
Wiejska 45 E, Bialystok 15 - 351, Poland

Abstract

Currently, the most important parameter describing structural elements is their durability. As a result of cyclic freeze/thaw, concrete undergoes degradation, which has a significant impact on the load-bearing capacity of structural elements. Moreover, high-strength concrete is a brittle material with a large number of structural defects, the occurrence of which is difficult to predict at the stage of structure design. The methods that will allow a good assessment of the state of degradation of high-strength concretes as a result of cyclic freeze/thaw are presently being sought. The introduction of fracture mechanics to the assessment of the degree of destruction of reinforced concrete elements, which were frequently frozen/thawed, gives a more complete understanding of the microstructural changes in concrete. The investigation was carried out mainly to assess the process of damage formation as a result of cyclic freeze/thaw of high strength concrete and HSC with fibers using a fracture mechanics method. Three types of high strength concretes were analyzed: concrete with compressive strength up to 90 MPa without fiber addition, concrete with 0.5 % steel fiber addition (39 kg/m^3) and concrete with a mix of steel and basalt fibers containing 0.25 % (19.5 kg/m^3) by volume of steel fibers and 0.25 % (6.8 kg/m^3) of basalt fibers. The test methods used are based on RILEM recommendations and ASTM C666. The fracture mechanics parameters were analyzed based on the relationship between load - deflection ($P-\delta$) and load - crack mouth opening displacement ($P\text{-CMOD}$), recorded for concrete samples after 150, 250, 300, and 350 freeze/thaw cycles. The changes of modulus of elasticity were also analyzed during this process to control the internal resistance to cyclic freeze/thaw by non-destructive methods, according to [2]. A new approach to the description of frost degradation of HSC with steel and basalt fibers was proposed.

Key words: high strength concrete, fibres, frost damage, fracture mechanics, frost resistance, steel fibre, basalt fibre, modulus of elasticity

1 Introduction

Nowadays, developing technologies make it possible to obtain building materials that are more and more beneficial in terms of strength and durability. The modern construction industry, which aims to create monumental buildings, breaking records of height and span, is looking for innovative solutions to use structural elements that are safe in terms of load capacity and resistance to external conditions. Due to the functionality and the economical approach of the building, the main reason for using high-strength concretes is to reduce the cross-sectional dimensions of the elements, simultaneously maximizing their spans. The key challenge for technologists, constructors, and contractors is to create a concrete structure that enables formation performance throughout its lifetime. High strength concretes, despite their numerous advantages, are brittle material. The addition of steel fibres to HSC concrete changes them into quasi-plastic materials, preventing a sudden brittle fracture in load conditions [3].

Durability is one of the most important parameters describing modern buildings. It has a significant impact on the behavior, appearance and usability of objects. The process of construction materials wearing out results from the destructive influence of external environment interaction and improper exploitation. The conventional calculations of the structural elements are based on the assumption that materials are an ideal continuum, have no defects, discontinuities and changes in the structure resulting from the influence of external conditions [4]. Despite the safety factors used in the construction dimensioning, the results of the analyses are characterized by high randomness. If there are internal defects in the material, then significant changes in strength parameters may occur with the progress of the service life. Severe discontinuities and defects of material may be the beginning of fracture development. However, concrete is not perfectly brittle because it has some tensile strength. HSC is

characterized by a rapid increase in initial strength, which leads to the initiation of numerous places with different characteristics of preliminary deformation [5]. Insignificant, in the initial period of existence of the concrete element discontinuities may, as a result of a destructive environmental impact, lead to the catastrophe of the structure, designed in accordance with generally applicable standards. The connection of fracture mechanics parameters with the degree of damage as a result of the destructive influence of cyclic temperature changes under the influence of de-icing agents, leads to a more complete description of the internal degradation of high strength concrete.

Numerous publications and works confirm the beneficial effect of adding fibres on the mechanical parameters of concrete, but so far little attention has been paid to the susceptibility of high-strength fibre-reinforced concrete to external environmental factors. According to [6], basalt fibres in the cement matrix significantly improve the flexural strength of concrete. Based on [7], the dynamic elasticity modulus of basalt fiber-reinforced concrete exposed to 100 freeze-thaw cycles was 1,47 times higher than normal concrete, while the addition of 2,50% of steel fibres has a positive effect on freeze-thaw durability factor [8]. The description of mechanical parameters of concrete with the addition of basalt fibres of different geometry has been presented in [9], indicating the variable character of concrete work during fracture before and after reaching the peak load. Concretes with basalt fibres showed better ductility and energy-absorbing capacity in comparison to normal concretes. The paper [10] indicates that the use of steel fibres in cement materials improves their acoustic properties and fire resistance. The addition of polypropylene fibre to ultra-high-strength concrete reduces the damage resulting from the influence of ambient temperature reaching over 300°C [11]. Steel fibres in concrete prevent the formation of shrinkage scratches in the early stages of curing and exploitation. The research on the influence of hybrid fibers on high strength concrete was presented in [12], showing advantages and disadvantages of mixing steel fibers of different dimensions, indicating the potential to achieve an optimal composition of HSC mixture. Comparative analysis of mechanical parameters of high strength fiber concrete compared to HSC without fiber addition was also carried out in the paper [13]. It was also found that the resistance to fracture of cement materials can be evaluated during the whole failure process [13].

The research aimed to determine the relationship between the degree of HSC frost degradation and the values of fracture mechanics parameters. The analysis led to the description of frost damage of high strength concrete, high strength fiber reinforced concrete with 0.5% steel fibre content and HSC with addition of a mixture of steel and basalt fibres in amounts constituting 0.25% by volume, using the stress intensity factor K_{Ic} and the critical crack mouth opening displacement (CMOD_C). The aim of the analysis was to show the effect of the presence of fibres in HSC mixture on fracture mechanics parameters and the degree of frost degradation, as well as to assess the adequacy of replacement of steel fibre parts with basalt fibres. High-strength concrete exposure to loads tend to be brittle material, therefore fibres have been selected that lead to a change in the characteristics of the material from brittle to quasi-plastic. The internal frost resistance was tested and the value of modulus of elasticity was determined after 150, 200, 250, 300 and 350 freeze/thaw cycles. Based on RILEM recommendation [1], the dependence of force as a function of the crack mouth opening displacement and deformation, under three-point bending test, was measured to determine the fracture mechanics parameters.

2 Experimental program

2.1 Materials and sample preparation

The tests were carried out on concrete with a compressive strength of 90 MPa. Portland cement CEM I 42.5 R in the amount of 440.5 kg/m³ was used for the samples, with a constant water-binder ratio ($w/c = 0.31$) in all series. The maximum grain size of the post-glacial grit used was limited to 11 mm. The absorbability and frost resistance of the aggregate was 0.7% and F_{NaCl7} , respectively [14]. River sand of 0 -2 mm grain size was applied. To obtain appropriate consistency at the S3 level to enable distribution of dispersed reinforcement in the mix, the superplasticizer Chrysto Optima 292 was added in the amount of 1.65% of the binder mix, with an increase in the amount to 1.85% of the binder volume for HSC with fibres addition. The superplasticizer produced based on modified polycarboxylates with a density of 1.085 g/cm³ at 20 °C was used. To obtain higher concrete strength and to obtain a tight structure silica dust, which accounts for 7% of the binder volume, was implemented. Three types of samples were made: MB1 - HSC without fibres, MB2 - HSC with 50 mm long steel fibre and MB3 - high-strength concrete with 50 mm steel fibre and 50 mm basalt fibre content. Physical and mechanical properties of the fibres are presented in Table 1. The addition of steel fibres in the MB2 mix was 0.5%

(39 kg/m³), while the addition of steel fibres in the MB3 mix was 0.25% (19.5 kg/m³) and basalt fibres 0.25% (6.75 kg/m³).

During the mixing process, the aggregate was mixed dry with cement and silica dust before applying half the water and superplasticizer. When the fibres were added to the concrete mix, the amount of superplasticizer was increased to maintain the consistency of the mix and to prevent the formation of empty spaces associated with worsened workability. The fibres were added to the concrete mix in stages, alternating with a mixture of water and a superplasticizer to prevent the formation of 'hedgehog' fibre clusters. The total mixing time was about 12 minutes. The samples were vibrated on a vibrating table. After 24 hours, the samples were disassembled and stored in a water bath at 18 +/- 2° C until the test started.

Table 1 Properties of the fibres used.

Properties	Steel fibres	Basalt fibres
Fibre shape	Hooked	Straight
Length (mm)	50	50
Diameter (mm)	1.0	0.02
Tensile strength (MPa)	900	1680
Modulus of elasticity (GPa)	200	89
Density (kg/m ³)	7850	2660

To analyze the mechanical parameters of HSC, 12 samples from each series were prepared: MB1, MB2, MB3, in the form of beam elements measuring 100 mm x 100 mm x 400 mm, with a notch. The initial notch, 30 mm deep and 3 mm wide, was made in the middle of the span, using a circular saw. The compression strength changes after 150, 250 and 350 freeze/thaw cycles were determined on cubes measuring 100 mm x 100 mm x 100 mm. Each series consisted of 3 elements. Tensile strength during the bending test was performed on beam elements measuring 100 mm x 100 mm x 400 mm.

2.2 Research methodology

The internal freeze/thaw tests were carried out according to the following procedure: the samples were frozen in air at - 18 ± 2 °C for 4 hours and thawed in water at +18 ± 2 °C for 4 hours. The assessment of frost resistance was made based on a decrease in compression strength and a decrease in mass after the next freeze/thaw cycle. Concrete series MB1 and MB2 were subjected to 350 freeze/thaw cycles. In case of the MB3 series of concretes, the cyclic freeze/thaw was carried out until the moment of loss of frost resistance of these concretes, found by non-destructive method after 150 cycles. After this period, numerous cracks and surface scratches were also observed. Every 50 cycles the decrease in HSC frost resistance was controlled by measuring the changes in the sample length and modulus of concrete elasticity, based on ASTM C 666 method [2]. The value of durability factor DF was determined according to formula (1). The standard [2] indicates that the value of DF below 0.6 indicates the lack of concrete resistance to frost. The measurements of resonance frequencies were carried out using a concrete scanner, as shown in the Figure 1.

The fracture mechanics parameters were determined on the basis of RILEM TC 89-FMT [1], under three-point bending test. The force was applied in such a way that the maximum load was reached within five minutes from the start of the test. An average load speed of 0.012 mm/s was assumed. The load was carried out by adjusting the displacement of the piston. The test assumptions were based on the method developed by Jenq and Shah [15]. The measurement of the crack mouth opening displacement during the test was performed using a plate extensometer. The tests were carried out under the conditions of the first load model using a Zwick/Roell Z250 testing machine. The diagram of load application (tensile) and support of the test pieces together with the specimen dimensions are shown in Figure 2.

$$DF = \frac{N}{M} \cdot \left(\frac{n_n}{n_0}\right)^2 \cdot 100 [\%] \quad (1)$$

where: M - number of freeze/thaw cycles, n_0 - resonance before the first freezing, n_n - resonance frequency after n cycles, $N = 300$.



Fig.1 Stand for resonance frequency measurement of concrete prism samples.

K_{IC} is the most popular and most commonly used parameter of fracture mechanics to describe the behaviour of concrete elements. It is a measure of the stress field at the tip of the initiated crack, assuming the linearly elastic material operation. The energy absorbed during the fracture process, related to the fracture propagation, is proposed to be determined according to [15]. The highest value of fracture energy is related to the subcritical deformation range and the critical point, while the subcritical range, to a lesser extent, affects the obtained values of this fracture mechanics parameter and represents only a few percent of total energy until the concrete element is destroyed. The test determined the dependence of the peak load and crack mouth opening displacement (P -CMOD), assuming that the measurement is completed when half of the maximum force is reached in the supercritical range. To determine the fracture energy, the force dependence on the deformation of the tested beams was determined (P - δ). The fracture mechanics parameters were determined based on the relationships (2),(3).

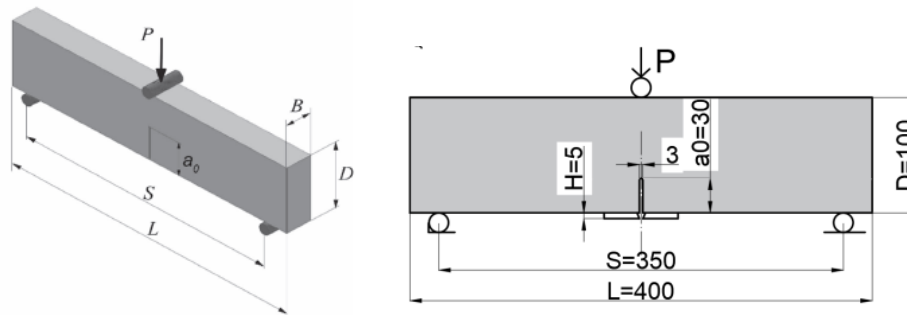


Fig.2 The load scheme of the test item. The following assumptions have been made: $L = 400$ mm; $S = 350$ mm; $D = 100$ mm; $B = 100$ mm; $a_0 = 30$ mm.

$$K_{IC} = \sigma_c \sqrt{\pi a_c} Y\left(\frac{a}{D}\right) \quad (2)$$

$$G_F = \frac{\int_0^{\delta_{max}} P(\delta) d\delta + mg\delta_{max}}{(D - a_0)B} \quad (3)$$

Where: δ_{max} - deformation at maximum load; a_0 - notch depth; $Y(a/D)$ - geometry influence function based on Lotto-Kesler dependencies [15]; D , B - beam width and height.

3 Results and discussion

Table 2 shows the average values of physical parameters of the tested high strength concretes, determined after 28 days of curing. The mean compressive strength f_{cm} , tensile strength f_{tm} , absorbability n , capillary action n_{cap} and volumetric density ρ were determined. Water absorption has been increased by about 30% when fibres are added to the cement matrix. Concrete with a mixture of steel and basalt fibres (MB3) was characterized by the biggest absorbability. The increase in absorbability in the case of the content of fibres in the concrete was caused by a decrease in the tightness of its structure and a noticeable loss of bonding of basalt fibres to concrete. The compressive strength of high-strength concretes with steel fibres (MB2) and mix of steel and basalt fibres (MB3) was reduced in comparison to HSC without fibres (MB1). The presence of fibres results in the formation of poor areas and voids in

HSC. Also, the tensile strength has deteriorated in the case of concrete with steel and basalt (MB3) fibres, which may have been caused by the weakening of the adhesion of the fibres to the concrete, due to the lack of continuity of the polymeric coating of basalt fibres. The deterioration of the mechanical properties of high-strength concrete with fibres in comparison to plain HSC was possibly caused by the incorrect distribution of fibres in the mixture, resulting in poor spots. The presence of fibres in the matrix of high-strength concrete caused a slight increase in volumetric density. The concrete of the MB2 series was characterized by the highest susceptibility to capillary suction 3% salt solution. The conversion of half of the steel fibres into basalt fibres in the MB3 series concretes made it possible to reduce the capillary pull-up ability. Insignificant inadequacies in spreading the fibres in the concrete mix can lead to an unbeneficial change in the characteristics of the mix with the addition of fibres in comparison to high strength concrete without fiber content. The tight structure of high-strength concrete has been disturbed.

Table 2 Properties of high strength concrete after 28 days of curing.

Type of concrete	f_{cm} [MPa]	f_{tm} [MPa]	n [%]	n_{cap} [$\frac{kg}{m^2}$]	ρ [$\frac{kg}{m^3}$]
MB1	93,66 (2,58) *	6,68 (0,15) *	1,96 (0,15) *	1,58 (0,19) *	2456 (13,00) *
MB2	91,62 (5,77) *	6,65 (0,14) *	2,38 (0,30) *	2,28 (0,20) *	2474 (22,77) *
MB3	86,88 (1,90) *	6,34 (0,02) *	2,57 (0,09) *	2,00 (0,16) *	2471 (64,16) *
*The standard deviation is given in brackets.					

Table 3 Analysis of fracture mechanics parameters K_{IC} and CTOD.

Concrete type	Number of freeze/thaw cycles	K_{IC} [MPa·m ^{1/2}]	CTOD [mm]	G_f (δ_{max}) [Nm/m ²]	Maximum load [kN]
MB1	0	0,688 (0,045)*	0,032 (0,0005)*	15,011	7122,8 (528,7)*
MB1	150	0,733 (0,032)*	0,032 (0,0031)*	35,932	7475,8 (560,4)*
MB1	250	0,756 (0,016)*	0,033 (0,0010)*	20,159	7677,9 (132,6)*
MB1	350	0,779 (0,043)*	0,034 (0,0017)*	19,885	7902,9 (356,8)*
MB2	0	0,782 (0,011)*	0,035 (0,0015)*	27,029	7943,4 (92,3)*
MB2	150	0,557 (0,047)*	0,025 (0,0017)*	41,161	5678,2 (389,2)*
MB2	250	0,865 (0,091)*	0,038 (0,0041)*	92,046	9247,2 (719,1)*
MB2	350	0,658 (0,068)*	0,029 (0,0035)*	18,639	6691,8 (565,5)*
MB3	0	0,774 (0,026)*	0,034 (0,0014)*	35,667	7861,8 (218,5)*
MB3	150	0,156 (0,098)*	0,053 (0,0797)*	23,570	1589,3 (895,0)*
*The standard deviation is given in brackets.					

Table 3 shows the results of the analysis of K_{IC} values, critical crack tip opening displacement of the CTOD_c and fracture energy G_f . The results show the improvement of fracture resistance of high strength concrete by adding steel fibres (MB2) and mixed fibres (MB3). After 150 freeze/thaw cycles, a decrease in the stress intensity factor value of concrete with steel and basalt fibres (MB3) is observed. In concretes without fiber addition, the value of stress intensity factor increases with the number of freeze/thaw cycles. The increase in fracture resistance of HSC without the addition of fibres is caused by the increase in the strength of the concrete over time and is an indicator of resistance to the effects of freeze/thaw. Concrete with a mixture of steel and basalt fibres (MB3) has lost its resistance to fracture and frost after 150 freeze/thaw cycles (Figure 7 and Table 3-4). The value of the critical tip opening displacement is highest in their case. The fibres did not stop the uncontrolled propagation of the critical crack mouth opening displacement and thus the brittle fracture. In the case of a limited amount of fibres

contained in the concrete, it is crucial that they are properly placed in the cement matrix. The stress intensity factor, which is a material characteristic of concrete, decreased by almost 80% in the case of the MB3 series compared to the initial value. The reason for this type of damage to high-strength concrete may be the heterogeneity of the concrete structure and the tendency of basalt fibres to join together. The DF index of the MB3 series concrete has fallen below the 60% limit, which indicates a loss of freeze/thaw resistance. HSC with steel fibres had the highest fracture energy after 250 freeze/thaw cycles. The fracture energy increases as a result of crack bridging by the more resistant steel fibre encountered. After 350 freeze/thaw cycles of MB2 series concretes, there was a sudden decrease in fracture resistance, which indicates the gradual degradation of concretes and the loss of their resistance to cyclic freeze/thaw. The content of steel fibres in high-strength concrete prevents the propagation of internal fractures and inhibits the development of cracks. When substantial stress is created as a result of cyclic freeze/thaw, the amount of fibres used in the concrete becomes insufficient and mechanical parameters become deteriorated. The highest susceptibility to fracture brittleness was found in high strength concrete without fibre content (MB1), not subjected to cyclic freeze/thaw. With the increase in the number of freeze/thaw cycles and the increase in strength, the resistance of MB1 series concretes to brittle fracture increases. These type of concrete up to 350 freeze/thaw cycles did not undergo the degradation, described by the deterioration of fracture mechanics parameters and DF coefficient.

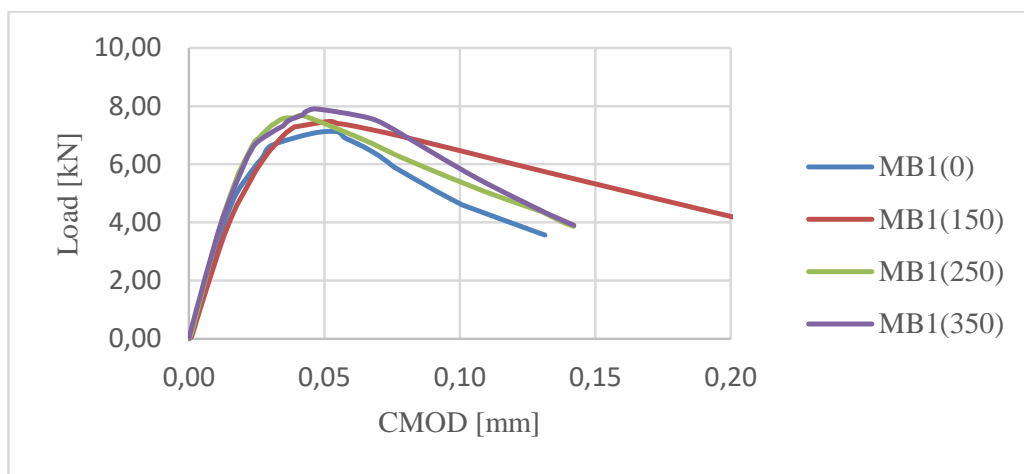


Fig.4 Typical curves of load dependence P in CMOD function for concrete of MB1 series after (n) freeze/thaw cycles.

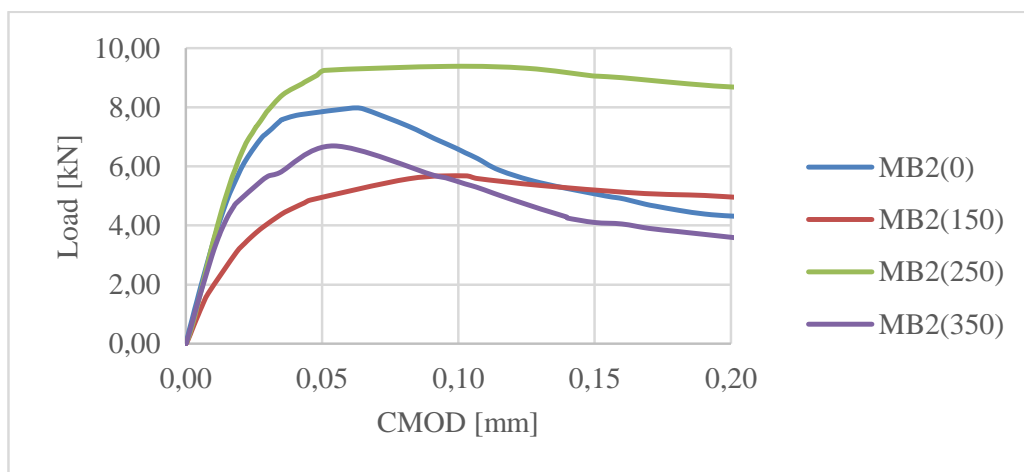


Fig.5 Typical load curves P in CMOD function for concrete of MB2 series after (n) freeze/thaw cycles.

Figures 4 - 6 show the maximum load as a function of crack mouth opening displacement CMOD. The measurement was made until the load was reduced by 50% of the maximum force. The ductile behavior of the MB3 series concretes after 150 freeze/thaw cycles were shown. Figure 5 gives the course of changes of maximum force as a function of CMOD for concrete with steel fiber content (MB2) after 150, 250 and 350 freeze/thaw cycles, with an increase of maximum force after 250 cycles and a decrease of its value again after 350 cycles. These changes indicate the susceptibility of high strength concretes

with the addition of steel fibres (MB2) to the influence of cyclic freeze/thaw, with a simultaneous increase in the value of strength parameters with the age of the concrete. The addition of basalt fibres in the cement matrix caused the elongation of the deformation segment until the maximum load is reached. The nature of the work of concrete with the addition of fibers in the cement matrix is clearly changed from quasi-brittle to quasi-plastic, and this is shown by the elongated shape of the MB2 and MB3 series curves in Figs. 5-6. After 350 cycles, no significant effect of freeze/thaw was observed on high strength concrete without fibers. These concretes are characterized by a larger range of elastic deformations, as shown in Figure 4, and at the same time lower resistance to fracture. Due to the more homogeneous structure and fewer voids, the MB1 series concretes did not degrade as a result of cyclic freeze/thaw after 350 cycles.

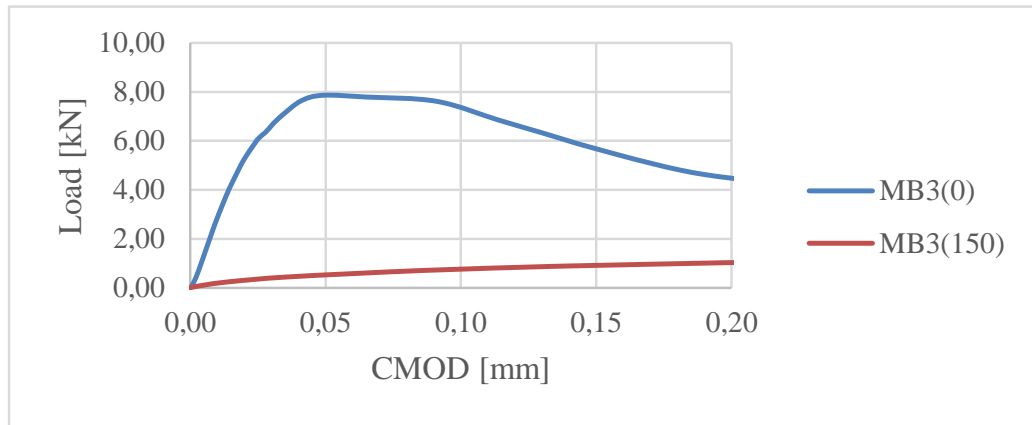


Fig.6 Typical load curves P in CMOD function for concrete of MB3 series after (n) freeze/thaw cycles.

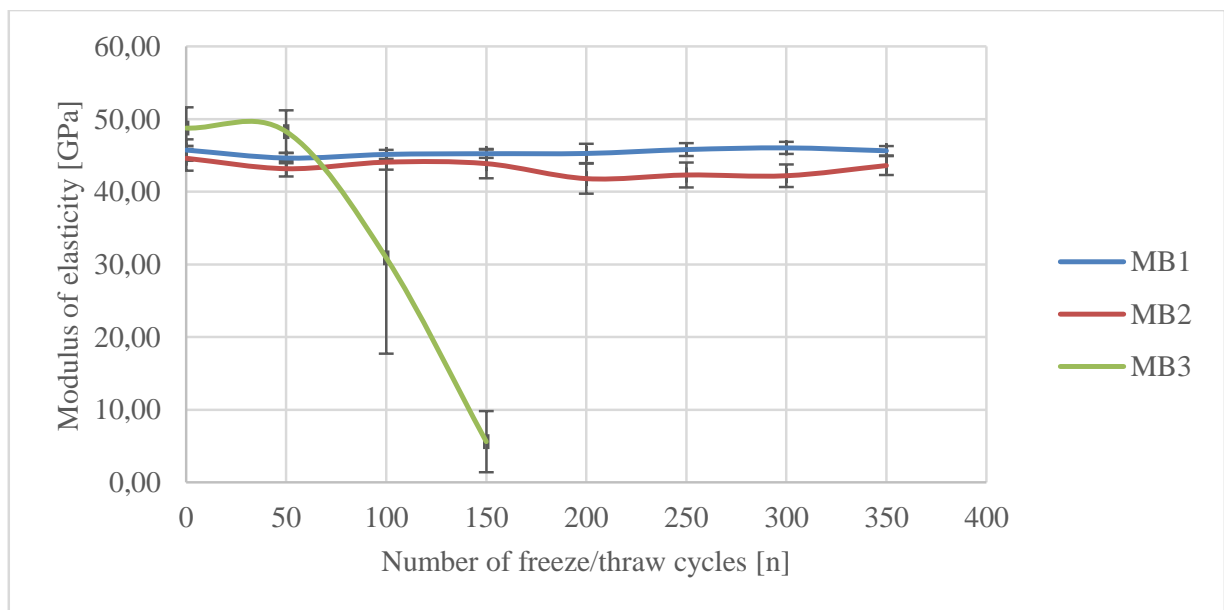


Fig.7 Changes in modulus of elasticity of high-strength concretes after (n) freeze/thaw cycles.

Table 4 DF value, compression strength loss and weight loss after (n) freeze/thaw cycles

Type of concrete	DF after 100 cycles [%]	DF after 150/350 cycles [%]	Δf_{cm} after 150/350 cycles [%]	Δm after 150/350 cycles [%]
MB1	97,39	97,83/99,56	2,83/8,30	0,70/1,49
MB2	97,62	96,73/95,56	7,55/13,26	0,50/1,22
MB3	83,04	21,23/[-]	15,18/[-]	2,62/[-]

None of the tested concretes showed a loss of resistance to cyclic freeze/thaw described by a decrease in mass and compression strength, as shown in Table 4. Concretes with mixed fibres: steel-basalt (MB3), after 150 freeze/thaw cycles, have undergone numerous cracks and their modulus of elasticity

has dropped by nearly 80%. The decrease in the value of modulus of elasticity after 150 cycles, in the case of the analysed HSC with mixed fibres (MB3) by 79.8% corresponds to a decrease in the value of the K_{IC} stress intensity coefficient by about 80%.

4 Conclusions

The fracture mechanics parameters of the MB2 and MB3 series of concretes improved due to the fibres presented in the HSC matrix but they deteriorated with subsequent freeze/thaw cycles. Theoretical strength and the value of the defects occurring are the factors that determine the strength of a material fracture in a brittle way. The higher the energy is absorbed during the fracture formation, the more resistant the material is to brittle fracture. The addition of fibres to the concrete increases the absorbed energy when the crack reaches the fibre through its propagation. The cyclic freeze/thaw led to the destruction of concretes with mixed steel and basalt (MB3) fibres. The fracture mechanics parameters of the MB3 series of concretes were significantly deteriorated. Similar CTOD_C values were observed for high strength concretes with mixed fibres and steel fibres before they were subjected to cyclic freeze/thaw. This means that the replacement of half the amount of steel fibres with basalt fibres does not cause significant changes in fracture inhibition. It is important that the steel and basalt fibre volume content of the concrete should be more than 0.5% in order to prevent the propagation of stress fractures caused by the cyclic freeze/thaw of HSC by crack-bridging fibre properties. The frost resistance of HSC is associated with absorbability. The presence of fibres in high-strength concrete significantly increases their absorbability. Steel and basalt fibres in concrete can withstand tensile stress, reducing the formation of cracks and limiting stress concentration at the tip of microcracks, preventing them from spreading, thus eliminating the formation of combined cracks. However, special care must be taken to ensure that the fibres are correctly distributed in the concrete mix and a proportionally higher number of fibres must be used to prevent the propagation of further fracture formation that occurs with subsequent freeze/thaw cycles. The decrease in the mechanical properties of concretes with fibres (MB3) was also caused by a decrease in the adhesion of the basalt fibre to concrete, due to the loss of continuity of the fibre outer coating. The stress intensity factor K_{IC} after freeze/thaw cycles changes accordingly to changes in DF in high strength concrete with the addition of mixed fibres (MB3). In the case of HSC without fibres (MB1), an improvement in fracture mechanics parameters, such as K_{IC} and CTOD_C value, becomes noticeable after being subjected to freeze/thaw cycles, with a slight deterioration in modulus of elasticity by about 4% and a slight decrease in mass (1.5%) and compressive strength (8.3%). In the case of HSC with steel fibres (MB2), there was an increase in the stress intensity factor after 250 cycles, while after 350 cycles there was a clear decrease in this parameter by over 16%, with a simultaneous decrease in modulus of elasticity by 4%. Cyclic freeze/thaw in the initial phase contributes to the increase of fracture energy. However, as the frost degradation progresses, the fracture mechanics parameters deteriorate. The increased absorbability of high strength concrete with fibres resulting from poor regions leads to a concentration of tensile stress in these areas as a result of cyclic freeze/thaw and as a consequence to internal degradation of the concrete.

5 Literature

- [1] Ferreira L.E.T.. 2007." Fracture analysis of a high – strength concrete and a high – strength steel – fiber – reinforced concrete". *Mechanics of Composite Materials*, 43/5.
- [2] RILEM Draft Recommendation TC 50-FMC.1985. "Determination of the fracture energy of mortar and concrete by means of three – point bend test on notched beams". *Materials and Structures* 18: 285 – 290.
- [3] Golewski G., Sadowski T. 2007. "Analysis brittle damages in concrete composites". *Technical Transactions*. Publishing House of The Cracow University of Technology. Poland: Cracow.
- [4] Gettu R., Bazant, Z. P., Karr M. E. 1990. "Fracture properties and Brittleness of High-Strength Concrete". *ACI Material Journal* 87/6: 608-618. November – December.
- [5] Neville A. M. 2012. *Properties of concrete*. Association of Cement Producers. Poland: Cracow.
- [6] Smarzewski P. 2019. "Influence of basalt – polypropylene fibers on fracture properties of high-performance concrete". *Composite Structures* 209: 23-33.
- [7] Fan X., Wu D., Chen H. 2014. "Experimental research on the freeze-thaw resistance of basalt fiber reinforced concrete". *Advanced Materials Research* 919-921: 1912-1915

- [8] Feo L., Ascione F., Penna R., Lau D., Lamberti M. 2020. "An experimental investigation on freezing and thawing durability of high performance fiber reinforced concrete (HPFRC)". *Composite Structures* 234:1-15.
- [9] Kosior – Kazberuk M., Krassowska J. 2015. "Fracture behavior of basalt and steel fiber reinforced concrete". *Civil and Environmental Engineering* 6: 73-80.
- [10] Ibrahim I.S, Che Baka M.B. 2011. "Effects on Mechanical Properties of Industrialized Steel Fibers Addition to Normal Weight Concrete". *International Journal of Recent Trends in Engineering* 2616:130-145.
- [11] Rios J. D., Cifuentes H., Leiva C. 2019. "Effect of polypropylene fibers on the fracture behavior of heated ultra – high performance concrete". *Internal Journal of Fracture*.
- [12] Ferreira L.E., de Hanai J.B., Ferrari V. J. 2016. "Optimization of a hybrid – fiber – reinforced high – strength concrete". *Mechanics of Composite Materials* 52/3.
- [13] ASTM C 666, Standard Test Method for Resistance of Concrete to Rapid Freezing and Thawing, Annual Book of ASTM Standards, 1991.
- [14] PN-EN 1367-1 Tests of thermal properties and resistance to weathering of aggregates - Part 1: Determination of frost resistance.
- [15] Jenq Y. S., Shah S.P. 1985. "A two parameter fracture model for concrete". *Journal of Engineering Mechanics* 111:. 1227-1241.
- [16] Bazant Z.P. 2002. „Concrete fracture models: testing and practice”. *Engineering Fracture Mechanics* 69:165-205

Leaching of cement-based mortar: sensitivity to calcium and carbonate ions

Aliénor Pouyanne - Gauthier^{1,2}, Benoît Hilloulin¹, Emmanuel Rozière¹, Ahmed Loukili¹, Van Quan Tran³

¹*Ecole Centrale de Nantes,
1 rue de la Noë, 44300 Nantes, France*

²*Edycem,
Rue du Fléchet, 85600 Boufféré, France*

³*University of Transport Technology,
Hanoi, Vietnam*

Abstract

Concrete structures can undergo several chemical deteriorations that can jeopardize their normal use, when in contact with their environment. The dissolution of cement hydration products in contact with water is one of them. As a first approach, a numerical model has been built, in order to reproduce the chemical phenomena that happen. Ionic concentrations and evolutions of mineral volumic proportions have been obtained. Several waters have been tested, from basic ones with demineralized water to real mineral water. The influence of calcium and carbonate ions is investigated in this study. A new performance indicator, which takes into account the variation of chemical elements, is discussed.

1 Introduction

In contact with environmental waters, structures made with cementitious materials can undergo chemical deteriorations that can jeopardize their serviceability. In order to take into account the durability, code models and standards like Eurocodes and European standards give specifications for the design, depending on the environmental actions. Recommendations are mainly about proportions of constituents and strength [1]. Based on experience feedbacks, these specifications allow easy implementation but they admit some simplifications. Although complying with these specifications, some water treatment plants have suffered premature deterioration. For instance, the deteriorated structure of drinkable water plant can be out of order and under renovation after only few years.

Another approach, called performance-based specifications, can be used to design the concrete mixtures. It does not only consider the mixture proportions, but also materials characteristics and properties, which allow to predict their actual resistance to the environmental action, during their service life. The approach is generally comparative. The tested sample is compared to a reference sample complying with prescriptive specifications. There must be an equivalence regarding the aggressive environment, and the concept of performance indicators is used. Their sensitivity is essential in order to distinguish different materials according to their performance level [2], as well as their representativeness: the indicator needs to be based on the real deterioration mechanism. Concerning leaching, existing indicators are mainly obtained by macroscopic measurements, like mass and volume variations, or by destructive tests, such as the evolution of water porosity. These indicators allow to highlight different behaviours of mortar samples in contact with different leaching solutions, but they are not always easily accessible due to their response time. In order to get other relevant and short-term performance indicators, it is necessary to understand the mechanisms involved in given chemical attack. Numerous studies have already modelled the case of leaching by unmineralized water, this study aim is to focus on mineralized waters. This paper offers a description of the attack thanks to a geochemical model, especially focused on quantities evolving during the attack, their concomitances, their specializations and temporalities. A new performance indicator, which takes into account the variation of chemical elements, is discussed.

Several leaching solutions are simulated and then compared, in order to analyse their influence on the chemical phenomena. Two artificial intermedial solutions are simulated, allowing to understand the influence of main ions presence in the leaching solution on chemical phenomena. A better understanding of the chemical aspect of this durability phenomenon is the first step forward constructions in any environment.

2 Numerical simulation

2.1 Numerical model

Simulations were performed using a reactive transport model called Toughreact, using the EOS9 module, for a unic aquous phase [3]. It is a geochemical code using an integral finite difference method. The saturation index is used to take into account the thermodynamic equilibria [4]. If the index is positive the mineral will be formed and if negative it will be dissolved. Flow and transport are modelled thanks to mass and energy conservation principle:

$$\frac{\partial M_j}{\partial t} = -\nabla F_j \quad (1)$$

were M_j cumulated mass of the aquous species j (kg) and F_j mass flow of the aquous species j ($\text{kg}\cdot\text{m}^{-2}\cdot\text{s}^{-1}$) [5]. Samples are initially water saturated, so diffusion of chemical species is the main transport phenomenon and it is considered that water and air do not flow. These lead to expressions of cumulated mass and mass flow as:

$$M_j = \phi S_l C_{jl} \quad (2)$$

$$F_j = u_l C_{jl} - (\tau \phi S_l D_l) \nabla C_{jl} \quad (3)$$

were C_{jl} is the concentration of the aquous species j in the liquid phase l ($\text{mol}\cdot\text{l}^{-1}$), D_l the diffusion of the aquous species l ($\text{m}^2\cdot\text{s}^{-1}$), τ the tortuosity, u_l the speed of the liquid phase (Darcy) ($\text{m}\cdot\text{s}^{-1}$), S_l the saturation of the liquid phase and ϕ the porosity [5]. Kinetics of dissolutions and precipitations are not considered in this model. In this model, the evolution of porosity during the attack is taken into account.

The modelled mortar sample is 2 mm deep and the surface exposed to environmental water is 1 cm high and 1 mm wide. It is meshed in one dimension by 200 similiary-sized cells (Fig. 1). The environmental water represents five cells with the same dimensions but a volume factor going from $1^{\text{E}5}$ to $1^{\text{E}80}$ to simulate an infinite volume of environmental water. The maximal time step has been set verifying Neumann condition:

$$\frac{2D_p \Delta t}{\Delta x^2} \ll 1 \quad (4)$$

were D_p is the diffusivity coefficient, Δx the size of cells and Δt the time step. Before performing the 6-month simulation, water and mortar have been equilibrated separately.

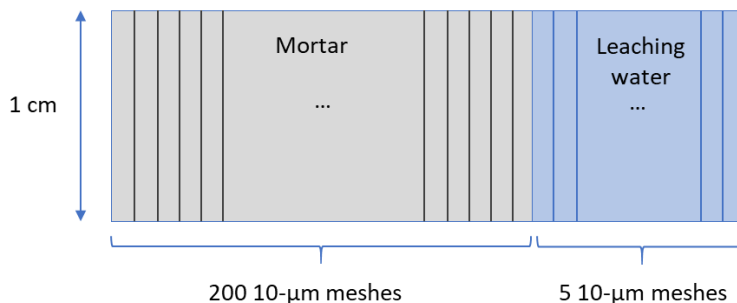


Fig. 1 General scheme of mesh used for the leaching simulation.

2.2 Mortar

Realistic chemical composition of poral solution (Table 1) and mineralogic composition of the solid part (Table 2) have been chosen, considering a water to cement ratio equal to 0.6. Tortosity was set to 0.0184 according to the equation: $D_e = \tau \times \phi \times D_{j,w}$ were ϕ is the porosity (0.1), D_e the effective diffusion coefficient ($1.84 \times 10^{-12} \text{ m}^2\cdot\text{s}^{-1}$) and $D_{j,w}$ the diffusivity coefficient in water ($1 \times 10^{-9} \text{ m}^2\cdot\text{s}^{-1}$). Precipitated minerals are calcite and ettringite (Table 2).

Table 1 Chemical characteristics of concrete poral solution.

Primary species	Molar concentration (mmol.l ⁻¹)
Ca ²⁺	1.548
pH	10
HCO ₃ ⁻	0.0
Al ³⁺	0.6587
K ⁺	182.5
Mg ²⁺	0.3345 × 10 ⁻⁵
Na ⁺	118.4
SO ₄ ²⁻	0.4447 × 10 ⁻¹
Cl ⁻	0.1 × 10 ⁻¹⁶

Table 2 Mineralogic composition of the reactive mortar portion.

Mineral	Volumic proportion
Calcite	0.0
Ettringite	0.0039
Monosulfoaluminate	0.0266
Portlandite	0.0646
C-S-H 1.6	0.1170

2.3 Leaching water

Four environmental waters were simulated from an unmineralized water (UW) to a mineral one (MW), by adding carbonate and calcium ions step by step. It is noteworthy that MW is a weakly mineralized natural water. Weakly mineralized waters often lead to chemical damage on concrete structures. Laboratory tests are generally performed with unmineralized water, hence the need to understand the influence of actual water composition.

Table 3 Chemical characteristics of leaching waters.

Primary species	Molar concentration (mol.l ⁻¹)			
	UW	Carb1	Carb1ca1	MW
Ca ²⁺	0.0	0.0	3.0 × 10 ⁻⁴	3.0 × 10⁻⁴
pH	7.0	7.0	7.0	7.0
HCO ₃ ⁻	0.0	1.2 × 10⁻³	1.2 × 10⁻³	1.2 × 10⁻³
Al ³⁺	0.0	0.0	0.0	0.0
K ⁺	0.0	0.0	0.0	1.5E-04
Mg ²⁺	0.0	0.0	0.0	3.3E-04
Na ⁺	0.0	0.0	0.0	5.2E-04
SO ₄ ²⁻	0.0	0.0	0.0	9.0E-05
Cl ⁻	0.0	0.0	0.0	4.2E-04

3 Results and discussions

3.1 Unmineralized water

In this study, a mortar is exposed to unmineralized water. Ionic concentrations, mineral proportions and porosity are plotted as a function of sample depth (Fig. 2). The sample can be divided into five zones. In zone 5, ionic concentrations, mineral proportions and porosity are unaffected, from 0.34 mm depth for a 6-month simulation. Then portlandite is dissolved progressively, increasing the sample porosity (zone 4). When portlandite is totally dissolved, monosulfoaluminates starts dissolving and ettringite is created (zone 3). Porosity is still increasing but with a smooth rope. When monosulfoaluminates are totally dissolved, the creation of ettringite follows a great increase and the mortar

sample gets denser (zone 2), until ettringite has filled the porosity at about 0.06 mm depth (zone 1). No calcite is created at the surface, because of the lack of carbonate ions in leaching water. The evolution of C-S-H cannot be quantified in this model, because their dissolution is not reproduced in a realistic manner by the thermodynamic database, which does not include intermediary states of C-S-H by decreasing progressively the proportion of calcium [6].

This attack has been studied experimentally by Planel et al., 2006 on a mortar with a water-to-cement ratio of 0.4. They used XRD analysis in order to obtain the profile of phase assemblage after a 12-week immersion in pure deionized water. They could also detect the formation of AFt from 0.4 to 1.5 mm depth. Contrary to our simulation, no ettringite is created at the very edge of the mortar sample. The main other difference is that ettringite starts to be created when portlandite is not totally dissolved yet. Barcelo et al. [8] have also modelled leaching with unmineralized water. They could also observe precipitation of AFt where AFm is dissolving. They noticed ettringite precipitation is only possible in the presence of supplementary calcium ions in the pore solution. Contrary to our results, they obtained dissolution of both portlandite and monosulfoaluminates at the same place.

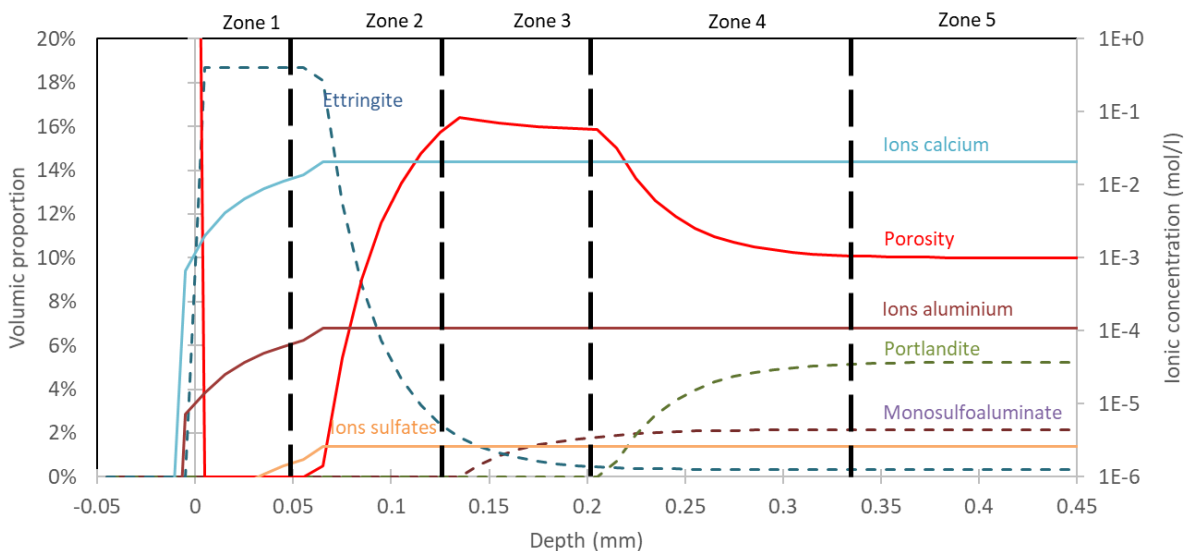


Fig. 2 Relative volumic quantities of solid species and ionic concentrations determined by the model after six months of simulated pure water leaching.

3.2 Mineralized water

3.2.1 Minerals and ions evolutions

The initial model has been adapted with natural mineralized water (MW) and with two artificial waters, in order to understand the differences between UW and MW. Carb1 contains carbonate ions and Carb1ca1 has both carbonate and calcium ions. Fig. 3 shows the amount of minerals formed at the end of 6-month simulation. Fig. 3a and 3b deal with dissolved minerals and Fig. 3c and 3d with precipitated minerals. Fig. 3e represents the global sum of minerals and give a clue to the porosity evolution. When carbonates are added to unmineralized water, the main phenomenon is the precipitation of calcite, due to the reaction with the carbonate ions of the leaching water and the calcium ions from the dissolution of portlandite and monosulfoaluminates. Both are more dissolved when carbonates are added, probably due to the precipitation of calcite. Calcium ions are consumed, and the reaction quotients stay below the equilibria constants, so that the amount of minerals dissolved is increased.

Carb1ca1 is an artificial water created from unmineralized water with the same amount of carbonate ions as Carb1 and MW and the same amount of calcium ions as MW. It creates a relatively high amount of calcite, probably due to the initial availability of calcium ions, and a significant dissolution of portlandite. Here again, the creation of calcite seems to be linked to the dissolution of portlandite. Less ettringite is formed, probably due to the huge creation of calcite.

Natural mineralized water (MW) has also been modelled. Results are close to Carb1, except for the amount of ettringite created, which is higher for MW. It can be observed that the presence of other ions reduces the impact of calcium ions, especially on their ability to create calcite, and thus to dissolve portlandite. The main difference is the presence of other ions like sodium, potassium and mag-

nesium. It can be assumed that studied mineral phases have a coupled stability and these ions influence their solubility.

The relative sum has been given in Fig. 3e. Contrary to what can be seen in experimental studies [9], UW does not present a volume loss, even if this is close to zero. It can be due to the modelled leaching conditions. In this study, no flow is applied on the leaching solution, which could foster the precipitation of ettringite at the edge of modelled mortar sample. Nevertheless it can be observed still that mineralized water has a greater amount of minerals created than UW.

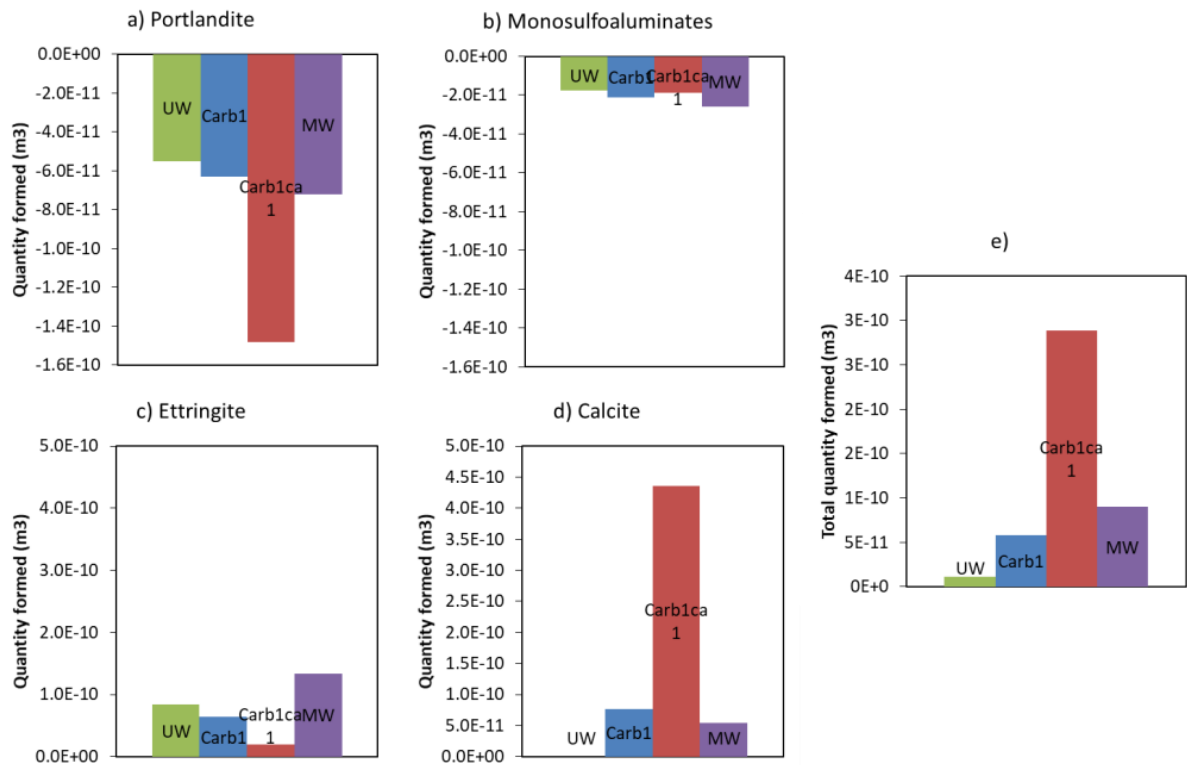


Fig. 3 Quantity of mineral formed at the end of 6-month simulation of leaching as a function of the leaching water. a) Portlandite. b) Monosulfoaluminates. c) Ettringite. d) Calcite. e) Total of dissolved and precipitated minerals.

Ionic concentrations, mineral proportions and porosity are plotted against depth (Fig. 4). The graph can be separated in five zones, as that obtained with unmineralized water (Fig. 2). No evolution occurs in the inner part of the modelled mortar sample (zone 5). Zone 4 and zone 3 are quite like Fig. 2: dissolution of portlandite and monosulfoaluminates respectively. Calcite and ettringite are created in zone 2, until porosity is filled (zone 1). The evolution of porosity is close to unmineralized water: a dense layer at the edge of the sample (zone 1), followed by a porous layer (zone 3) and a zone with initial porosity (zone 5, the heart).

It can be observed that calcite and ettringite start being created when portlandite is totally dissolved, but their precipitation increases when monosulfoaluminates have been totally dissolved. Badouix [10] has observed the same evolution of porosity when studying experimentally a Portland cement paste after seven months in a solution of NaHCO_3^- with a Scanning Electron Microscopy. They explained the dense zone at the edge of the sample by the formation of calcite.

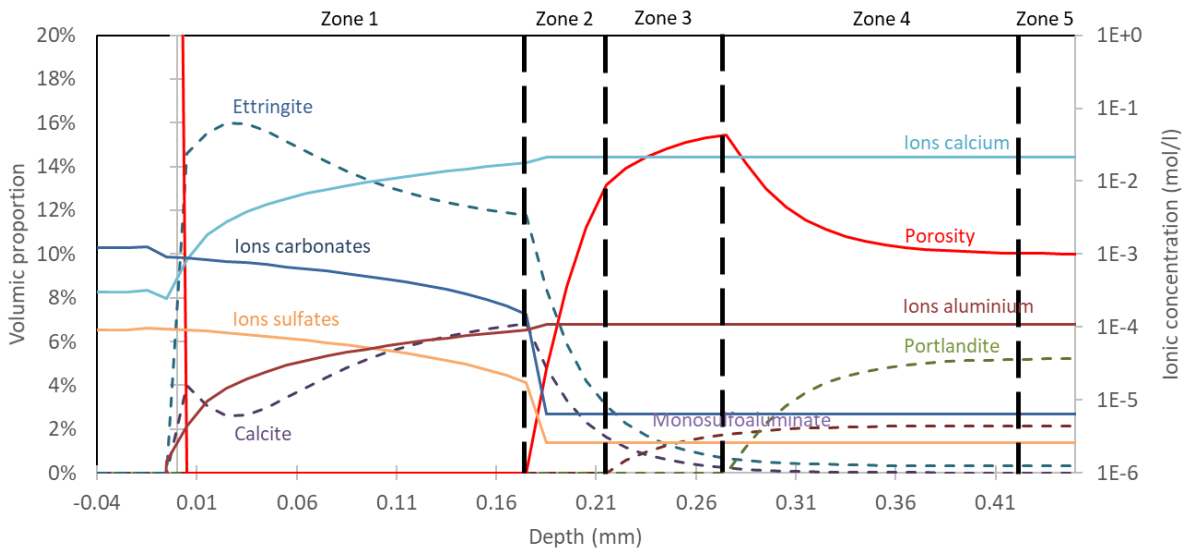


Fig. 4 Relative volumic quantities of solid species and ionic concentration vs depth of the materials determined by the model after six months of simulated natural mineralized water (MW) leaching.

Particular attention is paid to the volume occupied by the dissolved minerals, directly linked with the increase in porosity. Dissolved portlandite to dissolved monosulfoaluminates volumic ratio is given as a function of the leaching solution in Fig. 5a. The ratios are approximately the same whatever the solution. It shows the dissolution of portlandite is responsible for a greater increase of porosity. It is especially the case for unmineralized water, where dissolved portlandite volume is three times dissolved monosulfoaluminates volume. It was underlined by [11] when studying leaching by nitrate ammonium solution experimentally. They they also stated that portlandite dissolution is responsible for the commonly reported strength decrease. The volumic ratio of dissolved portlandite to dissolved monosulfoaluminates is lower when carbonates ions are added to the leaching solution (Carb1 vs UW), and it is also lower for natural mineralized water (MW).

During leaching, dissolution of minerals happens as deterioration fronts. Portlandite is dissolved before monosulfoaluminates and so the layer where portlandite is totally dissolved is deeper than this of monosulfoaluminates. Deteriorated thicknesses are given in Fig. 5b depending on the mineral considered. Portlandite is always totally dissolved at higher depths than monosulfoaluminates. The latter are never totally dissolved when the leaching solution is the artificial solution Carb1ca1. The dissolution depths of Carb1 are lower than unmineralized water whereas the amount of minerals dissolved is slightly higher with Carb1 than UW (Fig. 3): the depth difference between the start of dissolution and the total dissolution is lower is Carb1. Deterioration fronts are deeper for MW, which is in accordance with the amount of minerals dissolved (Fig. 3).

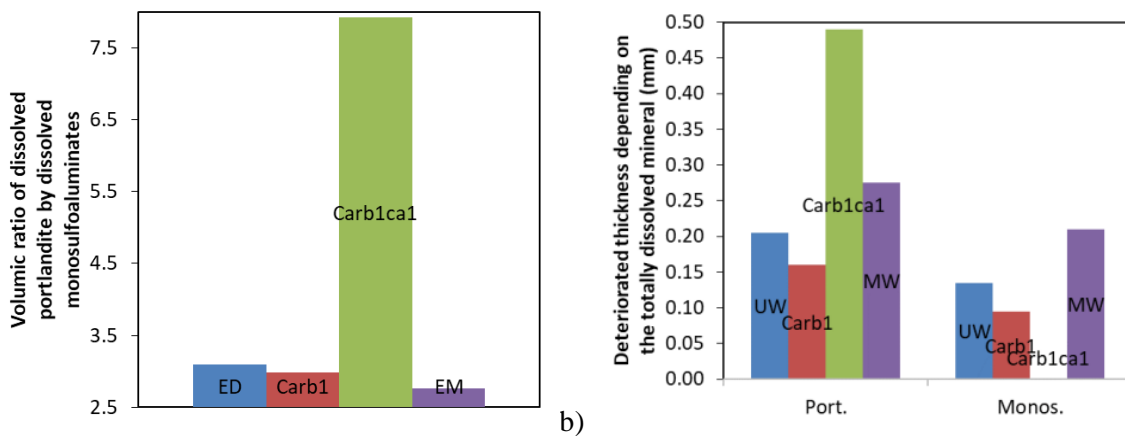


Fig. 5 Dissolved portlandite to dissolved monosulfoaluminates volumic ratio as a function of the leaching solution after a 6-month simulation (a). Dissolution front of totally dissolved minerals (portlandite and monosulfoaluminates) (b).

3.2.2 Cumulated variations of calcium ions

It can be observed that every mineral at stake in this chemical attack involve the release or consumption of calcium ions [12]. Calcium ions consumed due to dissolution / precipitation phenomena are calculated and given in Fig. 6. The relative sum of variations of calcium due to every phenomenon is an indicator particularly interesting because it can be monitored experimentally by following the calcium concentration in the leaching solution. The final ranking is in good agreement with variation of volume (Fig. 7): UW results is higher dissolution than precipitation, thus the indicator underlines the greater leaching of all tested waters in this study. This indicator underlines that dissolutions and precipitations phenomena tend to compensate in the case of Carb1 and MW. Carb1ca1 undergo a great consumption of calcium ions, due to the creation of calcite, which is indeed the main phenomenon in stake in Fig. 3. The graph (Fig. 6) underlines that the dissolution of monosulfoaluminates cannot be estimated when monitoring the consumption of calcium ions and ettringite has a limited impact. The main phenomena are the dissolution of portlandite and precipitation of calcite.

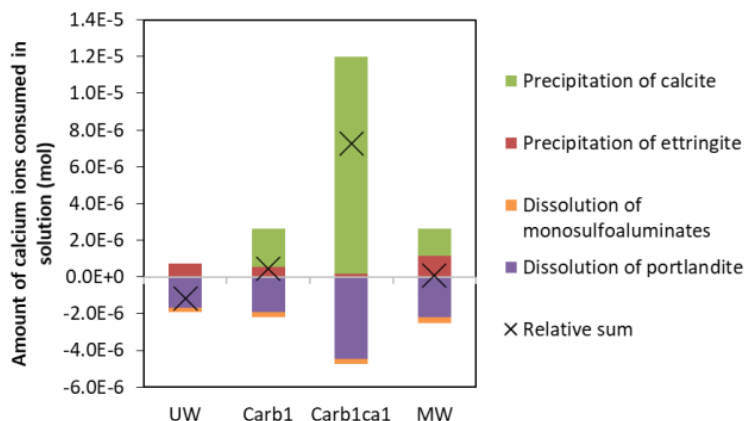


Fig. 6 Amount of calcium released after six-month modelled leaching depending on the dissolution / precipitation phenomena and the leaching solution.

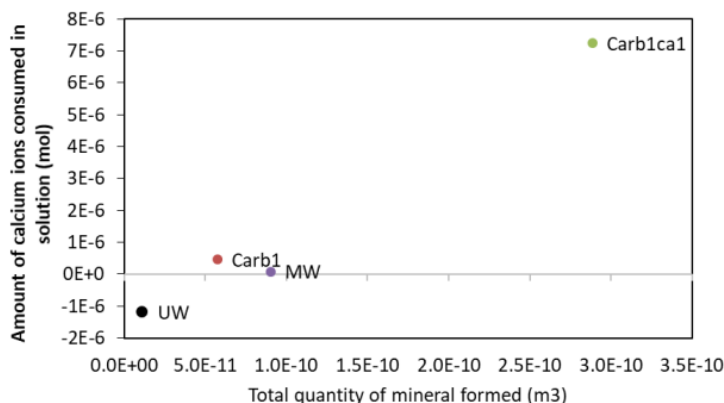


Fig. 7 Amount of calcium released after six-month modelled leaching and total volume of mineral formed.

4 Conclusion

The main purpose of this paper was to contribute to the understanding of the leaching mechanisms. The authors' attention was focused on the influence of the presence of calcium and carbonate ions and the main ions present in natural water. A simulation has been made thanks to a geochemical model, allowing a description of chemical phenomena taking place during the leaching of Portland cement-based mortar. The analysis is focused on quantities of dissolved ions and solid phases evolving during the attack, their coexistence in space and time.

From the outcome of our investigation it is possible to conclude that calcite and ettringite precipitations are due to portlandite dissolution, but they increase as monosulfoaluminates have been totally

dissolved, and thus calcite never coexists with portlandite, whereas monosulfoaluminates are still present when calcite and ettringite precipitations happen.

The new indicator, defined as the total amount of calcium consumed in solution, is discussed, based on the finding that every mineral at stake in this chemical attack involve releasing or consuming calcium ions. It leads to additional information in comparison to volume variations. This result could help designing performance tests and indicators.

The findings suggest in this paper could be useful clarifying the water parameters to consider designing concrete structures in their environment. Moreover, the performance-based approach requires indicators that are representative for the deterioration. Understanding the phenomena and the influence of the chemical composition of the leaching water will help provide relevant indicators. The next stage of our research will be to investigate if the calcium concentration can be one, by doing experimental leaching tests.

References

- [1] AFNOR, *NF EN 206-1 CN Spécification, performance, production et conformité — Complément national à la norme*. 2012.
- [2] E. Rozière, A. Loukili, and F. Cussigh, “A performance based approach for durability of concrete exposed to carbonation,” *Constr. Build. Mater.*, vol. 23, no. 1, pp. 190–199, 2009.
- [3] T. Xu, N. Spycher, and E. Sonnenthal, “TOUGHREACT User’s Guide: A Simulation Program for Non-isothermal Multiphase Reactive Transport in Variably Saturated Geologic Media, version 2.0,” *Lawrence Berkeley ...*, no. October, pp. 1–5, 2012.
- [4] A. Soive and V. Q. Tran, “External sulfate attack of cementitious materials: New insights gained through numerical modeling including dissolution/precipitation kinetics and surface complexation,” *Cem. Concr. Compos.*, vol. 83, pp. 263–272, 2017.
- [5] G. Massaad, “Stratégie performantielle d’évaluation de la résistance des matériaux cimentaires à l’attaque sulfatique externe, thèse de doctorat,” Ecole Centrale de Nantes, 2016.
- [6] B. Hilloulin, “Méthodes avancées et analyses multi-échelles pour l’étude de l’auto-cicatrisation des fissures dans les matériaux cimentaires, thèse de doctorat,” Ecole Centrale de Nantes, 2015.
- [7] D. Planel, J. Sercombe, P. Le Bescop, F. Adenot, and J. M. Torrenti, “Long-term performance of cement paste during combined calcium leaching-sulfate attack: Kinetics and size effect,” *Cem. Concr. Res.*, vol. 36, no. 1, pp. 137–143, 2006.
- [8] L. Barcelo, M. Moranville, and B. Clavaud, “Autogenous shrinkage of concrete: A balance between autogenous swelling and self-desiccation,” *Cem. Concr. Res.*, vol. 35, no. 1, pp. 177–183, 2005.
- [9] A. Cherki El Idrissi, E. Rozière, S. Darson-Balleur, and A. Loukili, “Resistance of alkali-activated grouts to acid leaching,” *Constr. Build. Mater.*, vol. 228, p. 116681, Dec. 2019.
- [10] F. Badouix, “Modélisation de l’altération à long terme des bétons : prise en compte de la carbonatation, thèse de doctorat,” ENS Cachan, 2000.
- [11] C. Carde and R. François, “Effect of the leaching of calcium hydroxide from cement paste on mechanical and physical properties,” *Cem. Concr. Res.*, vol. 27, no. 4, pp. 539–550, 1997.
- [12] T. Matschei, B. Lothenbach, and F. P. Glasser, “Thermodynamic properties of Portland cement hydrates in the system CaO-Al₂O₃-SiO₂-CaSO₄-CaCO₃-H₂O,” *Cem. Concr. Res.*, vol. 37, no. 10, pp. 1379–1410, 2007.

Numerical Modelling for Reactive Transport due to the Water-dependent Activities within Building Materials

Qing Xiang Xiong, Fekri Meftah

*Laboratoire Génie Civil et Génie Mécanique (LGCGM),
Institut National Des Sciences Appliquées Rennes,
20 avenue des Buttes de Cœsmes, Rennes(35700), France*

Abstract

Reactive transport is a critical issue in building materials because it is closely related to the durability of building materials, especially for the porous material with functional connectivity. When building material exposes to the aggressive environment during its service life, the microstructure will be altered because of water-dependent activities, such as salt precipitation/dissolution. This paper establishes a mathematical model for transport problems and chemical reactions intended to characterize the process of precipitation/dissolution in the porous medium. The main algorithm is implemented by the sequential iterative approach (SIA), which is based on two sets of equations. The transport problems are described by a set of partial differential equations based on mass conservation, and the chemical processes, under the assumption of equilibrium, are represented by a set of nonlinear algebraic equations based on the law of mass action.

To simplify the problem, this paper focuses on a material perspective of the porous medium, i.e., the development computes the chemical species and water as a function of time only. By adopting our model, transport properties such as ionic concentration and mass of chemical components were implemented. The porosity and the water saturation degree were also considered and examined in our work. Finally, the convergence rate of this numerical model was discussed based on two simulated cases. Such a method could be used as the extra reference when controlling experimental conditions is difficult, in refining the durability-related issues, such as salt intrusion and water transport.

1 Introduction

The durability analysis of porous medium, especially cement-based material requires modeling tools that can consider both the transport of moisture that contains dissolved species and chemical reactions. Therefore, the development of transport models that govern the partitioning of chemical species between aqueous and solid phases is fundamental to an understanding of processes such as salt precipitation/dissolution. The transport of moisture and dissolved chemical species through aqueous inside a porous medium is of interest to a variety of research. In recent decades, a large number of reactive transport models have been devised to provide this capability. In 1989, G.T Yeh et al. evaluated and discussed three models (the mixed differential and algebraic equation approach, the direct substitution approach, and the sequential iterative approach) for simulating the hydrogeochemical transport problems described by partial differential equations and nonlinear algebraic equations. It had been found that the use of the sequential iterative approach (SIA) models lead to the fewest constraints on computer resources in terms of CPU time and memory, which was recommended for the practicality and flexibility [1]. Valocchi et al. (1992) and Kaluarachchi et al. (1995) worked on another model-operator splitting approach for the numerical solution of advection-dispersion-reaction problems, especially the accuracy of this method were described [2], [3]. In 1994, Walter et al. developed a numerical model (MINTRAN) for the simulation of groundwater transport of multiple reacting chemical substances governed by the equilibrium equations of thermodynamics [4]. In 2000, E.Samson et al. reviewed and discussed various algorithms to model the effects of chemical reactions on ionic transport mechanisms in porous media [5]. Samson even considered the electro-chemical potential between different ions or the effect of temperature on the diffusion of ions [6], [7]. However, the most presented algebraic equation set is a general simulated model accommodating simultaneous reactions of adsorption, redox, complexation, ions exchange, acid based reactions, and precipitation/dissolution. Besides, equations for the description of models are functions of both time and position, which make the computer program a complex one, and some unexpected problems have emerged herein, for instance, the inherent error introduced by the operator splitting method.

In this paper, we mainly focus on the specific problem of precipitation/dissolution reaction. By adopting the sequential iterative approach (SIA), we will work out a computing method for solving transport problems, especially describing local chemical reactions (precipitation and dissolution). Then we take the sodium chloride as an example, the water transfer process, the ionic concentration variation, as well as the water saturation degree, will be implemented by our iterative procedure. Finally, a brief comment on our method will be given to the purpose of further improvement.

2 Coupling chemical reaction to water and ionic transport in an unsaturated porous media

A porous material consists of the following three phases. The solid phase is the composition of the solid matrix and precipitated salt. The aqueous solution is consisting of pure water (which is also the so-called solvent) and ionic species (which is also the so-called solute). The voids in the solid skeleton are filled partly with an aqueous solution and partly with a gaseous phase comprising dry air and water vapor.

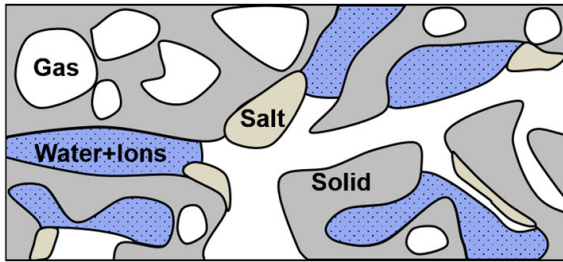


Fig. 1 Schematic of multi-components within the porous material.

In this given porous medium, the temperature and pressure are taken as constants. The liquid phase and solid phase are in an equilibrium state at the beginning. When the aqueous solution is disturbed, an amount of one or more chemical species will dissolve or precipitate to reach the new equilibrium state. Note that the gaseous phase, occupying a portion of the porous space, can be neglected in our research. Because according to the research by Marsily in 1986, for unsaturated porous material (salt dissolved aqueous), using the mobile air phase approach does not give results significantly different from the immobile approach, except for very special cases [8]. All the components in our system were described in molarity and molality units.

2.1 Transport Equations

Based on the mass conservation equation, water flow in the unsaturated porous medium can be written as

$$\frac{\partial m_w}{\partial t} + \text{div}(m_w \mathbf{v}_{w-s}) = 0 \quad (1)$$

where m_w is the relative mass of water which is denoted as $m_w = \rho_w S_w \phi$, \mathbf{v}_{w-s} is the velocity of water flow relative to the solid phase which can be determined by Darcy's law for multi-phase flow, ρ_w is the density of water, ϕ is the porosity for representing porous medium, and S_w is the water saturation degree (SD).

By substituting the expression of m_w into equation (1), one can get

$$\rho_w \phi \frac{\partial S_w}{\partial t} + \rho_w S_w \frac{\partial \phi}{\partial t} + Q_w = 0 \quad (2)$$

where $Q_w = \text{div}(m_w \mathbf{v}_{w-s})$ is the term of water flux.

At the same time, the transport equation for aqueous (dissolved) species based on mass conservation is given by:

$$\frac{\partial m_j}{\partial t} + \text{div}(m_j \mathbf{v}_{j-w}) + \text{div}(m_j \mathbf{v}_{w-s}) = 0 \quad (3)$$

where m_j is the relative mass of the j th aqueous species which is expressed as $m_j = c_j M_j S_w \phi$, \mathbf{v}_{j-w} is the velocity of the j th aqueous species relative to water that can be calculated by Darcy's law, c_j is the

concentration of the j th chemical species in the aqueous solution and M_j is the molar mass of the j th aqueous species.

Equation (3) can be rewritten as follows:

$$M_j \phi S_w \frac{\partial c_j}{\partial t} + c_j M_j \phi \frac{\partial S_w}{\partial t} + c_j M_j S_w \frac{\partial \phi}{\partial t} + Q_c = 0 \quad (4)$$

where $Q_c = \text{div}(m_j \mathbf{v}_{j-w}) + \text{div}(m_j \mathbf{v}_{w-s})$ represents the diffusion of the aqueous species.

The evolution equation for porosity in the process of precipitation/dissolution is given by

$$\frac{\partial \phi}{\partial t} = - \frac{\partial \phi_{salt}}{\partial t} \quad (5)$$

and ϕ_{salt} is expressed as

$$\phi_{salt} = -\omega_{salt}(c_{salt}^0 - c_{salt}) \quad (6)$$

where ω_{salt} is the molar volume of precipitated salt, c_{salt}^0 is the initial content of precipitated salt and c_{salt} is the content of precipitated salt.

By substituting equation (6) into equation (5), we have

$$\frac{\partial \phi}{\partial t} = -\omega_{salt} \frac{\partial c_{salt}}{\partial t} \quad (7)$$

2.2 Chemical reactions (Precipitation/dissolution)

Now let us propose that in the representing system of precipitation/dissolution there is a subset of N_x aqueous species as basis species, which are so-called components, primary species or ionic species. We also assume a subset of M_p precipitated species, which is also called as the secondary species. The number of secondary species is exactly equal to the number of reactions. The precipitated species can be represented as linear combinations of ionic species such as

$$\sum_{j=1}^{N_x} a_{ij} x_j \rightleftharpoons p_i \quad i = 1, 2, \dots, M_p \quad (8)$$

where a_{ij} is the stoichiometric coefficient of the j th aqueous component in the i th precipitated species; x_j is the j th aqueous component with $j = \overline{1, N_x}$; p_i is the i th precipitated species with $i = \overline{1, M_p}$.

The precipitation/dissolution of solid-phase are the chemical reactions that are described by a set of nonlinear algebraic equations under local equilibrium condition is governed by the following expression based on the law of mass action [9]:

$$\alpha_i \prod_{j=1}^{N_x} (c_j)^{a_{ij}} = 1 \quad i = 1, 2, \dots, M_p \quad (9)$$

where c_j is the concentration of the j th aqueous species ($mmol/l$) and α_i is the stability constant of the i th precipitated species which can be expressed as

$$\alpha_i = K_i \prod_{j=1}^{N_x} (\gamma_j)^{a_{ij}} \quad (10)$$

where K_i is the thermodynamic equilibrium constant of the i th precipitated species, which can be obtained according to equation (9). The chemical activity coefficient of the j th aqueous component species (a dimensionless quantity) is denoted as γ_j , which is related to the ionic strength of all aqueous species. In a very dilute solution, which is called as an ideal solution, the activity coefficients of aqueous species γ_j are equal to one. However, as the ionic concentration increases, the activity coefficient will significantly deviate from one. In this paper, the activity coefficient is calculated by Davies equation [10].

Note that equation (9) does not contain the concentration of precipitated species p_i because the activity of pure solid is considered one, which leads to significantly different from the models handling other types of chemical reactions, for instance, the complexation and sorption problems [9].

Furthermore, equation (9) can be extended to equation (11) by giving more details:

$$\alpha_i \prod_{j=1}^{N_x} \left(c_j^0 - \sum_{k=1}^{M_p} \alpha_{kj} \Delta c_{s-l,k} \right)^{a_{ij}} - 1 = 0 \quad i = 1, 2, \dots, M_p \quad (11)$$

where c_j^0 is the initial concentration ($mmol/l$) of the j th aqueous component species obtained from field measurements and $\Delta c_{s-l,k}$ is the increased concentration ($mmol/l$) (which is relative to the liquid in the porous medium) of the i th precipitated species p_i which can be obtained by solving equation (11).

3 Numerical solution

The coupled equations of reactive transport and chemical reactions will be implemented by the sequential iterative approach (SIA), which solves first the transport equations and then the chemical reactions [1], [4]. The sequential manner will follow an iterative procedure, repeating several times until convergence is attained.

For the iterative procedure, each time step Δt is defined as

$$\Delta t = t^{k+1} - t^k \quad (12)$$

in which k is the iteration number of transport and chemical reactions.

Thus, the porosity of each time step is computed as equation (13) by considering equation (7) and (12):

$$\phi^{t^{k+1}} = \phi_0 - \phi_{salt}^{t^{k+1}} \quad (13)$$

3.1 Solution of transport equations

Our model applies to problems of one-dimensional transport coupled with the chemical reaction of precipitation/dissolution. For simplicity, our numerical formulation for solving the transport equations (2) and (4) here is presented by two different cases based on some assumptions.

Case one where no chemical species diffusion is present. The porosity is constant; ignore the diffusion term of chemical species Q_c ($mmol/l.s$) and keep the term of water flux Q_w ($Kg/m^3.s$) as constant for each time step.

Then we could obtain the increment of water saturation degree at each time-lag Δt :

$$\Delta S_l^{t^{k+1}} = S_l^{t^{k+1}} - S_l^{t^k} = -\frac{Q_l}{\rho_l \phi^{t^{k+1}}} \Delta t \quad (14)$$

The increment of concentration for each ionic species at each time-lag Δt :

$$\Delta c_j^{t^{k+1}} = c_j^{t^{k+1}} - c_j^{t^k} = \frac{\Delta S_l^{t^{k+1}} c_j^{t^k}}{S_l^{t^{k+1}}} \quad (15)$$

We can formalize the iteration system by writing in time step form as follows:

$$S_l^{t^{k+1}} = -\frac{Q_l}{\rho_l \phi^{t^{k+1}}} \Delta t + S_l^{t^k} \quad (16)$$

and

$$c_j^{t^{k+1}} = \frac{S_l^{t^k} c_j^{t^k}}{S_l^{t^{k+1}}} \quad (17)$$

Case two where no water flux is present. Keep the diffusion term of chemical species Q_c ($mmol/l.s$) as constant and omit the water flux Q_w ($Kg/m^3.s$) in each iterative step.

Thus, we could obtain the increment of water saturation degree at each time-lag Δt :

$$\Delta S_l^{t^{k+1}} = S_l^{t^{k+1}} - S_l^{t^k} = -\frac{S_l^{t^k} \Delta \phi^{t^{k+1}}}{\phi^{t^{k+1}}} \quad (18)$$

The increment of concentration for each ionic species at each time step Δt :

$$\Delta c_j^{t^{k+1}} = c_j^{t^{k+1}} - c_j^{t^k} = -\frac{Q_c}{V \phi S_l^{t^{k+1}}} \Delta t \quad (19)$$

Finally, the equations for sequential solution are giving by

$$S_l^{t^{k+1}} = \frac{S_l^{t^k} \phi^{t^k}}{\phi^{t^{k+1}}} \quad (20)$$

and

$$c_j^{t^{k+1}} = -\frac{Q_c}{V \phi^{t^{k+1}} S_l^{t^{k+1}}} \Delta t + c_j^{t^k} \quad (21)$$

3.2 Solution of chemical reactions

The set of non-linear chemical reactions indicated in equation (9) is solved by the Newton-Rapson method. As is shown in equation (11), the initial concentration c_j^0 (at the beginning of the chemical reactions) is an input. Thus, the increased concentration of the secondary species or precipitated species $\Delta c_{s-l,k}$ is the essence to figure out, which are lumped into a vector of unknowns, \mathbf{X}_i ($i = 1, 2, \dots, M_p$). As we have M_p equations and M_p unknowns, then the unknowns can be updated as follows:

$$\mathbf{X}_i^{n+1} = \mathbf{X}_i^n + \Delta \mathbf{X}_i^n \quad (n = 0, 1, 2, \dots) \quad (22)$$

where n is the iteration number and $\Delta \mathbf{X}_i^n$ is the increment of unknowns denoted as

$$\Delta \mathbf{X}_i^n = J^{-1}(\mathbf{X}_i^n) \mathbf{f}(\mathbf{X}_i^n) \quad (23)$$

where J is the Jacobian matrix and $\mathbf{f}(\mathbf{X}_i^n)$ is the vector of residuals. The iteration will repeat until convergence is attained. In our research, the convergence criterion is that the L2-norm of $\Delta \mathbf{X}_i^n$ satisfied a specified tolerance, which is expressed as

$$\|\Delta \mathbf{X}_i^n\| \leq \text{err} \quad (24)$$

Once the increased concentrations of the secondary species are obtained, all of the aqueous species can be computed as follows:

$$c_j = c_j^0 - \sum_{i=1}^{M_p} \alpha_{ij} \Delta c_{s-l,i} \quad i = 1, 2, \dots, M_p \quad (25)$$

4 Numerical implementation

The model deals with the one-dimensional transport coupling with reactive chemical problems. Two sets of the iterative system are performed here. The first set subjects to equation (13), (16), (17) and (22), to analyze the influence of water flux on our system. The second set includes equation (13), (20), (21) and (22), to research the impact of diffusion of ionic species on our system. The numerical results for both two sets will be implemented with the time step of 1 hour. The most common chemical reaction is made as in equation (26). The Initialization of parameters of representing aqueous solution is listed in table 1.



Table 1 Initialization of parameters for representing aqueous solution.

Initialization	$C_{\text{Cl}^-} = C_{\text{Na}^+}$ [mmol/L]	Q_w [Kg/m ³ .h]	Q_c [mmol/L.h]	K_{eq}	ϕ_0	S_l
Case One	10	1	0	0.01246	0.2	0.9
Case Two	10	0	-1	0.01242	0.2	0.2

Case one-This case was carried out by considering water flux quantity while the effect of ionic diffusion was considered negligible. The parameters used in the numerical simulations were listed in table 1.

The water saturation degree (SD) proportionally decreased from 0.9 to 0 during the 180 hours (see Fig.2-a). The porosity, in this case, kept constant, which indicated only a few precipitated salts were generated that lead no significant difference to the solid volume. As shown in Fig.2-b, the mass of aqueous species decreased with the increase in the mass of precipitated salt. However, the total mass of the components remained constant despite the distribution between chemical species in both aqueous and solid phases because the mass of each chemical component was conservation in our system. The concentration of ionic species and salt increased as the SD decreasing (see Fig.2-c and Fig.2-d). This increment can be divided into two stages: the slight increase stage when SD decreased from 0.9 to 0.1 and the sharp increase stage until SD decreased to 0. It indicated that the significant chemical reaction occurred in the last period.

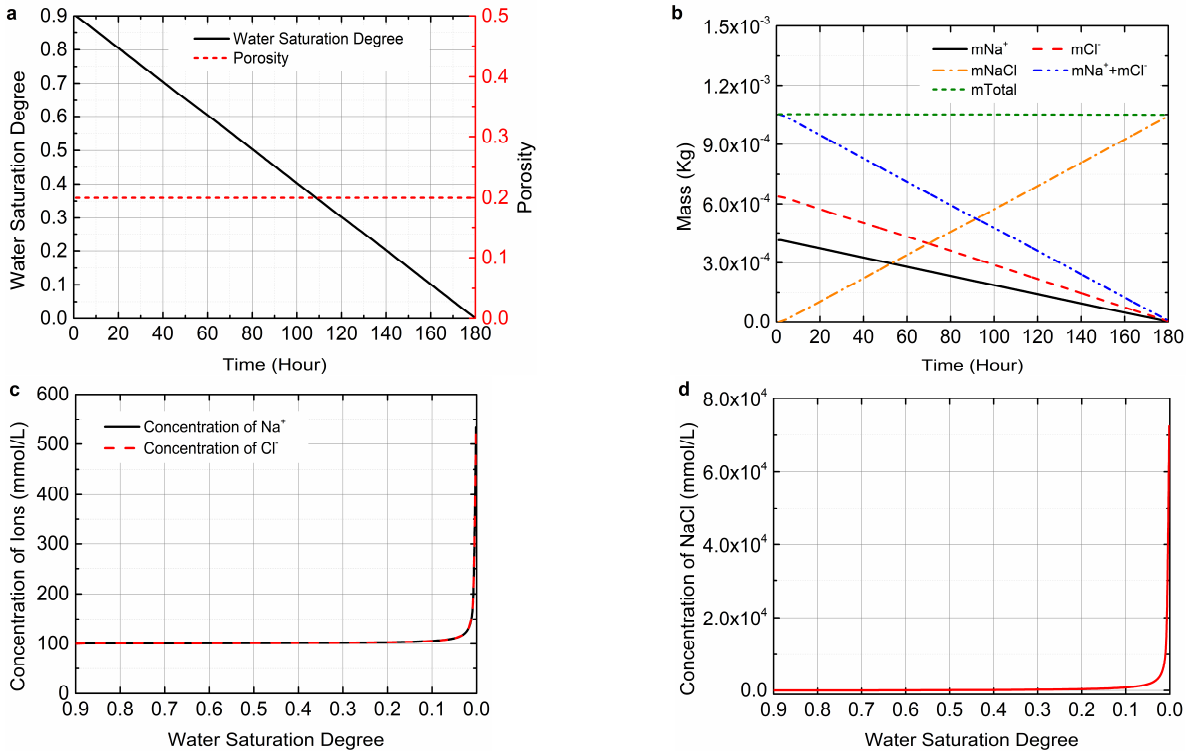


Fig. 2 Case one: **a** Water saturation degree is proportional to time; **b** Evolution of mass for each component in the reactive system; **c** Concentration of ionic species varies with water saturation degree; **d** Concentration of precipitated salt varies with water saturation degree.

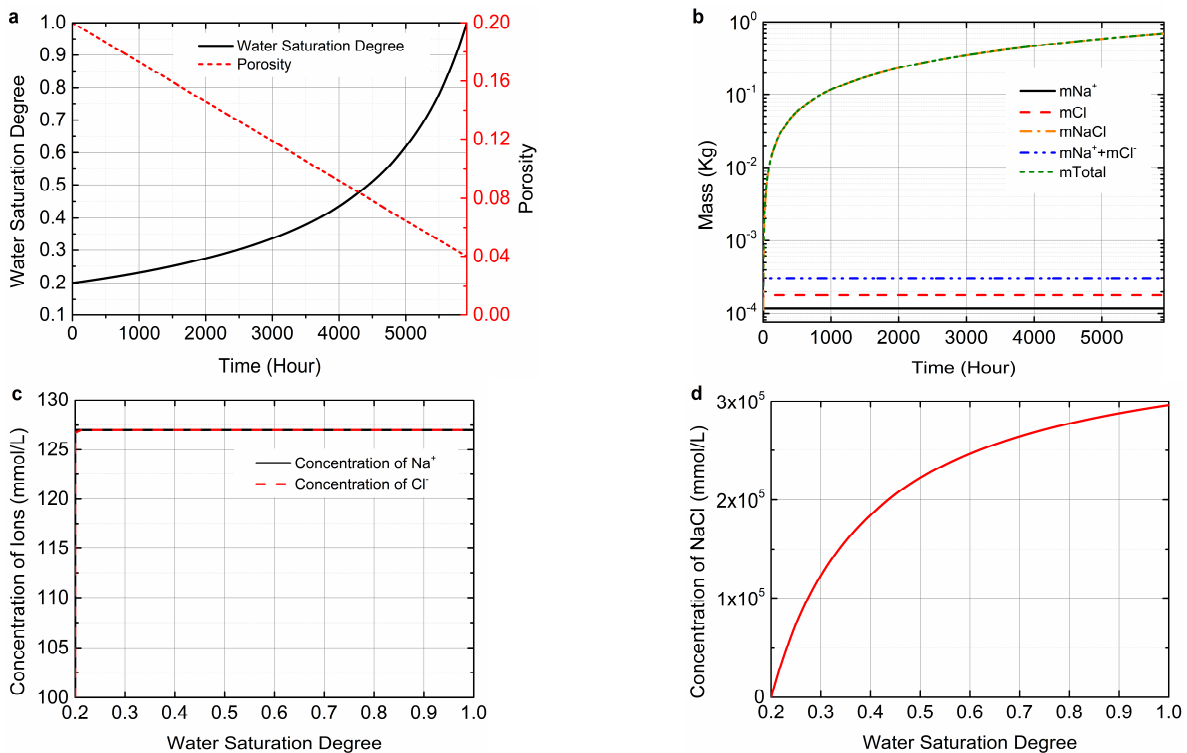


Fig. 3 Case two: **a** Water saturation degree varies with time; **b** Evolution of mass for each component in the reactive system; **c** Concentration of ionic species varies with water saturation degree; **d** Concentration of precipitated salt varies with water saturation degree.

Case two-This example gave an illustration of the controlling ionic diffusion processes while disregarding the water flux during the chemical reaction of precipitation/dissolution.

In this case, SD increased from 0.2 to 0.9 as time went by. It can be found that ionic diffusion affected the process of precipitation/dissolution by means of a pronounced increment in the mass of precipitated salt, which was over several orders of magnitude (see Fig.3-b). Simultaneously, the concentration of ionic species and precipitated salt were in a manner different from that for the case one (see Fig.3-c). Initially, the concentration of aqueous species increased to 126 (mmol/l) when SD was about 0.2, then it kept constant controlling by equilibrium. In contrast to case one for which the concentration of salt displayed variations that are more subdued, it increased over several orders of magnitude in case two, leading to more precipitated solids accumulate in the reactive system. Note that the increment of ionic concentration and precipitated mass were remarkable at the beginning period, then they kept stable, which revealed that the chemical reactions dominantly occurred at the beginning.

By comparing these two cases, we can find that the ionic transport influenced much salt precipitation than water transport. Besides, the water saturation degree also affected the transport and chemical reaction. It can be observed from Fig.2-c and Fig.2-d, during the process of the water saturation degree reduction, the concentration of components species and precipitated species did not change too much, causing a little bit of precipitated solid occurred in the system. While in case two (see Fig.3-c and Fig.3-d), as SD increasing, the ionic transport and chemical reactions were apparent. As a result, a considerable quantity of precipitated salt accumulated within the porous material. The computed results are consistent with most practical cases. The water saturation degree is a significant indicator of the moisture content, which affects the transport properties in the porous material. The augmentation of moisture content implies the better connectivity of water-filled path available for the transport of chemical species [11], [12]. Note that in our implemented examples, SD can be simulated as low as zero. However, it cannot be realized in reality because the certain moisture content is strongly absorbed on the pore surface and can no longer be depleted anymore.

Table 2 Comparison of CPU time required in case one and case two.

Case One				Case Two			
Q_w [Kg/ $m^3 \cdot s$]	Q_c [mmol/ l. s]	T(day)	CPU time [s]	Q_w [Kg/ $m^3 \cdot s$]	Q_c [mmol/ l. s]	T(day)	CPU time [s]
1	0	7.5	3.8	0	-1	246.5	18.5
0.1	0	74.7	5.5	0	-0.1	2464.5	158.3
0.01	0	746.8	34.6	0	-0.01	24644.9	1156.4

Table 2 showed the CPU time required by the two cases. The initial concentration of ionic species was 100 mmol/l, and initial porosity was 0.2 for both of the two cases. In case one, we added an identical quantity of water Q_w into the system for each time of iteration, the water saturation degree decreased from 0.9 to zero while the porosity kept constant. The iteration procedure stopped when the water saturation degree decreased as zero. In case two, we added an identical concentration of ions Q_c into the system for each time of iteration, when the water saturation degree increased from 0.2 to 1, the iteration stopped. The reactive time and convergence rate were dominated by Q_w or Q_c . For instance, when we added 1Kg/ $m^3 \cdot s$ of water into the target system for each time iteration, the convergence rate was very fast, and the computing time was about 4 seconds. On the contrary, it required more CPU time, such as 34.6 s, when the water flux was equal to 0.01Kg/ $m^3 \cdot s$. It revealed that the convergence rate of our iterative procedure depended on the quantity of water flux Q_w and the quantity of aqueous species diffusion Q_c .

5 Discussions and concluding remarks

The model is based on the mass conservation equation and the law of mass action theory, capable of handling hydro-chemical coupled problems. Even though much effort has been devoted to modeling chemical reactions and transport problems in many literatures, most of them mainly considered complexation and adsorption reactions. Very little research has been focused on the dissolution/precipitation reactions, especially the reactions in cement-based materials. This work focused on the precipitation/dissolution research within porous materials that evolved time-dependent only. By adopting this numerical model, we could conduct a quantitative analysis of salt precipitation during the water/ionic

transport process, which provided the possibility to elucidate the mechanism of local precipitation/dissolution in the pore scale.

By comparing two cases, it can be obtained that ionic transport influenced much chemical reaction than water transport. Besides, for the system that only water transport occurred, the chemical reaction mainly took place in the last period. However, for the system that only ionic transport existed, significant chemical reactions occurred in the beginning.

The convergence rate of our iterative procedure intimately depends on the quantity of water flux Q_w and the quantity of aqueous species diffusion Q_c . More obvious of water flux and ionic diffusion, faster the convergence of SIA attained.

However, it should be noted that this model is simplified in mathematical analyses with the variation of concentration with time, not with space, which may introduce differences from practical applications. Further research should be conducted to consider time and spatial dependent transport equations.

Acknowledgements

We are grateful to the valuable comments and suggestions of all reviewers for this paper.

References

- [1] Yeh, G. T., and V. S. Tripathi. 1989. "A Critical Evaluation of Recent Developments in Hydrogeochemical Transport Models of Reactive Multichemical Components." *Water Resources Research* 25(1): 93–108.
- [2] Valocchi, Albert J., and Michael Malmstead. 1992. "Accuracy of Operator Splitting for Advection-Dispersion-Reaction Problems." *Water Resources Research* 28(5): 1471–76.
- [3] Kaluarachchi, Jagath J., and Jahangir Morshed. 1995. "Critical Assessment of the Operator-Splitting Technique in Solving the Advection-Dispersion-Reaction Equation: 1. First-Order Reaction." *Advances in Water Resources* 18(2): 89–100.
- [4] Walter, A. L. et al. 1994. "Modeling of Multicomponent Reactive Transport in Groundwater: 1. Model Development and Evaluation." *Water Resources Research* 30(11): 3137–48.
- [5] Samson, E., J. Marchand, and J. J. Beaudoin. 2000. "Modeling the Influence of Chemical Reactions on the Mechanisms of Ionic Transport in Porous Materials: An Overview." *Cement and Concrete Research* 30(12): 1895–1902.
- [6] Samson, E., J. Marchand, K. A. Snyder, and J. J. Beaudoin. 2005. "Modeling Ion and Fluid Transport in Unsaturated Cement Systems in Isothermal Conditions." *Cement and Concrete Research* 35(1): 141–53.
- [7] Samson, E., and J. Marchand. 2007. "Modeling the Effect of Temperature on Ionic Transport in Cementitious Materials." *Cement and Concrete Research* 37(3): 455–68.
- [8] De Marsily, G. 1986. *Quantitative Hydrogeology*. New York: Academic Press.
- [9] Yeh, Gour-Tsyh, and Vijay S. Tripathi. 1991. "A Model for Simulating Transport of Reactive Multispecies Components: Model Development and Demonstration." *Water Resources Research* 27(12): 3075–94.
- [10] Samson, E., G. Lemaire, J. Marchand, and J. J. Beaudoin. 1999. "Modeling Chemical Activity Effects in Strong Ionic Solutions." *Computational Materials Science* 15(3): 285–94.
- [11] Guimarães, A. T. C. et al. 2011. "Determination of Chloride Diffusivity through Partially Saturated Portland Cement Concrete by a Simplified Procedure." *Construction and Building Materials* 25(2): 785–90.
- [12] Zhang, Mingzhong, Guang Ye, and Klaas van Breugel. 2014. "Multiscale Lattice Boltzmann-Finite Element Modelling of Chloride Diffusivity in Cementitious Materials. Part II: Simulation Results and Validation." *Mechanics Research Communications* 58: 64–72.

Numerical investigations on the influence of concrete cover on bond behaviour of reinforcement in concrete after fire

Arunita Das^{1*}, Akanshu Sharma¹, Josipa Bosnjak²

¹University of Stuttgart, Institute of Construction Materials, Stuttgart, Germany

²University of Stuttgart, Materials Testing Institute, Stuttgart, Germany

Abstract

The development of proper bond between steel and concrete in a reinforced concrete structure is essential for a safe and effective transfer of stresses between them. In case of realistic concrete covers, failure of bond between reinforcement and concrete can be limited by the premature splitting of concrete cover prior to bond pull-out failure. Moreover, bond in reinforced concrete structures or structural elements are vulnerable to fire. Under ambient temperature, bond behaviour has been extensively investigated so far and guidelines for assessing the bond strength are well-established (EC2, *fib* MC2010). However, relatively fewer investigations are carried out for estimating post fire bond strength.

In this study, degradation of bond behaviour after fire (residual state) has been studied using beam-end specimens, which simulates the boundary conditions more closely to reality than conventional pull-out specimen. ISO 834-1 fire scenario is considered for the heating of the specimens. First, the numerical investigations are carried out employing 3D finite element analysis for the specimens at ambient temperature to validate the modelling approach. Then the numerical models are utilized to investigate the influence of different concrete covers on post-fire bond behaviour considering different fire exposure durations. The obtained results clearly demonstrate that with realistic concrete cover, failure of concrete is almost always governed by splitting of concrete prior to bond pull-out leading to a limitation in usable bond strength and also a rather strong degradation of bond strength with fire exposure duration takes place, particularly for short exposure durations. The results also show that considering the degradation in bond strength only as a function of temperature for assessing residual bond capacity may be rather un-conservative. The results of the numerical analysis have been verified against a few experiments.

1 Introduction

Bond between concrete and steel is very important to assess the performance of a reinforced concrete structure or structural element. Bond strength might get strongly affected strongly when a structure undergoes fire accident resulting in a drastic reduction of the structural performance. Still, the topic of residual bond behaviour in post-fire scenarios is relatively less investigated resulting in insufficient guideline to assess the state of bond capacity in a structural member after fire accident. Standards and guidelines such as EN1992-1-1 (2004)¹ and *fib* Model Code 2010², provide analytical relationships to estimate the bond capacity at room temperature considering the effects of different parameters such as concrete strength, concrete cover, bar diameter, spacing of transverse reinforcement etc. However, it is also necessary to access the post fire bond behaviour to predict the residual capacity so that the structure can be reused without demolishing if it undergoes a fire accident. Moreover, several recent incidents of industrial and residential fires, fire explosions emphasise the necessity of the same. One of the most important parameters influencing the bond capacity especially in case of bond splitting failure is the concrete cover. Also for fire design of concrete structures, concrete cover is considered to be the most relevant parameter as it strongly affects the temperature of the reinforcement. The main objective of this present study is to numerically investigate the influence of concrete cover on post fire bond behaviour. Later, a model to assess the post-fire performance of bond in residual state will be worked out by considering all parameters influencing the behaviour.

2 Literature review

Research, performed so far to investigate the behaviour of bond under fire mainly by using pull-out specimen³(RILEM), obtained pull-out bond failure. In most of the cases slow heating rate was used

upto a certain duration to obtain the desired elevated temperature within the specimens and then they were cooled down to room temperature. Residual pull-out tests were performed on them thereafter.

Morley & Royles⁴ have studied degradation of bond strength with the increase of temperature in normal concrete using confined test setup considering two different scenarios: loading during heating and no loading during heating. They have concluded that there is an insignificant difference in the degradation of bond strength between these two cases. Similar studies have been performed by several other authors i.e. Diederichs and Schneider⁵, Bingöl and Gül⁶, Lublóy & Balázs⁷. List is only exemplary and not exhaustive. Sagar⁸ investigated the effect of different parameters on the bond strength and is the first to differentiate pull-out failure and splitting failure after exposure to elevated temperatures, thus demonstrating the concept of usable bond strength.

Recently Shamseldeen et al.⁹ have conducted several experiments to investigate the bond degradation on residual state. They have performed the tests using beam-end test specimen which represents well the real boundary conditions of a flexural member. Specimens were heated slowly using a heating rate of 2°C/min upto 800°C followed by a natural cooling down to room temperature. The degradation of bond stress matches well with that of the pull-out specimen.

Numerical investigations which are available so far on degradation of bond under fire don't offer much acuity on the residual bond capacity as well as mode of failure. Gao et al.¹⁰ performed numerical investigations on reinforced concrete beam subjected to fire and they concluded that incorporation of bond has a little impact on the residual strength. Hung¹¹ also performed numerical investigations on bond degradation and a model on that was proposed successively.

Sharma et al.¹² carried out a numerical study utilizing beam-end specimens to investigate the post-fire bond performance, which formed the basis of the current study. The detailed background of the development of the beam-end specimen utilized in this work is given in Bosnjak et al.¹³. A strong influence of realistic boundary conditions of the test specimen and fire scenario on post-fire bond performance was clearly demonstrated. This work is an extension of the work initiated in these studies and systematically investigates the influence of various parameters affecting bond performance in post-fire residual conditions. Here, only the influence of concrete cover is reported.

3 Significance of the study

Researches, which are conducted until now on behaviour of bond strength at elevated temperatures are mainly useful for the development of temperature dependent material model for bond. However, there are no such model available which gives due considerations with the influence of bond-splitting failure of reinforced concrete structure or structural member exposed to fire. Higher heating rate increases thermal stress and consequently cracking in concrete leading to a significant degradation of bond strength. Also, in most of the cases, thermally induced cracks result in a change of failure mode, therefore restricting to the achievement of complete bond stress. It is therefore essential to investigate the bond strength of a structural member considering i) different failure mode (splitting or pull-out) ii) heating rate on the concrete damage.

4 Numerical investigation

In this numerical investigation, the residual bond capacity is investigated considering different minimum concrete cover (c_{min}) for different fire exposure durations (see Table 1).

Table 1 Overview of the performed numerical investigations

Investigated parameter: Clear minimum concrete cover (c_{min})					
Name of the Specimen	Clear minimum concrete cover (c_{min})	Bonded length	Rebar dia.	Spacing of stirrups	Heating duration
	[mm]	[mm]	[mm]	[mm]	[min]
A	1.5* d_s =24mm	8* d_s =128mm	16	100	0,15,30,60,90
B	2.5* d_s =40mm	8* d_s =128mm	16	100	0,15,30,60,90
C	3.5* d_s =50mm	8* d_s =128mm	16	100	0,15,30,60,90

4.1 Specimen description

A beam-end specimen which simulates well the boundary conditions realistically is used to perform numerical investigations. It is previously shown that this specimen¹³ is more suitable for bond investigation under fire than the standard pull-out specimen. Figure 1 gives the overview of the specimen geometry and provides the details of the positions of the test rebar, stirrups, other longitudinal rebars etc. Standard test rebar (grade BSt 500) with a diameter of 16mm is used in this present numerical study. The test rebar in this case is provided with an initial debonded length of $7d_s$ followed by a bonded length of $8d_s$ (d_s is diameter of rebar) thereafter. The fundamental purpose of the debonded length is to prevent the formation of a concrete cone breakout body in the front. A minimum concrete cover of 24 mm is considered in this present study.

A total of four longitudinal rebars of 12 mm diameter are provided and 8mm diameter closed stirrups are provided with a spacing of 100mm in the bonded zone. Normal strength concrete conforming to the grade C16/20 according to EC2 is being considered. While simulating the post-fire residual pull-out behaviour, all the restrains are provided significantly far from the bonded zone to avoid influence of it.

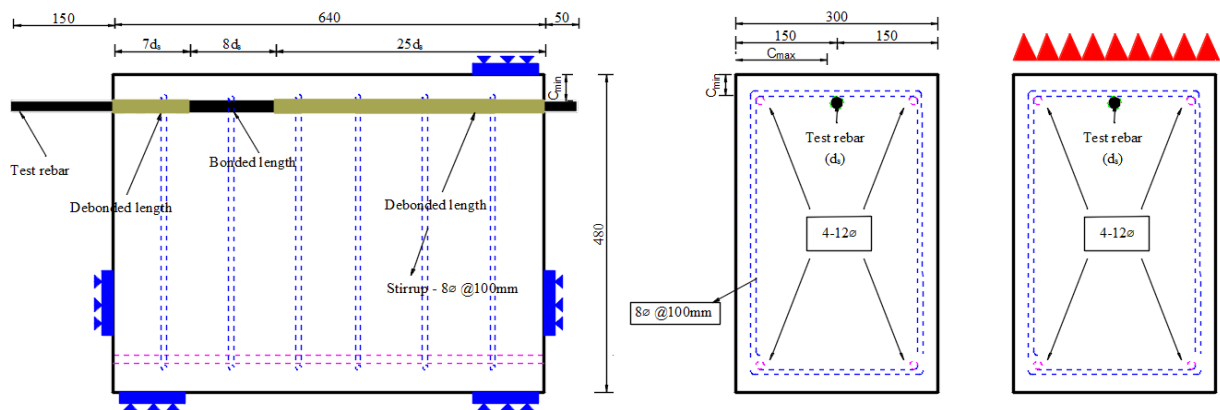


Fig. 1 Beam-end test specimen used for the present numerical investigation a) complete specimen b) cross-section of the specimen in ambient condition c) cross section displaying heating surface.

5 Thermo-mechanical modelling of concrete

In general, behaviour of RC members exposed to fire depends predominantly on the material and thermal properties of both concrete and reinforcing steel. The degradation of the material properties is governed by the changes occurring inside the material at the microscopic level, leading to a global weakening depending on the maximum attained temperature.

The numerical modelling is performed using the in-house developed 3D finite element software MASA. The constitutive law which is used to describe the behaviour of concrete at elevated temperature is a temperature dependent microplane model where the mechanical properties of concrete are coupled with temperature. To account the effect of temperature in concrete and steel thermo-mechanical model is used and briefly explained below. A detailed description can be found in Periskic, G¹⁷. In this thermo-mechanical model, the total strain of concrete at high temperature are splitted into three components.

$$\varepsilon_{total} = \varepsilon_m + \varepsilon_{fts} + \varepsilon_{lits}$$

Where, ε_m is mechanical strain, ε_{fts} is free thermal strain and ε_{lits} is load induced thermal strain. The temperature dependency of the microplane model is considered such that all the macroscopic properties of concrete - Young's modulus, compressive and tensile strength and fracture energy are temperature dependent. Though from the experimental investigations it is observed that with the increase of temperature free thermal strain increases, in this case it is considered that the tensor only depends on temperature and behaves alike in all directions.

Crack band method is used as localization limiter and smeared crack approach is considered for simulation of the cracks in concrete. A more detailed description can be found in Ožbolt et al¹⁴.

5.1 Numerical modelling approach

Mechanical properties of different materials used for the present numerical simulation are summarized in Table 2.

In this present numerical investigation, concrete is modelled using 4-noded tetrahedral elements and test rebar is modelled using 8-noded hexahedral elements. The material of the test rebar is considered as linear elastic because the aim of this work is to study influences of different parameters on bond of concrete. So, considering test rebar as linear elastic, yielding of steel can be avoided. Other longitudinal corner rebars and stirrups are modelled using 2-noded axial bar elements, for which a trilinear stress-strain law (elasticity modulus, yield strength, hardening modulus and ultimate strength) is defined.

Table 2 Material properties used in this present study

Material	unit	Concrete	Test rebar	Other longitudinal rebar	Stirrup
Compressive strength	[N/mm ²]	20	-	-	-
Tensile Strength	[N/mm ²]	2.25	-	550	550
Modulus of Elasticity	[GPa]	23.5	200	200	200
Poisson's ratio	[-]	0.18	0.33	0.33	0.33
Fracture energy	[N/mm]	0.06	-	-	-
Yield Strength	[N/mm ²]	-	-	500	500

5.2 Modelling bond behaviour

Interaction between reinforcing steel and concrete is modelled using one dimensional 2-noded bar element, which can bear shear and compression force only. A weak contact layer of 1mm thick, modelled using hexahedral solid element, is introduced between steel and concrete. An idealized trilinear bond stress-slip curve is specified in this present numerical investigation (figure 2). The maximum bond strength of the elements (τ_{max}) in the bonded zone and deboned zone are considered as 12 N/mm² and 0.1 N/mm², while the values of S1, S2 and S3 are 0.05mm, 1.5mm and 6 mm respectively.

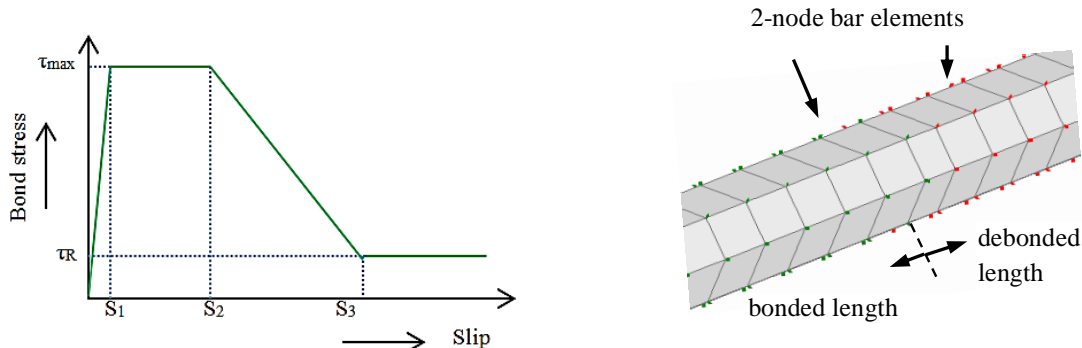


Fig. 2 a) Idealized bond stress-slip relationship used as constitutive law for 2-noded bar element.
b) Test rebar showing bonded and deboned bar elements

Figure 3 displays the complete FE model along with restrains and the positions of test rebar stirrups and other longitudinal rebars within the specimen. The increase of surrounding air temperature of the concrete is defined by the ISO 834-1 fire curve: $T = T_0 + 345 \log_{10}(8t+1)$. Where, T is actual temperature in °C, T_0 is initial temperature (which is considered as 20°C) and t is time in minutes.

In the present study, following fire durations are considered: no fire (reference case), 15min, 30 min, 60 min and 90 min. First the air temperature is increased upto the desired fire duration as per ISO 834-116 fire scenario. Upon finishing the heating, the air temperature is linearly cooled down to room temperature (20°C) and it is kept constant thereafter for a certain duration to assure a constant temperature of 20°C throughout the specimen. In this present numerical investigation heating and cooling is applied employing time steps, i.e. temperature profile within the specimen changes with each time step. After the completion of heating and cooling process, the rebar was pulled out in displacement control. The upper surface of the specimen is constrained in its rear end perpendicular to the loading direction

to prevent any kind of rotation or uplift. The front surface is constrained far from the test rebar towards loading direction to avoid sliding.

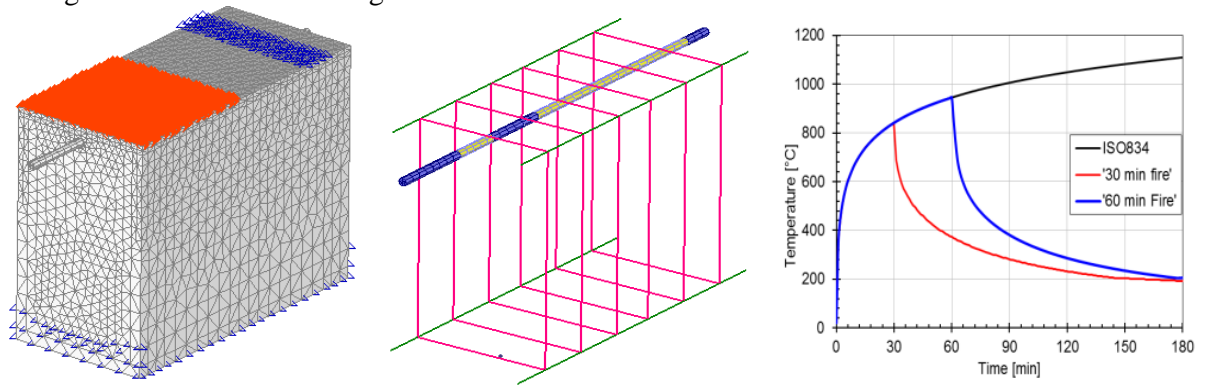


Fig. 3 FE model: a) Full model for one-sided heating scenario b) Full model for three-sided heating scenario c) ISO 834-1 fire scenario.

6 Experimental investigations

In this work, pull out tests in beam-end test specimens using unconfined test set-up are performed. Specimens are exposed into fire for a particular fire duration (such as 15, 30, 60 or 90 minutes) and allowed to cool down naturally to room temperature thereafter. Displacement control pull-out tests are performed on those cooled down specimens as well as reference specimens to understand the differences in bond strength-slip behaviour.

The average age of concrete at the time of testing was between 75 to 80 days at the time of fire tests. All contact surfaces are insulated using mineral wool. Thermocouples are used for each specimen to measure the temperatures inside the concrete surfaces. The heating was applied using oil burners. Furnace air temperature is measured and controlled by means of several sheath thermocouples.

The heating is applied according to ISO 834-1 fire scenario. Thereafter, the specimens are allowed to cool down naturally, inside the closed furnace.

6.1 Pull-out test



Fig. 4 a) beam-end specimens inside the furnace. b) pull-out test on beam-end specimen after fire

The test setup used to perform the pull-out tests is shown in Figure 4. The load, which is applied for every test is a displacement-controlled loading using a hydraulic cylinder. The applied load, the displacement of the bar (at the unloaded end) and the crack widths were measured and recorded continuously. LVDTs were used to measure crack widths and displacement of the rebar. All the restrains are provided significantly far from the bonded zone to avoid influence of it on the pull-out behaviour.

7 Outcome

The numerical results obtained from the present numerical simulations are in terms of applied load in the front of the test rebar with respect to the corresponding slip measured at the rear end of the test

rebar to eliminate the elastic elongation of it from the total displacement. The total applied load is converted to average bond stress over the entire bonded length considering the uniform bond stress approach:

$$\tau_b = P/(\pi d_s * l_b)$$

where, P is the total applied load, d_s is the diameter of test rebar and l_b is the length of the bonded zone.

The results of the numerical investigations of the pull-out tests (unconfined setup) performed using beam-end test specimens (Specimen type A, B and C; Refer Table 1) for different fire exposure durations are plotted in figure 5. It is observed that all investigated specimens exhibited concrete splitting, whereby the bond capacity decreased with decreasing minimum concrete cover (c_{min}).

The comparison of the bond stress v/s rear end slip curve obtained from the pull-out tests performed on the residual specimens and the specimens exposed to 60 mins of fire are plotted in figure. 5a. As the figure shows, both in ambient condition as well as post fire condition the bond stress-slip curve displays a typical splitting failure, having no plateau and steeper post-peak response contradictory to that of pull-out failure. Due to the reduced concrete cover towards the top of the specimen, the longitudinal splitting cracks reach the surface, implying a splitting failure. Therefore, full bond strength couldn't be achieved.

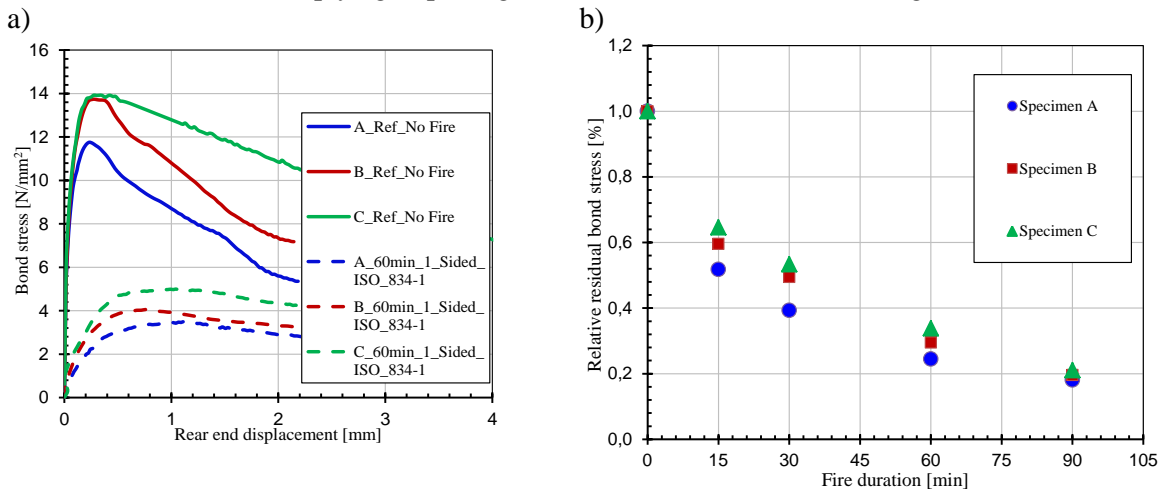


Fig.5 FE model a) Comparison of bond stress-slip curves for the reference case and after 60 minutes of fire b) Percentage degradation of bond stress with different fire durations.

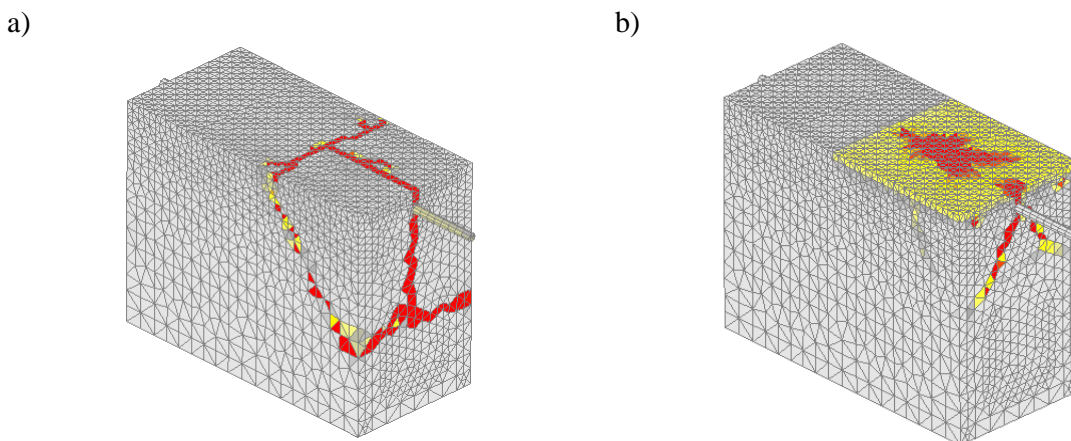


Fig. 6 Crack pattern for a specimen with 24 mm minimum concrete cover. a) Reference specimen b) Specimen subjected to 30 minutes of fire.

The relative residual bond stress of the specimens with different minimum concrete cover (c_{min}) for different fire exposure durations are plotted in fig. 5b. It can be noticed that, even in case of specimen with the highest concrete cover (specimen C with $c_{min} = 56$ mm), the residual bond strength only

after 15 min of fire is only approx. 65% of that under ambient condition. A gradual deduction of residual bond stress with the increment of fire exposure duration thereafter is also observed. This can be ascribed to ISO 834 -1 fire scenario which exhibits very high increase in temperature within a very short duration of fire exposure and much lower increase in later stage. Residual bond capacity is even lower for other specimen for the same fire exposure duration. As the conductivity of concrete is low, high heating rate leads to a very high temperature gradient between different layers of concrete. This immense temperature gradient enhances the thermally induced stresses inside the concrete layers leading to a several thermal cracks. Cooling process further aggravate the thermally induced damage. It can also be observed that slip corresponding to peak bond stress increases with increase fire exposure duration.

The crack pattern of a reference specimen and 30 mins fire exposed specimen with a minimum concrete cover (c_{min}) of 24 mm (specimen A) is depicted in figure. 6. A transverse crack at the end of the bonded zone can be noticed due to the tensile failure of concrete. A prominent longitudinal crack parallel to the test rebar can be observed thereafter. This can be attributed to the splitting failure of concrete cover prior to the pure bond pull-out failure limiting the usable bond strength. Very small concrete cover towards the top surface as compared to all other directions has provoked splitting cracks to propagate on top surface of the specimen.

8 Experimental validation

The results of the numerical simulations are validated with few experiments carried out on beam-end specimens. The validation is executed by comparing the load-slip curves, crack patterns, failure modes and temperature profiles with their respective experimental counterparts. Three tests are carried out for each type of specimen. The crack pattern obtained immediately after peak (numerically and experimentally) from the pull-out test of specimen A (min. concrete cover 24mm) exposed to 60 minutes of fire is outlined in fig. 7. It can be observed that similar to the FE model, the transverse tensile crack started to propagate from the end of the bonded zone owing to the growing longitudinal splitting cracks. It can be clearly observed that the crack pattern obtained numerically is in a very good agreement with its experimental counterpart. A very similar crack pattern is noticed for all other specimens subjected to different fire durations (15, 30, 90 minutes). The results of the load-slip curves and temperature profiles could not be shown here for brevity purpose.

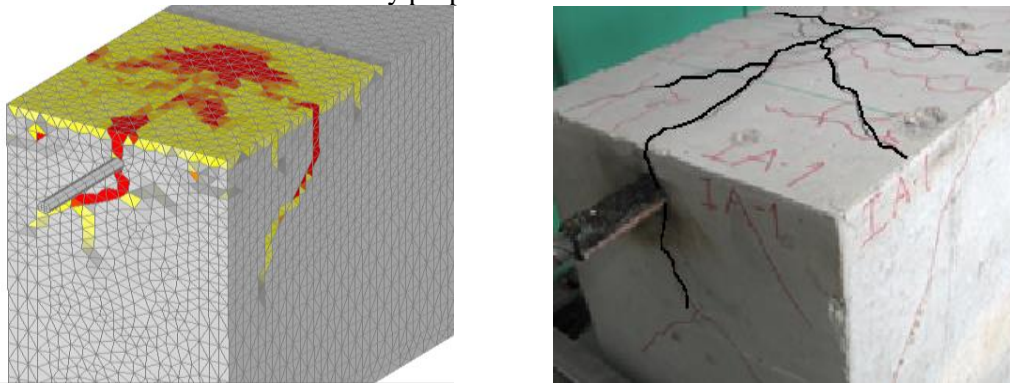


Fig. 7 A comparison of the crack pattern between numerical simulation and experimental investigation of a specimen (min. clear cover 24 mm) subjected to 60 minutes of fire.

9 Summary

In this present study, numerical investigations are carried out using beam-end specimens following ISO 834-1 fire scenario. The objective of the study was to understand the effect of the concrete cover on the reduction of post fire bond capacity compared to that of the residual state.

It is very much interesting to note that all investigated cases even specimens which are not exposed to fire (ambient condition) exhibit a typical splitting failure. Due to the reduced concrete cover towards the top surface, the longitudinal splitting cracks reach that surface, implying a splitting failure prior to pull-out failure. Hence, the full bond strength cannot be exploited.

Fire has two step repercussion on concrete namely material degradation and degradation due to thermally induced stresses. It is quite obvious that there will be a decrease in bond strength due to the degradation of material properties when a RC specimen undergoes fire. But it is observed from the

results that the residual bond strengths are adversely affected by fire loads and subsequent cooling (for example, about 40% after 15 minutes of fire exposure for a specimen with a concrete cover of 24 mm) even for a relatively short duration of fire exposure (15 minutes). This can not be justified only by the material degradation. Temperature gradient created between outer and inner layers of concrete while exposing to fire causes thermally induced damages in terms of thermal cracks. The cooling down of the specimens to room temperature further triggers these thermal cracks leading to a very severe degradation of bond strength.

It can also be noted from the results that the relative bond stress degradation is almost similar for all the investigated concrete minimum cover (c_{\min}) to diameter of rebar ratios. This can also be ascribed to the effect of thermally induced cracking. As the thermal conductivity of concrete is very low, huge thermal gradient arises between concrete layers as mentioned earlier. Unlike steel, concrete cannot regain its strength after cooling.

It is necessary to consider both the aspects; failure mode as well as percentage degradation of bond capacity for the design of bond strength in case of a fire accident. The authors are currently pursuing a detailed experimental and numerical study to investigate these and further parameters.

References

- [1] EN 1992-1-1:2004, *Eurocode 2: Design of concrete structures – Part 1-1: General rules and rules for buildings*, European Committee for Standardization, 2004.
- [2] *fib Model Code for Concrete Structures 2010*. Vol.55 Ernst & Sohn; 2013.
- [3] REILM. *Recommendations for the testing and use of construction materials*. REILM 1994;12:213-220.
- [4] Morley P, Royles R. *Response of bond in reinforced concrete to high temperature*. *Magazine of Concrete Research* 1983; 35:67-74.
- [5] Diedrichs U, Schneider U. *bond strength at high temperature*. *Magazine of concrete research* 1981; 33: 75-84.
- [6] Bingöl AF, Gül R. *Residual bond strength between steel bars and concrete after elevated temperature*. *Fire Safety journal* 2014; 69: 23-35.
- [7] Lublóy, Éva György, Balázs L. *Temperature effects on bond between concrete and reinforcing steel*. *Zbornik radova Građevinskog fakulteta journal* 2014;30: 27-35.
- [8] Sagar H. *Zum Einfluss hoher Temperaturen auf das Verbundverhalten von einbetonierten bewehrungsstäben*. *PhD Thesis*. Technical University of Braunschweig 1985. (in German).
- [9] A. Shamseldin, H. Elshafi, A. Rashad, M. Kohail, *Assessment and restoration of bond strength of heat-damaged reinforced concrete elements*, *Constr Build Mater* (2018) 169: 425-435.
- [10] WY. Gao, JG. Dai, JG. Teng, GM. Chen, *Finite element modelling of reinforced concrete beam exposed to fire*, *Eng Struct* (2013) 52:488-501.
- [11] Z. Huang, *Modelling the bond between concrete and reinforcing steel in a fire*, *Eng Struct* (2010) 32:3600-3669.
- [12] Sharma A, Bošnjak J, Ožbolt J, Hofmann J. *Numerical modelling of reinforcement pull-out and cover splitting in fire –exposed beam-end specimens*. *Engineering Structures*, 111, 2016, 217-232.
- [13] J. Bošnjak, A. Sharma, C. Öttl, *Modified beam-end test setup to study the bond behaviour of reinforcement in concrete after fire*, *Mater Struct* (2018) 51:13.
- [14] J. Ožbolt, I. Kožar, R. Eligehausen, G. Periškić, *Instationäres 3D Thermo-mechanisches Modell für Beton*, *Beton- Stahlbetonbau* (2005) 100:39–51.
- [15] EN 1992-1-2:2004, *Eurocode 2: Design of concrete structures – Part 1-2: General rules– Structural fire design*, European Committee for Standardization, 2004.
- [16] ISO 834-1: *Fire-resistance tests - Elements of building construction - Part 1: General requirements*, Geneva (Switzerland), International Organisation for Standardisation, 1999. Paragraph formats.
- [17] Periskic, G. *Entwicklung eines 3D thermo-hygro-mechanischen Modells für Beton unter Brandbeanspruchung und Anwendung auf Befestigungen unter Zuglasten*, *Institute of Construction Materials, University of Stuttgart*, 2009.

Monitoring and structural assessment

A new assessment methodology for fair-faced concrete surfaces based on digital image processing

Kitti Ajtayné Károlyfi¹⁾, András Horváth²⁾, Ferenc Papp¹⁾

¹⁾Faculty of Architecture, Civil Engineering and Transport Sciences; ²⁾Faculty of Mechanical Engineering, Informatics and Electrical Engineering

Széchenyi István University
Egyetem tér 1., Győr, 9026, Hungary

Abstract

Fair-faced concrete elements have become even more popular in architecture because of their pure aesthetics and favourable material properties. The European standards and guidelines are usually specifying four classes regarding to the surface quality. However, the standard assessment methodologies are based only on manual methods and they are very subjective in some cases. In order to increase the efficiency and accuracy of the evaluation a new methodology is proposed using digital image processing. In this paper the basis of the evaluation method made by using the Python 3.6 software is presented by focusing on the surface void ratio which is one of the most common surface defects of fair-faced concrete structures.

1 Introduction

Nowadays concrete is not only used because of its high load-bearing capacity and special cost/performance ratio, but also for its high surface quality and aesthetical appearance. The concrete and construction technology has improved rapidly, therefore special design and aesthetical requirements can be fulfilled easily. However, the assessment of the fair-faced concrete surfaces is usually based on references or on mainly subjective aspects. The European standards [1,2] and guidelines [3] define evaluation aspects and methodologies which are manual methods without exception. Therefore it is necessary to increase the efficiency of the evaluation process and exclude the human mistakes as far as possible. For that purpose the computer aided image processing method can be an effective solution, which has been already used in different engineering fields for decades. There are many methods [4,5,6] for automatic crack detection on concrete structures and some research works [7,8] have also been published with regard to the automatic evaluation of fair-faced concrete surfaces. However, a general method is not yet available for the purpose of assessing and classifying these surfaces by considering multiple aspects. In a previous study [9] a method for the evaluation of the surface void ratio was proposed by the authors. Results showed that the speed and accuracy of the assessment can be increased significantly using digital image processing techniques, therefore developing and extending this method to other aspects is preferable.

The aim of this research is to further develop and extend the program to recognize and identify as many surface defects as possible based on one photo in an efficient way. Therefore a new method was developed based on a background fitting with a two-variable cubic polynomial in order to define the differences between the original and the output image, which correspond with the different surface defects. In order to examine the accuracy of the method an experiment was carried out on the fair-faced concrete surfaces of the Széchenyi István University. (Fig. 1)



Fig. 1

Fair-faced concrete surfaces in Széchenyi István University, Győr, Hungary

A total number of 40 images were examined by focusing on the surface void ratio. Analyzing the test results allows not only to examine the precision of the method but also to find important relationships between the surface irregularities and the construction method or the concrete technology.

2 Methodology

The sampling was made on the fair-faced concrete surfaces of Széchenyi István University in Győr using a digital camera of the type of Sony DSC-HX350. For the digital image processing the Python 3.6 software was used. Measuring markers were used on every photo for scaling the images. Two input datas are needed for the program. The first is the original photo (Fig. 2a) taken from the surface containing a measuring marker. The second is an image (Fig. 2b) containing manually selected regions of the original photo which are free from any surface defects. The other parts of the image are filled with any color in order to exclude those pixels during the image processing. The basis of the methodology is fitting a third order polynomial to the three channel (R,G,B) of the image containing the selected regions (Fig. 2b) using the least squares approximation. The result is the fitted image (Fig. 2c), which is a new version of the original image that is free from surface defects. The program calculates the accuracy of the fitting step as well. After the fitting step, a reference surface is cutted out from the images (Fig. 3a), whose size can be determined based on the standard. In this study a reference area of 50x50 cm is used based on the Hungarian standard.

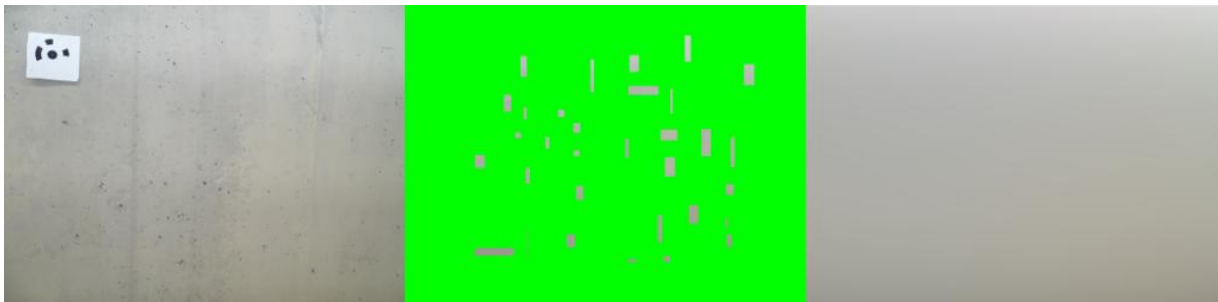


Fig. 2. (a) original image (b) selected regions (c) fitted image; maximal error = 0.0186

Thereafter the differences between the original and the fitted image will be the basis for identifying the different surface defects. The discoloration, the pores and additional surface irregularities can be detected very well based on the difference image, as it can be seen in Fig. 3b.

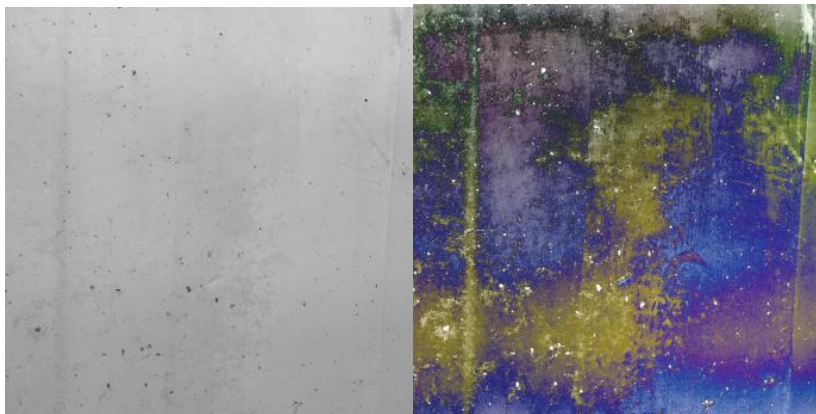


Fig. 3. (a) Reference surface (50x50 cm) (b) Difference between the original and the fitted image examined on the reference surface

Image segmentation method was used for separating the surface defects and the background. For that purpose the average value of the RGB components was calculated and compared with the RGB components of the original image. The allowed divergence from the average can be controlled by introducing a tolerance factor (TF). Therefore the image containing only the darker areas of the surface can be created by subtraction of the pixels below the average and the tolerance factor multiplied by the error of the fitting step. The image containing only the brighter areas can be created by summa-

rizing the previous values on each channel as well. The lower the tolerance factor is, the more precise the result is. (Fig. 4) The noise reduction was made by using a Gaussian blur with a kernel of 25x25 on the binary images.

For detecting and classifying the surface defects it is necessary to define the main characteristics of these irregularities. The evaluation aspects of the fair-faced concrete surfaces which can be examined by using digital image processing are the followings:

- surface void ratio
- honeycomb
- texture, panel joints
- color uniformity.

The following sections present the method of identifying some of these aspects and the results of an experiment with regard to the surface void ratio.

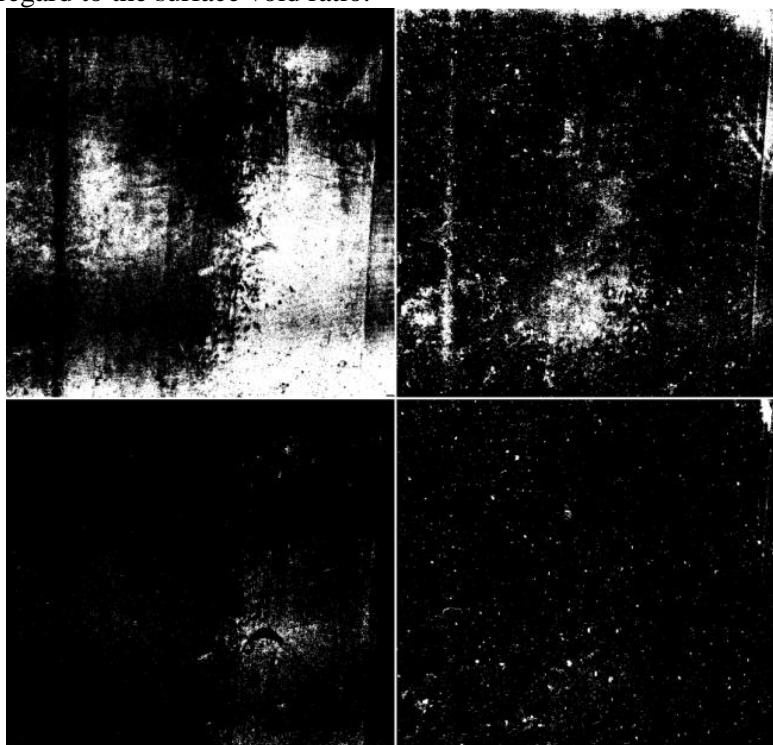


Fig. 4. (a) pixels above the average (TF=3.0); (b) pixels below the average (TF=3.0); (c) pixels above the average (TF=6.0); (d) pixels below the average (TF=6.0).

2.1 Detection of surface defects

2.1.1 Surface void ratio

For the image segmentation the FindContours function of the OpenCV library was used. The surface void ratio can be examined on the image containing the darker areas of the surface. The main characteristics of the pores were the allowable minimal and maximal diameter, the circularity and the solidity. The standards usually define the allowable diameters of the pores and the allowable surface void ratio in the test area. The diameter of the pores was calculated by defining the smallest enclosing circles of the detected contours. The limitation of the circularity and solidity was needed for separating the pores and other surface irregularities. The solidity of a shape is equal to the area of the contour area divided by the area of the smallest possible convex polygons that contain all of the points of the given contour. In this study the pores between 1 and 15 mm diameter were taken into account based on the Hungarian standard. The detected pores and the surface void ratio of the photo Fig. 3a can be seen in Fig. 5.

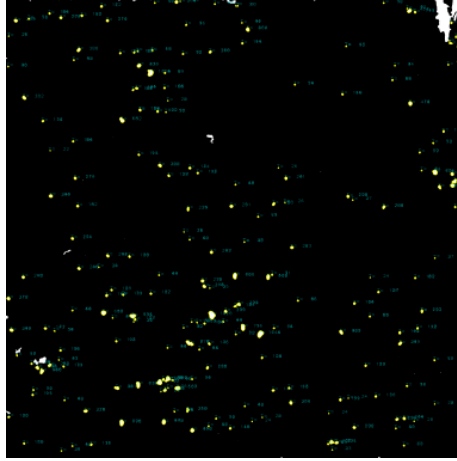


Fig. 5. Detected pores, surface void ratio = 0.943 %

2.1.2 Honeycomb

The honeycomb can be observed in both of the above- and below-the average images because of the sharper edges and lighter intermediate parts of the irregularity. For that reason the two images were summarized at first and the contour finding function was run on the output image. The contour of the honeycomb is more accurate if the noise reduction was made on the summarized image. The main properties of the honeycomb are the large area (greater, than the pores²), low circularity and usually the concave contour. Based on the standards the honeycomb is unacceptable in the case of the highest surface tolerance class, but there is no quantitative limitation. As in previous investigation, the ratio between the area of the honeycomb and the reference surface can be calculated, which allows a more accurate evaluation of this phenomenon (Fig. 6).

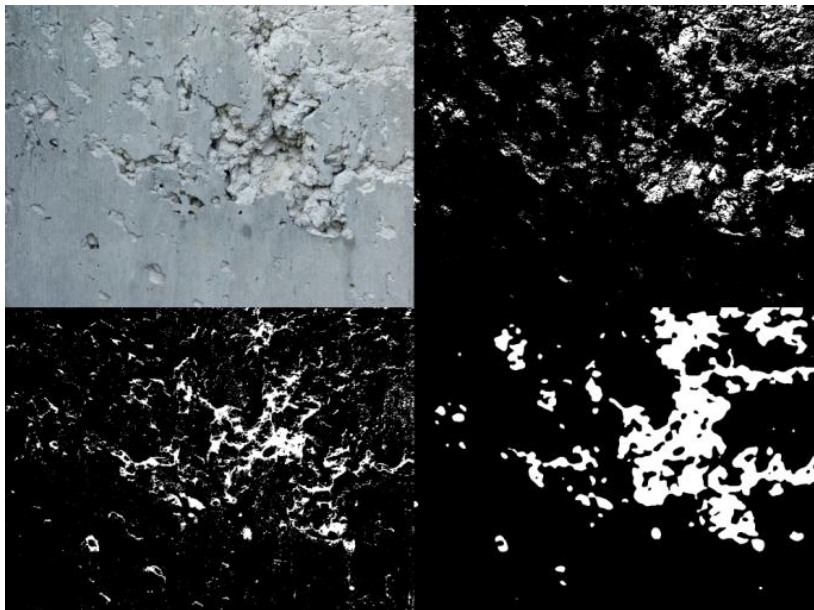


Fig. 6. (a) honeycomb on the original image; (b) pixels above the average (TF=2.0)
(c) pixels below the average (TF=2.0); (d) summarized and smoothed image

2.1.3 Cement residue

The mortar leakage (cement residue) is unacceptable in the case of the highest surface tolerance class. This surface defect can be observed in the above-the average image and can be identified by the small area and usually low solidity (Fig. 7).

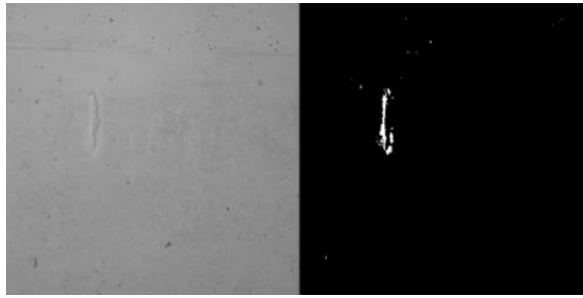


Fig. 7. (a) Cement residue on the original image; (b) Detected contour

2.2 Experiments

During the experiments a total number of 40 photos were examined; 20 photos (P01-P20) from inside the Széchenyi István University and 20 photos (P21-P40) outside the University, from the car park. Based on the results the mean diameter and the standard deviation were calculated of each reference surface and the distribution of the pores was presented on diagrams. As can be seen in Fig. 8, it is a non-normal distribution in all cases. The curtosis of the histograms are positive in almost all cases, which means, that the distributions have a peak around the diameters 1 and 2 mm and tend to decline rapidly with increasing diameter of the pores. Furthermore, they are positively skewed distributions without exception, which means that the tail of the distribution is toward the high diameters indicating an excess of low numbers of pores.

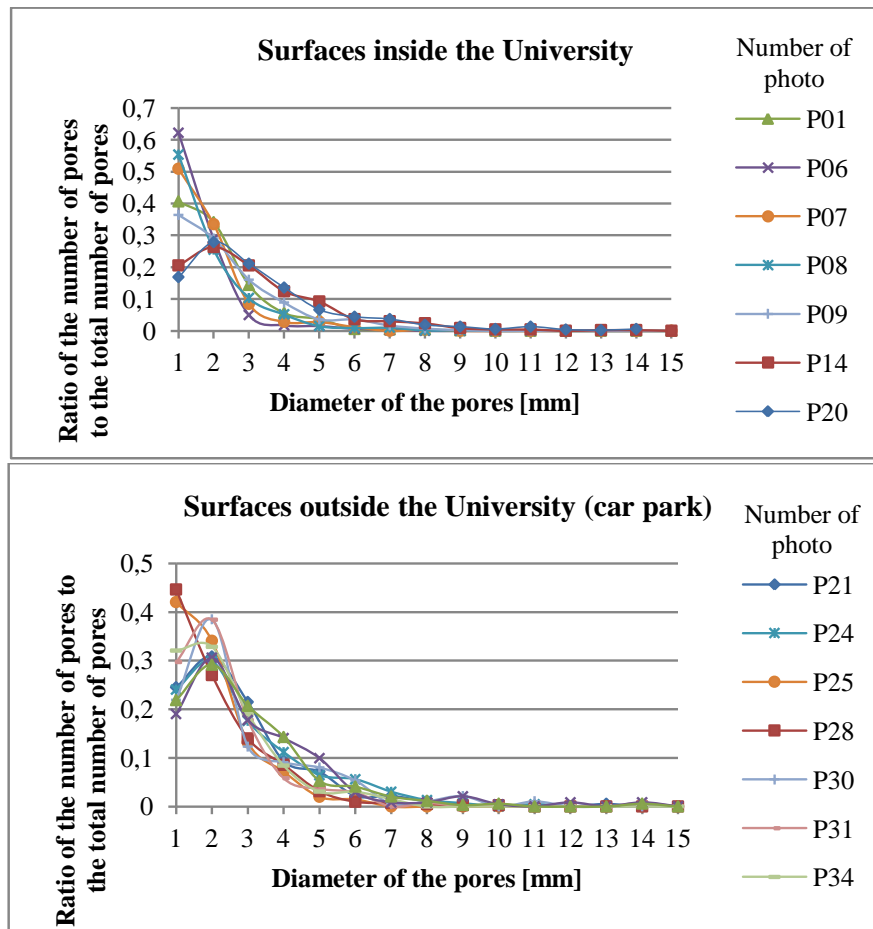


Fig. 8. Distribution of the pores

There is a difference between the distribution of the inside and outside surfaces. In the case of the outside surfaces, if the curtosis is relatively low, the distribution has a second frequent score around 5-6 mm. In these cases the standard deviation is even higher than in other cases. The mean diameter of the pores was 2,70 mm on inside surfaces and it was 2,97 mm on outside surfaces. As it can be seen in Fig. 9. the standard deviation is increasing with increasing mean diameter. Furthermore, a

strong decrease can be obtained in the curtosis with increasing mean diameter (Fig. 10). A clear relationship can be established between the skew and curtosis of the histograms, which means that the more the distribution is shifted to one site the more higher the peak is. (Fig. 11.) In Fig. 9-11. each point denotes one photo. The mean value of the skew is 2,04 on inside and 1,71 on outside surfaces, while the mean value of the curtosis is 2,98 and 1,61 on the two groups of test surfaces.

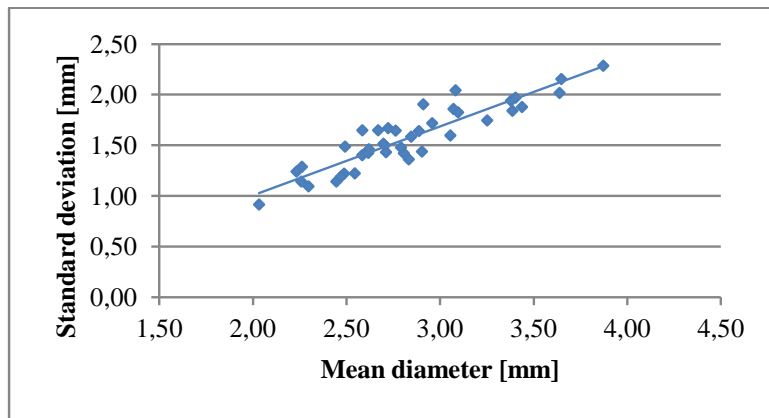


Fig. 9. Relationship between the mean diameter of the pores and standard deviation

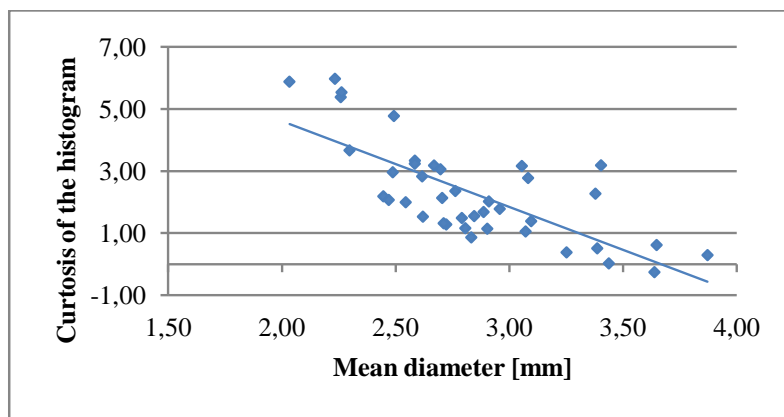


Fig. 10. Relationship between the mean diameter of the pores and curtosis of the distribution

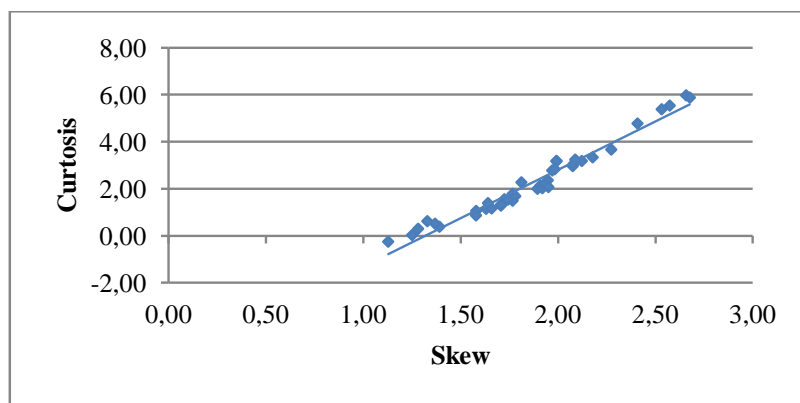


Fig. 11. Relationship between the skew and curtosis of the distribution curves

Based on these relationships of the datas it can be obtained that the pores were caused due to similar processes. The construction method and the applied form release agent was the same in the case of the inside and outside surfaces, while the applied formworks and concrete mixtures were different. It can be assumed that the second frequent score of the distribution about the diameter 5-6 mm was the result of these differences. Schubert et al. [10] proved, that the interaction between the formwork

surface, the form release agent and the fresh concrete has a significant effect on the surface quality. Based on their experiments they developed a four-steps model for the pore formation with regard to this interaction. The characteristics of the formwork, like the moisture absorption, the number of use and the surface texture, and the properties of the concrete mixture influence greatly this interaction and consequently, the pore formation, even under the same procedure and weather conditions. The surface void ratio of six samples was examined using the standardized manual method as well. These results are in good agreement with the measurements of the program. The surface void ratio values of the program is an average of 8% higher than the manual results. The reason of the difference is the different precision of the evaluation processes, since in the manual method the human mistake can not be excluded.

3 Conclusion and further research objectives

Experiments have shown that using the digital image processing the evaluation and classification of the fair-faced concrete surfaces can be done automatically and with proper precision between the examined frameworks. This method requires only one photo of the surface containing a measuring marker. After creating an image containing manually selected regions of the surface which are free from any surface defects, the evaluation and standardized classification of the surfaces can be done automatically in a few seconds. Based on the results further examinations can be carried out in order to find relationship between the surface defects and the construction technology.

The method allows identifying further surface irregularities, like color uniformity, as it can be seen in Fig. 3b, where the darker and brighter areas can be detected easily. The color uniformity is one of the basic characteristics of fair-faced concrete surfaces. In the practice usually reference surfaces or reference gray levels are used for that purpose. However, the evaluation of the homogeneity of color tone is quite subjective and sometimes results in disagreement between the developer and the contractor. [7] Digital image processing might be an effective and objective solution for that purpose. Therefore the authors' goal is to further develop the program with regard to this aspect. It requires determining objectively quantifiable criterias of the discoloration, with which its extent and degree can be obtained. In this case, the RGB color space applied hitherto should be replaced by the CIE-LAB color space, which was specially designed to encompass all colors the average human can see. It means that the same amount of numerical change in the L^*a^*b values corresponds to the same amount of visually perceived change. By using the difference image between the original and the fitted image the degree and direction of discoloration can be defined objectively.

Acknowledgements

This research is supported by the ÚNKP-19-3 New National Excellence Program of the Ministry of Human Capacities.

References

- [1] ÖNORM B 2211. 2009. Concrete, reinforced and prestressed concrete - Works contract.
- [2] Hungarian Standards Institution (MSZT). 2012. Requirements for the appearance of building structural elements. MSZ 24803-1:2012.
- [3] Bundesverband der Deutschen Zementindustrie e. V. (BDZ), Deutsche Beton- und Bautechnik-Verein e. V. (DBV). 2004. *Merkblatt Sichtbeton*. Berlin.
- [4] Mohan, Arun., and Poobal Sumathi. 2017. "Crack detection using image processing: A critical review and analysis." *Alexandria Engineering Journal*. (Article in press), doi:10.1016/j.aej.2017.01.020.
- [5] Yamaguchi, Tomoyuki, Hashimoto, Shuji. Fast crack detection method for large-size concrete surface images using percolation-based image processing. *Machine Vision and Applications* 21, 797–809 (2010). doi:10.1007/s00138-009-0189-8.
- [6] Prateek Prasanna, Kristin J. Dana, Nenad Gucunski, Basily B. Basily, Hung M. La, Member, IEEE, Ronny Salim Lim, and Hooman Parvardeh. Automated Crack Detection on Concrete Bridges. *IEEE Transactions on Automation Science and Engineering*, (Article in press), doi: 10.1109/TASE.2014.2354314.

- [7] Niki, Cauberg, Piérard, Julie and Bams, Veerle 2015. „Coloured fair-faced concrete – evaluation of colour tone“ Concrete – Innovation and Design, Proceedings of the 13th fib Symposium , pp. 228-229.
- [8] Stanke, Gerd, Roland, Herr, and Petra, Hoske. 2006. *Bildgeschützte Bewertungsverfahren für Sichtbetonoberflächen*. Schlussbericht, Gesellschaft zur Förderung angewandter Informatik e.V., Berlin.
- [9] Károlyfi, Kitti and Papp, Ferenc 2018. „Evaluation of fair-faced concrete surfaces using digital image processing“ Proceedings of the 12th International PhD Symposium in Civil Engineering, Prague, Czech Republic, August 28-31.
- [10] Schubert, Karsten 2011. „Neuse Sichtbetontechnik – *Integration der Erkenntnisse zu Wechselwirkungen zwischen Schalungshaut, Trennmittel und Betonoberfläche in die Prozesskette beim Sichtbeton*, Schlussbericht, Hochschule Karlsruhe – Technik und Wirtschaft, Institut für Angewandte Forschung

Carbon-fibred mortar: Effect of sand content and grain size distribution on electrical impedance

Allam Hamza¹, Duplan François¹, Clerc Jean-Pierre¹, Amziane Sofiane², Burt-schell Yves¹

1 Aix-Marseille Université, CNRS, IUSTI UMR 7343, 13453, Marseille, France

2 Univ. Clermont Auvergne, CNRS, Sigma, Institut Pascal, UMR 6602, Clermont-Ferrand, France

Abstract

Self-sensing concrete, also known as “Smart concrete”, is obtained by including electrically conductive fibers in cement-based materials. These fibers may allow to reduce electrical resistivity and develop a piezoresistive behaviour. Smart Concrete could therefore be simultaneously both a structural and a sensing material, which eliminates the need for external instrumentation in Structural Health Monitoring.

By increasing the fiber volume fraction within the cement matrix, the electrical resistivity (or impedance) of the material is reduced once percolation threshold is reached. Above this percolation threshold, the fiber content is high enough to allow conductive particles to be in contact or very close to each other, thus creating a continuous conductive network within the insulative matrix.

Sand’s presence was stated to have an influence on resistivity in case of fibred mortar: a high sand content may prevent the network of conductive fibers from percolating. This phenomenon is referred to as “double percolation”: the cement paste needs to be a continuous phase between sand aggregates in order to allow fibers to maintain their efficiency in reducing the electrical resistivity of composites.

However, little attention has been given to the impact of the size of sand grains on the electrical percolation. This work intends to study the effect of the grain size distribution and volume fraction of sand within mortars containing various fiber volume fractions. The results confirm the “double percolation” phenomena: when the volume fraction of sand is close to its maximum packing density, the addition of fibres was not as effective in reducing the electrical impedance of mortar samples. In addition, sand’s grain size distribution proved an influence on impedance of mortar: fine sand showed higher impedance compared to standard sand, especially in case of high sand volume fraction. This could be related to the smaller maximum packing density in case of fine sand, where distance between particles would be in average reduced. This effect, combined with the higher number of insulative particles, could probably disrupt the continuity of the conductive network of fibres within mortar.

KEY WORDS: mortar, carbon fibers, electrical properties

1 Introduction

Self sensing mortar, developed by adding electrically conductive fibers to ordinary cementitious matrix, is an innovative construction material able to detect a stress or deformation in the material due to a mechanical or thermal action. Above the percolation threshold, conductive fibers are able to create conductive paths inside the insulative cementitious matrix, thus reducing its resistivity [1]. Starting even from very low fiber volume fraction, fibred mortar develops a piezoresistive behaviour, where strains caused by external solicitations may be monitored through the exploitation of their relationship with the electrical resistivity [2] [3] of the material. Potential applications of monitoring include the detection of actions such as mechanical loads in compression [4] or tension [5], or thermal variations [6], electromagnetic shielding and pavement’s heating have also been under investigation [7][8].

The relation between hydrating cement systems and AC impedance in absence of fibers was well studied previously [9]. The efficiency of conductive fibers as “doping agent” depends on fiber’s volume fraction (FVF) [1]. The evolution of mortar’s impedance (impedance is the ratio of applied voltage on the specimen to the current flowing through it in case of AC measurements) function of FVF consists in three main phases: an insulation zone, a percolation transition zone and a conductive zone. In the insulative zone, ie where fiber concentration is below the percolation threshold, the electrical current

cannot flow continuously within the fiber exclusively, and still have to go through the insulative matrix; therefore, the reduction of the resistivity of the material is not very significant yet. A strong transition zone is observed around the percolation threshold, when continuous conductive paths start to be established within the matrix, and most of the electrical current may be able to flow through this network. Therefore, the resistivity is being reduced drastically. Above the percolation threshold, increasing the content of fibers may still improve the density and connectivity of the conductive paths within the fiber network, but its beneficial effect on electrical resistivity may not be significant [10].

Various studies have treated the percolation of fiber-shaped inclusions within a homogeneous matrix medium. Balberg [11] proposed a model to estimate percolation threshold for thin spheroids depending on the complexion of their morphology. Celzard [12] developed it to be applied on thin fibers with high aspect ratio. Berhan [13] estimated percolation thresholds for high aspect ratio fibers considering two different possible approaches for fiber's percolation inside a hosting environment. Those studies could be applied to fiber's percolation in cement paste, considering cementitious matrix as a homogeneous phase. In case of mortar, the fibers are not able to penetrate insulative sand particles, and these theoretical approaches may not be valid.

In mortar, the connectivity of cement paste within sand particles has been reported to be a necessary condition for the percolation of fibers at low volume fractions [14]. This criterion is referred to as "double percolation". Garboczi et al. [15] has estimated in 1995 the connected fraction of sand's interfacial transition zone function of its volume fraction. The study showed that the phase surrounding sand particles starts to be connected around 33% and total percolation is reached around 50-55%. Baeza et al. [16] stated that in case of concrete, a multiscale "triple percolation" is necessary to allow the percolation of the fibers: within concrete matrix, mortar could be able to percolate through coarse aggregates, in combination of cement paste percolating through fine sand aggregates within the mortar phase.

While the effect of sand content on the resistivity of carbon fibred mortars has been treated in various works [14][16][17], there seems to be little information on the effect of its grain size distribution within the literature. This study intends to provide a contribution on the effect of sand grain size distribution and volume fraction on the electrical impedance of mortars containing carbon fibres. This study would provide, using AC impedance measurements, a better understanding of the interaction between sand grain size and volume fraction from one side, with the possibility of carbon fibers to create conductive paths through it.

It compares mortars produced with a Standard sand (well distributed sand) (diameter between 0 and 2 mm) and a finer grain size fraction of the same sand (diameter between 0 and 0.5 mm) with four sand volume fractions: 0, 15, 40 and 50%. Different sand volume fractions cover the various sand structure connectivity status. Real and imaginary impedances would be illustrated, permitting the assessment of of the several interactions in the composite.

2 Materials and experimental setup

Carbon fibers present a length of 6 mm and a diameter of 7 μm . Fibers surface is virgin from treatments. The cement matrix is made of: Cement CALCIA CEMI 52.5 R, Water-to-cement ratio (W/C) =0.4. Superplasticizer BASF MasterGlenium ACE 550 was increased proportionally to fiber's volume fraction to ensure workability, not exceeding 4% of cement weight to avoid bleeding effect. Two sand granulometries tested are illustrated in the figure below.

The standard sand (well distributed 0/2mm sand) is normalised in accordance with EN 196-1. The fine sand was obtained by taking the fraction 0/0.5mm of the standard sand, meaning that both sands have the same nature. The importance of 0/0.5 mm sand in this study is to physically provide a better understanding of changing grain size distribution on the efficiency of conductive fibers.

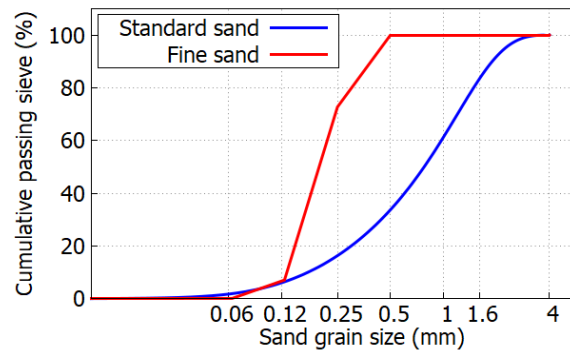


Fig 1: Grain size distribution of two used sands

Sand's volume fraction varies between 0%, 15%, 40% and 50% for both sands. For each of them, 6 carbon fiber contents ranging from 0 to 0.6 % of total volume. This range permits to have a reference mortar (0% fibers), low fibred mortars (0.1% & 0.2%) and High fibred mortar (0.3%, 0.4% & 0.6 %).

A Perrier mixer with 140 rpm was used to mix the components respecting the following procedure: 1 min mix for cement, carbon fibers with sand particles, after water was added with superplasticizer and all the components are mixed for other 2 minutes [18]. Mortar was then poured in a steel mold of 3 samples of 4 X4 X 16 cm. Samples were demolded after 24h then emerged in water for 28 days. They were then kept in stable conditions (20 °C, 50 % RH) for 120 days before measuring their AC impedance. Electrodes were made of copper plates with nickel conductive spray installed on the edges of the samples. AC impedance at 1 KHz was measured using a Hioki impedance analyzer IM3750 [], under a voltage of 0.1 V.

3 Results

Response of fibred cement paste and fibred mortar with different volume fraction of standard sand is illustrated in Fig 2. Real and imaginary impedances at 1 KHz are shown function of fiber's volume fraction. Due to the very high aspect ratio of carbon fibers, the percolation threshold in cement paste is very low and the typical insulative zone below percolation threshold does not show on the graph. The percolating transition zone shows a decrease of real impedance from $10E4$ at 0% FVF to $10E1 \Omega$ at 0.2% FVF. The conductive zone shows a slight decrease of real impedance from $10E1$ at 0.2% FVF to 5Ω . Capacitance decreased from $5*10E3 \Omega$ to 0.03Ω at 0.6 %. The very low value of capacitance above 0.2 % FVF are typical of an almost ideal resistive type behavior.

In presence of a EN 196-1 standard sand volume fraction (SVF) of 15%, real and imaginary impedances were almost identical to the ones of cement paste. With a 40% SVF, sand seemed to reduce the apparent percolation threshold of carbon fibers, with real impedance values of mortar lower than in cement paste below a FVF of 0.3 %. Beyond that point, real and imaginary impedance seemed to remain constant when the FVF was increased from 0.3 to 0.6% surpassing slightly cement paste impedance beyond 0.3% FVF. With a 50% SVF of standard sand, the real and imaginary impedance were higher than for cement paste or mortars with lower sand contents, regardless of the FVF, but followed a similar trend than previously described, with a significant decrease when the FVF was increased from 0 to 0.2 % FVF, while it remained almost constant with FVF ranging from 0.2 to 0.6%.

Real and imaginary impedance of mortar with fine sand measured at 1 KHz are illustrated in Fig 3. Presence of 15% of fine sand volume fraction did not seem to have any significant effect on impedance for all the range of fiber volume fraction. With 40% of fine sand volume fraction, real and imaginary were higher than for cement paste and mortar with a 15% SVF, especially with FVF above 0.3 %, when the SVF of fine sand was 50% of fine sand in mortar, real and imaginary impedance decreased slowly with increasing FVF, with a continuous decrease up to a 0.6% FVF. The real impedance decreased from $10E5$ to $10E3 \Omega$, while the imaginary impedance decreased from $10E4$ to $10E1 \Omega$. In comparison, for the highest FVF of 0.6%, the real and imaginary impedances of cement paste reached values of $10E1$ and $10E-1 \Omega$.

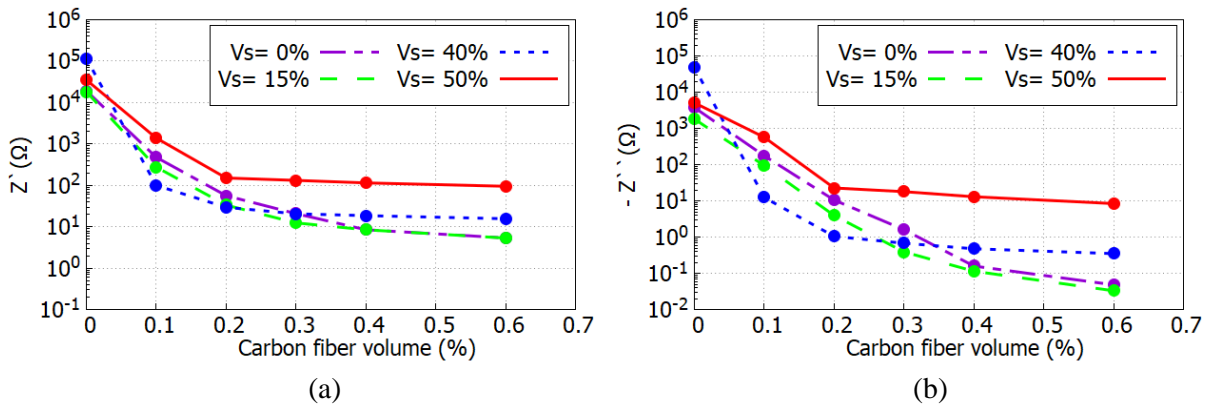


Fig 2: Electrical impedance at 1 KHz function of fiber's volume fraction for different normalized sand volume (a) real part (b) imaginary part

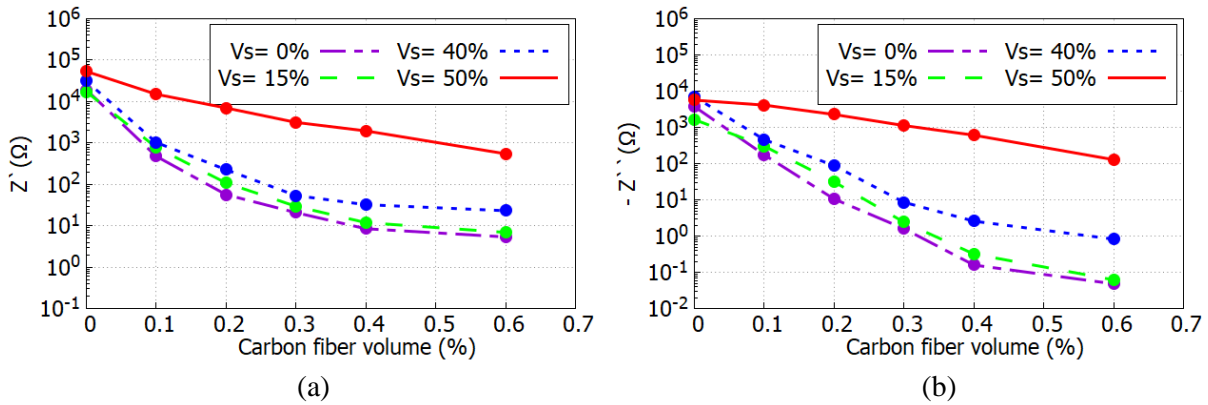
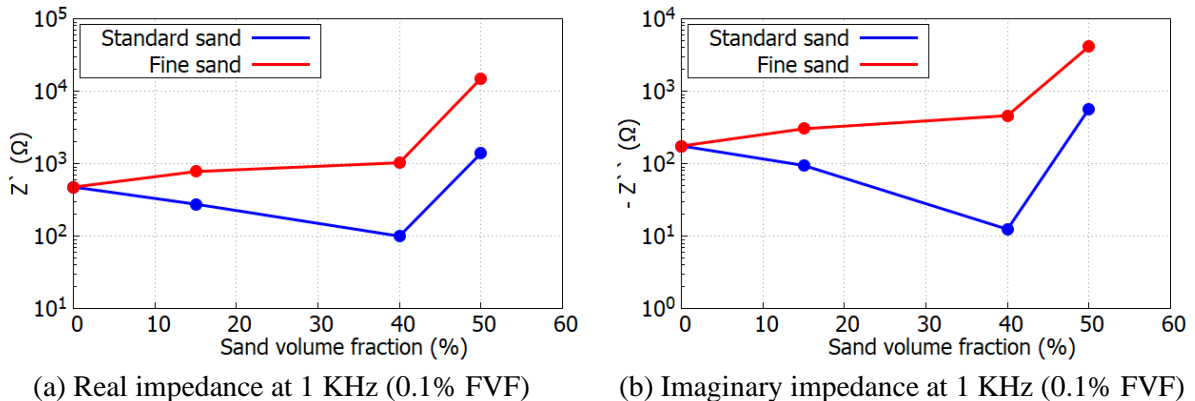


Fig 3: Electrical impedance at 1 KHz function of fiber's volume fraction for different fine sand volume (left) real part (right) imaginary part

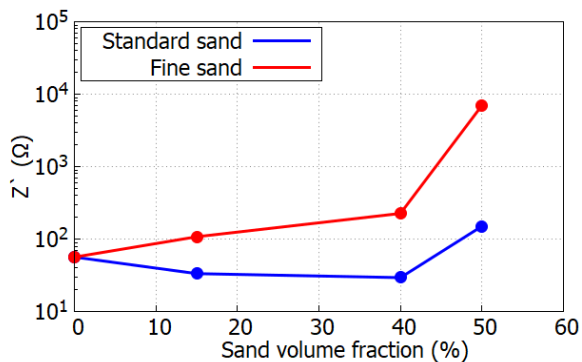
Fig 4. shows real and imaginary impedances of standard sand and fine sand mortars for a given FVF. For all FVF, the real and imaginary impedance of mortars with standard sand were decreasing when the SVF was increased to 15 and 40%, then increasing when the SVF reached 50%. For mortars containing fine sand the real and imaginary parts of impedance increased with an increasing SVF, regardless of the FVF. This increase, however, showed two clear phases, since it was way more significant when the SVF was increased from 40 to 50% than from 0 to 40%.

With 15 % (theoretically diluted sand particles), results for both sands are in the same order of magnitude of cement paste as mentioned above. The deviation between mortars impedance with different sands is seen more clearly with 40% of sand volume fraction (theoretically sand volume is partially connected), where especially at low fiber volume fraction, standard sand seems to reduce mortar's impedance; on the other hand, fine sand tends to increase this apparent impedance, the gap is considerable between both sands at low FVF (< 0.2%).

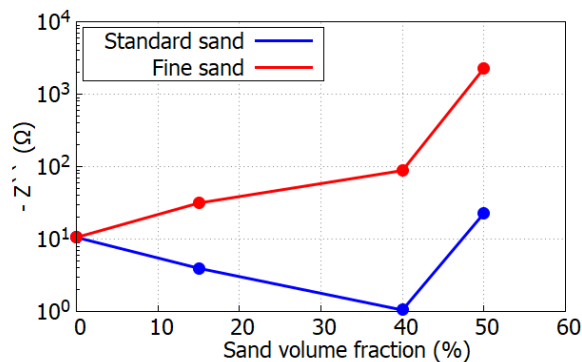


(a) Real impedance at 1 KHz (0.1% FVF)

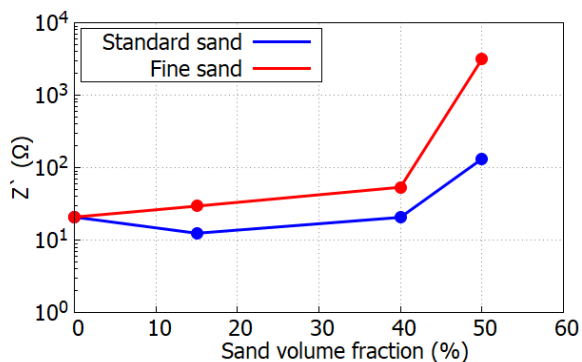
(b) Imaginary impedance at 1 KHz (0.1% FVF)



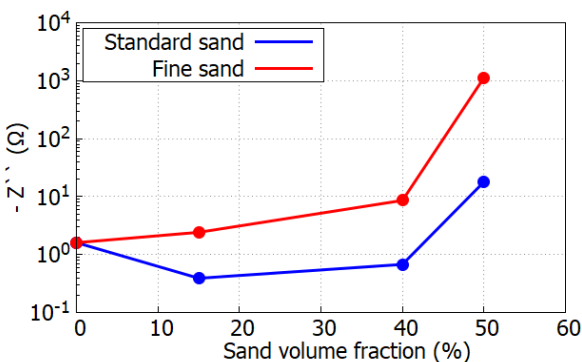
(c) Real impedance at 1 KHz (0.2% FVF)



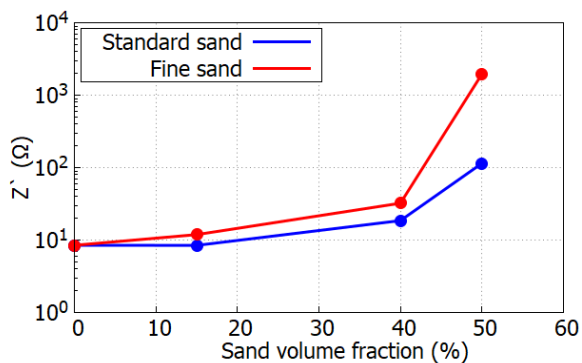
(d) Imaginary impedance at 1 KHz (0.2% FVF)



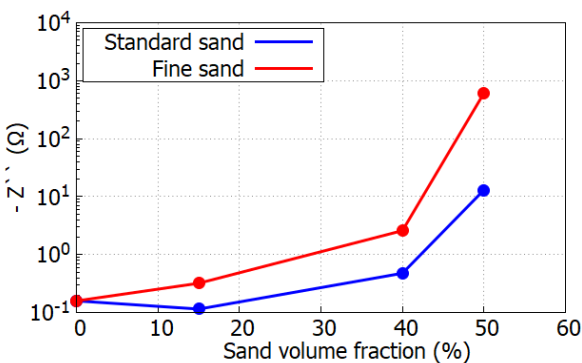
(e) Real impedance at 1 KHz (0.3% FVF)



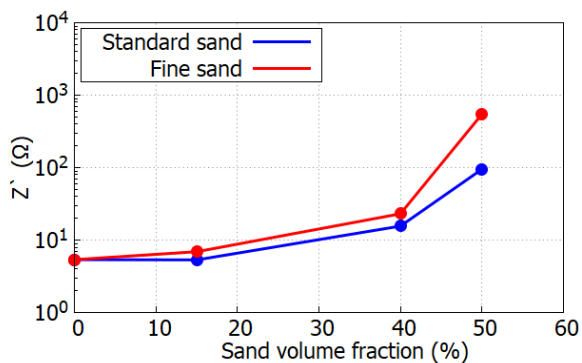
(f) Imaginary impedance at 1 KHz (0.3% FVF)



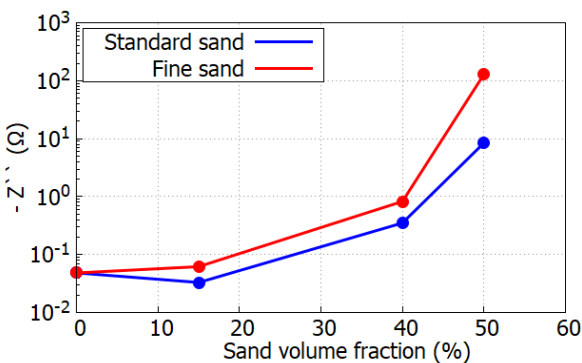
(g) Real impedance at 1 KHz (0.4% FVF)



(h) Imaginary impedance at 1 KHz (0.4% FVF)



(i) Real impedance at 1 KHz (0.6% FVF)



(j) Imaginary impedance at 1 KHz (0.6% FVF)

Fig 4: Electrical impedance at 1 KHz function of sand's volume fraction for well distributed sand and fine sand

4 Discussion

Equations developed in previous studies to estimate percolation threshold base their estimations on fibers morphology [11]. In the case of carbon fibers with a diameter of 7 μm and a length of 6 mm randomly dispersed in a homogeneous matrix, the percolation threshold would be approximatively of 0.14 % according to Celzard [12], and around 0.08% according to Helsing [19]. For cement paste, indeed, those estimations seemed to be relevant since percolation threshold was reached around 0.1 and 0.2% of FVF.

It is however crucial to note that for a given FVF, the relative volume fraction of carbon fibers within cement paste is higher in a mortar than in cement paste. For instance, with a 40% SVF and a 0.2% FVF, the actual volumic proportion of carbon fibers within cement paste would be $0.2/0.6 = 0.33\%$. As a matter of fact, for standard sand, the electrical impedance of mortar with a 40% SVF are lower than for cement paste when the FVF is below 0.33 %. In other words, sand aggregates do not allow carbon fibers to penetrate them and promote the percolation of fibers within cement paste, thus having a beneficial effect on the conductivity of the phase of fibred cement paste within the mortar material. Therefore, the overall electrical impedance of mortar samples was indeed lower than cement paste when the FVF was around the percolation threshold. At higher FVF, however, the insulative nature of the sand aggregates showed a slightly detrimental effect on the overall electrical impedance of the mortar samples.

With fine sand, the presence of sand aggregates did not seem to present any beneficial effect on the electrical impedance of mortars, thus showing that even if the relative volumic proportion of fibres in cement paste was higher, their percolation was not enhanced by the presence of sand at SVF of 15 and 40%.

The results were in clear accordance with the double percolation theory [14], since the only mortar matrices that seemed to hinder the effect of the FVF on the electrical impedance were the ones with the highest SVF of 50 %. This was clear for both standard and fine sand, the latter showing significantly higher values of impedance. Those observations are persistent with previous studies [15][20] stating that the double percolation may not be ensured when the SVF is above the range of 40-50% and sand aggregates might start to be in contact of each other, thus causing discontinuities within the conductive phase of fibred cement paste.

Presence of high standard sand volume fraction limited fibred mortar from reaching low values of impedance, values that were reached with cement paste and mortar with sand volume fraction lower than cement matrix percolation threshold. On the other hand, the effect of high fine sand volume was more radical on continuity of fibers conductive paths, where impedance persisted at high values even with fiber volume fractions that were efficient to reduce drastically impedance of cement paste.

Electrical impedance seemed to be significantly influenced by the grain size distribution as shown in the results above. Reducing grain size interval to finer sand with high volume fraction increased the electrical impedance and slowed percolation phenomenon. Maximum packing density of sand's arrangement inside the mortar could represent one of the key parameters. Experimentally, maximum packing density for both standard (between 0 and 2 mm) and fine sand (between 0 and 0.5 mm) were determined experimentally equal to $\Phi_{c1} = 64\%$ and $\Phi_{c2} = 54\%$ respectively. Mean diameters of both sands were calculated based on grain size distribution showed in figure 1 equal to $d_1 = 744 \mu\text{m}$ and $d_2 = 232 \mu\text{m}$ respectively. Spacing s between particles is calculated based on the assumption that for dense sand presence [21]:

$$\varphi \simeq d^3 / (s + d)^3 \quad (1)$$

Knowing that for $s = 0$, $\varphi = \varphi_c$, mean spacing between sand grains is estimated using Eq. 2:

$$\frac{\varphi}{\varphi_c} = \frac{1}{(1 + s/d)^3} \quad (2)$$

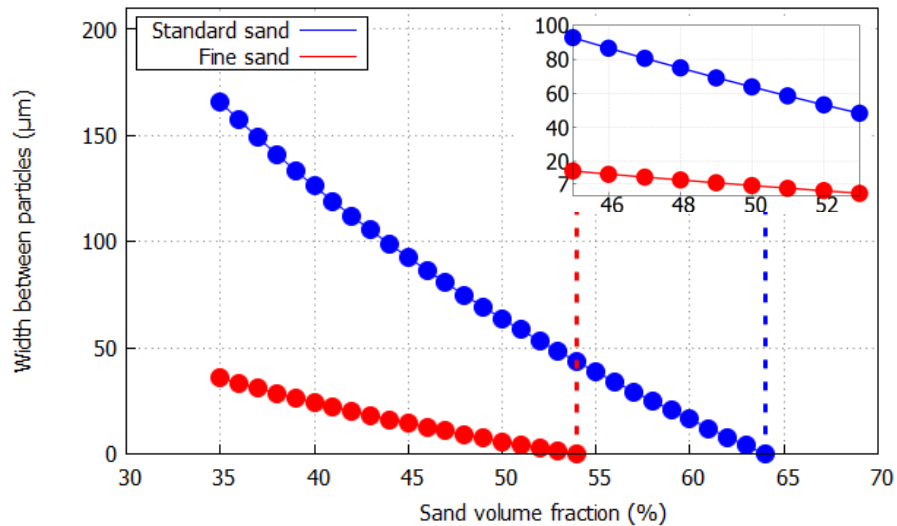


Fig 5: Distance between sand particles function of sand's volume fraction

Reducing sand's distribution interval minimises its maximum packing density. This effect, combined with the smaller diameter of sand particles, reduces the mean paste width between sand particles according to eq (2) and as shown in Fig 5. The reduction of mean distance between particles to small values of few μm s, in case of dense fine sand, would reflect a heavier presence of sand spacing width equal or smaller than fibers diameter. This effect combined with the increase in particles number (in case of fine sand), would multiply the narrow spacings between sand particles. therefore, having negative effect on the continuity of fibred cement paste phase. This effect of hindering the continuity of the conductive phase, more pronounced in case of fine sand, would increase the impedance value of mortar in case of high sand volume fraction. In such case, the presence of sand is expected to have a detrimental effect on the homogeneity of fiber dispersion within the cement paste phase by creating a strong disparity in the local volumetric concentration of fibers within cement paste

Further publications will be focused on showing the Nyquist plots of mortar with different sand volume fraction and different grain size distribution, and their sensing behavior under mechanical loads.

5 Conclusion

Fibers prove efficiency as doping agents to reduce resistivity by a factor of $10E4$ when the double percolation is ensured (percolation of fibers within cement paste and percolation of cement paste within mortar) in presence of enough conductive volume fraction to create conductive paths inside mortar. Percolation threshold of carbon fibers within a homogeneous matrix was estimated between 0.1 and 0.2% by percolation theories [12][19] and were in accordance with experimental results with cement paste.

Fibers efficiency was confirmed to depend on hosting matrix. Increasing sand's volume fraction proved significant influence on fibers percolation. This influence dependend on the grain size distribution of sand, as well as its volume fraction. For SVF up to 40%, the standard sand had a beneficial effect on the electrical impedance at FVF below 0.3%, and a very slight detrimental effect for FVF above 0.3%. For fine sand, no beneficial effect of sand aggregates on the impedance was observed. For both sands, the impedance of mortars with a 50% SVF was way higher than for cement paste, thus confirming the relevance of the double percolation theory [14].

The effect of grain size distribution of sand was illustrated. Finer sand proved higher impedance, i.e., less continuous conductive paths compared to cement paste, causing a slow decrease in resistivity function of carbon fibers. This could be related to its arrangement closer to monodisperse, reducing maximum packing density, and consequently for a given sand volume fraction, decreases mean spacing between sand particles. This effect, combined with the higher number of sand particles, could potentially cause more considerable discontinuities in fibred cement paste and consequently higher impedance values. The sand aggregates might have a negative effect on the dispersion of fibers within cement

paste phase, as well as creating insulative blocking points within the network of fibres, therefore mitigating the expected beneficial effect of the percolation of fibers on impedance reduction.

Further work is needed to study sand's effect on fibers tortuosity, that could have significant effects as well, especially with high aspect ratio fibers as well as as a better understanding of effect of fine sand effect on porosity of cementitious matrix.

References

- [1] P. Xie, P. Gu and J.J. Beaudoin, (1996) Electrical percolation phenomena in cement composites containing conductive fibres. *Journal of materials science*.
- [2] Z.Q. Shi and D. D. L Chung. (1999) Carbon fiber-reinforced concrete for traffic monitoring and weighing in motion. *Cement and Concrete Research*.
- [3] B. Han, S. Ding, X. Yu (2015) Intrinsic self-sensing concrete and structures: A review.
- [4] D. D. L. Chung. (2002) Piezoresistive Cement-Based Materials for Strain Sensing. *Journal of intelligent Material Systems and Structures*.
- [5] L.X. Zheng, X. Song, L; Zhuo (2002) Investigation on the Method of AC Measurement of Compression Sensibility of CF, *Cement Journal of Wuhan Urban Construction Institute*.
- [6] E. Teomete (2016) The effect of temperature and moisture on electrical resistance, strain sensitivity and crack sensitivity of steel fiber reinforced smart cement composite smart *Materials Structures*
- [7] Jeng-Maw Chiou, Qijun Zheng, D.D.L. Chung, (1989) Electromagnetic interference shielding by carbon fiber reinforced cement, *Composites*,
- [8] Sassani, A et al. (2018) Carbon fiber-based electrically conductive concrete for salt-free deicing of pavements, *Journal of cleaner production*.
- [9] Ping Xie, Ping Gu, Zhongzi Xu, and J. J. Beaudoin., (1993) A rationalized a.c. impedance model for microstructural characterization of hydrating cement systems. *Cement and Concrete Research*, 23(2):359-367.
- [10] B. Han, X. Yu and J. Ou, (2014) Chapter 6 - Sensing Mechanisms of Self-Sensing Concrete, Editor(s): Baoguo Han, Xun Yu, Jinping Ou, *Self-Sensing Concrete in Smart Structures*, Butterworth-Heinemann,
- [11] I. Balberg (1985) Universal percolation-threshold limits in the continuum. *Physical Review B*
- [12] A. Celzard, E. McRae, C. Deleuze, M. Dufort, G. Furdin, and J. F. Maréché. (1996) Critical concentration in percolating systems containing a high-aspect-ratio filler. *Physical Review B*
- [13] L. Berhan and A. M. Sastry. (2007) Modeling percolation in high-aspect-ratio_ber systems. I. Soft-core versus hard-core models. *Physical Review E*.
- [14] S. Wen, D.D.L. Chung, (2007) Double percolation in the electrical conduction in carbon fiber reinforced cement-based materials, *Carbon*
- [15] E. J. Garboczi, L. M. Schwartz, and D. P. Bentz. (1995) Modeling the influence of the interfacial zone on the DC electrical conductivity of mortar. *Advanced Cement Based Materials*.
- [16] F.J. Baeza, D.D.L. Chung, E. Zornoza, L.G. Andi6n and P. Garc6s (2010). Triple Percolation in Concrete Reinforced with Carbon Fiber. *ACI Materials Journal* volume 107 – 4
- [17] B. Chen, K. Wu, W. Yao, (2004) Conductivity of carbon fiber reinforced cement-based composites, *Cement and Concrete Composites*.
- [18] H. Allam, F. Duplan, J.P. Clerc, S. Amziane, and Y. Burtschell, (2019). Etude comparative de techniques de mesure et de malaxage pour mortiers fibr6s type « smart concrete ». *Academic Journal of Civil Engineering*, 36(1), 562-566. <https://doi.org/10.26168/ajce.36.1.120>
- [19] J. Helsing, A. Helte, (1991) Effective conductivity of aggregates of anisotropic grains, *Journal of Applied Physics*
- [20] D.N. Winslow, M.D. Cohen, D.P. Bentz, K.A. Snyder, E.J. Garboczi, (1994) Percolation and pore structure in mortars and concrete, *Cement and Concrete Research*
- [21] B. Andreotti, Y. Forterre, and O. Pouliquen. (2012) *Les milieux granulaires - Entre fluide et solide: Entre fluide et solide*. EDP Sciences.

Transmission length test for prestressing cable after loss of mechanical anchorage

Rafał Walczak and Wit Derkowski – supervisor

*Chair for Reinforced Concrete and Prestressed Concrete Structures,
Cracow University of Technology,
24 Warszawska Street, Cracow 31-155, Poland*

Abstract

The test of transmission length for a prestressing cable in case of loss of its mechanical anchorage is presented in the paper. In order to determine the work of the prestressing cable in the case of anchorage failure, a controlled cut-off of the prestressing cable located in the upper flange of the member was conducted. The test was carried out on the precast post-tensioned concrete crane beam that was operated for over 50 years. During the test, the strain variation was recorded using four methods: electrofusion strain gauges, DIC, DOFS, and High-frequency DOFS. The test results indicate that after losing the cable anchorage, the prestressing force is transmitted through the bond of the prestressing wires to the cement grout, providing that the injection was done properly and the prestressing wires are tightly wrapped. The article also highlights the problem of the partial filling of the cable ducts.

1 Definition of the research problem

Plenty of post-tensioned concrete structures which were erected throughout Europe in the mid-20th century are still in operation. It is estimated, that currently there are about 100,000 precast post-tensioned concrete elements built into building structures in Poland. Figure 1 illustrates a track for the overhead cranes made of post-tensioned beams – one example of the precast post-tensioned structures that are still frequently used.

Such structures have been reaching the period of their designed durability or they have exceeded it, hence the question on durability and safety of such structures is still being asked and actual. One of the most important issues in the assessment of existing post-tensioned concrete structures is how to determine safety of the structure in the situation of loss of tendons' mechanical anchorage (due to corrosion or mechanical damage of the uncovered anchorage).



Fig. 1 Post-tensioned beam track for the overhead cranes inside the industrial plant (left) and external post-tensioned beam track for the overhead cranes (right).

It is assumed that, when the cables are properly injected with cement grout, after the loss of the mechanical anchorage, the prestressing force will be bond transmitted over a certain transmission length. Destructive experiments of post-tensioned, precast crane beams were conducted by Derkowski and Walczak [1], but their results are not sufficient to accurately assess the technical condition of precast

post-tensioned elements after their designed period of use. It seems necessary to broaden the knowledge and create the tools which are needed to determine the actual safety of structures which are exposed to the loss of prestressing cable anchors. Research on the transmission length for Freyssinet type prestressing cables, commonly used in the 1960s and 1970s, consisting of a parallel smooth wires, have probably not been conducted in any scientific centre in the world so far.

The previous researches of post-tensioned structures [2] have shown that cable ducts are relatively often only partially filled with injection grout. This may be caused for example by leaks between the cable duct and anchoring, poor consistency of the grout, sedimentation of the injection grout or improper ventilation of the duct [3]. This situation not only causes the corrosion hazard of unprotected fragments of prestressing tendons, but also makes the cables work as unbounded tendons.

2 Experimental test

The subject of the experimental tests are prestressed concrete crane beams disassembled after more than fifty years of being used in an industrial plant with favourable environmental conditions (low chemical aggressiveness, low humidity). During their service life, they served as a track for overhead cranes with a lifting capacity of 12.5 tons. These are typical I-section prefabricated post-tensioned concrete crane beams, with the height of 800 mm and modular span of 6.0 m. Each beam is prestressed with five bonded cables. The prestressing cables are anchored in steel cone anchorages with block dimensions of 100x100 mm. The cross-section and the view of the beam with cable anchorages are demonstrated in Fig. 2. In the test beams, the anchorages of prestressing cables have never been protected against corrosion. The anchor blocks and protruding ends of the prestressing wires are covered with corrosive coating, however no significant corrosion damage has been observed. According to the catalogue of Typical Projects of Industrial Construction [4], the beams correspond to the KBP 80/6 type with the I-st variant of prestressing reinforcement, which provides for one upper and four lower prestressing cables (see Fig. 2). The design assumes prestressing with rectilinear 12Ø5 mm cables of II-nd grade steel with a nominal strength of 15,000 at, which after conversion to SI units yields the value of 1,471 MPa.

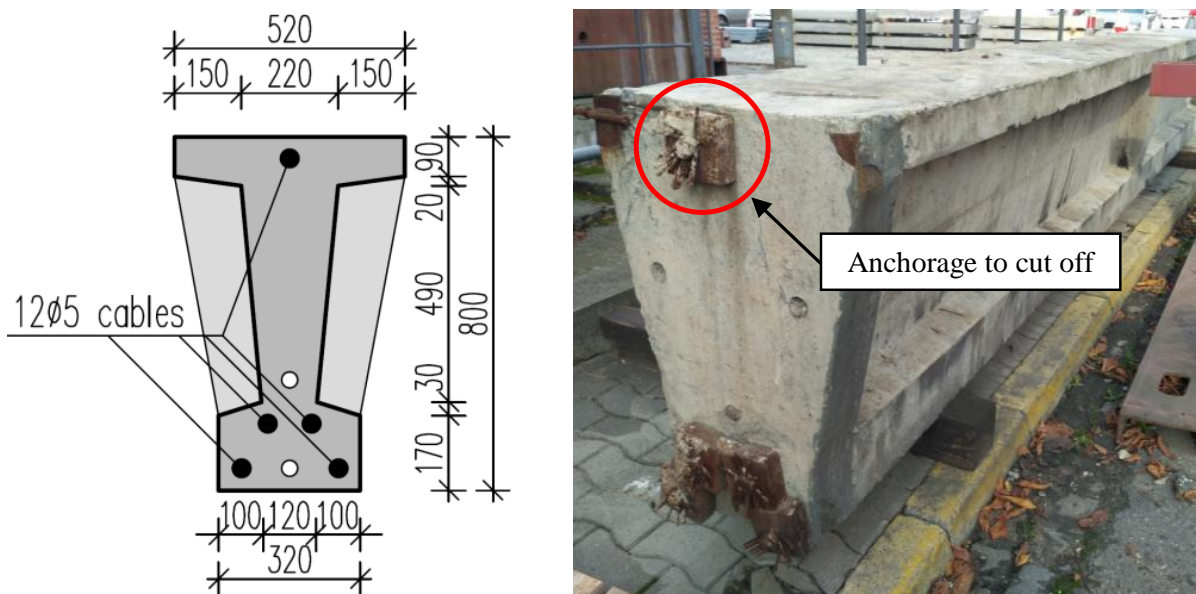


Fig. 2 Cross-section (left) and view (right) of the tested beam.

The aim of the test was to measure the transmission length for the prestressing cable made of parallel smooth wires in the cable duct injected with cement grout at the situation of cutting off the cable anchorage. The cut off was performed by a circular saw (Fig. 4 left), which caused a gradual release of the tension of individual wires of the cable.

During the cutting off the upper prestressing cable's anchorage, the changes of the concrete strain at the prestressing cable area were measured. Data acquisition with four measuring systems were applied: strain gauge system, digital image correlation method (DIC), static distributed optic fiber sensing (DOFS) and high-frequency distributed optic fiber sensing (High-frequency DOFS). Fig. 3 shows schematically the tested element and the arrangement of measuring sensors.

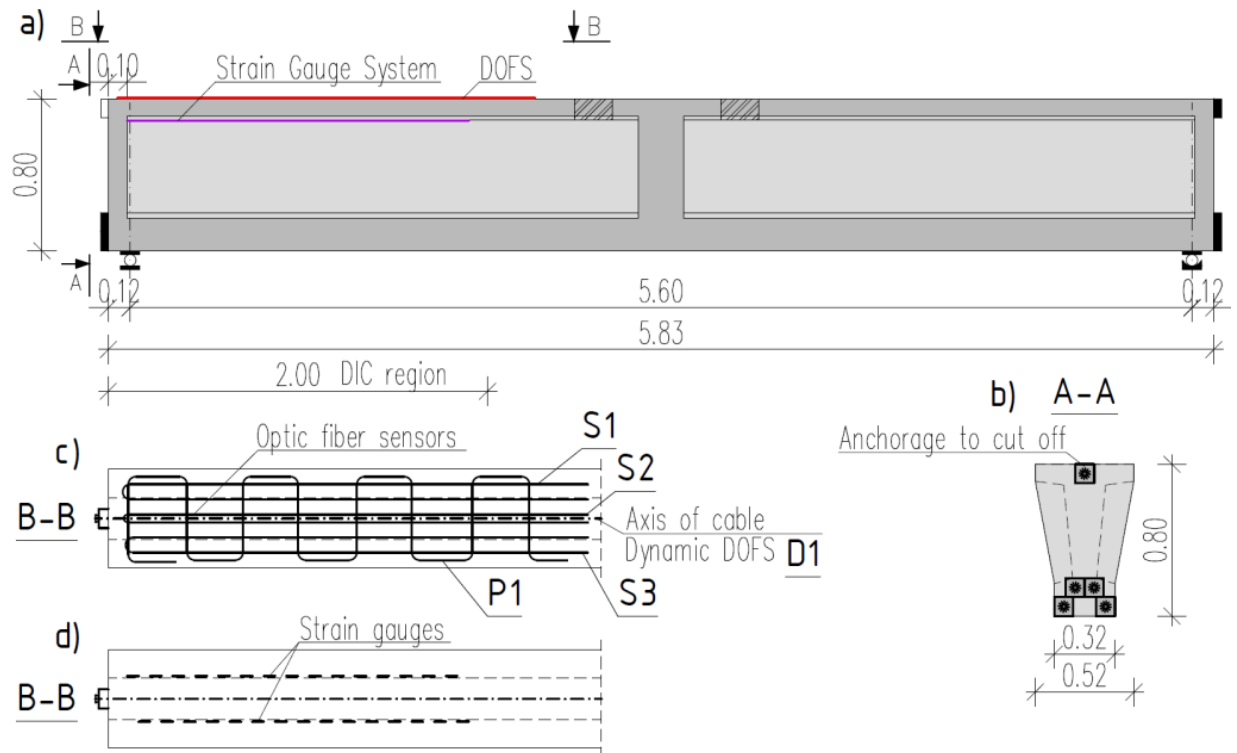


Fig. 3 Scheme of the tested element with the arrangement of measuring points a) longitudinal view; b) front view; c) top view (DOFS); d) top view (strain gauges).

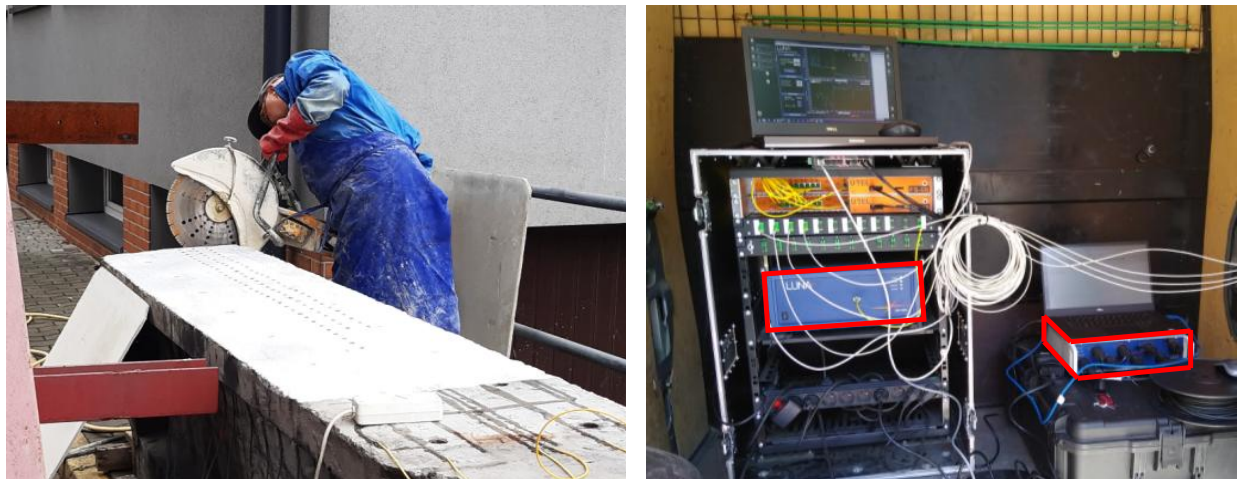


Fig. 4 Cutting process using circular saw (left), optical backscatter reflectometer OBR and optical interrogator in use (right).

During the research, two DFOS measuring approaches based on Rayleigh scattering were introduced: dedicated for static measurements using optical backscatter reflectometer OBR and high-frequency measurements using optical interrogator (see Fig. 4 right). Standard telecom fibre SM9/125 in its primary acrylic coating was selected, as it is the most relevant for short-term surface measurements. The optical fibres were primary shaped and stabilise by a tape and then glued with two-component epoxy resin (structural adhesive). Five measuring fibers were finally installed, four for static measurements and one for high-frequency. Static DOFS are increasingly used for strain and crack analysis of concrete members [5] however, the High-frequency DOFS technology was used to measure the strain of the structural element for the first time ever in Poland.

Moreover above the beam's top surface, the camera was installed in order to take pictures for digital image correlation (DIC) method application.

Also, an additional measuring technique was applied in the form of conventional electrofusion spot strain gauges with the base of 60 mm, arranged in series over the side surfaces. Selection of the side surface rather than the top surface was determined not to cover the DIC measured top surface. In

addition to check if the location of the sensors can influence the final determination of the transmission length.

Vary of measuring methods were assumed to verify results since this was a preliminary test such type. As well as to choose the most advantageous measurement methods for further research. After the test, a top cable duct was opened halfway along the length of the beam to verify the filling with cement grout and a cross-section was cut out of the tested beam.

3 Results of the experiment

After cutting off the anchorage, incomplete filling of the cable duct was observed (Fig. 5 left). The opening of the cable duct (Fig. 5 right) showed that along the whole length of the cable the injection did not fully fill the duct. In the first 0.3 m from the anchorage, the four upper prestressing wires were not covered with grout (see Fig. 5 left). At a distance of 1.4 m from the anchorage, two wires remained uncovered (see Fig. 5 right), while one prestressing wire remained uncovered on the rest of the beam. Observations of the cross-section cut out of the tested element (Fig. 6) showed that the problem of incomplete infectivity occurs in all of the cable ducts.



Fig. 5 Front view of prestressing cable (left) and opened cable duct view (right).



Fig. 6 Unproperly filled lower cable ducts on cut out cross-section of the tested beam.

Fig. 7 illustrates the longitudinal strain variation recorded by the static DOFS measurement by all 3 longitudinal optical fibre ducts (6 fibre lines - 3 measurements on each line + reference zero measurements). Based on the distribution of fibre optical sensors on the beam surface, it was also possible to create a map of longitudinal strain variations which is demonstrated in Fig. 8.

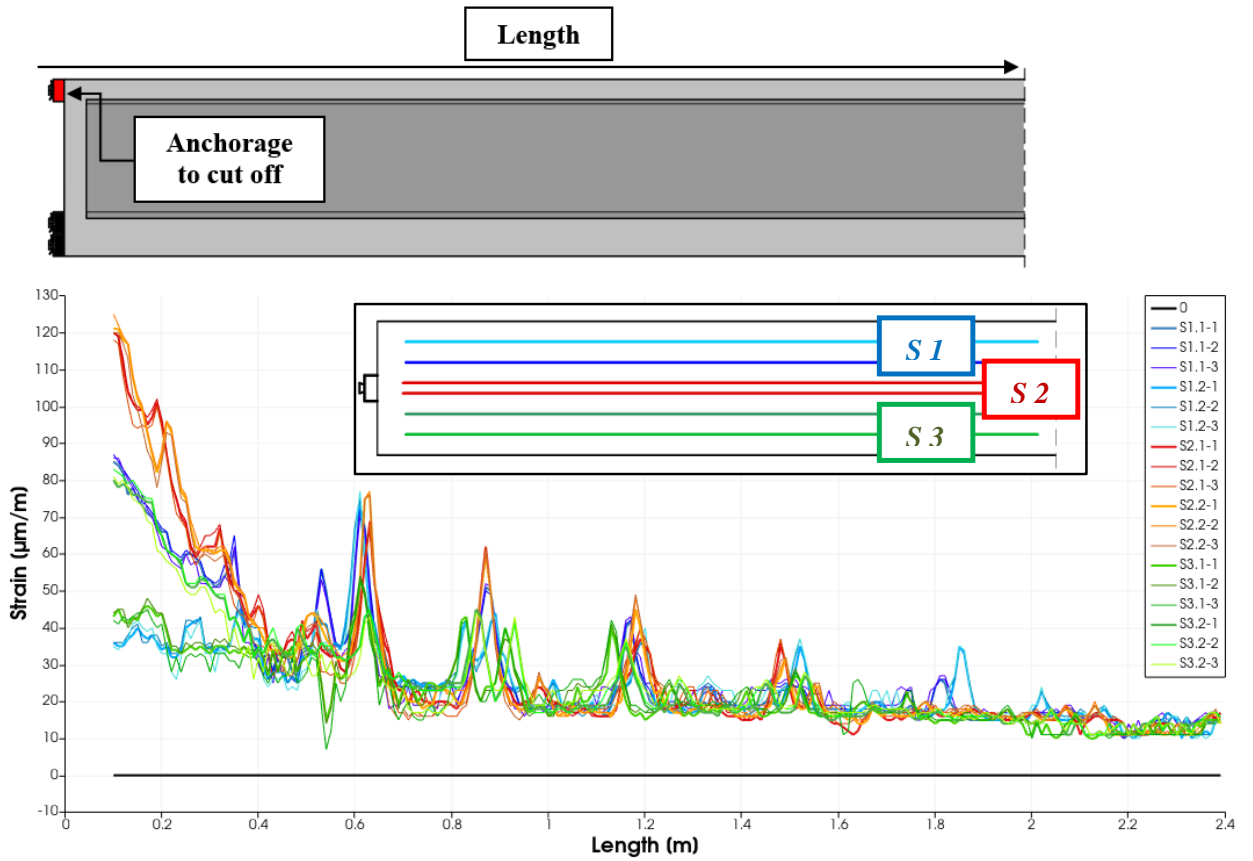


Fig. 7 Graphs of longitudinal strain changes along the length of optical fibre sensors (all optical fibre ducts). Static DOFS measurements.

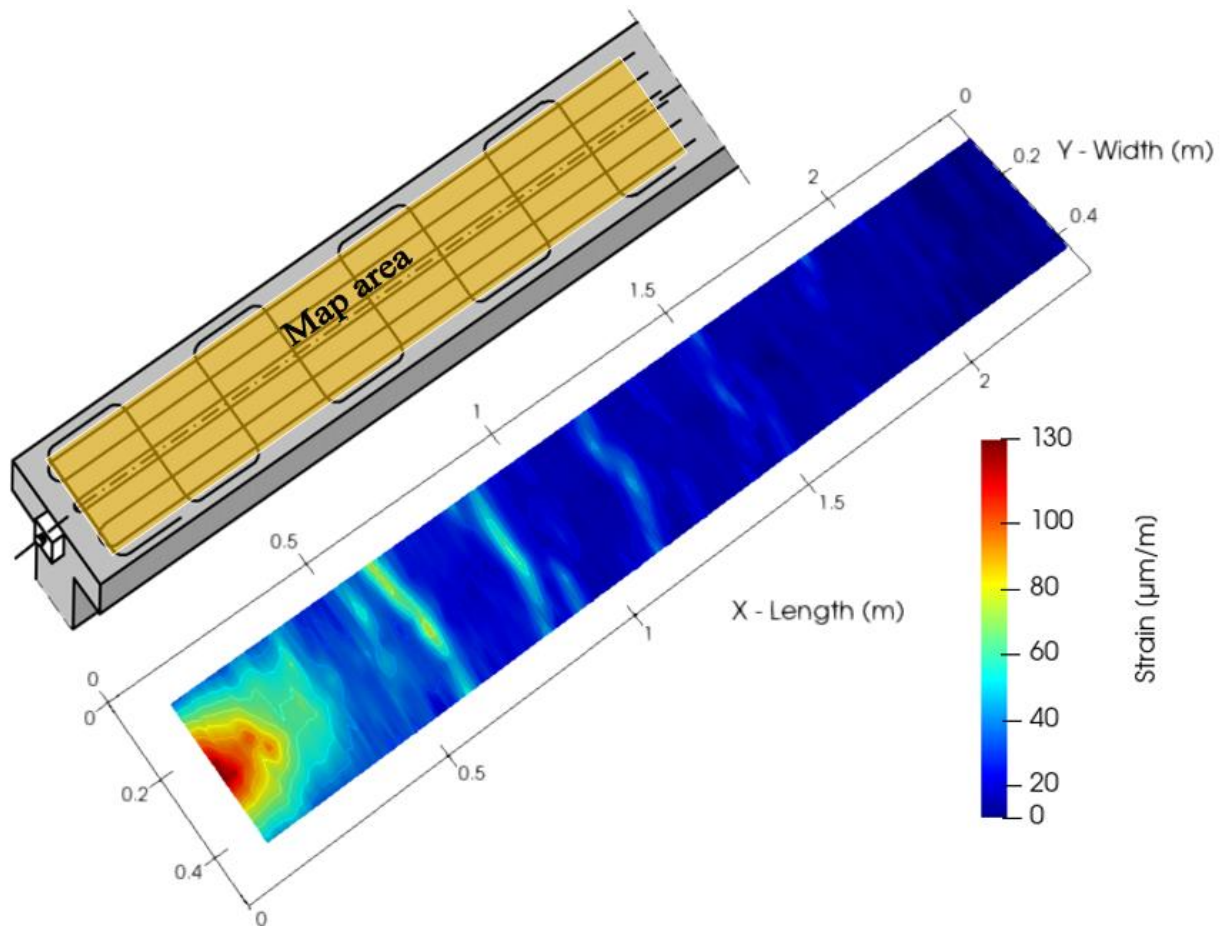


Fig. 8 Map of longitudinal strain variations. Static DOFS measurements.

High-frequency DOFS and Strain Gauge System recorded the change of concrete strain not only along the element also in the time domain as well. Fig. 9 shows the variation in time of the increment of longitudinal strains obtained by High-frequency DOFS and by electrofusion strain gauges. The values of strain variations were presented for representative measuring points, for the optical fibre at a distance of 100 mm and for the strain gauge at a distance of 190 mm from the beam face. The abscissa represents the time of the test in seconds, while the ordinate represents the increment of strains in micro-deformations.

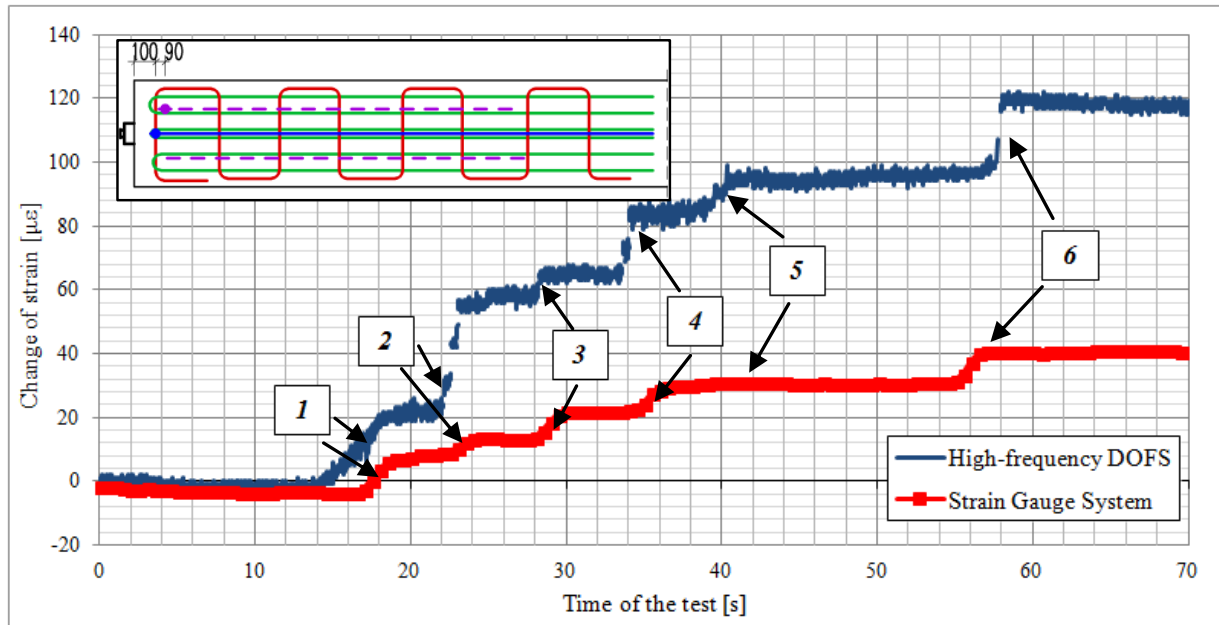


Fig. 9 Comparison of longitudinal strain variation during the test for electrofusion strain gauges and High-frequency DOFS measurements.

The graph illustrates the gradual increments of strain. Six strain increments can be distinguished and each increment is observed when a given batch of wires is cut through. The graphs representing that both measurement methods are consistent, and the stepped strain increments overlap in time (the value of the step no. 5 recorded with a strain gauge was $8 \mu\epsilon$ and it is hardly visible on this scale of the graph). The maximum longitudinal strain variation total $122 \mu\epsilon$ (High-frequency DOFS) and $47 \mu\epsilon$ (Strain Gauge System). The value of strain variation recorded by strain gauges is much smaller than the one recorded by optical fibre measurements, which is a consequence of the different location of the strain gauges, glued at the connection with the web (125 mm from the cable axis).

Difficult test conditions resulted in the inability to record a relatively small strain variation that occurred at the surface of the tested member by using the DIC method. This was associated with the large area being observed, so the size of a single-pixel in the image was relatively large. Another difficulty was the presence of splashing water while cutting the anchorage off. Water changes the texture and shape of the measurement markers during the cut-off, and as a result, interfere with the test results.

The strain variation maps obtained by the DIC method have only revealed the background noise, and therefore the decision was made that DIC measurements will not be used in the further tests of transmission length.

4 Results summary

Fig. 10 shows the concrete strain changes recorded with optic fiber sensors - static measurement of longitudinal deformations along the fiber length, static measurement of transverse deformations presented along the tested element and high-frequency measurement of longitudinal deformations along the fiber length. The diagrams also present the changes of longitudinal deformations along the tested element obtained from strain gauge measurements. The graph has been completed with the reference zero measurement (made before cutting off the anchorage).

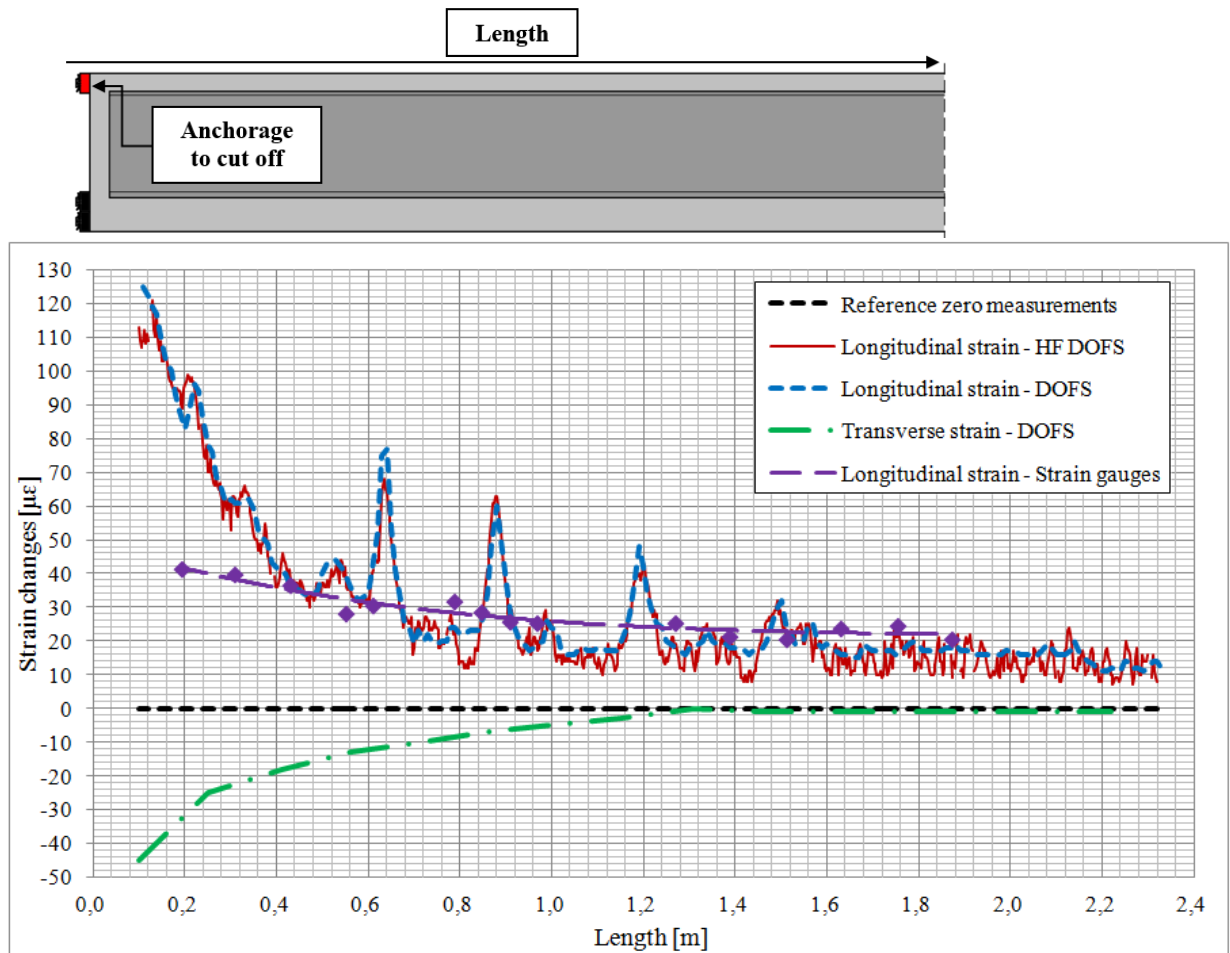


Fig. 10 Graphs of the longitudinal and transverse strain variations along the tested element.

The results of the test which contains the transmission length, maximum longitudinal strain and maximum transverse strain obtained during the test with each measurement method are summarised in the Table 1. Positive strain values (+) represent the tension resulting from loss of prestressing force over transmission length of the cable, while negative values (-) represent compression. The approximate transmission length is arbitrarily considered to be the distance from the front of the element on which the increase of concrete strain disappears asymptotically.

Table 1 Summary of the test results.

Measurement method	Transmission length [m]	Maximum longitudinal strain [$\mu\epsilon$]	Maximum transverse strain [$\mu\epsilon$]	Comment
DFOS	~ 1.1 m longitudinal	125	- 45	Nearest sensor 54 mm to the cable axis
	~ 1.2 m transverse			
High-frequency DFOS	~ 1.1 m	122	-	Sensor 50 mm directly above the cable axis
Strain Gauge System	~ 1.2 m	47	-	Strain gauges 125 mm from the cable axis
DIC	n\	n\	n\	No results acquired

The accuracy of transmission length estimation depends on the spatial resolution. In case of longitudinal, both static and high-frequency DFOS measurements, it is greater than 10 mm. However, for static DFOS in transverse direction the accuracy is about 300 mm and for spot strain gauges is about 100 mm.

5 Conclusions

The graphs of strain changes recorded on the length and width of the beam show their clear asymptotic disappearance. In the analysis of the results of the test it was assumed that the maximum distance at which changes in longitudinal and transverse deformations were recorded can be considered as the transmission length of the cable. However, it should be noted that the loss of mechanical anchorage of the prestressing wires, that were not covered with injection grout, causes a constant change of strain along the whole element. In this case, the prestressing force resulting from the tension of the uncovered wires is completely lost. The transmission length for the tested beam was determined on the basis of the experiment results. Each measuring method indicates very similar results and transmission length is about 1.1 - 1.2 m.

The presented test has shown that the measurements conducted with the distributed optic fibers enable to precisely determine the transmission length of the prestressing force. In the case of using High-frequency DOFS, it also gives the opportunity of a precise analysis continuous in length and time. Furthermore, it is possible to analyse the action of the element in case of rupture the individual wires in the cable and gradually transmitted prestressing force.

Acknowledgements

The authors acknowledge the support of the PROM programme no.PPI/PRO/2019/1/00018/U/0000 1 which is co-financed by the European Social Fund under the Knowledge Education Development Operational Programme.

References

- [1] Derkowski, Wit, and Walczak Rafał. 2019. "Problem of Condition Assessment of Precast, Posttensioned Concrete Crane Beams in an Extended Period of Use." Paper presented at fib Symposium 2019, Cracow, Poland, May 27-29.
- [2] Moravčík, Martin, and Bujňáková, Petra, and Krkoška, Lukáš, and Koteš, Peter. 2016. "Diagnostic assessment of one of the first generation of prestressed concrete bridges in Slovakia." *Procedia Engineering* 156:257–263. Accessed March 9, 2020. doi:10.1016/j.proeng.2016.08.295.
- [3] Jaromniak, Andrzej. 2019. "Zagrożenia mostów kablobetonowych powodowane wadliwym iniektem." *Inżynieria i Budownictwo* 12:564–570.
- [4] Zieliński, Zenon. 1961. "Typowe belki podsuwnicowe z betonu sprężonego." *Inżynieria i Budownictwo* 2(14):5–10.
- [5] Sieńko, Rafał, and Zych, Mariusz, and Bednarski, Łukasz, and Howiacki, Tomasz. 2019. "Strain and crack analysis within concrete members using distributed fibre optic sensors." *Structural Health Monitoring* 18:1510–1526.

Validation of a numerical model for singly reinforced corroded concrete beams

Hussein Nasser, Charlotte Van Steen, Rutger Vrijdaghs, Lucie Vandewalle, Els Verstrynghe

*Department of Civil Engineering,
Katholieke Universiteit Leuven (KU Leuven),
Kasteelpark Arenberg 40, Heverlee, 3001 Belgium*

Abstract

Numerical models of corroded reinforced concrete beams are often based on damage relations. The choice of relations and modelling approaches have varied in the literature. Therefore, the paper explains the choice of a proper set of damage relations and validates the approach on the results of three-point bending tests in terms of load-displacement relations, crack patterns and failure mode. The damage to the reinforcement is input as average and variable cross-section loss which is coupled by a model to reduce its material properties. The bond loss is based on calibrated multi-linear curves from pull-out tests done in the framework of the same project. The results show that reducing the steel material properties is important while both the average and the variable section loss yield good predictions for the considered corrosion range. Incorporating the suggested bond-slip law in the corroded beam model affects the cracking pattern, however, no full agreement between numerical and experimental crack patterns was obtained.

1 Introduction

Many existing reinforced concrete (RC) structures suffer from chloride-induced corrosion damage. Due to rust formation, excessive cracking and spalling, they pose serviceability and safety concerns. Besides the level of damage determined by inspection, predicting the residual structural capacity can be helpful for the process of decision making with regards to renovation and lifetime extension of existing structures. Therefore, numerical modelling becomes an essential tool.

Many attempts were made to model the mechanical behaviour of corroded reinforced concrete beams. These models were based on the reduction of section and material properties using damage relations. Steel section loss is modelled using a pitting factor which varies between 2 and 10 [1], spherical pit models were also used [2] and most authors opted for total average cross-section loss without taking into account the variation of the corrosion damage. Moreover, steel material properties were altered in addition to section loss [3]. Cover cracking has been modelled as a reduction to the concrete tensile and compressive strength [4, 5]. Furthermore, as bond degradation causes a shift in failure mode, it was suggested to model it using a power decay law based on pull-out tests [6], scaling the fib bond-slip law [7] or shifting the curve as a function of the corrosion level [8]. The variety of the empirical damage relations is a result of the different experimental conditions upon which they were calibrated. This makes it challenging to choose the relation that would simulate the corroded beam under certain conditions. The literature also shows different modelling methods. For example, beams of Rodriguez et al. [9] were modelled differently by different authors [7, 10] who applied modifications according to different damage relations. Therefore, there is a need to obtain an understanding of the effect of different modelling approaches so that the choice of damage relation can be made in an informed manner.

In this paper, firstly, the experimental test program and results are presented of accelerated corrosion and bending tests performed by the authors. The availability of detailed test data regarding material properties, cracking and corrosion measurements offer an enhanced method of validating the numerical models. Secondly, the developed numerical model is presented. The model takes into account both average and variable cross-section loss as opposed to the literature, where only the average section loss is investigated. This aims to investigate the importance of taking the spatial variation of corrosion damage into account. Furthermore, a corrosion-dependent bond-slip law is implemented. The empirical relation is based on the results of pull-out tests from a related experimental campaign [11] at KU Leuven. Finally, numerical predictions are compared with experimental data in terms of load-deflection

curves and cracking patterns as obtained from LVDT's and digital image correlation (DIC), respectively.

2 Overview of the experiments

The experimental program consisted of accelerated corrosion followed by three-point bending tests on singly reinforced concrete beams. They were reinforced with one ribbed rebar of diameter 14 mm and no stirrups were used. The beam section has a dimension of 150x200 mm and a length of 1.8 m. Nine beams were tested in total. Three were non-corroded while the others were subjected to accelerated corrosion, in pairs, up to 5%, 10% and 15% of mass loss. Finally, naming the beams is done by using three characters, for example; 10R1, where the first number indicates the corrosion level, the letter indicates the type of rebar (Ribbed), and the final number indicates the sample number (one pair per batch).

2.1 Material properties

Each pair of beams was produced from the same concrete mix along with cubes and prisms that were tested at 28 days. Three additional cubes were made for the batches of corroded beams which were tested after the corrosion process (on the day of the bending test). The corrosion process of 10R1 and 10R2 was started a month apart; therefore nine additional cubes were made for this batch. Fig. 1 shows the variation of the compressive strength which also shows that it increases after 28 days. The average flexural strength varies between 4 MPa and 5.4 MPa. Finally, the applied steel grade for the rebar is BE500, with an average yield strength of $f_{ym}=550$ MPa.

2.2 Corrosion experiment

The beams were subjected to an accelerated corrosion process by placing them upside-down and using a bottomless tank placed on top and filled with 5% NaCl solution [Fig. 2]. A metal plate was immersed in the solution, which acted as the cathode. Both the steel rebar and the plate were connected to a power supply which provided a current density of $100 \mu\text{A}/\text{cm}^2$. Only 1.5 m of the length of the rebar was exposed to the salt solution while the rest was coated with an anti-rust primer. Even though the salt contamination was uniform, cutting the rebar into pieces of 20 cm showed variation in the cross-section loss, see Fig 3.

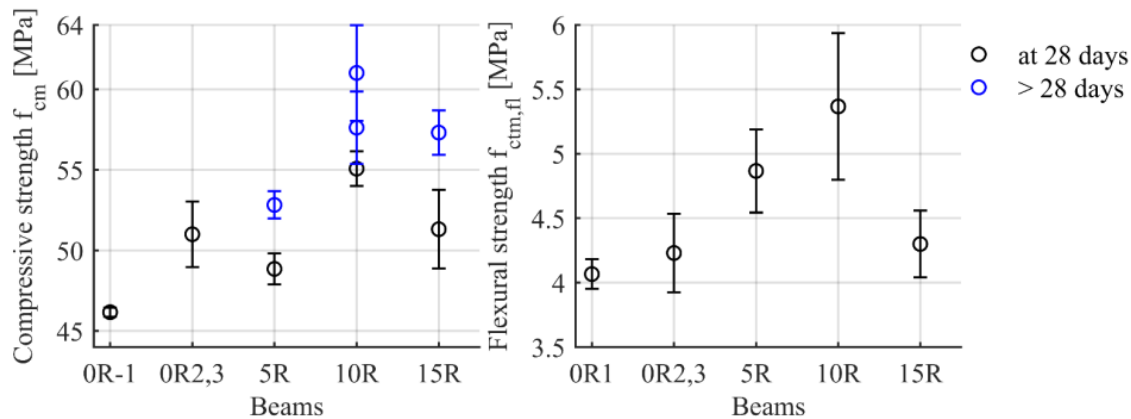


Fig. 1 The average compressive strength of three cubes (left) and the average flexural strength of three prisms (right).

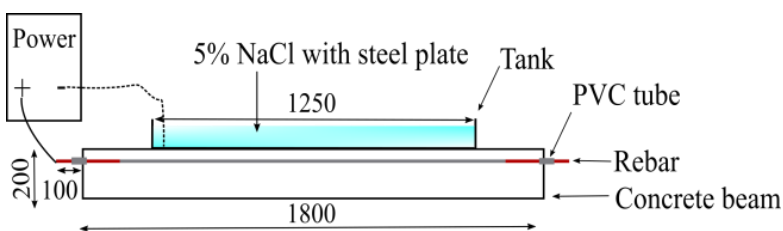


Fig. 2 Corrosion set-up.

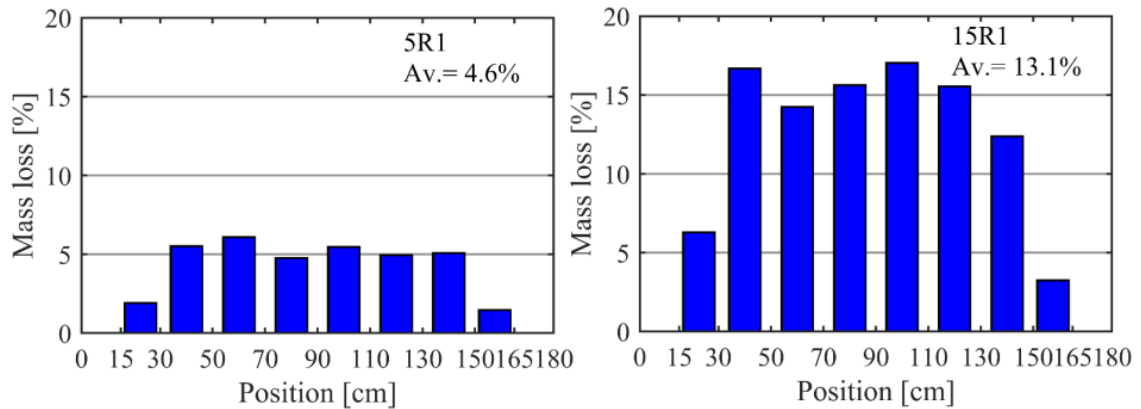


Fig. 3 Example of the measured mass loss variation along the rebar with the average (Av.) indicated.

2.3 Three-point bending

After the target corrosion level was reached, the beams were subjected to a three-point bending test. During the test, the deflection of the beams was recorded using two LVDT's at mid-span, placed opposite to each other, while the load applied was recorded using a load cell of 500 kN. The load was introduced at a load rate of 0.03 kN/s by means of a rectangular steel plate of 3 cm thickness and 15 cm x 7 cm contact surface placed at mid-span. Additionally, digital image correlation (DIC) was used to monitor the evolution of the bending cracks over an area of 90x20 cm. The load-deflection results are presented in [Fig. 4] which clearly show a reduction in the bending capacity upon an increase of the corrosion level. The cracking patterns, obtained from DIC [Fig. 4 right], show that the non-corroded samples developed closely spaced flexural cracks while those corroded developed a less number of cracks (2 or 3) which have wider spacing [Fig. 4-6]. These cracks propagated in an inclined manner and splitting cracks formed along the level of the rebar. The splitting cracks were more developed in the case of 5R1, 10R1 and 10R2 while 15R1 and 15R2 had limited propagation of the inclined cracks but developed wider vertical cracks.

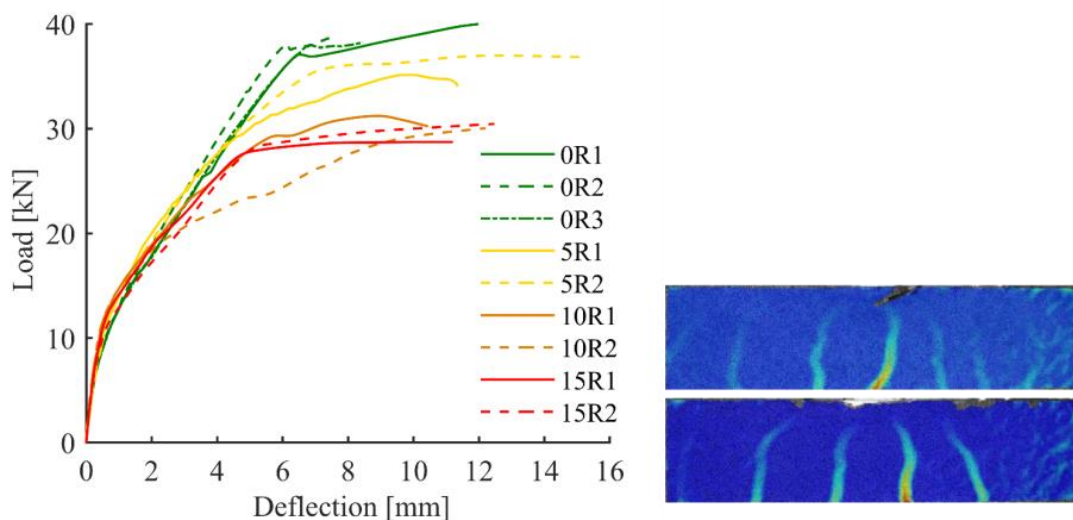


Fig. 4 [Left] Load deflection curves for the beams. [Right] DIC strain images of 0R2 (top) and 0R3 (bottom).



Fig. 5 Picture of cracks developed in the case of 5R1 (left) and 5R2 (right).

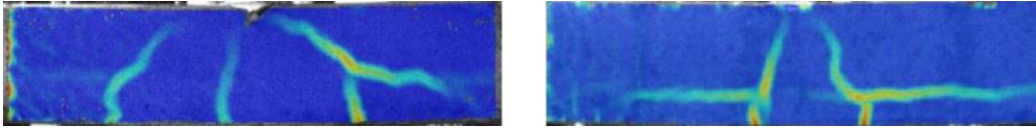


Fig. 6 DIC strain image of 10R1 (left) and 10R2 (right).

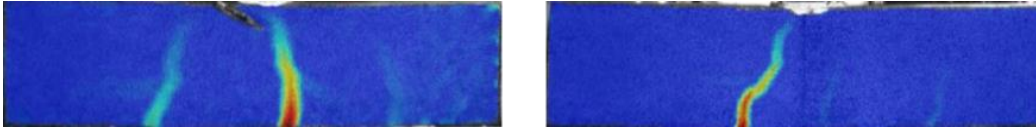


Fig. 7 DIC strain image of 15R1 (left) and 15R2 (right).

3 Numerical modelling of non-corroded beams

The finite element (FE) model is developed in the FE software DIANA. The model is built in 2D using 8-node plane-stress quadrilateral elements with a mesh size of 10 mm. A small load plate, as well as support plates, are modelled with elastic steel properties to simulate the loading and support conditions and prevent local stress concentrations. Moreover, a small region below the load plate is modelled using elastic concrete properties to prevent early prediction of concrete crushing.

3.1 Model parameters and settings

The concrete is modelled with tension softening according to Hordijk and parabolic softening in compression. The compressive strength is taken to be the average cylindrical strength calculated from the obtained cube strength while the lower bound characteristic uni-axial tensile strength is used, which is obtained from the flexural tests on prisms. The steel reinforcement was modelled as a bond-slip truss element with a bi-axial hardening curve. The yield strength is considered to be the average value of BE500 ($f_{ym}=550$ MPa) while the ultimate strength is taken as 25% higher ($f_{um}=688$ MPa). The bond-slip curve is defined as a multi-linear curve, based on average results of pull-out tests on non-corroded samples [Fig. 8]. These curves were fitted as the intersection of an initial power function, ascending polynomial (d^5 or d^6) and a descending polynomial branch (d^4 or d^5) after which the average of each part was calculated [Fig. 9]. Finally, because the test was load-controlled, a load-controlled quasi-newton (BFGS) procedure was implemented with load increments of 0.5 kN and convergence criteria according to the force (0.01) and energy (0.001) norms.

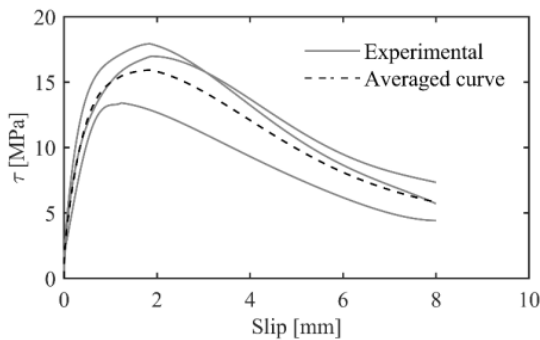


Fig. 8 Average bond-slip curve used as an input in DIANA.

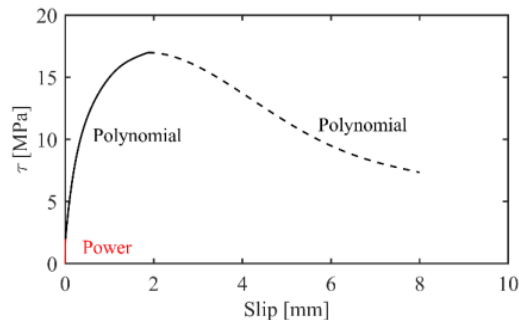


Fig. 9 Method to describe the experimental bond-slip curve by different functions.

3.2 Results

The results of the numerical analysis of the non-corroded samples show good agreement with the experimental load-deflection curves [Fig. 10]. The average experimental bending capacity is 37.6 kN while the numerical is 37.2 kN. Additionally, the cracking pattern in the case of a fixed crack model agrees with that observed experimentally [Fig. 12], while that of the rotating crack model shows the formation of a splitting crack and an exaggerated propagation of the inclined cracks [Fig. 11]. Because shear cracking in beams without stirrups is resisted by the concrete, the shear retention factor (β) in the

case of a fixed crack model plays the role of aggregate interlock, which stabilizes the propagation of the inclined cracks. Moreover, it was observed that a higher value of the shear retention factor changes the cracking pattern and increases the yield capacity since it tends to make the post-cracking concrete behaviour more ductile. The model yielded good agreements in terms of cracking and load capacity with $\beta=0.01$ and a tensile fracture energy $G_f=0.2 \text{ N/mm}^3$.

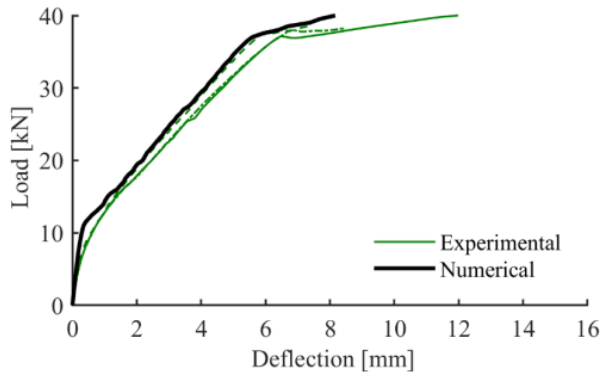


Fig. 10. Numerical and experimental load-deflection curves of the non-corroded beams.

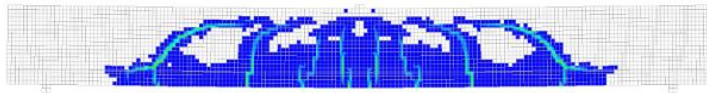


Fig. 11 Formation of splitting cracks in the case of a rotating crack model.

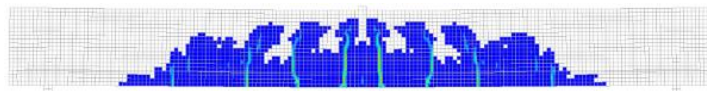


Fig. 12 Stable inclined cracks in the case of a fixed crack model ($\beta=0.01$).

4 A Numerical model for the corroded beams

After validating the behaviour of the non-corroded samples, the following section provides appropriate damage relations that are incorporated into the corroded beam models as a function of the measured corrosion level.

4.1 Damage relations

4.1.1 Concrete material properties

For the models of the corroded samples, the compressive strength at the age of the bending test was used while the uniaxial tensile strength at 28 days was used.

4.1.2 Cross-section loss

Cross-section loss due to pitting corrosion is modelled using the average section loss, called model 1, and the variable section loss, called model 2, as measured on the rebar segments [Fig. 3]. The yield strength and tensile strength of the rebar are linearly reduced while the ultimate strain follows an exponential reduction according to [12]. It has been observed that an overestimation occurs when disregarding the reduced material properties while the chosen reduction models provided good predictions. For both models, [Fig. 13], the initial stage shows similar stiffness while the post-crack localization phase shows a slight reduction for model 2. The crack pattern does not correspond well with the experiment since that of the models does not show the formation of splitting cracks [Fig. 14]. The cracking pattern of model 1 was similar to the non-corroded case. In the case of the variable section loss, model 2, the cracking pattern was slightly non-symmetric and showed that only one of the middle cracks widened.

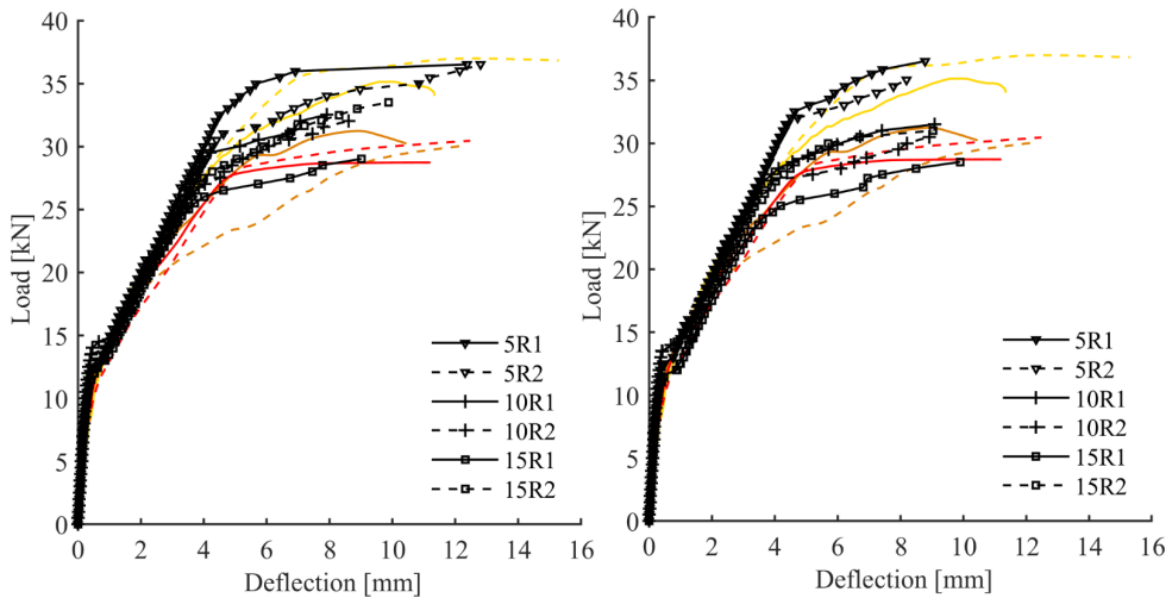


Fig. 13 Numerical load deflection curves of model 1 (left) and model 2 (right). [unmarked curves=experimental].

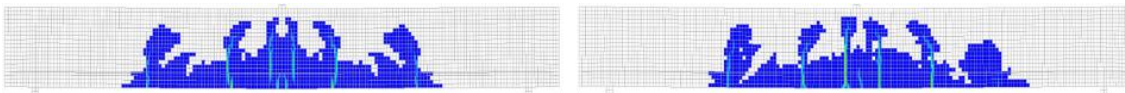


Fig. 14 Crack patterns of 10R1 in case of model 1 (left) and model 2 (right).

4.1.3 Bond deterioration [model 3]

Concrete cover cracking due to the pressure build-up of the rust causes a decrease in the bond strength in addition to shifting the failure mode from pull-out to splitting. Kagermanov et al. [10] showed that the effect of bond loss is secondary and associated with splitting mode of failure of the beams. For the present model, the residual bond strength (τ_r) is calculated as follows. (1) the amount of mass loss (ΔA) to cause surface cracking (A_{cr}) is calculated according to [13]. This is done because the beams have smaller cover compared to the prisms of the pull-out tests [11] and thereby they crack at a lower corrosion level. (2) Because the calculated period until cracking of 6 days is relatively short, it is assumed that no increase in bond strength is observed. (3) The bond degradation is assumed to follow a decreasing power law ($\tau = \alpha \Delta A^{-\gamma}$) with α and γ to be determined. (4) γ is calculated from the pull-out testing while α is calculated from point ($A_{cr}, 1$). For the present study, this results in the following equation: $\tau_r = 0.9 \Delta A^{-0.2}$ [Fig. 15]. Finally, the corroded bond-slip curve is assumed to ascend linearly on the non-corroded curve up to the calculated τ_r after which it decreases following $\tau = \alpha' s^{-0.6}$ [Fig. 16]; α' is calculated from point τ_r and its corresponding slip (denoted s) on the non-corroded curve.

After inputting the degraded bond-slip curves to model 1, the shear and normal stiffnesses of the bond-slip interface were adapted to the values given by the slope of the linear ascending part. The resulting load-deflection curves of model 3 are shown in Fig. 17. Slight changes in terms of stiffness along with a slight increase in the yield capacity can be observed. It is also noticed that the cracking pattern changes towards the formation of a single wide crack in the middle [Fig. 18]. Yet, formations of widely spaced cracks and splitting cracks were not noticed from adapting the bond-slip behaviour.

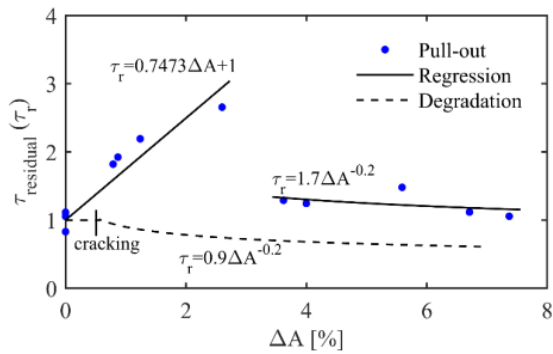


Fig. 15 Determining the residual bond strength based on [11].

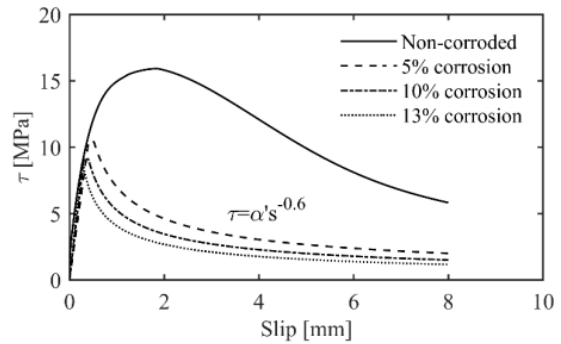


Fig. 16 Bond deterioration curves for $\gamma = -0.2$

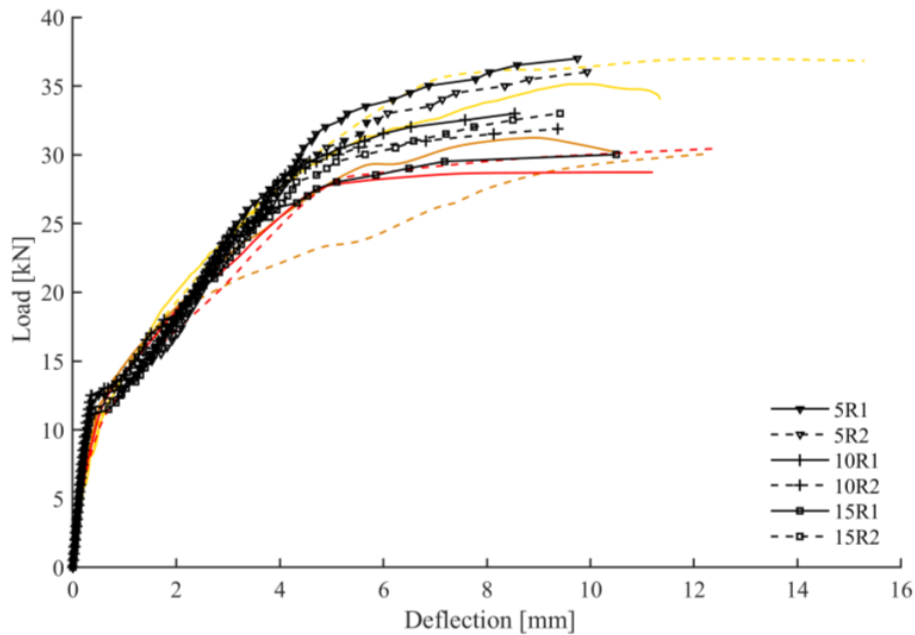


Fig. 17 Numerical and experimental load-deflection curves with average section loss and bond loss [model 3]. [unmarked curves=experimental]

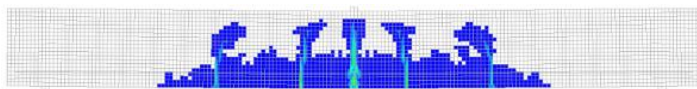


Fig. 18 The crack pattern of 10R1 in case of model 3.

4.1.4 Comparing the different models

The three modelling approaches show slight differences regarding the stiffness and the yield capacity with more difference regarding the crack pattern. But, considering the stochastic nature of the corrosion process and the cracking of the concrete cover, the three approaches seem to correctly fall within the range for each corrosion level (based on two samples for each level) [Fig. 19]. Moreover, the calibrated bond deterioration model affects the stiffness and the cracking pattern, yet it does not trigger the formation of splitting cracks as observed experimentally. The reason can be due to the rate of cracking which is more severe for the beams than the pull-out samples. Consequently, the degradation rate (γ) needs to be calibrated based on the level of cracking. Even though using damage relations related to the steel is seen to be sufficient to predict the structural capacity, calibrating a degraded bond-slip relation is important. It can probably assist in predicting the early formation of splitting cracks in the case of beams with insufficient shear resistance. Finally, it should be noted that the current research does not include local pit modelling, as no rebar rupture was observed in the experiments. Additionally, the simple bending setup and singly reinforced beams do only allow an initial evaluation of the numerical predictions, and more complex load conditions and rebar lay-outs are required for a detailed evaluation.

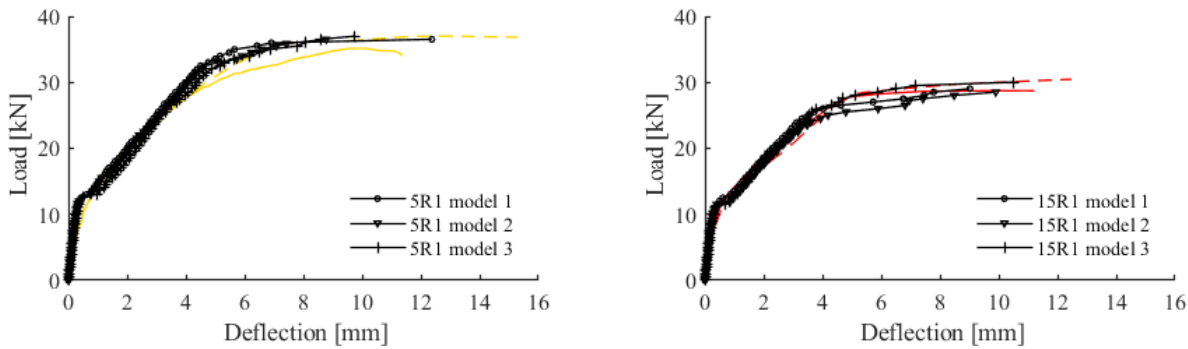


Fig. 19 Comparing the different models for the case of 5R1 and 15R1. [unmarked curves=experimental]

5 Conclusion

The paper presented a modelling approach for singly reinforced concrete beams validated on experimental results done by the author. The damage to the steel section can be taken as average uniform loss which should be coupled by an adequate damage law to account for the reduction in the rebar's tensile and ultimate strength and the ultimate strain. Considering the bond degradation by the approach presented provides bond deterioration curves as a function of the corrosion level. Yet, the change in the cracking pattern, as observed experimentally, was not reproduced by the bond loss model and it did not affect the ultimate capacity. Furthermore, while the current modelling approach yields good predictions, the shift in cracking can be investigated by studying its sensitivity to the reduction of the tensile strength of the cracked cover and higher degradation rates of the bond law. Finally, the sensitivity of the model to the variability in the cross-section loss can be further assessed using a smaller discretised length of the rebar, which is of importance for high corrosion levels where rebar rupture might occur.

6 References

- [1] Rodriguez, J., et al. 2006. Calculation of structural degradation due to corrosion of reinforcement. Springer
- [2] Val, D. and Melchers, R. 1997. "Reliability of Deteriorating RC Slab Bridges." *Journal of Structural Engineering* 123(12):1638-1644.
- [3] Kioumars, M., Marqueset, G. and Hooshmandi, S. 2017. "Effect of Pit Distance on Failure Probability of a Corroded RC Beam." *Procedia Engineering* 171(2017):526-533.
- [4] Coronelli, D. and Gambarova, P. 2004. "Structural Assessment of Corroded Reinforced Concrete Beams: Modeling Guidelines." *Journal of Structural Engineering* 130(8):1214-1224.
- [5] Nasser, H., et al. 2019. "Numerical modelling of corroded reinforced concrete beams based on visual inspection data." Paper presented at the Fifth SMAR Conference, Potsdam, Germany, August 27-29.
- [6] Rao, A. 2014. "Structural Deterioration and Time-Dependent Seismic Risk Analysis." Phd diss., Stanford University.
- [7] Saether, I. and Sand, B. 2012. "FEM simulation of Reinforced Concrete Beams attacked by corrosion." *ACI Structural Journal* 109(2):15-31.
- [8] Blomfors, M., et al. 2018. "Engineering bond model for corroded reinforcement." *Engineering Structures* 156(2014):394-410.
- [9] Rodriguez, J., Ortega, L. and Casal, J. 1997. "Load Carrying Capacity of Concrete Structures with Corroded Reinforcement." *Construction and Building Materials* 11(4):239-248.
- [10] Kagermanov, A. and Markovic, I. 2019. "FE-Modelling Techniques for Structural Capacity Assessment of Corroded Reinforced Concrete Structures." Paper presented at the Fifth SMAR Conference, Potsdam, Germany, August 27-29.
- [11] Van Steen, C., et al. 2019. "Assessing the bond behaviour of ribbed and smooth rebars with acoustic emission monitoring." *Cement and Concrete Research* 120(2019):176-186.
- [12] Imperatore, S., Rinaldi, Z. and Drago, C. 2017. "Degradation relationships for the mechanical properties of corroded steel rebars." *Construction and Building Materials* 148(2017):219-230.
- [13] Lundgren, K., et al. 2012. "Analytical model for the bond-slip behaviour of corroded ribbed reinforcement." *Structure and Infrastructure Engineering* 8(2):157-169.

Author Index

- Abu-Salma Deema, 216–223
Ajtayné Károlyfi Kitti, 288–295
Al-Kaimakchi Anwer, 165–172
Allam Hamza, 296–303
Amziane Sofiane, 296–303
Anthiniac Patrice, 246–253
Anton Ana, 40–47
- Baktheer Abedulgader, 134–141
Barylyak Bogdan, 179–186
Beddaa Hamza, 18–24
Ben-Fraj Amor, 18–24
Benmebarek Mohamed Amine, 86–93
Borowska Sylwia, 254–262
Bosnjak Josipa, 279–286
Botte Wouter, 200–207
Burtschell Yves, 296–303
- Camps Benjamin, 134–141
Caspeelee Robby, 200–207
Chudoba Rostislav, 134–141
Clerc Jean-Pierre, 296–303
Csanády Dániel, 10–17
- Dangla Patrick, 238–245
Das Arunita, 279–286
Davydenko Yurii, 2–9
Dillenburger Benjamin, 40–47
Ding Luchuan, 200–207
Djerbi Tegguer Assia, 238–245
Domingo Magi, 157–164
Dovzhenko Oksana, 63–69, 193–199
Drobotia Oleksandr, 173–178
Duc Myriam, 78–85
Duplan François, 296–303
- Elat Emmanuel, 78–85
- Fenyvesi Olivér, 10–17
Fernandez Pablo, 157–164
Fiorio Bruno, 55–62
Fladr Josef, 110–117
- Gallias Jean Louis, 55–62
Garnevičius Mantas, 33–39
Garrecht Harald, 118–124
Gauthier - Pouyanne Aliénor, 263–270
Gebhard Lukas, 40–47
Gelu Zaharia, 126–133
Glock Christian, 224–229
Gribniak Viktor, 33–39, 94–101
- Harkava Olha, 179–186
- Hasenko Anton, 173–178
Hausi Sorin Bogdan, 126–133
Hegger Josef, 134–141
Hilloulin Benoit, 263–270
Horb Oleksandr, 2–9
Horváth András, 288–295
- Ibrahim Sarah Khaleel, 208–215
- Karel Seps, 110–117
Kaufmann Walter, 40–47, 70–77
Kiesche Martin, 48–54
Kohoutkova Alena, 110–117
Kosior-Kazberuk Marta, 254–262
Kruse Heiner, 224–229
Kuznietsova Iryna, 63–69
- Lacombe Clement, 246–253
Lavergne Francis, 18–24
Lazik Piotr-Robert, 118–124
Lee Minu, 70–77
Lorenz Dirk, 102–109
Loukili Ahmed, 263–270
- Macorini Lorenzo, 216–223
Mari Antonio, 157–164
Mata-Falcón Jaime, 40–47, 70–77
Mbessa Michel, 78–85
Meftah Fekri, 271–278
Movahedi Rad Majid, 86–93, 208–215
Mytrofanov Pavlo, 2–9
- Nadim Abdel Nour, 149–156
Nasser Hussein, 312–319
Nemes Rita, 25–32
Noret Christine, 246–253
Noumowé Albert, 78–85
Nunes Sandra, 142–148
- Oller Eva, 157–164
Omikrine-Metalssi Othman, 238–245
Ovidiu Nechita, 126–133
- Pahn Prof. Dr.-Ing. Matthias, 48–54
Papp Ferenc, 288–295
Pavlikov Andrii, 179–186, 230–236

Pierre Alexandre, 78–85
Pimentel Mário, 142–148
Plioplys Linas, 33–39
Pliya Prosper, 78–85
Pohribnyi Volodymyr, 63–69, 193–199
Prosek Zdenek, 110–117
Prykhodko Yuliia, 230–236

Rambo-Roddenberry Michelle, 165–172
Rimkus Arvydas, 94–101
Rozière Emmanuel, 263–270

Scherer Thomas, 102–109
Schreiberova Hana, 110–117
Sellier Alain, 246–253
Semko Olexandr, 173–178
Sereng Marie, 238–245
Seyam Ahmed, 25–32
Sharma Akanshu, 279–286
Shihada Samir, 25–32
Shkurupii Oleksandr, 2–9
Sine Aurelio, 142–148
Sirobaba Vitalij, 173–178
Slama Anne-Claire, 55–62
Sokolov Aleksandr, 94–101
Spartali Homam, 134–141
Sultani Haji Akbar, 94–101

Thiele Catherina, 102–109, 224–229
Torrenti Jean-Michel, 18–24, 238–245
Torres Lluís, 94–101
Trtik Tomas, 110–117

Usenko Dmytro, 193–199
Usenko Iryna, 63–69

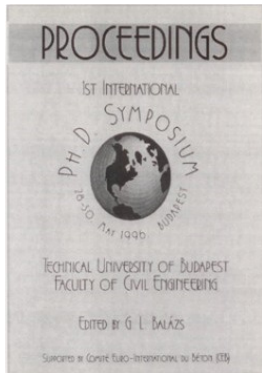
Valente Rui, 142–148
Van Coile Ruben, 200–207
Van Steen Charlotte, 312–319
Vandewalle Lucie, 312–319
Vasatko Radek, 187–192
Verstryngge Els, 312–319
Vidal Thierry, 246–253
Vollum Robert, 216–223
Vrijdaghs Rutger, 312–319

Walczak Rafał, 304–311

Xiong Qingxiang, 271–278

Zyma Oleksandr, 193–199

Previous *fib* International PhD Symposia

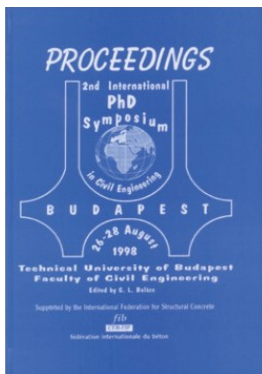


1st *fib* International PhD Symposium in Civil Engineering

May 1996, Technical University of Budapest, Budapest, Hungary

Order info:

Balazs, Gyorgy (Ed.)
Sokszorosította a Muegyetemi Kiado
Risograph technologiaival
Fedelos vezető: Veress Janos
Munkaszám: 96-Mk10
E-mail: fib@eik.bme.hu
ISBN 963 420 504 6

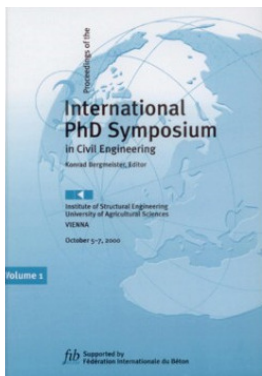


2nd *fib* International PhD Symposium in Civil Engineering

August 1998, Technical University of Budapest, Budapest, Hungary

Order info:

Balazs, Gyorgy (Ed.)
Publishing Company of Technical University of Budapest
Head: Janos Veress
Offset printing No: 98-0134
E-mail: fib@eik.bme.hu
ISBN 963 420 560 7



3rd *fib* International PhD Symposium in Civil Engineering

October 2000, University of Agricultural Sciences Vienna, Austria

Order info:

IKI - Institute for Structural Engineering
BOKU – University of Agricultural Sciences
Peter Jordanstr. 82, A-1190 Vienna, Austria
Phone: +43 1 47654 5250
Fax: +43 1 47654 5292
E-mail: lilo@iki.boku.ac.at
ISSN 1028-5334

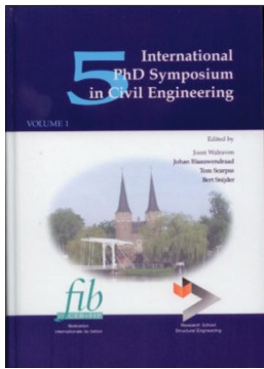


4th *fib* International PhD Symposium in Civil Engineering

September 2002, Technische Universität München
Universität der Bundeswehr München, München, Germany

Order info:

Springer-VDI-Verlag GmbH & Co. KG
Düsseldorf, Germany
ISBN 3-935065-09-4



5th fib International PhD Symposium in Civil Engineering

June 2004, Delft University of Technology, Delft, The Netherlands

Order info:

W. Sutjiadi
Faculty of Civil Engineering and Geosciences
Delft Univ. of Technology
Stevinweg 1, 2628 CN Delft, The Netherlands
Tel: +31 15 278 4665
Fax: +31 15 278 7313
E-mail: w.sutjiadi@ct.tudelft.nl
ISBN Vol 1: 90 5809 677 7
ISBN Vol 2: 90 5809 678 5



6th fib International PhD Symposium in Civil Engineering

August 2006, ETH Zurich, Zurich, Switzerland

Order info:

fib secretariat
Case Postale 88
CH-1015 Lausanne, Switzerland
Phone: + 41 21 693 2747
Fax: + 41 21 693 6245
E-mail: fib@epfl.ch



7th fib International PhD Symposium in Civil Engineering

September 2008, University of Stuttgart, Stuttgart, Germany

Order info:

PhD Symposium Secretariat
IWB Universitat Stuttgart
Pfaffenwaldring 4
70569 Stuttgart, Germany
Phone: +49 711 685 63320
Fax: +49 711 685 67681
E-mail: stumpp@iwb.uni-stuttgart.de

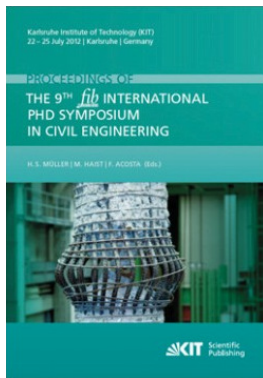


8th fib International PhD Symposium in Civil Engineering

June 2010, Technical University of Denmark, Kgs. Lyngby, Denmark

Order info:

Technical University of Denmark
Department of Civil Engineering, Brovej, Building 118
DK-2800 Kgs. Lyngby, Denmark
Phone: + 45 45 25 17 00
Fax: + 45 45 88 32 82
E-mail: byg@byg.dtu.dk



9th *fib* International PhD Symposium in Civil Engineering

July 2012, Karlsruhe Institute of Technology (KIT), Karlsruhe, Germany

Order info:

KIT Scientific Publishing
 Strasse am Forum 2
 D-76131 Karlsruhe
 Germany Phone: + 49 721 608 43104
 Fax: + 49 721 608 44886
 E-mail: info@ksp.kit.edu
 Available as download at: <http://www.ksp.kit.edu>

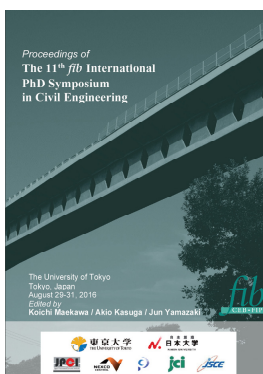


10th *fib* International PhD Symposium in Civil Engineering

July 2014, Universite Laval, Quebec, Canada

Order info:

Research Centre on Concrete Infrastructure (CRIB)
 Universite Laval
 Quebec (Quebec)
 Canada, G1V 0A6
 Phone: + 418-656-3303
 E-mail: josee.bastien@gci.ulaval.ca
 Available as download at: <https://www.fib-phd.ulaval.ca>

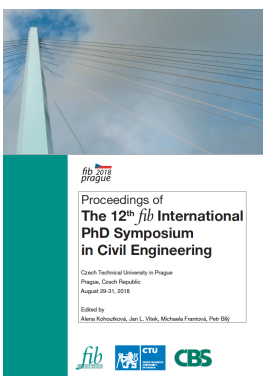


11th *fib* International PhD Symposium in Civil Engineering

August 2016, The University of Tokyo, Japan

Order info:

The University of Tokyo
 7-3-1 Hongo, Bunkyo-ku
 113-8656, Tokyo, Japan
 Phone: + 81-3-5841-6010
 E-mail: fib-phd2016@concrete.t.u-tokyo.ac.jp
 Available as download at:
http://concrete.t.u-tokyo.ac.jp/fib_PhD2016/
 ISBN 978 4 9909148 0 6



12th *fib* International PhD Symposium in Civil Engineering

August 2018, Czech Technical University in Prague, Czech Republic

Order info:

Czech Technical University in Prague
 Jugoslávských partyzánů 1580/3
 160 00 Prague 6 - Dejvice
 Czech Republic
 Available as download at:
www.fib-international.org/publications/fib-proceedings.html
 ISBN 978-80-01-06401-6

Proceedings of the 2020 session of the
13th *fib* International PhD Symposium in Civil Engineering
held in Paris, France,
August 26-28, 2020.

Edited by: Fabrice Gatuingt & Jean-Michel Torrenti

The *fib*, Fédération internationale du béton, is a not-for-profit association formed by 45 national member groups and approximately 1000 corporate and individual members. The *fib*'s mission is to develop at an international level the study of scientific and practical matters capable of advancing the technical, economic, aesthetic and environmental performance of concrete construction.

The *fib* was formed in 1998 by the merger of the Euro-International Committee for Concrete (the CEB) and the International Federation for Pre-stressing (the FIP). These predecessor organizations existed independently since 1953 and 1952, respectively.